CONF-9505204--
ORNL/FMP-95/1

U.S. Department of Energy
Fossil Energy
Advanced Research and Technology Development

Proceedings of the Ninth Annual Conference On Fossil Energy Materials

May 16-18, 1995
Oak Ridge, Tennessee

Fossil Energy AR&TD Materials Program

OAK RIDGE NATIONAL LABORATORY
MANAGED BY
LOCKHEED MARTIN ENERGY SYSTEMS, INC.
FOR THE
U.S. DEPARTMENT OF ENERGY
UNDER CONTRACT DE-AC05-84OR21400

Fossil Energy Program

CONF-9505204--
ORNL/FMP-95/1

U.S. Department of Energy
Fossil Energy
Advanced Research and Technology Development

Proceedings of the Ninth Annual Conference On Fossil Energy Materials

May 16-18, 1995
Oak Ridge, Tennessee

Fossil Energy AR&TD Materials Program

OAK RIDGE NATIONAL LABORATORY
MANAGED BY
LOCKHEED MARTIN ENERGY SYSTEMS, INC.
FOR THE
U.S. DEPARTMENT OF ENERGY
UNDER CONTRACT DE-AC05-84OR21400

Fossil Energy Program

CONF-9505204
ORNL/FMP-95/1

PROCEEDINGS OF THE NINTH ANNUAL CONFERENCE ON FOSSIL ENERGY MATERIALS

May 16-18, 1995
Oak Ridge, Tennessee

Compiled by
N. C. Cole and R. R. Judkins

Date Published: August 1995

Prepared by the
Department of Energy
Fossil Energy Office of Advanced Research
and
Oak Ridge Operations Office
AA 15 10 10 0

Prepared by the
OAK RIDGE NATIONAL LABORATORY
Oak Ridge, Tennessee 37831-6285
managed by
LOCKHEED MARTIN ENERGY SYSTEMS, INC.
for the
U.S. DEPARTMENT OF ENERGY
under Contract DE-AC05-84OR21400

PREFACE

The Ninth Annual Conference on Fossil Energy Materials was held in Oak Ridge, Tennessee, on May 16-18, 1995. The meeting was sponsored by the U.S. Department of Energy's (DOE) Office of Fossil Energy through the Advanced Research and Technology Development (AR&TD) Materials Program. The objective of the AR&TD Materials Program is to conduct research and development on materials for longer-term fossil energy applications as well as for generic needs of various fossil fuel technologies. The management of the program has been decentralized to the DOE Oak Ridge Operations Office with Oak Ridge National Laboratory (ORNL) as the technical support contractor. The research is performed by staff members at ORNL and by researchers at other national laboratories, universities, and in private industry. The work is divided into the following categories: (1) structural ceramics, (2) new alloys and coatings, (3) functional materials, and (4) technology assessment and transfer.

This conference is held each year to review the work on all of the projects of the Program. The final program for the meeting is given in Appendix A, and a list of attendees is presented in Appendix B.

These proceedings have been published from camera-ready masters supplied by the authors. All of the contributions have been checked for errors but have not been subjected to peer reviews. However, most of the papers have already undergone technical review within the individual organizations before submission to the Program Office.

The successful completion of the conference and publication of the proceedings has required help from several people. The organizers wish to thank Judy Fair for her superb coordination work; Gloria Donaldson for her assistance with preparations for the conference; Judy and Gloria for their excellent work at the registration desk; the ORNL Conference Office for their help in the many arrangements; and the numerous staff and support personnel associated with the conference. Finally, we express our sincere appreciation to the authors whose efforts are the very basis of the conference.

SESSION I - CERAMIC COMPOSITES

TABLE OF CONTENTS

SESSION II - CERAMICS AND NEW ALLOYS

OXIDATION-RESISTANT INTERFACIAL COATINGS FOR CONTINUOUS FIBER CERAMIC COMPOSITES

D. P. Stinton, T. M. Besmann and A. Bleier
Oak Ridge National Laboratory, Oak Ridge, TN 37831-6063

S. Shanmugham and P. K. Liaw
University of Tennessee, Knoxville, TN 37996-2200

ABSTRACT

Continuous fiber ceramic composites mechanical behavior are influenced by the bonding characteristics between the fiber and the matrix. Finite modeling studies suggest that a low-modulus interfacial coating material will be effective in reducing the residual thermal stresses that are generated upon cooling from processing temperatures. Nicalon^{TM}/SiC composites with carbon, alumina and mullite interfacial coatings were fabricated with the SiC matrix deposited using a forced-flow, thermal gradient chemical vapor infiltration process. Composites with mullite interfacial coatings exhibited considerable fiber pull-out even after oxidation and have potential as a composite system

INTRODUCTION

Continuous fiber ceramic composites (CFCCs) are being developed for high temperature structural applications, many of which are in oxidative environments.[1,2] Such composites are attractive since they are light-weight and possess the desired mechanical properties at elevated temperature and in aggressive environments. The most significant advantage is their toughness and their non-catastrophic failure behavior.[3,4]

The mechanical properties of CFCCs have been characteristically linked with the nature of the interfacial bond between the fibers and the matrix.[5,6] Weakly bonded fiber-matrix interfaces allow an impinging matrix crack to be deflected such that the fracture process occurs through several stages: Crack deflection, debonding at the interface, fiber slip and pull-out, and ultimately fiber failure.[7] Such a composite will fail in a graceful manner and exhibit substantial fracture toughness. Currently, carbon interface coatings

are used to appropriately tailor interface properties, however their poor oxidation resistance has required a search of an appropriate replacment.

Generally, metal oxides are inherently stable to oxidation and possess thermal expansion coefficients relatively close to those of Nicalon^{TM} (Ceramic Grade Nicalon, Nippon Carbon Company, Tokyo, Japan) nd SiC. However, the metal oxides must also be chemically compatible with the fiber and matrix. If the fiber/interface/matrix system is chemically compatible, then the interfacial bonding stress is influenced by the thermal residual stresses that are generated as the composite is cooled from processing to room temperature. In the current work, thermomechanical computational results were obtained from a finite element model (FEM) for calculating the thermal residual stresses.[8] This was followed by experimental evaluation of Nicalon^{TM}/SiC composites with carbon, alumina, and mullite interfacial coatings.

DISCUSSION OF CURRENT ACTIVITIES

Finite Element Modeling

A finite element model has been developed in order to understand the effect of interfacial coating materials on the profile of thermal residual stresses. The elementary cell comprises a fiber (radius =7 μm) surrounded by an interfacial coating, the matrix (radius = 11 μm) and the bulk material (Fig. 1). The bulk material is represented as having the average properties of the composite determined from the rule of mixtures. The fiber volume fraction is 40% and the interfacial and the matrix volume fraction varies with interfacial coating thickness.

The model is based on an axisymmetric system and the meshing was done with two dimensional elements (rectangular with eight nodes) in a plane. The boundary conditions are the following: 1. Displacement is permissible only along the axis of

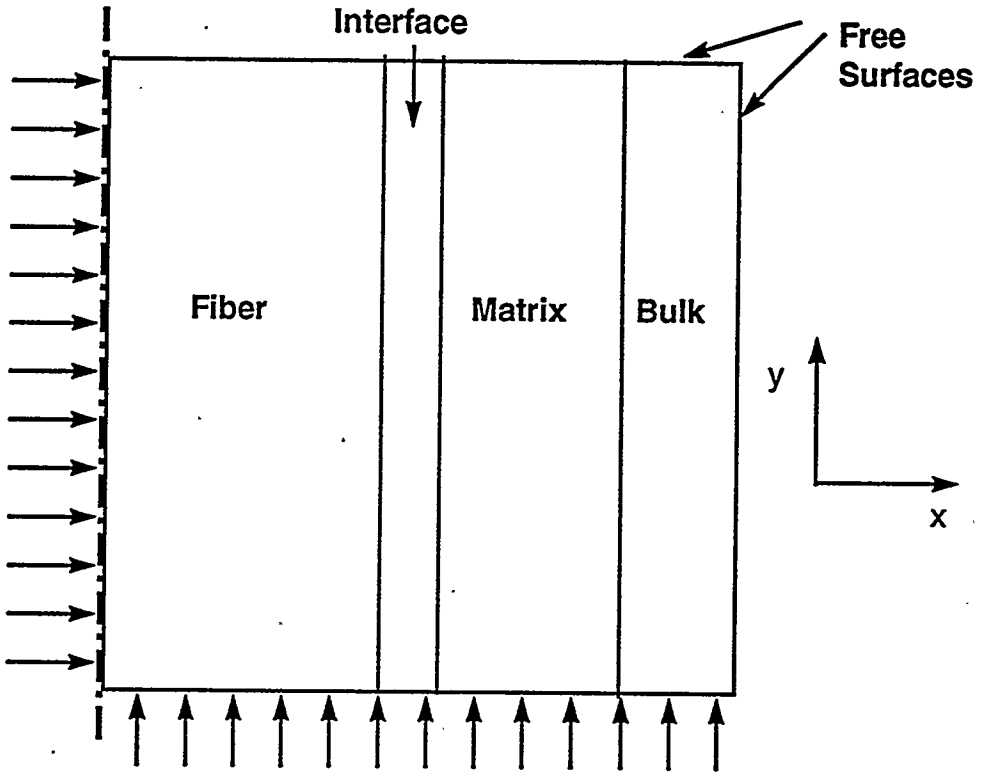

Fig. 1 Schematic of an elementary cell in the finite element model

symmetry, 2. the bottom of the cell can not be displaced in the direction of the axis of symmetry and the bulk cannot rotate around this axis and has its outer surface free, and 3. a temperature differential of 1175 K is assumed due to cooling from the maximum processing temperature of 1473 K.

A variety of potential interfacial coating materials (carbon, aluminum titanate, barium zirconium phospate silicate or BaZPS, alumina and mullite) which represent a wide range of mechanical properties (Young's modulus, coefficient of thermal expansion, and Poisson's ratio) were considered. The properties of Nicalon^{TM}, SiC matrix, and the interfacial coating materials are summarized in Table 1. The finite element model was used to compute the effect of carbon coating thickness on the radial thermal residual stresses (σ_x) at the fiber-coating interface and the coating-matrix interface (Fig. 2). The residual radi-

al stress for the fiber-matrix interface in the absence of any coating is based on Hsueh's[10] model. With a thin coating (0.1 μm), the residual radial stresses at both of the interfaces are compressive, although they become tensile with increasing coating thickness. The effect of alternative coating materials with a thickness of 0.5 μm on the radial stresses developed at the interfaces are shown in Fig. 3 and compared with that for 0.1 μm carbon.

Table 1. Material properties utilized in the FEM analysis [9]

Material	Young's modulus E (GPa)			Coefficient of thermal expansion ($\times 10^{-6}$/K)			Poisson's ratio v		
	E_x	E_y	E_z	α_x	α_y	α_z	υ_x	υ_y	υ_z
Nicalon	200	200	200	3	3	3	.12	.12	.12
SiC	350	350	350	4.6	4.6	4.6	.2	.2	.2
Carbon	12	40	40	28	2	2	.4	.12	.12
Alumina	380	380	380	8.3	8.3	8.3	.22	.22	.22
Mullite	220	220	220	5	5	5	.27	.27	.27
BaZPS with x=0.25	50	50	50	1	1	1	.2	.2	.2
Al_2TiO_5	11	11	11	1	1	1	.22	.22	.22

Based on the FEM results, among the three parameters, Young's modulus, coefficient of thermal expansion and Poisson's ratio, the Young's modulus plays a more

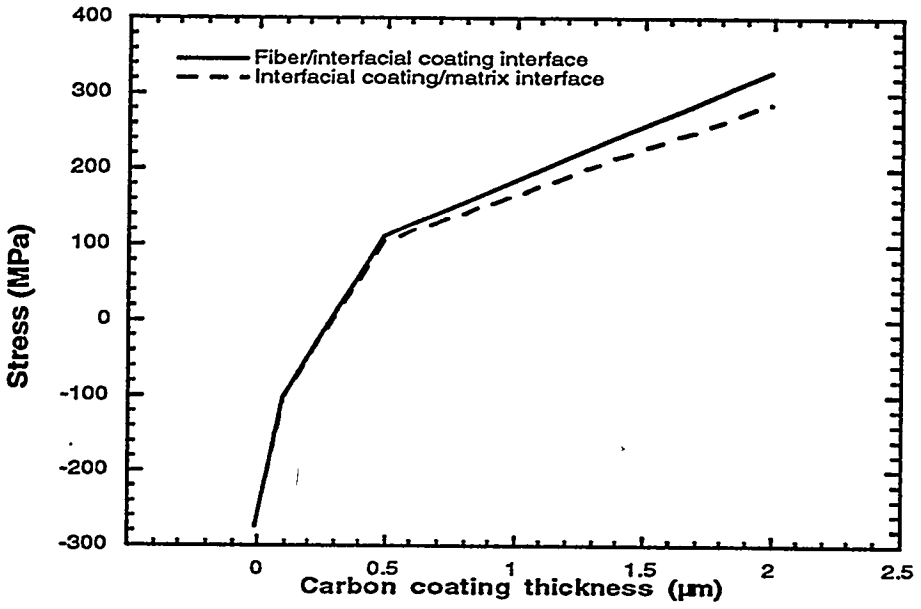

Fig. 2 Effect of carbon coating thickness on the calculated residual radial thermal stresses derived from the finite element model

dominant role. For example, as the modulus of the coating is decreased (e.g., from alumina to aluminum titanate) the difference in residual stresses that are generated at the fiber/interfacial coating and interfacial coating/matrix interfaces are reduced (Fig. 3). Further, the materials with low Young's modulus (e.g., aluminum titanate) cause a reduction in compressive thermal residual stresses similar to that for the 0.1 μm thick carbon coating.

Moreover, for interfacial materials with the same modulus, a material with a higher thermal expansion coefficient than that of the fiber and matrix is more effective in reducing radial stresses than is a material with a lower or similar thermal expansion. Trends similar to those reported here were observed with Hsueh's[10] model as well.

Experimental Results

Nicalon^{TM} (Ceramic Grade Nicalon, Nippon Carbon Company, Tokyo, Japan) fibrous preforms were prepared by stacking multiple layers of plain weave cloth in a 0±30

sequence within the cavity of a graphite holder. The preform was compressed by hand

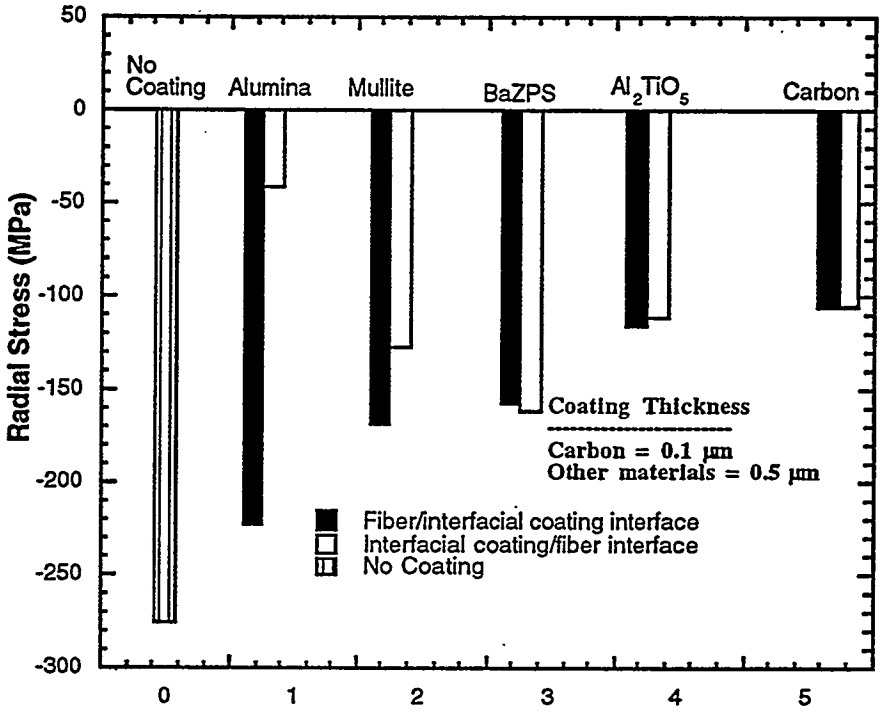

Fig. 3 Finite element computations indicate that low modulus interfacial coatings reduce compressive radial stresses

and held within the graphite holder with a graphite lid. The cloth sizing was removed by heat treatment at 973 K in argon for 2 h. The average fiber content of the resulting fiber preforms was 40 vol% with sample dimensions of 45 mm in diameter and 12.25 mm in thickness.

The carbon interfacial coating was deposited from a dilute argon/propylene mixture at 1373 K and 3 kPa pressure. The alumina (Grade RCHP-DBM, Reynolds Aluminum,) and mullite (Baikowski International Corporation, North Carolina) interfacial coatings were applied starting from powders using a novel colloidal process developed at Oak Ridge National Laboratory. Preforms with alumina and mullite interfacial coatings were then sintered in argon at 1373 K for 2 h.

The coated preforms were infiltrated with SiC matrix using the forced-flow, thermal-gradient chemical vapor infiltration (FCVI) process.[2] The SiC matrix was deposited from the decomposition of methyltrichlorosilane (MTS) in hydrogen. The process parameters are as follows: Hot surface temperature of 1473 K; MTS flow of 0.307 g/min; hydrogen flow of 500 cm^3/min; and exhaust pressure of 101 kPa. Typically, the matrix infiltration was completed within 20 hours.

The infiltrated Nicalon^{TM}/SiC composites were cut into twenty-four flexural bars of average size 2.5 x 3.0 x 40 mm. The dimensions of the cut flexural bars were measured and they were weighed to determine densities. Half of the flexure bars were then heat treated at 1273 K for 24 h in air to determine their oxidation behavior. The bars were loaded perpendicular to the layers of the cloth and the fracture surfaces were examined by scanning electron microscopy.

Fracture surface examination of composites with carbon interfacial coatings showed considerable fiber pull-out before oxidation (Fig. 4a). However, after oxidation they exhibited brittle fracture with very little fiber pull-out (Fig. 4b) due to the oxidation of the carbon interlayer and the subsequent formation of silica that bonded the fibers to the matrix.[5,11] The fracture surface of a composite with an alumina interfacial coating also showed very little fiber pull-out after oxidation (Fig. 5) and Langley et al.[12] reported that the tensile strength of Nicalon^{TM} fibers coated with alumina by plasma CVD were reduced by 30-40% compared to fibers similarly coated with carbon. The fiber damage was attributed to either chemical reaction or mechanical damage resulting from the thermal expansion mismatch between fiber and coating, or a combination of both. Walukas[13] observed that sol-gel derived alumina interfacial coating reacted with silica in the Nicalon^{TM} fiber during composite densification to form mullite. The fracture surface of the composite with a mullite interfacial coating, however, displayed considerable fiber

pull-out before and after oxidation (Fig. 6), however, the non-uniformity of the coating is a problem, and regions with considerable fiber-pull out are adjacent to regions of brittle fracture (Fig. 7). The accumulation of coating material around the fibers in certain areas also resulted in the lack of matrix in those areas. Preliminary thermodynamic calculations indicate that mullite coatings are likely to be stable with the Nicalon^{TM}/SiC system.

In order to overcome the non-uniformity problem a sol-gel approach is being pursued to deposit mullite coatings. Mullite sols with yield of the oxides ranging from 1-5% were used for coating Nicalon^{TM} fabric. The sizing on the Nicalon^{TM} was removed by heat treatment at 600°C for 1 h. The Nicalon was coated just after the removal of the sizing and pretreatment with methanol as well. The fabric was dipped into the mullite sol and dried either in air or in the presence of saturated methanol solution. Several combinations were tried and it was found that mullite sols with 1 wt% yield and dried in the presence of a saturated methanol atmosphere produced the best coatings. Figures 8a and 8b show the mullite coating on untreated Nicalon^{TM} fabric after 1 and 3 dips, respectively and dried in air. Figure 9 shows the mullite coating on a Nicalon fabric pretreated in alcohol and dried in the presence of a saturated methanol atmosphere. Coatings obtained under controlled drying conditions (Fig. 9) exhibited better uniformity than the coatings dried in air (Fig. 8).

Conclusions

FEM analysis revealed that a low modulus interfacial coating may be effective in reducing radial residual stresses that result from cooling from processing temperatures. Further, for the interfacial materials with the same modulus, a material with a higher thermal expansion coefficient than that of the fiber and matrix is more effective in reduc-

ing the radial stresses than is a material with a lower or similar thermal expansion coefficient.

Composites with carbon and alumina interfacial coatings exhibited brittle fracture after oxidation. However, a composite with a mullite interfacial coating retained considerable fiber pull-out, suggesting that it may be a desirable interfacial coating. Colloidal coating application, however, resulted in non-uniform mullite coatings. Potentially, the use of sol-gel methods may result in coatings with much better uniformity.

REFERENCES

1. N. Chawla, P. K. Liaw, E. Lara-Curzio, R. A. Lowden and M. K. Ferber, Symposium on "High Performance Composites," TMS, Warrendale, PA, K. K. Chawla, P. K. Liaw and S. G. Fishman, eds., 291, 1994.
2. T. M. Besmann, B. W. Sheldon, R. A. Lowden, and D. P. Stinton, Science, 253, 1104, 1991.
3. D. P. Stinton, A. J. Caputo, and R. A. Lowden, Am. Ceram. Soc. Bull., 65 (2), 347, 1986. 4. K. M. Prewo and J. J. Brennan, J. Mater. Sci., 15, 463, 1980.
5. A. G. Evans and D. B. Marshall, in Fiber Reinforced Ceramic Composites: Materials, Processing and Technology, ed. by K. S. Mazdiyasni, Noyes Publications, Park Ridge, NJ, 1, 1990.
6. D. B. Marshall and A. G. Evans, J. Amer. Ceram. Soc., 68 (5), 225, 1985.
7. R. W. Rice, Ceram. Eng. Sc. Proc., 2 (7-8), 661, 1981.
8. F. Rebillat, Unpublished work
9. Engineered Materials Handbook, Vol. 4, Ceramics and Glasses, ASM International, 1991.
10. C. H. Hsueh, P. F. Becher, and P. Angelini, J. Am. Ceram. Soc., 71 (11), 929, 1988.
11. B. A. Bender et al., Ceramic Eng. Sci. Proc., 5 (7-8), 614, 1984.
12. N. R. Langley et al., in Metal Matrix, Carbon and Ceramic matrix Composites,, ed. by J. D. Buckley, 1987.
13. D. M. Walukus, A Study of the Mechanical Properties and Oxidation Resistance of Nicalon-SiC composites With Sol-Gel-Derived Oxide Interfacial Coatings, M. S. Thesis, University of Tennessee, May 1993.

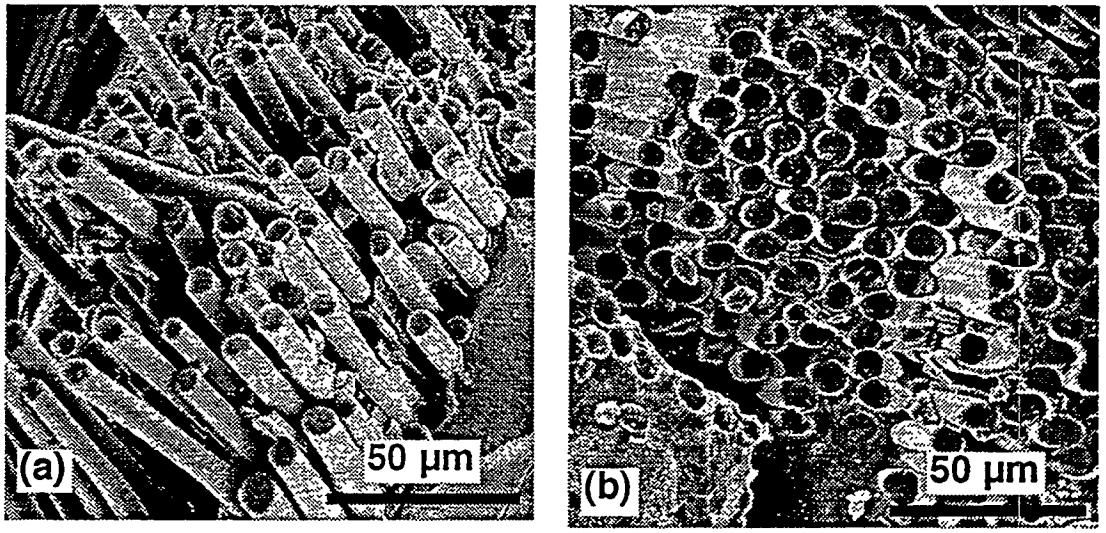

Fig. 4 Fracture surface of a composite with carbon interfacial coating
(a) before oxidation and (b) after oxidation in air for 24 h at 1273 K

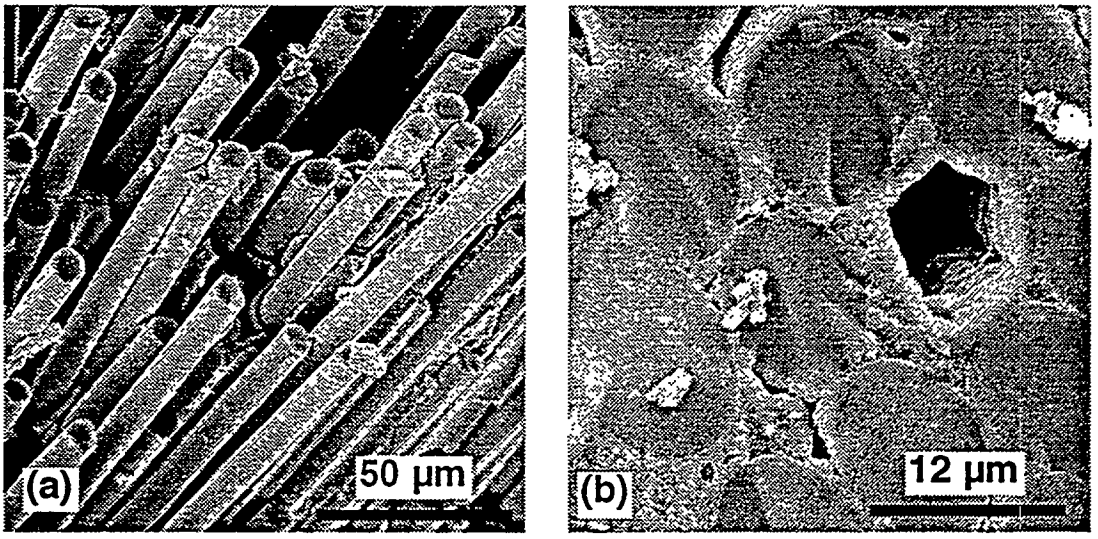

Fig. 5 Fracture surface of a composite with an alumina interfacial coating
(a) before oxidation and (b) after oxidation in air for 24 h at 1273 K

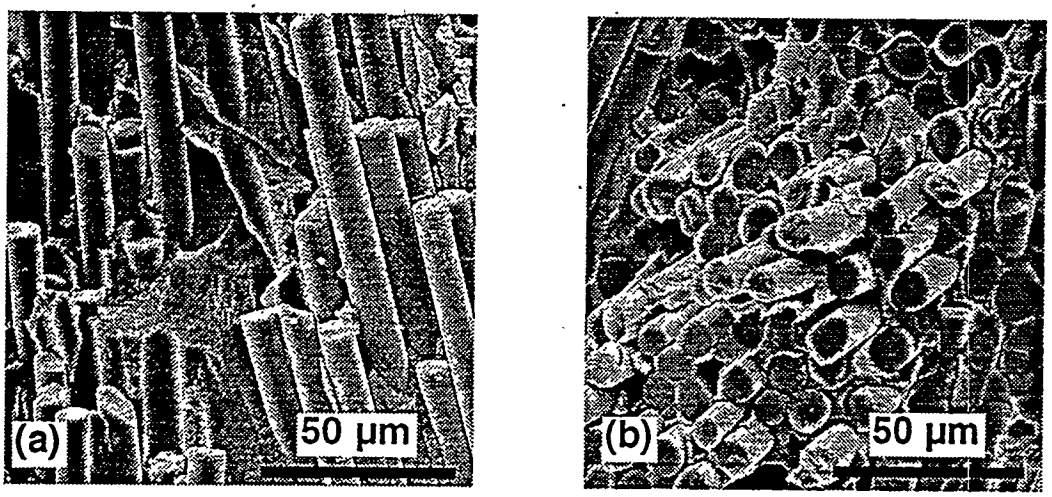

Fig. 6 Fracture surface of a composite with a mullite interfacial coating (a) before oxidation and (b) after oxidation in air for 24 h at 1273 K

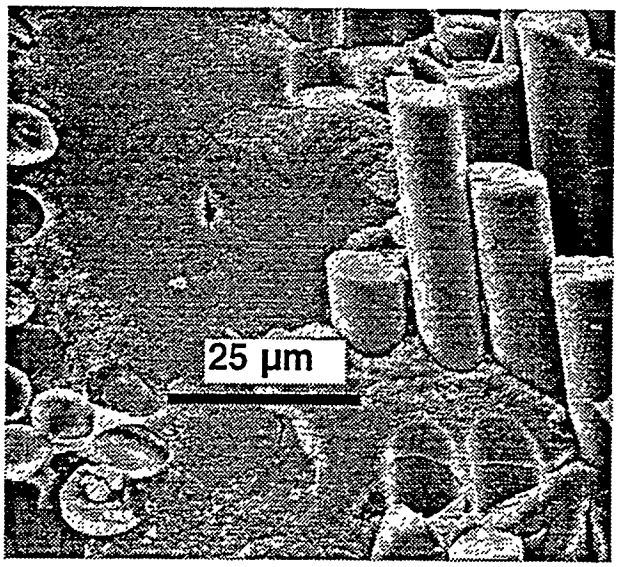

Fig. 7 Non-uniformity of the mullite interfacial coating resulted in fiber pull-out in certain regions and brittle fracture in other areas

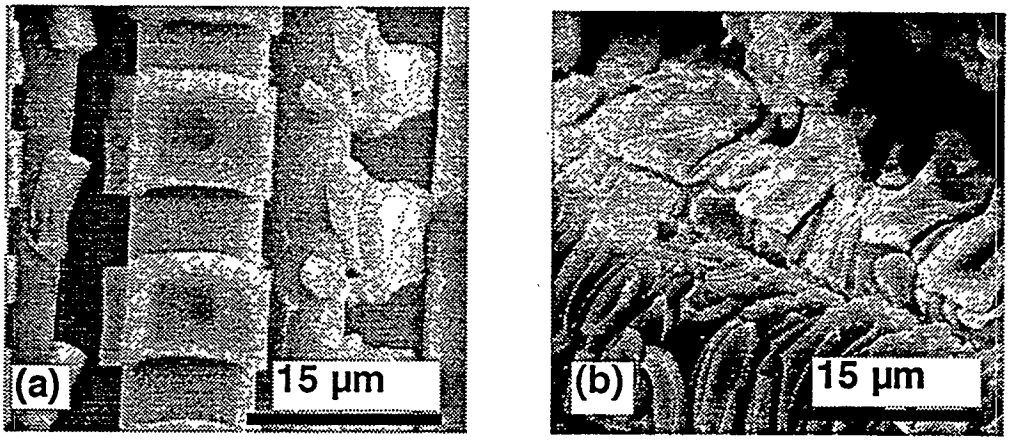

Fig. 8 Mullite coating on the untreated Nicalon fabric (a) after 1 dip and (b) after 3 dips

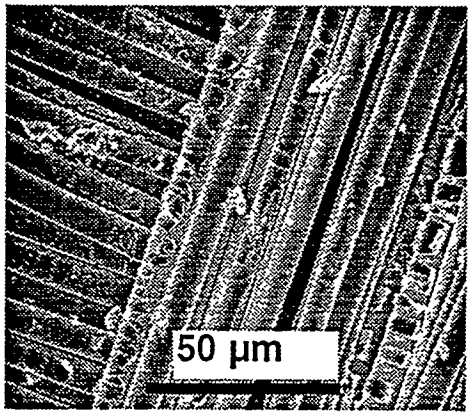

Fig.9 Mullite coating on Nicalon fabric after pretreatment with methanol and dried in the presence of a saturated methanol atmosphere

MODELING OF FIBROUS PREFORMS FOR CVI FABRICATION

T.L. Starr and D.Y. Chiang

School of Materials Science and Engineering
Georgia Institute of Technology
Atlanta, Georgia 30332-0245

This program involves modeling the chemical vapor infiltration (CVI) of tube shapes in support of experimental process development at Oak Ridge National Laboratory (ORNL). The previously developed tube model, including radiative heat transfer, has been modified to match the new, larger reactor at ORNL. For infiltrating tubes 4" OD and 12-18" L, higher reactant flow rate is needed for rapid densification.

Two new processing schemes are being investigated. In the first, the processing parameters - temperature, flow rate, etc. - are varied through the run in order to maintain optimum densification performance. In the second, processing conditions near the end of the run are adjusted to close residual porosity and to produce a gas-tight tube. For each of these, model runs will identify process schedules prior to experimental runs at ORNL.

INTRODUCTION

Chemical vapor infiltration is an effective method for fabrication of tube shapes for fossil energy applications. Equipment design and process conditions are significantly different than for disk-shaped components fabricated previously. A new, larger tube infiltration system has been installed at ORNL. Our previously developed process model is being modified to match this new reactor. Initial model runs have focused on the temperature profile in the system and its effect on infiltration performance. In the future, the model will be used to identify variable condition runs for reduction of densification time and hybrid processing for production of gas-tight tubes.

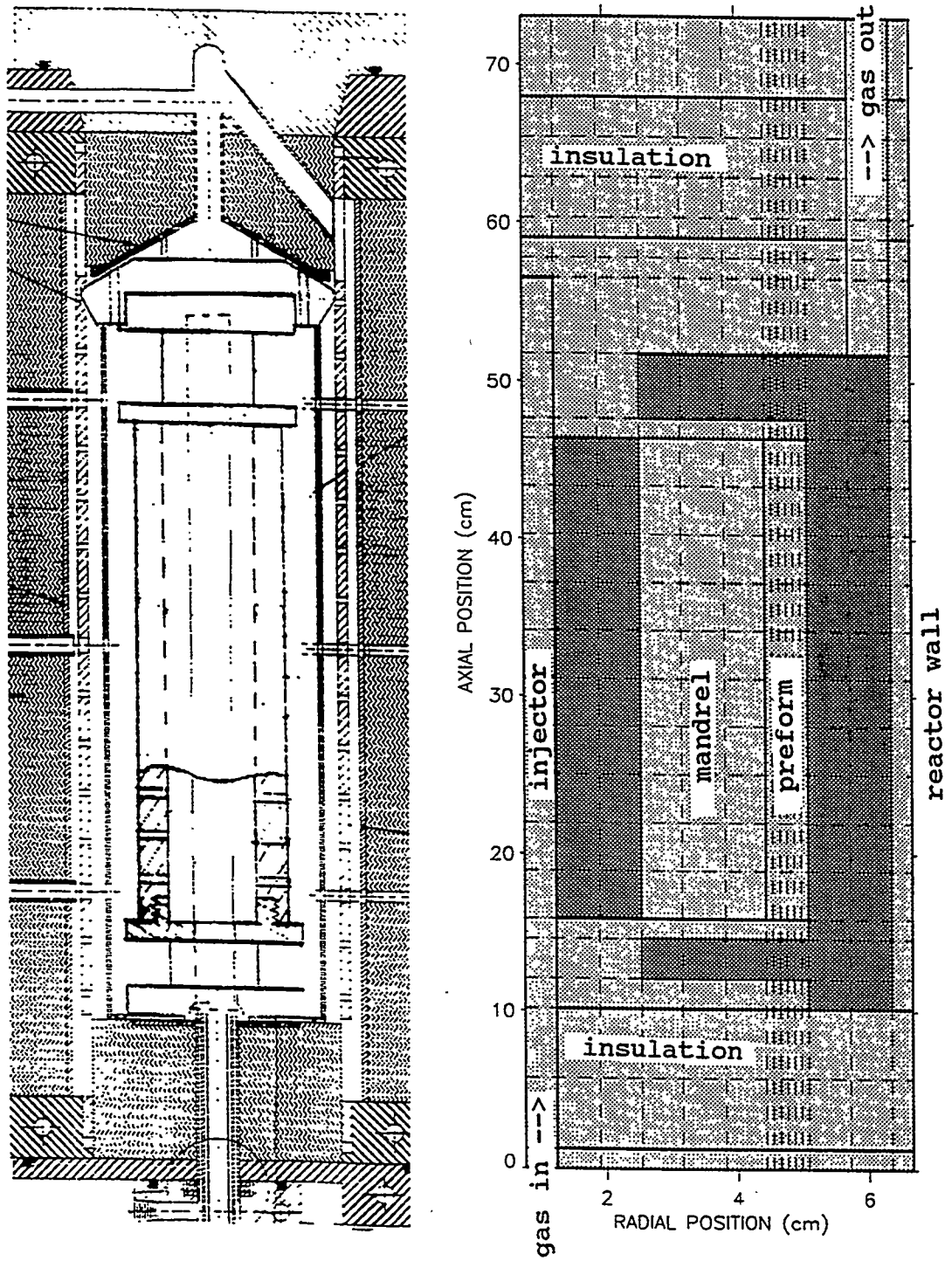

Figure 1. The new tube CVI system at Oak Ridge National Laboratory (left) is modeled using a 15x26 volume element grid (right). (Note that the radial and axial scales are different.)

as our model predictions are compared to actual temperature profiles measured at ORNL.

Table I. Thermal conductivity for materials in ORNL tube infiltration system.

MATERIAL	LOCATION	THERMAL CONDUCTIVITY (W/cmK)
graphite H451	Mandrel, endcap	$73.7xT^{-2/3}$ (0.87@500°C)
aluminum	furnace enclosure	2.3
carbon-carbon composite	reactor wall	$73.7xT^{-2/3}$ (0.87@500°C)
carbon fiber insulation	ends of reactor	$7.37xT^{-2/3}$ (0.087@500°C)
stainless steel	gas injector	0.30
Nicalon fiber cloth layup	preform - radial - axial	.00708/(1.012-ρ) .0539/(1.077-ρ) ρ=fraction dense

Using these values the CVI model predicts the temperature profile shown in Figure 2 for a reactor wall temperature of 1300°C. The ends of the preform are significantly cooler than the center of the tube. In the end regions there is good thermal contact to the cool injector through the high thermal conductivity H451 graphite. In the tube middle the thermal contact relies on radiation across the gas space which is inefficient at the temperature involved.

The temperature profile through the preform is plotted in Figure 3 for three different wall temperatures and for the middle and ends of the tube. Overall the temperature difference between the cool and hot side of the preform is in the range 300-450°C. The cool side temperature at the tube end nearest the gas inlet is approximately 170°C lower than in the middle, while the other end of the tube is 150°C cooler than the

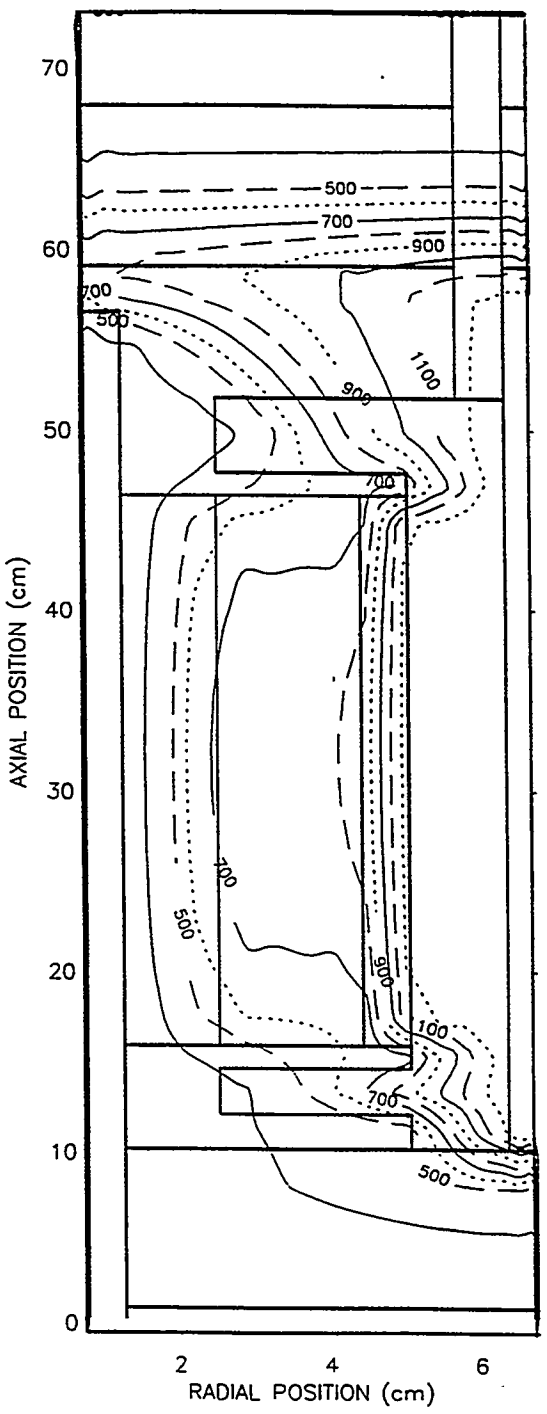

Figure 2. Model predicts the above temperature profile for a reactor wall temperature of 1300°C. Ends of preform are significantly cooler than the middle.

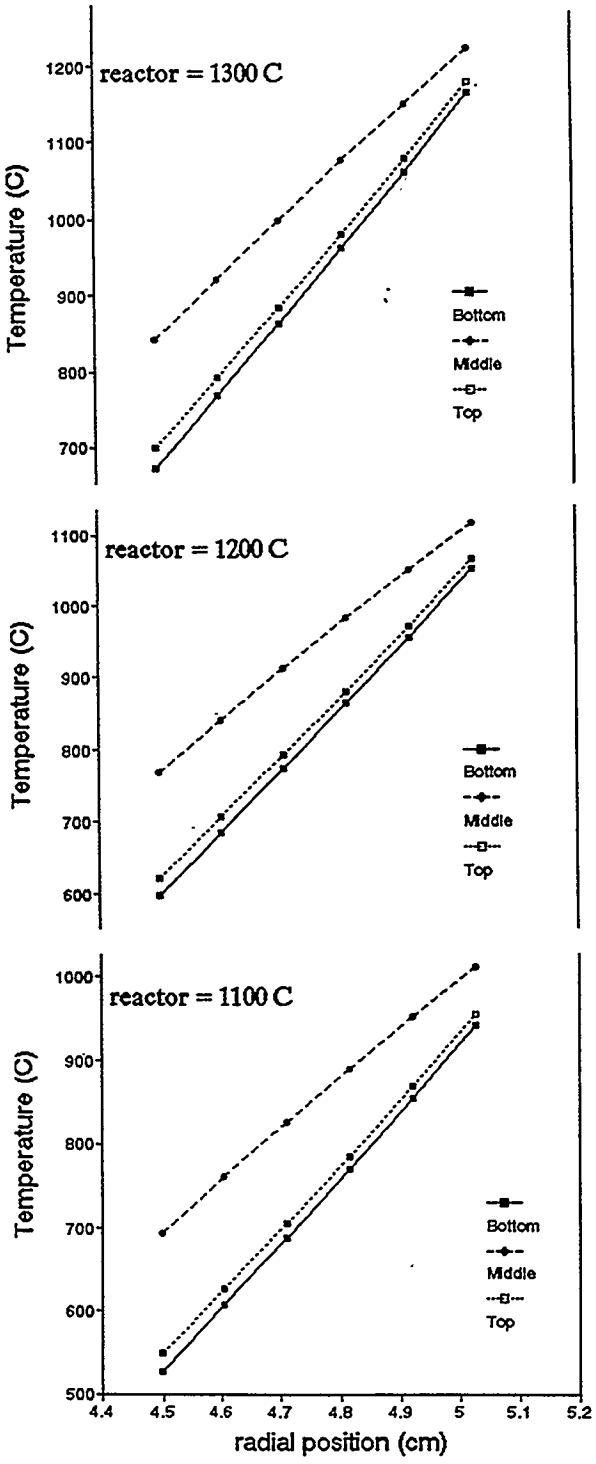

Figure 3. Temperature profile through preform depends on reactor wall temperature and on position along tube length.

middle. This suggests that densification may be significantly slower in these regions although the gas flow pattern also will influence densification behavior.

PROCESS OPTIMIZATION

Once the model is verified by comparison to experimental results, it will be used to "optimize" the tube densification process. This optimization has two objectives: reduce the processing time and produce gas-tight tubes. Achieving these goals will require two distinct approaches.

Optimized processing conditions for reduced process time will involve adjustment of the furnace temperature, reactant concentration, and gas flow rates throughout the run according to the changing physical properties of the preform. Processing using these variable conditions is expected to result in significantly reduced infiltration times as compared to current practice where process conditions are held constant for the duration of the run. In particular, we have seen previously that the preform temperature drops during a run as the composite becomes denser, with a higher thermal conductivity, and provides better thermal contact to the cool injector. We will devise an increasing reactor temperature schedule to counteract this effect and maintain the preform at the highest temperature consistent with fiber stability and uniform densification.

Secondly, we plan to reduce the overall gas flow rate near the end of the run as the composite becomes less permeable. This will allow continued infiltration for some period of time beyond the normal process endpoint.

While this optimized processing will produce tubes with less than 10% porosity, "hybrid" processing techniques will be identified that utilize diffusion-driven CVI to further reduce permeability. At the point where forced flow can no longer be maintained, the process will be adjusted to allow diffusion of reagent from the cool side into the preform. This one-sided infiltration is capable of producing true, gas-

tight materials. The model will be used to identify suitable conditions for this process.

SUMMARY

Initial modeling of the new ORNL tube infiltration system has been completed. Comparison of model predictions with experimental temperature profile and densification performance will be made.

The verified process model will be used to identify process conditions for reduction of densification time and for production of gas-tight tubes.

REFERENCES

1. T.L. Starr and A.W. Smith, "Modeling of Forced Flow/Thermal Gradient Chemical Vapor Infiltration", Oak Ridge National Laboratory Report ORNL/sub/85-55901/03 (September 1993).

ENGINEERING SCALE DEVELOPMENT OF THE VAPOR-LIQUID-SOLID (VLS) PROCESS FOR THE PRODUCTION OF SILICON CARBIDE FIBRILS AND LINEAR FIBRIL ASSEMBLIES

Michael Tenhover and Joseph Biernacki

The Carborundum Company
Technology Division, P.O. Box 832
Niagara Falls, NY 14320

Kathleen Schatz and Frank Ko

Advanced Product Development, Inc.
2500 Pearl Buck Road
Bristol, PA 19007

ABSTRACT

In order to exploit the superior thermomechanical properties of the VLS fibril, the feasibility of scaled-up production of the SiC fibril is demonstrated in this study. Through time series study and computer simulation, the parameters affecting the growth process and properties of the fibrils were examined. To facilitate translation of the superior mechanical properties into higher level preform structures, conventional and unconventional processing methods were evaluated. As revealed by scanning electron microscopic examination and X-ray diffractometry, high level alignment of the fibrils was achieved by the wet-laid process.

INTRODUCTION

The development of high-temperature ceramic composite reinforcement materials is critical for the continued development of fracture-resistant, high-temperature ceramic composite materials for high-temperature applications in DOE Fossil Energy programs. The VLS SiC fibrils, being single-crystal SiC, have unmatched high-temperature tensile strength, modulus, and creep resistance compared to other ceramic composite reinforcement materials. The SiC fibrils could be a critical, enabling reinforcement for DOE Fossil Energy program applications requiring high-temperature (>2400°F) ceramic composite materials.

In order to develop a reliable supply source for the VLS SiC fibril, the feasibility of scale-up of the VLS process for producing SiC fibrils was examined through time series growth experiments and a computer simulation model. Laboratory scale post processing methods have been developed to facilitate fibril harvesting and beneficiation of medium and short length fibrils as well as reducing the undesirable small diameter fibrils.

In order to maximize the translation of fibril properties to the composite and facilitate the ceramic composite manufacturing process conventional and unconventional textile fiber processing methods were evaluated for the processing of the fibrils. It was concluded that a fluid-based (wet)

process will provide the most gentle media for the dispersion, alignment, and integration of the fibrils. A manual batch process was established to produce linear fibrous assemblies through dispersion and subsequent alignment of the fibrils by fluid flow. The inter-fibril cohesion was provided both by the use of chemical binders and different auxiliary sheath techniques. As illustrated by SEM observations and X-ray diffractometry, a high level of fibril alignment was achieved by the wet process. These aligned fibril linear assemblies will be fabricated into a ceramic matrix composite by the CVI process for preliminary characterization of the properties of the ceramic composite system.

THE VLS SiC FIBRIL GROWTH PROCESS

The chemistry of the VLS process for producing SiC fibrils has been described elsewhere. [1,2] The Carborundum development reactor incorporates many features of the Los Alamos National Laboratory (LANL) reactor design.[2,3] Figure 1 shows the reactor design concept. The critical difference between the Carborundum and LANL reactor is its vertical dimension. The Carborundum reactor is 30.5 cm high (two times the height of the LANL reactor), which allows for the determination of critical scale-up parameters in the vertical dimension. It was expected that vertical scale-up of the process would produce the highest risk in increasing the reactor dimensions, and subsequent process development experiments have confirmed this assumption.[4]

Carborundum has explored the key process factors in the macroscopic growth process and has identified the effect of critical process and scale-up parameters. Delivery of both SiO and CH_4 control the fibril growth rate. The SiO and CH_4 concentration profiles exhibit different behavior as a function of reactor position, resulting in a continuous variation in the chemical conditions in the reactor. Despite this continuous variation, acceptable fibril morphologies can be grown throughout the reactor height. (Figure 1.)

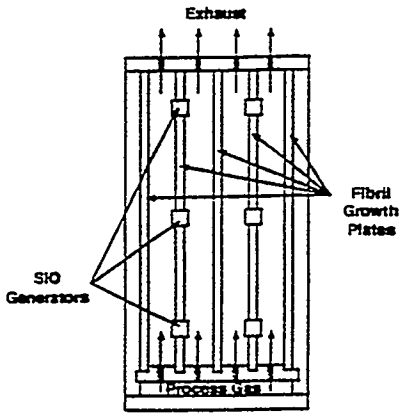

Figure 1. Carborundum development reactor.

Kinetic data obtained in development experiments have been incorporated in a simulation model. Three reactions control the fibril growth process -- SiO supply, CH_4 decomposition and the SiC fibril formation reaction. Taken together, these reactions interact to produce varying growth rates at different process conditions. The simulation model can predict critical trends in the SiO generation. CH_4 delivery and SiC fibril formation using kinetic constants derived from experimental data. Figure 2 shows the effect of processing condition on fibril growth rate profile.

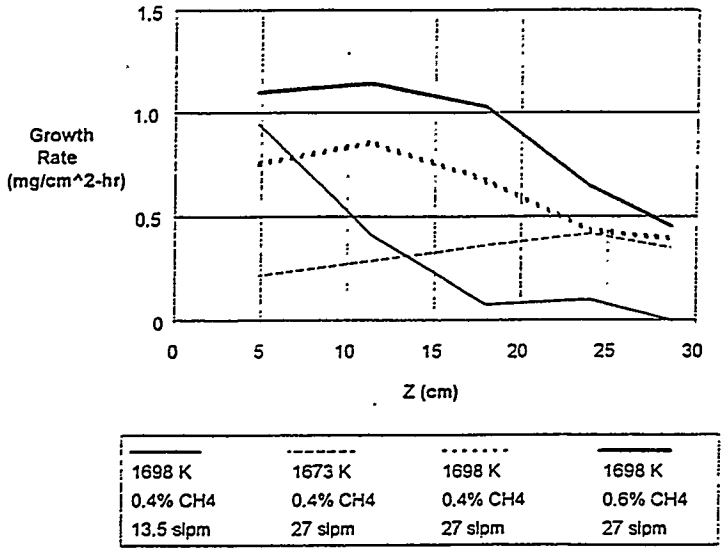

Figure 2. Effect of synthesis process conditions on fibril growth rate profiles.

Both the fibril post-processing and process gas recycle portions of the process are important to the viability of the process. Harvesting/beneficiation has focused on identifying process steps to remove residual catalyst and product beneficiation to remove undesirable by-products. The beneficiation step needs to be tied to the desired fibril product characteristics, since this process step can modify the product characteristics.

PROPERTIES OF SiC FIBRILS

VLS SiC fibrils have a number of attractive properties, which are the result of their single crystal structure. Table 1 summarizes different areas of fibril characterization and highlights some of the attractive features of the VLS SiC fibril.

Characteristic	Examples	Attractive Fibril Features
Physical	Morphology Length Diameter	Single crystal B-SiC Length: to 7 cm Diameter: 5 - 10 μm
Chemical	Bulk Chemistry Trace impurities	High purity
Mechanical	Tensile strength	Tensile strength ≥ 6 GPa
Thermal	Creep resistance Oxidation resistance	Creep resistance better than other SiC reinforcements

Table 1. Important areas of VLS SiC fibril characterization and attractive fibril features.

Diameter Analysis

Fibril diameter has important ramifications on the commercial viability of the VLS SiC fibril process. The diameter and its distribution may affect composite performance. The potential health hazard associated with fine diameter fibrils is a concern. This has promoted efforts to improve control of the product diameter. To guide these efforts, a quantitative measurement technique based on optical microscopy combined with automated image analysis was used.

This technique involves the preparation of a dilute sample of shortened fibrils on an optical microscope slide. The slide was scanned across the viewing area at a magnification of 1250x and 100 diameter data points were accumulated. The diameter was measured using image analysis software and the diameter distribution was calculated by this software.

MECHANICAL PROPERTIES OF VLS SIC FIBRILS

The attractiveness of VLS SiC fibrils can be attributed to their high strength and unmatched thermal resistance, which results from the single crystal structure of the fibrils. VLS SiC fibril mechanical properties have been reported in other studies. [5,6] These results are summarized in Table 2.

Property	Measured By	Result
Tensile strength	Single fiber tensile testing - LANL [7]	8.5 GPa (1200 ksi)
Elastic modulus	Single fiber tensile testing - LANL [7]	580 GPa (85000 ksi)
Creep resistance	Bend stress relaxation - NASA-LRC [2]	m = 1 @ 1673 K for 1 hour

Table 2. Mechanical and thermal resistance properties of VLS SiC fibrils from the literature.

To avoid potential inaccuracies associated with this methodology, Carborundum is evaluating the feasibility of using single fiber composite testing (SFC) techniques to evaluate the fibrils strength. [7] This technique has been used to obtain useful strength data of materials down to very small gauge lengths without the potential artifacts introduced by the single fiber tensile testing technique. [8] The test involves imbedding a single fibril in an epoxy matrix and stressing the matrix. By measuring the number and location of the fibril breaks as a function of the stress on the sample, the fibril strength and the statistical analysis of the strength can be obtained. This preliminary work has been performed by Anil Netravali at Cornell University. The preliminary tests indicated fibril strengths of 6 - 9 GPa at a 2.54 cm gauge length, with a Weibull modulus of 3 - 3.5.

Another attractive property of the VLS SiC fibril is its unmatched creep resistance relative to other SiC reinforcements. An article describing a simple technique of measuring creep resistance and it application to the evaluation of fiber reinforcements has been published. [5] In testing at temperatures of 1673 K for 1 hour, the VLS SiC fibril exhibited the highest degree of creep resistance relative to any other SiC reinforcement. No creep was noted, leading to an m value of 1.

DEVELOPMENT OF LINEAR FIBRIL ASSEMBLIES

Preform fiber architecture has been demonstrated to play an important role in facilitating the processing and enhancing the toughness of ceramic matrix composites.[9] In order to exploit fully the superior strength, modulus and thermal stability of the SiC fibril produced by Carborundum considerable effort has been devoted in the industry to convert the fibrils to linear fibrous assemblies. [9,10] As illustrated in Figure 3 plotting critical fiber diameter as a function of tensile modulus, the SiC fibril (which has a modulus of approximately 600 GPa and diameter of 5 ± 3 μm) is on the fringe of being processable as a textile fiber because its fine diameter could compensate for its high modulus.

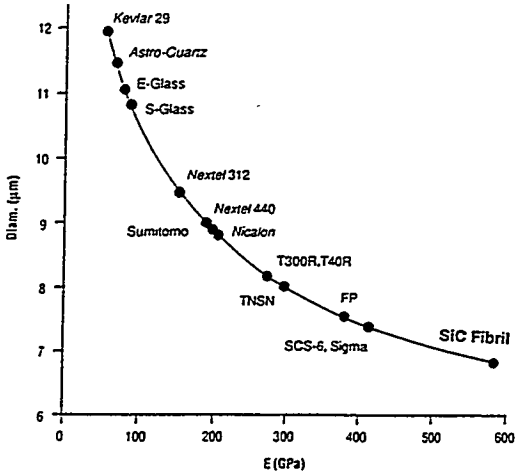

Figure 3. Critical fiber diameter for successful textile processing.

In order to assess the feasibility of converting the SiC fibril to fibrous assemblies, the key technical issues in the processing of SiC fibrils were examined. It was identified that, similar to conventional textile yarn processing, dispersion, alignment and integration of the fibril assemblies are the essential ingredients for the successful conversion of the fibril to a textile-like linear fibrous assembly. In this program, the feasibility of the conventional textile yarn processes were first examined followed by an evaluation of alternate unconventional processes. A summary of the operations corresponding to the conventional and unconventional processing methods is shown in Table 3.

	Conventional Textile Processing	Adhesive Tape Processing	Wet-Laid Processing
1) Separation	Opening, Carding	Aligning on growth Plate	Dispersion in liquid medium
2) Alignment	Carding	Aligning on growth Plate	Alignment in flow of dispersion medium
3) Attenuation or other control of linear density of fibrils	Drafting	None; Dependent on fibril growth density and length	Accumulation
4) Integration	Spinning Twist insertion or Fiber entanglement	Adhesive Tape Application	Binder and auxiliary tape substrate

Table 3. Basic processing steps in conventional and unconventional methods.

CONVENTIONAL PROCESSES

The conventional yarn spinning process which converts short fibers into continuous yarns consists of four steps: separation, alignment, attenuation, and integration. In traditional yarn manufacturing, separation and alignment steps are achieved by carding, producing a web of fiber. This web is condensed into a thick untwisted rope which is attenuated and further aligned through a drafting process. Spinning re-entangles the well aligned fibers in a controlled manner through a twisting process to give the yarn strength. With a focus on achieving fibril alignment and creating structural integrity our research was focused on the carding and spinning process.

Carding

Carding is a well established process for the orientation of textile fibers wherein the fibers are subjected to the opposing action of metallic wires as shown in Figure 5. Due to the limited availability and the high modulus nature of the SiC fibril, a model SiC fiber Nicalon (which has 50% lower modulus than the fibril) was used to test a laboratory scale carding machine constructed for this study. It was founded that , besides the formation of fiber clusters, a great deal of damage was done to the Nicalon fibers and the yield was extremely low. Accordingly, it was concluded that the carding process is

unsuitable for processing fibers such as Nicalon even with the aid of a carrier fiber. Therefore, no further trial was attempted to align the fibril with the carding process.

Air Vortex Spinning

In order to minimize the contact of fibrils with mechanical surfaces in traditional spinning operations, a laboratory scale air vortex spinning apparatus (Figure 6) was constructed to align and integrate the fibril into a linear assembly. It was found that a great deal of carrier fibers would be needed even with the Nicalon model fiber in order to obtain a linear strand. Substantial damage occurred on the Nicalon fiber due to the whipping/twisting motion and contact with the wall of the air duct. It was concluded that it would be difficult for the fibril to survive the air vortex spinning process.

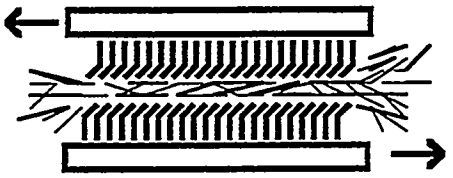

Figure 5. Carding operation.

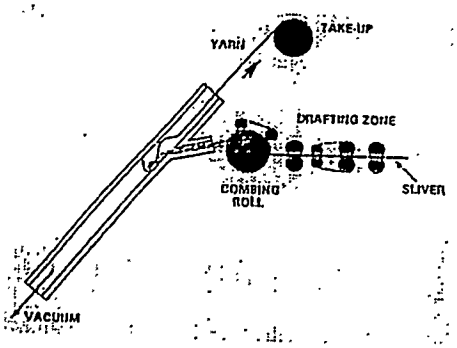

Figure 6. Air vortex spinning.

UNCONVENTIONAL PROCESSES

It was clear from the lessons learned in the unconventional processes that in order to process ultra-high modulus materials such as SiC fibril, one must keep handling to its minimum, the fibrils to fibril contact should be minimized, and the fibrils should be well separated during the gentle/non

twisting alignment process. Out of a list of ten candidate unconventional processing methods, the adhesive tape and the wet-laid processes were selected for further examination.

Adhesive Tape Process

In the adhesive tape method is a direct process wherein separation and alignment would occur while the fibrils were still anchored on the growth plate, through a combing or brushing step. Like hair on a scalp, fibril entanglement is limited to the entanglement which is formed as the fibrils grow together, and can be modified by controlling growth density and fibril growth length. Once oriented, the fibrils can be removed from the plate by applying and removing an adhesive tape, which provides the integration. In this process, an attenuation step does not occur, as the linear weight is dictated by the fibril growth on the plate. (Figure 7.)

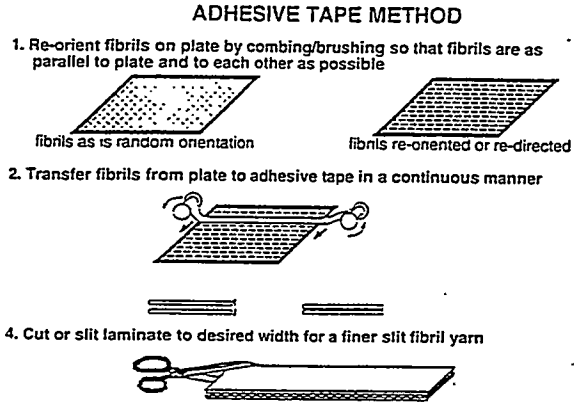

Figure 7. Adhesive tape process.

Wet-Laid Process

The wet-laying process is a gentle process wherein the fibrils can be protected from each other through surface charge modification and orientation is induced by fluid flow. The first operation of wet-laying is the dispersion (or separation) of fibrils in a liquid medium to the degree that the fibrils are *discretely* suspended. Alignment occurs when the liquid medium is allowed to flow in a controlled manner and the dispersed fibrils align in the flow onto a porous screen where the liquid is removed. Attenuation can occur at two points. The first opportunity for attenuation occurs when the fibrils are rinsed of the dispersion medium by a flow of plain water, after which a binder is applied to give the fibrous array enough strength to be lifted from the screen. A second opportunity for attenuation can occur when the still-wet fibrils slide past each other as they are transferred from one surface to another. (Figure 8)

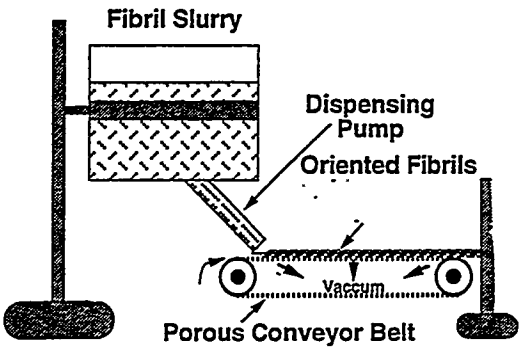

Figure 8. Wet-laid process.

CHARACTERIZATION OF FIBRIL ALIGNMENT

A major objective in the formation of linear fibril assembly is to create high level of fibril alignment. The degree of alignment can be studied by scanning electron microscopic(SEM) observation and X-ray diffractometry by examination of the peak height ratio between (220) and (210) . An examination of the SEM photographs of the adhesive tape and the wet-laid fibrils as shown in Figures 9 and 10 respectively, demonstrated that the wet-laid process produced a well aligned linear assembly whereas fibril assembly produced by the adhesive tape process tends to be random. This difference in alignment was further confirmed by X-ray diffractometry as shown in Figures 11 and 12.

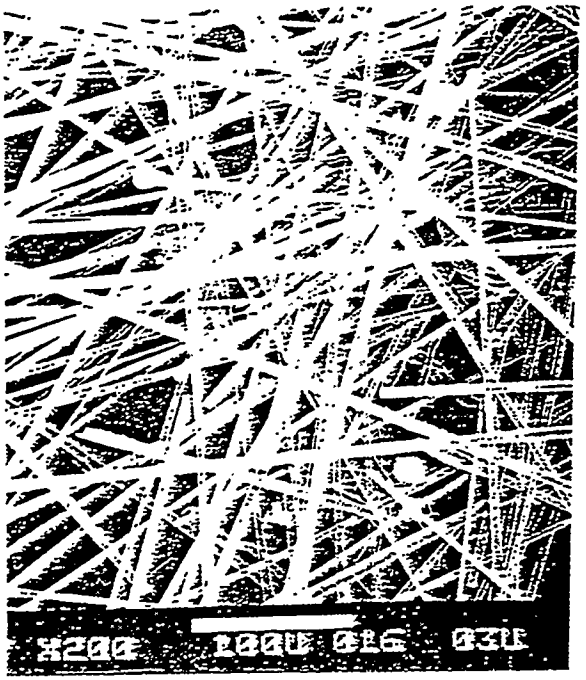

Figure 9. SEM photograph of fibrils aligned by adhesive tape process.

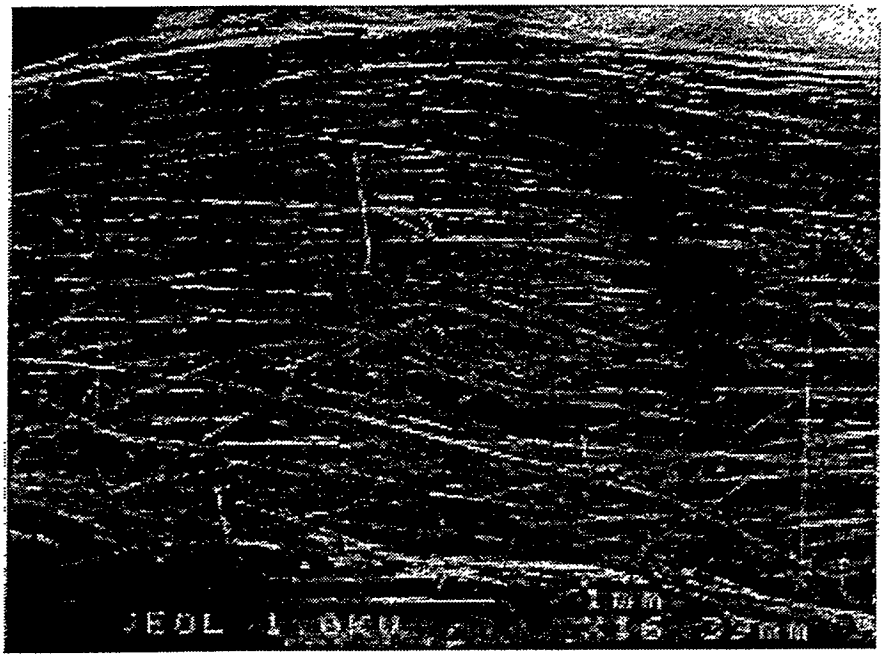

Figure 10. Photograph of fibrils aligned by wet processing.

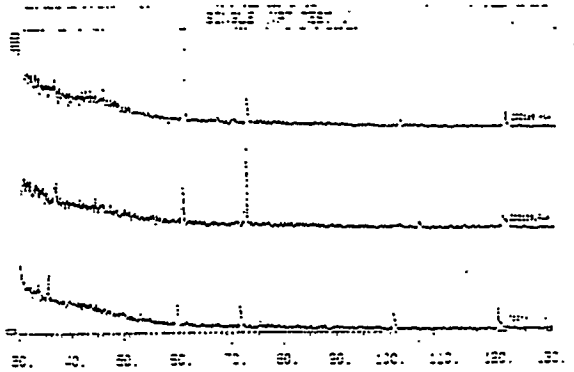

Figure 11. X-Ray diffractometry of fibrils aligned by adhesive tape process.

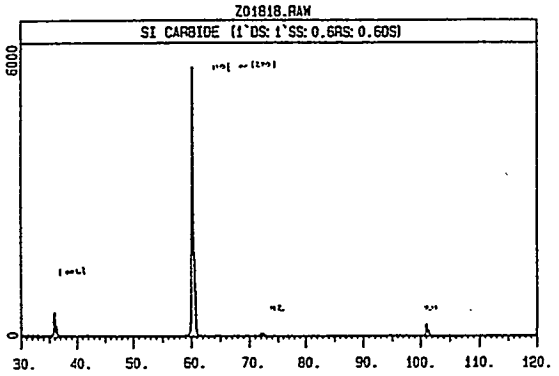

Figure 12. X-Ray diffractometry of fibrils aligned by the wet-laid process.

CONCLUSIONS

This study demonstrated that engineering scale production of SiC fibril is feasible and high level of fibril alignment can be achieved by the wet-laid process. By time-series experiments the critical variables in the growth process of SiC fibril were identified and evaluated. A computer simulation model was established to predict fibril growth rate as a function of process parameters which will facilitate future reactor design and development .With an average growth rate of 0.65 mg/cm^2/hr , the diameter of 99% by weight of the fibril were above 3μm. The tensile strength of the fibril was also confirmed to be consistent with the literature, at the level of 6-9 GPa. In order to maximize the translation of the unique tensile properties to a higher level structure and finally the composite, conventional and unconventional fiber processing methods were examined. It was concluded that conventional methods such as carding and spinning, even with modification, are not applicable to the processing of SiC fibril due to excessive fiber damage and inability to separate and align the high modulus fibers. Of the unconventional processes such as the adhesive tape and the wet-laid method, although substantial simplification can be made with the adhesive tape process the level of fibril alignment and volume fraction are lower than that by the wet-laid process.

This study has established the necessary foundation for a scale up process for the fibril growth, harvesting and conversion into well oriented linear, planar and 3-D assemblies with controlled fibril fractions suitable for the production of ceramic matrix composites. A follow-on program has been planned to optimize the wet-laid process and establish a pilot scale wet-laid production facility capable of near net shape production of fibril preforms for heat exchangers and other CMC products of interest to the DOE Fossil Energy AR & TD Program.

REFERENCES

1. Hollar, W.E. and J. J. Kim, "Review of VLS SiC Whisker Growth Technology," *Ceram. Eng. Sci. Proc..*, 12[7-8], p 979 - 991 (1991).

2. Shalek, P.D., D.E. Christiansen, F.D. Gac. R.E. Honnell, G.F. Hurley, J.D. Katz, W.J. Parkinson, J.J. Petrovice and D.S. Phillips, "Scale-up and Optimization of the VLS Growth Process for Beta-SiC Whiskers for the Period KApSiptember - 1989," DARPA Final Report & DOE/OAR&TD Topical Report, Los Alamos National Laboratory Report #LA12119 (1992).

3. Hollar, W.E., J.J. Kim and W.H. Mills, "The Growth Kinetics of VLS SiC Whiskers," presented at the 16th Annual Conference on Composites and Advanced Ceramics, Cocoa Beach, FL, January 1992.

4. Kim, J.J., W.E. Hollar, S. Chwastiak and W.H. Mills, "Engineering Scale Development of the Vapor-Liquid-Solid (VLS) Process for the Production of Silicon Carbide Whiskers."

5. Morscher, G.N. and J.A. DiCarlo, "A Simple Test for Thermomechanical Evaluation of Ceramic Fibers". *J. Am. Cer. Soc.*, 75 [1], 136 - 140 (1992).

6. Petrovic, J.J., J.V. Milewski, D.L. Rohr and F.D. Gac, "Tensile Mechanical Properties of SiC Whiskers," *J. Mat. Sci.*, 20, 1167 - 1177 (1985).

7. Netravali, A.N., L.T.T. Topoleski, W.H. Sachse and S.L. Phoenix, "An Acoustic Emission Detection Technique for Measuring Fiber Fragment Length Distributions in the Single-Fiber-Composite Test," *Comp. Sci. and Tech.*, 35, 13 - 29 (1989).

8. Srinivasan, G.V. and V. Venkateswaran, "Tensile Strength Evaluation of Polycrystalline SiC Fibers," presented at the 17 Annual Conference on Composites and Advanced Ceramics, Cocoa Beach, FL, January 12, 1993.

9. Ko, F., Preform Fiber Architecture for Ceramic Matrix Composites, Bulletin of American Ceramic Society, Vol. 68 No. 2 1989.

10. NASA Contractor Report CR-795, May 1967.

MECHANICAL PROPERTIES OF CERAMIC COMPOSITE TUBES

W. A. Curtin[1], L. L. Oleksuk[1], K. L. Reifsnider[1], and D. P. Stinton[2]
[1]Materials Response Group, Department of Engineering Science and Mechanics
Virginia Polytechnic Institute and State University, Blacksburg, VA 24061
[2]Oak Ridge National Laboratory, Oak Ridge, TN

ABSTRACT

Results of axial tension tests on SiC/SiC tubular ceramic composite components fabricated by a forced-CVI technique are presented. Axial elastic modulus measurements on a number of tubes show that the Young's modulus varies along the length of the tube, with occasional very stiff or very soft regions. Tests to failure on a few tubes show the initiation of non-linear stress-strain behavior to be in the range of 3-9 ksi, followed by extensive non-linear deformation up to failure. For one tube, the failure stress obtained was 20.1 ksi, but the strains to failure at various axial locations varies from 0.19% to 0.24%. The correlation between modulus and proportional limit is considered within the ACK matrix cracking theory and within a model in which matrix cracking between fiber tows occurs, both modified to account for matrix porosity. The crack size required to cause stress concentrations large enough to cause failure at the observed strength is considered. Predictions for both matrix cracking and strength suggest that the current generation of tubes are controlled by microstructural defects.

I. INTRODUCTION

Two of the major fossil energy technology applications for ceramic matrix composite (CMC) materials are heat exchangers and hot-gas filters. Both of these are tubular components with specific mechanical property requirements. The goal of the present effort is to assess the mechanical properties of tube components, rather than simple flat coupons, and to guide the development of advanced processing techniques used to fabricate such CMC components. In this paper, we will present and discuss results on elastic modulus, microcracking, and tensile failure, and the variations of these properties within a single component.

The CMC tubes studied here are composed of Nicalon™ fibers reinforced by a SiC matrix deposited by a forced-CVI technique[1]. The fiber preform is created by rolling 2d, plain weave mats woven from fiber tows. One set of fiber tows are aligned along the tube axis and the other tows are perpendicular and wind around the circumference. A thin carbon coating is deposited onto the fibrous preform prior to infiltration by CVI-SiC. The final components are 8 inches in length, with approximately 1" i.d. and 1.25" o.d.; the total fiber volume fraction is about 32%, while the porosity is between 10% and 25%, and is predominantly in the form of "interlaminar" pores between the 0° and 90° fiber tow. (Fig. 1).

II. EXPERIMENTAL RESULTS

Tensile testing along the axial direction of the tubes is performed using either an Instron or MTS servohydraulic testing device. Gripping, and prevention of grip failure, by the use of tapered end plugs has been discussed previously[2]. Because of the varying porosity observed qualitatively along the tube length, and the large size of the sample, we have investigated the axial Young's modulus at a number of

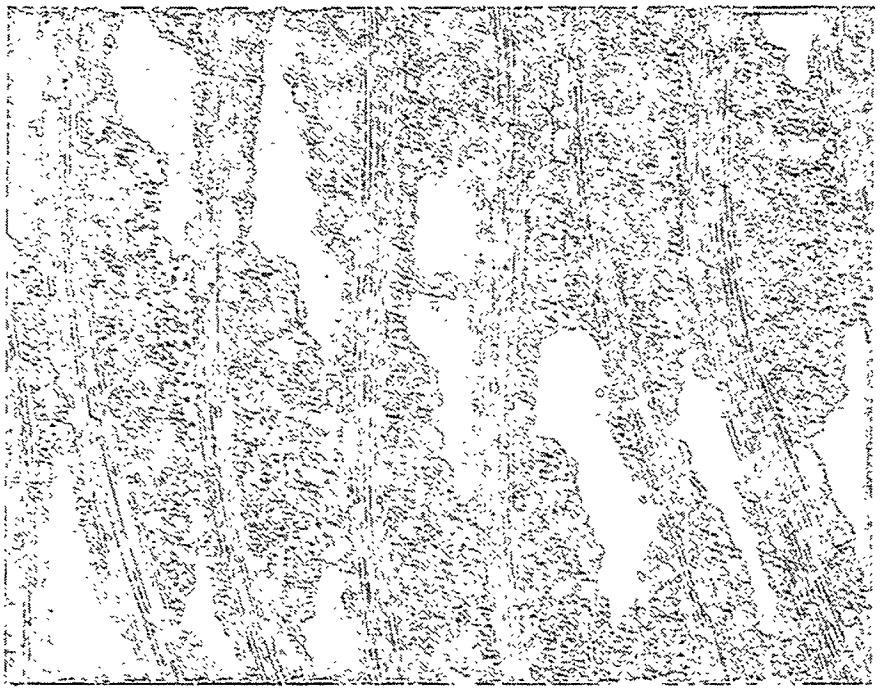

Figure 1. Optical micrograph of a typical tube cross-section. Dark regions are interlaminar porosity. Typical tow dimensions are 1000 μm x 150 μm. Upon matrix and 90° tow failure, "unbridged" regions between the 0° tows have a typical width of about 800 μm.

locations along and around the tube. Strain gauge pairs are equally spaced along the 6" gauge length of each specimen, and pairs at 90° rotation are also used to check angular modulus variations. The modulus measurements are carried out using strains less than 10^{-3} to avoid non-linearities associated with microcracking, and 3 load cycles are run to insure reversability and repeatability. Results on 4 different tubes (each with varying number of strain gauges) are shown in Figure 2. The axial modulus exhibits

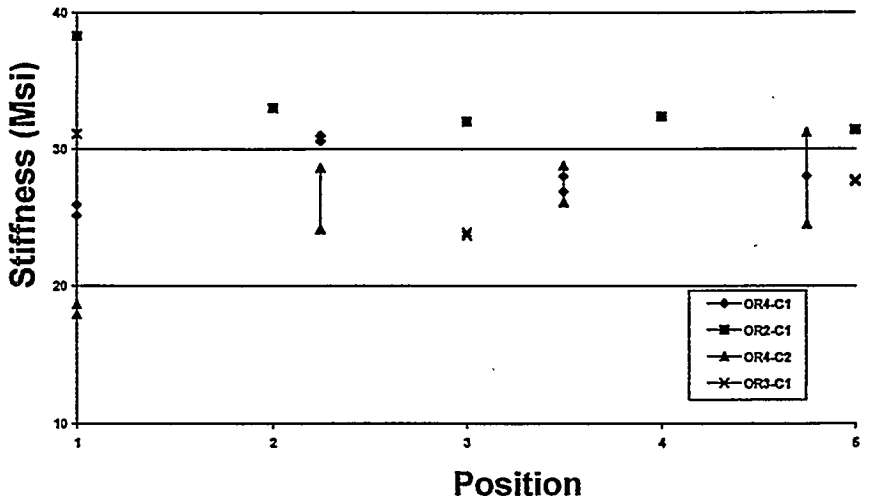

Figure 2. Modulus (Msi) versus axial position along tube, for four different tubes. Angular variations at fixed axial position are shown by multiple symbols.

rather large point-to-point variations along each tube and each tube shows distinct behavior. 3 of the 4 tubes exhibit a modulus which is either high or low (by as much as 50%) at one end of the tube, with mild variations away from the one end. The 4th tube, however, has a low modulus in the middle of the tube. The modulus at any axial location, but for angular locations differing by 90°, shows much smaller variations, indicating angular homogeneity at a fixed axial position

The observed modulus variations are generally attributable to variations in densification along the length, potentially caused by thermal gradients along the tube length during processing. Microscopy of high and low modulus regions indicate "low" and "high" degrees of porosity, respectively. These qualitative results are consistent with a correlation of modulus and density made by Becher et al. on similar F-CVI materials (Fig. 3).[3] Variations observed here, interpreted using Fig. 3, suggest variations in porosity from 10-25% along the length in these tube components.

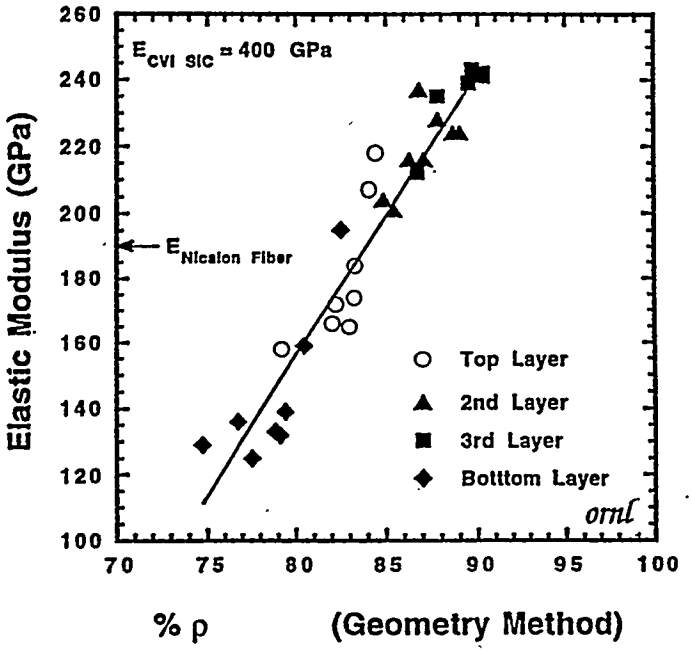

Figure 3. Modulus (Gpa) versus volumetric density (from Becher et al.)

Two tubes have been tested beyond the linear range. The stress-strain curves for the six pairs of strain gauges (two pairs at each of three locations) are shown in Fig. 4 for the one sample which failed in the gauge section at 137 Mpa (20.1 ksi). It is evident that the entire stress-strain response of the material is influenced by the local property variations, and that axial variations are more severe than angular variations. Table I shows the modulus, proportional limit stress and strain, strain at failure, and tangent modulus at failure, for the six pairs of gauges. The lower moduli regions exhibit a slight tendency toward lower proportional limit stresses. The softest region with the lowest σ_{pl} exhibited the largest strains up to failure. At failure, the strains differ by up to 25% from point to point. Near failure the tangent moduli are fairly constant with strain but again vary by 25%, at $\approx 28 \pm 5$ GPa. There is no apparent correlation between initial composite modulus and final tangent modulus, however. This overall behavior suggests that the initial response is controlled by matrix modulus and residual stresses whereas, after extensive cracking and non-linear reponse, the final response is much less dependent on matrix properties and is controlled primarily by the response of the fiber tows. For reference, the response of the 0° fibers alone

suggests a final tangent modulus of ½ $V_f E_f \approx 30$ GPa. Progressive damage to the fibers, followed by fiber slipping against the matrix, can cause the tangent modulus to be below ½ $V_f E_f$ and, in an ideal composite, to approach zero at composite failure. More detailed analysis of these results is presented in the following section.

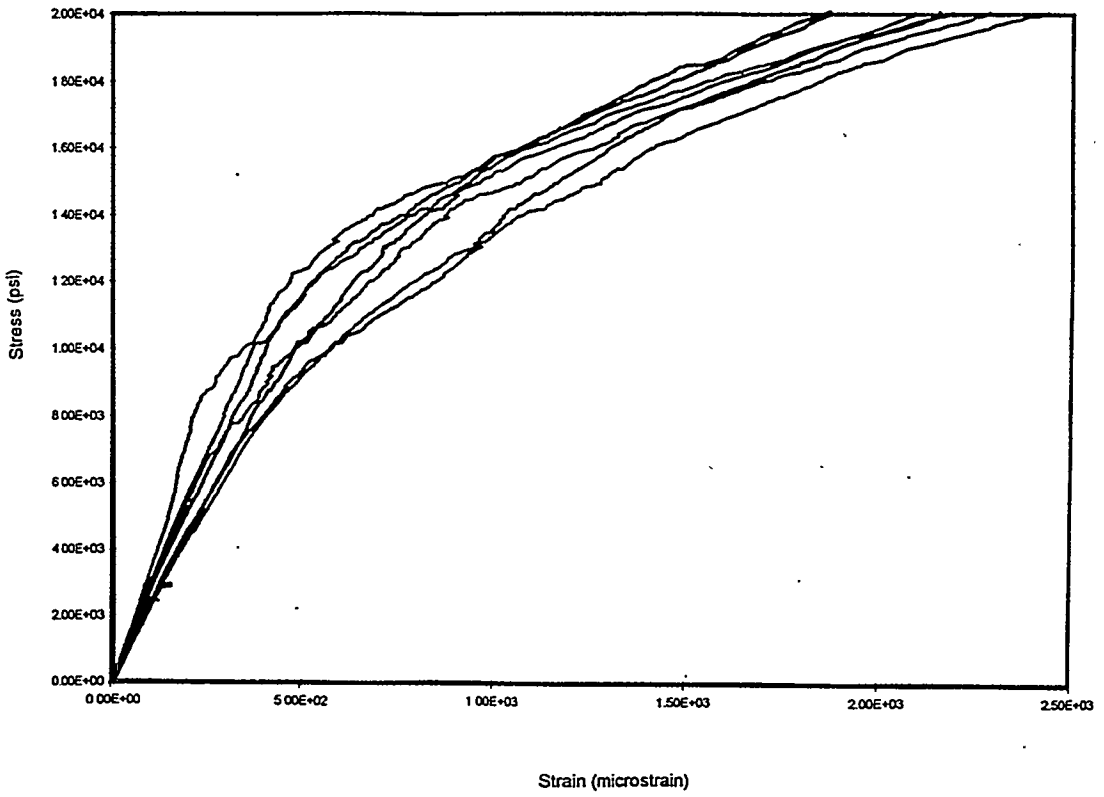

Figure 4. Stress-strain curves for six pairs of strain gauges on sample OR3-C1. Variations in the proportional limit and strain at failure are clearly evident.

Site	E (msi)	σ_{pl} (ksi)	ε_{pl} (microstrain)	$\varepsilon_{failure}$ (microstrain)	E_{final} (msi)
1 - front	29.8	9.1	300	2190	3.4
- back	31.05	5.0	151	2090	4.1
3 - front	23.9	3.1	140	2440	3.9
- back	23.0	6.3	287	2150	4.3
5 - front	27.3	6.9	259	2280	3.7
- back	28.5	4.0	150	1870	4.9

Table I. Initial modulus, porportional limit stress and strain, failure strain, and tangent modulus at failure (from 17.5 ksi to 20 ksi), for six pairs of strain gauges on tube OR3-C1.

III. ANALYSIS

Matrix Cracking

We first consider the observed variations in proportional limit stress, and any correlations with initial modulus. Due to bridging of cracks by the 0° fibers, Aveston, Cooper and Kelly showed that large cracks cannot propagate across the matrix of a uniaxial composite below a "matrix cracking stress" σ_{mc}, which therefore established a minimum proportional limit[4]. σ_{mc} is given by

$$\sigma_{mc} = \left[\frac{6\Gamma f^2 E_f E_c^2 \tau}{(1-f)E_m^2 r}\right]^{1/3} - q\frac{E_c}{E_m}$$

where f = 0° fiber volume fraction, E_f, E_c, E_m are fiber, composite and matrix Young's moduli, r is fiber radius, Γ is the matrix fracture energy, τ is the interfacial sliding resistance between fibers and matrix, and q is the residual tensile stress in the matrix. To utilize the above result in a porous-matrix composite with 90° fibers, the quantities E_m and Γ must be considered properties of an effective homogeneous matrix. We estimate E_m from the known E_f and measured E_c by a simple rule of mixtures:

$$E_c = fE_f + (1\text{-}f)\,E_m$$

where $f = \frac{1}{2} V_f$ in this case. The effective matrix fracture energy is the true matrix energy reduced by i) the porosity in the matrix, which is related to the true porosity as $V_p/(1\text{-}f)$, and ii) the surface area of the 90° fibers, which are assumed to be weakly bonded to the matrix because of the weak carbon interlayer. Hence,

$$\Gamma = \Gamma_{SiC}\left(1 - \frac{V_p + f}{1-f}\right)$$

V_p is obtained from the measured E_c using the correlation of Fig. 3. Predictions for σ_{mc} versus E_c can be made from the above, and here we use E_f = 190 GPa, τ = 25 MPa,[5] V_f = 0.32, $\Gamma^{SiC} = 1.0 \times 10^{-8}$ GPa - m. The result is $\sigma_{mc} \approx 90$ GMa = 13 ksi nearly independent of the matrix porosity or E_c. If residual thermal stresses exist, the proportional limit can be shifted down but q is not expected to vary with porosity, and so the shift does not, in fact, depend on either E_m or E_c. Thus, σ_{mc} can be reduced to smaller values but does not exhibit any strong correlation with E_c.

As an alternative to full matrix cracking, we also consider cracking around the 0° infiltrated fiber tows, with no slip at the tow-matrix interface[6]. This deformation mechanism corresponds to cracking around the tows and through the 90° tows without penetration into the 0° tows, and is analogous to the onset of tunnel cracking in the 90° plies of 0°/90° laminate composites. In this case, the onset of extensive cracking occurs at a stress

$$\sigma_{mc} = \left[\frac{f_T E_T E_c \Gamma \rho}{a E_m}\right]^{1/2}$$

where a is the fiber tow diameter, f_T is now the 0° tow volume fraction, E_T the tow modulus, E_m and Γ the modulus and fracture energy of the effective matrix material outside of the fiber tows and ρ a calculated parameter.[4] Assuming the fiber tows to be 60% fiber and fully densified with 40% SiC matrix, (E_{SiC} = 400 GPa) we have

$$E_T = 0.6\,E_f + 0.4\,E_{SiC}$$

and $f_T = f/0.6$. The remaining "matrix" material has a modulus E_m obtained again from

$$E_c = f_T E_T + (1-f_T) E_m$$

and the effective Γ is

$$\Gamma = \Gamma_{SiC}\left(1-\frac{V_p+f}{1-f_T}\right) .$$

The prediction of this model, with the parameter ρ ranging from 1.7 - 2.0 and a = 220 μm, (effective tow diameter) for the proportional limit versus E_c are also nearly independent of E_c or V_p and are σ_{mc} = 47 Mpa (6.8 ksi) . These values are somewhat lower than the ACK results, but still slightly higher than observed experimentally. Residual stresses could easily be the difference between these predictions and the observed range.

Considering these results, the onset of cracking and non-linear deformation in these materials may thus occur by formation of multiple small matrix cracks which initiate at large pores and grow across 90° tows but do not grow through or around the 0° tows. Normally such microcracks do not contribute substantially to the non-linear strain of the composite. But here the extensively distributed porosity may permit considerable local microcracking at low stresses. The microcracks would then grow into, at higher loads, fully-extended "matrix cracks" in the traditional sense. The initial cracking failure may thus mimic the response of very heterogeneous materials such as cements, and the onset of non-linearity would than be strongly coupled to the extent and size distribution of porosity. If this mechanism prevails, it is not accompanied by cracking of the 0° tows, and the 0° load-bearing fibers are not exposed to deleterious environmental degradation. The low proportional limit may then not be a design limit for long-term durability. This will be investigated in our future work.

Ultimate Strength

Ideally, the UTS is controlled by failure of the fiber bundles. The final tangent moduli shown in Table 1 are close to 1/2 $V_f E_f$ = 30 Gpa, suggesting that the system is controlled by the fiber loading at this point. Under the "Global Load Sharing" assumption widely successful in a number of other CMC materials, the UTS σ_u is predicted to be[7]

$$\sigma_u = \left(\frac{1}{2}V_f\right)\left(\frac{2}{m+2}\right)^{\frac{1}{m+1}}\left(\frac{m+1}{m+2}\right)\sigma_c$$

where σ_c is the in-situ fiber strength at a characteristic gauge length $\delta_c = r\sigma_c/\tau$ and m is the Weibull modulus describing the statistical variability in fiber strength around σ_c . Several recent studies have assessed the in-situ strength of Nicalon in CVI-SiC and found fiber degradation on processing with σ_c = 1.75 ± .25 GPa and m = 5 ± 1.[8] Using the median values suggests predicted strengths in the range of

$$\sigma_u \approx 195 \pm 35 \text{ MPa}$$

and a failure strain of

$$\varepsilon_f \approx \frac{\sigma_c}{E_f}\left(\frac{2}{m+2}\right)^{\frac{1}{m+1}} = 0.75 \pm 0.11\%$$

These values are larger than the observed strength and failure strain, particularly for the failure strain, and prompt us to consider below the strength of these materials in the presence of the unbridged matrix regions, which can cause stress concentrations and "premature" failure.

The stress concentrations on the fibers at the tips of unbridged matrix region (cracks) has recently been investigated by Xia et al.[9] They have found that, including fiber slip controlled by the interfacial τ, the fiber tensile stresses σ_f at the tip of a crack of diameter 2a are enhanced relative to the applied stress σ as

$$\sigma_f = \frac{\sigma}{V_f}\lambda(\eta)$$

where $\lambda(\eta)$ is a computed function of

$$\eta \approx \frac{3\pi V_f^2 E_f E_c}{V_m^2 E_m^2}\frac{a\tau}{r\sigma}$$

For 2-d cross-ply materials that approximate the present woven structure, the function λ is roughly linear. At $V_f = 0.40$, and $E_m = E_f$ (the only case calculated),

$$\lambda(\eta) \approx 2\left(1+\frac{1}{60}\eta\right) \qquad 0 < \eta < 30$$

Since $\sigma\eta$ is independent of σ, the fiber stress is increased by a fixed amount over the "global" load sharing value of $2\sigma/V_f$. To initiate failure, we must then have $\sigma_f \approx \sigma_c$ so that the applied failure stress is

$$\sigma_u = \frac{V_f}{2}\sigma_c - \frac{\sigma\eta}{60}$$

For "typical" intermediate porosity $V_p = 15\%$ and E_f, E_c, E_m, V_f, V_m, τ as given earlier, we find

$$\sigma_u = \frac{V_f}{2}\sigma_c - 0.11a(\mu m)\ \text{MPa}$$

The strength degradation is approximately linearly dependent on the "crack" size a. For 2a = 800 μm, a typical width of the interlaminar pore region (see Fig. 1) we obtain

$$\sigma_u = 236\ \text{Mpa}$$

which is larger than to the global load sharing prediction, suggesting that typical tow spacings/crack sizes

do not degrade strength. For a "high" porosity region with $V_p = 25\%$ ($E_c \approx 125$ Gpa), the stress concentrations increase, and

$$\sigma_u = \frac{V_f}{2}\sigma_c - 0.217a(\mu m)MPa\,.$$

With typical "crack" widths of 2a = 800σm, the predicted strength is

$$\sigma_u = 194 \text{ Mpa},$$

almost identical to the global load sharing result. However, if a width of 2a = 1200 μm (slightly larger than a tow length) occurs,

$$\sigma_u = 150 \text{ Mpa}$$

is predicted, a value approaching the measured value of 139 Mpa. Interestingly, the failure plane of the failed tube is quite close to the low-modulus region (position 3, $E_c = 159$ Gpa), which is consistent with the above estimate. Fluctuations in the microstructure which lead to local regions with both low density/modulus and in which the tow separation is somewhat larger than average could thus be responsible for the observed reduced strength.

The above predictions are only qualitative in the sense that they do not account for the fiber/matrix moduli differences; nor has the influence of multiple matrix cracks been considered, which tends to decrease stress concentrations. Also, uncertainty in the precise values τ and σ_c certainly exists. Further analysis of the fracture surfaces, in-situ fiber strengths, interfacial sliding τ, and microstructural variations will be carried out on the present materials to make these calculations more quantitative.

IV. Summary

The analysis of both σ_{mc} and σ_u indicates that local microstructural variations, such as porosity and tow spacing, can play an important role in determining the mechanical properties of these CMC materials. Such a situation is clearly undesirable in that, although tougher and exhibiting "graceful" failure, this composite tends to be controlled by "defects" as in a monolithic ceramic. In contrast, many other CMC materials exhibit behavior consistent with the theoretical predictions and are far less sensitive to matrix porosity and "damage" in various forms. Improved forced-CVI processing approaches are now being investigated to eliminate thermal gradients and large inter-laminar pores, and to improve the microstructure. Modified preform fabrication to increase fiber volume fraction and improve homogeneity will also improve mechanical performance. Interface manipulation is not clearly necessary at this stage: reducing τ reduces the matrix cracking stresses but can lessen stress concentrations and thereby improve ultimate strength; increasing τ might increase matrix cracking in better-densified materials but could also increase stress concentrations. The initial cracking in the present materials may not, however, expose 0° fibers and the carbon interface to external environments, and so durability at loads somewhat above the initial cracking loads may not be an issue. In any case, if processing defects can be better eliminated, as accomplished in traditional CVI SiC/SiC systems, the initial cracking events will be pushed up to higher stresses and these materials will be suitable for heat exchanges applications at moderate temperatures and loads.

REFERENCES

1. T. M. Besmann, B. W. Sheldon, R. A. Lowden and D. P. Stinton, "Vapor-Phase Fabrication and Properties of Continuous-Filament Ceramic Composites," Science, Vol. 253, 1104-1109 (1991).

2. W. A. Curtin, K. L. Reifsnider, L. L. S. Oleksuk and W. W. Stinchcomb, "Investigation of Properties and Performance of Ceramic Composite Components: Final Report on Phase II." Oak Ridge National Laboratory, October 31, 1994.

3. P. F. Becher and H. T. Lin, CFCC Program Bimonthly Progress Report, Feb.-Mar. 1994, pg. 37.

4. M. Sutcu and W. B. Hillig, "The Effect of Fiber-Matrix Debond Energy on the Matrix Cracking Strength and the Debond Shear Strength," *Acta metall. mater.* Vol. 38, 2653 (1990); B. Budiansky, J. W. Hutchinson and A. G. Evans, "Matrix Fracture in Fiber-Reinforced Ceramics," *J. Mech. Phys. Solids*, Vol. 34, 167, (1986).

5. E. Lara-Curzio, M. K. Ferber and R. A. Lowden, "The Effect of Fiber Coating Thickness on the Interfacial Properties of a Continuous Fiber Ceramic Matrix Composite," *Ceram. Eng. Sci. Proc., Vol.*15, 989 (1994).

6. This is analogous to the no-slip condition at the fiber-matrix interfaces, as discussed in Ref. 4.

7. W. A. Curtin, "Theory of Mechanical Properties of Ceramic-Matrix Composites," Journal of the American Ceramic Society, Vol. 74, 2837 (1991).

8. A. G. Evans, and F. W. Zok, "Review: The Physics and Mechanics of Fibre-Reinforced Brittle Matrix Composites." Journal of Materials Science, 29, 3857 (1994); D. Singh, J. P. Singh, M. J. Wheeler, "Mechanical Behavior of Sic(f)/SiC Composites and Correlation to In-Situ Fiber Strength at Room and Elevated Temperatures," Submitted to the Journal of the American Ceramic Society, January 1995.

9. Z. C. Xia, J. W. Hutchinson, A. G. Evans and B. Budiansky, "On Large Scale Sliding in Fiber-Reinforced Composites," in press (1993).

JOINING OF SiC CERAMICS AND SiC/SiC COMPOSITES

B. H. Rabin

Idaho National Engineering Laboratory
P.O. Box 1625
Idaho Falls, ID 83415-2218

ABSTRACT

This project has successfully developed a practical and reliable method for fabricating SiC ceramic-ceramic joints. This joining method has the potential to facilitate the use of SiC-based ceramics in a variety of elevated temperature fossil energy applications. The technique is based on a reaction bonding approach that provides joint interlayers compatible with SiC, and excellent joint mechanical properties at temperatures exceeding 1000°C. Recent efforts have focused on transferring the joining technology to industry. Several industrial partners have been identified and collaborative research projects are in progress. Investigations are focusing on applying the joining method to sintered α-SiC and fiber-reinforced SiC/SiC composites for use in applications such as heat exchangers, radiant burners and gas turbine components.

INTRODUCTION

SiC ceramics have considerable potential as elevated temperature structural materials in fossil energy applications. Ceramic-to-ceramic joining methods are needed to allow the fabrication of large or complex shaped parts, and ceramic-to-metal joining methods are needed to allow integration of ceramic components into existing engineering systems. Although considerable efforts have been devoted to understanding the processing, microstructures and properties of SiC-based structural materials, joining remains largely an unresolved issue, particularly with respect to elevated temperature applications. Ideally, joined components should exhibit mechanical properties (including reliability), elevated temperature capabilities and environmental resistance comparable to the base material. Furthermore, the joining method should be practical, cost effective and applicable to different types of SiC ceramics, including SiC fiber-reinforced composites.

This project has successfully developed a reaction processing method for fabricating SiC ceramic-to-ceramic joints [1,2]. The processing method involves tape casting thin sheet SiC+C interlayer precursors, clamping the tape between the SiC parts, and infiltrating the joint with molten Si to form a reaction bonded silicon carbide (RBSC) joint interlayer. This method is attractive since the interlayer material is compatible with SiC, and excellent room and elevated temperature mechanical properties can be achieved.

In addition, as with brazing, external pressure is not required, thus making the process inexpensive and practical compared to alternative joining methods. Details of the joining procedure as well microstructural and mechanical property characterization results have been described previously [1,2]. This paper reports on the status of technology transfer efforts involving a number of industrial partners.

PROGRESS STATUS

Laboratory Joining Studies

Recently, efforts have been made to demonstrate the applicability of the joining method to different joint geometries and materials. Figure 1 shows examples of several joined structures that were fabricated from sintered α-SiC using the laboratory scale localized induction heating apparatus at INEL. Of particular interest is the ability to fabricate tube-to-tube butt joints, since long ceramic tube structures are required in applications such as heat exchangers and radiant burners.

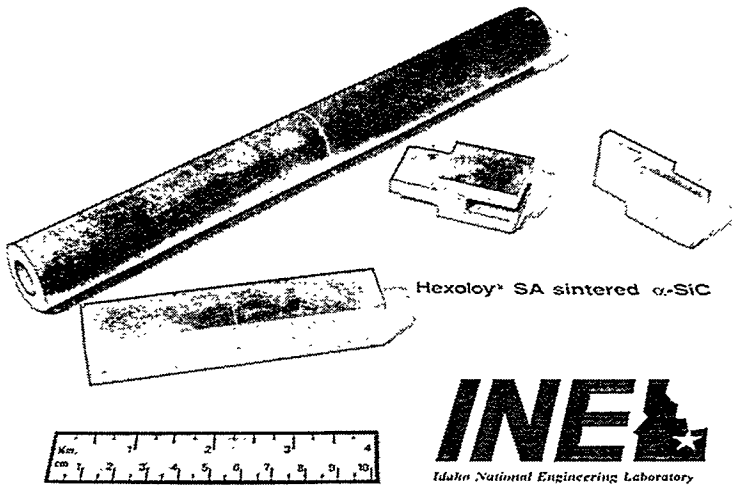

Figure 1. Examples of joined α-SiC structures produced using the reaction processing method developed under this project.

Technology Transfer Activities

Several industry contacts have been made and detailed discussions have taken place regarding industrial needs for the SiC joining methods in general, and the potential uses of the method developed under this program in particular. Table 1 lists the various industry contacts and the associated applications being explored. As a result of these discussions, several technology transfer activities are now in progress, as discussed below.

contact	material	applications
DuPont Lanxide Composites, Inc.	CVI SiC/SiC	gas turbines, radiant burners
Allied-Signal Aerospace	α-SiC	heat exchangers
Hague International	α-SiC, RBSC, SiC/$MoSi_2$	heat exchangers
Stone & Webster	α-SiC, SiC/SiC	reformers
Amercom, Inc.	SiC/SiC	heat exchangers, radiant burners, gas turbines
Textron Specialty Materials, Inc.	NBSC	heat exchangers, radiant burners, reformers
Dow Corning	SiC/SiCN	gas turbines, chemical pump

Table 1. Potential Industrial Uses for SiC Joining Technology

Cooperative work with DuPont Lanxide has been initiated under funding from the DOE Continuous Fiber Ceramic Composites (CFCC) Program. In this work, the joining method is being applied to CVI SiC/SiC composite materials for potential use in a variety of energy conversion devices including gas turbine components. These studies are examining the suitability of different joint configurations, and joint microstructures and properties are being studied at both INEL and DuPont Lanxide.

In another effort, a Phase I Joint Development Program is being carried out in collaboration with Allied Signal Aerospace Corp., a subcontractor to Foster Wheeler Development Corp., involved in the development of the Ceramic Air Heater for the DOE High Temperature Advanced Furnace. This work is being conducted under funding from

the DOE-PETC High Performance Power Systems Program. This work will apply the joining technique to sintered SiC, and specifically includes the fabrication and elevated temperature high pressure testing of tube-to-tube structures. A CRADA involving Allied-Signal and Carborundum is currently being negotiated.

A CRADA is also being negotiated with Hague International to investigate the fabrication of tube-to-tube joints for use in ceramic heat exchangers. This work will involve a variety of SiC-based materials, and seeks to improve the elevated temperature mechanical properties and corrosion resistance of the joints.

SUMMARY

Reaction processing methods have been developed for fabricating SiC-to-SiC joints for potential use at elevated temperatures. Technology transfer activities are in progress.

REFERENCES

1. B. H. Rabin and G. A. Moore, "Joining of SiC Ceramics and SiC/SiC Composites," ORNL/FMP-93/1, Oak Ridge National Laboratory, July 1993, pp. 33-42.

2. B. H. Rabin and G. A. Moore, "Reaction Processing and Properties of SiC-to-SiC Joints," Mat. Res. Soc. Symp. Proc., Vol. 314, 1993, pp. 197-203.

COMPARISON OF HIGH TEMPERATURE MECHANICAL PROPERTIES OF TWO MONOLITHIC SiC CERAMICS AND AN Al_2O_3 / SiC COMPOSITE

Kristin Breder

Oak Ridge National Laboratory
High Temperature Materials Laboratory
Oak Ridge, TN 37831-6069

ABSTRACT

Fast fracture strength, slow crack growth, and creep properties have been evaluated for three ceramics in air at room temperature and two elevated temperatures. The ceramics are candidate materials for heat exchangers in fossil energy systems, therefore, retained strength after coal ash exposure was also measured. At 1100°C the ceramics had acceptable mechanical properties, but two of them exhibited strength loss due to coal ash corrosion. At 1400°C creep and slow crack growth were observed in two of the materials, and the material which exhibited best resistance to coal ash showed unacceptably high creep rates.

INTRODUCTION

The purpose of this project is to compare structural ceramic materials proposed for use in the air heater of a coal fired high temperature advanced furnace (HITAF) for power generation. This work will provide necessary initial structural ceramic parameters for design of a prototype system. Two teams are currently funded by Pittsburgh Energy Technology Center (PETC) under the Combustion 2000, Phase 1, program to develop such a system. One team is led by the United Technologies Research Center, and the other team is led by Foster Wheeler Development Corporation[1, 2] Proposals for Phase 2 and 3 of the Combustion 2000 are currently under evaluation by DOE. Phase 2 will be engineering development and testing, consisting of subsystem and materials testing, and Phase 3 will consist of the detailed design, construction, operation, and evaluation of a prototype plant. The work presented here consists of evaluation of the mechanical properties of three structural

ceramics at high temperatures in air and a preliminary evaluation of mechanical properties of these structural ceramics after exposure to coal ash.

MATERIALS AND EXPERIMENTAL PROCEDURE

The following properties were measured for use as base line data: (1) Fast fracture strength at room temperature, 1100, and 1400°C; (2) Statistical analysis in the form of a Weibull analysis; (3) Necessary fractography; (4) Slow crack growth properties evaluated by the dynamic fatigue method; and (5) Creep/creep-rupture effects measured through interrupted static fatigue experiments. Initial corrosion experiments were performed in cooperation with the University of North Dakota Energy and Environmental Research Center (UNDEERC), where ORNL performed fast fracture measurements of corroded specimens.

For the mechanical properties measurements three materials have been compared. These are β-SiC from Coors Ceramics Company, NT230 siliconized SiC from Saint-Gobain/Norton and Lanxide DIMOX $SiC_{particulate}/Al_2O_3$ from DuPont Lanxide Composites. β-SiC is sintered silicon carbide with a fine grain structure and high density. NT230 SiC is siliconized silicon carbide and contains free silicon alloy (8 vol%) and some residual porosity. The SiC_p/Al_2O_3 which is manufactured by the Lanxide Direct Oxidation process (DIMOX) contains 48 vol% SiC_p, 38 vol% Al_2O_3 and 13 vol% Al-alloy, and some residual porosity. The SiC ceramics were tested as machined while the Lanxide DIMOX was reoxidized by the manufacturer after machining. For the corrosion studies the β-SiC was replaced (due to limited availability) by an α-SiC from the Carborundum Company, and an experimental grade of the Lanxide DIMOX material which was not reoxidized before the test was included.

The fracture strength of ceramic materials is most commonly measured in four-point flexure.[3] In this test, a specimen of 4x3x50 mm is subjected to bending in a fixture providing an inner span of 20 mm and an outer span of 40 mm. The specimen is loaded to fracture while load and deflection are monitored, and the flexure strength is calculated according to standard beam theory. The high temperature fixtures were SiC fixtures with pins that were free to rotate. The experiments were carried out in the flexure test system (FTS) which is a hydraulic system with SiC push rods in load control. The flexure method offers the possibility of testing a large number of samples at a reasonable cost, and, since the load train arrangement is relatively simple, three specimens may be tested simultaneously in the furnace.

Weibull analysis is the statistical tool most commonly used to analyze fracture data for structural ceramics.[4] Due to the brittle nature of ceramic materials, the fracture strength of a set of specimens may vary as much as 100% from the average strength,

necessitating a statistical analysis of the data. The Weibull modulus, m, and the Weibull scaling factor, σ_0, were obtained by the maximum likelihood method.[5,6]

The term "fatigue" as used for structural ceramics is different from that commonly used for metals. For ceramics the term fatigue is often used to describe the decrease in strength due to the combined action of *static* stress and degrading environment. The mechanism which causes this is known as slow crack growth (SCG) and is the growth of small preexisting cracks or voids at stress levels less than those needed to cause catastrophic failure. This happens because the individual atomic bond strength is decreased by exposure to certain environments. Eventually, a small crack will grow to a size large enough to cause catastrophic failure at a given stress level. In order to predict the lifetime for components in a given environment, the velocity at which cracks grow under a given stress and specific environment must be known.[7, 8]

Flexure creep tests were carried out in four-point bending in fixtures as described above. Two types of tests have been done; static tests at a fixed load for 300 hours and stepped loads of 100 h duration each. The static tests were performed at 1400°C, i.e. the temperature at which creep was observed in the dynamic fatigue experiments, and the loads were chosen such as to correspond to 25% and 70% of the fast fracture strength at that particular temperature. The stepped tests were carried out at 1200, 1300 and 1400°C at loads corresponding to stress levels of 50 MPa, 100 MPa, 150 MPa and so on up to 250 MPa (i.e. 500 h) or to failure. For these tests two of the three stations were loaded with fixtures and specimens while the third station was loaded with a dummy fixture only.

As a first approximation and for comparison between the materials and with previous experiments[9,10] the analysis by Hollenberg et al.[11] was used.

RESULTS AND DISCUSSION

Fast fracture of the unexposed materials as a function of temperature is shown in Fig. 1. The Weibull distributions of the three materials are shown in Figs. 2, 3, and 4 for room temperature, 1100, and 1400°C, respectively. The measured strengths as a function of stressing rate are shown in Figs. 5 and 6 for the three materials at 1100°C and 1400°C, respectively.

NT230 at 1400°C was the only material-temperature combination which showed any strength degradation over time and the SCG parameter n was calculated to be equal to 15.5[12] The Lanxide DIMOX material could only be tested up to stressing rates of 0.01 MPa/s at 1400°C because at the slower stressing rates creep became so pronounced that the four-point flexure fixtures could no longer accommodate the specimens. Also, at the 0.01 MPa/s stressing rate the creep was measurable, so the strength values calculated according to beam theory overestimate the strength of Lanxide DIMOX at this condition.

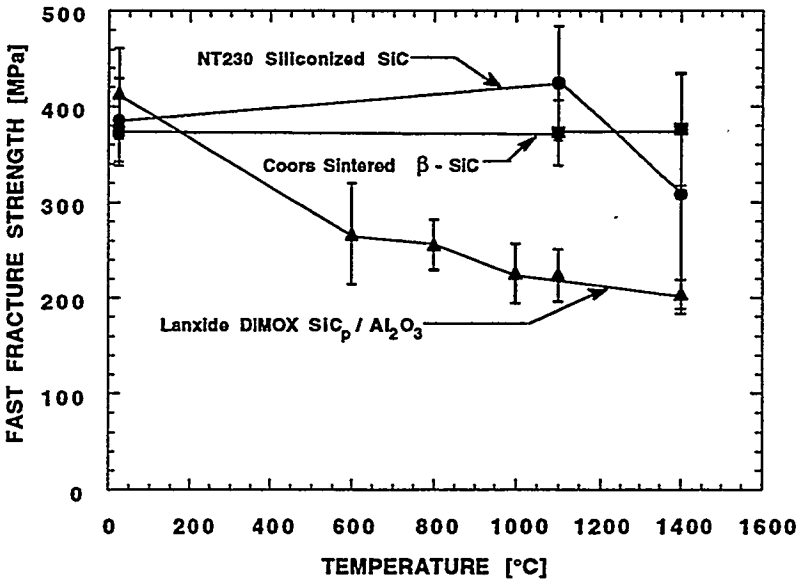

Figure 1. Fast fracture strength as a function of temperature for NT230 SiSiC, sintered β-SiC and Lanxide DIMOX.

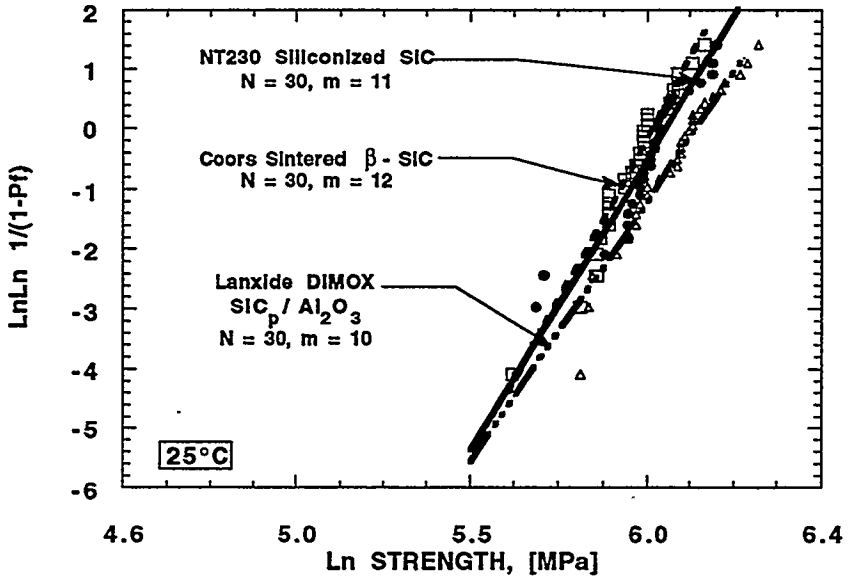

Figure 2. Weibull distribution of the room temperature fast fracture strength for NT230 SiSiC, sintered β-SiC and Lanxide DIMOX.

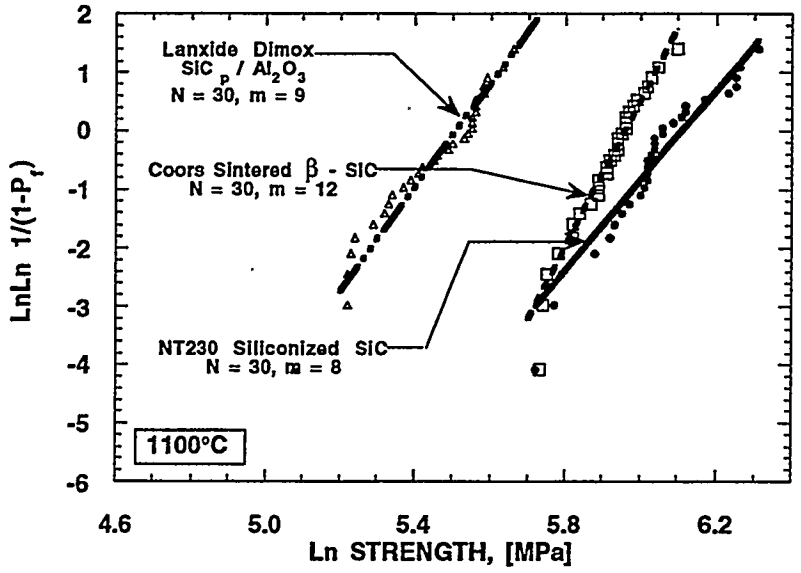

Figure 3. Weibull distribution of the 1100°C fast fracture strength for NT230 SiSiC, sintered β-SiC and Lanxide DIMOX.

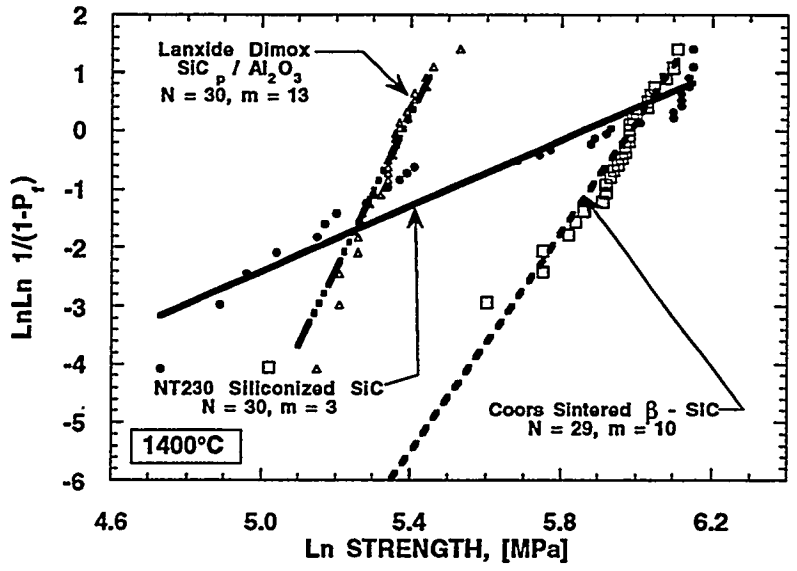

Figure 4. Weibull distribution of the 1400°C fast fracture strength for NT230 SiSiC, sintered β-SiC and Lanxide DIMOX.

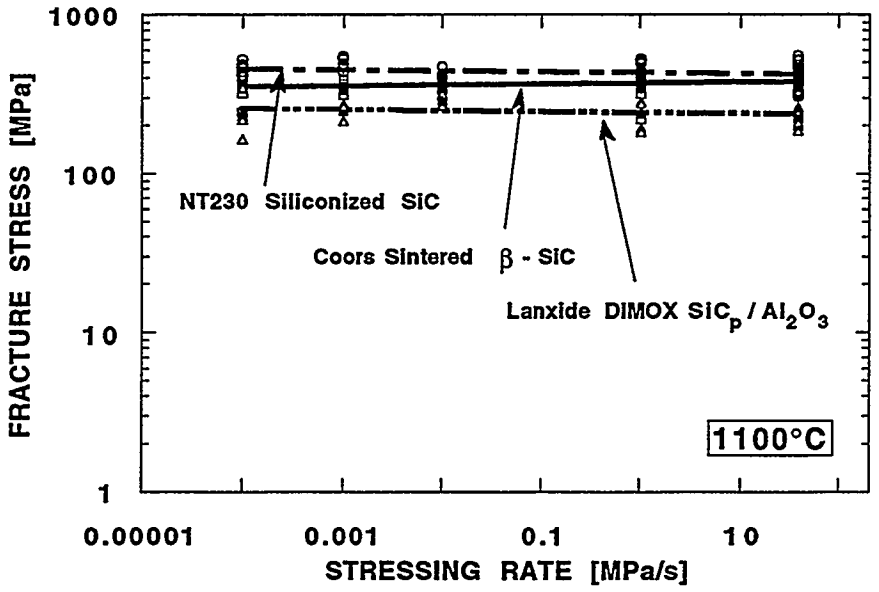

Figure 5. Strength as a function of stressing rate at 1100°C for NT230 SiSiC, sintered β-SiC and Lanxide DIMOX.

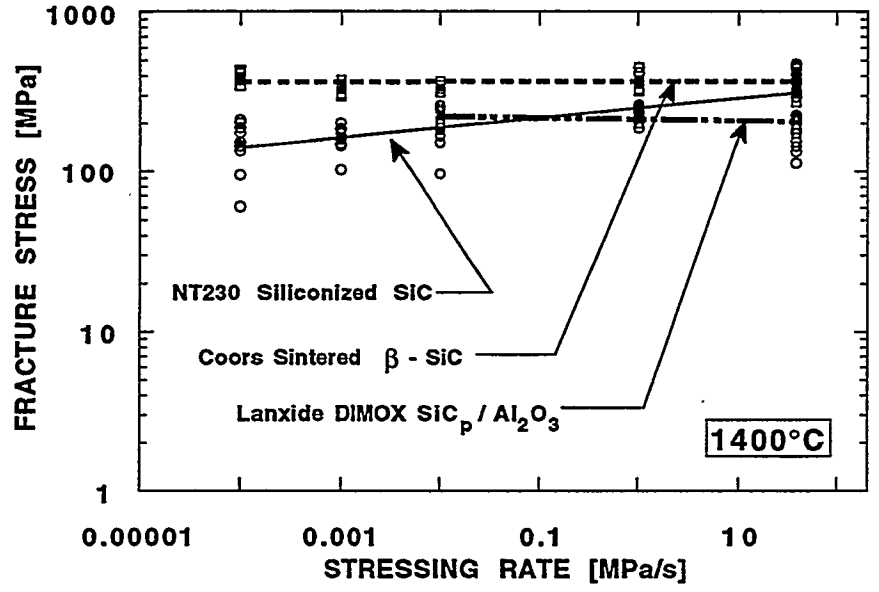

Figure 6. Strength as a function of stressing rate at 1400°C for NT230 SiSiC, sintered β-SiC and Lanxide DIMOX.

The fractography results confirmed the dynamic fatigue results. In general the failure mode for Coors β-SiC was fast fracture from pores in the microstructure, and this did not change as a function of stressing rate or temperature. Lanxide DIMOX failed in general from metal rich areas, but at 1400°C at the slower stressing rates creep became pronounced and the specimens failed due to accumulated creep damage. NT230 was delivered to ORNL in two batches, probably with a slight difference in Si - alloy content or composition. At room temperature and at 1100°C the failure modes for both batches were similar; fast fracture from pores in the microstructure. At 1400°C there was a clear difference between the two batches in the fast fracture test; one batch failing from a combination of pores and metal-rich inclusions, the other failing from pores as was observed at the lower temperatures. At the slower stressing rates where strength degradation was observed, the specimens failed from pore-like cracks (often containing metal-rich inclusions) that had grown in size during the test, and the batch difference became insignificant.

The base line strength of the three ceramics under consideration as a function of temperature was as expected. The Coors β-SiC showed no strength reduction at the temperatures under consideration, while the two other materials exhibit a drop in strength at the temperatures where the metal in these materials softens and melts. The Weibull analyses of the three ceramics reveal some important differences. At room temperature both the Weibull modulus and characteristic strength are comparable for the three materials, as can be seen in Fig. 2. At the elevated temperatures, however, it is seen that the Weibull modulus stays relatively unchanged for Lanxide DIMOX and Coors β-SiC, while for NT230 a gradual reduction of the Weibull modulus is seen. At 1400°C the Weibull modulus was m = 2.8, an unacceptably low value for a structural material. The lower Weibull modulus at 1100 and 1400°C for NT230 is due to the variability in the size of pores in the material and due to the fact that the NT230 was delivered in two batches with slight difference in Si-alloy content or composition. This effect is most pronounced at 1400°C as seen in the fast fracture results. Microstructural and fractographic investigations revealed differences in fracture initiating flaws between the batches, see ref. 12.

The dynamic fatigue experiments, shown in Figs. 3 and 4, show that there is no strength reduction with time at 1100°C for any of the ceramics. At 1400°C a pronounced strength reduction is seen for NT230. This strength reduction is due to the subcritical growth of pore-like cracks, often containing metal rich inclusions.

The stepped load deflection data typically look as shown in Fig. 7, where the load point deflection data corrected for the deflection in the dummy fixture are shown as a function of time for Lanxide DIMOX at 1400°C. As can be seen the creep does not reach a constant rate during the 100 hours, and as can be seen from Fig. 8 a steady state creep rate is not achieved even after 300 h at a constant stress. The deflection rates at the various stress levels were therefore obtained as the slope of the deflection curve towards the end of the 100 h test interval. A thorough description of the creep measurements will be reported elsewhere.[13]

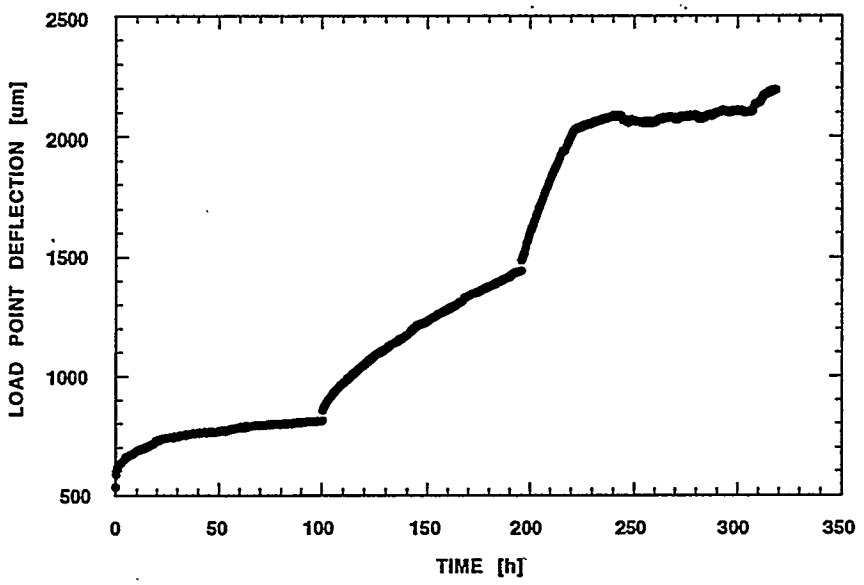

Figure 7. Load point deflection for a Lanxide DIMOX flexure bar stressed for 100 h each in increments of 50 MPa at 1400°C. The flattening out of the curve after approximately 220 h indicates that the specimen reached the bottom of the fixture.

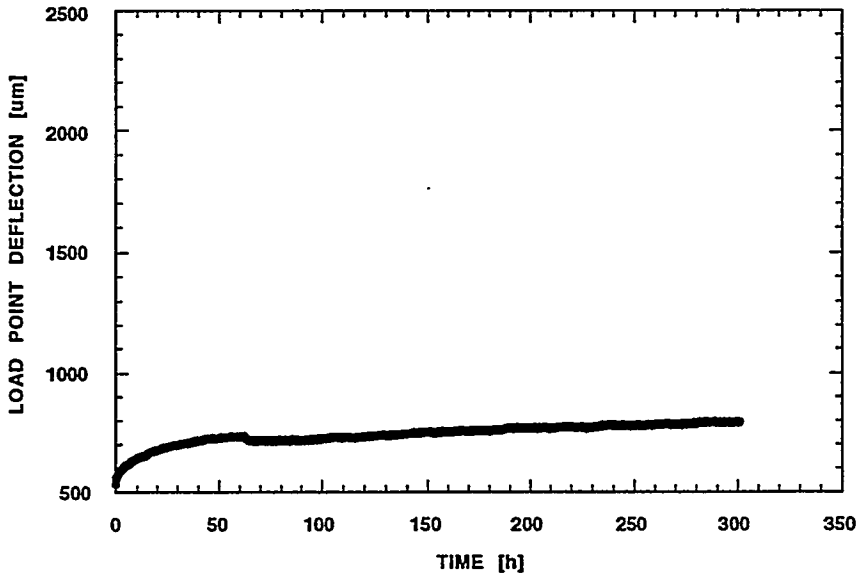

Figure 8. Load point deflection for a Lanxide DIMOX flexure bar stressed at 50 MPa for 300 h at 1400°C.

The materials exposed to coal ash at UNDEERC were fractured at room temperature in four point flexure. The resulting fracture strengths are shown in Fig. 9. The coal ash exposure experiments show several important features. The present experiments were intended as an initial set of conditions to compare several materials, coal slags and temperatures. By exposing the ceramics to static coal slag in a muffle furnace, significantly different levels of corrosion attack were observed, and reduction in strength values was observed for some of the combinations of ceramics, coal ash and temperature. The subsequent fractography showed that the materials which experienced a strength reduction also had a change in failure mode and that the coal ash in some cases produces severe corrosion pits. The material which had strengths that were unaffected by the exposure (Lanxide DIMOX) failed in a similar manner before and after exposure. A thorough discussion of the strength degradation and coal ash corrosion mechanisms can be found elsewhere.[14,15 16]

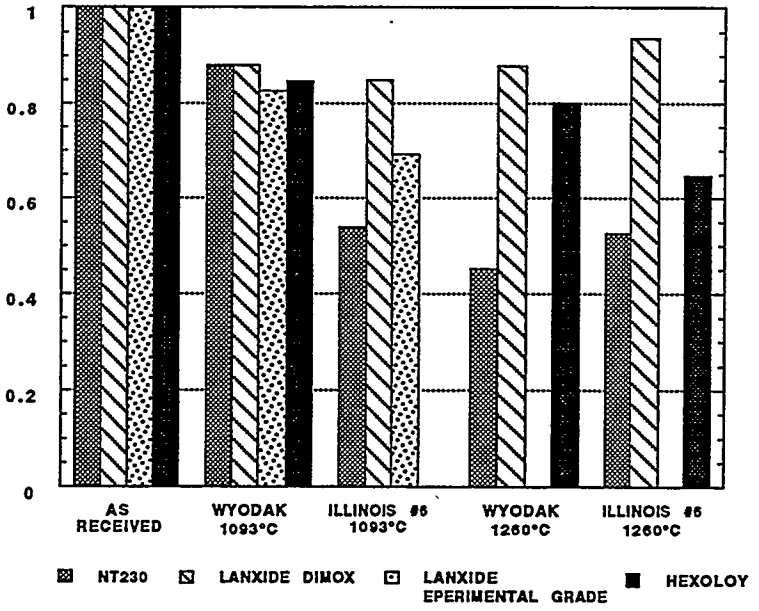

Figure 9. Retained fast fracture flexure strength in percent of the as received strength for specimens tested after exposure to Wyodak and Illinos #6 coal ash at 1093°C and 1260°C.

SUMMARY

The results show that the unexposed Coors β-SiC had good mechanical properties at the two temperatures considered. No SCG was observed during testing

times up to 1000 h at 1400°C. This material was, however, not tested for coal ash corrosion, but the very similar α-SiC showed strength degradation after coal ash exposure. The unexposed Lanxide DIMOX material showed loss of strength at 600°C, and considerable creep was observed at 1400°C. At 1100°C, the material showed no SCG or creep during the dynamic fatigue experiment. The Lanxide DIMOX withstood the corrosive coal ash environment well, and experienced only insignificant loss of strength after 300 h of coal ash exposure. Unexposed NT230 had good mechanical properties at 1100°C with a reasonable strength and no SCG. At 1400°C, however, the ceramic showed loss of strength and SCG. This ceramic was attacked by both coal ashes at both experimental temperatures.

The present results have implications for the proposed application, i.e. high temperature heat exchangers. The creep rates for Lanxide DIMOX at 1400°C are quite high, and in a design where even moderate localized stresses will occur, the components may be out of tolerance in an unacceptably short time. However, at 1200°C both the magnitude of the strain rates and the creep exponent are considerably lower, and this temperature may constitute a possible design temperature for this material. However, in order to ensure a reliable estimation of the life-time of components at this temperature, further measurements will be needed. Creep in tension and compression should be performed, as well as time to failure experiments in tension. It is further necessary to investigate the creep and long time failure mechanisms for the temperatures under consideration. The NT230 SiSiC exhibited improved creep properties compared to similar siliconized silicon carbides.[17,18] Especially at 1200 and 1300°C the material exhibited very little creep. At 1400°C some creep was measured, and further measurements in tension might be warranted also for this material. It is, however, important to keep in mind that the NT230 exhibited SCG at 1400°C, and strength degradation after coal ash exposure. The result may be an unacceptable short lifetime at 1400°C because of this.

Future research needs to concentrate on establishing the properties of the materials under a combined action of stress and environment. The various coal ashes have different viscosities at different temperatures, and temperature regimes must be established in which the combination of mechanical properties and corrosion resistance will give the specific ceramic under consideration an appropriate lifetime.

ACKNOWLEDGMENTS

Research sponsored by the U.S. Department of Energy, Office of Fossil Energy, Pittsburgh Energy Technology Center, Advanced Combustion Technology Program, DOE/FE AA 20 10 00 0, and Advanced Research and Technology Development Materials Program, [DOE/FE AA 15 10 10 0, Work Breakdown Structure Element

ORNL-1(G)] under contract DE-AC05-84OR21400 with Martin Marietta Energy Systems, Inc.

REFERENCES

1. D. J. Seery et al., "Engineering Development of Coal-Fired High -Performance Power Generation Systems," pp 188-195 in Proceedings of the Eighth Annual Coal Preparation, Utilization, and Environmental Control Contractors Conference, U.S. DOE, Pittsburgh Energy Technology Center, Pittsburgh, PA, 1992.

2. J. Shenker, "Development of a High-Performance Coal-Fired Power Generating System with a Pyrolysis Gas and Char-Fired High Temperature Furnace," pp. 183-187 in Proceedings of the Eighth Annual Coal Preparation, Utilization, and Environmental Control Contractors Conference, U.S. DOE, Pittsburgh Energy Technology Center, Pittsburgh, PA, 1992.

3. ASTM C 1161, "Standard Test Method for Flexural Strength of Advanced Ceramics at Ambient Temperature."

4. W. A. Weibull, "A Statistical Theory of the Strength of Materials," Ingeniørsvetenskapsakademien Handlingar, No. 151, Stockholm, Sweden, 1939.

5. W. Nelson, Applied Life Data Analysis, J. Wiley & Son, New York, NY, 1982.

6. K. Breder and V. J. Tennery, "Comparison of the Dynamic Fatigue Behavior of Two Monolithic SiC Ceramics and an Al_2O_3/SiC Composite," to be published in Ceramic Engineering Science Proceedings, **15** [4] 23-31, 1994.

7. S. M Wiederhorn, "Subcritical Crack Growth in Ceramics'" pp. 613-646 in Fracture Mechanics of Ceramics, Vol. 2, R. C. Bradt, D. P. H. Hasselman and F. F. Lange, Eds., Plenum Press, New York, NY, 1974.

8. J. E. Ritter, "Engineering Design and Fatigue Failure of Brittle Materials'" pp. 667-687 in Fracture Mechanics of Ceramics, Vol. 4, R. C. Bradt, D. P. H. Hasselman and F. F. Lange, Eds., Plenum Press, New York, NY, 1978.

9. H. T. Lin and P. F. Becher, "Creep behavior of a SiC-Whisker-Reinforced Alumina," *J. Am. Cer. Soc.* **73** [5] 1398-81 (1990).

10. H. T. Lin and P. F. Becher, "High-Temperature Creep Deformation of Alumina-SiC-Whisker Composites," *J. Am. Cer. Soc.* **74** [8] 1886-93 (1991).

11. G. W. Hollenberg, G. R. Terwilliger, and R. S. Gordon, "Calculation of Stress and Strain in Four-Point Bending creep Tests," *J. Am. Cer. Soc.* **54** [4] 196-99 (1971).

12. K. Breder, "Time-Dependent Strength Degradation of a Siliconized Silicon Carbide Determined by Dynamic Fatigue," accepted for publication in Journal of the American Ceramic Society, 1995.

13. K. Breder and H. T. Lin, "Creep Deformation of an Alumina-Silicon Carbide-Particulate Composite," manuscript in preparation, 1995.

14. T. M. Strobel, J. H. Hurley, "Coal-Slag Corrosion of SiC-Based Ceramics in a Combustion Environment," published in the Proceedings from the Am. Cer. Soc. PAC RIM Meeting, Nov. 1993.

15. T. M. Strobel, J. P. Hurley, K. Breder and J. E. Holowczak, "Coal-Slag Corrosion and Strength Degradation of Silicon Carbide-Alumina Composites," to be published in Ceramic Engineering Science Proceedings, 1994.

16. K. Breder, J. P. Hurley, T. M. Strobel and J. E. Holowczak, "Strength Degradation of Monolithic SiC and Al_2O_3 / SiC Composites After Exposure to Coal Slag," submitted to the Journal of the American Ceramic Society, 1995.

17. T-J. Chuang and S. M. Wiederhorn, "Damage-Enhanced Creep in a Siliconized Silicon Carbide: Mechanics of Deformation," *J. Am. Cer. Soc.* **71** [7] 595-601 (1988).

18. S. M. Wiederhorn, D. E. Roberts, T-J. Chuang, and L Chuck, "Damage-Enhanced Creep in a Siliconized Silicon Carbide: Phenomenology," *J. Am. Cer. Soc.* **71** [7] 602-608 (1988).

FACTORS AFFECTING THE CORROSION RATES OF CERAMICS IN COAL COMBUSTION SYSTEMS

John P. Hurley
Energy & Environmental Research Center
University of North Dakota
PO Box 9018
Grand Forks, ND 58202-9018

ABSTRACT

The concentrations of approximately a dozen elements in the products of coal combustion affect the corrosion rates of ceramics used to construct the combustion system. The elements, including H, O, Na, Mg, Al, Si, P, S, Cl, K, Ca, and Fe, affect corrosion rates in three ways: as primary corrodants of the materials, as secondary corrodants that affect the activities of the primary corrodants, and by affecting the mass transport rate of the primary corrodants. A full factorial study of corrosion rates performed by varying the concentrations of these elements would involve X^n tests, where X is the number of variations of each element and n is the number of different elements. For three variations (low, medium, and high concentrations) of each of 12 elements, the number of tests is 531,441 for a single temperature and pressure condition. The numbers can be reduced with the use of a fractional factorial test matrix, but the most effective way to perform corrosion tests is to base them on realistic system conditions. In this paper, the effects of the composition and physical state of the products of coal combustion on ceramic corrosion rates are given along with suggestions of appropriate test conditions for specific system components.

INTRODUCTION

To increase national energy self-sufficiency for the near future, energy systems will be required to fire low-grade fuels and use more efficient energy cycles than those available today. The coal-fired steam cycle used at present is limited to a maximum steam temperature of 550°C and, thus, a conversion efficiency of 35%. Higher working-fluid temperatures are required to boost efficiency. This means that subsystems will be exposed to much more corrosive environments than those currently used. Problems of special concern are corrosion and fatigue of directly fired turbine blades, corrosion and blinding of hot-gas cleanup filters, and catastrophic failure of high temperature heat exchangers. To prevent those structures from failing will require the use of advanced materials, particularly ceramics, for construction.

Silicon- and alumina-based ceramics are most often considered for the construction of large subsystems because of their relatively low cost and familiarity. However, only a few studies have been performed with the materials in actual coal combustion environments.[1] Testing is made especially difficult because of the complexity of a coal combustion environments and the great variability in coal composition.

In this paper, we describe fuel and operational factors that affect the corrosion rates of structural ceramics in coal-fired combustor systems, with examples of the corrosion of silicon carbide-based materials. We focus in particular on two subsystems, hot-gas particulate filtration and high-temperature heat exchangers. The objective of the paper is not to present specific data on rate factors, but to help the experimentalist measuring these factors to better design their tests.

FACTORS AFFECTING THE COMPOSITION OF ASH DEPOSITS

All surfaces of a coal-fired combustor upstream of particulate removal systems are quickly covered with ash. The composition of the ash deposits depends on the composition of the coal, the mechanisms of ash deposition, and the temperature of the deposits.

Coal-Related Factors

Coal is composed primarily of carbon, lesser amounts of heteroatoms such as hydrogen, oxygen, sulfur, and nitrogen, and ash-forming constituents such as mineral matter and organically associated alkali and alkaline-earth cations. The quantity and form of the major elements in the coal are determined by the depositional environment of the original coal-forming plants, and the interaction of the buried material with groundwater both before and after coalification.

Coals from the eastern United States are typically high-rank coals that form ash from microscopically observable mineral grains. The most prevalent minerals in U.S. coals are quartz (SiO_2), kaolinite ($Al_2Si_2O_5[OH]_4$) and other aluminosilicate clays such as montmorillonite ($[Al,Mg]_8[Si_4O_{10}]_3[OH]_{10}\cdot 12H_2O$) and illite ($KAl_5Si_7O_{20}[OH]_4$), and pyrite ($FeS_2$). These minerals are rich in silicon, aluminum, and iron, so the coal ashes are alkaline. Coals from the western United States also contain these minerals, but they are primarily lower-rank coals that have undergone less lithification than the eastern coals and so contain much more oxygen in their organic structures. The oxygen is commonly present in carboxylic acid functional groups. During interaction with groundwater, these acids can undergo ion exchange to fix sodium, potassium, magnesium, and calcium in an atomically disbursed form within the organic structure. The addition of the alkali metal and alkaline-earth elements to the ash make it much more alkaline than eastern coal ash.

Because of the large range of depositional environments, degrees of coalification, and interactions with groundwater, U.S. coal ashes have a wide range of compositions. Table 1 shows the range as given in a standard text on coal-fired energy systems[2]. This wide range of coal ash compositions requires the materials experimentalist to consider specific coals that may be used in the energy system of interest.

Table 1. Coal-Ash Chemical Composition Ranges

Oxide Component	Percentage
SiO_2	10–70
Al_2O_3	8–38
Fe_2O_3	2–50
CaO	0.5–30
MgO	0.3–8
Na_2O	0.1–8
K_2O	0.1–3
SO_3	0.1–30

Factors Related to Ash Deposition Mechanisms

In addition to the type of coal that may be used in the energy system, the experimentalist must consider which fractions of the ash will come in contact with the ceramic. This information is best obtained experimentally, although approximations can be made based on extensive testing performed at utility boilers. During combustion of the coal, the minerals can vaporize, fragment, or coalesce depending on the initial association of the mineral with the coal, on the temperature and gas composition of the local combustion environment, and on the morphology of the original mineral grains. In general, mineral grains that are included within coal particles will experience temperatures 200°–300°C higher and much more reducing environments than the excluded mineral grains that were separated from the carbonaceous particles during processing. The included minerals commonly fuse with other mineral grains in the particle to form larger, much more compositionally complex ash particles. The excluded mineral grains are much less likely to interact with other mineral grains and will experience lower temperatures and more oxidizing atmospheres than the included mineral grains. In such situations, they may be much more likely to fragment to form smaller ash particles than the original mineral.

In contrast to the mineral grains, the organically associated elements vaporize during combustion and become extremely reactive. The alkaline-earth elements rapidly oxidize to form submicron ash particles on the surface of the burning char particle. These can be shed as oxide particles or coalesce with quartz- and clay-derived ash to form complex aluminosilicates[3,4]. In contrast, the vaporized alkali metals exist as gaseous sulfates, hydroxides, and chlorides that can condense far downstream of the fireball. The vaporization and subsequent condensation of the organically associated elements causes them to concentrate in smaller ash particles.

The size and composition interdependence in the ash means that the composition of the ash depositing on and possibly corroding the material of interest depends on the local gas flow

conditions. If the object of interest is a tube placed directly in the gas flow, then larger ash particles will separate from the gas flow and strike the tube as they diverge around it, while the smaller ash will stay entrained with the gas. Figure 1 illustrates this concept. It compares the compositions of an ash deposit formed at 2100°F on the upstream side of a steam tube with four aerodynamic size-ranges of particulate ash collected from the boiler at the same location as the deposit. The boiler was firing a high-calcium subbituminous coal at the time. The bulk composition of deposit shows that it is formed primarily from particles with aerodynamic diameters of over 10 μm. The most striking variations in elemental concentration versus ash particle size occur for silicon and calcium. The average concentration of silicon in the ash particles is directly related to particle size whereas the average concentration of calcium is inversely related. This characteristic of the ash is typical of most high-calcium U.S. coals.

Figure 2 shows the compositions of another type of ash deposit along with aerodynamically sized ash collected in the vicinity. This type of deposit also forms on the upstream sides of steam tubes when firing high-calcium coals but forms at temperatures below approximately 1700°F. A comparison of the compositions shows that these deposits form predominantly from particles with aerodynamic diameters below 3 μm and so are much enriched in calcium and depleted in silicon. Materials prone to calcium corrosion would be much more severely attacked by this type of deposit than by the first. In addition, Figure 2 shows that the deposit contains a high level of sulfur, and that the sulfur condenses after ash deposition. The sulfur also can be quite corrosive, especially to alloys.

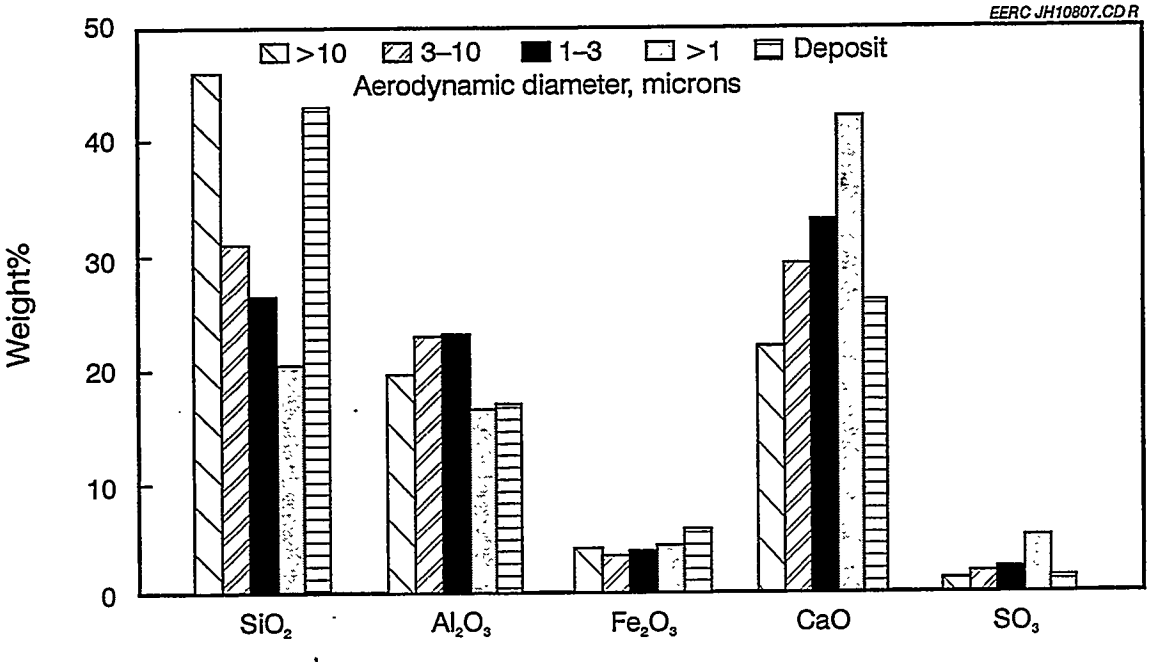

Fig. 1. Comparison of the compositions (SO_3-free) of the aerodynamically sized entrained ash particles and a conventional fouling deposit.

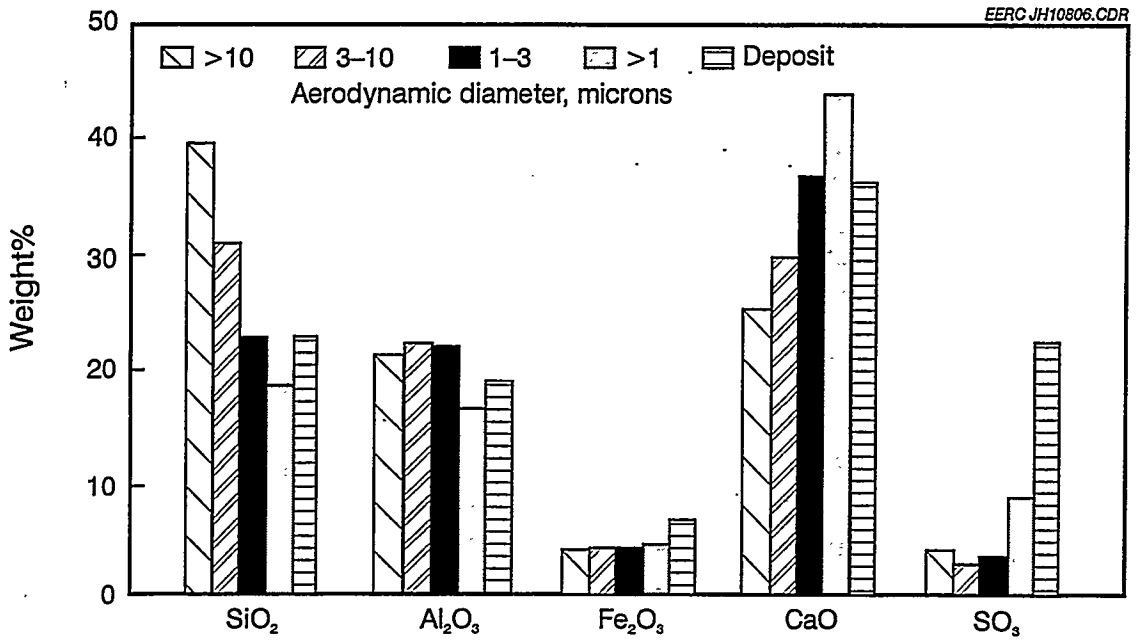

Fig. 2. Comparison of the compositions (SO_3-free) of the aerodynamically sized entrained ash particles and an upstream enamel deposit.

Factors Related to the Temperature of the Material

The temperature of the subsystem of interest affects both the composition of the ash deposit on its surface and the physical nature of the deposit. Figure 3 shows the concentrations of silicon, calcium, and sulfur in ash deposits collected from steam tubes in a boiler firing a high-calcium coal. It shows that the sulfur concentration in the deposits increases dramatically at temperatures below 2000°F. Laboratory experiments show that the mechanism of increase is chemical vapor deposition caused by the conversion of calcium in aluminosilicates to calcium sulfate below 1900°F. Figure 4 shows the concentrations of sodium, potassium, and phosphorus in the same deposits. They also increase significantly, but not as much as that of the sulfur. The sodium concentration increases primarily through physical vapor deposition, or condensation, of sodium sulfate. This indicates that materials cooled to below approximately 1900°F will be especially subjected to alkali sulfate corrosion. This situation may be especially prevalent for heat exchangers operating at gas temperatures above 1900°F but surface temperatures below that; however, depending on the local gas flow characteristics, the material can be rapidly covered with ash and, thus, protected from this type of corrosion. Hot-gas cleanup filters may also experience this type of corrosion if most of the larger ash is efficiently removed by upstream cyclones. Heat exchangers producing working fluids with temperatures above 1900°F would not be expected to experience this type of corrosion.

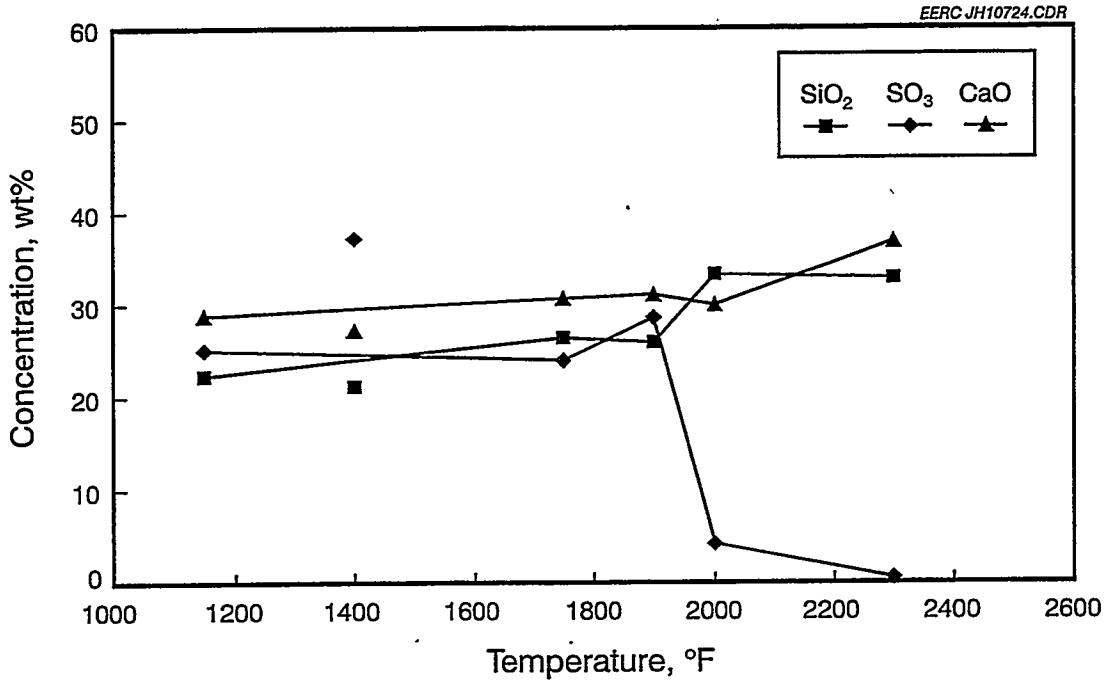

Fig. 3. Temperature-dependent concentrations of silicon, sulfur, and calcium (reported as oxides) in deposits collected from the convective pass of a pulverized coal-fired utility boiler burning a subbituminous coal from the western United States.

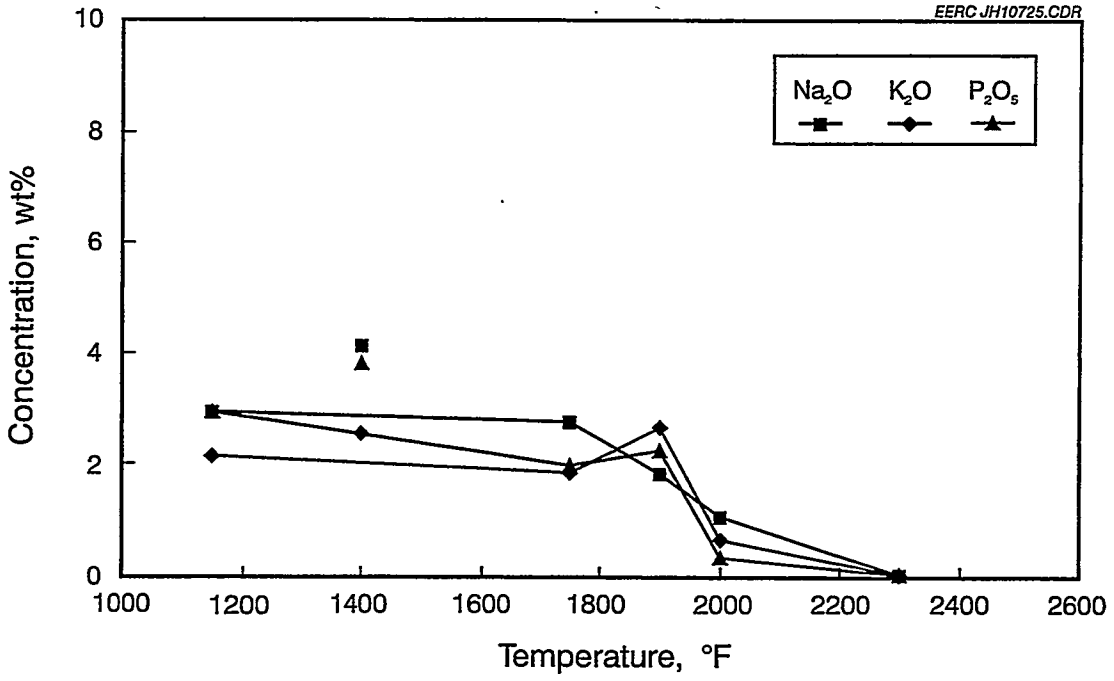

Fig. 4. Temperature-dependent concentrations of sodium, potassium and phosphorus (reported as oxides) in deposits collected from the convective pass of a pulverized coal-fired utility boiler burning a subbituminous coal from the western United States.

In addition to affecting the composition of the deposits, temperature will affect the physical nature of the deposits. Figure 5 shows a viscosity-versus-temperature plot for fused slag formed in a boiler burning Illinois No. 6 bituminous coal to which limestone has been added to reduce the viscosity of the slag. The measurements were made in air and in a reducing environment in the presence of 10% water vapor. It shows that, at temperatures above 2500°F, the slag has a viscosity below 250 poise and will flow well and can, therefore, be very erosive as well as corrosive. However, the flow of the slag is expected to result in a uniform recession rate of the surface, instead of pitts. Other measurements have shown that this type of slag can be liquid down to at least 2300°F[5]. Although much less erosive than the higher-temperature slags, these liquid slags are still able to dissolve the protective oxide scale on most ceramic materials, causing the corrosion rate to be linear rather than parabolic with time.

Figure 6 is a scanning electron micrograph of a cross section of Hexoloy SA silicon carbide exposed to a nonlimestone-doped Illinois No. 6 slag at 2300°F in a static slag corrosion test performed in air[5]. The bright spheres are composed of iron silicide that are often found near pits in the silicon carbide. In such cases, the protective silica layer is dissolved into the slag, and the pitting may weaken the material, although the recession rate is reduced as compared to higher-temperature slag corrosion. At still lower temperatures, the ash may sinter but does not dissolve the protective oxide layer. Figure 7 is a scanning electron micrograph of the interface between

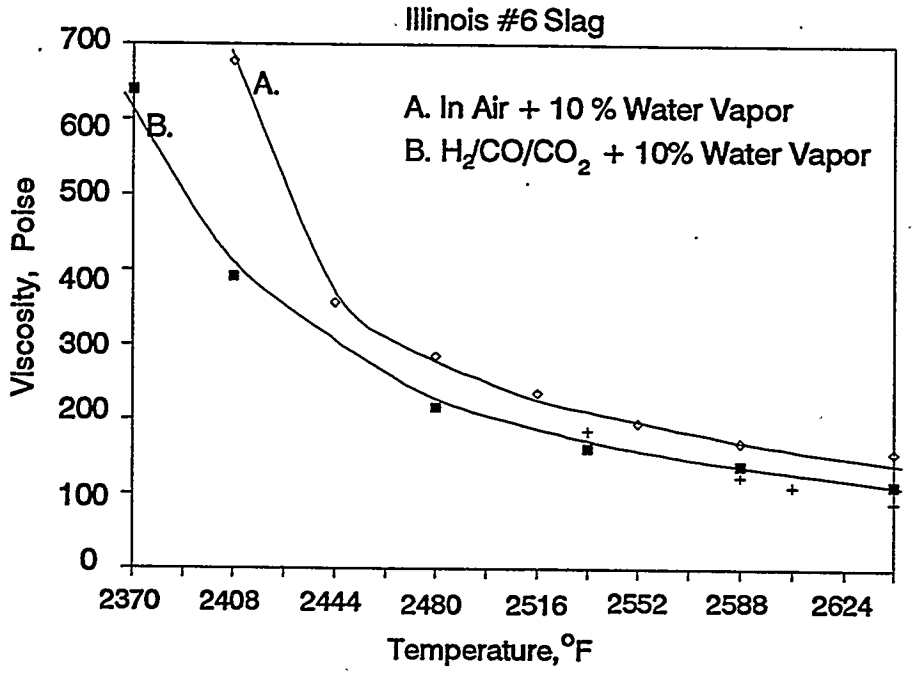

Fig. 5. Viscosity-versus-temperature plot for a slag produced in a boiler firing Illinois No. 6 bituminous coal to which limestone had been added to reduce slag viscosity.

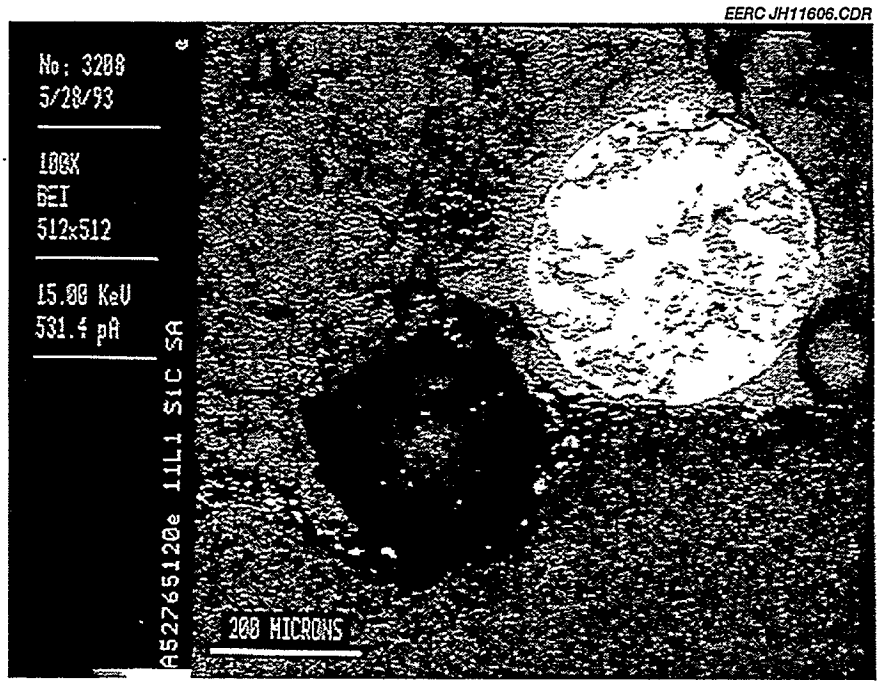

Fig. 6. Scanning electron micrograph of a cross section of Hexoloy SA silicon carbide (bottom) exposed to Illinois No. 6 slag at (top) 2300°F in a static slag corrosion test in air.

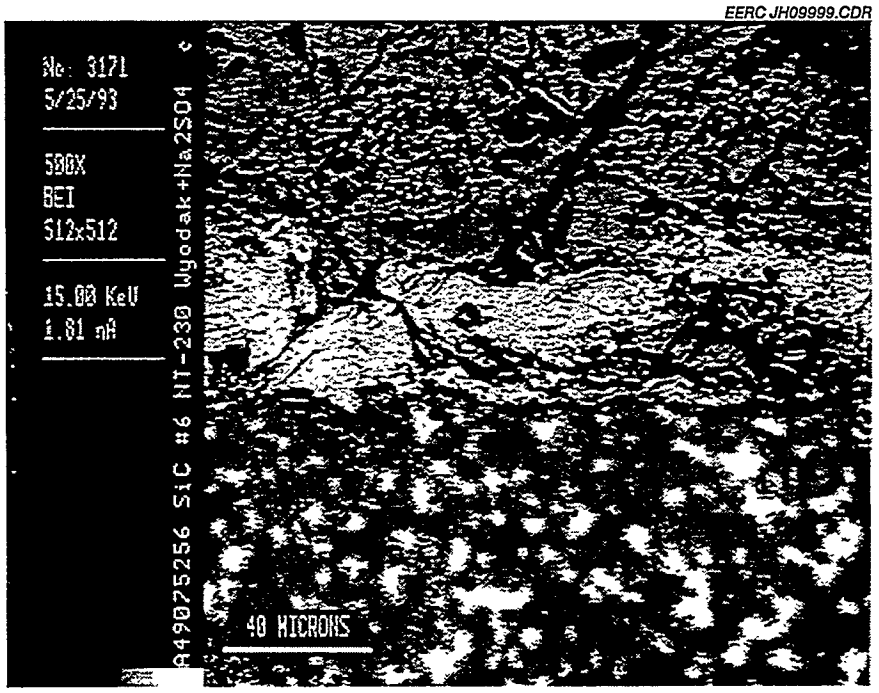

Fig. 7. Scanning electron micrograph of the interface between siliconized silicon carbide (bottom) and a high-calcium ash doped with excess sodium sulfate (top) reacted at 1790°F.

siliconized silicon carbide and a high-calcium ash doped with excess sodium sulfate reacted at 1790°F. These conditions simulate a situation in which a heat exchanger may be protected from the bulk of ash deposition by a slag screen but still exposed to fine ash and sodium sulfate condensation[6]. SEM analyses show that the scale is composed of calcium and magnesium silicate. Only very low levels of sodium could be measured in the scale, but similar experiments made without the condensed sodium sulfate (but with the vapor) show that the oxidation rate of the material is greatly increased by the presence of the sodium. Sodium silicate does not form extensively, because it is not stable as a silicate in the presence of aluminosilicate ash.

THE EFFECTS OF SPECIFIC ELEMENTS IN THE CORROSION OF SILICON-BASED CERAMICS

Approximately a dozen inorganic elements in the products of coal combustion affect the corrosion rates of silicon-based ceramics used to construct subsystems. The elements, including H, O, Na, Mg, Al, Si, P, S, Cl, K, Ca, and Fe, affect corrosion rates in three main ways: as primary corrodants that form reaction products with the material; as secondary corrodants that affect the activity of the primary corrodants; or by affecting the rate of mass transfer of the primary corrodants. Although many of the elements participate as more than one type of corrodant, they are listed here under what we believe is the most active role.

The primary corrodants of silicon-based ceramics in coal-fired combustion systems include O, Mg, Ca, and Fe. These elements form silicates or silicides that are stable in the presence of the other constituents of the ash in contact with the ceramic surface. Examples of their corrosion products are shown in Figures 6 and 7. When ash is not present, such as the interior or down stream of a particulate removal device like a filter, a vapor-phase sodium can also be a primary corrodant of silicate ceramics, forming a sodium silicate reaction layer through which oxygen can more rapidly diffuse than through a pure silica layer[7].

In contrast to the primary corrodants, the secondary corrodants have not been observed in EERC tests to form corrosion products with silica- or alumina-based ceramics in the presence of coal ash. They are known, however, to affect the activities of some of the primary corrodants. The elements mainly having this role are H, Al, S, and Cl. Hydrogen, along with the carbonaceous part of the fuel, is most important in gasification conditions because it affects the concentration of O, and in combustion conditions, it helps to form volatile hydroxides such as $Si(OH)_4$ or NaOH which will affect corrosion rates when no other ash is present. Similarly, S and Cl affect the vapor-phase concentrations of Na_2SO_4 and NaCl, which will affect corrosion rates when ash is not present.[8] In addition, Al affects the activity of Na, Mg, and Ca. Since these elements are more stable in an aluminosilicate condensed phase than in a silicate corrosion product, they are less corrosive to silicate ceramics when aluminum is present in the ash.

Finally, the major role of several other major elements is in their effects on the rate of transport of the primary corrodants. These elements include Na, Si, P, and K. They are most important in their effect on the viscosity of a melt, as well as on the rate of ion diffusion in a glass. They have not been observed to form corrosion products except in minor roles.

Because the concentrations of many of these elements affect the activities of the primary corrodants, the surest experimental design to determine all of the interdependencies is the full factorial matrix, where the concentration of each element in the system is varied dependently on the others. However, the number of tests in such a matrix would involve X^n tests, where X is the number of variations of each element, and n is the number of different elements. For three variations (low, medium, and high concentrations) of each of 12 elements, the number of tests is 531,441 for a single temperature and pressure condition. The numbers can be partially reduced with the use of a fractional factorial test matrix, but the most cost-effective way to perform corrosion tests is to base them on realistic system conditions.

The best method to obtain appropriate test conditions is to expose the material in an operating combustor system. This can be expensive as a 100-hour pilot-scale combustor test may cost $50,000. As the scale of the test is reduced, so are the costs, but the accuracy of the conditions may also be compromised. To improve the accuracy of laboratory-scale test conditions, the EERC has been funded under a project entitled "Support Services for Ceramic Fiber-Ceramic Matrix Composites," administered under the Advanced Research and Technology Development (AR&TD) Materials Program at Oak Ridge National Laboratory, to assemble 55-gallon drums of coal ash and slag from four utility power plants. Quantities of each of these ashes will be supplied to any materials researcher for their testing at no charge to the researcher.

The samples were gathered by utility plant workers from areas of the power systems where they best simulate the state of the ash in contact with two types of possible ceramic subsystems. For testing of materials used in hot-gas filter systems, ash was provided by the American Electric Power Company Tidd plant from the Westinghouse Advanced Particle Filter while firing a Pittsburgh No. 8 coal and using a dolomite sorbent. Suggested conditions for such testing are 1650°F (although many other researchers do not use temperatures above 1550°F) in 15% CO_2, 15% H_2O, 3% O_2, 0.5% SO_2, 0.05% HCl, and 10 ppm NaCl, with a balance of N_2. The concentrations of HCl, SO_2, and NaCl were chosen to approximate high-end partial pressures for pressurized fluidized-bed reactors[9,10]. The correct partial pressures of the other gases cannot be produced in an atmospheric test, so we use the approximate relative concentrations of those species. This ash can also be used to test heat-exchanger materials that will operate in a pressurized fluidized-bed combustor downstream of a particulate removal device at temperatures below the sulfation temperature of the ash (approximately 1900°F), although it may be necessary to condition the ash to more appropriate gas concentrations before the start of the exposure.

To simulate the type of ash that will strike a high-temperature heat exchanger upstream of ash removal devices, slags were gathered from the taps of three cyclone-fired boilers. Subbituminous coal slag was provided by the Northern States Power Company Riverside plant, which was burning a coal from the Powder River Basin in Wyoming. Illinois No. 6 bituminous coal slag was provided by the Central Illinois Public Service Coffeen plant. Our analyses showed abnormally high calcium concentrations in this slag due to limestone additions to the coal to reduce slag viscosity. Therefore, another drum of Illinois No. 6 slag was provided by the Illinois Power Company Baldwin plant. Suggested initial conditions for slag testing are 1090°C for sintered ash conditions, 1260°C for viscous molten ash, and 1430°C for runny molten ash. We have run all of our tests in air, although viscosity tests show that water vapor may significantly affect slag viscosity and perhaps should be included at a level of about 15%. We are still investigating this

effect. The slag layer thickness should be approximately 3–5 millimeters to ensure appropriate oxygen transport. The compositions of the ashes are shown in Table 2.

SUMMARY

For a given temperature, the rate of corrosion of ceramic materials in advanced coal-fired energy systems is affected by the composition of the gas and condensed species in contact with the material. These compositions are dependent on the fuel (and sorbent in a fluidized-bed system) which determines that species will be present, the temperature of the material which determines whether vaporized species will have condensed and whether the ash is molten, and the local gas flow conditions which determine the size range of ash depositing and, therefore, the composition of the ash. Approximately 12 elements affect the corrosion rates of silicon-based ceramics. Oxygen, Mg, Ca, Fe, and Na (when no ash is present) are primary corrodants in that they have been observed to form corrosion products with silicon carbides. Secondary corrodants—H, Al, S, and Cl—have not been observed to form primary corrosion products under coal combustion conditions but do affect the activity of the primary corrodants. The other major elements, including Na, Si, P, and K, affect the rate of transport of the primary corrodants by affecting slag viscosity and ion mobility.

To improve the accuracy of laboratory-scale test conditions, the EERC has assembled 55-gallon drums of coal ash and slag from four utility power plants, which will be provided free of charge to investigators. The samples were gathered by utility plant workers from areas of the power systems where they best simulate the state of the ash in contact with two types of possible ceramic subsystems. For testing of materials used in hot-gas filter systems, ash from such a system is available. Suggested conditions for such testing are 1650°F (although many other researchers do not use temperatures above 1550°F) in 15% CO_2, 15% H_2O, 3% O_2, 0.5% SO_2, 0.05% HCl, and 10 ppm NaCl, with a balance of N_2.

Table 2. Chemical Compositions of Standard Ashes

Oxide, wt%	Tidd	Riverside	Coffeen	Baldwin
SiO_2	24.1	47.0	52.5	53.4
Al_2O_3	7.7	18.6	16.3	18.6
Fe_2O_3	6.4	5.3	13.5	17.6
TiO_2	0.3	1.4	0.7	0.7
P_2O_5	0.2	0.6	0.2	0.0
CaO	28.8	19.7	13.1	7.1
MgO	16.2	5.7	1.2	0.9
Na_2O	0.2	0.9	0.8	0.0
K_2O	0.8	0.3	1.6	1.7
SO_3	15.2	0.3	0.1	0.0

To simulate the type of ash that will strike a high-temperature heat exchanger upstream of ash removal devices, slags are available from three cyclone-fired boilers. Suggested initial conditions for slag testing are for sintered ash conditions, 2300°F for viscous molten ash, and 2600°F for runny molten ash. We have run all of our tests in air, although viscosity tests show that water vapor may significantly affect slag viscosity and perhaps should be included at a level of about 15%. The slag layer thickness should be approximately 3–5 millimeters to assure appropriate oxygen transport.

REFERENCES

1. Ferber, M.K.; Tennery, V.J. "Behavior of Tubular Ceramic Heat Exchanger Materials in Acidic Coal Ash from Coal–Oil Mixture Combustion," *Ceram. Bull.* **1983**, *62* (2), 236–243.

2. Ferber, M.K.; Tennery, V.J. "Behavior of Tubular Ceramic Heat Exchanger Materials in Basic Coal Ash from Coal–Oil Mixture Combustion," *Ceram. Bull.* **1984**, *63* (7), 898–904.

3. Combustion Engineering Inc. *Combustion*, 3rd ed.; Rand McNally: Chicago, 1981; pp 35–57.

4. Hurley, J.P.; Schobert, H.H. "Ash Formation During Pulverized Subbituminous Coal Combustion, 1. Characterization of Coals and Inorganic Transformations During Early Stages of Burnout," *Energy & Fuels* **1992**, *6* (1), 47–58.

5. Hurley, J.P.; Schobert, H.H. "Ash Formation During Pulverized Subbituminous Coal Combustion, 2. Inorganic Transformations During Middle and Late Stages of Burnout," *Energy & Fuels* **1993**, *7*, 542–553.

6. Walsh, P.M.; Sayre, A.N.; Loehden, D.O.; Monroe, L.S.; Beér, J.M.; Sarofim, A.F. *Prog. Energy Combust. Sci.* **1990**, *16*, 327–346.

7. Benson, S.A.; Jones, M.L.; Harb, J.H. "Ash Formation and Deposition," In *Fundamentals of Coal Combustion for Clean and Efficient Use*; Smoot D., Ed.; Elsevier: Amsterdam, 1993; 299.

8. Baxter, L.L.; DeSollar, R.W. *Fuel* **1993**, *72*, 1411.

9. Wibberley, L.J.; Wall, T.F. *Fuel* **1982**, *61*, 93–99.

10. Hurley, J.P.; Benson, S.A.; Erickson, T.A.; Allan, S.E.; Bieber, J. *Project Calcium Final Report*, DOE/MC/10637-3292, 1995.

11. Strobel, T.M.; Hurley, J.P.; Senior, C.L.; Holowczak, J.E. "Coal Slag Corrosion of Silicon Carbide-Based Ceramics in a Combustion Environment," *In* Proceedings of the Symposium on Silicon Carbide-Based Structural Ceramics; American Ceramic Society PAC RIM Meeting, Honolulu, HI, Nov. 7–10, 1993, pp 327–334.

12. Strobel, T.M.; Hurley, J.P.; Breder, K.; Holowczak, J.E. "Coal Slag Corrosion and Strength Degradation of Silicon Carbide–Alumina Composites," *Ceramics Engineering & Science Proceedings* **1994**, *15*(4), 579–586.

13. Senior, C.L.; Moniz, G.A.; Hurley, J.P.; Strobel, T.M. "Corrosion of Silicon Carbides by Ash and Vapor in a Coal Combustion Environment," *In* Proceedings of the Symposium on Silicon Carbide-Based Structural Ceramics; American Ceramic Society PAC RIM Meeting, Honolulu, HI, Nov. 7–10, 1993, pp 335–342.

14. Zheng, Z., Tressler, R.E.; Spear, K.E. "A Comparison of the Oxidation of Sodium Implanted CVD Si_3N_4 With the Oxidation of Sodium-Implanted SiC Crystals" *Corrosion Science* **1992**, *33* (4), 569–580.

15. Mann, M.D.; Swanson, M.L.; Yagla, S.L. "Characterization of Alkali and Sulfur Sorbents for Pressurized Fluidized-Bed Combustion" *In* Proceedings of the 13th International Fluid Bed Conference, ASME, 1995.

CORROSION PERFORMANCE OF MATERIALS FOR ADVANCED COMBUSTION SYSTEMS*

K. Natesan
Argonne National Laboratory
Argonne, IL 60439

and

M. Freeman and M. Mathur
Pittsburgh Energy Technology Center
Pittsburgh, PA 15236

ABSTRACT

Conceptual designs of advanced combustion systems that utilize coal as a feedstock require high-temperature furnaces and heat transfer surfaces capable of operating at much higher temperatures than those in current coal-fired power plants. The combination of elevated temperatures and hostile combustion environments requires development and application of advanced ceramic materials for heat exchangers in these designs. This paper characterizes the chemistry of coal-fired combustion environments over the wide temperature range of interest in these systems and discusses some of the experimental results for several materials obtained from laboratory tests and from exposures in a pilot-scale facility.

INTRODUCTION

Coal is a complex and relatively dirty fuel that contains varying amounts of sulfur and a substantial fraction of noncombustible mineral constituents, commonly called ash. Recently, the U.S. Department of Energy has embarked on programs to develop coal-fired boilers with advanced steam cycles, fluidized-bed combustion cogeneration systems, high-performance power system (HIPPS), and a low-emission boiler system (LEBS). Conceptual designs of advanced combustion systems that utilize coal as a feedstock require high-temperature furnaces and heat transfer surfaces capable of operating at higher temperatures than those used in current coal-fired power plants. The combination of elevated temperatures and hostile combustion environments necessitates the use of ceramic materials at least in the first few passes of the heat exchangers in these designs.

The HIPPS would employ a combined cycle that uses a gas turbine driven by a working fluid (air) that is separately heated in a high-temperature advanced furnace, in addition to conventional steam turbines.[1] The ultimate goal is to produce electricity from coal with an overall thermal efficiency of 47% or higher (compared with ≈35% for current systems) and to reduce CO_2 emissions by 25 to 30%. The targeted requirements for an HIPPS system are:

---

*Work supported by the U.S. Department of Energy, Office of Fossil Energy, Advanced Research and Technology Development Materials Program, Work Breakdown Structure Element ANL–4, under Contract W–31–109–Eng–38.

- A minimum conversion efficiency of 47%.
- NO_X < 0.06 lb (as NO_2) per million Btu of fuel input.
- SO_X < 0.06 lb (as SO_2) per million Btu of fuel input.
- Particulates < 0.003 lb per million Btu of fuel input.
- All solid waste streams must be benign.
- Initially, fuels will be coal and natural gas, with coal providing at least 65% of heat input and ultimately increasing to 95%.
- The commercial plant will have a 65% annual capacity factor and generate electricity at a 10% lower (than present) cost.

The pulverized-coal high-temperature advanced furnace (HITAF) in the HIPPS concept will heat air to an intermediate temperature of ≈1000°C and burn supplemental clean fuel to boost the temperature of air to the turbine inlet temperature of ≥1300°C. Use of supplemental fuel can be reduced as the HITAF technology evolves to permit air to be heated to higher temperatures in the furnace. HITAF represents a major departure from conventional pulverized-coal-fired boilers in which only steam is raised to a maximum of 530-620°C. The purpose of the HITAF is to heat the clean working fluid – air – to the required turbine inlet temperatures. At the elevated temperatures of the HITAF, transfer of heat from the combustion gases to the working fluid will be dominated by radiative heat transfer, and the design of the heat transfer surface will be critical for success of the system. Several concepts are under development for the design of the heat transfer surfaces in the HITAF system. The concept proposed by the Foster Wheeler Development Corporation uses a pyrolysis process to convert the coal into low-Btu fuel gas and char.[2] The cleaned fuel gas is burned in areas of the HITAF where ash deposition could be a problem. The concept proposed by the United Technologies Research Center uses a combustor with a controlled fuel distribution/long axial flame in which the heat release is stretched out, allowing for progressive heat removal.[3] The compressed air is heated to 700°C in a convective air heater and then to 1000°C in a radiative air heater. A protective refractory layer on the fire side of the radiant air heater prevents corrosion of air passages by ash and slag, which inevitably will be deposited on the heat transfer surface. This concept also involves heating of the air with supplemental natural gas firing to achieve a 1300°C turbine inlet temperature.

Irrespective of which of these (or any other) concepts becomes viable for a commercial-scale HIPPS, it is evident that the heat transfer surfaces will be exposed to much higher temperatures than are prevalent in conventional coal-fired steam-turbine systems. For temperatures in the range of 1000-1300°C, conventional metallic materials do not possess adequate strength properties and/or corrosion resistance for long-term service. In addition, an important difference between the conventional boiler system and the HIPPS is seen in the chemical and physical characteristics of the ash layers that can deposit on the heat transfer surfaces. The deposits are likely to be dominated by alkali sulfates and coal slags in HIPPS rather than by pyrosulfates or alkali-iron-trisulfates (which are prevalent in conventional pulverized coal-fired boilers) and by the increased mobility of corrosion-accelerating agents in the deposit layers due to the much higher temperature of the heat transfer surfaces in HIPPS. A major challenge is to develop methods to combat severe deposition, erosion,

and corrosion (DEC) of heat transfer surfaces exposed to higher-than-normal temperatures. These methods could include fuel selection, cleaning of aggressive contaminants from coal, fine grinding of coal, use of additives, and selection of advanced corrosion-resistant ceramic materials, coatings, and advanced alloys for vulnerable heat transfer sections.

The objectives of the present program are to evaluate (a) the chemistry of gaseous and condensed products that arise in combustion of coal and (b) candidate materials for application in the combustion environments. Chemistry calculations determine the types and amounts of combustion products over the wide temperature range of 700-1700°C and at 1 atm pressure. The experimental program on heat exchanger materials will develop mechanistic information on the roles of material composition, ash constituents, combustion deposits, chlorine, alkali sulfates, and sulfur sorbents in the corrosion process. The program emphasizes corrosion evaluation of materials in air, salt, and coal/ash environments at temperatures between 1000 and 1400°C, as well as measurement of residual fracture properties of the materials after corrosion. Coal/ash chemistries synthesized on the basis of thermodynamic/kinetic calculations, together with slags from actual combustors, are used in the program. The paper will present selected results on several materials exposed in both laboratory tests and in the Combustion and Environmental Research Facility (CERF) at DOE's Pittsburgh Energy Technology Center.

Thermodynamic calculations were used to evaluate the chemistries of gaseous and condensed phases that occur during combustion of an Illinois bituminous coal. The computer program used for the calculations is based on calculating the equilibrium concentrations of various species by minimizing the free energy of the system. Details of the calculations are presented in Ref.4. Calculated results for the chemistry of condensed phases and the gaseous phase at the combustion air:coal stoichiometric ratio of 1.3 showed that coal combustion results in a liquid phase that is essentially a silica-saturated silicate and/or sulfate condensate, with the components made up largely of SiO_2, Al_2O_3, CaO, Fe_2O_3, Na_2SO_4, and NaCl (see Fig. 1). At temperatures below 1180°C, the partial pressures of NaCl(g), HCl(g), NaOH(g), and Na(g) change abruptly; a complex sodium aluminosilicate, $Na_2O{:}Al_2O_3{\cdot}6SiO_2(s)$, tends to form; and the liquid silicate-sulfate condensate disappears. Formation of the complex silicate requires intimate contact among several gaseous and condensed phases, the probability of which is expected to be low in real systems. Under nonequilibrium conditions, where such reactions are constrained, stability of the liquid sulfate–silicate condensate extends to temperatures as low as 890°C.

Above 1330°C, the solution consists mostly of $Al_2O_3{\cdot}SiO_2$, $CaO{\cdot}SiO_2$, $Na_2O{\cdot}SiO_2$, and $FeO{\cdot}SiO_2$, as well as traces of Na_2SO_4. As the temperature decreases, the concentration of $FeO{\cdot}SiO_2$ decreases and that of Na_2SO_4 increases. At 1130°C, Na_2SO_4 concentration may be relatively high (about 12 mol% for high-sulfur coal) and may increase very rapidly with a decrease in temperature. Under nonequilibrium conditions, the solution phase is rich in Na_2SO_4. For high-sulfur coal at temperatures below 930°C, the solution phase consists of more than 90 mol% sulfate. A solution phase consisting of sodium, magnesium, and calcium sulfates is stable below 880°C. The transition from silicate sulfate to sulfates occurs within the temperature range of 1130-980°C.

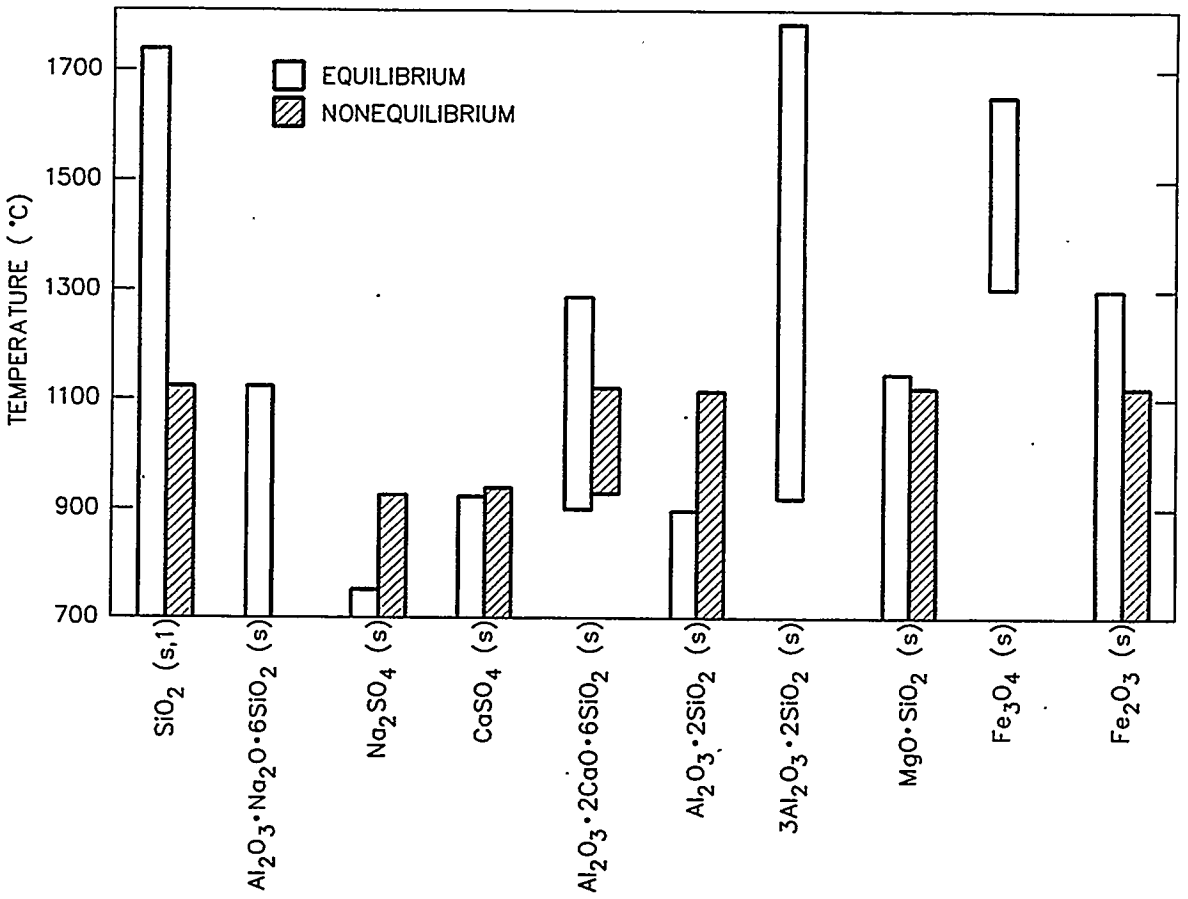

Fig. 1. Approximate temperature ranges for stability of condensed phases during combustion of high-sulfur coal with 30% excess oxygen.

Based on the results of these calculations, the general behavior of the solution phase under oxidizing conditions can be described as follows. A liquid solution phase, consisting mostly of silicates of aluminum, calcium, sodium, magnesium, and iron, is present at 1730°C. The mole fraction of Na_2SO_4 phase in the liquid is <0.01 above 1280°C. The concentration of Na_2SO_4 rises rapidly as the temperature decreases and becomes a major component of the solution at 980°C. The mole fraction of Na_2SO_4 may increase to 0.9 or more at 980°C. These compositional changes can have implications for the corrosive behavior of the liquid condensates. In the temperature range of interest in HIPPS, the predominant deposits are either mullite or Ca-rich aluminosilicates. The silicate liquid may be even more corrosive and have worse fouling tendencies than sulfates because of (a) high temperature conditions, (b) adhesive behavior of the silicates, and (c) solubility of ceramic materials, which are probably higher in silicate than in sulfate melts.

EXPERIMENTAL PROCEDURE

Laboratory Experiments. The materials selected for the laboratory experimental program include advanced metallic alloys, monolithic ceramic materials, and ceramic-matrix ceramic composites; they are listed

in Table 1, together with their manufacturers. Coupon specimens measuring 2 cm x 2 cm x 2-3 mm were prepared from several of the above–listed materials for salt- and slag-exposure experiments. Dimensions and initial weights of the specimens were measured prior to exposure. Salt tests were conducted at 1000 and 1200°C in the presence of Na_2SO_4 or a mixture of Na_2SO_4 and NaCl for 168 h. Tests in the presence of three different slags were conducted at 1200°C for a test time of 200 h. Table 2 lists the compositions of slags and the coals that were combusted to obtain these slags. Analysis shows that the slag obtained from Illinois #6 coal was richer in Fe_2O_3 and leaner in CaO and MgO, while the reverse is seen for slag from the Rochelle coal. Slags #43 and XX typify the slags derived from coals in the eastern U.S. while the slag #47 is typical of that derived from western coals.

Combustor Experiments. High-temperature materials were tested by exposing samples of several ceramic materials in the CERF at the Pittsburgh Energy Technology Center. The CERF is a state-of-the-art, 0.5 millionBtu/h pilot-scale combustion facility designed to achieve similarity with full-scale utility and industrial boilers. The CERF is designed to closely duplicate typical full-scale specifications for:

- Solid fuel fineness or liquid fuel atomization quality.
- Burner relative mass flow (fuel and air) and velocities.
- Furnace temperature distributions.
- Radiant furnace residence time.
- Convective section gas velocity.

Table 1. Materials selected for corrosion tests

Material	Manufacturer
Alumina	Coors Ceramics
Hexoloy SA	Carborundum
SiC (I) particulate in alumina	Lanxide/Du Pont
Siliconized SiC (NT230)	Norton/TRW
Silicon Nitride (NT154)	Norton/TRW
SiC fibers in SiC matrix	Du Pont
SiC fibers in Si_3N_4 matrix	ORNL

Table 2. Compositions of slags for laboratory study

Compound	Slag 43/ Illinois #6	Slag 47/ Rochelle	Slag XX/ Illinois #6
SiO_2	52.9	47.1	53.3
Al_2O_3	16.6	18.8	18.6
Fe_2O_3	12.9	5.2	17.6
CaO	13.0	19.6	7.2
MgO	1.3	5.8	1.0
Na_2O	0.8	0.9	0
K_2O	1.6	0.3	1.7
SO_3	0.1	0.3	0

Materials exposures in CERF are being conducted in a piggyback mode, whereby normal CERF testing would proceed in terms of evaluating combustion of various coals and coal blends. Figure 2 is a cross section of the radiant and convective portions of CERF, showing locations where samples are being exposed for corrosion evaluation. With this approach, comparative assessments of many materials at different locations could be made economically before pursuing dedicated-materials CERF tests that would require continuous operation of the facility for 1000 h or more. To minimize thermal stresses during exposure, samples were placed in the CERF prior to the start of each test and removed after the CERF was cooled to room temperature. Coupon samples of several of the ceramic materials (see list in Table 1) were mounted on a water-cooled, high-temperature materials testing probe that uses welded clips and pins to hold the samples, as shown in Fig. 3.

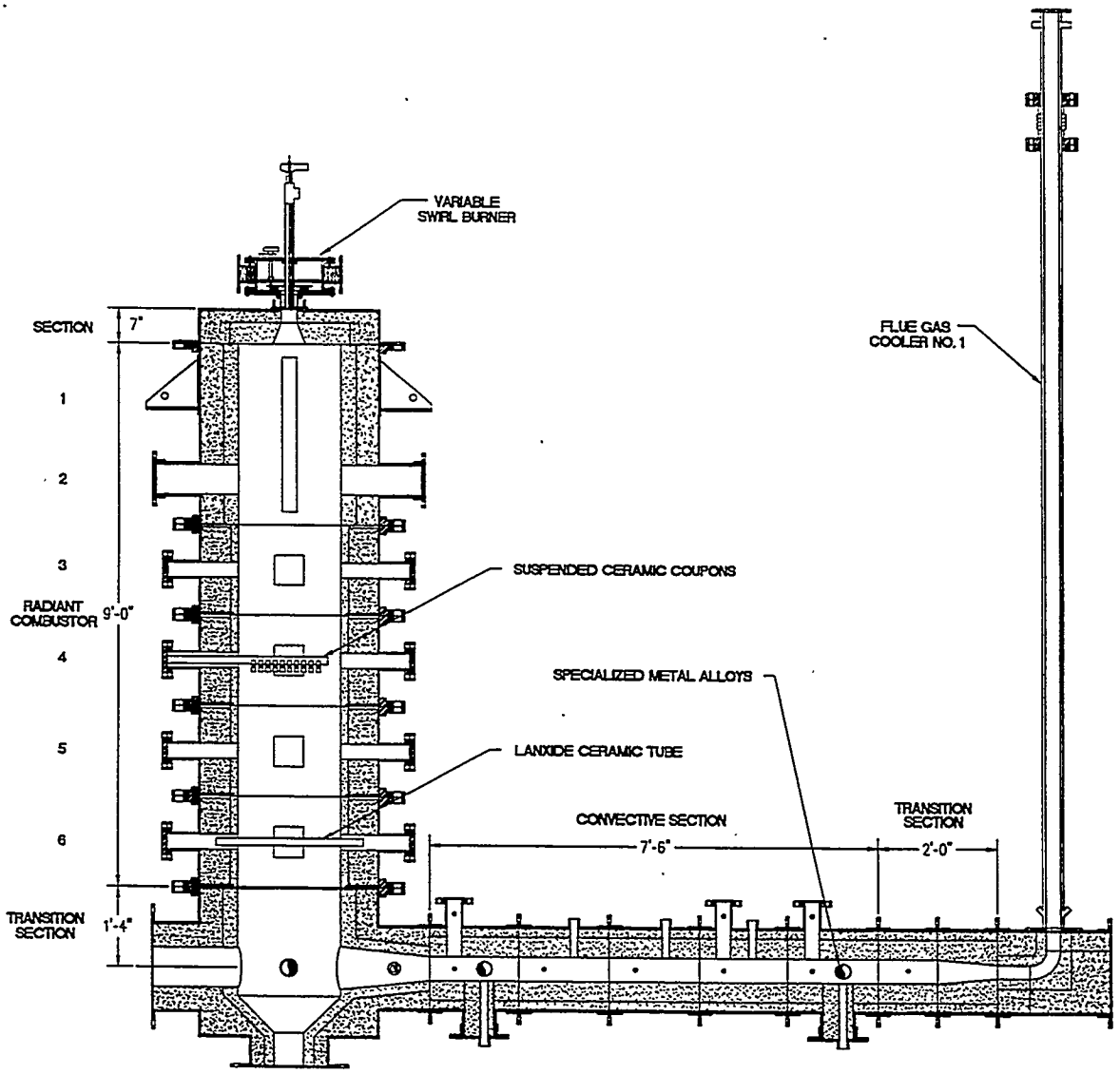

Fig. 2. CERF cross section of radiant and convective section and high-temperature materials test locations.

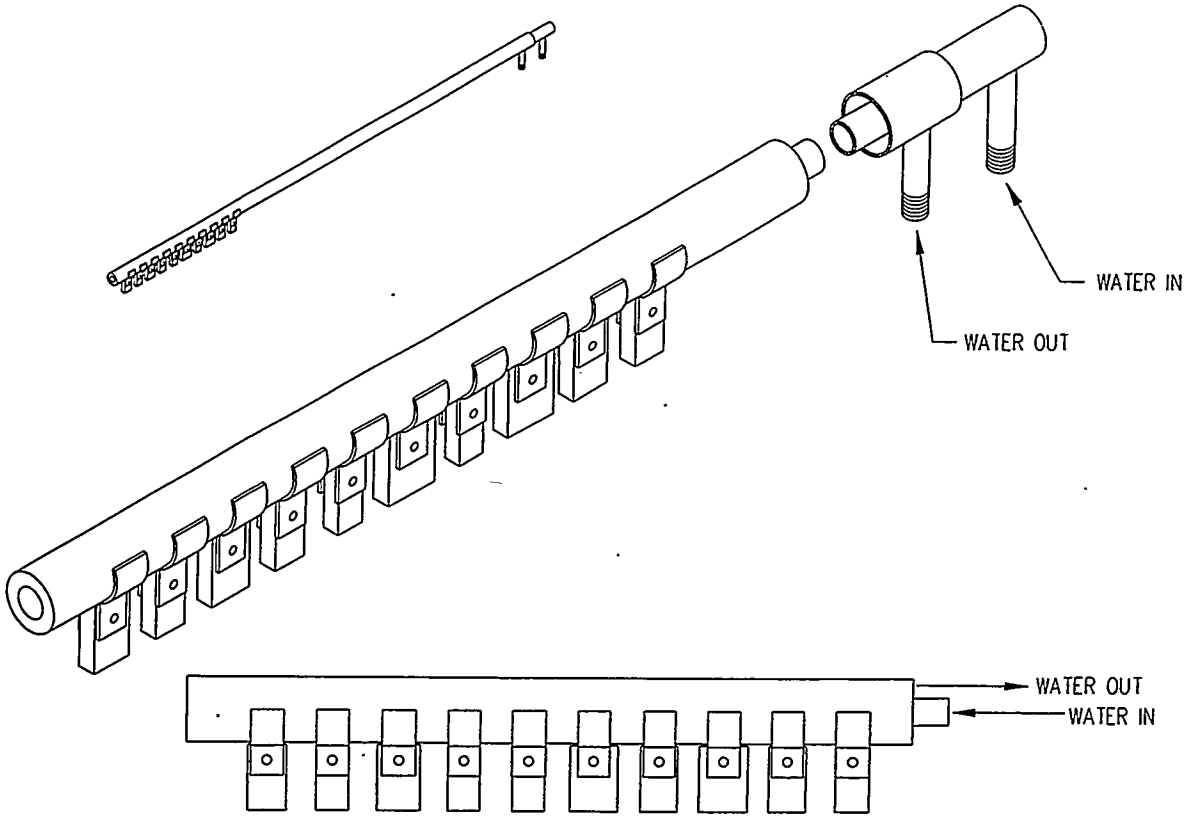

Fig. 3. Materials test probe for exposure of small coupons in CERF.

Table 3. Compositions (in wt.%) of coal ash

Compound	Ash 43/ Illinois #6	Ash 47/ Rochelle	Ash XX/ Illinois #6	Ash 1/ Pittsburgh	Ash 2/ Alaskan
SiO_2	56.5	32.1	51.6	41.5	43.1
Al_2O_3	20.8	18.0	19.2	21.5	17.0
Fe_2O_3	9.6	4.9	17.4	17.9	8.7
CaO	3.0	23.1	3.2	8.5	20.6
MgO	1.1	9.9	1.0	0.8	2.6
Na_2O	1.7	1.5	0.9	0.6	0.6
K_2O	2.5	0.3	2.4	1.3	1.2
SO_3	1.8	8.0	2.3	4.0	5.6
Ash Fluidity Temperature (°C)	1405	NA	1400	1388	1288

Ceramic specimens were exposed during two 100-h runs in which Pittsburgh coal and a blend of Alaskan/Russian coal were burned. Table 3 shows compositions of coals used in CERF runs, along with coals that generated slags for the laboratory test program.

EXPERIMENTAL RESULTS

Hexoloy SA: This material is a sintered form of alpha silicon carbide with >98% of theoretical density. It has a very fine grain structure (8 μm) for excellent wear resistance, contains no free silicon, and has been reported to be chemically resistant in both oxidizing and reducing environments. In air tests, the Hexoloy SA oxidized to form a silica layer, as evidenced by the oxygen content of the surface regions of the air-exposed specimens. At 1400°C, all of the carbon in the surface region was reacted and oxygen enrichment was substantial. The material exhibited passive oxidation of SiC to SiO_2.

In the salt tests at 1200°C, the specimen melted, indicating formation of a low-melting compound (i.e., melting point <1200°C) by reaction of salt and silicon. Based on the Na_2O-SiO_2 phase diagram, additions of even a small amount of Na_2O to silica can lead to $Na_2O{\cdot}xSiO_2$ with melting temperature decreasing as Na_2O content increases. Because pure Na_2SO_4 will establish a fairly high Na_2O activity, especially at 1200°C, formation of the low-melting (Si,Na,O) compound is most likely. In a 50:50 mixture of salt and slag, oxidation of silicon carbide to silicon oxide was virtually complete in 168 h of exposure. At longer exposure times, the reaction between silicon oxide and sodium oxide will occur, resulting in a low-melting (Si,Na) compound observed in pure salt tests.

In laboratory slag tests, the materials behaved differently than in salt tests. The specimen showed significant surface cracking but the slag itself didn't seem to penetrate the sample, as evidenced by energy-dispersive X-ray (EDX) analysis of specimen cross sections. Because Na_2O activity in the slag is relatively low, the deposit did not melt, but significant bubbling of the slag was noted, probably due to formation of SiO vapor in a reducing condition established locally by entrapped carbon in slag. All three slags exhibited similar appearance after the test and also all three specimens exposed to different slags appeared similar, indicating that coal slag chemistry has little influence in these short exposures. Figure 4 shows SEM photomicrographs of specimen cross sections after exposure in the three slags. In the first CERF exposure conducted with Pittsburgh coal, the specimen exhibited a thin layer of deposit after ≈100 h of testing. X-ray diffraction analysis of the deposit indicated predominantly mullite ($3Al_2O_3{\cdot}2SiO_2$) with some ordered albite [(Na,Ca)Al(Si,Al)$_3O_8$] along with traces of hematite. No significant degradation of the sample was observed in scanning electron microscopy (SEM) and EDX analysis. The sample from the second run, in which a blend of Alaskan and Russian coals was combusted, was lost even though the pin and the clip holding the sample were intact. This may qualitatively indicate that the material may be susceptible to cracking at elevated temperatures by particle impingement.

SiC (p) in Al_2O_3: This material was fabricated by Du Pont-Lanxide by a direct metal oxidation process and has an Al_2O_3 matrix with SiC particulates dispersed throughout the matrix. The surface regions of the samples exposed to either salt or slag were devoid of SiC particulates, based on EDX analysis. Reactions between alumina, silica, and sodium oxide in salt experiments can lead to corrosion products with several possible compositions, but microscopic observations of the reacted layers indicate that no liquid phase formed and that the Na_2O activity is low enough to form higher-melting compounds enriched in alumina and silica. Coupons of this material tested in laboratory slag tests also showed SiC conversion to silica, but corrosion or internal penetration of the material was negligible. Moreover, CERF tests showed that the

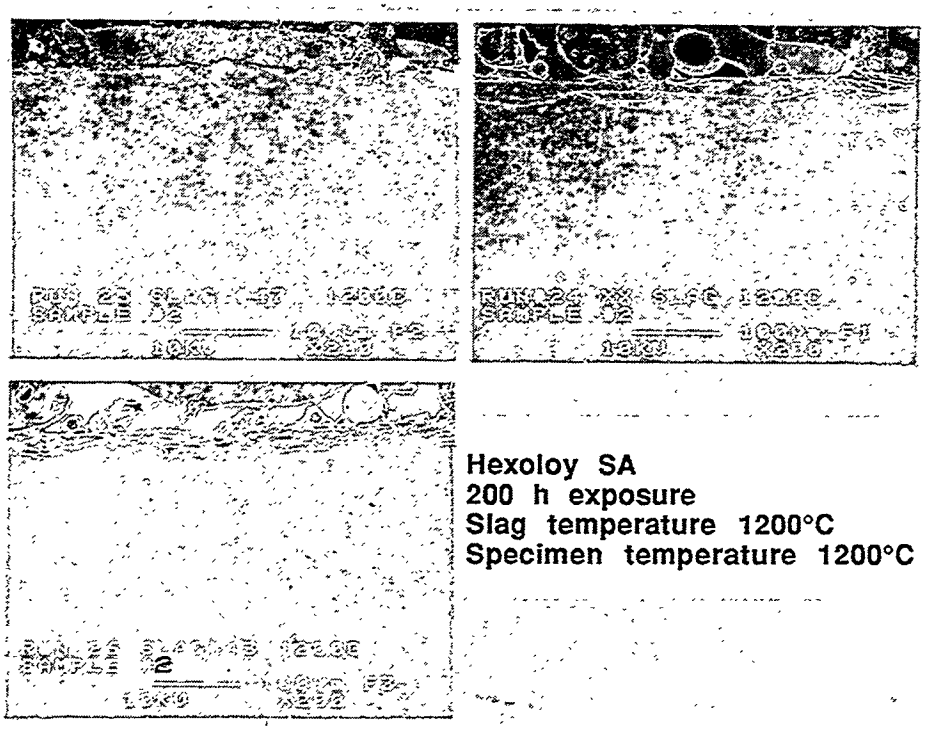

Fig. 4. SEM photomicrographs and EDX analysis of cross sections of Hexoloy SA specimens after exposure in CERF during combustion of Pittsburgh coal.

compositions of the deposit layers were somewhat different between the two runs. In the run with Pittsburgh coal, the deposit contained significant iron oxide, while the run with Alaskan blend exhibited a high concentration of CaO. The deposit composition seems to have a significant effect on stickiness and subsequent accumulation on the specimen surface. The deposit in CERF run 2 was at least twice as thick as in run 1 for the nominal operating conditions and same time of exposure. Figures 5 and 6 show the SEM photomicrographs of specimen cross sections and deposits obtained in the two runs. Also shown is the EDX elemental distribution for several elements of interest from the corrosion standpoint.

Siliconized SiC: This material (identified as NT 230) made by Norton/TRW was tested in salt and slag environments in the laboratory and in CERF. In the salt experiments, the surface regions of the specimens lost carbon, but from the standpoint of corrosion the material was virtually unaffected. In the slag experiments at 1200°C, the specimens exhibited surface cracks (similar to Hexoloy SA) but corrosion degradation was minimal or nonexistent. In CERF tests, the material developed a silica-rich region but from the corrosion standpoint, the material was virtually unaffected (similar to Hexoloy SA).

SiC Fiber/SiC Matrix: This material is made by Du Pont with a chemical vapor infiltration process. It is recommended for service requiring high strength, high-temperature properties, and light weight. The material exhibits creep deformation at temperatures >1200°C, contrary to behavior of Hexoloy SA and NT 230, in which creep was virtually absent.

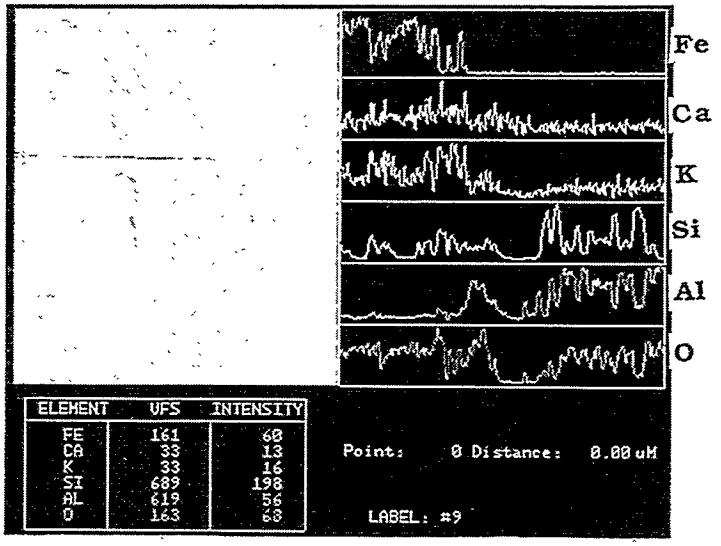

Fig. 5. SEM photomicrographs and EDX analysis of cross sections of SiC(p)/Al_2O_3 specimens after exposure in CERF during combustion of Pittsburgh coal.

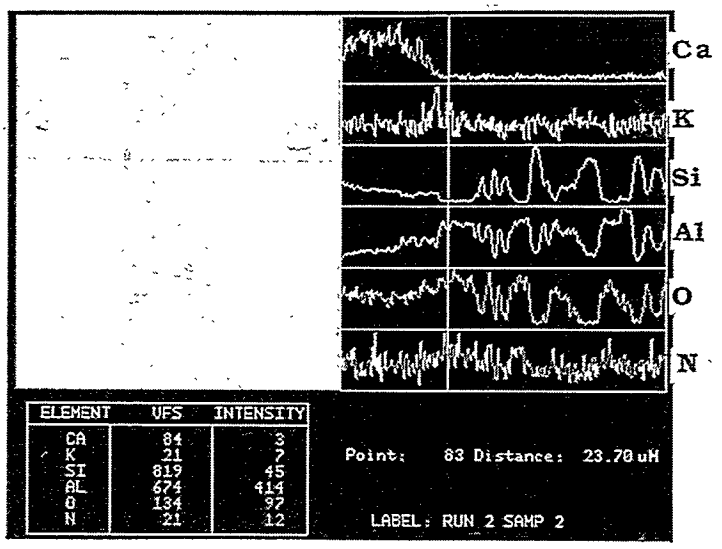

Fig. 6. SEM photographs and EDX analysis of cross sections of SiC(p)/Al_2O_3 specimens after exposure in CERF during combustion of Alaskan/Russian blend coal.

In salt exposures conducted in the laboratory, the material behaved similarly to monolithic SiC from the reaction standpoint. Surface regions were devoid of SiC, while the interior was unaffected by the salt during 168 h of exposure. In slag experiments at 1200°C, the material developed only a solid reaction product and the reaction was confined to the surface regions of the specimens. The behavior of the material in CERF exposures was similar to those of monolithic SiC such as Hexoloy SA and NT 230.

DISCUSSION

Corrosion of ceramic heat exchanger surfaces in coal-fired systems can occur via three different mechanisms dictated by the material composition and exposure environment (which includes temperature, gas chemistry, and deposit chemistry). The gas and deposit chemistries, in turn, will be dictated by the coal and ash chemistry, combustion conditions, and gas and particulate flow conditions determined by furnace design. The first mode of degradation of ceramic materials such as monolithic and composite SiC, Si_3N_4, and SiC-dispersed Al_2O_3 is by oxidation of SiC and Si_3N_4 in air. Oxidation can occur via either the passive mode in which a solid SiO_2 phase forms and can offer protection against further oxidation, or via active oxidation in which the SiO phase forms and can volatilize, resulting in accelerated oxidation of the material. The air oxidation experiments conducted with these materials at temperatures in the range 1000-1400°C in dry air environment showed that the materials undergo passive oxidation. However, the effect of water vapor on oxidation needs further evaluation.

The second mode of degradation of these materials involves reactions between the ceramic materials and alkali sulfates such as Na_2SO_4 and K_2SO_4 and alkali chlorides such as NaCl and KCl. In the combustion gas environment, the concentrations of oxygen and of sulfur as SO_2 and SO_3 determine the sodium oxide activity via the reaction $Na_2SO_4 = Na_2O + SO_3$. Subsequently, the silica phase that forms on the ceramic materials can react with Na_2O to form compounds such as $Na_2O{\cdot}XSiO_2$, where X can be 0.5, 1, 2, or 4. These sodium silicates have melting temperatures in the range of 875-1110°C. This mode of degradation of ceramic materials requires that Na_2O activity be sufficiently high and is usually possible in gas turbine systems where slag constituents are virtually absent. In such instances, the liquid phase can dissolve the protective SiO_2 scale and also result in penetration of the liquid reaction products into the substrate ceramic material, thereby mechanically weakening the material. In coal-fired combustion systems, the presence of slag constituents determine the thermodynamic activity of various deposit constituents, and alkali-sulfate-induced corrosion is generally not dominant.

The third mode of degradation of ceramic materials in coal-fired combustion systems is via reactions with coal ash. This type of degradation depends on material composition, slag chemistry (acidic or basic), and gas-phase environment (either oxidizing or reducing). The slag generally contain phases such as SiO_2, Al_2O_3, CaO, Fe_2O_3, Na_2O, a combination of these phases, and other ash constituents depending on the coal feedstock. X-ray diffraction data for the deposits, obtained in a CERF run with combustion of Pittsburgh coal, showed the dominant phases to be mullite ($3Al_2O_3{\cdot}2SiO_2$), ordered calcian albite [(Na,Ca) Al (Si,Al)$_3O_8$], and hematite (Fe_2O_3). The melting temperatures of these phases are >1400°C (see Table 4 for a listing of melting temperatures of various compounds); reactions between these compounds and the ceramic materials occur primarily in the solid state, and little or no penetration of the ceramics occurs by liquid phase

Table 4. Melting temperatures of coal slag components

Compound	Melting Temperature (°C)
Al_2O_3	2020
SiO_2	1610-1723
Fe_2O_3	1594
CaO	2614
$Na_2O{\cdot}SiO_2$	1089
$Na_2O{\cdot}2SiO_2$	874
$Na_2O{\cdot}4SiO_2$	1112
$2Na_2O{\cdot}SiO_2$	1018
$3Al_2O_3{\cdot}2SiO_2$	1850
$Na_2O{\cdot}Al_2O_3{\cdot}2SiO_2$	1526
$Na_2O{\cdot}Al_2O_3{\cdot}4SiO_2$	1138
$Na_2O{\cdot}Al_2O_3{\cdot}6SiO_2$	1118
$Na_2O{\cdot}Fe_2O_3{\cdot}4SiO_2$	1310
$CaO{\cdot}SiO_2$	1544
$2CaO{\cdot}SiO_2$	2130
$CaO{\cdot}Al_2O_3{\cdot}2SiO_2$	1553
Na_2SO_4	884

from coal combustion environment. Similarly, X-ray diffraction data for the deposits, obtained in a CERF run with combustion of Alaskan/Russian blend coal, showed the dominant phases to be anorthite ($CaO{\cdot}Al_2O_3{\cdot}2SiO_2$), calcium aluminum silicate ($CaO{\cdot}Al_2O_3{\cdot}SiO_2$), and ordered sodium anorthite (Ca,Na)$(Al,Si)_2\ Si_2O_8$. These Ca-rich silicates also have melting temperatures >1400°C (see Table 4), and reactions between the coal ash deposit and the ceramics occur predominantly in the solid state. The experimental results also indicate that Na_2O activities in the deposits (with combustion of coals containing Fe_2O_3 and CaO) are sufficiently low to form liquid sodium silicates of various types in coal-fired systems. At present, long-term experiments are in progress in the laboratory and in CERF to evaluate the corrosion performance of several ceramic and advanced metallic materials and to assess their residual mechanical properties.

SUMMARY

Thermodynamic calculations were performed to evaluate the chemistries of gaseous and condensed phases that arise during combustion of an Illinois bituminous coal. Coal combustion results in a liquid phase that is essentially a silica-saturated silicate-sulfate condensate, with the components being largely $CaO{\cdot}SiO_2$, $Na_2O{\cdot}2SiO_2$, $FeO{\cdot}SiO_2$, $MgO{\cdot}SiO_2$, Na_2SO_4, and NaCl. At temperatures below 1180°C, the partial pressures of NaCl(g), HCl(g), NaOH(g), and Na(g) change abruptly; a complex sodium aluminosilicate, $Na_2{\cdot}Al_2O_3{\cdot}6SiO_2$(s), tends to form; and the liquid silicate-sulfate condensate disappears. Formation of the complex silicate requires intimate contacts among several gaseous and condensed phases, the probability of which is expected to be low in real systems. Under nonequilibrium conditions, where such reactions are constrained, stability of the liquid sulfate–silicate condensate extends to temperatures as low as 890°C. Calculations also indicate that the silicate phases such as mullite and calcium aluminum silicate will dominate the deposit composition and that alkali-sulfate-induced corrosion, prevalent in gas turbine systems that use coal-derived gases, may not be of concern for heat exchangers in HIPPS.

An experimental program has been initiated to evaluate materials for advanced combustion systems. Several candidate materials are being examined in a laboratory test program to assess their performance in the presence of salt and slag environments. The candidates included advanced metallic alloys, monolithic ceramics, ceramic particulate/ceramic matrix composites, ceramic fiber/ceramic matrix composites, and ceramic whisker/ceramic matrix composites. In addition, materials are being exposed in CERF at the Pittsburgh Energy Technology Center to assess their performance in a pilot-scale system that simulates combustion and flow/temperature conditions of a full-scale boiler. Extensive microstructural analyses are conducted on the exposed specimens to evaluate the corrosion performance of the materials for service in air and fireside environments of advanced coal–fired boilers.

ACKNOWLEDGMENTS

The authors thank the ceramics manufacturers for supplying specimen materials. D. L. Rink assisted in the corrosion tests and microstructural analysis of exposed specimens.

REFERENCES

1. L. A. Ruth, "Combustion 2000," PETC Review, Issue 4, p. 4, Fall 1991.

2. J. Shenker, "Development of a High-Performance Coal-Fired Power Generating System with a Pyrolysis Gas and Char-Fired High Temperature Furnace," Proc. 9th Annual Coal Preparation, Utilization, and Environmental Control Contractors' Conf., July 19-22, 1993.

3. D. J. Seery, J. J. Sangiovanni, F. L. Robson, W. M. Proscia, J. E. Holowczak, M. Bak, J. D. Freihaut, M. Heap, D. W. Pershing, and P. J. Smith, "Combustion 2000: Burning Coal in the Twenty-First Century," ibid., p. 356.

4. K. Natesan, M. Yanez-Herrero, and C. Fornasieri, "Corrosion Performance of Materials for Advanced Combustion Systems," Argonne National Laboratory Report ANL/FE-93/1, Dec. 1993.

MULLITE COATINGS FOR CORROSION PROTECTION OF SILICON CARBIDE

R. Mulpuri, and V.K. Sarin

Boston University
Department of Manufacturing Engineering
Boston, MA 02215

ABSTRACT

SiC based ceramics have been identified as the leading candidate materials for elevated temperature applications in harsh oxidation/corrosion environments. It has been established that a protective coating can be effectively used to avoid problems with excessive oxidation and hot corrosion. However, to date, no coating configuration has been developed that can satisfy the stringent requirements imposed by such applications. Chemical Vapor Deposited (CVD) mullite coatings due to their desirable properties of toughness, corrosion resistance, and a good coefficient of thermal expansion match with SiC are being investigated as a potential candidate. Since mullite has never been successfully grown via CVD, the thermodynamics and kinetics of its formation were initially established and used as a guideline in determining the initial process conditions. Process optimization was carried out using an iterative process of theoretical analysis and experimental work coupled with characterization and testing. The results of theoretical analysis and the CVD formation characteristics of mullite are presented.

INTRODUCTION

SiC and SiC based ceramics are leading candidate materials for high temperature applications due to their unique combination of high strength and thermal conductivity, low thermal expansion, high temperature stability and oxidation resistance. The presence of impurities in the environment or a gas stream can considerably increase the rate of passive oxidation by modifying the transport rate of oxygen through the protective scale, causing active oxidation via formation of SiO. This can accelerate the degradation process, and

depending on gaseous impurities produce compounds such as Na_2SiO_3 which chemically attack the ceramic resulting in accelerated corrosion. Studies have shown that substantial improvements can be made by the application of thin protective coatings. [1] It is of course imperative that these coatings be adherent, oxidation/corrosion, and thermal shock resistant in order to withstand the stringent conditions and protect the ceramic components. None of the coating configurations that have been developed so far are capable of withstanding, for extensive periods, the conditions imposed by such applications. Most coating configurations to date have failed mainly due to poor adhesion. A large mismatch in coefficient of thermal expansion (CTE) between the coating and the substrate is often a major contributing factor to this problem. Mullite ($3Al_2O_3 \cdot 2SiO_2$) is an excellent candidate for a coating material by virtue of its CTE match with SiC and its excellent high temperature stability and strength as well as oxidation and corrosion resistance characteristics.[2]

Mullite is a solid solution of Al_2O_3 and SiO_2 and is the only stable crystalline compound in the $Al_2O_3.SiO_2$ system under normal atmospheric pressure. It has a chemical composition of approximately $3Al_2O_3.2SiO_2$ (71.8 wt% Al_2O_3) and crystallizes in the orthorhombic system. [3] In spite of years of research on bulk mullite, controversy still exists regarding the solid solubility range of mullite and the exact phase diagram of the SiO_2-Al_2O_3 system. Variation in solid solubility (70 to 82% Al_2O_3) has been reported to be dependent on the method of synthesis.[4] In light of this uncertainty and the technical challenges of growing CVD mullite, two approaches were investigated; (i) Laminated structures: Formation of mullite via diffusion across multi-layers of Al_2O_3 and SiO_2, and (ii) Co-deposition: Simultaneous formation of Al_2O_3 and SiO_2 in appropriate ratios.

MULTI-LAYERED COATINGS

Multilayers of α-Al_2O_3 and vitreous SiO_2 were grown on SiC substrates by chemical vapor deposition (CVD). Equilibrium thermodynamic analysis was performed in order to establish theoretical trends and aid in determining the initial process conditions. CVD formation of individual Al_2O_3 and SiO_2 coatings is well studied. The CVD reactor was modified so that the alternating layers could be deposited using the same fixturing without interruption between layers. The thickness of the layers was adjusted such that the overall composition of the coating was that of theoretical stoichiometric mullite.

SiO_2 was deposited by pyrolysis of Tetraethoxysilane ($Si[OC_2H_5]_4$) which resulted in amorphous coatings. The deposition reaction was carried out at 800 °C and 50 torr pressure. The projected chemical reaction is as follows [5]:

$$(Si[OC_2H_5]_4) \longrightarrow \mathbf{SiO_2} + 2CO + 2CH_4 + 2C_2H_4 + 2H_2$$

Al_2O_3 was formed from $AlCl_3$ by a hydrolysis reaction. $AlCl_3$ can be formed in-situ by flowing Cl_2 or HCl with a carrier gas such as H_2 through Aluminum chips maintained at a constant temperature. H_2 and CO_2 were used to obtain the water-gas-shift reaction and form H_2O in-situ in the CVD reactor. The reaction was carried out at 950 °C and 75 torr pressure. The resulting alumina coatings had a corundum (α) structure. The chemical reactions are as follows

Source: $2Al + 3Cl_2 \longrightarrow \mathbf{2AlCl_3}$

Water-gas-shift: $CO_2 + H_2 \longrightarrow \mathbf{H_2O} + CO$

Deposition: $2AlCl_3 + 3H_2O \longrightarrow \mathbf{Al_2O_3} + 6HCl$

As deposited, the multi-layers had definite interfaces with abrupt changes in composition, which resulted in large levels of residual stresses in the coating, and in some cases crack formation. The multilayered coatings were annealed at different temperatures to facilitate the formation of mullite via interfacial reactions. Figure 1 is a TEM micrograph of an Al_2O_3-SiO_2 interface after a 2 hour anneal at 1200 °C, showing the presence of a 50 nm reaction zone. Chemical analysis of this reaction layer in the STEM using a 1 nm electron probe showed the formation of a compound in which the Al:Si atomic ratio was measured to be 65:35 (see EDS spectra in Figure 1) which is close to the theoretical ratio in stoichiometric mullite. This coating exhibited no visible signs of cracking on cooling.

In order to widen the diffusion zone, the temperature of the post deposition anneal was increased to 1350 °C. This treatment resulted in the delamination of the Al_2O_3 layer. TEM micrograph (Figure 2) of this sample shows partial transformation of the amorphous SiO_2 layer immediately next to the Al_2O_3 coating into crystalline silica. Cracks were observed at the crystalline SiO_2 layer and Al_2O_3 interface indicating that phase transformation may be responsible for coating delamination. It is felt that for any coating configuration to maintain

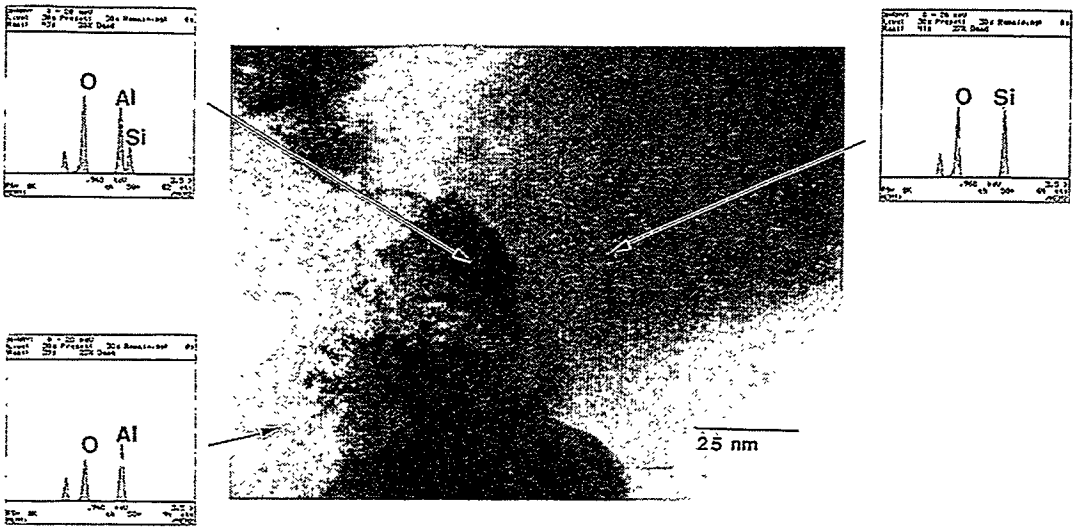

Figure 1: TEM micrograph of Al_2O_3-SiO_2 interface after a 2 hour anneal at 1200 °C.

adherence at elevated temperatures on Si based substrates, this problem needs be addressed since there is a naturally present silica layer on all Si substrates. To quantify the dependence of devitrification of SiO_2 on pressure and temperature, experiments were conducted on bulk silica powders. Details of this work were presented elsewhere. [6] It was concluded that vitreous to crystalline transformation in silica leads to coating spallation due to cracking caused by volume changes. This transformation is affected by stresses within the coating. Work is currently underway to quantify the stresses at the interfaces in multi-layered Al_2O_3/SiO_2 coatings.

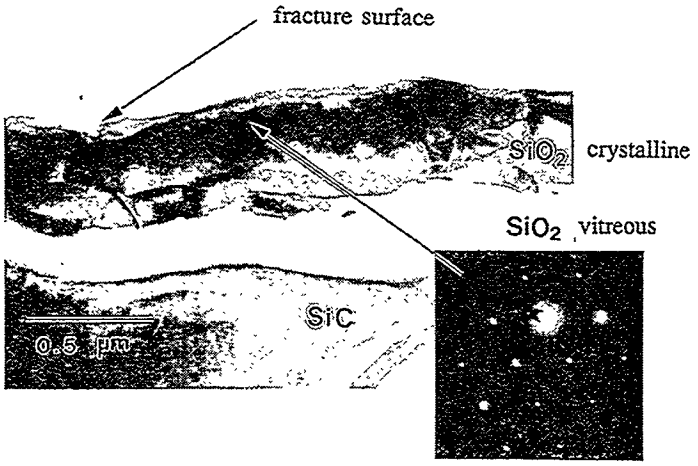

Figure 2: TEM micrograph of the multilayered coating annealed at 1350 °C for 2 hours.

CODEPOSITED COATINGS

Mullite is hypothesized to be formed by the following reaction:

$$6AlCl_3 + 2SiCl_4 + 13CO_2 + 13H_2 \longrightarrow 3Al_2O_3 \cdot 2SiO_2 + 13CO + 26HCl$$

In order to establish the initial process conditions for the formation of mullite via CVD, equilibrium thermodynamic analysis using the modified SOLGASMIX-PV program [7] was performed on the $AlCl_3$-$SiCl_4$-CO_2-H_2 system. The results of the calculations were presented in the form of "CVD phase diagrams". These diagrams help in identifying the phases that would be present if a particular set of process parameters were to be used under equilibrium conditions. However, since CVD is rarely an equilibrium process, the information from the CVD phase diagrams can only be useful in establishing trends from theoretical analysis rather than for predicting the type and concentration of the phases that would be present under experimental conditions.

Thermodynamic Analysis

Figure 3 shows a ternary CVD phase diagram of $AlCl_3$-$SiCl_4$-CO_2-H_2 system at 1000 °C and 75 torr. The ratio of H_2:($AlCl_3$+$SiCl_4$+CO_2) was maintained at 5:1. Since the concentration of H_2 was fixed at 500 moles, the total moles of $AlCl_3$+$SiCl_4$+CO_2 was 100.

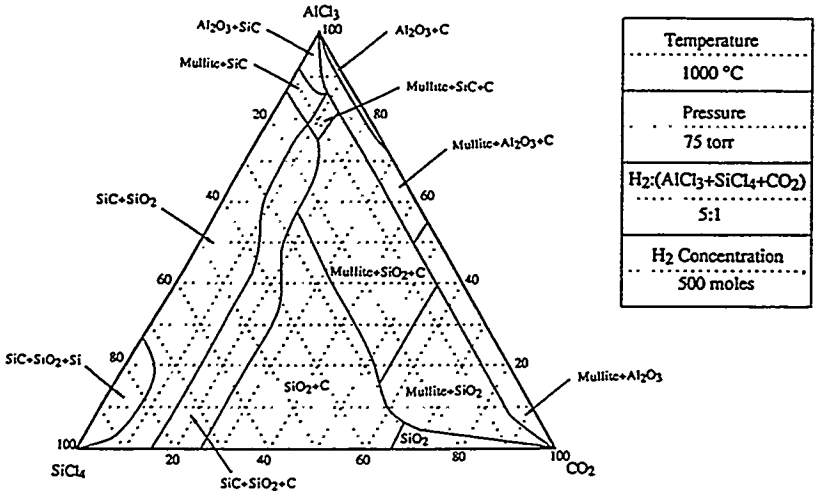

Figure 3: CVD ternary phase diagram of $AlCl_3$-$SiCl_4$-CO_2-H_2 system at 1000 °C and 75 torr.

As one would expect, Al_2O_3-based products form along the $AlCl_3$-CO_2 line, and SiO_2-based products form along the $SiCl_4$-CO_2 line. Pure oxides form at high CO_2 concentrations, oxides+carbon in the medium CO_2 concentration, and oxides+carbides in the low CO_2 concentration. To avoid carbon in the deposit, operating in the regime where there is excess CO_2 available for the reaction is necessary. Excess carbon towards the left portion of the diagram is the result of the lack of availability of O_2 in the reaction to form the gaseous bi-product, CO. According to the phase diagram, pure mullite can only be obtained as a line compound, in between the mullite+Al_2O_3 and mullite+SiO_2 regions. However, mullite will have a composition range when produced via CVD, just as in the bulk stage. Since the Gibbs free energy of formation of SiO_2 is lower than that of mullite, which is lower than that of Al_2O_3, all the oxygen available is first used to form SiO_2, then mullite, and then Al_2O_3.

Effect of Temperature

Temperature was varied from 800 °C to 1200 °C in steps of 200 °C. The results are shown in the CVD phase diagrams in Figure 4. When the temperature was reduced to 800 °C, the formation of mullite was not predicted. Instead, sillimanite (Al_2O_3•SiO_2) is formed in the high CO_2 concentration range. At 1200 °C, many phases such as carbon that were present at 1000 °C were absent throughout the phase diagram. Based on the analysis of output gas stoichiometry at 1200 °C, gaseous products such as CH_4 were formed, rather than formation of carbon as a solid deposit. At this temperature, carbon free deposits of mullite can be obtained over a much broader range of input parameters compared to 1000 °C.

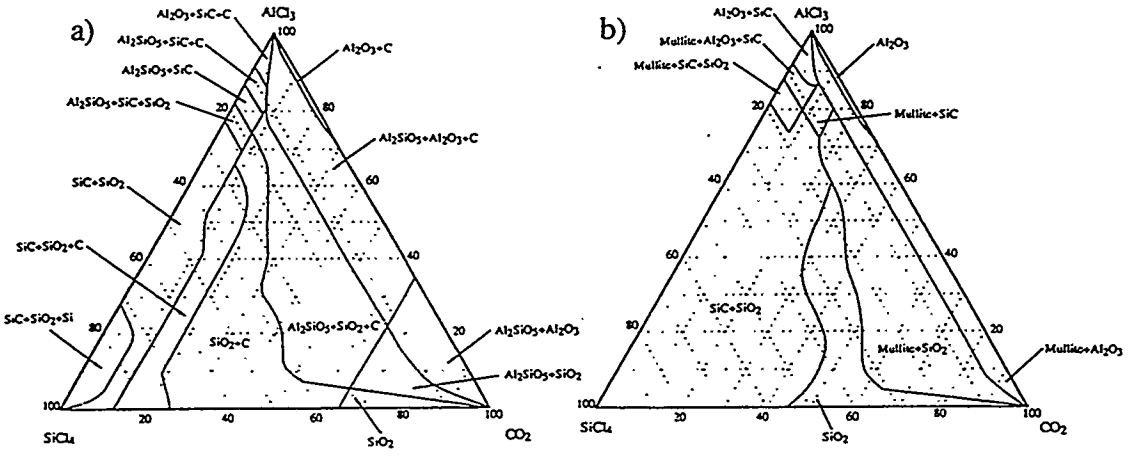

Figure 4: CVD ternary phase plot of $AlCl_3$-$SiCl_4$-CO_2-H_2 system at 75 torr and a) 800 °C, and b) 1200 °C.

Effect of Pressure

Pressure was varied from 2 torr to 150 torr. The results are shown in the CVD phase diagrams in Figure 5. As the pressure is increased from 2 to 150 torr, the region over which mullite can be formed widens, and a fewer number of phases are present. Additionally, as the pressure is decreased from 150 to 2 torr, the level of free carbon is reduced. Lower pressures are preferred for obtaining carbon-free deposits, since at lower pressures, carbon has a higher affinity to form gaseous products such as CH_4 than forming a solid deposit. Thus there is a trade-off between the extent of formation of mullite and obtaining carbon-free deposits.

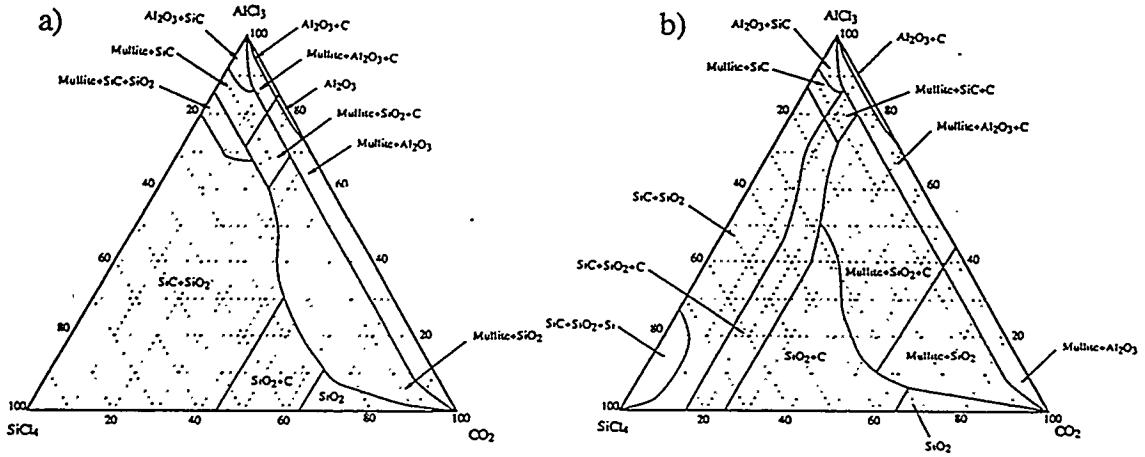

Figure 5: CVD ternary phase plot of $AlCl_3$-$SiCl_4$-CO_2-H_2 system at 1000 °C and a) 2 torr, and b) 150 torr.

Effect of Stoichiometry

To determine the appropriate ratios of the Al and Si species in the reactant mix, $AlCl_3$ and $SiCl_4$ concentrations were varied at the 1000 °C and 75 torr condition. The region over which the compositions were varied is shown on the ternary diagram with the lines AA, and BB in Figure 6. CO_2 concentration throughout the line AA was maintained at 90 moles. Thus, the total ($AlCl_3$+$SiCl_4$) concentration is 10 moles. $AlCl_3$ composition was varied from 0 to 10 moles, and the results were plotted in terms of composition of the reaction products and the $AlCl_3$ deposition efficiency. The deposition efficiency is calculated by dividing the number of moles of the product by the number of moles of $AlCl_3$ that contributes to that product. Mullite concentration was found to increase gradually with increasing $AlCl_3$ concentration with the highest at 7.5 moles of $AlCl_3$, which also matches with theoretical stoichiometric mullite. The SiO_2 concentration in the deposit increases to the left, and the Al_2O_3 concentration increases to the right of this point. The efficiency of mullite

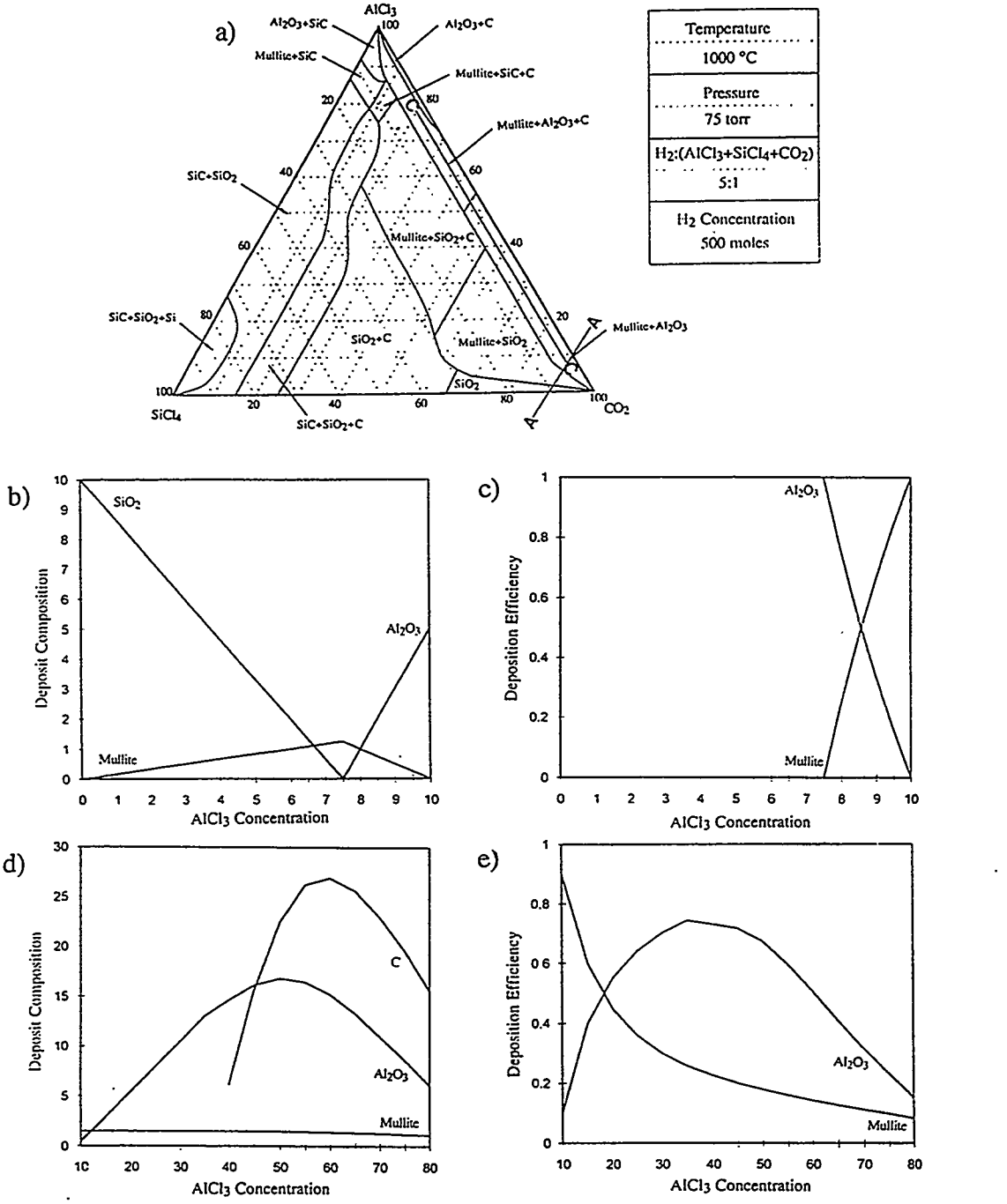

Figure 6: a) CVD ternary phase plot of $AlCl_3$-$SiCl_4$-CO_2-H_2 system at 1000 ° C and 75 torr showing the regions varied, b) effect of stoichiometry on concentration at CO_2: 90 moles, c) effect of stoichiometry on deposition efficiency at CO_2: 90 moles, d) effect of stoichiometry on concentration at $SiCl_4$: 3 moles, and e) effect of stoichiometry on deposition efficiency at $SiCl_4$: 3 moles.

formation is 100 % from 0 to 7.5 moles of $AlCl_3$ (at which point Al_2O_3 starts to form) and decreases gradually to the right. In addition, it was also observed that the efficiency has not increased when the temperature was increased from 1000 °C to 1200 °C.

Section BB was taken at a constant $SiCl_4$ concentration of 3 moles. Thus, the total ($AlCl_3$+CO_2) concentration is 97 moles. $AlCl_3$ concentration was varied from 10 to 80 moles (87 to 17 moles of CO_2). The concentration of the resulting mullite remains fairly constant throughout the diagram. However, the efficiency of mullite formation is the highest at the low $AlCl_3$ concentration. It is evident from the phase diagram that it is important to operate in the low $AlCl_3$ concentration range in order to obtain pure mullite deposits. This also points out however, that $AlCl_3$ concentration can be varied gradually to be able to effectively obtain a mullite+Al_2O_3 composite. This becomes especially useful and extremely important in cases where functional grading of the CVD coatings is desired.

Experimental Work

Initial parameters for experimentation were chosen from equilibrium thermodynamic analysis and the corresponding CVD phase diagrams that were constructed. The phase diagrams were very useful in effectively identifying initial process conditions. In general, low chloride concentrations were chosen for experimentation. CVD mullite coatings were successfully grown from $AlCl_3$-$SiCl_4$-CO_2-H_2 mixtures.

$AlCl_3$ was formed in-situ by flowing Cl_2 or HCl with a carrier gas such as H_2 through Aluminum chips maintained at a constant temperature. $SiCl_4$ was evaporated from liquid stage at room temperature. $AlCl_3$ and $SiCl_4$ were mixed in appropriate ratios prior to entering the CVD reactor. H_2 and CO_2 were used via the water-gas-shift reaction in order to form H_2O in-situ in the CVD reactor. The reaction was carried out at 950 °C and 75 torr.

Figure 7 shows the scanning electron micrograph of a typical mullite coating on a SiC substrate. X-ray diffraction analysis confirmed that the only crystalline phase present in this coating was mullite. The coating was dense, uniform in thickness and composition, with a fine grained, equiaxed structure. Further experimentation is necessary to establish the effect of process parameters on structure/property correlations, and to optimize the process conditions based on performance measures.

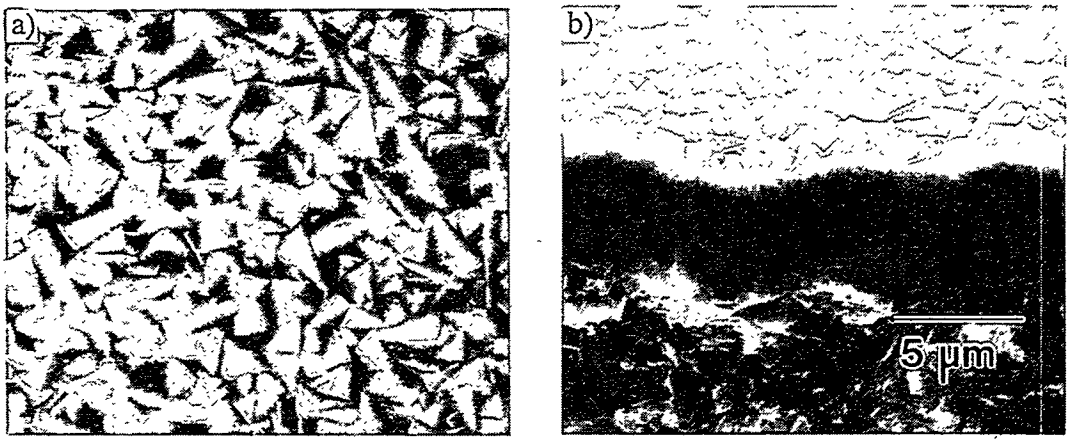

Figure 7: Scanning electron micrograph of a mullite coating on SiC, a) surface, b) cross-section.

SUMMARY

Two processing routes to grow CVD mullite coatings were investigated. Localized mullite formation was achieved with multi-layered coatings, but could not be extended to total formation throughout the coating due to devitrification of the silica layer. It was determined that residual stresses in the multi-layers contributed to the phase transformations. Equilibrium thermodynamic analysis was performed on the $AlCl_3$-$SiCl_4$-CO_2-H_2 system for the formation of mullite via codeposition. The results of the analysis were presented in the form of "CVD phase diagrams" that show that low concentrations of the chlorides is necessary in order to obtain high deposition efficiency and carbon-free deposits. This information was very effectively used in identifying the initial process conditions for experimentation. Based on this, dense, adherent mullite coatings were successfully grown via CVD. Initial corrosion testing shows that these coatings performed well under Na_2SO_4 environments at elevated temperatures.

ACKNOWLEDGMENTS

The authors wish to acknowledge the help from Mr. D. Doppalapudi, and Dr. S.N. Basu with the TEM analysis. This project was initiated through funding by Office of Transportation Technologies, as part of the Ceramic Technology Project of the Propulsion System Materials Program. Research sponsored by the U.S. Department of Energy, Assistant Secretary for Energy Efficiency and Renewable Energy, Fossil Energy AR&TD Materials Program under contract number SC-19X-SS110C with Martin Marietta Energy Systems, Inc.

REFERENCES

1. K.N. Lee, N.S. Jacobson, and R.A. Miller, "Refractory Oxide Coatings on SiC Ceramics," MRS Bulletin, Vol. 19, No. 10, p. 35 1994.

2. J.I. Federer, Adv. Ceram. Mater., Vol. 3, No. 1 p. 56 1988.

3. R.F. Davis, and J.A. Pask, "Mullite," High Temperature Oxides, Part IV, A.M. Alper, Ed., Academic Press, New York 1971.

4. I.A. Aksay, and J.A. Pask, J. Am. Ceram. Soc., Vol. 58, No.11-12 p. 507 1975.

5. G. Oertel, and H. Flietner, "Isolationsschichten Auf Germanium Und Deren Elektrische Eigenschaften," Proceedings of the Second Colloquium on thin Films, p. 626-635 1967.

6. D. Doppalapudi, R. Mulpuri, S.N. Basu, and V.K. Sarin, "Phase Transformations in Multilayered CVD Mullite Coatings," MRS Proceedings, Vol. 363, Chemical Vapor Deposition of Refractory Metals and Ceramics III, W. Lee, B. Gallois, and M. Pickering, Eds. MRS Fall Meeting, Boston, MA, Nov/Dec 1994.

7. T.M. Besmann, "SOLGASMIX-PV for the PC," Oak Ridge National Laboratory 1989.

MECHANICAL BEHAVIOR OF CERAMIC COMPOSITE HOT-GAS FILTERS AFTER EXPOSURE TO SEVERE ENVIRONMENTS

D. J. Pysher, B. L. Weaver, R. G. Smith, J. H. Eaton, and J. L. Kahnke

Ceramic Technology Center
3M Company
St. Paul, MN 55144-1000

ABSTRACT

A novel type of hot-gas filter based on a ceramic fiber reinforced ceramic matrix has been developed, as reported at previous Fossil Energy Materials Conferences, through research activities at Oak Ridge National Laboratory (ORNL) and at the 3M Company. Simulated testing has been done at the Westinghouse Science and Technology Center. This filter technology has been extended to full size, 60 mm OD by 1.5 meter long candle filters and a commercially viable process for producing the filters has been developed. Filters are undergoing testing and demonstration use throughout the world for applications in pressurized fluidized-bed combustion (PFBC) and integrated gasification combined cycle (IGCC) plants. Demonstration tests of this ceramic composite filter along with other filters are in progress at the Tidd PFBC plant.

Mechanical tests were performed on the 3M brand Ceramic Composite Candle Filter after exposure to various corrosive environments in order to assess its ability to function as a hot gas filter in coal-fired applications. Due to the different construction of ceramic composite filters and the thin composite wall versus the typical thick-walled monolithic filter, standard mechanical property tests had to be refined or modified to accurately determine the filter's properties. These tests and filter property results will be described.

Longitudinal tensile and diametral O-ring compression tests were performed on as-produced candle filters as well as on filters which had been exposed to various environments. The exposures were for 1000 hrs at 850°C in wet air, in wet air containing Na_2CO_3, and in wet air containing NaCl. In addition, a filter which had been coated with ash (Old Grimethorpe) was exposed to wet air at 850°C for 1000 hours.

INTRODUCTION

A novel type of hot-gas filter based on a ceramic fiber reinforced ceramic matrix has been developed through research activities at Oak Ridge National Laboratory (ORNL) and at the 3M Company under a contract with the U.S. DOE Office of Fossil Energy's Advanced Research and Technology Development (AR & TD) Materials Program. This filter development has been extended from a laboratory sample stage to the fabrication of full size, 60 mm OD by 1.5 meter long candle filters with a commercially viable process for producing the filters.[1,2]

As reported at previous Fossil Energy Materials Conferences, simulated pressurized fluidized-bed combustion (PFBC) testing of two sets of the ceramic composite filters has been completed at the Westinghouse Science and Technology Center.[3,4] Filters are currently undergoing testing and

demonstration use in various university test laboratories and industrial facilities throughout the world for applications in pressurized fluidized-bed combustion (PFBC) and integrated gasification combined cycle (IGCC) plants.

Demonstration tests of the 3M Ceramic Composite Candle Filters along with other filters are in progress at the Tidd PFBC plant under the sponsorship of Morgantown Energy Technology Center (METC), American Electric Power (AEP), and Westinghouse (WSTC). One 3M filter removed during 4th Quarter 1994 from the Tidd Power Plant test has been divided between 3M and Westinghouse for analysis. An additional ten filters were installed and tested during the 1st Quarter of 1995. These ten filters are waiting to be removed from the system for analysis. At this point the details of the Tidd test cannot be discussed until METC, AEP, and Westinghouse release the test information.

Traditional (monolithic) mechanical property tests which utilize bend bars or tensile coupons cannot be adapted to tubular, low-density composite geometries without undue complications. Therefore, test methodologies were developed which subject candle filters to conditions they are expected to experience in service in order to assess their ability to function as a hot gas filter in coal-fired PFBC and IGCC applications. Sections of composite were tested in longitudinal tension and in diametral compression in both the as-produced state as well as after exposure to oxidative/corrosive environments which simulated those encountered in service. The results of the mechanical property testing of the 3M Ceramic Composite Candle Filter used at Tidd are presented along with retained baseline samples and samples exposed to various corrosive environments in the laboratory.

EXPERIMENTAL PROCEDURE

A 60" candle filter was sectioned as shown in Figure 1. Tensile, O-ring diametral compression, and filtration tests were performed on both exposed and unexposed portions to allow comparisons to be made.

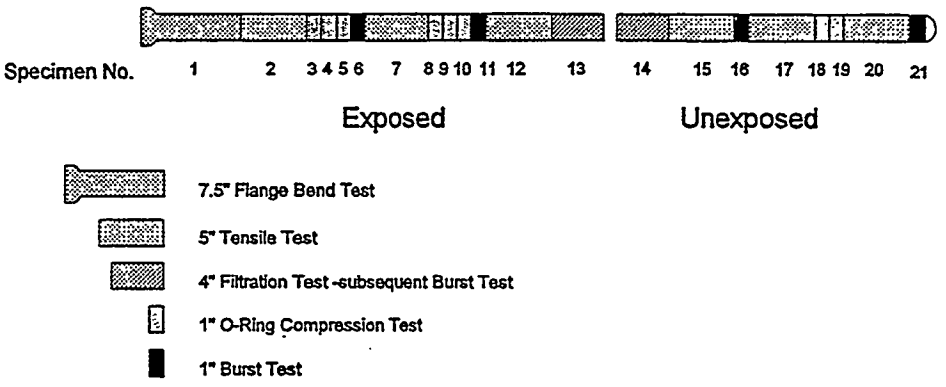

Figure 1. Sectioning of 60" candle filter.

For oxidation experiments, 36" of the flange end of an as-fabricated candle filter was placed into a preheated tube furnace. The rate of air flow through a bubbler containing water into the furnace was 1 l/min. Exposures were performed at 850°C for 1000 hours. Weights of the entire section were recorded before and after exposure and each test specimen was weighed after exposure as well. For corrosion/oxidation experiments, the candle filters were dipped in a solution of either Na_2CO_3 or NaCl prior to oxidation. The solutions were prepared so as to give a uniform concentration of about $1x10^{17}$ Na ions/cm^2.[5]

Filtration testing was performed using a commercial filter tester.[a] The filtration test utilized NaCl particles with a mean diameter of 0.1 μ at a concentration of 100 mg/m3. The filtration test was performed at a given flow rate of 30 liters/min, corresponding to a face velocity of 3.0 cm/sec for a 4" filter tube section. Face velocity equals flow rate divided by surface area. Efficiency is calculated by dividing the concentration of particles exiting the filter by the input concentration.

Maximum pore diameter and permeability were determined by standard methods[6]. The maximum pore diameter was determined by submerging the filter in a liquid medium (water) and measuring the pressure at which bubbling first occurs. Permeability was determined by measuring the pressure drop across the filter at various air flow rates.

Tensile specimens were fabricated by epoxying standard iron pipe reducer fittings into the ends of a 5" section of tube using epoxy[b]. Fixtures were then screwed into the fittings and attached to the test frame and load cell using orthogonally-oriented pins to minimize non-axial loading. A crosshead speed of 2.0 mm/min was used.

Although it does not directly simulate stresses encountered in service, the O-ring compression test is a simple and effective test for monitoring process variables or service conditions which affect composite failure behavior. Tests were performed by diametrically compressing a 1" section of filter tube. A crosshead speed of 4.0 mm/min was used and tests were halted after a crosshead displacement of 5 mm.

RESULTS & DISCUSSION

Filter sections subjected to the wet oxidation and the Na_2CO_3/NaCl dip + oxidation treatments developed a uniform golden hue and experienced a minimal weight gain, consistent with passive oxidation of the SiC matrix.

a TSI Automated Filter Tester, model 8110.

b 3M Scotch-Weld™ 1838-L B/A

Filtration Test Results

Filtration results for filter samples subjected to wet oxidation are presented in Figure 2. Results for samples coated with ash prior to oxidation are presented in Figure 3. For both exposures, filtration efficiency reached 99.9% within 10 minutes of the test, which is typical of the 3M filter. Pressure drop for the wet oxidized sample was slightly lower after exposure. The filtration results for samples coated with Na_2CO_3 and NaCl fall between these two extremes.

Mechanical Test Results

The tensile strengths were calculated using

$$\sigma_{tensile} = \frac{F}{\pi(r_o^2 - r_i^2)} \qquad (1)$$

where F is the fracture load (in Newtons), and r_0 and r_i are the outer and inner tube radii, respectively. Tensile stiffness values were determined from the maximum slope of the load-displacement curves.

For stress analyses, the composite filter is treated as a thin-wall cylinder (i.e. the assumption of constant stress across the wall results in negligible error) since its internal diameter-to-thickness ratio is greater than 10 (≈ 30)[7]. The equation used to calculate the maximum stress in an O-ring is that for a thin-walled cylinder and is given by[8]

$$\sigma_{O-Ring} = \frac{2Fr_a}{\pi dt^2}\frac{(6r_a - t)}{(2r_a - t)} \qquad (2)$$

where r_a is the average radius ($r_a = [r_0 + r_i] / 2$), t is the wall thickness, and d is the specimen width.

A critical parameter in determining accurate stresses is a wall thickness (see Equation 1 and 2 above), which describes the true cross-sectional area. For the 3M Ceramic Composite Candle Filter, the thin-walled, high-porosity construction makes it difficult to decide on a representative wall thickness. Work has begun on determining an "effective" wall thickness from the true density (based on submerged weight measurements). This effective wall thickness would be the thickness of a 100% dense tube having the same average radius and length.

Mechanical testing at this point has focused on the substrate layer of the 3M Ceramic Composite Candle Filter as this is the principal load supporting layer of the filter. The other layers are not intended

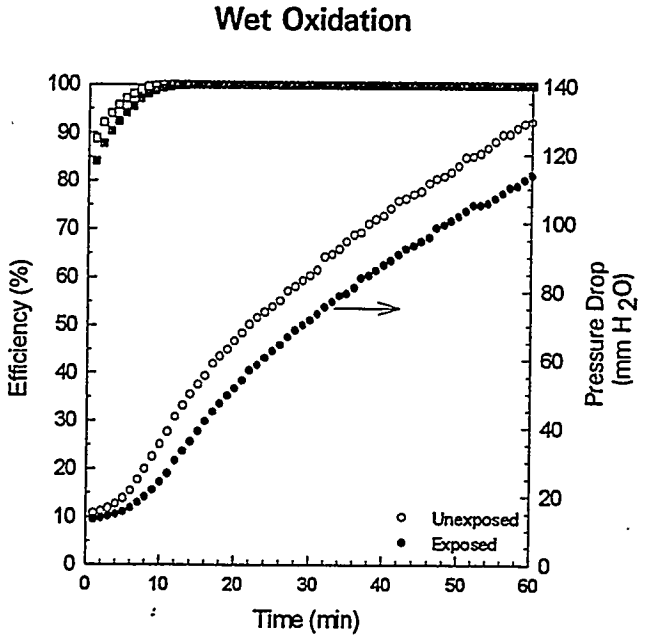

Figure 2. Filtration efficiency and pressure drop for ceramic composite candle filter oxidized at 850° C for 1000 hours.

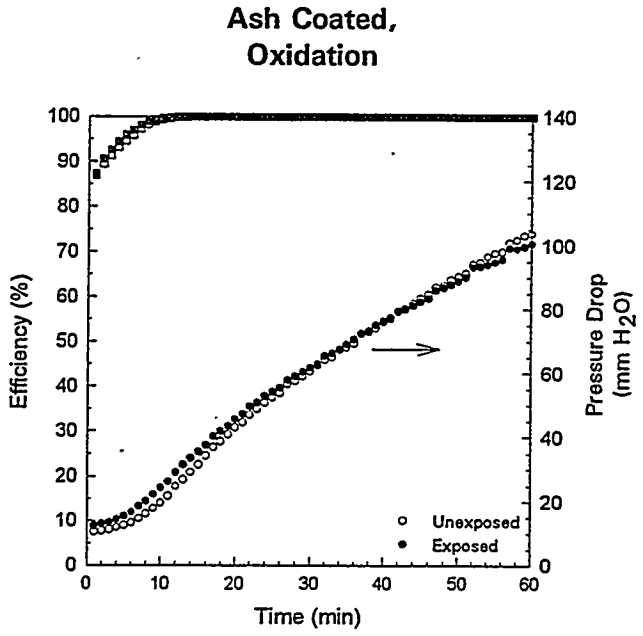

Figure 3. Filtration efficiency and pressure drop for ceramic composite candle filter coated with ash and oxidized at 850° C for 1000 hours.

to be structural, but may or may not contribute to the overall strength of the filter. Work has begun on determining what affect, if any, these outer layers have on mechanical properties.

OBSERVATIONS

A summary of the mechanical test results is given in Table 1. In the laboratory exposure tests the samples retained approximately 50% of the as-produced peak tensile stress. The Tidd PFBC exposed sample retained 69% of the as-produced peak tensile stress. Representative tensile load-displacement curves are shown in Figure 4.

Table 1. Results from tensile and O-ring compression tests of as-produced and exposed filters.

		Oxidized	Na_2CO_3 dipped, oxidized	NaCl dipped, oxidized	Ash coated, oxidized	Tidd PFBC
Peak Tensile Stress (MPa)	As-Produced	50	51	47	46	(48)
	After Exposure	27	24	28	23	34
	Retained	**54%**	**46%**	**59%**	**50%**	**69%**
Tensile Stiffness (Kg/mm)	As-Produced	2236	2426	2552	2501	(2446)
	After Exposure	2099	2236	2353	1793	2158
	Retained	**94%**	**92%**	**92%**	**72%**	**88%**
Peak O-Ring Stress (MPa)	As-Produced	10.8	9.8	7.8	6.1	(8.7)
	After Exposure	6.8	5.0	4.6	4.8	9.3
	Retained	**63%**	**51%**	**59%**	**79%**	**107%**
O-Ring Stiffness (Kg/mm)	As-Produced	12.7	11.2	8.2	10.4	(10.6)
	After Exposure	5.3	4.4	5.1	4.2	11.5
	Retained	**42%**	**39%**	**62%**	**40%**	**109%**

Numbers in parentheses are retained baseline samples.

The laboratory exposure O-ring test specimens retained slightly more than 50% of the as-produced stress values. Again, the Tidd PFBC exposed samples retained more of the as-produced stress than the laboratory exposed samples. Representative O-ring load-displacement curves are shown in Figure 5.

The values for percent of retained tensile stiffness do not indicate a clear trend. The O-ring stiffness retention does indicate that there was very little effect on this value in the Tidd PFBC exposure test.

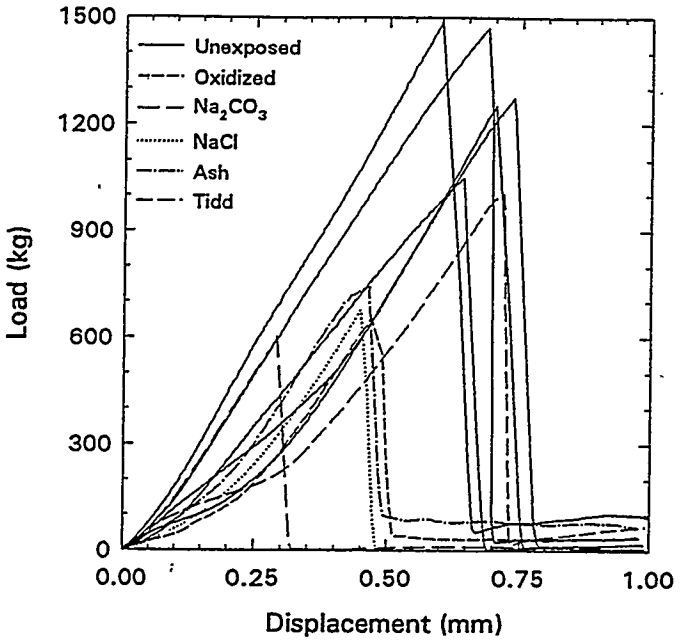

Figure 4. Load-displacement curves from tensile tests on unexposed and exposed filters.

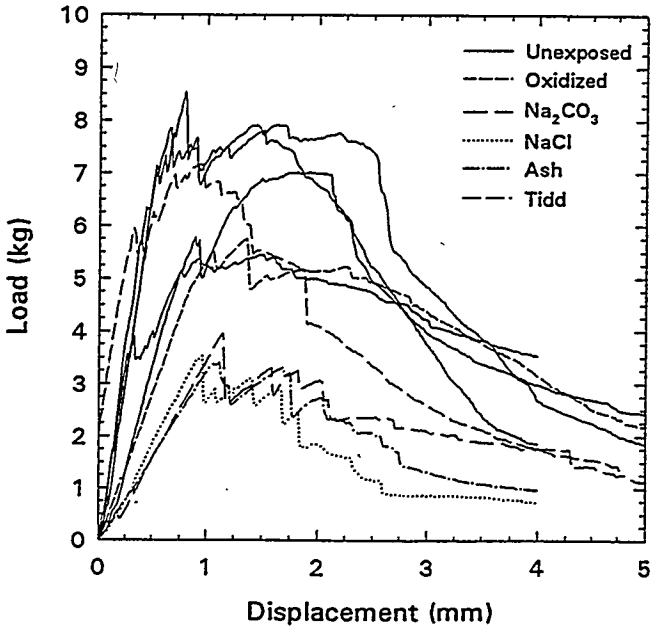

Figure 5. Load-displacement curves from O-ring tests on unexposed and exposed filters.

The similarity in stress retention between the oxidized samples, and the Na_2CO_3, NaCl, and ash coated samples, seems to indicate a similar mechanism at work in these samples. All of these samples were exposed to wet air at high temperatures, this indicates that oxidation is the primary factor in the reduction of strength in these samples. From 3M studies on other ceramic composite parts the initial strength decrease which occurs in the first hours of oxidation exposure is felt to be due to oxidation of the interface materials.

The Tidd PFBC exposed samples did not degrade as much as the laboratory exposed samples. This indicates that the conditions in the PFBC exposure are not as harsh as the conditions used in these laboratory exposures.

FUTURE PLANS

Future testing plans include both exposure and analysis of laboratory samples, and placement and analysis of filters in real industrial environments. Specific plans include the following:

1. A mechanical burst test has been developed as part of the set of composite filter mechanical property tests. Several one inch wide sections have been retained from each of the exposed and baseline filter samples for burst testing in the immediate future.

2. Additional shorter and longer duration laboratory exposure tests will be run to better understand mechanical and filtration durability.

3. A range of exposure specimens will be examined microscopically to determine microstructure changes that correspond to decrease of mechanical properties.

4. Interactions will continue with various outside laboratories and industrial groups to place and test filters in additional real environment PFBC and IGCC applications.

ACKNOWLEDGMENTS

This research was sponsored by U. S. Department of Energy, Office of Fossil Energy, Martin Marietta Energy Systems, Inc., Oak Ridge National Laboratory, and 3M Company. The assistance of D. P. Stinton and R. R. Judkins of Oak Ridge National Laboratory, and T. E. Lippert, M. A. Alvin, E. E. Smeltzer, all of Westinghouse is gratefully acknowledged.

REFERENCES

1. R.G. Smith and J.H. Eaton, "Fabrication of Commercial-Scale Fiber-Reinforced Hot Gas Filters by Chemical Vapor Deposition," Final Technical Report on subcontract No. 93X-SB482C with Martin Marietta Energy Systems, Inc. April, 1994.

2. R.G. Smith and J.H. Eaton, "Fabrication of Commercial-Scale Fiber-Reinforced Hot Gas Filters by Chemical Vapor Deposition," Addendum to Final Technical Report on subcontract No. 93X-SB482C with Martin Marietta Energy Systems, Inc. September, 1994.

3. J.P. Oberst and E.E. Smeltzer, "3M CVI Hot Gas Candle Filter Test Program," Test under General Order No. MP-12775-CE for 3M Company, May 20, 1993.

4. E.E. Smeltzer, "3M CVI Hot Gas Candle Filter Test Program," Test under General Order No. MP-12775-CE for 3M Company, Jan. 27, 1994.

5. Z. Zheng, R.E. Tressler, and K.E. Spear, Fundamental Studies of Corrosion of Nonoxide Structural Ceramics, Vol. 1, Single Crystal Silicon Carbide, Center for Advanced Materials, The Pennsylvania State University, October 1988.

6. ASTM E128-94, "Standard Test Method for Maximum Pore Diameter and Permeability of Rigid Porous Filters for Laboratory Use", 1994 Annual Book of ASTM Standards, vol.14.02, pp. 53-55.

7. p. 5-49 in Marks Standard Handbook for Mechanical Engineers, 9th edition.

8. G. DeWith, "Note on the Use of the Diametral Compression Test for the Strength Measurement of Ceramics," J. Mater. Sci. Lett., 3 [11] 1000-1002 (1984).

FRACTURE BEHAVIOR OF ADVANCED CERAMIC HOT-GAS FILTERS

J.P. Singh, D. Singh, J. Smith, and H. Volz

Energy Technology Division
Argonne National Laboratory
Argonne, IL 60439

ABSTRACT

Microstructural, mechanical, and thermal-shock behavior of hot-gas candle filters obtained from different manufacturers have been evaluated. These filters include both monolithic ceramic and composite materials. Based on the results obtained so far, composite filters perform better than monolithic ceramic filters in a thermal-shock environment. During thermal-shock testing, the monolithic ceramic filters failed in a brittle (catastrophic) mode, while composite filters showed a non-catastrophic mode of failure and very little degradation in ultimate strength. Fractographic evaluations were performed to identify and characterize critical flaws in Nextel fibers for the determination of in-situ fiber strength in Nextel/SiC filters. Average in-situ fiber strength was determined to be 1.7 GPa.

INTRODUCTION

Hot dirty gas exiting from a gasifier or an advanced combustor contains sufficient particulates to warrant it undesirable for direct utilization in gas turbines and heat engines. Today's hot dirty gas cleanup systems, such as cyclones, can remove only the fraction containing the larger particulates. Smaller particulates can be removed only by cooling and filtering the gas. The resulting enthalpy loss causes a significant decrease in overall system efficiency. Because of the enthalpy loss and decrease in overall efficiency, there is a critical need for cleaning hot dirty gas with little or no cooling. The U.S. Department of Energy and others are currently supporting the

development of ceramic/composite filter technology for combined-cycle power generation with coal gasification. Ceramic filters should essentially remove all of the fines from a hot dirty gas stream and be stable in hot dirty gas environments.

This project supports the development of candle ceramic/composite filters for cleanup of hot dirty gases. Effort has been directed toward developing materials qualification technology in order to ensure satisfactory performance of filters in a hot dirty gas stream. To predict long-term performance of such filters, it is important to understand and evaluate the fracture behavior of filters in service environments. Mechanical properties should be evaluated to establish baseline data. Thermal-shock resistance should be measured to predict filter performance in a service environment.[1] Failure modes must be identified and failure mechanisms must be established.

In this paper, results are presented on the evaluation of strength and thermal-shock resistance for the first set of filters obtained from 3M, Du Pont Lanxide, and Industrial Filter and Pump (IFP).

SPECIMENS FOR FRACTURE STUDIES

Initial effort concentrated on filters obtained from the three industrial sources: Nextel/SiC composite filters from 3M, PRD-66 filters from Du Pont Lanxide, and monolithic SiC filters from IFP. The 3M filters consist of layered composite structures, with a tubular filter element sandwiched between two Nextel/SiC composite tubes. Bonding between the Nextel/SiC composite tubes and the filter layer is achieved by chemical vapor infiltration (CVI) of SiC. The inner and outer diameters of these filters are ≈2.54 and ≈2.86 cm, respectively. The PRD-66 is an all–oxide ceramic consisting of a layered microstructure of alumina, mullite, cordierite, and some amorphous material. Inner and outer diameters of the filters are ≈2.26 and ≈2.98 cm, respectively. The monolithic SiC filters consist primarily of SiC grains; inner and outer diameters are ≈2.05 and ≈2.96 cm, respectively.

EVALUATION OF STRENGTH AND THERMAL–SHOCK RESISTANCE

Strength of the candle filters was evaluated on 1–in.–long O-ring specimens machined from each of the three filters. These specimens were loaded to failure in a

diametrical compression mode at a crosshead speed of 0.13 cm/min. Maximum stress is at the inner diameter across the load points, which simulates the thermal-shock stresses developed during pulse-cleaning cycles. The fracture stress, σ_f, is given by the following equation:[2]

$$\sigma_f = PK/\pi bl, \quad (1)$$

where P is the fracture load, K is a function of the ratio of inner and outer diameters,[2] and l is the length of the ring. As shown in Fig. 1, load-deflection plots for the filter specimens in as-fabricated condition indicated a nonbrittle mode of failure for the Nextel/SiC composites and PRD-66 filters, while the IFP monolithic SiC filters showed brittle failure.

Thermal-shock testing of these filters was performed on 1-in.-long ring specimens machined from the filters and insulated on the outer surfaces to simulate heat transfer conditions in service. The specimens were heated to preselected temperatures (25-1100°C) in an electric furnace, as shown in Fig. 2. Subsequently, they were quenched in silicone oil at room temperature (≈25°C). Thermal-shock damage was estimated by measuring the strength of each ring specimen before and after thermal quenching.

Results of the thermal-shock experiments are given in Fig. 3, which shows the retained strength of specimens when subjected to varying degrees of thermal quenching (ΔT). Vertical bars represent standard deviation when three to four specimens were tested. Other data points represent values for single specimens.

Limited results obtained so far indicate that the 3M Nextel/SiC composite filters and Du Pont Lanxide PRD-66 filters show little or no strength degradation when quenched from temperatures up to ≈1000°C. On the other hand, the monolithic SiC filters from IFP showed strength degradation when quenched from temperatures >800°C. Further experiments are currently in progress to confirm the statistical reliability of these results. Microstructural evaluations are also underway to evaluate failure modes and mechanisms for improved prediction of filter performance.

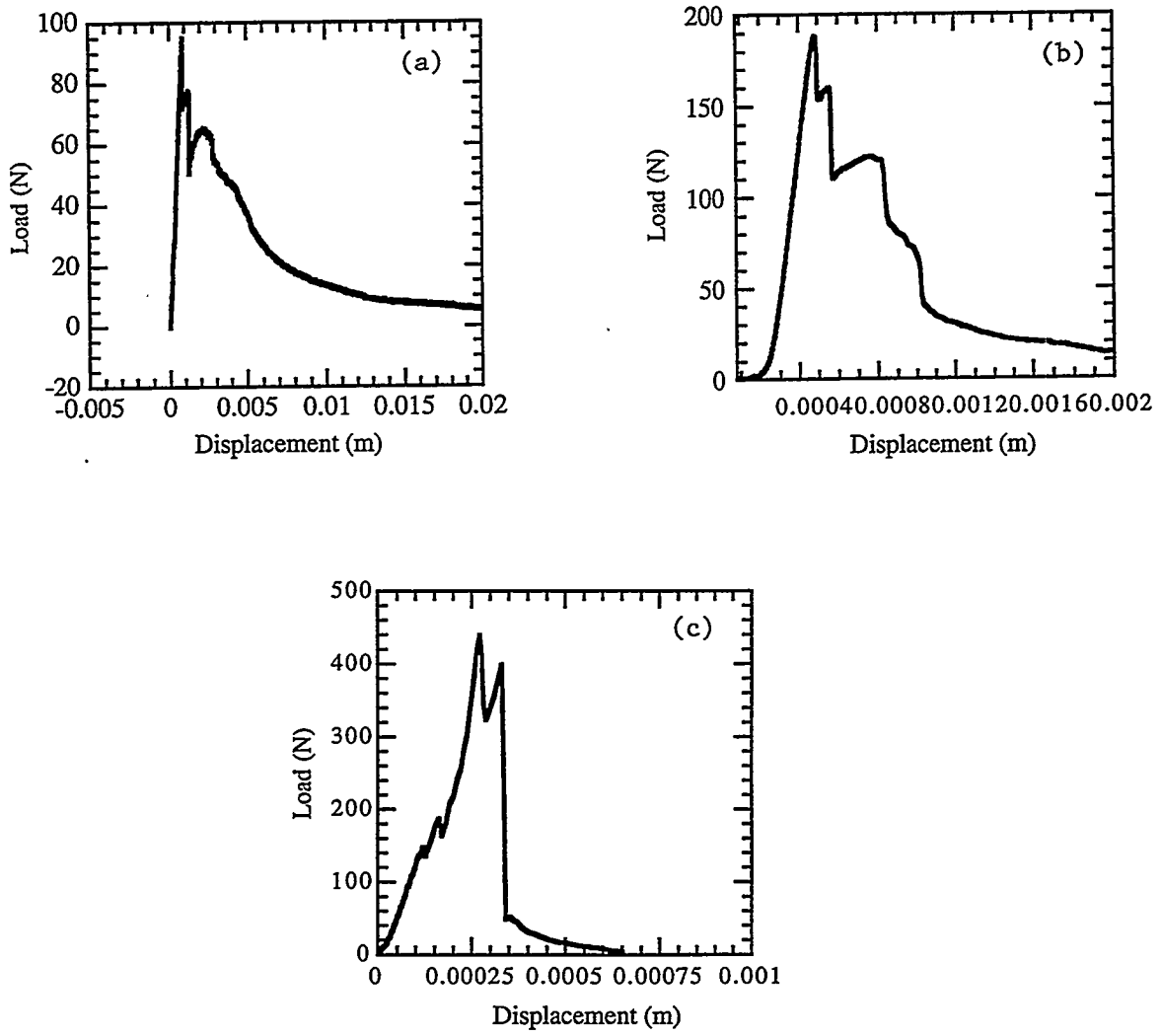

Fig. 1. Load-displacement plots for (a) Nextel/SiC, (b) PRD-66, and (c) IFP SiC filters, showing nonbrittle and brittle fractures.

As noted in other studies,[3,4] a substantial degradation of in-situ strength of Nicalon fibers in Nicalon-fiber-reinforced SiC matrix composites was observed during composite processing and in elevated-temperature service environments. Therefore, a study has been initiated to evaluate the nature of flaw generation and resulting strength degradation of Nextel fibers in the Nextel/SiC composite filters during filter processing and in service. Strength of in-situ Nextel fibers in the Nextel/SiC composites after filter processing has been determined by evaluating critical flaw sizes using fractographic techniques, as described below.

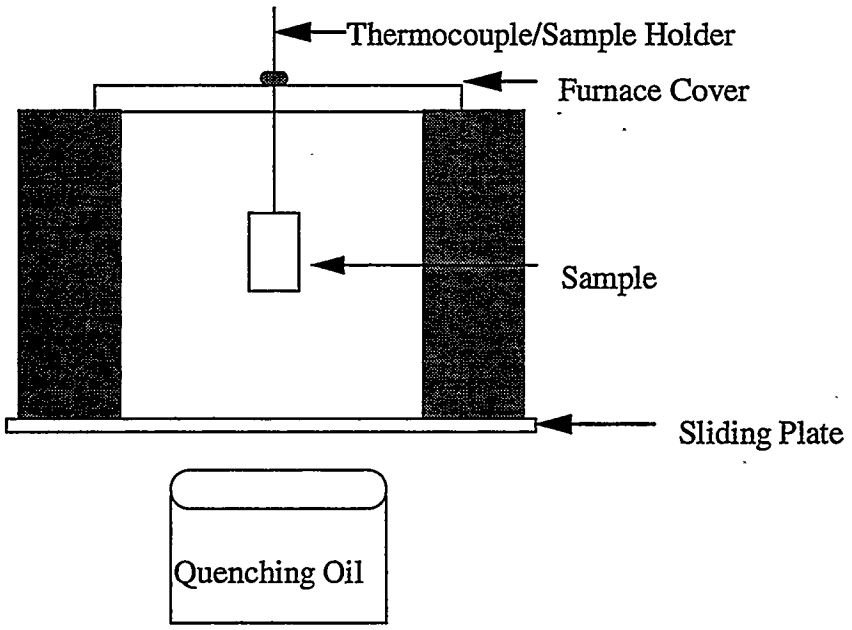

Fig. 2. Schematic diagram of thermal–quench test apparatus.

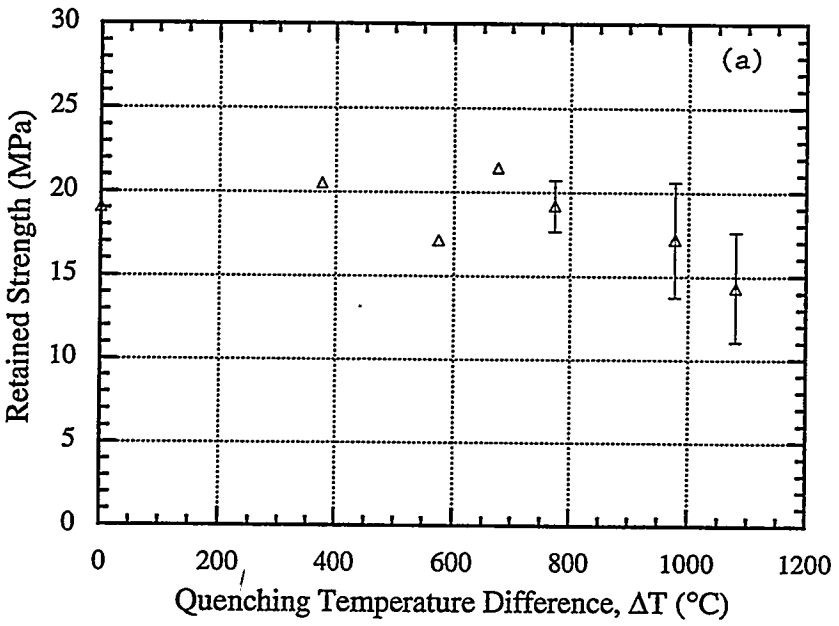

Fig. 3. Dependence of retained strength of ring specimens on quenching temperature difference (ΔT): (a) Nextel/SiC composite filters, (b) PRD-66 filters, and (c) monolithic IFP SiC filters.

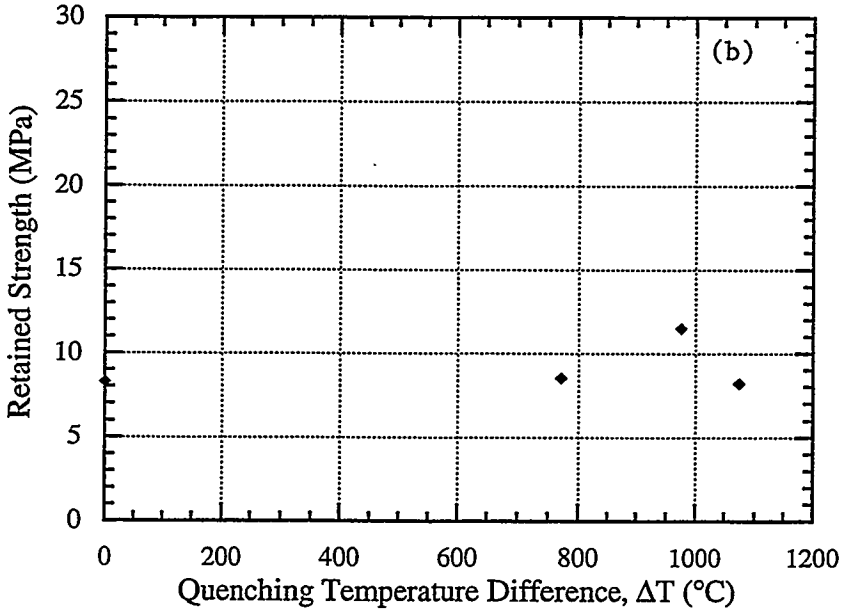
(b)
Retained Strength (MPa)
0
5
10
15
20
25
30
0
200
400
600
800
1000
1200
Quenching Temperature Difference, ΔT (°C)

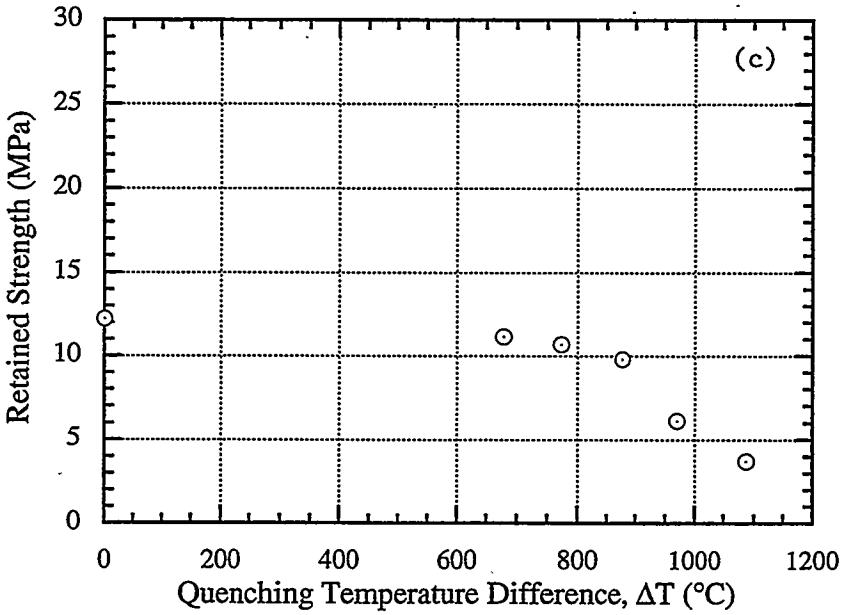
(c)
Retained Strength (MPa)
0
5
10
15
20
25
30
0
200
400
600
800
1000
1200
Quenching Temperature Difference, ΔT (°C)

Fig. 3. (Contd.)

IN–SITU FIBER STRENGTH BEHAVIOR

In-situ strength of fibers in the Nextel/SiC composite filters tested at room temperature was evaluated from characteristic fracture features of the fibers. Strength of fractured fibers was determined from the measured values of fracture mirror radii, as discussed in regard to use of the empirical relationship proposed by Kirchner and Gruver[5] and as given in

$$\sigma_f \sqrt{r_m} = A_m, \tag{2}$$

where σ_f is the fiber fracture strength, r_m is the measured fiber mirror radius, and A_m is the mirror constant and is taken to be 3.5 MPa$\sqrt{m}$.

The measured values of in-situ fiber strengths were described by the Weibull strength distribution function, as shown in

$$F(\sigma) = 1 - \exp\left[-\left(\frac{\sigma}{\sigma_o}\right)^m\right], \tag{3}$$

where $F(\sigma)$ is the cumulative failure probability at an applied stress σ, σ_o is the scale parameter signifying a characteristic strength of the distribution, and m is the Weibull modulus that characterizes the flaw distribution in the material.

Figure 4 shows the distribution of in-situ Nextel fibers in Nextel/SiC composite filters. Average fiber strength is approximately 1.7 GPa. An effort was also made to evaluate the strength of as-fabricated fibers by fiber bundle testing.[6] Average strength of as–fabricated Nextel fibers, obtained from preliminary fiber bundle tests, was 2.1 GPa. This suggests that there is an approximately 20% degradation in the strength of as–fabricated Nextel fibers during filter processing. Further experiments are being conducted to validate the results obtained from bundle tests.

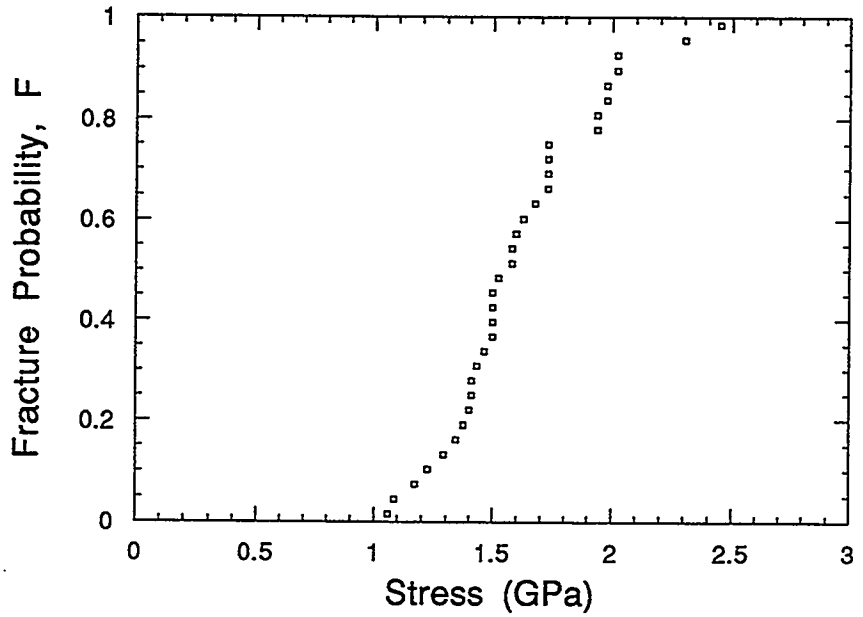

Fig. 4. Weibull strength distribution of Nextel fibers in Nextel/SiC composite filters.

ACKNOWLEDGMENT

The work was supported by the U.S. Department of Energy, Office of Fossil Energy, Advanced Research and Technology Materials Program, under Contract W-31-109-Eng-38. The authors thank D. J. Pysher, B. L. Weaver, and R. G. Smith of the 3M Company, J. A. Chambers of Dupont Lanxide Composites Inc., and P. Eggerstedt and J. Zievers of the Industrial Filter & Pump Manufacturing Company for providing filter specimens and for their helpful discussions.

REFERENCES

1. J. P. Singh, S. Majumdar, A. S. Wagh, T. Wenzel, and R. B. Poeppel, "Materials Qualification Technology for Ceramic Cross-Flow Filters," Argonne National Laboratory Report ANL/FE-91/1, July 1991.

2. E. A. Ripperger and N. Davis, "Critical Stress in Circular Ring," Trans. Amer. Soc. Civ. Engr., Paper No. 2308, pp. 619-35 (1948).

3. J. P. Singh, D. Singh, and R. A. Lowden, "Effect of Fiber Coating on Mechanical Properties of Nicalon Fibers and Nicalon-Fiber/SiC Matrix Composites," Ceram. Eng. Sci. Proc., **15**, [4] 456-464 (1994).

4. D. Singh and J. P. Singh, "Effect of Processing on Strength of Nicalon Fibers in Nicalon Fiber-SiC Matrix Composites," Ceram. Eng. Sci. Proc., **13** [7-8] 257-266 (1992).

5. H. P. Kirchner and R. M. Gruver, "Fracture Mirror in Alumina Ceramics," Phil. Mag. ,**27** 1433–1446 (1973).

6. Z. Chi, T. W. Chou, and G. Shen, "Determination of Single Fiber Strength Distribution from Fiber Bundle Testings," J. Mater. Sci. ,**19** [10], 3319–3324 (1984).

HIGH TEMPERATURE CORROSION OF ADVANCED CERAMIC MATERIALS FOR HOT-GAS FILTERS AND HEAT EXCHANGERS

E. R. Kupp, M. F. Trubelja, K. E. Spear and R. E. Tressler

Materials Science and Engineering
The Pennsylvania State University
University Park, PA 16802

ABSTRACT

Experimental corrosion studies of hot gas filter materials and heat exchanger materials in oxidizing combustion environments have been initiated. Filter materials from 3M Co. and DuPont Lanxide Composites Inc. are being tested over a range of temperatures, times and gas flows. It has been demonstrated that morphological and phase changes due to corrosive effects occur after exposure of the 3M material to a combustion environment for as little as 25 hours at 800°C. The study of heat exchanger materials has focused on enhancing the corrosion resistance of DuPont Lanxide Dimox™ composite tubes by adding chromium to its surfaces by (1) heat treatments in a Cr_2O_3 powder bed, or (2) infiltrating surface porosity with molten chromium nitrate. Each process is followed by a surface homogenization at 1500°C. The powder bed method has been most successful, producing continuous Cr-rich layers with thicknesses ranging from 20 to 250 μm. As-received and Cr-modified DuPont Lanxide Dimox™ samples will be reacted with commonly encountered coal-ash slags to determine the Cr effects on corrosion resistance.

INTRODUCTION

The objectives of this work are to: (a) study the corrosion and resulting changes in mechanical properties of candidate hot gas filter materials exposed to a combustion environment, and (b) compare the corrosion rates of the as-received and Cr-infiltrated $Al/Al_2O_3/SiC_p$ DuPont Lanxide Dimox™ heat exchanger materials in contact with the two commonly encountered coal-ash slags of a typical Illinois #6 composition, and a CaO-enriched Illinois #6. Our progress toward achieving these objectives is summarized below.

SCREENING ANALYSIS OF CANDIDATE CERAMIC HOT GAS FILTER MATERIALS

The corrosion testing of ceramic hot gas filters currently involves 3M's Type 203 filters (a SiC matrix-Nextel fiber composite) and DuPont Lanxide's SiC-SiC composite tubes with Nicalon fibers. In both cases the SiC matrix is produced by a chemical vapor

infiltration process. The initial tests involve flow-over exposures to a combustion atmosphere of ash-coated rings cut from tubes of these materials. The ash used to coat the rings was collected at the Tidd plant and is a product of the combustion of Pittsburgh #8 coal. A parametric study of time, temperature and total gas flow has been initiated to study corrosion effects and to generate systematic corrosion data. Time permitting, a study of the effect of gas composition on corrosion rates will also be undertaken. These data will provide a baseline for corrosion testing of mini-candles in a flow-through configuration.

Experimental Conditions

The experimental conditions involved in the parametric study of time, temperature and gas flow are presented in Table 1. The baseline gas composition is the same as that used at the University of North Dakota Energy and Environmental Research Center (UNDEERC), where it was determined to be representative of the combustion environment experienced by hot gas filters in a pressurized fluidized bed combustor (PFBC). The range of temperatures was chosen because it is also representative of the conditions to which candle filters are exposed during use. Flow rates and exposure times were chosen to be practical for running laboratory tests and generating systematic corrosion data in a reasonable time frame. Short duration exposures have not been reported previously and a

Table 1: Experimental conditions used in a flow-over configuration to study corrosion effects on filter materials in simulated coal combustion environments.

Parameter	Values
Temperature (°C)	800, 870, 950
Time (hr)	10, 25, 50
Flow rate (slm)	1, 2.5, 5
Baseline gas composition: N_2 (%)	66.5
CO_2 (%)	15
O_2 (%)	3
H_2O (%)	15
SO_2 (%)	0.5
NaCl (ppm)	10

significant amount of corrosion may occur in the early exposure of filter materials to combustion environments.

Results and Discussion

Corrosion effects were observable for test conditions of 800°C, 25 hours and a flow rate of 2.5 slm. Figure 1 contains scanning electron micrographs of SiC-coated fibers in the middle layer of a 3M filter as-received (Fig. 1a) and after exposure to these conditions (Fig. 1b). This layer is the part of the material which actually filters the ash from the combustion gases. The morphology of the coating is significantly altered by this exposure. In the as-received sample, the SiC grains are observed to have a typical CVD film structure sometimes referred to as a "cauliflower" morphology. After only 25 hours in a combustion environment, the surface of the SiC coating has a glazed or glassy appearance and is less uniform. The surface appears to have been coated with reaction products of the gas phase species or to have reacted with the combustion gases. It has not yet been determined whether the thicknesses of the fibers are increasing or decreasing as a result of this interaction. No changes were observed on the surface of the inner, or support, layer of the exposed filter ring.

Pieces of the middle layers of the samples shown in the micrographs in Fig. 1 were crushed in a mortar and pestle and mounted on glass slides for x-ray diffraction (XRD) analysis. The resulting spectra are shown in Fig. 2. SiC was the only phase positively identified on both patterns. The SiC is probably a mixture of polytypes, but it most closely matches the powder diffraction pattern for the 15R polytype of SiC (JCPDS file number 39-1196). A trace amount of mullite (JCPDS file number 15-776) may also be present. The only discernible difference between the spectra is a broad hump between 20 and 30 degrees 2-theta, indicating an amorphous component, on the pattern for the sample which was exposed to the combustion environment (scan b in Fig. 2). No discernible differences were observed on the XRD patterns for the inner layer of the filter before and after exposure. In addition to SiC, mullite was identified as a minor phase on these spectra.

Summary and Future Research on Hot Gas Filter Materials

Initial exposure testing of 3M's fiber composite hot gas filter material has confirmed that corrosive effects are observable after short term exposure times to PFBC conditions.

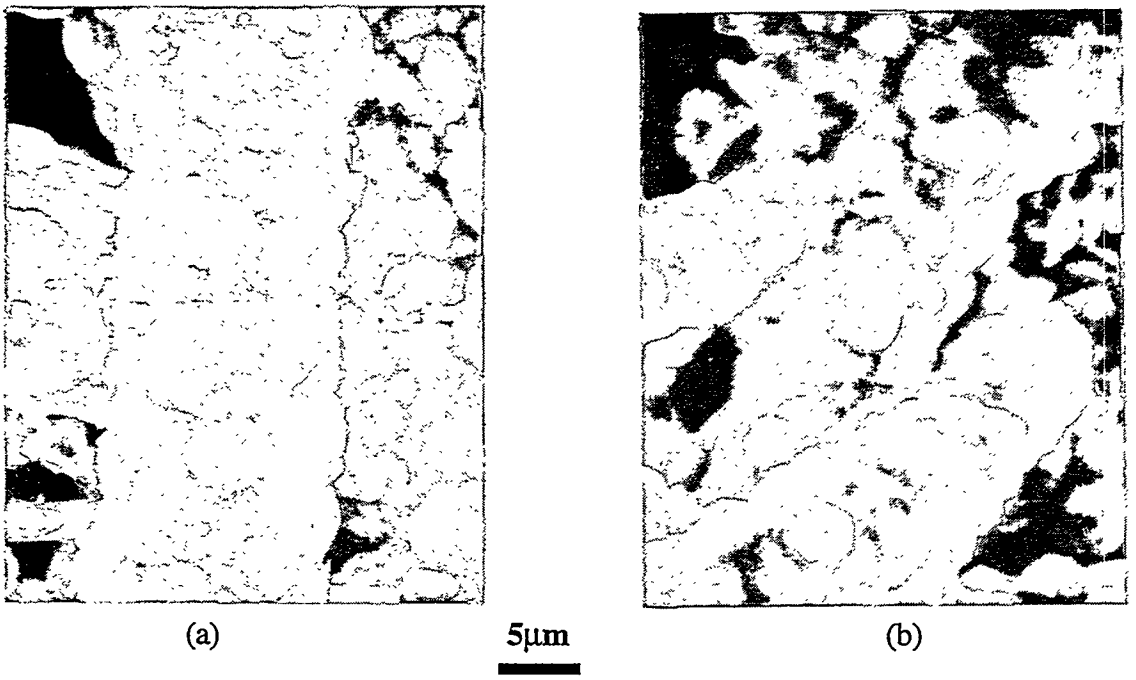

Fig. 1. Scanning electron micrographs of fibers from a 3M hot gas filter (a) as-received and (b) exposed to a combustion environment at 800°C for 25 hours at a flow rate of 2.5 slm.

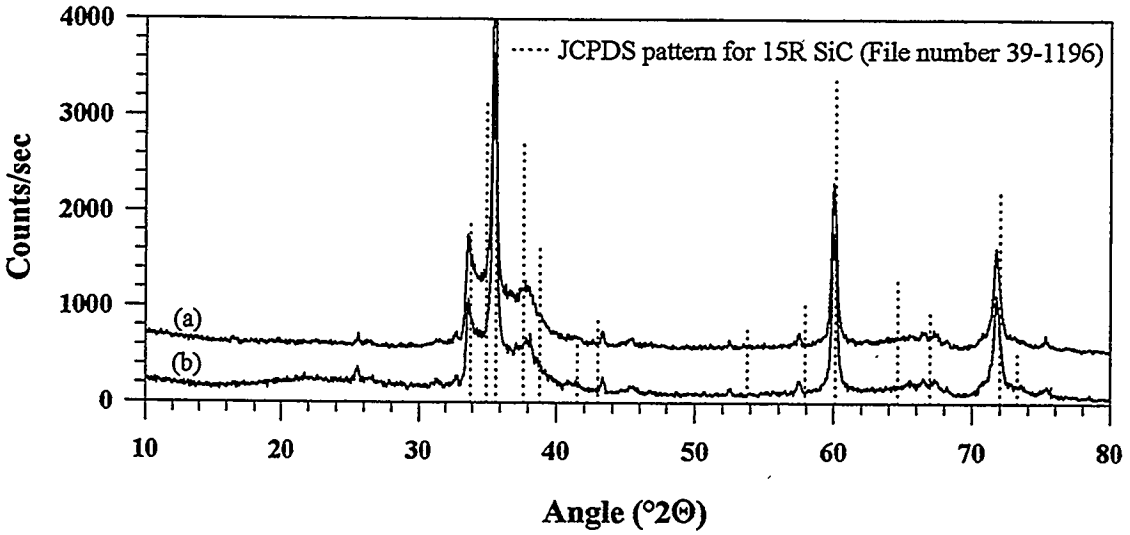

Fig. 2. X-ray diffraction spectra for the middle (filtering) layer of a 3M hot gas filter (a) as-received and (b) exposed to a combustion environment at 800°C for 25 hours at a flow rate of 2.5 slm.

Morphological changes were seen on the surfaces of the coated fibers in the filtering layer of the filter material. XRD analysis showed the presence of an amorphous component in this layer as well. This result correlates with the glassy or glazed appearance of the fiber surfaces observed using scanning electron microscopy. The matrix of experiments presented in Table 1 is currently being run on the 3M material to develop systematic corrosion data at these combustion conditions. The same set of experiments will be run on the DuPont Lanxide material when it is received.

Longer term, 200 hour, exposures of mini-candles will be initiated when the baseline corrosion data has been determined using rings of candles exposed in the flow-over tests. The experimental parameters for these tests will be chosen based on results from the flow-over tests in conjunction with thermochemical calculation results. The exposed candles will be analyzed in the same way as the rings in the flow-over tests as well as being cut into rings for mechanical property testing. The expected result will be correlations of exposure conditions with corrosion effects and mechanical properties.

CERAMIC HEAT EXCHANGER MATERIALS WITH CHROMIUM SURFACE TREATMENTS FOR CORROSION RESISTANCE

Ceramic heat exchangers in coal-fired power plants are exposed to extremely harsh environments, with the temperatures reaching up to 1600°C and a variety of coal combustion products causing both corrosive and erosive damage to the material.[1] Candidate DuPont Lanxide Dimox™ Al/Al_2O_3/SiC_p composites have shown a favorable combination of thermal conductivity, mechanical properties (creep resistance and hot strength), oxidation/corrosion resistance in fossil fuel environments, and thermal shock resistance.[2] However, when in contact with the alkali and alkaline-earth rich slags, accelerated corrosion of the composite is likely because of the formation of the low-melting silicate phases on the surface. Since chromium oxide has a very low solubility in silica and molten silicates, and the corrosion rate of alumina–chromia solution phases in CaO–MgO–Al_2O_3–SiO_2 melts decreases with an increase in Cr_2O_3 concentration,[3] it is expected that a DuPont Lanxide Dimox™ composite surface modified with Cr_2O_3 will resist liquid formation and provide improved corrosion resistance as compared to the Cr_2O_3-free composite. The following sections describe two methods of infiltrating Cr_2O_3 into the DuPont Lanxide Dimox™ composite, and present the results of the SEM and EDX analyses of the infiltrated material.

Experimental Procedure

The chromium infiltration of the $Al/Al_2O_3/SiC_p$ DuPont Lanxide Dimox™ heat exchanger material was accomplished by one of two methods: (1) heating the composite in a Cr_2O_3 powder bed, and (2) heating the composite in molten $Cr(NO_3)_3 \cdot 9\ H_2O$. Both types of infiltrated samples were subjected to a heat treatment at 1500°C prior to corrosion testing. This heat treatment was performed to ensure the Cr in-diffusion, as well as to reoxidize and homogenize the specimen surfaces. The experimental conditions employed in methods (1) and (2) are summarized in Tables 2 and 3, respectively.

Table 2. Experimental conditions for DuPont Lanxide Dimox™ composite surface modification in Cr_2O_3 powder bed.

Sample #	Infiltration Temperature/Time	Equilibration Temperature/Time
1	1000°C/2 h	1500°C/2 h
2	1100°C/2 h	1500°C/2 h
3	1100°C/12 h	1500°C/2 h
4	1100°C/12 h	1500°C/6 h

Table 3. Experimental conditions for DuPont Lanxide Dimox™ composite surface modification in molten $Cr(NO_3)_3 \cdot 9H_2O$.

Sample #	Surface Pre-treatment	Cr-Nitrate Infiltration*	Cr-Nitrate Decomposition	Surface Equilibration
5	1100°C/12 h	80°C/24 h	600°C/1 h	1500°C/2 h
6	1100°C/12 h	80°C/24 h	600°C/1 h	1500°C/6 h
7	conc HCl / 12 h	80°C/24 h	600°C/1 h	1500°C/2 h
8	conc HCl / 12 h	80°C/24 h	600°C/1 h	1500°C/6 h

* Subsequent drying at room temperature for 48 h.

In method (1), the purpose of the low-temperature heat treatment at 1000° or 1100°C was to recreate the conditions for the Dimox™ process which causes the simultaneous melting, growth and oxidation of the residual Al from the composite. Consequently, the Cr_2O_3 from the powder bed could be trapped within the molten Al on the composite surfaces. In method (2), the heat treatment at 1100°C (equivalent to the

Dimox™ process) or, alternatively, the chemical treatment in concentrated HCl (by etching the residual Al) allowed for the formation of residual porosity on the specimen surfaces. The molten chromium (III) nitrate subsequently penetrated the surface pores by capillary action. Prior to surface equilibration at 1500°C, the Cr-nitrate was decomposed into an oxide at 600°C. SEM and EDX analyses of the polished cross sections of the specimens heat treated at 1500°C were performed to determine the extent of Cr penetration.

The as-received and selected Cr-infiltrated composite materials are being reacted with typical slags for various times and temperatures, and will be characterized to determine the effects of the chromium surface treatments on corrosion resistance. The slags are commonly encountered coal-ash slags of an Illinois #6 composition, and a CaO-enriched Illinois #6.

Results and Discussion

The results of the SEM and EDX analyses performed on the specimens heated in Cr_2O_3 powder bed are summarized in Table 4, indicating the dramatic effects of heat treatment time and temperature on the thickness and continuity of the Cr-rich layer, and the roughness of the resulting specimen surfaces. It appears that a satisfactory compromise among the surface characteristics to warrant further corrosion studies was achieved in Specimens #1 and #4.

Table 4. SEM and EDX results for specimens infiltrated in a Cr_2O_3 powder bed.

Sample #	Average Cr-Layer Thickness (μm)	Cr-Layer Continuity	Surface Roughness
1	20 ±2	Yes	Minimal
2	outer surf. 100 ±10 inner surf. 200 ±60	No	Substantial
3	200 ±25	No	Substantial
4	250 ±40	Yes	Acceptable

An SEM micrograph of the near-surface layer of Specimen #4 is shown in Fig. 3. It was found by the EDX analysis that the Cr-rich layer observed in the upper portion of the photograph consisted of the Cr_2O_3 grains (brighter phase) embedded in a chromia–alumina–silicate matrix (darker phase). The appearance and distribution of the darker phase suggested that it had been formed from a liquid and was probably glassy. Minor amounts

of Ca were found within the darker phase, suggesting that the Ca was present in the as-received composite material.

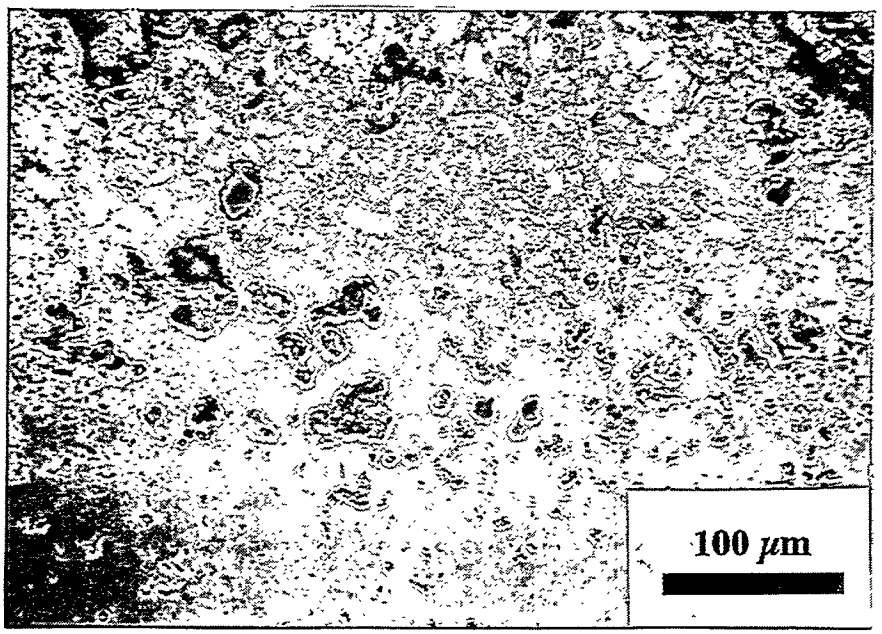

Fig. 3. SEM photograph of the near surface layer of a DuPont Lanxide Dimox™ Al/Al_2O_3/SiC_p composite infiltrated in a Cr_2O_3 powder bed for 12 h at 1100°C and equilibrated for 6 h at 1500°C.

Similar morphologies and compositions were observed in the other specimens. However, extensive regions of discontinuity in Cr distribution were found in the near-surface layers of Specimens #2 and #3. In addition, the average thickness of the Cr-rich layer in Specimen #2 was found to be substantially higher (approximately by a factor of 2) on the inner wall of the specimen as compared to the outer wall. This unexpected effect was not observed in any of the other specimens infiltrated in the Cr_2O_3 powder bed. It is also believed that the substantial amount of damage and porosity observed in the Cr-rich layers were in part caused by the sample preparation procedure, which involved high-speed cutting and diamond-wheel grinding of the cross sections.

Among the specimens infiltrated with Cr-nitrate, minor amounts of chromium were detected only in the outer surface of Specimen #8 (leached for 12 h in HCl and equilibrated for 6 h at 1500°C). The SEM photograph of this specimen is presented in Fig. 4, and shows the formation of a 50 ± 8 μm thick modified surface layer only slightly enriched

with Cr. Apparently, surface porosity created in Specimens #5 through #8 was insufficient to allow any substantial penetration of molten Cr-nitrate by capillary action at 80°C. It is possible, however, that an additional heat treatment step at 1100°C, after the decomposition of the nitrate had been completed, might have improved the infiltration and yielded higher surface concentration of chromium in Specimen #8. At this stage, however, it was concluded that the Cr-nitrate treatment did not yield the surface characteristics required to improve the corrosion resistance.

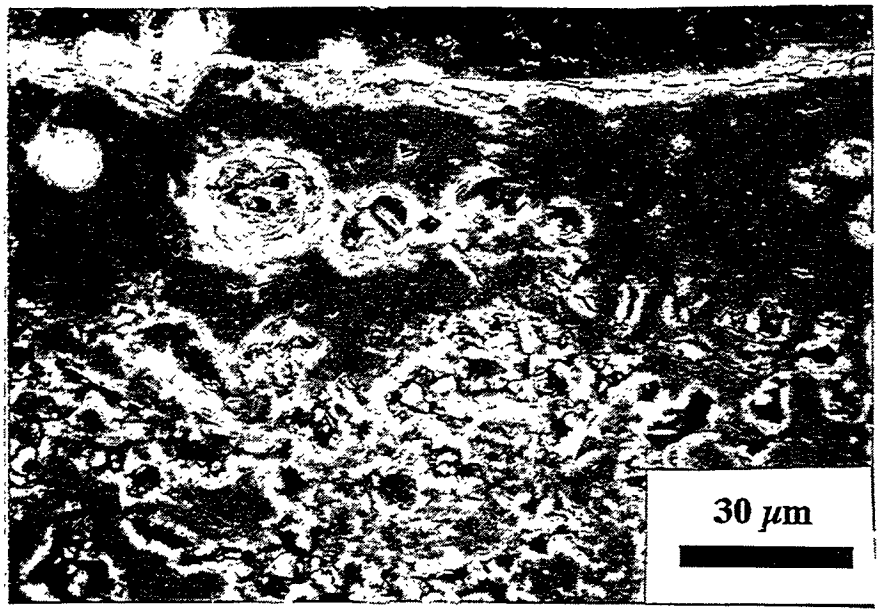

Fig. 4. SEM photograph of a near surface layer of the outer wall of a DuPont Lanxide Dimox™ $Al/Al_2O_3/SiC_p$ composite etched for 12 h in concentrated HCl, infiltrated with $Cr(NO_3)_3 \cdot 9\ H_2O$ for 24 h at 80°C, and equilibrated for 6 h at 1500°C.

Summary and Future Research on Heat Exchanger Materials

(1) The Cr-infiltration of the DuPont Lanxide Dimox™ $Al/Al_2O_3/SiC_p$ composites in a Cr_2O_3 powder bed generated continuous Cr-rich layers with the thicknesses ranging from 20 to 250 μm.

(2) The Cr-infiltration in molten $Cr(NO_3)_3 \cdot 9\ H_2O$ was found to be insufficient to produce any substantial penetration of Cr into the composite surfaces.

The composite specimens heat treated in Cr_2O_3 powder bed under two different sets of conditions were selected for further corrosion studies in contact with Illinois #6 and

CaO-enriched Illinois #6 slags. The corrosion tests are currently under way and will be followed by a detailed examination of the morphologies and compositions of the surface reaction layers formed at the composite/slag interfaces.

ACKNOWLEDGMENTS

We would like to thank D. Pysher (3M Co.), P. Gray (DuPont Lanxide Composites Inc.), and D. Landini (DuPont Lanxide Composites Inc.) for providing the samples for this work, and J.P. Hurley (UND EERC) for helping us obtain the ash and slags for corrosion testing. This research was sponsored by the United States Department of Energy, Office of Fossil Energy, Advanced Research and Technology Development Materials Program (DOE/SE AA 15 10 10 0), Subcontract 38X-SS111C, WBS Element PSU-4 administered by Martin Marietta Energy Systems, Oak Ridge, TN 37831.

REFERENCES

1. K. Breder and V. J. Tennery, "Materials Support for the Development of High Temperature Advanced Furnaces (HITAF)—A Comparison of Selected Mechanical Properties for Three SiC-Based Ceramics"; A Discussion of DOE-Sponsored Fossil Energy Research Projects. The Pennsylvania State University, University Park, PA (1994).

2. C. R. Kennedy, "Reinforced Ceramics Via Oxidation of Molten Metals," *Ceram. Ind.*, 26–29, December 1994.

3. K. H. Sandhage and G. J. Yurek, Indirect Dissolution of $(Al,Cr)_2O_3$ in CaO–MgO–Al_2O_3–SiO_2 (CMAS) Melts," *J. Am. Ceram. Soc.*, **74** [8] 1941–54 (1991).

THERMAL AND STRUCTURAL ANALYSIS OF A FILTER VESSEL CERAMIC TUBESHEET

R.H. Mallett

Mallett Technology, Inc.
PO Box 14407
Research Triangle Park, NC 27709-4407

R.W. Swindeman

Oak Ridge National Laboratory
PO Box 2008
Oak Ridge, TN 37831-6084

J.F. Zievers

Industrial Filter & Pump Mfg. Co.
5900 Ogden Avenue
Cicero, IL 60650-3888

ABSTRACT

A ceramic tubesheet assembly for a hot gas filter vessel is analyzed using the finite element method to determine stresses under differential pressure loading. The stresses include local concentration effects. Selection of the stress measures for evaluation of structural integrity is discussed. Specification of stress limits based upon limited data is considered. Stress results from this ongoing design analysis technology project are shown for one design concept.

INTRODUCTION

A transport combustor is being commissioned at the Southern Services facility in Wilsonville, Alabama to provide a gaseous product for the assessment of hot-gas filtering systems. Foster-Wheeler will install a Pressurized Fluidized Bed Combustor (PFBC) to burn carbonizer product and a hot gas filter will be installed in the PFBC gas stream. One of the barrier filters incorporates a ceramic tubesheet to support the candle filters. The ceramic tubesheet system, designed and built by Industrial Filter and Pump Manufacturing Company (IF&PM), is somewhat unique and offers distinct advantages over metallic systems. This design analysis project is applying a design methodology applicable to the thermal-mechanical analysis of an all-ceramic system.

TECHNICAL APPROACH

A design analysis problem is defined by its geometry, material properties and applied loading. This step has been formalized into creation of a Design Analysis Specification [1].

Tubesheet Geometry

The geometry of the tubesheet is defined in design drawings. The tubesheet is circular with an outside diameter of approximately 55 inches and an inside diameter of 11 inches. The tubesheet is supported at the outside diameter by a ledge attached to the filter vessel. The inside diameter of the tubesheet is attached to an inlet downcomer pipe through which dirty gas enters the filter vessel.

The tubesheet contains many penetrations into which filter candles are inserted. The hot gas is filtered as it passes from the lower dirty gas plenum through the filter candles into the upper clean gas plenum. The penetration pattern repeats at 60° intervals around the circle formed by the tubesheet.

The thickness of the illustrative tubesheet design analyzed herein is a composite construction. Upper and lower layers of 3-inch thickness are separated by a 5-inch layer. This sandwich construction relies on the outer layers to resist bending while shear resistance is provided by the core layer.

Tubesheet Materials

The upper and lower layers of the tubesheet are aluminosilicate composite materials. Further details are beyond the scope of this design analysis project and test data are very limited.

The shear core in this design concept is specified as a Fibrosics™ material constructed from a blend of aluminosilicate fibers and binders of silica and alumina. This shear core is a low density material.

Tubesheet Loading

The design analysis specification of Reference 1 defines the service which the tubesheet must withstand. This includes thermal and mechanical loadings from various operating conditions and transients including backflow pulses to dislodge the dustcake from the filter candles.

The differential pressure across the tubesheet rises to 4 psi as dustcake accumulates. At 4 psi, backflow pulses dislodge the dustcake and the differential pressure returns to a nominal 1.5 psi. Nevertheless, a differential design pressure of 15 psi is specified for the tubesheet. This is a dominant load case and is the loading used for preliminary evaluation of tubesheet design concepts.

ANALYSIS RESULTS

Figure 1 shows the finite element analysis model used for the tubesheet. This is a 30° sector of the tubesheet. This model is sufficient for determining stresses throughout the 360° tubesheet because of the repetitive pattern of the candle filter penetrations [2]. Figure 2 is a close-up view of the region near the inside diameter of the tubesheet.

The thickness of the analysis model includes separate sections for the upper and lower layers and for the shear core. Thin bond layers are also provided between the major material layers.

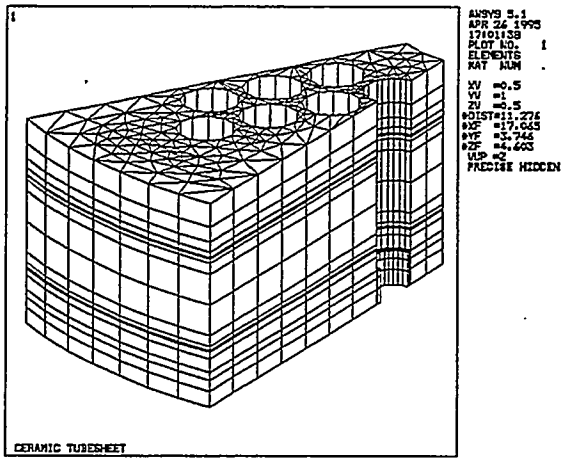

Figure 1. Overall Analysis Model

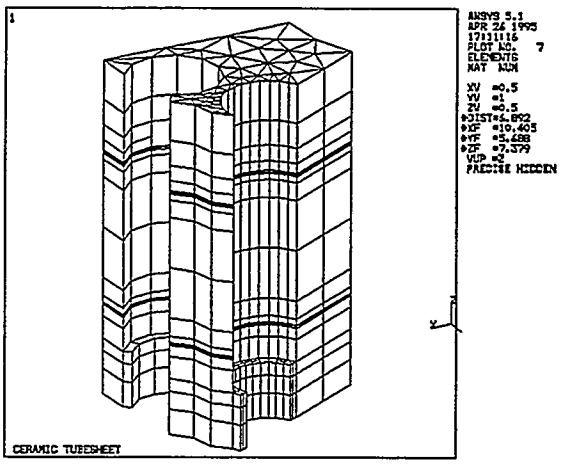

Figure 2. Local Analysis Model

Figure 3 shows a contour plot of the stress intensity distribution caused by a differential pressure of 15 psi. The maximum stress intensity occurs in the ligaments between the penetrations and at the support ledge.

Figure 4 focuses on the high stress region near the inside diameter of the tubesheet. Figure 5 shows a profile of the hoop stress up the edge of the hole.

The maximum stress intensity value in the upper and lower layers is 490 psi. The maximum stress intensity in the shear core is 97 psi. The maximum stress intensity in the bond layer is 129 psi.

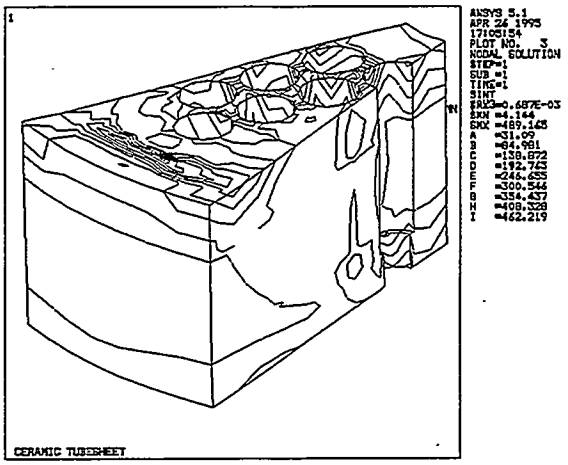

Figure 3. Stress Distribution

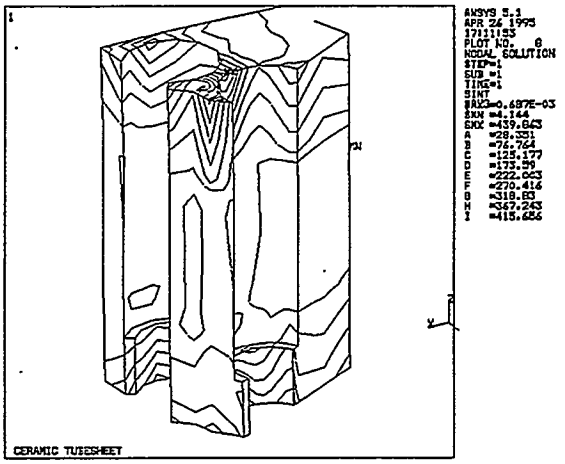

Figure 4. Local Stress Distribution

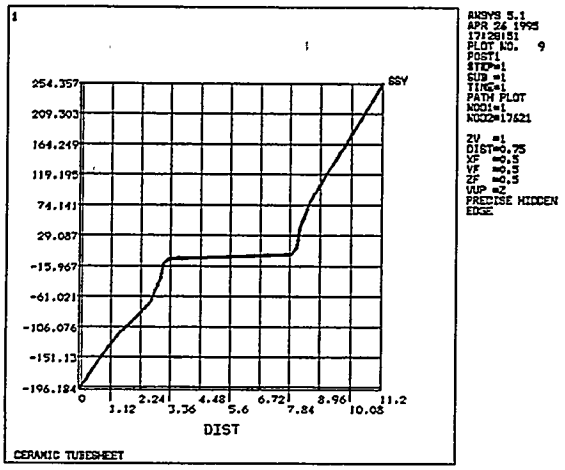

Figure 5. Hoop Stress Through Thickness

DESIGN EVALUATION

If a material has sufficient ductility, local peak stresses are attenuated by local strains without causing failure of the component although repeated applications may cause fatigue crack initiation. The determination of sufficient ductility is complex. Low ductility materials are often excluded from consideration because of material property variations and uncertainty in local stress concentration conditions and applied loadings.

Herein, we judge that the stress quantity which should be limited in the tubesheet bending case is the total (peak) stress. This judgement is based upon observation that the stress peaks in Figure 5 are not highly localized. This judgement also is made on the assumption that the material strength data will be determined using bend tests. Such tests are considered to represent conditions similar to the in-situ conditions in the tubesheet under differential pressure.

In summary, the materials are considered to have low ductility; not zero ductility. The stress distribution in the tubesheet is bending somewhat similar to a bend test. We will use the maximum bending stress from the bend test to limit the total (peak) stress in the tubesheet.

It remains to determine the design stress limit such that there is sufficient margin to the failure stress. Very few data are available. There is no statistical characterization of the failure stress.

We proceed on judgement. The failure distribution is judged to lie largely with a range of +/- 33% about the average test failure stress. On this basis, the design stress limit is taken as 1/3 of the average failure stress. For example, if the average failure stress is 2,700 psi, the range of data is taken to be from 1,800 psi to 3,600 psi and the design stress limit is specified as 900 psi.

CONCLUSIONS

The design analysis rationale for the ceramic tubesheet includes encouragement to develop a mechanical design concept with inherent ductility. The use of a relatively soft shear core is an example of this.

The design analysis rationale is also encouraging the use of a mechanical design concept with inherently low stress. The key to low stress in the tubesheet is to use a large thickness value.

Finally, the design evaluation is encouraging the use of feature tests for determination of mechanical and strength properties. Using tests which are representative of conditions in-situ can compensate for the limited data and understanding regarding the material properties.

REFERENCES

1, R.H. Mallett, "Design Analysis Specification for Filter Vessel Ceramic Tubesheet (Draft)", Mallett Technology Report MTI-TR-825, February 3, 1995.

2. R.H. Mallett, "Preliminary Design Analysis for a Filter Vessel Ceramic Tubesheet", Mallett Technology Report MTI-TR-845, February 6, 1995

PROCESSING OF SILICON NITRIDE AND ALUMINA NANOSIZE POWDERS

Eduardo J. Gonzalez, Gasper Piermarini, Bernard Hockey and
Subhas G. Malghan

Ceramics Division
National Institute of Standards and Technology
Gaithersburg, MD 20899

ABSTRACT

The effects of pressure on the compaction and subsequent processing of nanosize γ alumina powders were studied. A 3 mm diameter piston/cylinder die was used to compact the nanosize powders to pressures of 1 and 2.5 GPa. The green bodies were sintered at temperatures up to 1600 °C. Results show that green body density can be increased by higher compaction pressures. It appears that as a result of the γ-to-α transformation in alumina, higher green density does not necessarily produce a higher density sintered alumina body. The microstructures of the sintered bodies are described in terms of porosity and phase content.

INTRODUCTION

The primary objective of this project is to develop a novel compaction process to produce a dense green-state compact from nanosize powders that subsequently can be sintered to form a dense ceramic, possibly with nanoscale microstructure. Earlier work involved efforts to compact nanosize (average particle size, 17 nm) amorphous silicon nitride powders into dense green body compacts followed by sintering to produce a dense ceramic with nanoscale microstructure. The results of those efforts led to the following conclusions: (1) a random packing green body density of about 57% of theoretical can be achieved by dry compaction of the nanosize powder to 2.5 GPa. Green body density can be increased to 64% by using liquid nitrogen as a lubricant during the compaction process. The transparent green compacts were pressureless sintered at 1400 °C and yielded a sintered piece with a Vickers hardness of about 6 GPa. Not a very promising result. Hot pressing the transparent green body followed by pressureless sintering improved the hardness to 11 GPa, but still not anywhere near the 25-30 GPa values characteristic of conventional silicon

nitride ceramic. Sintering at temperatures higher than 1400 °C produced a phase transformation to α silicon nitride with a loss of transparency and no improvement in hardness. The interpretation of these compaction and sintering results is difficult because the amorphous nanosize silicon nitride powder experiences a crystallization to α phase and an additional transformation to β phase at higher temperatures.

To better understand the effects of phase transformation on the densification process occurring during sintering, nanosize γ alumina powder was studied. The existence of a variety of transitional alumina phases already has attracted considerable attention because of their importance in affecting the processing parameters for alumina ceramics [1]. One of the main interests in the transitional alumina phases is their possible effects on densification which occurs in the sintering process during which the α Al_2O_3 ceramic is formed. Some authors have reported that the transformation process enhances the densification kinetics and lowers the sintering temperature required to produce dense samples of α Al_2O_3 [2]. It is well known that the phase transformation in alumina occurs by a nucleation and growth process, but the mechanisms by which the transformation enhances densification are not well understood. Nevertheless, polycrystalline, dense α Al_2O_3 ceramics have been made by sintering transitional γ phase green bodies at temperatures as low as 1150 °C, while maintaining almost the original grain size of the starting powder in the sintered body. Kumagai and Messing [2], for example, studied the effects of seeding sol-gel derived transitional oxides of aluminum with submicrometer size α Al_2O_3 crystals. These authors showed that the θ-to-α transformation temperature was reduced to 1200 °C by seeding, and that the transformed α alumina sinters to full density with a submicrometer grain size. Yeh and Sacks [3] used a somewhat different approach and made slurries of fine grain α Al_2O_3 (0.2 - 0.3 μm) using conventional suspension techniques. The slurries were slip-casted into pellets of relatively high densities (69%). These pellets were sintered at 1150 °C to almost full density with very little increase in grain size. They demonstrated that the transformation was not necessary to achieve high densities at low sintering temperatures.

Another method of increasing the rate and lowering the temperature of the transformation in alumina was reported by Ishitobi *et al*, [4] and later by Dynys and Halloran [1]. Ishitobi *et al*, [4] demonstrated that sintering η Al_2O_3 or θ Al_2O_3 under pressures of several gigapascals decreases the transformation temperature significantly. Dynys and Halloran, on the other hand, showed that cold compaction at different pressures changes the transformation kinetics under pressureless sintering in a similar fashion. The residual stresses in the green body produced by compaction of the starting powder is thought to increase the number of nuclei at which the transformation initiates.

In the present work, we describe the microstructure and densification that develops as a result of the γ-to-α transformation in nanosize γ Al_2O_3 powder, and show how it is affected by the magnitude of the initial compaction pressure used to fabricate the green body. The results have implications concerning the difficulties experienced in the processing of nanosize silicon nitride powders where transformations from the amorphous state to α and β Si_3N_4 crystalline forms occur.

EXPERIMENTAL PROCEDURES

The starting nanosize γ Al_2O_3 powder used in this work is a commercially available material, Aluminum Oxide C, supplied by Dugussa*, AG, Geschäftsbereich Anorganische Chemieprodukt, Frankfurt, Germany. The powder, consisting of equiaxed particles with an average diameter of 20 nm, is primarily γ phase with some δ phase, estimated from diffraction intensities to be <10% by volume, as determined by transmission electron microscopy (TEM) and x-ray powder diffraction (XRPD) techniques. The powder is strongly agglomerated with no evidence of partial sintering. Green body samples of 3 mm diameter were pressed to 1 and 2.5 GPa in an Instron Press described in detail elsewhere [5]. Sintering experiments were conducted in an alumina tube-furnace under the rough vacuum of a

*Certain commercial names are identified in this paper to foster understanding. Such identification does not imply recommendation or endorsement by the National Institute of Standards and Technology.

mechanical pump. Samples were sintered at 1000, 1100, 1200, 1300, 1500, and 1600 °C for 5 h, employing heating and cooling rates of 300 °C/h. After the heat treatments, the weight and volume of the samples were remeasured to determine the extent of densification. To further understand the densification process, optical microscopy, x-ray diffraction, TEM and surface area analysis were used to characterize the microstructure of the samples. The details of the green body preparation, sintering procedure and microstructural determination are described in a recent report [6].

RESULTS AND DISCUSSION

Densification Results

To summarize our results the average density at each sintering temperature and compaction pressure is illustrated in Figure 1. The density increases monotonically for both compaction pressures.

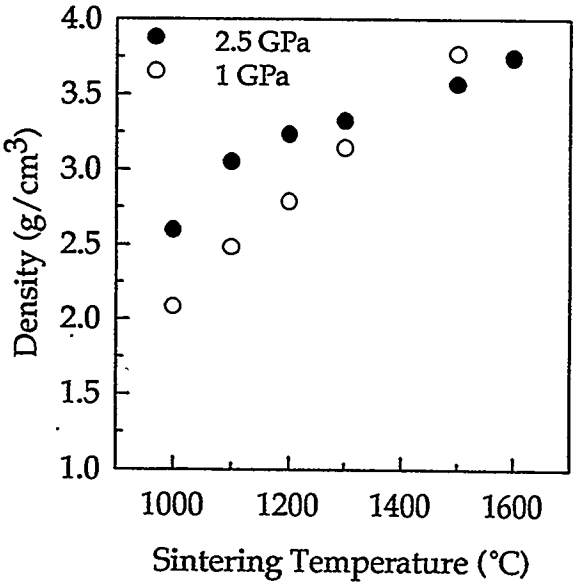

Figure 1. Plot shows monotonic increase in density with sintering temperature for γ-alumina samples compacted at 1 and 2.5 GPa.

However, it is of interest that the average density of the samples pressed to 1 GPa and sintered at 1500 °C was higher than the average density of the samples pressed to 2.5 GPa and also sintered at 1500 °C. The measured densities of the 1 GPa and 2.5 GPa pressed samples are 3.80 and 3.58 g cm^{-3}, or 96% and 90% relative density, respectively (theoretical density of α Al_2O_3, 3.98 g cm^{-3}). However, after sintering at 1600 °C, the difference in relative density is more subtle.

Microstructure

Figure 2 shows a TEM micrograph of a green body compacted at 2.5 GPa. Both XRPD and electron diffraction results on these samples confirmed that they are predominantly γ Al_2O_3. The γ particles are equiaxed with an average size of $\approx$ 20 nm.

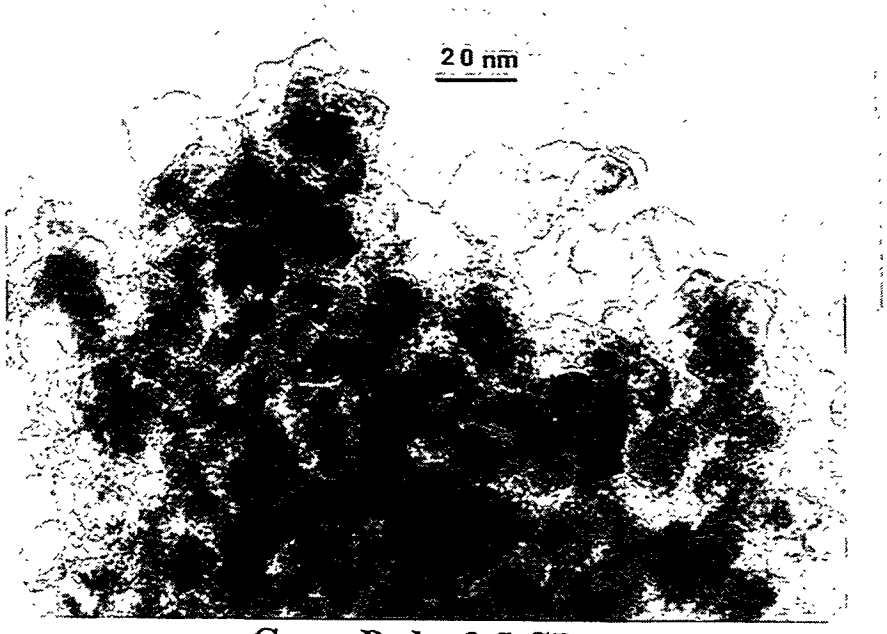

Figure 2. TEM brightfield image shows the microstructure of a green body of γ-Al_2O_3 compacted at 2.5 GPa.

More generally, observations on samples compacted to 1.0 and 2.5 GPa indicate a random dense packed particle structure with uniform interconnected porosity. For both compaction pressures, the pore dimensions were less than the particle size. As a consequence, the 16% difference in packing density between the samples compacted at 1 and 2.5 GPa was not resolved by TEM.

Figures 3 (a and b) show, in comparison, TEM micrographs of the samples sintered at 1000 °C for the 1 and 2.5 GPa compaction pressures.

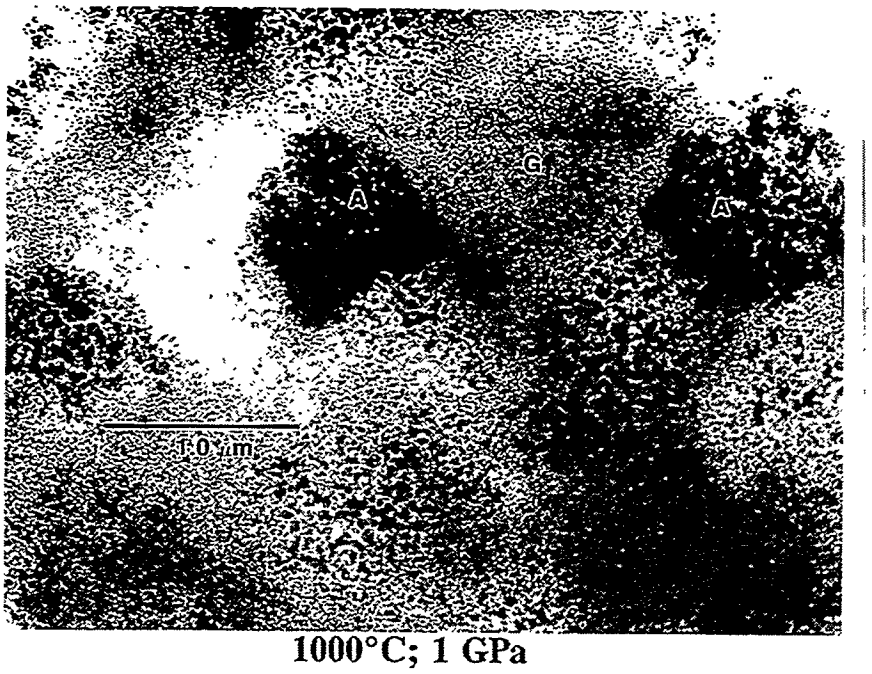

Figure 3a. Brightfield image in TEM shows the typical microstructure of γ-alumina samples sintered at 1000 °C for a) 1 GPa.

The sample compacted at 1 GPa is made of a mixture of equiaxed particles of γ phase and isolated clusters of predominantly α phase. Even at this temperature, necking between γ particles, indicative of partial sintering, was not observed by TEM. The isolated α clusters grow in a spongy structure with continuous porosity. XRPD results confirmed that both α and γ phases were present in the samples pressed to 1.0 GPa.

In contrast, the samples pressed to 2.5 GPa consisted of all α phase, with spongy microstructure morphology and continuous porosity similar to the isolated α clusters in the 1 GPa pressed samples. Again, XRPD confirmed that the 2.5 GPa pressed samples are exclusively α Al_2O_3.

It should be noted that the spongy α phase microstructure consists of interconnected individual grains, ranging in size from about 100 nm to nearly 1 μm. As illustrated in Figure 3b, regions of dark contrast define areas of common orientation, the grains have a complex morphology, and the boundaries connecting adjacent grains are typically 50 to 100 nm long.

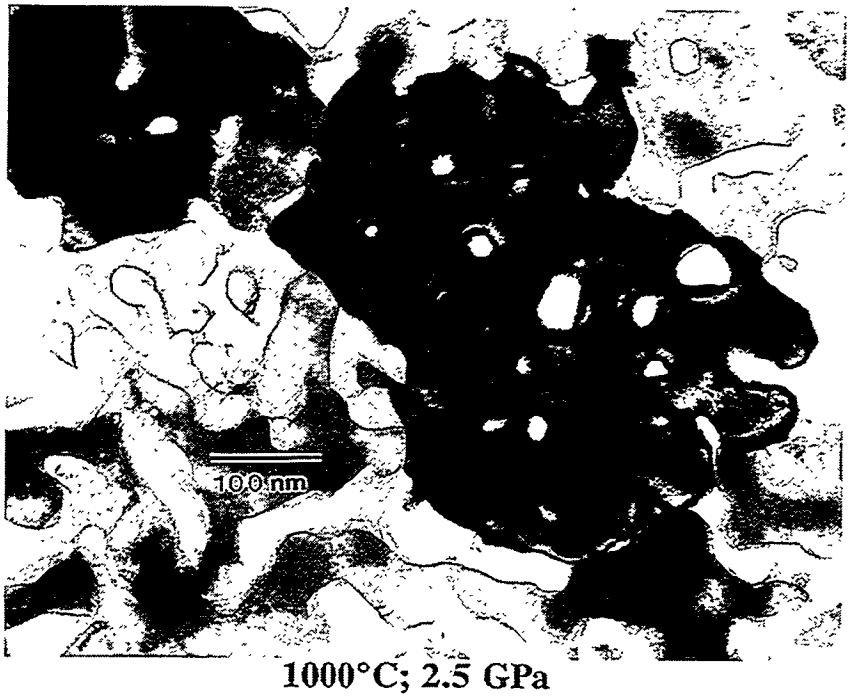

Figure 3b. Brightfield image in TEM shows the typical microstructure of γ-alumina samples sintered at 1000 °C for b) 2.5 GPa.

Surface area and pore size distribution analysis was done on selected green and sintered bodies. The results indicate that for fully transformed samples (all α phase), the average pore radius increases by a factor of 4 to 5 and the surface area decreases by a factor of 3 to 5, in agreement with the TEM observations.

The samples pressed at 2.5 GPa, which already transformed to α Al_2O_3, experienced some shrinkage during transformation to the α phase for the

same mass of material, and, as a result, these samples have a higher bulk density. Likewise, because the transformed volume in the 1 GPa samples is small compared to the 2.5 GPa material, the measurements cannot resolve this volume change. We have also done careful microstructural studies on samples sintered at 1300 °C. The density of these samples did not exceed 83% of theoretical. It was determined by XRPD that the samples are all α Al_2O_3 for both 1 and 2.5 GPa compacted samples. The 1 GPa samples are made up of a combination of the spongy grain structure and equiaxed micrometer size grains. Significant porosity and necking between grains is evident. In contrast, the 2.5 GPa compacted sample exhibited only an equiaxed grain morphology, and no evidence of spongy α phase structure.

The microstructures of the samples sintered at 1600 °C, shown in Figures 4(a and b), clearly illustrate the difference in volume fraction porosity and grain morphology. The sample compacted to 1 GPa has attained almost full density with some trapped porosity inside grains. Porosity in the 2.5 GPa compacted sample, on the other hand, is mostly intergranular with very little trapped porosity within grains.

In connection with the work of Dynys and Halloran [1], pressure does have an effect in the transformation kinetics. The 1 GPa compacted samples are partially transformed at 1000 °C, whereas the 2.5 GPa compacted samples have completely transformed to α Al_2O_3 under the same heat-treatment conditions. However, it is difficult to determine if the increase in pressure during compaction reduces the time and temperature for densification. Moreover, the nanoscale grain size is already lost when sintered at 1300 °C. It is unclear if the individual grains that form are the α Al_2O_3 clusters with reduced internal porosity. If this is the case, the starting size of the clusters determines the initial size of the grains. Therefore, it is necessary to control the cluster size or to start with α Al_2O_3 nanosize powders to avoid the transformation which appears to be responsible for cluster formation. This would have the effect of decreasing the final grain size after sintering.

The microstructures created at low temperatures in these studies are interesting for a number of reasons, however. The spongy structure of α Al_2O_3, for example, can be used as high temperature submicron ceramic

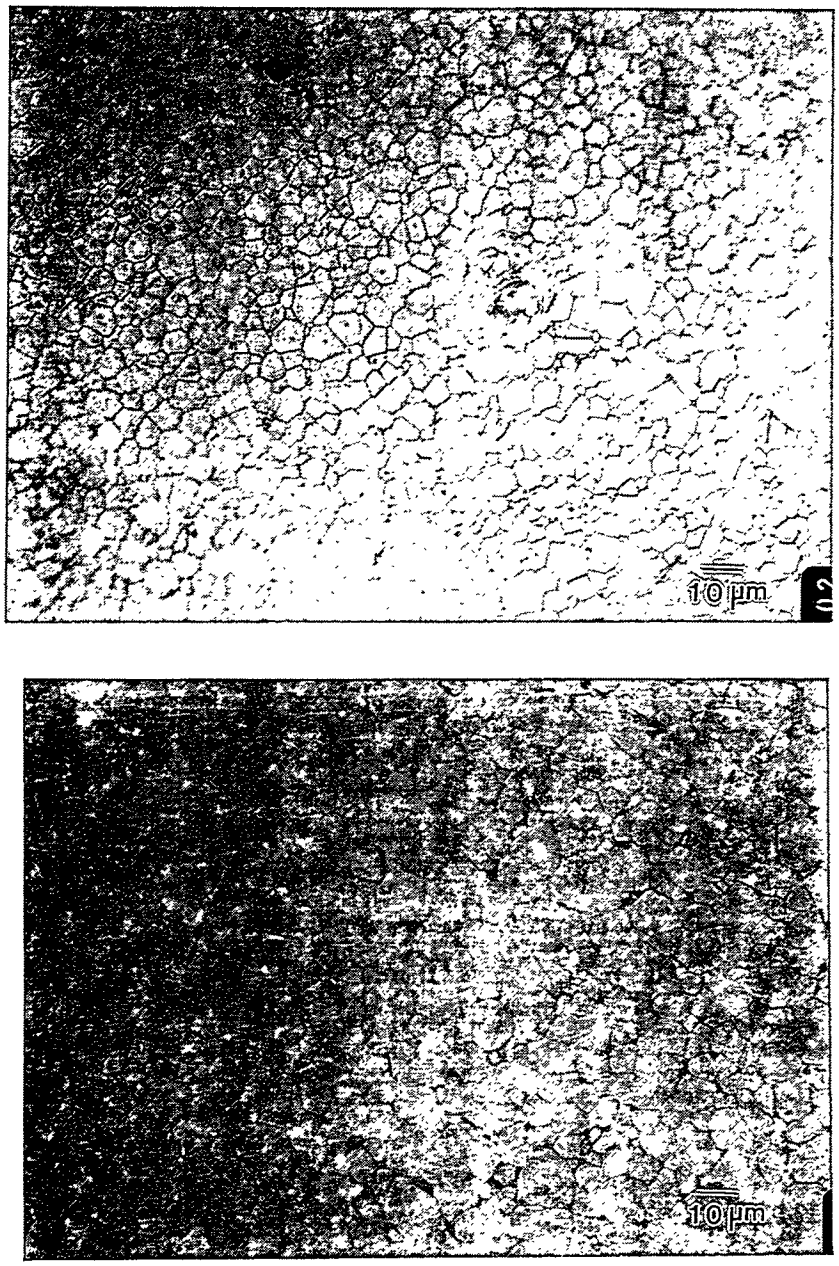

(a)

(b)

Figure 4. Microstructures of samples sintered at 1600 °C of (a) 1 GPa and (b) 2.5 GPa green compact.

filter, assuming that size distribution can be controlled over narrow ranges. Furthermore, some of these materials can be infiltrated with liquid metals to form composites with interesting properties.

CONCLUSIONS

The compaction pressure has an enhancing effect on (1) the green body density, (2) the γ-to-α transformation rate, and (3) the γ-to-α transformation temperature. In general, samples compacted to 1 GPa and sintered at temperatures below 1300 °C yielded consistently lower densities than the samples pressed to 2.5 GPa and sintered at the same temperatures. However, the densities of both samples approached the same value ($\approx$ 3.2 g cm^{-3}) for sintering at temperatures near 1300 °C. At higher sintering temperatures, the 1 GPa samples sintered at 1500 °C attained a higher density than the 2.5 GPa samples sintered at the same temperature, and for sintering at 1600 °C, the densities for the two samples appear to be nearly the same ($\approx$3.8 g cm^{-1}) at 96% of theoretical. In the case of silicon nitride processing, the mechanisms described here for alumina such as pressure effects on green body density, pressure effects on crystallization and on phase transformation, may also be relevant.

REFERENCES

1. F. W. Dynys and J. W. Halloran, "Alpha Alumina Formation in Alum-Derived γ Alumina", J. Am. Ceram. Soc., **65**, 442-448 (1982).

2. M. Kumagai and G. L. Messing, "Controlled Transformation and Sintering of a Boehmite Sol-Gel by α-Alumina Seeding", J. Am. Ceram. Soc., **68** [9] 500-505 (1985).

3. T. Yeh and M. D. Sacks, "Low-Temperature Sintering of Aluminum Oxide", J. Am. Ceram. Soc., **71** [10] 841-844 (1988).

4. Y. Ishitobi, M. Shimada and M. Koizumi, "Reactive Pressure Sintering of Alumina", Ceramic Bulletin, **59**, [12] 1208-1211 (1980).

5. W. Chen, A. Pechenik, S. J. Dapkunas, G. J. Piermarini and S. G. Malghan, "Novel Equipment for the Study of the Compaction of Fine Powders", J. Am. Ceram. Soc., **77**, [4] 1005-1010 (1994).

6. Eduardo J. Gonzalez, Gasper Piermarini, Bernard Hockey and Subhas G. Malghan, "Low Temperature Fabrication From Nanosize Ceramic Powders", Final Report to DOE, ORNL/Sub/92-22041/02, April 28, 1995.

SESSION II - CERAMICS AND NEW ALLOYS

DEVELOPMENT OF NONDESTRUCTIVE EVALUATION METHODS AND PREDICTION OF EFFECTS OF FLAWS ON THE FRACTURE BEHAVIOR OF STRUCTURAL CERAMICS

W. A. Ellingson, J. P. Singh, E. A. Sivers, J. B. Stuckey,
D. Christopher, S. L. Dieckman, and D. Singh

Energy Technology Division
ARGONNE NATIONAL LABORATORY
Argonne, Illinois 60439

ABSTRACT

Continuous fiber ceramic matrix composites are being developed for turbine engine components, heat exchangers, and hot-gas filters in fossil energy systems. Reliable application requires nondestructive evaluation (NDE) methods that provide data for quality assurance and inputs to life time prediction models and that aid in process development. NDE developments at Argonne have focused on methods to assess density distribution, fiber orientation (for mechanical properties), and defect detection in both SiC/SiC and Al_2O_3/Al_2O_3 materials, and that also assess the chemical state at fiber/matrix interfaces. 2-D cloth lay-up and 3-D weave CVI-infiltrated SiC/SiC specimens were studied by X-ray imaging methods now under development. Microfocus X-ray computerized tomography (MXCT) methods are being developed to provide these data. Multinuclear Nuclear Magnetic Resonance spectroscopy (13C, 29Si, and 11B) is under development for quantifying B content at fiber/matrix interfaces. Magic angle spinning techniques on SiC/SiC specimens with different coating thicknesses showed that quantification of B at the interface is achievable.

NDE data are being coupled to room- and elevated-temperature fracture studies to evaluate effects of fiber orientation and fiber coating thickness on resulting flaw morphology and mechanical properties of Nicalon-fiber–reinforced SiC matrix composites. Specifically, composites with fiber cloth lay-up sequences of varying coating thicknesses were evaluated. For room-temperature mechanical evaluation, composites with carbon-fiber coating thicknesses of 0 and 0.2 μm were used, while elevated-temperature studies used composites with a coating thickness of 0.4 μm. Composites with uncoated fibers failed in a brittle mode, while composites with 0.2 μm fiber coating showed noncatastrophic failure. Comparison of these results with previously obtained data for composites with coating thickness of 0.4 μm indicate that a coating thickness of 0.2 μm provides optimal mechanical performance.

INTRODUCTION

Nondestructive evaluation (NDE) technology is being developed to advance the reliable application of ceramic materials to fossil energy systems for improved efficiency and better environmental control. NDE technology is evaluating and characterizing continuous fiber ceramic matrix composite (CFCC) materials such as SiC/SiC and Al_2O_2/Al_2O_3, with matrix infiltration by a variety of processes. NDE technology is being developed to provide data for quality assurance, process

development, and component lifetime prediction. CFCC materials are being developed for several applications in fossil energy systems. As an example, the development of improved hot-gas clean-up technology would have a significant impact on combined-cycle coal gasification, combined cycle pressurized fluidized bed combustion (PFBC), direct coal-fired gas turbines and coal gasification/fuel cell technology. Hot-gas filter applications require large numbers of components and thus NDE methods must be cost-effective. In addition the mechanical performance of CFCC materials have been shown to be strongly dependent on reinforcing fiber strength, fiber/matrix interface, and fiber architecture (fiber cloth lay-up sequence). The strength of the fibers and the fiber/matrix interface can become degraded in elevated temperature service environments. Such degradation is related to the generation of flaws and changes in the flaw morphology during processing and in service; if possible, these should be detected by NDE methods. Therefore, this research effort has continued to evaluate effects of fiber cloth lay-up sequence, fiber/matrix interface, and high-temperature environments on flaw generation and the resulting mechanical properties of reinforcing fibers and composites.

NDE CHARACTERIZATION OF AS-PROCESSED CFCC MATERIALS

X-ray computed tomographic imaging technology with high spatial resolution capability has been under development to evaluate CFCC materials for process development and "flaw" data for input to life-time prediction models.[1-4] The spatial resolution, speed of acquisition and part size that can be handled have been significantly improved to the point where many applications are now possible. Examples of results of applying this NDE method to several fiber architectures are given below.

a) 3-D Braided SiC/SiC with CVI Infiltration

As part of process development technology for CVI of 3-D braided SiC/SiC, MXCT has been shown to be capable of detecting delaminations, void distributions and areas of low infiltration density. Figure 1 shows a single transaxial X-ray CT image of a nominally 2 in. (50 μm) diameter tube being studied for process develop-ment. Note that voids < 100 μm can now be easily detected and, with image processing, porosity size distribution can be determined as a function of radial position. Such information is very helpful for process development and can be used to adjust infiltration parameters.

b) 2-D Laminated SiC/SiC and CVI Infiltration

X-ray CT imaging data has also been demonstrated to be capable of detecting delaminations and radially varying infiltration density in 2-D cloth lay-up SiC/SiC components infiltrated by isothermal CVI. Figure 2 shows three X-ray CT sections of a 50 mm diameter SiC/SiC tubular component fabricated by hand cloth layup and subsequently infiltrated by CVI. Note the detection of the cloth overlap region, the low density infiltration region near the inner surface and the detection of delaminated regions or laminar regions of poor infiltration. For heat-exchanger applications, such information may be necessary to predict component behavior.

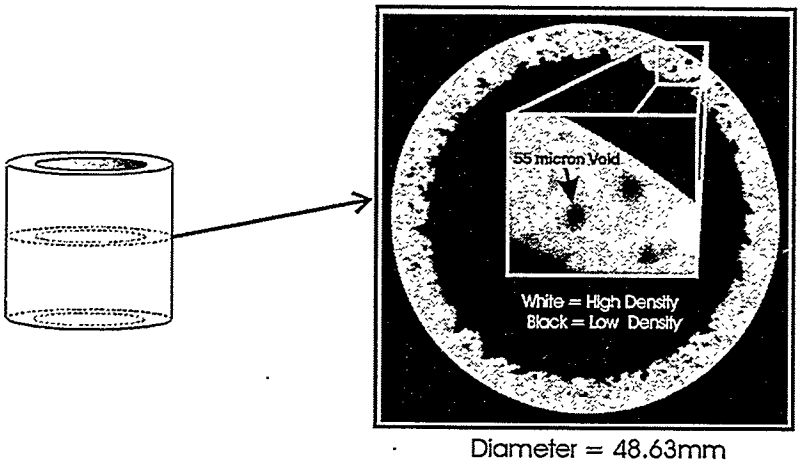

Fig. 1. Microfocus-based X-ray CT image of one section of a 50 mm diameter 3-D weave SiC/SiC infiltrated by CVI as part of infiltration process development.

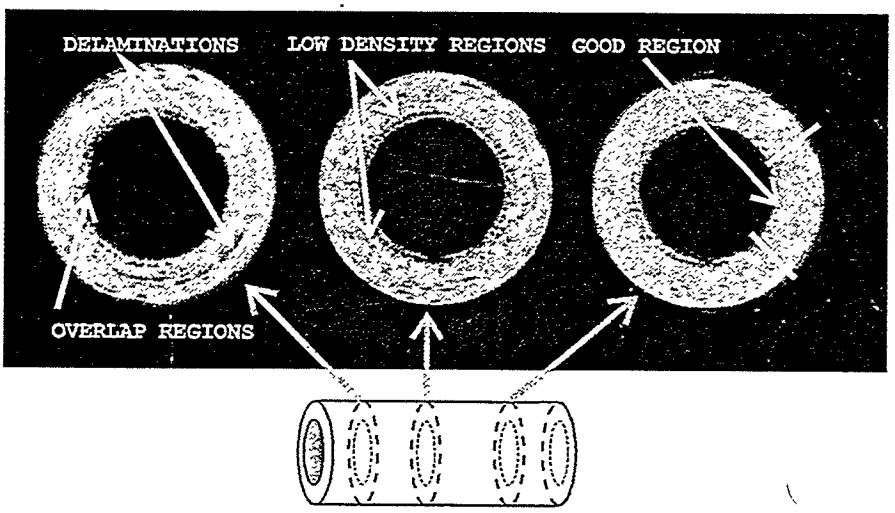

Fig. 2. Micro focused based X-ray CT images of 3 sections of a 50 mm diameter 2-D lay-up SiC/SiC CVI infiltrated tubular component.

c) 3-D Weave Oxide/Oxide Infiltrated by Sol-Gel Methods

X-ray CT imaging data have demonstrated the ability to detect fiber architecture and density variations in 20 cm diameter 3-D weave Sol-Gel infiltrated Al_2O_3/Al_2O_3 turbine engine combustor liners. Figure 3 shows a typical segment of an X-ray CT cross-section of a 3mm thick wall.

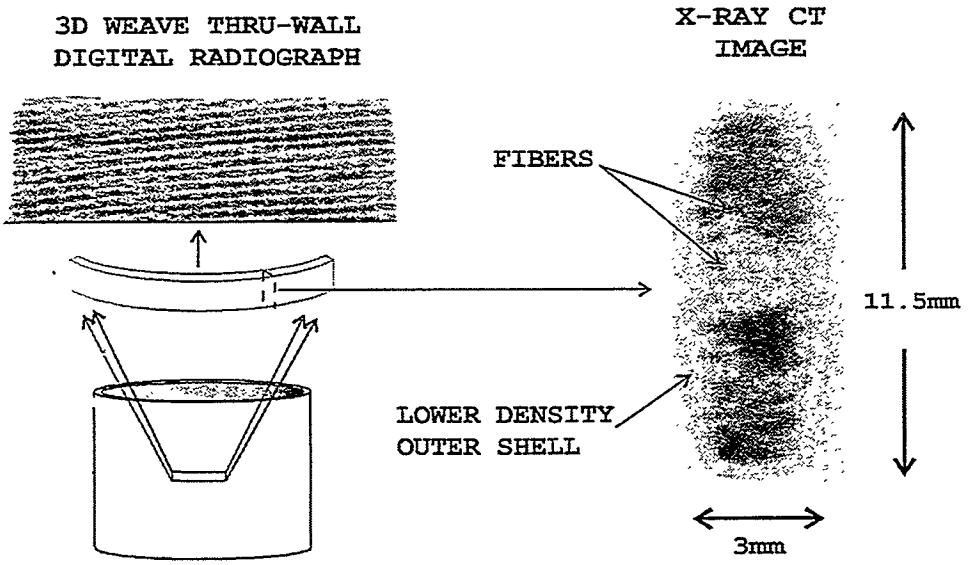

Fig. 3. X-ray computed tomographic images of a segment of a 20 cm diameter 3-D weave Al_2O_3/Al_2O_3 combustor liner infiltrated by Sol-Gel methods. (a) through-wall, X-ray digital radiograph, (b) high-resolution X-ray CT images.

d) Large Scale Component Inspection

The developed X-ray CT scanner technology now allows large components (>20cm) to be accommodated and thus provide high-spatial resolution image data.[2,3] Figure 4 shows a typical CT cross-section of a 20 cm diameter 3-D weave SiC/SiC turbine combustor liner. The image quality detail (spatial resolution) allows fiber architecture detection and large (>1 mm) regions of low infiltration. This information has been demonstrated to correlate with component performance prediction in turbine engine test rig tests.

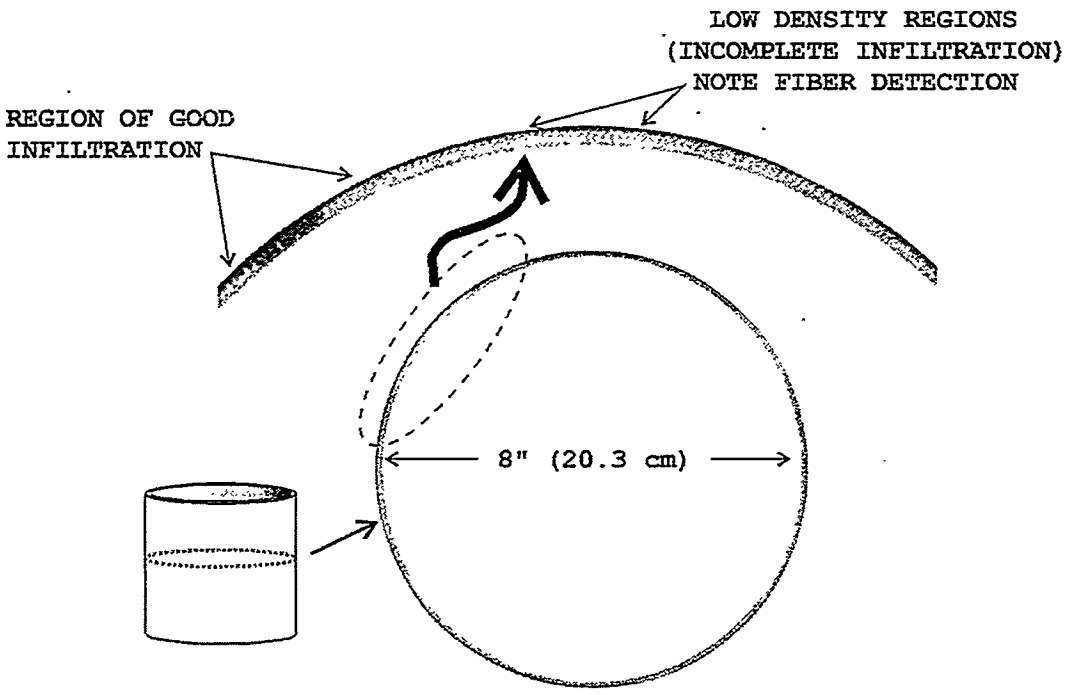

Fig. 4. Microfocus X-ray CT cross-section image of a 20 cm diameter 3-D weave SiC/SiC, CVI infiltrated turbine engine combustor liner showing regions of low-density infiltration and the ability of high resolution CT to detect fiber architecture within the 3 mm combustor liner wall.

FIBER/MATRIX INTERFACES: MEASUREMENT OF CHEMICAL COMPOSITION

Nuclear Magnetic Resonance Spectroscopy of Ceramic Composites

Experimental studies were conducted to examine the applicability of ^{11}B NMR spectroscopy for the determination of boron-doped carbon and BN coating microstructures on Nicalon fiber in SiC matrices. Specifically, experiments were initiated on a series of specimens provided by ORNL. The specimens were produced with 40 vol. % Nicalon plain-weave fabric rotated in the typical 0-30^{o} orientation, and with varying boron-to-carbon ratio and thickness of BN coatings in the doped and BN coated fibers, respectively. Initial experiments were performed to determine the overall sensitivity of the nucleus and various experimental parameters, including appropriate spinning speeds and pulse repetition rates.

To verify the utility of ^{11}B NMR spectroscopy, solid-state magic angle spinning (MAS) NMR experiments were performed on samples containing high concentrations of boron. ^{11}B NMR studies of the samples were performed at a magnetic field strength

of 7.1 T. Figure 5(a) shows NMR spectra of boric acid. It was shown that ^{11}B NMR analysis is capable of providing resolution and sensitivity exceeding the analytical requirements for quantitative measurements of boron in ceramic composites.

Experiments were also performed on a specimens containing BN-coated Nicalon fibers in SiC matrices to examine the applicability of ^{11}B NMR spectroscopy for the determination of boron-doped carbon and BN coating microstructures on Nicalon fibers in SiC matrices, as shown in Fig. 5(b). It was determined that the favorable spectroscopic properties (i.e., an isotopic natural abundance of approximately 80.5 %, a spin of 3/2 that provide efficient spin-lattice relaxation in the solid state, and an overall high relative receptivity approximately 13% of that of ^{1}H) of the ^{11}B nucleus provides significant sensitivity and allows accurate classification of the chemical environment of the boron. A new NMR and imaging system is now completely functional, and automated variable-temperature studies, and MAS 8 KHz will be performed to further understand the application of ^{11}B NMR spectroscopy for the determination of boron-doped carbon and BN coating microstructures on Nicalon fibers in SiC matrices.

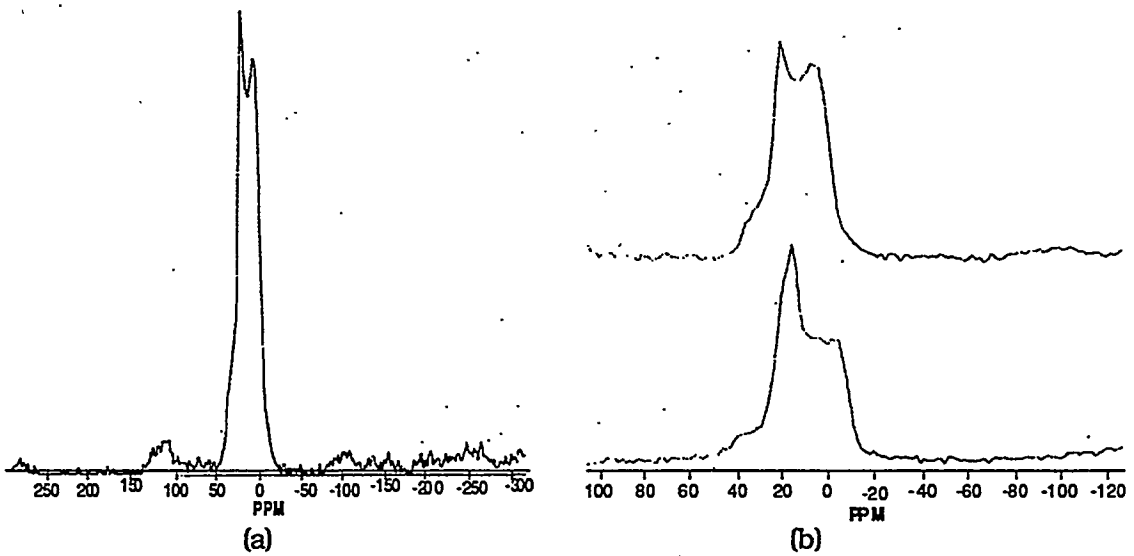

Fig. 5 (a) NMR spectra of boric acid. (b) ^{11}B NMR spectra of specimen containing BN-coated Nicalon fibers in SiC matrices.

EFFECTS OF FLAWS ON FRACTURE BEHAVIOR

To evaluate the effects of fiber cloth lay-up sequence and elevated-temperature service environments on flaw generation and resulting mechanical properties, Nicalon-fiber-reinforced SiC matrix composites (fabricated by CVI) with various cloth lay-up sequence and fiber coating thicknesses were obtained from Ceramic Composites, Inc., of Millerville, MD. To date, composites with fiber lay-up sequences of 0°/45° and 0°/20°/60° and carbon coating thickness of 0-0.4 μm have been evaluated. These composites were received in plate form, from which rectangular bars (≈3 x 4 x 40 mm) were machined. The tensile edges of the test bars were beveled to eliminate stress concentrations and thus avoid edge failures. Density of composites was measured by the Archimedes' principle. Approximately five specimens were tested per condition.

ROOM-TEMPERATURE MECHANICAL PROPERTY EVALUATIONS AND CORRELATIONS WITH FIBER ARCHITECTURE

Mechanical testing of 0°/45°, 0°/20°/60°, and 0°/40°/60° SiC/SiC composites was conducted in a four-point-bending mode on a universal testing machine at a loading rate of 1.27 mm/min. The loading and outer support spans were 20 mm and 40 mm, respectively. Both sets of specimens were observed to fail in a graceful manner, accompanied by extensive fiber pullout. The first matrix cracking stress was determined from the load at the first deviation from linearity on the load-displacement plot, whereas ultimate strength was measured from the peak load. Work-of-fracture was estimated from the area under the load-displacement plots. Room-temperature mechanical properties are shown in Table 1.

Table 1. Room-temperature mechanical-property data for SiC/SiC CFCCs with different fiber cloth lay-up sequences

Fiber Architecture	Coating Thickness (μm)	Composite Density (g/cm^3)	First Matrix Cracking Stress (MPa)	Ultimate Stress (MPa)	Work-of-Fracture (kJ/m^2)
0°/45°	0.0	-	-	105±28	0.16
	0.2	-	95.0	321±131	17.8±6
	0.4	2.25	86±23	153±41	9.8±2
0°/20°/60°	0.4	2.40	115±25	287±48	15.7±4
0°/40°/60°	0.4	2.46	116±28	312±28	14.4±4

As shown in the table, mechanical properties of composites are dependent on both fiber coating thickness and fiber cloth lay-up sequence. For a lay-up sequence of 0°/45°, mechanical properties (first matrix cracking stress, ultimate stress, and work of fracture) initially increase with coating thickness and reach peak values at a coating thickness of 0.2 μm. Further increases in coating thickness do not improve mechanical properties. This is believed to be related to the role of the coating in protecting fibers from damage during processing and in service.[7] These results indicate an optimal coating thickness of 0.2 μm for fibers in these composites. Similar results have been obtained for CVI SiC/SiC composites obtained from Oak Ridge National Laboratory.[7]

For a given fiber coating thickness, mechanical properties of composites with 0°/20°/60° and 0°/40°/60° fiber lay-up sequences were similar in magnitude, whereas composites with a fiber lay-up sequence of 0°/45° had relatively lower values. The decrease in mechanical properties for composites with a fiber lay-up sequence of 0°/45° is believed to have two causes. First, composites with a lay-up sequence of 0°/45° had a lower density (2.25 g/cm^3) than composites with other sequences (Table 1). The second cause could be the lower fiber fraction in the loading direction for composites with a 0°/45° fiber lay-up sequence as compared to composites with other fiber lay-up sequences.

These results provide much-needed information for optimizing composite processing in terms of fiber architecture and fiber coating thickness.

IN-SITU FIBER STRENGTH BEHAVIOR AND ITS CORRELATION WITH CRITICAL FLAWS

For evaluating the effects of fiber architecture and coating thickness on in-situ strength of fibers in composites, the fracture surfaces of composites with different fiber architectures and coating thicknesses (as shown in Table 1) were evaluated by standard fractography. Critical flaws in fibers (as shown in Fig. 6) were located and their sizes were measured. Subsequently, flaw sizes were correlated with fiber strength, as discussed below.

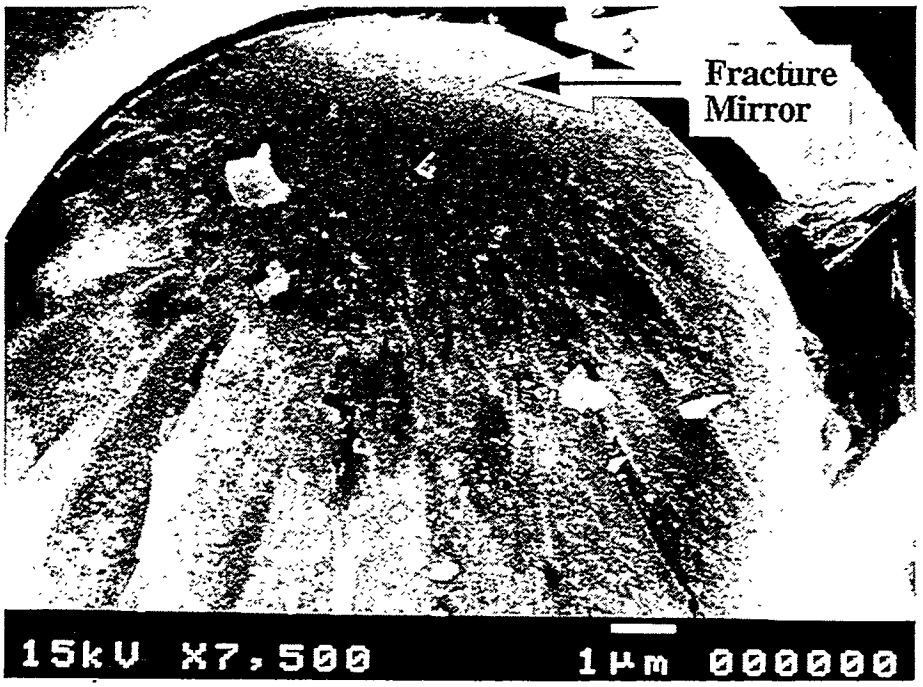

Fig. 6. Photomicrograph of fractured Nicalon fibers in SiC matrix composite, showing characteristic fracture features and fracture originating at fiber surface.

CRITICAL FLAW SIZE EVALUATIONS

In-situ strength of fibers in composites tested at room temperature as a function of fiber cloth lay-up sequence and coating thickness was evaluated from characteristic fracture features of the fibers. Strength of the fractured fibers was determined from the measured values of fracture mirror radii, as discussed by Kirchner and Gruver,[8] who provided the empirical relationship given in Equation 1.

$$\sigma_f \sqrt{r_m} = A_m , \tag{1}$$

where σ_f is the fiber fracture strength, r_m is the measured fiber mirror radius, and A_m is the mirror constant and is taken to be 3.5 MPa$\sqrt{m}$.

The measured values of in-situ fiber strengths were described by the Weibull strength distribution function, as shown in .

$$F(\sigma) = 1 - \exp\left[-\frac{L}{L_o}\left(\frac{\sigma}{\sigma_o}\right)^m\right], \tag{2}$$

where F(s) is the cumulative failure probability at an applied stress s, L_o is the fiber gage length at which Weibull parameters are estimated, L is the standard gage length taken to be 10 mm, s_o is the scale parameter signifying a characteristic strength of the distribution, and m is the Weibull modulus that characterizes the flaw distribution in the material.

Figure 7 compares the room-temperature in-situ fiber strength distributions of Nicalon fibers in composites with fiber lay-up sequences of 0°/45° and 0°/20°/60°. The figure also shows the effect of fiber coating thickness for composites with 0°/45° fiber lay-up. It can be clearly seen that for the same coating thickness of 0.4 μm, composites with a fiber lay-up sequence of 0°/45° have a higher (41%) in-situ fiber strength retained after processing than composites with 0°/20°/60° fiber lay-up sequence. In addition, for composites with 0°/45° fiber lay-up sequence, retained in-situ strength was higher (>100%) with a coating thickness of 0.4 μm. Further studies are in progress to optimize processing parameters for improved in-situ fiber strength.

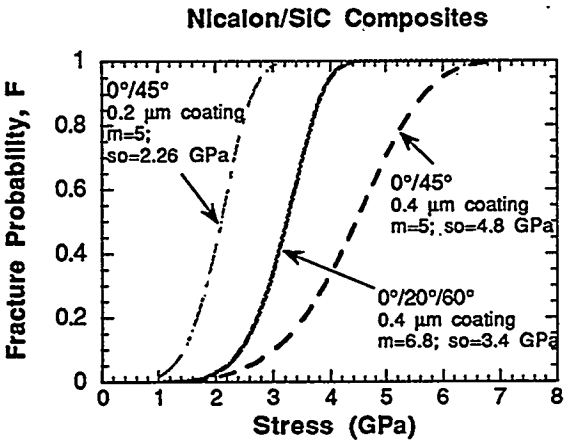

Fig. 7. Weibull strength distribution of Nicalon fibers in composites with different fiber lay-up sequences and coating thicknesses.

SUMMARY

Nondestructive evaluation (NDE) methods which can provide information about uniformity of material processing, e.g., axial and radial density, uniformity of fiber spacing, and the chemical state of the fiber matrix, have been demonstrated for applicability to several material systems. Distribution of void sizes of <100 μm can be

detected by high spatial resolution X-ray computed tomographic imaging on CFCC materials and density distribution can be determined. NMR has demonstrated the capability to measure the chemical state of fiber/matrix interfaces. Fracture behavior as a function of coating characteristics, fiber orientation, and flaw morphology show that coating thickness and fiber orientation are indeed affected by mechanical properties.

In the future, NDE technologies will be evaluated relative to joining applications of CFCC materials and for in-process data acquisition.

REFERENCES

1. E. A. Sivers, D. A. Holloway and W. A. Ellingson, "Predicting the Performance of 3-D X-ray Computerized Tomography Systems," in Nuc. Instr. and Meth. in Physics Research A, **345** (1994) pp. 179-197.

2. E. A. Sivers, D. A. Holloway, and W. A. Ellingson, "Use of Local X-ray Computerized Tomography for High-Resolution Region of Interest Inspection of Large Ceramic Components for Engines," ASME Int. Gas Turbine and Aero Engine Conf. May 1993, paper 93-GT-42, Cincidnnati, OH.

3. E. A. Sivers, W. A. Ellingson, S. A. Snyder, and D. A. Holloway," CT Multi-Scan Using Small Area Detectors to Image Large Dense Ceramic Components," to be presented to the ASME Int. Gas Turbine and Aeroengine Conf., June 1995, Houston, TX

4. P. Rizzo and W. A. Ellingson, "An Initial Comparison between Two 3-D X-ray CT Algorithms for Characterizing Ceramic Materials," in Conf. on NDE of Modern Ceramics, July 1990, Columbus, OH.

5. A. G. Evans and D. B. Marshall, "The Mechanical Behavior of Ceramic Matrix Composites," Overview No. 85, Acta Metall., **37** (10) 2567–2583 (1989).

6. T. Mah, M. G. Mendiratta, A. P. Katz, R. Ruh, and K. S. Mazdiyasni, "Room Temperature Mechanical Behavior of Fiber–Reinforced Ceramic Matrix Composites," J. Am. Ceram. Soc., **68** (1) C–27 – C–30 (1985).

7. J. P. Singh, D. Singh, and R. A. Lowden, "Effect of Fiber Coating on Mechanical Properties of Nicalon Fibers and Nicalon-Fiber/SiC Matrix Composites," Ceram. Eng. Sci. and Proc., **15** (4) 456–464 (1994).

8. H. P. Kirchner and R. M. Gruver, "Fracture Mirror in Alumina Ceramics," Phil. Mag. **27** 1433–1446 (1973).

FABRICATION OF FIBER-REINFORCED COMPOSITES BY CHEMICAL VAPOR INFILTRATION

W.M. Matlin*, D.P. Stinton**, and T. M. Besmann**
*Department of Materials Science and Engineering, University of Tennessee
Knoxville, TN 37996-2200

**Oak Ridge National Laboratory, Oak Ridge, TN 37831

ABSTRACT

A two-step forced chemical vapor infiltration process was developed that reduced infiltration times for 4.45 cm dia. by 1.27 cm thick Nicalon+ fiber preforms by two thirds while maintaining final densities near 90 %. In the first stage of the process, micro-voids within fiber bundles in the cloth were uniformly infiltrated throughout the preform. In the second stage, the deposition rate was increased to more rapidly fill the macro-voids between bundles within the cloth and between layers of cloth. By varying the thermal gradient across the preform uniform infiltration rates were maintained and high final densities achieved.

INTRODUCTION

Due to their high temperature strength and damage tolerant behavior, fiber reinforced ceramic matrix composites produced by chemical vapor infiltration are candidate materials for a number of high temperature applications. However, major obstacles in the commercialization of these materials are posed by the materials' high cost and the difficulty in fabricating thick components. In an attempt to reduce this cost and enable fabrication of thicker components, Oak Ridge National Laboratory has developed forced chemical vapor infiltration (FCVI) [1].

In spite of the significant advantages of FCVI, the composites produced may still be too expensive to be commercially viable. Furnace operation during preform infiltration make up the largest fraction of the composite's cost [2]. Therefore, reducing the time to infiltrate the preforms would have the greatest impact on the economics of the process.

Sheldon [3] has approached optimization of the isothermal, isobaric chemical vapor infiltration (ICVI) process by dividing the process into two steps. In the first step, intrabundle infiltration would be optimized [3]. In the second step, the much larger interbundle voids would be more efficiently filled [4]. Since the

+ Nippon Carbon Company, Tokyo, Japan

transport phenomena for ICVI,diffusion, is different than for FCVI, forced convection, the conclusions from this work could not be directly applied to FCVI optimization. However, the general two-step approach should be applicable.

In previous experimental FCVI optimization efforts, reductions in processing time have always corresponded to reductions in final density [5]. If this trend was to be reversed a better understanding of time dependent relationship between process variables would be required. The Georgia Tech. Chemical Vapor Infiltration Model (GTCVI) [6], a three dimensional finite volume program for modeling chemical vapor infiltration processes, was used to gain a phenomenological understanding of the process and as a guide in identifying the relative importance of each of the involved variables.

Several sets of modeling runs were performed to identify the optimum conditions for a two step process to infiltrate a 4.45 cm dia. by 1.27 cm thick preform, comprised of 52 layers of Nicalon cloth, with SiC deposited from CH_3SiCl_3 in hydrogen. The object of these runs was to develop a first step optimized to fill the micro-voids within the fiber bundles, and a second step optimized to fill the macro-voids between bundles in the cloth and between layers of fabric. This process scheme should result in much shorter infiltration times.

FIRST STAGE MODELING

A set of modeling runs was performed to identify conditions that resulted in uniform bundle infiltration from the hot side to the cool side of the preform. Six modeling runs were preformed by varying the initial cool side temperatures from 750 °C to 1000 °C at 50 °C increments. The hot-side of the control volume was fixed at 1200 °C and 100 kPa. The cool-side of the control volume was set to 750 °C, total flow of 550 cm^3/min, and a CH_3SiCl_3 flow of 45 cm^3/min. A time increment of 30 minutes was used between iterations and the runs were terminated after 8 simulated hours of infiltration. Density, deposition rates, temperature, pressure, CH_3SiCl_3 concentration, product HCl concentration and gas flow values were saved for each of the time increments.

The 750 °C cool side temperature run resulted in rapid deposition on the hot face with little or no deposition on the cool face. After 8 hours the cool-side of the preform has barely started to infiltrate, while the hot side was well past the point where bundles are fully infiltrated. Increasing the cool side temperature increased the deposition rate there. Since more reactant was consumed and HCl etchant produced on the cool side of the preform, the concentration of reactant on the hot-side decreased, resulting in lower deposition rates. At a cool-side temperature of approximately 950 °C the temperature gradient offsets the depletion of the reactant and uniform deposition results. Above 950 °C the density gradient is reversed with higher densities occurring near the cool-side and lower densities occurring near the hot-side.

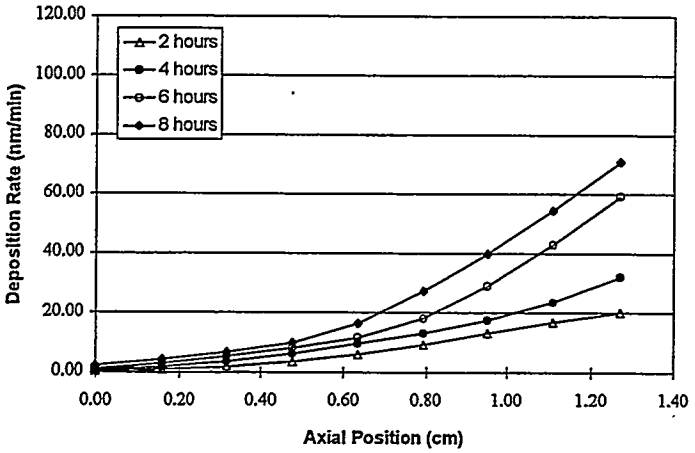

Figure 1. Deposition rate vs. axial position for 750 °C cool-side GTCVI simulation.

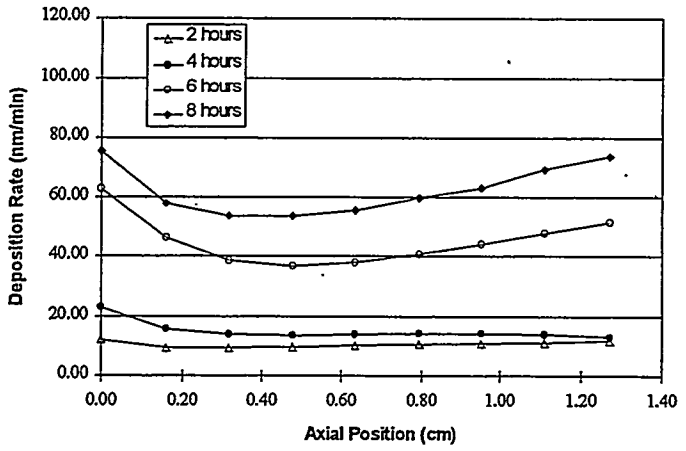

Figure 2. Deposition rate vs. axial position for 950 °C cool-side GTCVI simulation.

SECOND STAGE MODELING

Process conditions to more rapidly fill the macro voids between bundles and layers in the preforms were then investigated by using a response surface experimental design. The goal of this investigation was to optimize the process conditions to rapidly fill the large voids between bundles. In this design the top temperature was fixed at 1200 °C; higher temperatures were not investigated because they would result in damage to the Nicalon fiber. The thermal gradient, H_2 gas flow, CH_3SiCl_3 molar ratio and outlet pressure were varied using a central composite design with 16 cube points and 8 star points. A center point of 1200 °C top temperature, 545 cm^3/min total flow, 0.0827 CH_3SiCl_3 molar ratio (CH_3SiCl_3 moles/total gas moles), and 100 kPa outlet pressure was used. Intervals of 100 °C, 100 cm^3/min total flow, 0.025 CH_3SiCl_3 molar ratio, and 25 kPa

were used to generate the cube and star conditions. Infiltration at each of these conditions was then simulated using GTCVI, as shown in Table 1.

The interrelationship between and relative importance of the process variables on times and density was then determined by fitting first order response surfaces from the data points in Table 1. Density and process time were determined to be much more sensitive to temperature variations than other variables. Pressure was the next variable of importance due to the fact that increasing the inlet pressure while maintaining a shutdown inlet pressure of 200 kPa resulted in lower allowable pressure drops across the preform; thus, lower final densities. Density and process time had similar sensitivities to total gas flow and CH_3SiCl_3 concentration.

Additionally, increases in temperature, pressure, and gas flow rates reduced processing times and lowered final densities. In contrast, increases in concentration tended to both lower processing time and increase final density (Figs. 3 and 4).

Table 1. Response Surface Points used in the GTCVI model for second stage infiltration.

File Name	Response Surface Intervals				Temp. (°C)	Pressure (kPa)	H_2 (cm^3/min)	CH_3SiCl_3 (cm^3/min)	Time (h)	Density (%)
tst401	-1	-1	-1	-1	1100	75	420	25.75	29	88.1
tst402	1	-1	-1	-1	1300	75	420	25.75	9	87
tst403	-1	1	-1	-1	1100	125	420	25.75	24.5	85.7
tst404	1	1	-1	-1	1300	125	420	25.75	7.5	84.2
tst405	-1	-1	1	-1	1100	75	580	35.5	22.5	86.7
tst406	1	-1	1	-1	1300	75	580	35.5	6.5	85.1
tst407	-1	1	1	-1	1100	125	580	35.5	17	82.9
tst408	1	1	1	-1	1300	125	580	35.5	6	82.9
tst409	-1	-1	-1	-1	1100	75	420	25.75	24	88.5
tst410	1	-1	-1	1	1300	75	420	50.7	7	87.9
tst411	-1	1	-1	1	1100	125	420	50.7	11	87.9
tst412	1	1	-1	1	1300	125	420	50.7	5.5	84.4
tst413	-1	-1	1	1	1100	75	580	70	18	86.6
tst414	1	-1	1	1	1300	75	580	70	5.5	87
tst415	-1	1	1	1	1100	125	580	70	14.5	83.8
tst416	1	1	1	1	1300	125	580	70	4	82.3
tst417	0	0	0	0	1200	100	500	45	10.5	85.9
tst418	0	0	0	0	1200	100	500	45	10.5	85.9
tst419	-2	0	0	0	1000	100	500	45	56.5	87
tst420	2	0	0	0	1400	100	500	45	4.5	84.9
tst421	0	-2	0	0	1200	50	500	45	12.5	88.2
tst422	0	2	0	0	1200	150	500	45	8	82.1
tst423	0	0	-2	0	1200	100	340	30.5	15	88
tst424	0	0	2	0	1200	100	660	59.5	8	84
tst425	0	0	0	-2	1200	100	500	17	19	86.4
tst426	0	0	0	2	1200	100	500	76.5	8.5	86.6
tst427	0	0	0	0	1200	100	500	45	10.5	85.9

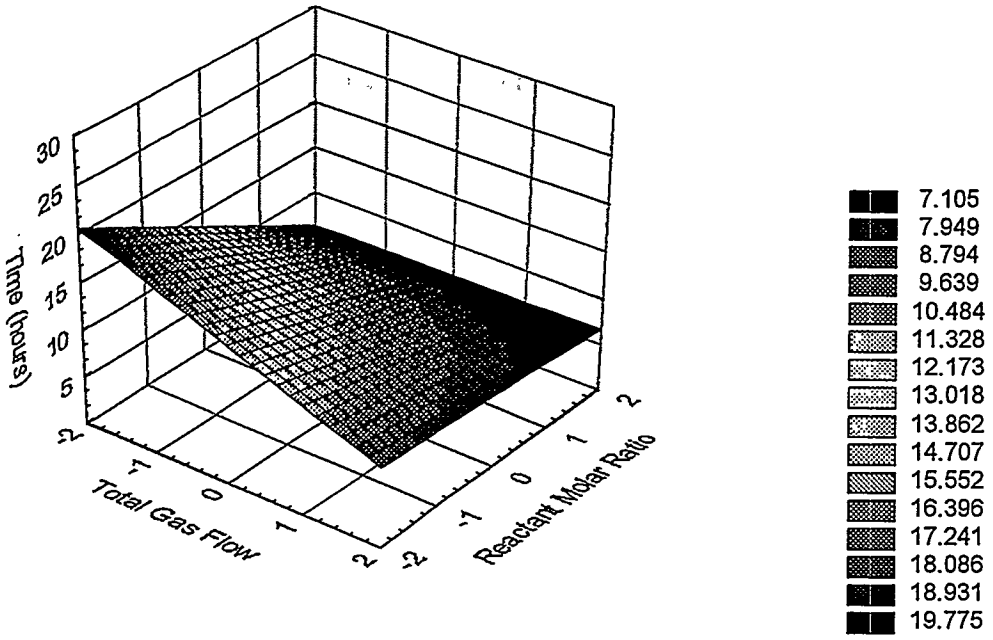

Figure 3. Time, flow, and concentration response surface generated from the GTCVI model data for the second phase of the two-step process.

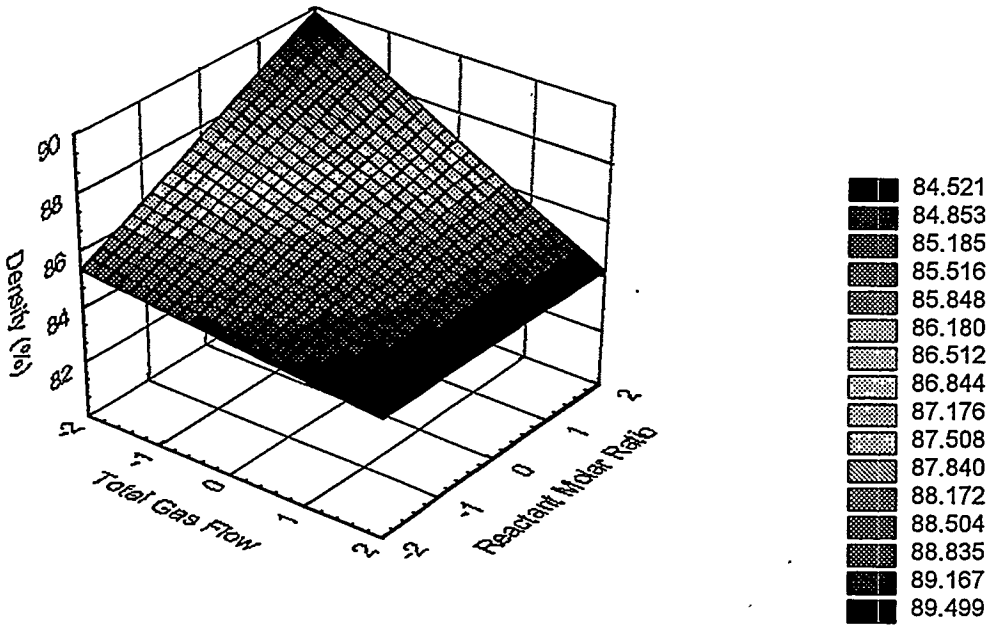

Figure 4. Density, flow, and concentration response surface generated from the GTCVI model data for the second phase of the two-step process.

TWO STEP MODELING

A two-step process, consisting of the optimized conditions from each of the stages previously described, was modeled and compared to the original one-step process. In the first set of computations, one-step conditions were used: 1200 °C hot-side temperature, 750 °C cool-side temperature, 500 cm^3/min H_2, 45 cm^3/min CH_3SiCl_3. The simulation ran until the pressure drop across the preform reached 100 kPa. The second run combined the thermal gradient optimization of the first stage with the increased CH_3SiCl_3 concentration of the second stage. The first five hours of the run used a 1200 °C hot-side temperature, 950 °C initial cool-side temperature, 500 cm^3/min H_2, and 45 cm^3/min CH_3SiCl_3. After the first five hours, the cool-side temperature was decreased to 850 °C and the CH_3SiCl_3 was increased from 45 cm^3/min to 83 cm^3/min. This simulation ran until a back-pressure of 100 kPa was reached.

The two-step simulation predicted a processing time 25 % shorter than the one-step process, with more uniform final density (Figs. 5 and 6).

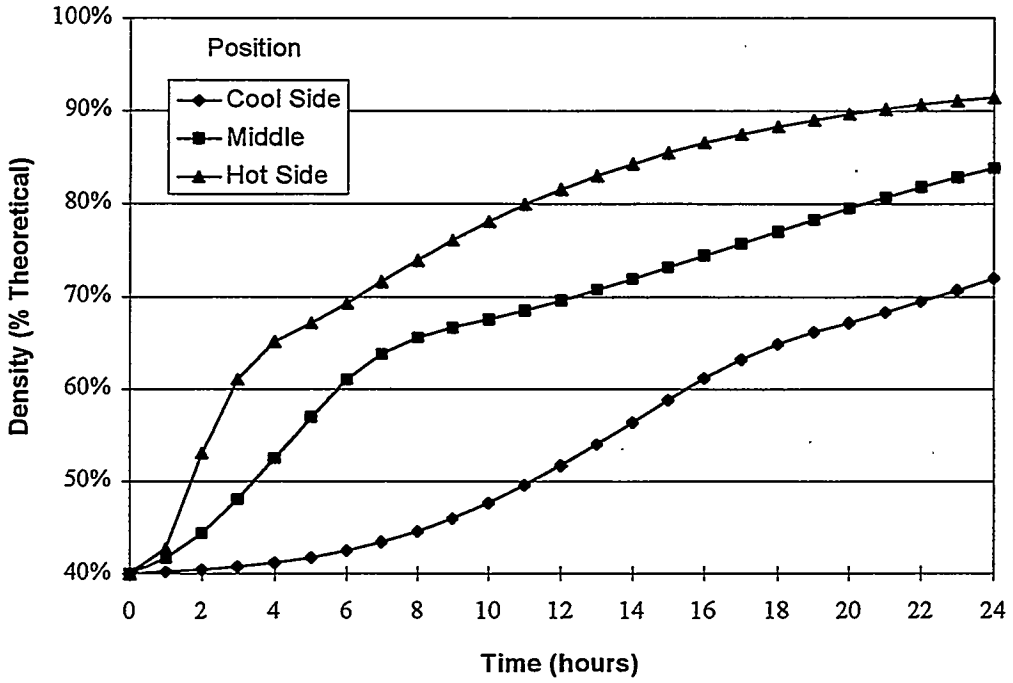

Figure 5. Density vs. time for 750 °C cool-side, one-step GTCVI simulation.

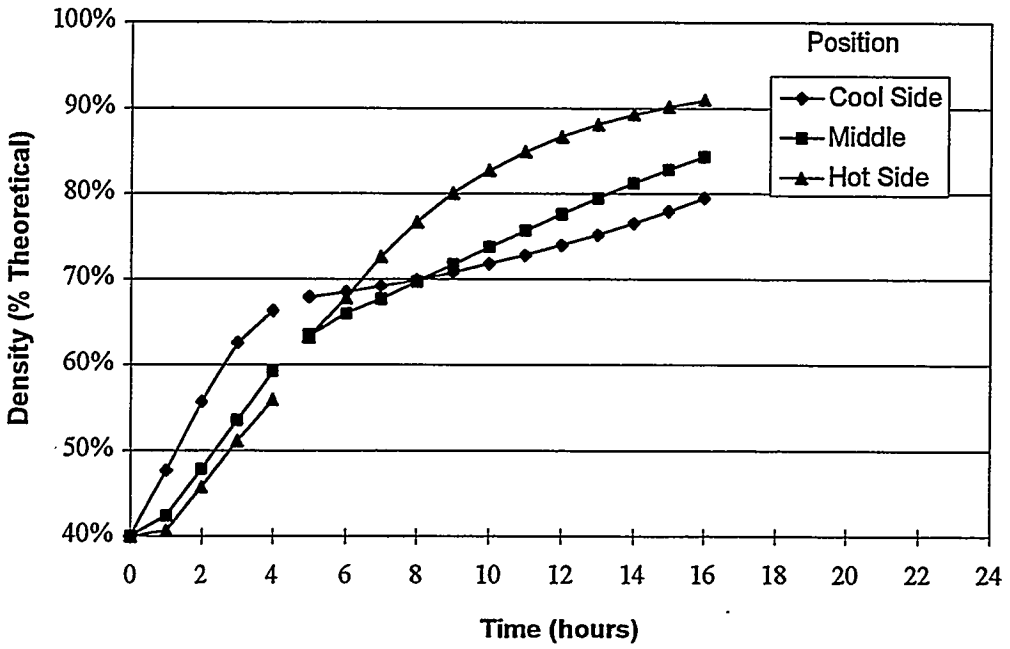

Figure 6. Density vs. time for 950 °C cool-side, two-step GTCVI simulation.

EXPERIMENTAL VERIFICATION

Two experimental runs were preformed and compared to the model predictions. In the first run (907) the preform was infiltrated for five hours using a 1200 °C hot-side temperature, 920 °C cool-side temperature, 500 cm^3/min H_2, and 45 cm^3/min CH_3SiCl_3. Process conditions were then changed to 1200 °C hot-side temperature, 825 °C cool-side temperature, 500 cm^3/min H_2, and 83 cm^3/min CH_3SiCl_3. The process automatically shutdown when a back-pressure of 170 kPa was reached.

The second preform (906) was infiltrated using standard conditions, i.e., 1200 °C hot-side temperature, 750 °C cool-side temperature, 500 cm^3/min H_2, and 45 cm^3/min CH_3SiCl_3. The process, again, automatically shutdown when a back-pressure of 170 kPa was reached.

The two step process required ten hours for infiltration and displayed a relatively uniform density averaging 89.8% (Table 2). In contrast, the run using standard conditions took 4.4 hours longer and had an average density 6.6% lower (Table 2). Additionally, the density gradients were significantly larger. Image analysis of the specimens was used to characterize the relative percentage of micro-porosity and macro-porosity. The sample fabricated using standard conditions had a total porosity of 15.4%, consisting of 8.7% macro porosity and 6.8% micro porosity (Table 3). The sample fabricated using the two-step process

had a total porosity of 14.5%, consisting of 9.4% macro porosity, and 5.1% micro porosity (Table 3).

Table 2. Experimental verification runs.

Process Number	Process Time (h)	Cool side Temp. (°C)	CH_3SiCl_3 Flow (cm^3/min)	Density (% Theoretical) Radial Position				
				Center				Edge
One-Step (906)	14.4	750	45	Hot side	89.8	89.7	89.5	88.9	86.6
				Middle	80.6	87.3	86.8	84.1	84.4
				Cool side	75.1	75.6	75.9	77	77.1
Two-Step (907)	5 + 5 = 10	920 + 750	45 + 83	Hot side	90.4	92.7	92	94.1	93.2
				Middle	92.8	92.2	92.5	92	91.6
				Cool side	85.6	86.2	86.3	85	80.9

Table 3. Porosity measurements using optical image analysis.

	One-Step (906)			Two-Step (907)		
	Macro Porosity	Micro Porosity	Total Porosity	Macro Porosity	Micro Porosity	Total Porosity
Hot Side	9.4%	6.7%	16.2%	15.5%	5.2%	20.7%
	6.7%	6.9%	13.7%	5.3%	5.3%	10.6%
	4.7%	7.1%	11.8%	5.6%	5.3%	10.9%
	5.4%	7.0%	12.5%	4.7%	5.3%	10.1%
	11.0%	6.6%	17.6%	8.2%	5.1%	13.3%
	7.4%	6.9%	14.3%	9.0%	5.1%	14.1%
	9.4%	6.7%	16.1%	12.1%	4.9%	17.0%
Cool Side	15.1%	6.3%	21.4%	14.6%	4.8%	19.4%
Average	8.7%	6.8%	15.4%	9.4%	5.1%	14.5%

SUMMARY

The two-step process significantly reduced processing time without reducing final density or uniformity. The key to this success was focusing on maintaining uniform infiltration rates, which prevent density gradients from forming within the preform. Gradients are caused by closure of macro-voids within one section of the preform while other sections remain relatively porous.

The utility of the GTCVI model was also demonstrated. Based on the accuracy of the GTCVI simulations for the 4.45 cm diameter furnace, GTCVI is expected to be instrumental in developing similarly optimized processing conditions for larger-scale furnaces [7].

REFERENCES

1. T. M. Besmann, B. W. Sheldon, R. A. Lowden, and D. P. Stinton, "Vapor phase fabrication and properties of continuous-filament ceramic composites", Science, Vol. 253, pp 1104-9 (1991).

2. Y.G. Roman, D. P. Stinton, "The preparation and economics of Silicon Carbide matrix composites by chemical vapor infiltration"; in Symposium Proceedings, Ceramic Matrix Composites (Boston, MA, 1994). Edited by R.L Lowden and J. R. Hellman, Materials Research Society, Pittsburg, PA, 1994 (in press).

3. H.C. Chang, T.F. Morse, B.W.Sheldon, "Minimizing infiltration times during the initial stage of isothermal chemical vapor infiltration", Journal of Materials Processing & Manufacturing Science, Vol. 2, pp 437-455 (1994).

4. B.W. Sheldon, H.C. Chang, "Minimizing densification times during the final stage of isothermal chemical vapor infiltration", Silicon-Based Structural Ceramics, B.W. Sheldon, S.C. Danforth (eds.), Ceramic Transactions, Vol. 42, American Ceramic Society, (1994).

5. R.A. Lowden, A.J. Caputo, D.P. Stinton, T.M. Besmann, and M.D. Morris, "Effect of infiltration conditions on the properties of SiC/Nicalon composites", Oak Ridge National Laboratory Report ORNL/TM-10403, (1987).

6. T.L. Starr, "Model for rapid CVI of ceramic composites" Proc. 10th Int. Conf. CVD, (The Electrochemical Society, Inc., Pennington, NJ, 1987), pp 1147-1155, (1987).

7. D. P. Stinton, O.J. Schwarz, and J. C. McLaughlin, "Fabrication of fiber-reinforced composites by chemical vapor infiltration", Proceedings of the Eight Annual Conference on Fossil Energy Materials, Oak Ridge National Laboratory Report ORNL/FMP-94/1, pp 1-9, (1994).

TRANSPORT PROPERTIES OF CERAMIC COMPOSITES

T.L. Starr

School of Materials Science and Engineering
Georgia Institute of Technology
Atlanta, Georgia 30332-0245

This project involves experimental and modeling investigation of the transport properties of chemical vapor infiltration (CVI) preforms and densified composites, with particular emphasis on gas permeability and mass diffusivity. The results of this work will be useful both for on-going CVI process development and for evaluation and optimization of composite materials for fossil energy applications.

With preforms made with 500 filaments/tow Nicalon at 40 vol% fiber loading, permeability values are similar for square-weave cloth layup and 3-D weave at low density. At greater densification the 3-D weave permeability is lower and approaches zero with significantly more closed porosity than the cloth layup. For filament wound preforms we were unable to make reliable measurements with the available materials.

A model for gas transport in these materials utilizes percolation theory concepts. The ultimate achievable density is related to the closing of a continuous gas path through the preform. As the density approaches this limit the gas permeability and diffusivity vanish exponentially. The value of this limit is controlled primarily by the preform fiber architecture. The observed difference between the cloth layup and 3-D weave materials is due to the larger pores at tow crossing points found in the 3-D weave.

INTRODUCTION

Of the various methods for fabricating ceramic matrix composites, chemical vapor infiltration (CVI) is strongly controlled by the transport properties of the preform and partially densified composite. These properties include gas permeability, mass diffusivity (effective diffusion coefficient) and thermal conductivity, and depend on the density and microstructure of the composite. For forced flow CVI, the gas permeability is the critical factor that determines the ultimate density that can be achieved. Mass diffusivity is a controlling property for isothermal CVI where it limits the densification rate and

density uniformity. For thermal gradient CVI the thermal conductivity of the composite controls the steepness of the thermal gradient and how this gradient changes with processing time.

This paper describes our ongoing investigation of the gas permeability of CVI preforms and densified composites, involving both experiment and modeling. The results of this work will be used both for CVI process development and for evaluation and optimization of composite materials for fossil energy applications.

GAS PERMEABILITY MEASUREMENTS

Our experimental apparatus for measuring gas permeability is shown schematically in Figure 1. Measurement consists of concurrent determination of gas flow rate and pressure difference across the specimen. While simple in principle accurate measurements with small specimens at low permeability require careful attention to detail. In particular we have added a second, downstream flowmeter to the apparatus to ensure there are no leaks in the gas lines and in the specimen mounting fixture.

A critical factor in these measurements is extraction and mounting of the test specimen. It must be large enough to encompass a number of unit cells of the composite architecture, but small enough to have uniform density throughout. Earlier measurements used very small, cube shaped specimens[1]. For recent measurements we have used two types of larger specimens.

One type of permeability specimen has the form of a right circular cylinder approximately 10 mm in diameter and 5-10 mm in length and is machined from a larger piece of composite. Recent results for composites made with 40 vol% Nicalon fiber are shown in Figure 2. Permeability values for 3-D weave and cloth layup materials are similar at low density, however, at high density the 3-D weave permeability is lower and approaches zero with significantly more closed porosity than the cloth layup. These results are analyzed below in the discussion of transport property modeling. Sections of filament wound composite also

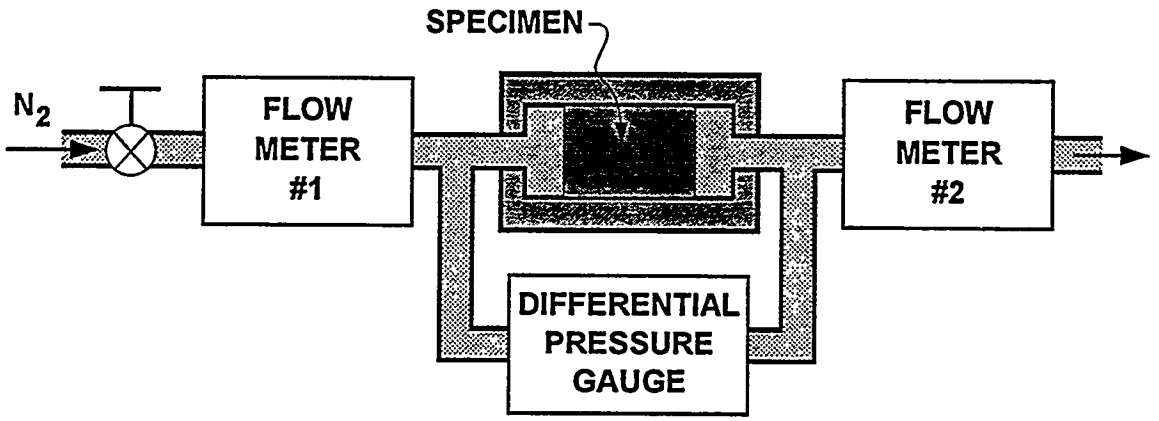

Figure 1. Apparatus for performing gas permeability measurements. Downstream meter provides redundant flow measurement as check for gas leaks in mounting fixture.

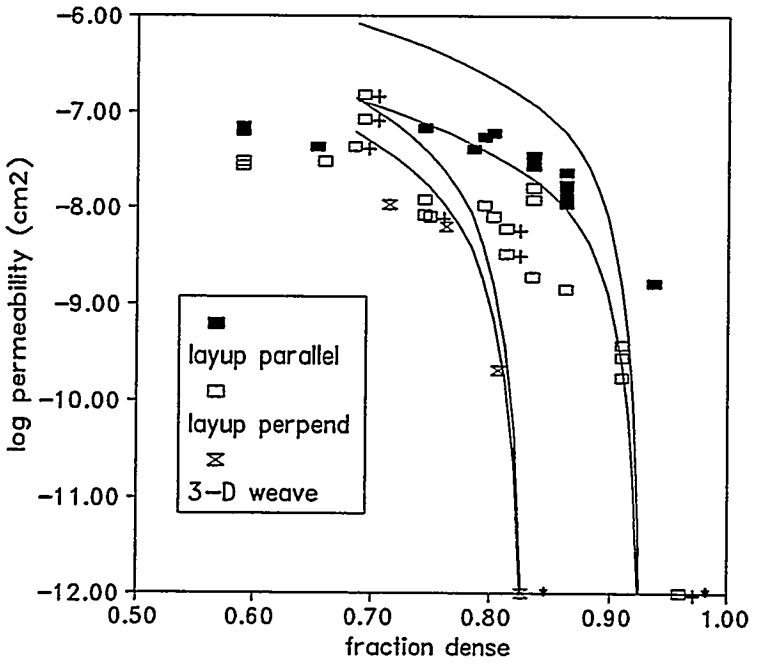

Figure 2. Gas permeability for cloth layup and 3D weave composites. Layup points with + are recent measurements. Points with * had no measurable permeability. Solid lines are model calculations discussed in text.

were available but due to their size and configuration we were unable to machine specimens suitable for reliable measurements.

An additional type of specimen is fabricated using a small, forced flow CVI apparatus, providing specimens 18 mm in diameter and up to 20 mm thick. This approach has the advantages that it allows us to measure permeability prior to densification and at different densities, and to fabricate various layup patterns. Permeability measurements with these specimens have not been completed at this time.

TRANSPORT PROPERTY MODEL

A general model has been proposed for the microstructure and gas permeability of woven fiber preforms and composites based on a node-bond model[2]. In this model the porosity is represented as a network of spherical "nodes" connected by cylindrical "bonds" (Figure 3). The network geometry is directly related to the regular structure of the woven preform. Nodes correspond to the large pores created at tow crossing points while bonds correspond to the smaller channels that connect neighboring nodes. The spatial arrangement of the nodes and their coordination number (number of nearest neighbors) is fixed by the weave architecture i.e. tow spacing and weave or braid pattern. The node and bond diameters exhibit a distribution of values around an average which is set to match the overall volume fraction of intertow porosity.

The gas permeability of this network is calculated assuming Poiseuille flow through the cylindrical bonds with the given distribution of diameters. Densification is simulated by incrementally reducing the bond and node dimensions and recalculating the network pore volume, surface area and permeability. As densification proceeds the smaller bonds close (Figure 4) and as the fraction of open bonds approaches the percolation limit the accessable pore fraction and the network permeability both vanish exponentially.

The model can be used to estimate the surface area and permeability of woven fiber preforms during CVI. A commonly used

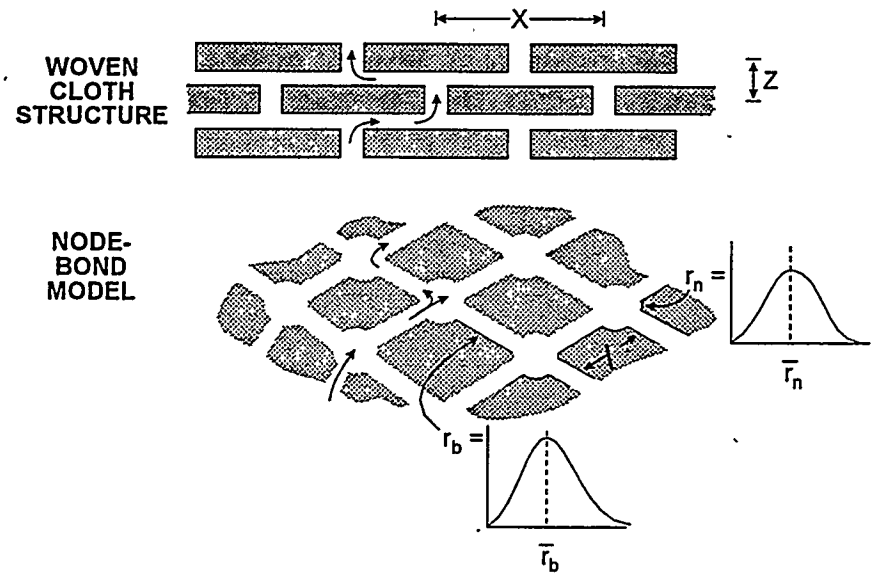

Figure 3. Node-bond model for gas transport through woven fiber preform relates to fiber architecture.

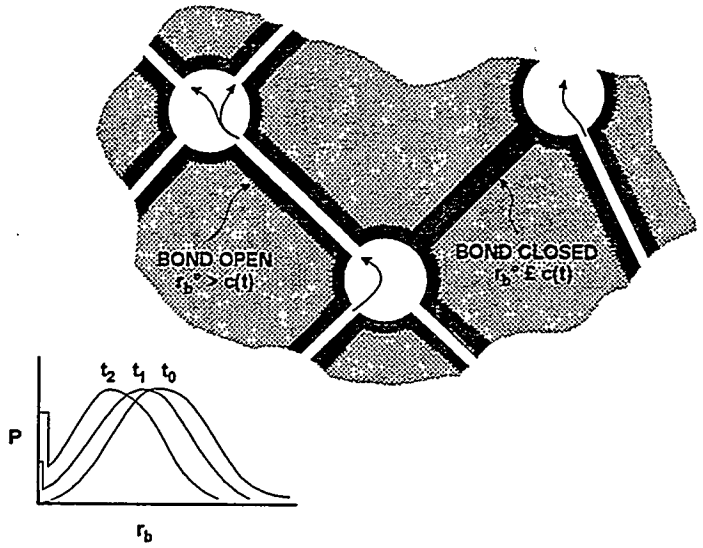

Figure 4. During densification bonds close at different times until no continuous gas path remains.

preform consists of several layers of square-weave cloth stacked to give 40% fiber by volume. A typical preform uses tows of 15 μm fibers with 500 filaments/tow, tow spacing of 0.150 cm in the cloth (X and Y directions) and a layer spacing of 0.030 cm. The 60% porosity in the preform is considered to be divided equally between fine porosity within the tows and coarse porosity between the tows. The coarse porosity consists of relatively large pores (nodes) in the plane of the cloth and smaller, tortuous pores (bonds) connecting these to eight similar nodes in adjoining cloth layers. A critical parameter in this model is the ratio of the node and bond radii, r_n/r_b. Model estimate of permeability is shown as the upper pair of curves in Figure 2 for $r_n/r_b = 3.0$. The match to experiment is reasonably good although the model values are systematically high.

Microscopic examination of the 3-D weave composite used for permeability measurements shows a tow spacing in two directions of 0.150 cm but only 0.100 cm in the third direction. This anisotropy is expected to yield a somewhat anisotropic permeability. However, all experimental measurements were made parallel to the small spacing direction. Also, compared to the cloth layup composite, the "nodes" constitute a larger fraction of the intertow porosity. Using these observations the model yields the lower pair of curves in Figure 2 for $r_n/r_b = 6.0$. Again, the match with experiment is reasonably good with a percolation limit significantly lower than that of the cloth layup. From the model we can see that this results from the relatively large pores found at the crossing points of the three orthogonal yarns.

SUMMARY

This experimental investigation of the transport properties of CVI preforms and densified composites aims to produce consistent data useful both for on-going CVI process development and for evaluation and optimization of composite materials for fossil energy applications. The ultimate goal is to understand the microstructure-transport property

relationship well enough to design fiber architectures for optimum processing behavior.

The node-bond percolation model for gas transport builds on a representation of the coarse porosity in woven fiber structures during CVI densification. While this structure is idealized, model parameters relate to real structural features such as filament size, number of fibers per tow and spacing of tows in the weave. Some uncertainty exists in the proper partition of the porosity between "node" and "bond" and between intra-tow and inter-tow, although the total is constrained by the known fiber loading.

Applied to cloth layup and 3-D weave preforms the model gives reasonably good agreement with experimental measurements although model predictions are systematically high. The observed higher amount of closed porosity for the 3-D weave is due to a larger fraction of intertow porosity deriving from the large pores at tow crossing points.

REFERENCES

1. G.B. Freeman, T.L. Starr and T.C. Elston, "Transport Properties of CVI Preforms and Composites," Mat. Res. Soc. Symp. Proc. 168, 49-54 (1990).

2. T.L. Starr, "Gas Transport Model for Chemical Vapor Infiltration," J. Mat. Sci., in press.

DEVELOPMENT OF MATERIALS FOR MICROWAVE-HEATED DIESEL PARTICULATE FILTER

Mark A. Janney and David P. Stinton
Oak Ridge National Laboratory
Oak Ridge, Tennessee 37831-6087

ABSTRACT

Ceramic fiber filters are being fabricated and tested for use as diesel particulate filters. The filters are to be heated by microwave energy to remove carbon and regenerate the filters.

INTRODUCTION

The purpose of this research is to help develop microwave-heated diesel engine particulate filter/burner devices. The goal is to develop materials that will perform both as filter and heater in such a device. A Cooperative Research and Development Agreement (CRADA No. ORNL93-0172) between Martin Marietta Energy Systems (MMES) and the Cummins Engine Company is in place that supports this work. The Department of Energy (DOE) CRADA monies come from both the Fossil Energy AR&TD Materials Program and the Energy Efficiency and Renewable Energy - Office of Transportation Technologies (EE-OTT), Heavy Duty Transport Program.

Diesel engines will soon be required (1998) to emit essentially no particulate exhaust into the environment. One of the approaches to prevent such emissions is to trap the particles in a filter, then burn the trapped particles on a regular cycle. An approach that has been proposed by Cummins Engine Co. is to build a system based on a ceramic filter that can be heated with microwaves. We will fabricate such filters

and determine how they interact with microwaves to heat and burn the carbon particulates trapped in the filter material.

We propose to develop a ceramic composite structure of SiC-coated ceramic fiber that can be used as a diesel engine particulate filter. For commercial usage a particulate filter must: 1) filter carbon particles from high temperature diesel exhaust gas at an acceptable (low) backpressure; 2) survive thousands of thermal transients caused by regeneration (cleaning) of the filter by oxidizing the collected carbon; (3) be durable and reliable over the life of the filter, which is in excess of 300,000 miles (10,000 hours of operation); and, (4) provide a low overall operating cost which is competitive with other filtering techniques.

SiC-coated ceramic fiber was selected as the filter material because it can be readily heated by microwave energy. Particulate traps must be regenerated by heating the carbon particles to approximately 600°C to oxidize the carbon. Heating by microwaves is expected to provide more uniform heating of the filter and result in a lower cost, more reliable regeneration system. Previous methods of regeneration used diesel-fired burners or electrical resistance heating for regeneration. Uneven heating and use of weak ceramic materials resulted in cracking of the trap and loss of filtration capability. Fiber composites have excellent thermal shock capability. Producing a filter by manufacturing a fiber-reinforced ceramic paper has inherent advantages since it is possible to tailor the filtration characteristics of the ceramic paper while maintaining a strain tolerant material.

The idea of using microwave heating combined with ceramic filters to trap and burn carbon particulate emissions from

diesel engines represents a large-scale, near term consumer and industrial application of two technologies, microwave heating and chemical vapor infiltration, developed under the AR&TD materials program. As such, it has the potential to be an excellent example of technology transfer and cooperative research and development between a national laboratory and U.S. industry. This approach represents the front runner in the thinking of one of the nation's foremost diesel manufacturers.

TECHNICAL PROGRESS

We are investigating the development of materials for diesel particulate filters. We have devoted our efforts to evaluating various candidate materials concerning: (1) how well they can be fabricated into filter elements; (2) how they interact with a microwave field - i.e., how they heat;; and, (3) how well they withstand a corrosive (oxidative) high temperature environment.

CVD Coating

Filter papers made from ceramic fibers were received from Fleetguard, a division of Cummins Engine Company. These papers were coated at ORNL with CVI SiC containing various levels of additives. It had been observed last year that CVD conditions that should have produced high-quality, stoichiometric SiC coatings instead produced poor coatings. It was hypothesized that excess carbon had formed in the filter papers during pyrolysis of the organic constituents used in the papermaking process. Excess silicon was added to some of the CVI runs to compensate for the residual carbon. Figure 1 shows micro-structures of the CVD-coated papers made under stoichiometric and excess silicon CVD conditions. Clearly, the coating made

with excess silicon is superior to that made under stoichiometric conditions.

Characterization of Filter Materials

The various filter materials made above were tested under long term oxidation conditions (500h, 800°C). Figure 2 shows that the samples with coatings containing excess silicon performed the best. They exhibited only a small change in weight, losing weight in the short term, and gaining slightly in the long term. This behavior is consistent with the fibers being coated by a dense, adherent silicon carbide coating.

Filter materials were also characterized in terms of their microwave absorption properties. Figure 3 shows the behavior of a typical sample that had been coated with CVD silicon carbide under "stoichiometric" conditions. The initial properties of the sample showed that it absorbed microwaves very strongly at ambient temperature. Its penetration depth (see below) was on the order of 1 cm. On heating the first time, the properties of the material changed dramatically. At about 600°C, the sample became much less absorptive and its penetration depth increased by a factor of 10, and then fell again as temperature was further increased. Upon a second heating, the sample behaved very differently. Its penetration depth at ambient temperature was about 1000 cm. This value decreased with increasing temperature and at 700°C matched the values obtained during the first heating. There were no additional changed in microwave properties with additional heatings (3,4, and 5).

The drastic changes in microwave absorption (penetration depth) during the first heating is consistent with burnout of

carbon in the sample. The semilog relationship of penetration depth with temperature during cycles 2 though 5 is consistent with the exponential increase in the electrical conductivity of silicon carbide with increasing temperature.

Penetration Depth and Applicator Design

Microwaves are absorbed in materials according to the Beer-Lambert Law:

$$P = P_o \exp(-\alpha X) \qquad (1)$$

where P is the power at any point, P_o is the incident power, α is the absorption coefficient, and X is the distance of penetration into the material. The absorption coefficient, α, is related to more fundamental properties:

$$\alpha = (\omega \sqrt{e'_r} \tan \delta) / c \qquad (2)$$

where ω = frequency, e'_r = relative dielectric constant, $\tan \delta$ = dielectric loss tangent, and c = speed of light. One may define a characteristic distance, called the penetration depth, which is related to the absorption coefficient. The penetration depth is defined as the distance into the material at which the incident energy has been reduced by a factor of 1/e (where e = 2.7183, the base of the natural logarithms). Figure 4 shows this relationship graphically.

The importance of penetration depth (absorption coefficient) as a design parameter is shown in Figure 5. This figure shows a simplified design for a microwave filter heater. For a material having a very large absorption coefficient (small penetration depth), $\alpha r >> 1$ and all of the microwave energy is deposited at the outer surface of the filter. For very small

absorption coefficients (large penetration depths), $\alpha r << 1$ and the microwave energy is absorbed very slowly by the filter material. Standing waves build up inside the applicator, which lead to "hot spots" and "cold spots" in the filter. For moderate absorption coefficients (moderate penetration depths), $\alpha r \approx 1$, most of the microwave energy is absorbed in one or two passes through the filter. This leads to the most uniform heating of the filter by the microwaves. The penetration depths of the materials being developed in this study range from 10 to 1000 cm for an individual layer of CVD coated filter material. The actual filters will contain multiple layers of filter material. This will produce a composite having a penetration depth that is of the order of the size of the microwave applicator, i.e., 10 to 20 cm.

System Testing

In February 1995, a prototype filter cartridge was tested at Cummins Engine Company in a developmental microwave applicator as a first proof-of-concept test for the microwave regenerated filter. The filter removed carbon particles from the exhaust of a test diesel engine and the microwave heater successfully regenerated the filter by burning out the carbon.

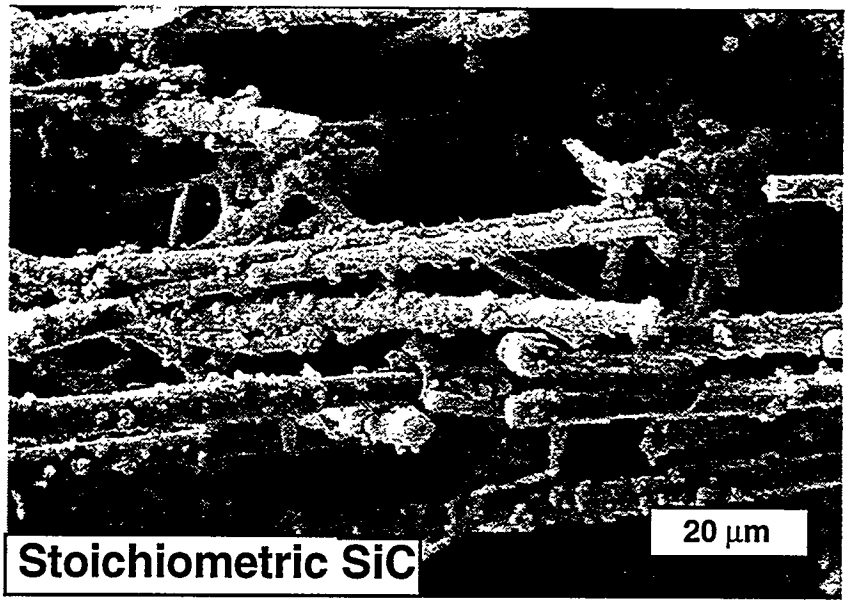

(a)

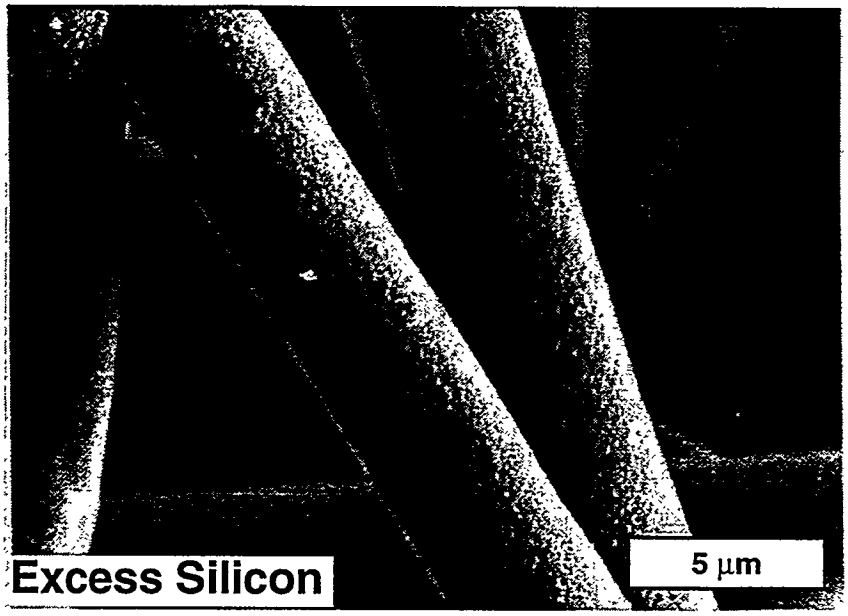

(b)

Figure 1. The addition of excess silicon to the CVI coating on the filter preforms produced a superior coating: (a) stoichiometric SiC; (b) excess silicon. SEM micrographs.

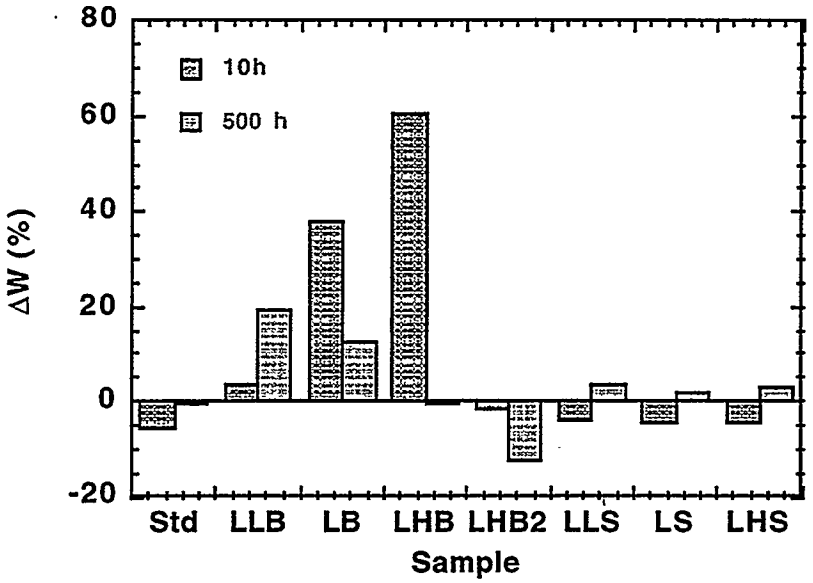

Figure 2. Samples containing excess silicon in the CVI coating were the most resistant to oxidation.

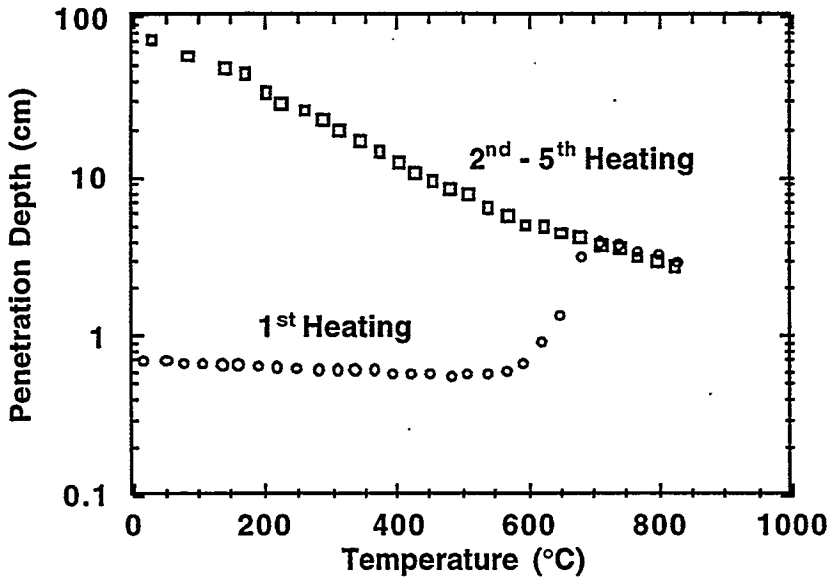

Figure 3. SiC coated alumina fiber filter materials "aged" on first heating. They were stable on subsequent heating. Filter coated with "stoichiometric" SiC CVI mixture.

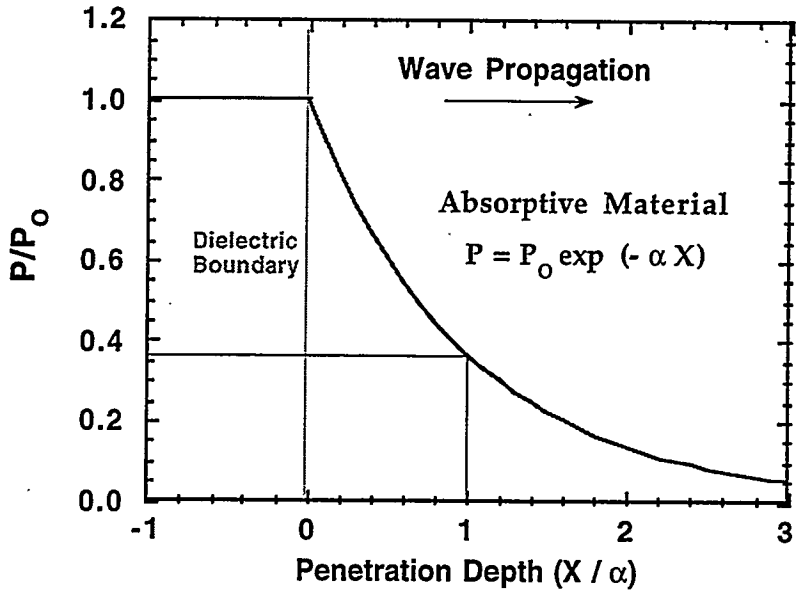

Figure 4. Most of the power in a microwave beam is lost in the first penetration depth.

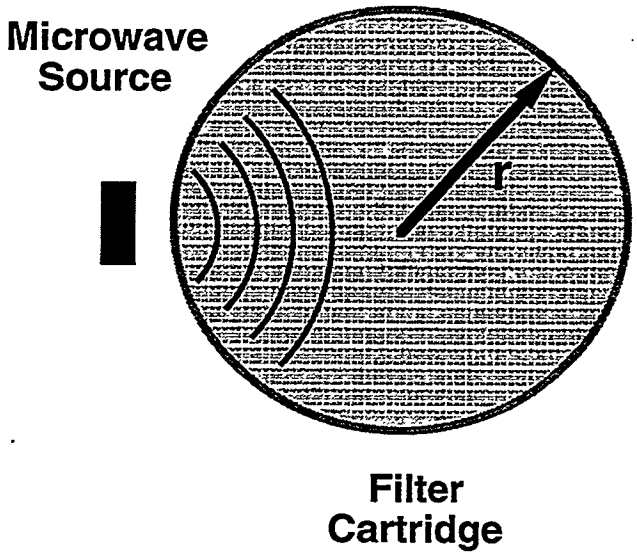

Figure 5. Penetration depth is an important factor in developing a microwave applicator the heats uniformly.

HIGH TEMPERATURE INORGANIC MEMBRANES FOR SEPARATING HYDROGEN

D. E. Fain and G. E. Roettger

Oak Ridge K-25 Site*
P. O. Box 2003
Oak Ridge, Tennessee 37831-7271

ABSTRACT

Effort has continued to accumulate data on the transport of gases over the temperature range from room temperature to 275°C with inorganic membranes having a range of pore radii from approximately 0.25 nm to 3 nm. An experimental alumina membrane having an estimated mean pore radius of 0.25 nm has been fabricated and tested. Extensive testing of this membrane indicated that the separation factor for helium and carbon tetrafluoride at 250°C was 59 and the extrapolated high temperature separation factor was 1,193. For safety reasons, earlier flow measurements concentrated on helium, carbon dioxide, and carbon tetrafluoride. New data have been acquired with hydrogen to verify the agreement with the other gases. During the measurements with hydrogen, it was noted that a considerable amount of moisture was present in the test gas. The source of this moisture and its effect on permeance was examined. Improvements were implemented to the flow test system to minimize the water content of the hydrogen test gas, and subsequent flow measurements have shown excellent results with hydrogen. The extrapolation of separation factors as a function of temperature continues to show promise as a means of using the hard sphere model to determine the pore size of membranes. The temperature dependence of helium transport through membranes appears to be considerably greater than other gases for the smallest pore sizes. The effort to extend temperature dependence to the hard sphere model continues to be delayed, primarily because of a lack of adequate adsorption data.

INTRODUCTION

The goal of this project is to develop methods for fabricating ceramic membranes that will separate hydrogen efficiently from gasified coal at temperatures of 1,000°F or higher. To be economically useful, the membranes must have a high separation factor. Very high separation factors can be achieved with ceramic membranes if the pores are small enough to separate gas molecules by molecular sieving. A molecular sieve membrane ideally would have pores that are slightly smaller than the larger gas molecule but larger than the smaller gas molecule. Such a membrane permits only the

---

*The Oak Ridge K-5 Site is managed by Martin Marietta Energy Systems, Inc. For the U.S. Department of Energy under contract No. DE-AC05-84OR21400.

smaller gas molecule (such as hydrogen) to pass through the pores, as shown conceptually in Fig. 1, providing an infinite separation factor. Actual membranes always have a distribution of pore sizes with some pores considerably larger than ideal; hence, there is some limit on the separation factor actually achievable. The hard sphere diffusion model, discussed earlier, shows how the separation factor changes from square root of molecular weight ratio for Knudsen flow to infinite for a molecular sieve as the pore radius decreases.[1] Membranes having a tubular geometry, such as those being fabricated for this project, could be assembled into a useful separation module of the tube and shell type. A simplified module containing a single membrane tube is shown conceptually in Fig. 2. A single stage of membrane separation, using molecular sieve membranes having a high separation factor, could be adequate for many gas separation applications.

The primary objective of this project during the past year has been to develop and demonstrate through testing a ceramic membrane having sufficiently small pores to achieve a separation factor of 50 or higher. Another important objective was to upgrade the high temperature flow test system to permit hydrogen to be used as an additional test gas for measuring the permeance and separation factors of membranes. Key results and data pertaining to these objectives are summarized below.

DISCUSSION OF CURRENT ACTIVITIES

Alumina Membrane Having 0.25 nm Mean Pore Radius

An experimental alumina membrane has been produced and tested that has an estimated mean pore radius of about 0.25 nm (2.5Å). The membrane was tested in our high temperature flow test system using helium and carbon tetrafluoride as test gases. Flow measurements were made on the membrane over a range of pressures at room temperature, 100°C, and 250°C. Since the pore size of this membrane was considerably smaller than any previously available, the membrane was extensively tested to verify separation factors and to study the transport properties. Separation factors calculated from the ratios of specific flows were determined for the He/CF_4 gas pair. Repeat cycles of testing resulted in twelve separation factors being determined. One of these values proved to be a statistical outlayer and was omitted. A total of four He/CF_4 separation factors were determined at 250°C and their mean value was 59, which met the separation factor target of 50. An Arrhenius-type plot (ln separation factor plotted against the reciprocal of the absolute temperature) for the eleven separation

ORNL-DWG 95M-5199

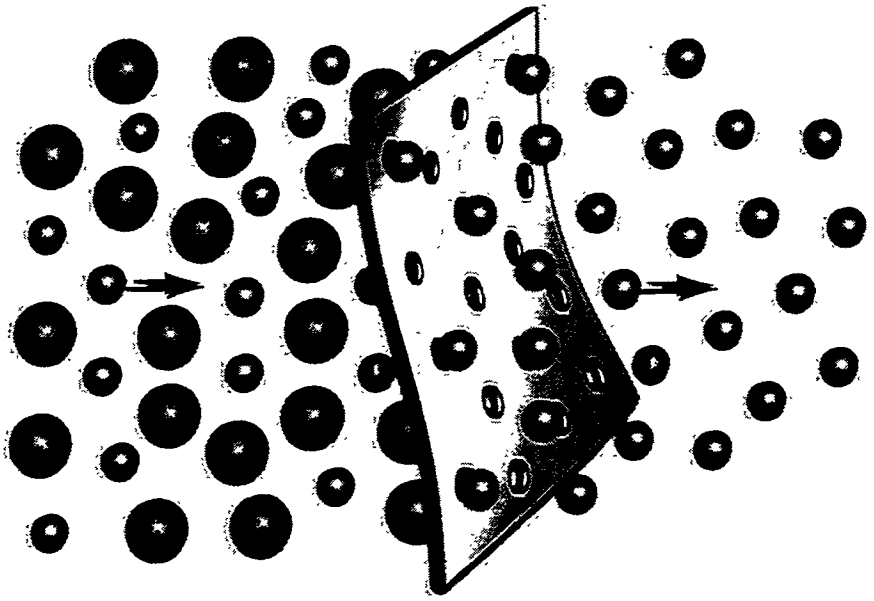

Fig. 1. Molecular sieve membrane for separating gas molecules.

ORNL-DWG 95M-5211

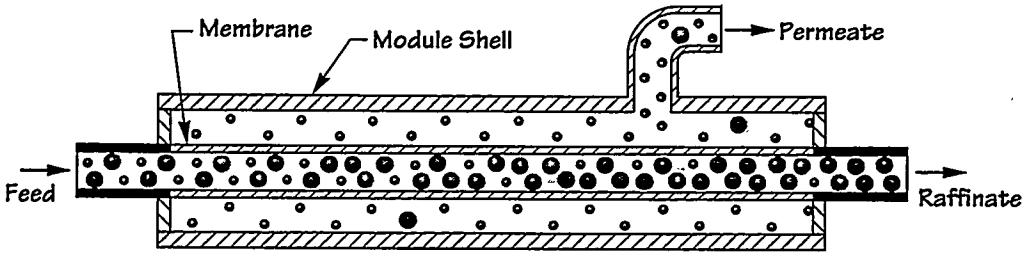

Fig. 2. Separation module using molecular sieve membrane to separate gases.

factors is shown in Fig. 3. A least squares fit of the data is extrapolated to a zero value of 1/T (infinite temperature) to estimate the separation factor at the high temperature limit where pure diffusive flow should exist. The high temperature extrapolated separation factor determined for the membrane was 1,193. This high temperature separation factor can be interpreted by the hard sphere model to provide an estimate of the membrane pore size. This calculation indicates that a mean pore radius of 0.25 nm is required to provide a He/CF_4 separation factor of 1,193 at the high temperature limit. Using the least squares fit of the data, a separation factor of 336 is calculated for 1,000°C and 164 is calculated for 1,000°F.

A typical example of the flow data measured on this membrane with carbon tetrafluoride at room temperature, 100°C, and 250°C is shown in Fig. 4. The flow data are plotted as a permeance (sccm/sq cm/cm Hg) versus average pressure (average of the forepressure and backpressure). The CF_4 permeance is highest at room temperature and declines as the temperature is increased to 250°C. This trend toward lower permeance at higher temperature has been observed with other small pore size membranes and appears to result from decreasing surface flow of adsorbed molecules as temperature is increased.

A typical example of the helium flow data measured on the membrane at the same three temperatures is shown in Fig. 5. The measurements show much higher helium permeance at 250°C than at the lower temperatures. This phenomenon, which was observed in several repeat cycles of testing of the membrane, has not been observed with previous membranes and is not yet understood.

The permeance data shown in Figs. 4 and 5 may be converted to transport probabilities and extrapolated to zero pressure, as described earlier, to provide a zero pressure transport probability for each gas at each temperature.[1] For free molecule or Knudsen flow, the zero pressure transport probability should be a function of the properties of the membrane and independent of the type of gas molecule and temperature. The zero pressure transport probabilities determined for He and CF_4 at the three temperatures are shown in Fig. 6. The trends noted earlier in permeance values with temperature are very prominent in the plotted transport probabilities and indicate large deviations of the actual gas transport from free molecule or Knudsen flow.

High Temperature Flow Test System Upgraded to Use Hydrogen

The high temperature flow test system is used routinely to evaluate the separation factors of membranes using inert gases such as helium and carbon tetrafluoride as discussed above. Since

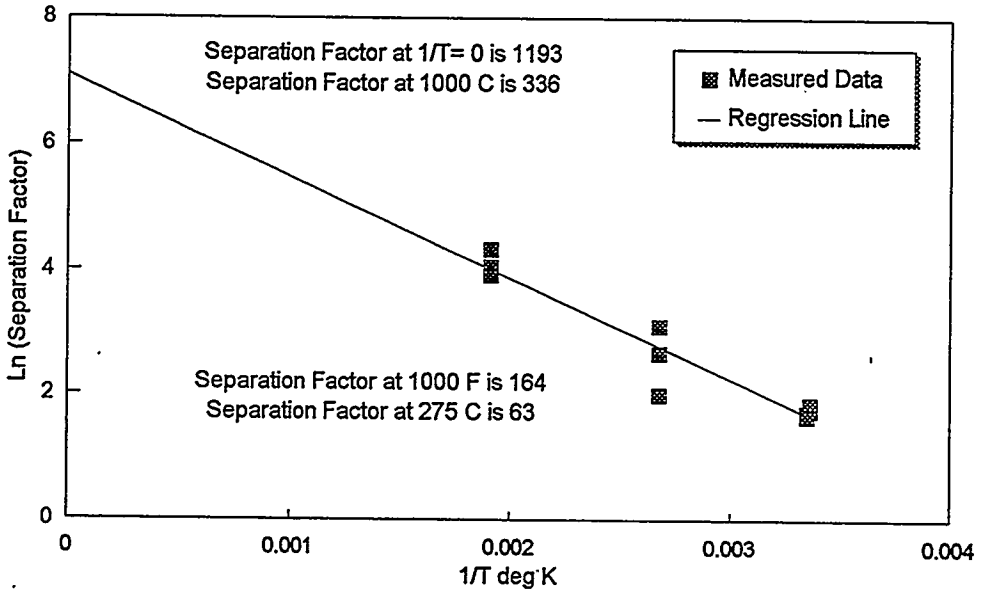

Fig. 3. He/CF_4 separation factors measured on alumina membrane having mean pore radius of 0.25 nm.

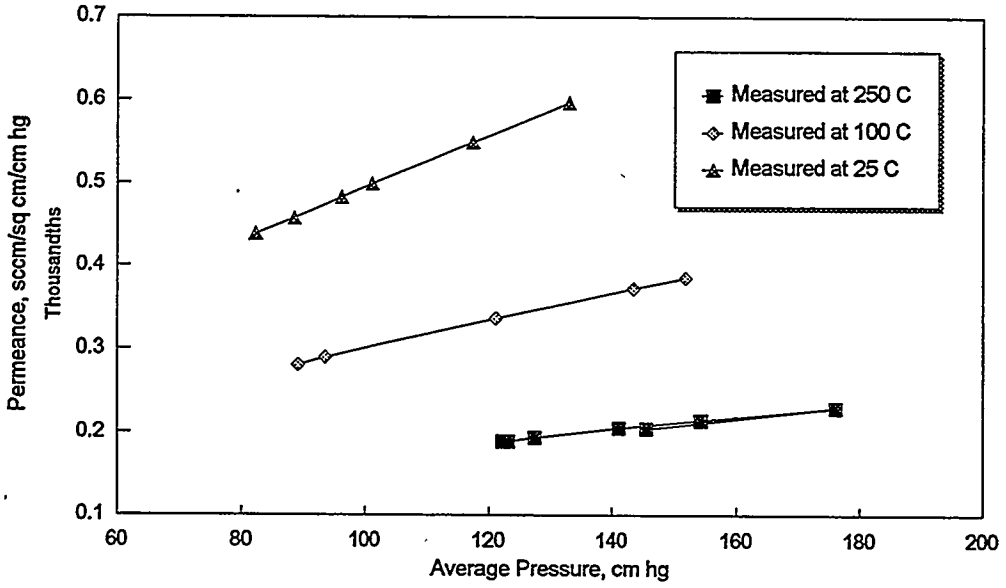

Fig. 4. Carbon tetrafluoride flow data measured at three temperatures through alumina membrane having mean pore radius of 0.25 nm.

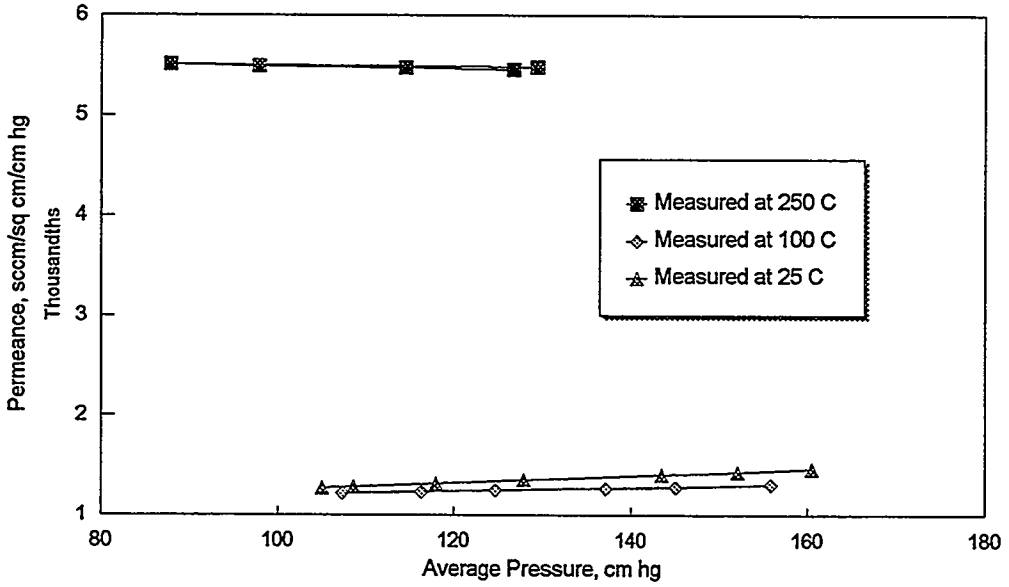

Fig. 5. Helium flow data measured at three temperatures through alumina membrane having mean pore radius of 0.25 nm.

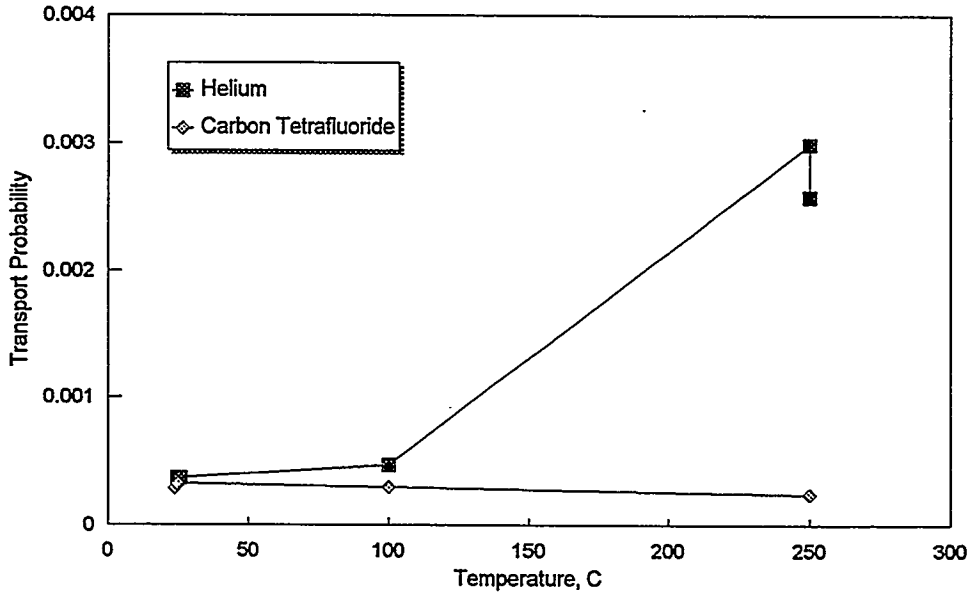

Fig. 6. Zero pressure transport probability measured at three temperatures on alumina membrane having mean pore radius of 0.25 nm.

hydrogen separation is a primary goal of this task, the test system has been upgraded to permit hydrogen to be used as an additional test gas. Several modifications of equipment and procedures were made to assure safe operation with hydrogen at elevated temperatures.

During initial operations with hydrogen in the test system, it was found that the hydrogen test gas contained a high concentration of moisture. A moisture analyzer (with sensor designed for use in hydrogen) was used to analyze the test gas. Analyses showed that the water content of the hydrogen exiting the test system was greater than 1,000 ppm, and the water content of the research grade hydrogen fed to the system was about 85 ppm. These surprisingly high water contents were of concern because water in the test gas can adsorb on the walls of the small pores and affect the flow data, and the magnitude of such effects would differ with temperature.

Several improvements were made to the test system to minimize the water content of the hydrogen. These improvements included the replacement of some copper tubing in the system with stainless steel since hydrogen can react with copper oxide to produce water vapor, particularly at elevated temperatures. In addition, a molecular sieve dryer was installed in the feed gas stream to dry the hydrogen entering the test system. Other minor modifications were made to minimize opportunities for ambient moisture to enter the system. These improvements reduced the water content of the hydrogen test gas by nearly two orders of magnitude. For example, moisture analyses indicated that the water content of hydrogen entering the test system was being limited to a satisfactory level of approximately 1 ppm. Subsequent flow measurements made over a range of temperatures have shown excellent results with hydrogen. Hydrogen flow data measured on a recent membrane are discussed below and compared to helium flow data.

Hydrogen Flow Data on 0.75 nm Mean Pore Radius Membrane

An alumina membrane, having a mean pore radius of 0.75 nm, was tested recently in the high temperature flow test system at several temperatures up to 275 °C using helium, carbon tetrafluoride, and hydrogen as test gases. These data were the first measured with hydrogen after implementing several improvements (described above) to minimize the water content of the hydrogen test gas. From the flow data, separation factors were determined for He/CF_4 and for H_2/CF_4 at each of the

temperatures and are plotted in Fig. 7. The separation factors for H_2/CF_4 were higher than values for He/CF_4 at each of the five temperatures. The extrapolated high temperature separation factor for H_2/CF_4 was 10.5 compared to 8.3 for He/CF_4. The hard sphere model was used to calculate the membrane pore size from these high temperature separation factors. The membrane mean pore radius calculated from the H_2/CF_4 data was 0.75 nm, and the value calculated from the He/CF_4 data was 0.74 nm. The excellent agreement of these results supports the hard sphere diffusion model and indicates that the hydrogen flow data are of high quality. Similar measurements with hydrogen will be made using membranes having smaller pores.

Separation factors for He/CF_4 and for H_2/CF_4 at the high temperature limit can be calculated from the hard sphere model. These model calculations are plotted in Fig. 8 as a function of the membrane pore size. The calculations indicate that the H_2/CF_4 separation factors should be moderately higher than the He/CF_4 separation factors for pore radii down to about 0.3 nm. For pore radii of 0.3 nm and smaller, the He/CF_4 separation factors should be higher.

REFERENCES

1. D. E. Fain and G. E. Roettger, "Hydrogen Production Using Inorganic Membranes" in Proceedings of the Eighth Annual Conference on Fossil Energy Materials, Oak Ridge, Tennessee, May 10-12, 1994, p. 51-61.

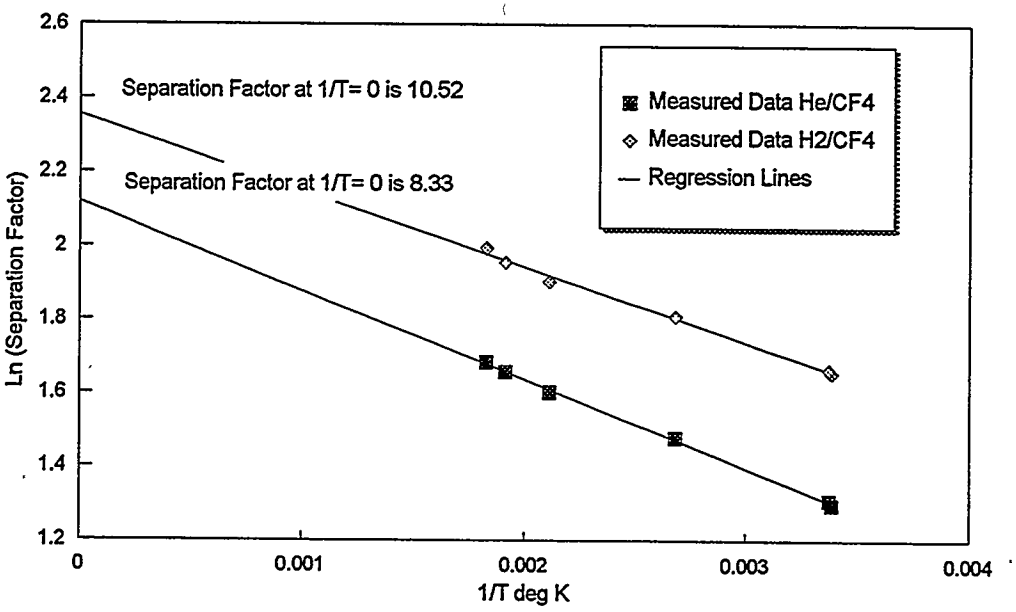

Fig. 7. Separation factors for He/CF_4 and H_2/CF_4 measured on alumina membrane having mean pore radius of 7.5Å.

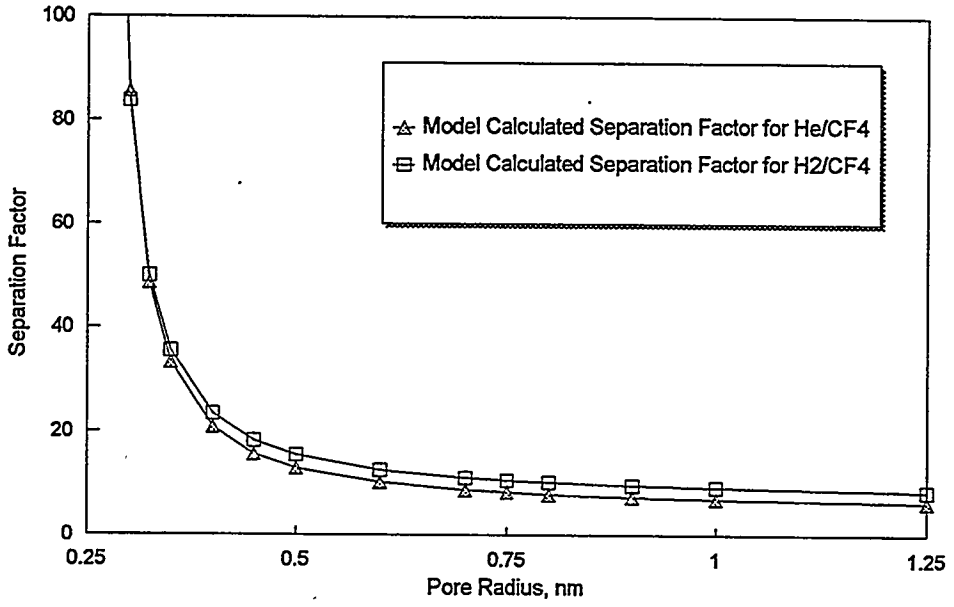

Fig. 8. Separation factors calculated from transport model for He/CF_4 and H_2/CF_4 at high temperature limit.

MIXED OXYGEN ION/ELECTRON-CONDUCTING CERAMICS FOR OXYGEN SEPARATION

J.W. Stevenson, B.L. Armstrong, T.R. Armstrong,
J.L. Bates, L.R. Pederson, and W.J. Weber

Pacific Northwest Laboratory†
P.O. Box 999
Richland, WA 99352

ABSTRACT

Solid mixed-conducting electrolytes in the series $La_{1-x}A_xCo_{1-y}Fe_yO_{3-\delta}$ (A=Sr,Ca,Ba) are potentially useful as passive membranes to separate high purity oxygen from air and as cathodes in fuel cells. All of the compositions studied exhibited very high electrical conductivities. At lower temperatures, conductivities increased with increasing temperature, characterized by activation energies of 0.05 to 0.16 eV that are consistent with a small polaron (localized electronic carrier) conduction mechanism. At higher temperatures, electronic conductivities tended to decrease with increasing temperature, which is attributed to decreased electronic carrier populations associated with lattice oxygen loss. Oxygen ion conductivities were higher than that of yttria stabilized zirconia and increased with the cobalt content and also increased with the extent of divalent A-site substitution. Thermogravimetric studies were conducted to establish the extent of oxygen vacancy formation as a function of temperature, oxygen partial pressure, and composition. These vacancy populations strongly depend on the extent of A-site substitution. Passive oxygen permeation rates were established for each of the compositions as a function of temperature and oxygen partial pressure gradient. For 2.5 mm thick membranes in an oxygen vs nitrogen partial pressure gradient, oxygen fluxes at 900°C ranged from approximately 0.3 sccm/cm^2 for compositions high in iron and with low amounts of strontium A-site substitution to approximately 0.8 sccm/cm^2 for compositions high in cobalt and strontium. A-site substitution with calcium instead of strontium resulted in substantially lower fluxes.

INTRODUCTION

Perovskite compositions in the $(La,Sr)(Co,Fe)O_{3-\delta}$ system have been studied as candidate materials for applications such as solid oxide fuel cell cathodes, oxygen separation membranes, and membrane reactors.[1-10] At elevated temperatures, these compositions exhibit substantial mixed (anionic and electronic) conductivity. The oxygen

† Operated by Battelle Memorial Institute for the US Department of Energy under contract DE-AC06-76RLO 1830

anion conductivity in these materials can be quite large relative to other oxygen conductors, such as yttria-stabilized zirconia (YSZ). The mixed conducting behavior results in a spontaneous flux of oxygen through dense sintered materials in an oxygen partial pressure ($P(O_2)$) gradient. Under these conditions, gaseous oxygen on the high $P(O_2)$ side of the material is reduced to anionic oxygen at the surface, transported ionically through the material to the low $P(O_2)$ side, and re-oxidized to O_2. The ionic current due to the flux of oxygen ions is offset internally by an electronic current, eliminating the need for electrodes and external circuitry.

Teraoka et al[1-3] investigated several $(La,Sr)(Co,Fe)O_{3-\delta}$ compositions using oxygen permeation and four-probe dc techniques. At 800°C, ionic conductivities were on the order of 0.01-1 S/cm, while electronic conductivities exceeded 100 S/cm. The ionic conductivity increased sharply with increasing Sr content and decreased slightly with increasing Fe content. The increasing ionic conductivity with increasing Sr content was attributed to an increase in the oxygen vacancy concentration as trivalent La cations were replaced by divalent (acceptor) Sr cations. While compositions highest in Sr and Co tend to offer the highest oxygen fluxes, other factors must also be considered. For example, $SrCo_{0.8}Fe_{0.2}O_{3-\delta}$ provides very high oxygen permeability but exhibits very limited chemical and structural stability in reduced $P(O_2)$ environments.[4] Kruidhof et al[7] observed that, at lower temperatures (e.g., 750°C), the oxygen flux through several compositions high in Sr and/or Co (e.g., $La_{0.6}Sr_{0.4}CoO_{3-\delta}$ and $SrCo_{0.8}Fe_{0.2}O_{3-\delta}$) decreased substantially with time. This degradation in behavior was attributed to an order-disorder transition which caused the oxygen vacancies to become immobile below a composition-dependent transition temperature. The purpose of the present study is to increase the understanding of the synthesis and electrochemical properties of materials within the $La_{1-x}(Sr,Ca,Ba)_xCo_{1-y}Fe_yO_{3-\delta}$ system, in order to assist their successful utilization in electrode and oxygen membrane applications.

DISCUSSION OF CURRENT ACTIVITIES

A simple code is used to refer to the compositions under study. Compositions in the system $La_{1-x}Sr_xCo_{1-y}Fe_yO_{3-\delta}$ are designated by LSCF followed by numerals indicating the relative proportions of each cation. For example, $La_{0.6}Sr_{0.4}Co_{.2}Fe_{0.8}O_{3-\delta}$

is designated LSCF-6428, $La_{0.2}Sr_{0.8}Co_{.8}Fe_{0.2}O_{3-\delta}$ is designated LSCF-2882. $La_{1-x}Ba_xCo_{1-y}Fe_yO_{3-\delta}$ compositions and $La_{1-x}Ca_xCo_{1-y}Fe_yO_{3-\delta}$ compositions are designated by LBCF and LCCF, respectively. The required compositions were prepared using the glycine-nitrate combustion synthesis technique.[11] The LSCF compositions were essentially single phase perovskites after calcination at 850°C, while the LCCF and LBCF compositions tended to require higher temperature treatment before yielding a high proportion (>95 wt.%) of the desired perovskite phase.

Thermogravimetric analysis was performed on calcined powder specimens using a heating rate of 5°C/min and a cooling rate of 2°C/min. The TGA measurements were performed in several different atmospheres (air; 10,000 ppm O_2 in Ar; 1,000 ppm O_2 in Ar; 100 ppm O_2 in Ar). TGA results for the LSCF compositions when heated and cooled in air are shown in Figure 1. Substantial reversible weight loss was observed at elevated temperatures. This weight loss was due to a partial loss of lattice oxygen, so that the oxygen deficiency, δ, increased with increasing temperature. The temperature at which oxygen loss began to occur decreased as the Sr content increased. The magnitude of the oxygen loss increased with increasing Sr content. This behavior is consistent with previously reported results for two of these compositions (LSCF-6428,4628).[5] The effect of ambient $P(O_2)$ on weight loss behavior was examined by performing TGA measurements in various atmospheres. The magnitude of the oxygen loss upon heating increased only slightly as the ambient $P(O_2)$ was reduced. In 10,000 ppm O_2, full re-oxidation was observed in high Co materials upon cooling (as in air), but re-oxidation did not occur in atmospheres of 1,000 and 100 ppm O_2 (Figure 2). Compositions containing less cobalt did not experience full re-oxidation in the 10,000 ppm O_2 environment. For a given Sr content (e.g., $x = 0.6, 0.8$), the degree of re-oxidation during cooling in the 10,000 ppm O_2 atmosphere decreased with increasing substitution of Fe for Co.

The ionic transport number in these compositions is less than 1%, so that bulk electrical conductivities obtained by 4-probe pulsed dc measurements on sintered specimens provided a measure of the electronic conductivities of the materials. Typical sintering temperatures were 1150-1250°C with dwell times of 2-4 hours. Plots of log σT vs. 1000/T (σ is conductivity (in S/cm) and T is absolute temperature) for the LSCF compositions are shown in Figure 3. At lower temperatures, conductivities increased

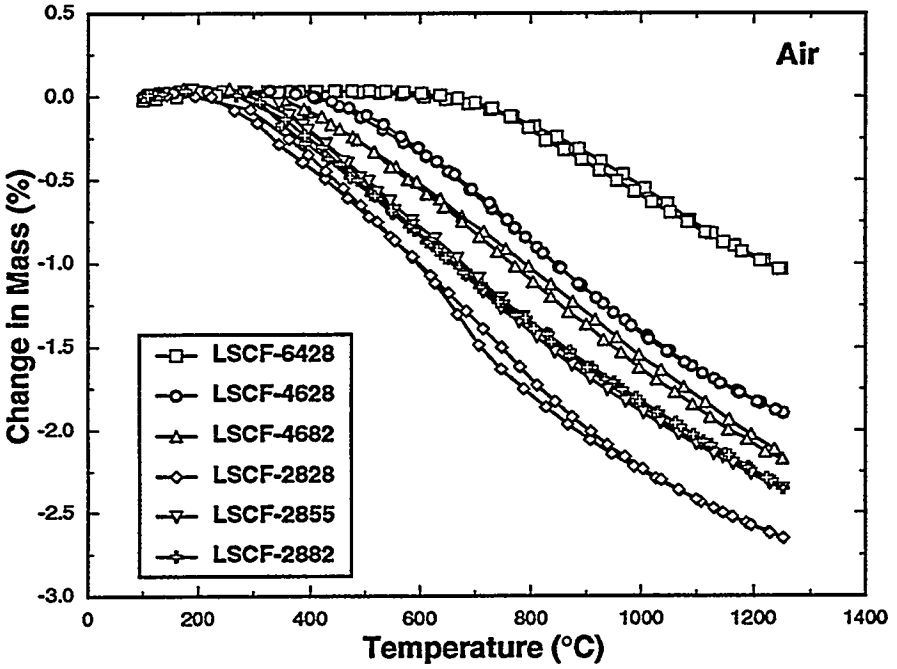

Fig. 1. Thermogravimetric measurements on LSCF compositions in air.

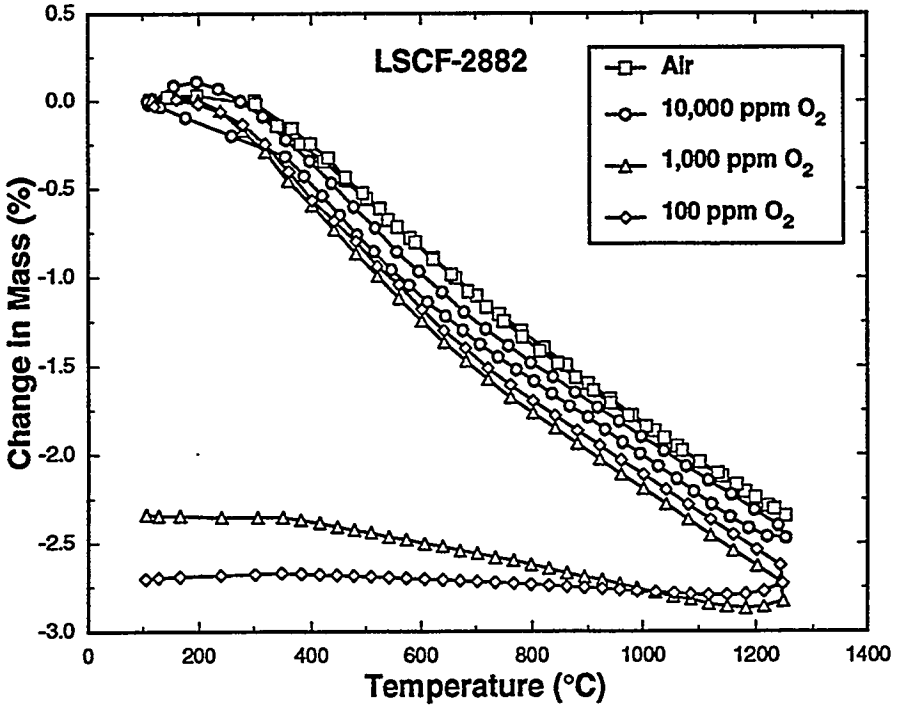

Fig. 2. Thermogravimetric measurements on LSCF-2882 in various atmospheres.

linearly with increasing temperature, with activation energies on the order of 0.05-0.16 eV. This behavior is consistent with a small polaron conduction mechanism (i.e., localized electronic carriers with a thermally activated mobility).[12] At higher temperatures, conductivity was observed to decrease substantially with increasing temperature. This exaggerated decrease at high temperatures is attributed to a decreasing concentration of electronic charge carriers (electron holes, $h^{\bullet}$) as the oxygen content of the material decreases. This process can be represented (Kroger-Vink notation)[13] as:

$$2h^{\bullet} + O_O^{x} \Rightarrow V_O^{\bullet\bullet} + \tfrac{1}{2}O_2 \qquad [1]$$

Thus, two electron holes are eliminated for each oxygen ion leaving the lattice. While this decrease in oxygen stoichiometry with increasing temperature reduces the electronic carrier concentration, it simultaneously increases the concentration of the ionic charge carriers (oxygen vacancies). Plots of σT vs. 1000/T for the LCCF compositions tended to remain relatively linear at temperatures where the LSCF composition exhibited the pronounced decline in conductivity, suggesting that the electronic carrier concentrations in these materials remain essentially constant over a wider temperature range than is the case for the LSCF materials.

Passive oxygen permeation was measured using sintered disc specimens sealed in an alumina test cell with gold gaskets. Air and oxygen were used as source gases with nitrogen as the carrier gas. Oxygen flux was measured as a function of temperature using heating and cooling rates of 0.65°C/min and gas flow rates of 25-30 sccm. Temperature-dependent oxygen permeation rates (in oxygen vs. nitrogen) through sintered specimens of several LSCF, LBCF and LCCF compositions (2.3 - 3.1 mm thick) are shown in Figure 4. For the LSCF compositions, increased Sr content resulted in a substantial increase in flux. This was consistent with the TGA results which showed that the degree of oxygen deficiency increased with increasing Sr content. The increase in oxygen flux with increasing temperature can thus be attributed to two factors: increasing mobility of the lattice oxygen ions, and increasing concentration of lattice oxygen vacancies. Fluxes for the LCCF compositions were significantly lower than for the LSCF compositions.

Ionic conductivities were calculated from the flux rates using the relation:[14]

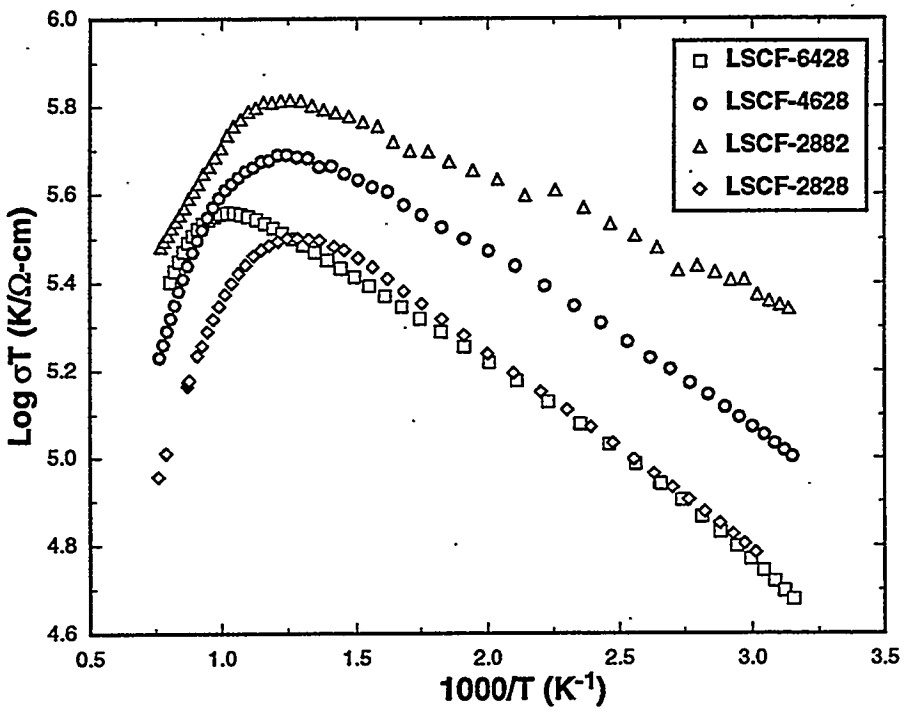

Fig. 3. 4-probe dc conductivity data for the indicated LSCF compositions.

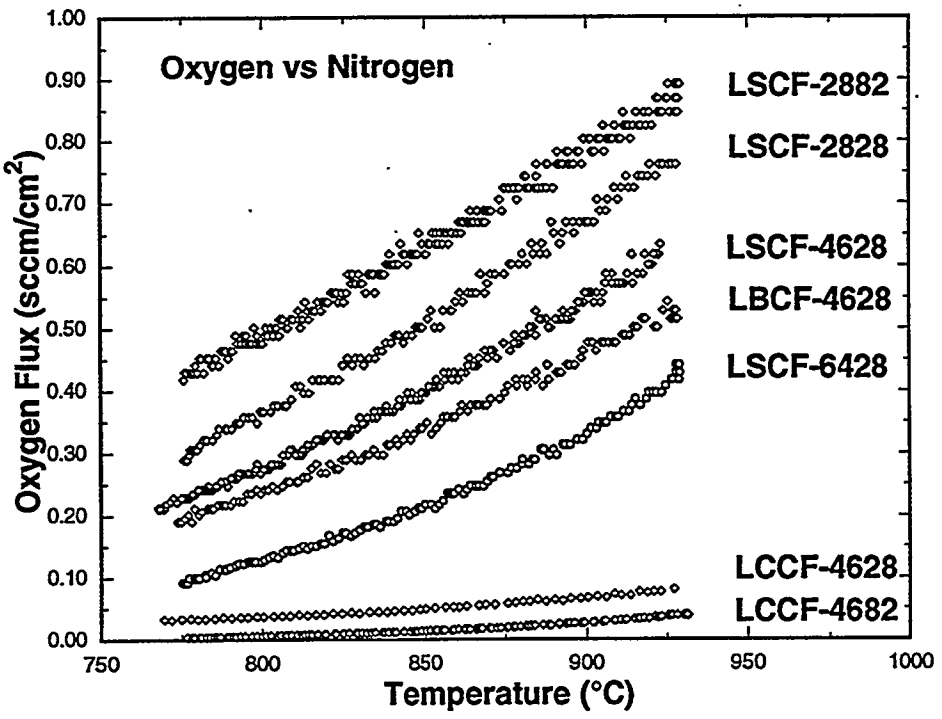

Fig. 4. Oxygen permeation as a function of temperature for the indicated compositions.

$$\sigma_i = \frac{4 F J t}{R T \ln\left[P(O_2^I)/P(O_2^{II})\right]} \qquad [2]$$

where F is Faraday's constant, J is flux (in A/cm2), t is specimen thickness, R is the gas constant, T is absolute temperature, and $P(O_2^I)$ and $P(O_2^{II})$ are the oxygen partial pressures on each side of the specimen. The calculated ionic conductivities at 900°C are shown in Table I. The LSCF compositions exhibited significantly higher conductivities than YSZ (also shown in Table I). These values are similar to conductivities obtained with a 4-probe dc technique by Teraoka et al.[2] Ionic transport numbers were calculated by dividing the ionic conductivity by the total conductivity.

Table I. Ionic and Electronic Conductivities at 900°C

Composition	Ionic Conductivity (S/cm)	Electronic Conductivity (S/cm)	Ionic Transport Number
LSCF-6428	0.23	252	9.1×10^{-4}
LSCF-4628	0.40	219	1.8×10^{-3}
LSCF-2828	0.62	120	5.2×10^{-3}
LSCF-2882	0.87	310	2.8×10^{-3}
LCCF-4628	0.03	52	5.8×10^{-4}
LCCF-4682	0.01	296	3.4×10^{-5}
YSZ	0.10	--	1

Aging effects on oxygen flux behavior are being studied through long term permeation measurements. Kruidhof et al[7] reported that, for some compositions in the LSCF system, substantial degradation of flux occurred at temperatures below a composition-dependent order-disorder transition temperature as the oxygen vacancies within the structure became ordered and, therefore, immobile. Figure 5 shows their data

for $La_{0.6}Sr_{0.4}CoO_{3-\delta}$ at 750°C. In the present study, flux through a different LSCF composition (LSCF-2882) was measured at 775°C (Figure 5). Only a slight decrease (approx. 4%) in flux was observed after operation for 340 hours. This behavior indicates that LSCF compositions remain viable candidate materials for oxygen permeation applications at intermediate temperatures (e.g., 750-800°C).

The removal of lattice oxygen from the perovskite structure results in a volumetric expansion in the material. This phenonenon is being investigated using controlled atmosphere dilatometry on sintered bars to measure linear expansion as a function of ambient $P(O_2)$. Results for LSCF-6428 at three temperatures are shown in Figure 6. It is apparent that even mildly reducing conditions altered the oxygen stoichiometry sufficiently to cause significant linear expansion. The magnitude of the expansion was similar to that observed in lanthanum chromite materials, but the expansion occurred in much higher oxygen partial pressures due to the lower enthalpy of oxygen vacancy formation in cobaltite-ferrite perovskites.

Ease of fabrication is an important factor in the successful utilization of these materials; a tubular geometry is desirable for oxygen separation applications. Open end tubes have been fabricated from LSCF-6428 powders using rubber bag tooling and 22 ksi cold isostatic pressure. Sintered densities (after heat treatment at 1250°C for 4 hours in air) were 95% of theoretical. Final inner and outer diameters were approximately 0.28 and 0.40", respectively.

REFERENCES

1. Y. Teraoka, H. Zhang, S. Furukawa, and N. Yamazoe, "Oxygen Permeation through Perovskite-Type Oxides," Chemistry Letters, 1743-1746 (1985).

2. Y. Teraoka, H. Zhang, K. Okamoto, and N. Yamazoe, "Mixed Ionic-Electronic Conductivity of $La_{1-x}Sr_xCo_{1-y}Fe_yO_{3-\delta}$ Perovskite-Type Oxides," Mat. Res. Bull., **23**, 51-58 (1988).

3. Y. Teraoka, T. Nobunaga, K. Okamoto, N. Miura, and N. Yamazoe, "Influence of Constituent Metal Cations in Substituted $LaCoO_3$ on Mixed Conductivity and Oxygen Permeability," Solid State Ionics, **48**, 207-212 (1991).

4. U. Balachandran, S. Morissette, J. Picciolo, J. Dusek, and R. Peoppel,"Fabrication of Ceramic Membrane Tubes for Direct Conversion of Natural Gas," Proc. International Gas Research Conference, Ed. H. Thompson, Government Institutes, Rockville, MD, pp. 565-573 (1992).

5. L. Tai, M. Nasrallah, and H. Anderson, "$(La_{1-x}Sr_x)(Co_{1-y}Fe_y)O_3$, A Potential Cathode for Intermediate Temperature SOFC Applications," Proc. 3rd Int. Symp. on SOFC, Electrochem. Soc., Vol. 93-4, 241-251 (1993).

6. H. Anderson, C. Chen, L. Tai, and M. Nasrallah, "Electrical Conductivity and Defect Structure of (La,Sr)(Co,Fe)O_3," Proc. 2nd Int. Symp on Ionic and Mixed Conducting Ceramics, Ed. T. Ramanarayanan, W. Worrell, and H. Tuller, Electrochem. Soc., Vol. 94-12, 376-387 (1994).

7. H. Kruidhof, H. Bouwmeester, R. v. Doorn, and A. Burggraaf, "Influence of Order-Disorder Transitions on Oxygen Permeability through Selected Nonstoichiometric Perovskite-Type Oxides," Solid State Ionics, **63-65**, 816-822 (1993).

8. H. Bouwmeester, H. Kruidhof, and A. Burggraaf, "Importance of the Surface Exchange Kinetics as Rate Limiting Step in Oxygen Permeation through Mixed-Conducting Oxides," Solid State Ionics, **72**, 185-194 (1994).

9. U. Balachandran, J. Dusek, S. Sweeney, R. Peoppel, R. Mieville, P. Maiya, M. Kleefisch, S. Pei, T. Kobylinski, C. Udovich, and A. Bose,"Methane to Syngas via Ceramic Membranes," Am. Cer. Soc. Bulletin, **74**, 71-75 (1995).

10. C.C. Chen, M.M. Nasrallah, H.U. Anderson, and M.A. Alim, "Immittance Response of $La_{0.6}Sr_{0.4}Co_{0.2}Fe_{0.8}O_3$," J. Electrochem. Soc., **142**, 491-496 (1995).

11. L.A. Chick, L.R. Pederson, G.D. Maupin, J.L. Bates, L.E. Thomas, and G.J. Exarhos, "Glycine-Nitrate Combustion Synthesis of Oxide Ceramic Powders," Materials Letters, **10**, 6-12 (1990).

12. D. P. Karim and A.T. Aldred, "Localized Level Hopping Transport in La(Sr)CrO_3," Phys. Rev. B, **20**, 2255-2263 (1979).

13. F.A. Kroger, The Chemistry of Imperfect Crystals, North-Holland, Amsterdam (1964).

14. M. Liu and A. Joshi, "Characterization of Mixed Ionic-Electronic Conductors," Proc. First Int. Symp. Ionic and Mixed Conducting Ceramics, Eds. T.A. Ramanarayanan and H.L. Tuller, Electrochem. Soc, Proc. Vol. 91-12, 231-246 (1991).

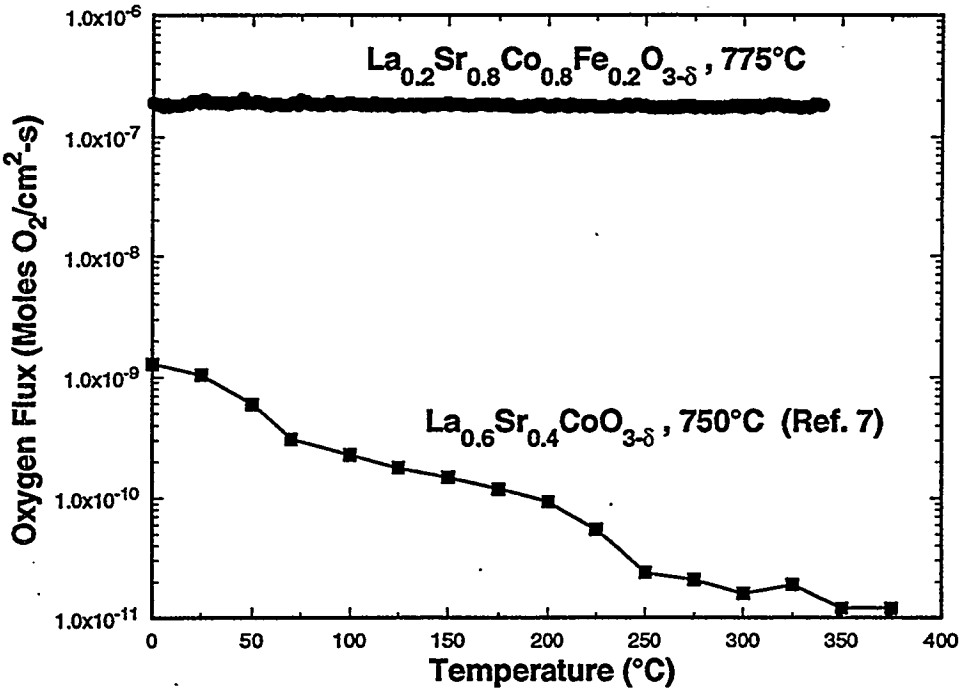

Fig. 5. Oxygen permeation as a function of time for the indicated compositions.

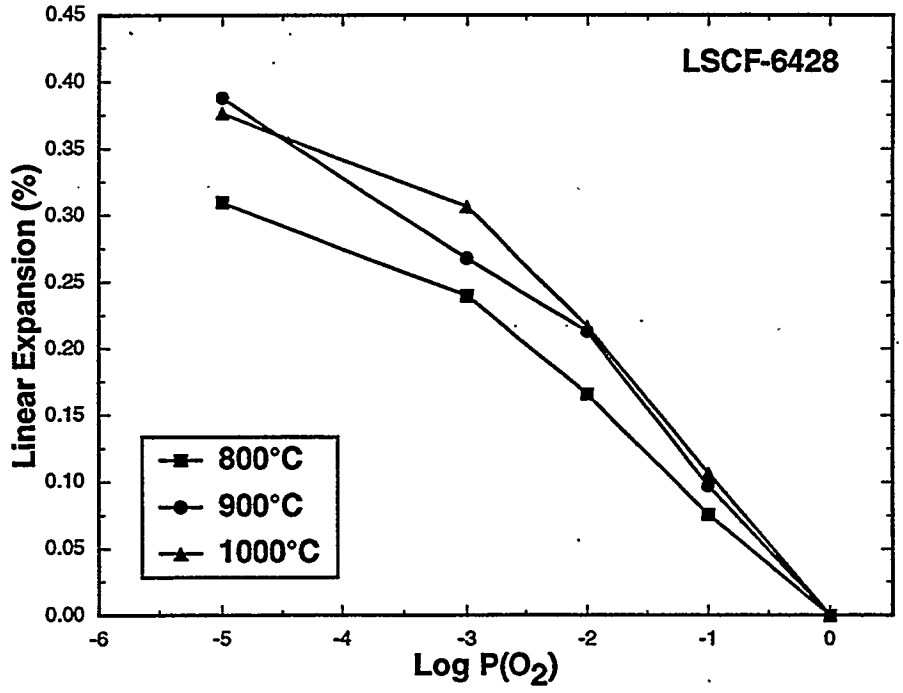

Fig. 6. Linear expansion of LSCF-6428 as a function of ambient $P(O_2)$.

PROTON CONDUCTING CERATE CERAMICS

G. W. Coffey, L. R. Pederson, T. R. Armstrong, J. L. Bates and W. J. Weber

Pacific Northwest Laboratory[1]
P. O. Box 999
Richland, Washington 99352 USA

ABSTRACT

Cerate perovskites of the general formula $AM_xCe_{1-x}O_{3-\delta}$, where A = Sr or Ba and where M = Gd, Nd, Y, Yb or other rare earth dopant, are known to conduct a protonic current. Such materials may be useful as the electrolyte in a solid oxide fuel cell operating at intermediate temperatures, as an electrochemical hydrogen separation membrane, or as a hydrogen sensor. Conduction mechanisms in these materials were evaluated using dc cyclic voltammetry and mass spectrometry, allowing currents and activation energies for proton, electron, and oxygen ion contributions to the total current to be determined. For $SrYb_{0.05}Ce_{0.95}O_{3-\delta}$, one of the best and most environmentally stable compositions, proton conduction followed two different mechanisms: a low temperature process, characterized by an activation energy of 0.42±0.04 eV, and a high temperature process, characterized by an activation energy of 1.38±0.13 eV. It is believed that the low temperature process is dominated by grain boundary conduction while bulk conduction is responsible for the high temperature process. The activation energy for oxygen ion conduction (0.97±0.10 eV) agrees well with other oxygen conductors, while that for electronic conduction, 0.90±0.09 eV, is affected by a temperature-dependent electron carrier concentration. Evaluated by direct measurement of mass flux through a dense ceramic with an applied dc field, oxygen ions were determined to be the majority charge carrier except at the lowest temperatures, followed by electrons and then protons.

INTRODUCTION

Certain perovskite-type oxides are known to conduct a protonic current through a fully densified structure.[1-3] The best proton-conducting oxides, ytterbium-doped strontium cerate and neodymium-doped barium cerate, have proton conductivities of approximately 0.01 S/cm at 800°C. These compositions are potentially useful as solid electrolytes in solid oxide fuel cells, as hydrogen sensors, as hydrogen pumps, and as steam electrolyzers to produce hydrogen from water.[3, 4]

Because these perovskite-type metal oxides often contain several types of point defects, they support conduction by multiple charge carriers.[2] At low temperatures, proton

---

[1]Operated by Battelle Memorial Institute for the U. S. Department of Energy under Contract DE-AC06-76RLO 1830.

hopping between oxide ions is believed to be the dominant conduction mechanism,[3] whereas electronic and oxygen ion contributions to the overall current become important at high temperatures.[5] Conduction mechanisms are not well established in these materials, partially the result of a practical difficulty in achieving electrolytes without interconnected porosity. For example, it has been proposed that hydrogen is carried by negatively charged hydroxyl ions rather than by protons.[6] A good understanding of the relative importance of each charge carrier is essential if these materials are to be utilized in a practical device.

EXPERIMENTAL PROCEDURES

Homogeneous $AM_xCe_{1-x}O_{3-\delta}$ powders, where A = Sr or Ba and where M = Gd, Nd, or Yb, were prepared by calcination of combustion-derived precursors.[7,8] This material was then calcined at temperatures <950°C for several hours and uniaxially and isostatically pressed into discs and bars. Most compositions sintered to greater than 98% of full density at 1500°C for 12 hours.

Discs of $AM_xCe_{1-x}O_{3-\delta}$, 2 to 3 mm thick and approximately 25 mm in diameter, were sealed in an alumina cell with gold gaskets. Porous platinum electrodes were previously applied to each surface. The seals were verified to be helium leak-tight using quadrupole mass spectrometry. Pt-Pt,10%Rh thermocouples provided local temperature measurements on each side of the samples as well as electrical leads for cyclic voltammetry and emf measurements. Cyclic voltammetry measurements were performed on these concentration cells, with either hydrogen, oxygen, or nitrogen gas flows on the source side of the cell and either nitrogen or oxygen flows on the collection side of the electrolyte. Gas fluxes (hydrogen, oxygen, or water) were monitored by mass spectrometry, using a stainless steel capillary tube to sample the gas stream. Oxygen fluxes were additionally determined using zirconia oxygen sensors.

RESULTS AND DISCUSSION

Cyclic voltammetry measurements performed with different choices of gas streams on each side of cerate perovskite sample in an electrochemical concentration cell allowed an estimate of currents carried by electrons, protons, and oxygen ions to be made over a range of temperatures. Simultaneous mass spectrometry measurements provided an independent

means to determine mass fluxes through the sample as a function of applied voltage, temperature, and environment, in a configuration very similar to that required in a solid oxide fuel cell, electrochemical hydrogen separation membrane, or related device. In general, the agreement between mass fluxes determined by mass spectrometry and those calculated from current/voltage responses was very good.

Electron contributions to conduction in the cerate perovskites were calculated from the slope of current versus voltage responses when nitrogen streams were applied to both sides of the sample. For $SrYb_{0.05}Ce_{0.95}O_{3-\delta}$, linear responses were obtained in the voltage range of ±0.5 volts in at 900°C, as shown in Figure 1. Water electrolysis was apparent outside that voltage range at the highest temperatures, leading to transport of hydrogen or oxygen ions in addition to the electronic current, depending on the sign of the voltage. Concurrent fluxes of hydrogen or oxygen were observed by mass spectrometry. The presence of water is essential for these perovskites to conduct a protonic current. Water will react with oxygen vacancies to create protonic carrier sites; the exact nature of the lattice defect is not well understood.[1-4]

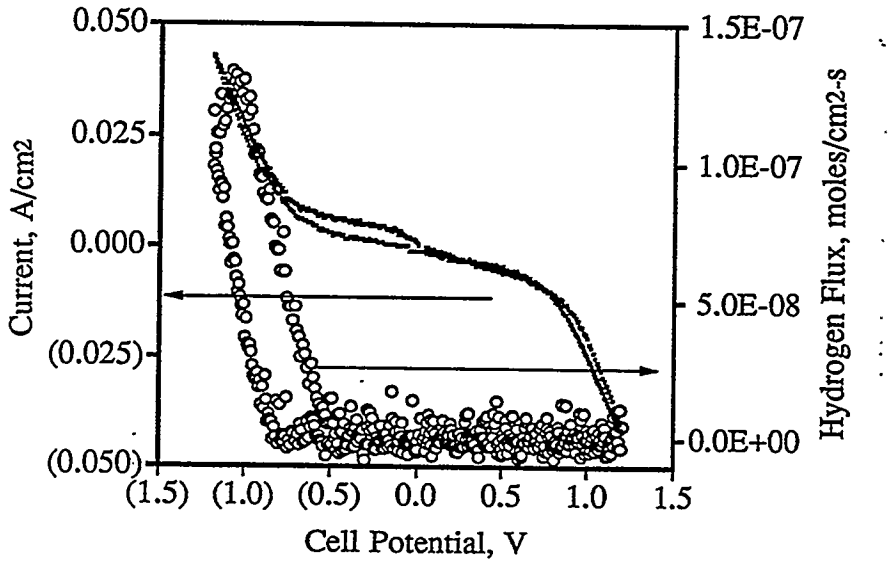

Figure 1. Cyclic voltammogram for $SrYb_{0.05}Ce_{0.95}O_{3-\delta}$ at 900°C for wet nitrogen versus nitrogen. Water electrolysis was apparent for -0.5V>cell potential>0.5V.

Proton currents were determined from current/voltage responses where a stream of 4% hydrogen in argon was applied on one side of the ceramic and a nitrogen stream was applied to the other side. Similarly, oxygen currents were determined using an air stream on one side and nitrogen on the other. Results for 4% hydrogen versus nitrogen and for air versus nitrogen are given in Figures 2 and 3, respectively. Electronic currents were subtracted from the overall current versus voltage curves in both cases. Asymmetric responses were obtained, as expected. Higher currents were found when a negative dc bias (collection side relative to the source side of the electrolyte) was applied with hydrogen on the source side; a positive dc bias gave higher currents with oxygen on the source side. This behavior is as expected for protonic and oxygen ion currents in addition to an electron current. With 4% hydrogen on the source side and air on the opposite side, the cerate supported proton, oxygen ion, and electron currents simultaneously. This arrangement is similar to that used in a solid oxide fuel cell.[10]

Activation energies were calculated for electron, oxygen ion, and proton transport as a function of temperature from cyclic voltammetry and mass spectrometry data. These results are given in Figures 4 and 5 for oxygen ion and proton transport, respectively. The activation energy for electronic transport was found to be 0.90±0.09 eV. From electron hole transport in $BaSm_{0.1}Ce_{0.9}O_{3-\delta}$ reported by Iwahara et al.,[4] an apparent activation energy of 1.1 eV can be calculated, similar to present results. Such higher than expected activation energies for electronic conduction probably reflect the creation of additional carriers (Ce^{4+}/Ce^{3+} equilibrium) with increased temperature as well as increased mobility. The activation energy for oxygen ion conduction was found to be 0.97±0.10 eV, in good agreement with results for cerates[4] and other oxygen conductors such as yttria-stabilized zirconia.[11] Currents calculated from oxygen fluxes determined by mass spectrometry were in good agreement with those determined from current/voltage curves. Activation energies for oxygen ion conduction determined from the two methods likewise were in good agreement.

Results for hydrogen conduction (see Figure 5) show two different regimes. At low temperatures (300 to 600°C), an activation energy of 0.42±0.04 eV was obtained from current/voltage responses, whereas at higher temperatures (600 to 900°C), an activation energy of 1.38±0.13 eV was found. Hydrogen fluxes determined by mass spectrometry were in fairly good agreement with those calculated from current/voltage curves. It is believed that proton currents at low temperatures are dominated by grain boundaries, while

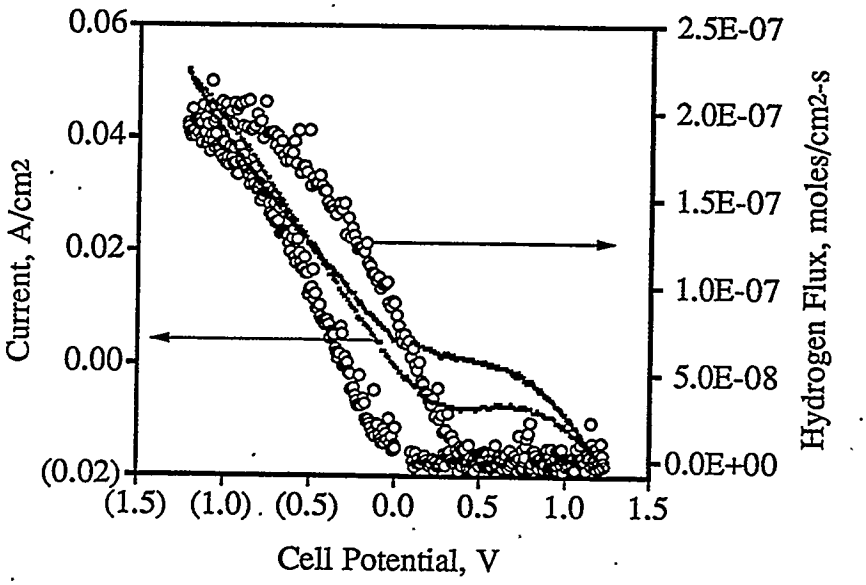

Figure 2. Cyclic voltammogram for $SrYb_{0.05}Ce_{0.95}O_{3-\delta}$ at 900°C for 4% hydrogen in argon versus nitrogen. Cathodic potentials led to hydrogen transport through the electrolyte.

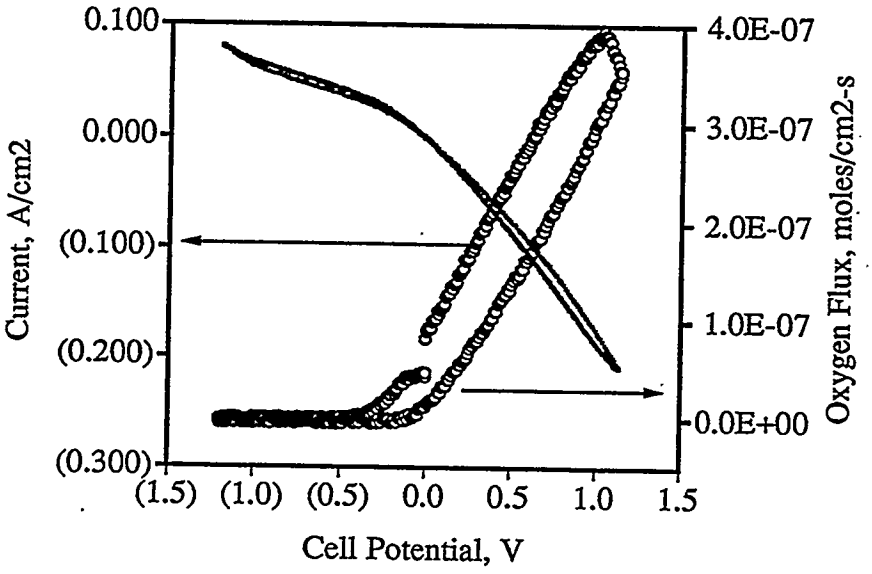

Figure 3. Cyclic voltammogram for $SrYb_{0.05}Ce_{0.95}O_{3-\delta}$ at 900°C for wet air versus nitrogen. Anodic potentials led to oxygen transport throught the electrolyte.

those at high temperatures are due to bulk conduction. A grain boundary component in proton currents in barium cerate compositions has been previously reported, attributed to a separate grain boundary phase.[12] In the strontium ytterbium cerates, however, no microscopic evidence for a grain boundary phase or segregation could be found.

From the ion and electron currents determined by cyclic voltammetry and mass transport (Figures 4 and 5), transference numbers for each charge-conducting species can be determined, as shown in Figure 6 for $SrYb_{0.05}Ce_{0.95}O_{3-\delta}$. The protonic contribution was the least important of the three, falling at first with increasing temperature to approximately 500°C (grain boundary contribution) and then rising with temperature (bulk contribution). For temperatures at which a practical electrochemical device could be operated, oxygen ions clearly were the most important charge carrier.

The kinetics of water uptake by $SrYb_{0.05}Ce_{0.95}O_{3-\delta}$ was evaluated by thermogravimetry and found to follow a two-stage process. The first, rapid uptake stage is attributed to hydration of the grain boundaries and near surface regions, whereas the much slower, long-term hydration is attributed to hydration of the bulk grains. Below approximately 700°C, times required to reach full hydration any of the bulk cerates were prohibitively long (>days). In previous studies of water uptake by similar compositions, complete hydration of the bulk was reported to be reached within a few hours even for temperatures below 600°C.[9] To fully remove water from the sample following each hydration experiment in the present study, it was necessary to heat to 1300°C in dry, flowing air for at least 24 hours. Activation energies were determined for both stages of water uptake by the perovskite. For the early stage of water uptake, which is attributed to grain boundary and near surface hydration, an activation energy of 0.39±0.09 eV was found. The second stage of hydration yielded a much higher activation energy: 2.8±0.4 eV, which is attributed to bulk hydration. Clearly, two substantially different processes contribute to the overall hydration of this material.

Environmental stability, in particular the reaction of strontium or barium cerates to form strontium or barium carbonate, may ultimately limit the applicability of these unique materials in fuel cells and other such devices. Barium cerates are particularly susceptible to decomposition to barium carbonate plus metal oxides and hydroxides. Sintered barium cerate samples will revert to a powder when exposed to the ambient atmosphere for a few days; strontium cerates, however, appear stable. From thermodynamic considerations,

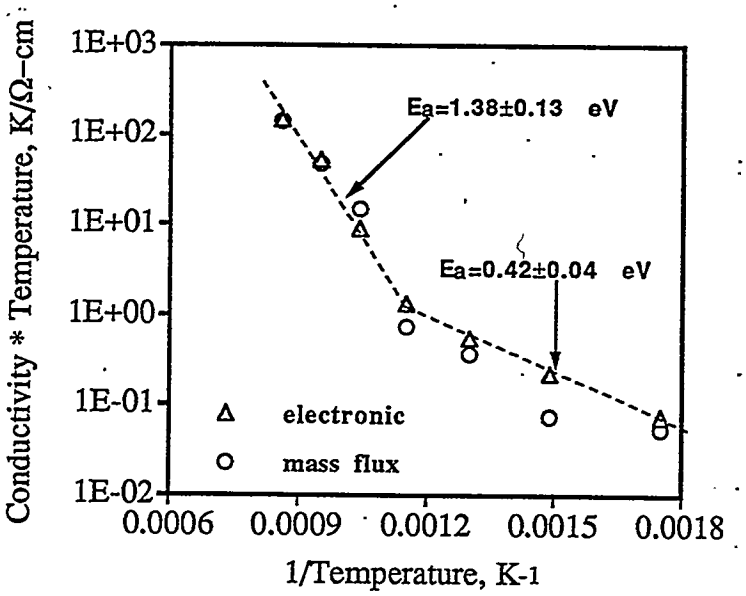

Figure 4. Proton conductivity-temperature product versus reciprocal temperature for $SrYb_{0.05}Ce_{0.95}O_{3-\delta}$. Low temperature conduction is dominated by grain boundary processes, while bulk processes are responsible for high temperature proton conduction.

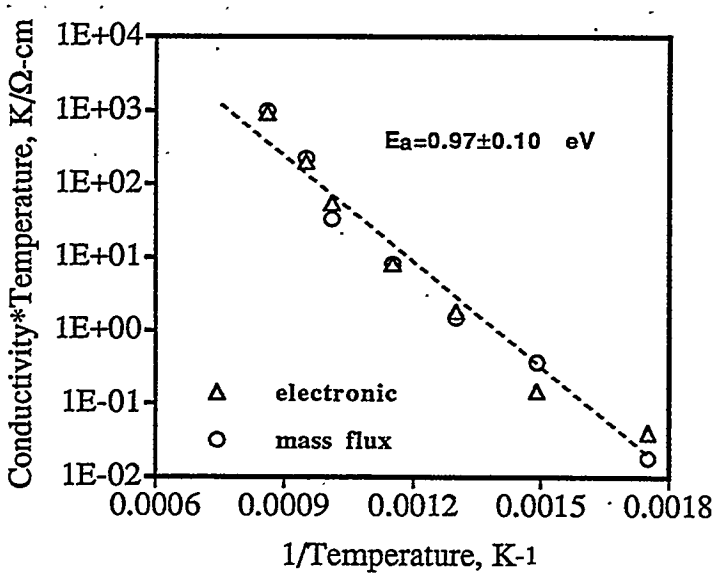

Figure 5. Oxygen ion conductivity-temperature product versus reciprocal temperature for $SrYb_{0.05}Ce_{0.95}O_{3-\delta}$.

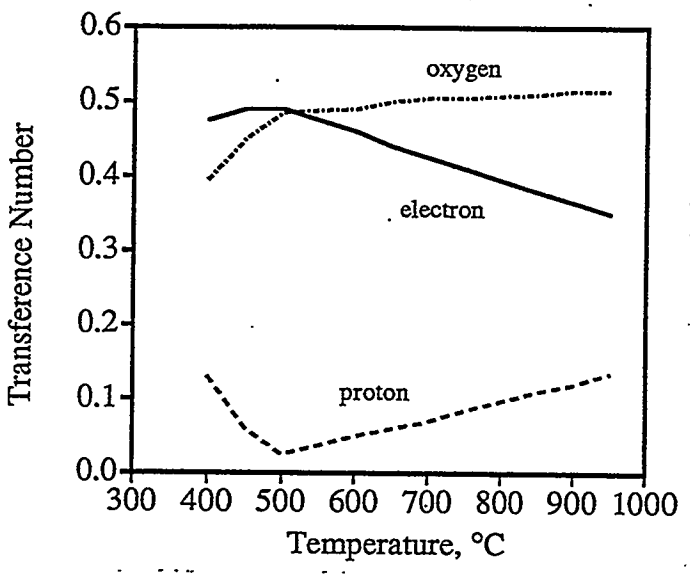

Figure 6. Transference numbers for protons, oxygen ions, and electrons in $SrYb_{0.05}Ce_{0.95}O_{3-\delta}$ as a function of temperature.

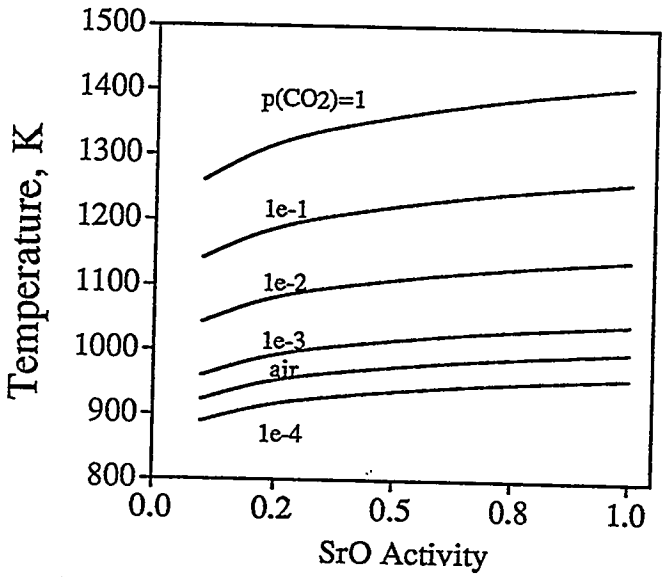

Figure 7. Calculated maximum temperature of stability of strontium carbonate as a function of SrO activity for several carbon dioxide partial pressures.

alkaline earth carbonates are expected to be stable to relatively high temperatures, as shown for strontium carbonate in Figure 6 for various carbon dioxide partial pressures. Assuming a(SrO)=0.5 (equal to its mole fraction in the cerate), strontium carbonate formation is expected in pure carbon dioxide up to approximately 1050°C. In air, strontium carbonate should decompose above ≈700°C. Barium carbonate is more stable than strontium carbonate, and should persist to even higher temperatures. Although predicted from thermodynamic data, carbonate formation in a pure carbon dioxide environment has not been observed to date above 800°C for either the strontium or barium cerates.

SUMMARY

Contributions to electrical conductivity in substituted cerate perovskites have been evaluated by cyclic voltammetry and mass transport, under conditions similar to those required for a practical electrochemical device. Measurements were facilitated by the development of synthesis and sintering methodologies to prepare fully dense ceramics, free of interconnected porosity. Protonic conduction followed two different mechanisms: a low temperature, grain boundary process having a small activation energy, and a high temperature, bulk process having a relatively high activation energy. Oxygen was the primary charge carrier over temperatures at which a practical electrochemical device could operate. Conductivities in the cerate perovskites were sufficiently high to be useful as the electrolyte in a fuel cell operating at intermediate temperatures, despite the fact that an electronic contribution to the overall current was apparent, which would lessen the efficiency of the fuel cell.

ACKNOWLEDGEMENTS

The authors gratefully acknowledge R. W. Stephens for technical assistance in performing transport measurements, D. E. McCready for performing x-ray diffraction analyses, N. T. Saenz for preparing specimens for microscopy, and J. E. Coleman for SEM analyses. Research was supported by the Advanced Research and Technology Development Materials Program, Office of Fossil Energy, U. S. Department of Energy.

REFERENCES

1. T. Norby, Solid State Ionics 40/41, p. 857 (1990).

2. N. Bonanos, Solid State Ionics 53-56, p. 967 (1992).

3. H. Iwahara, Solid State Ionics 28-30, p. 573 (1988).

4. H. Iwahara, T. Yajima, T. Hibino, and H. Ushida, J. Electrochem. Soc. 140 [6], p. 1687 (1993).

5. T. Yajima, H. Iwahara, and H. Uchida, Solid State Ionics 47, p. 117 (1991).

6. R. L. Cook and A. F. Sammells, Solid State Ionics 45, p. 311 (1991).

7. L. A. Chick, L. R. Pederson, G. D. Maupin, J. L. Bates, L. E. Thomas, and G. J. Exarhos, Materials Letters 10, p. 6 (1990).

8. T. R. Armstrong, J. L. Bates, G. W. Coffey, J. J. Kingsley, L. R. Pederson, J. W. Stevenson, W. J. Weber, and G. E. Youngblood, Proc. 8th Annual Conf. on Fossil Energy Materials, CONF-9405143, Oak Ridge National Laboratory, Oak Ridge, Tennessee, p. 89 (1994).

9. H. Iwahara, Solid State Ionics 52, p. 99 (1992).

10. H. Iwahara, T. Yajima, T. Hibino, and H. Ushida, J. Electrochem. Soc. 140 [6], p. 1687 (1993).

11. H. L. Tuller, in Ceramic Materials for Electronics, ed. R. C. Buchanon, Marcel Dekker, New York p. 425 (1986).

12. K. D. Kreuer, E. Schonherr, and J. Maier, Proc. 14th Int. Symp. Materials Science, eds. F. W. Poulson, J. J. Bentzen, T. Jacobsen, E. Skou, and M. L. J. Ostergard, Riso National Laboratory, Roskilde, Denmark p. 297 (1993).

SYNTHESIS OF SILICON NITRIDE POWDERS IN PULSED RF PLASMAS

R. J. Buss, S. V. Babu* and P. Ho

Sandia National Laboratories
Albuquerque, NM 87185-0367

ABSTRACT

Nanometer size silicon nitride particles are synthesized using a pulsed radio frequency plasma technique. The plasma is modulated with a square-wave on/off cycle of varying period to control size and morphology and to deduce the growth kinetics. *In situ* laser light scattering and *ex situ* particle analysis are used to study the nucleation and growth. For SiH_4/Ar plasmas which nucleate silicon particles, an extremely rapid initial growth phase is followed by a slower growth rate, approaching the rate of thin film deposition on adjacent flat surfaces. In SiH_4/NH_3 plasmas, silicon nitride particle size can be tightly controlled by adjusting the plasma-on time. The size dispersion of the particles is large and is consistent with a process of continual nucleation during the plasma-on period. Our observed polydispersity differs dramatically from that reported from other laboratories.

INTRODUCTION

It has been recognized for many years that silicon nitride has excellent high temperature structural properties such as high strength and low weight which would make it ideal for many applications such as engine parts. Unfortunately, the low temperature properties of hardness and brittleness make manufacturing processes difficult. It is known that materials formed from nanometer size subunits can exhibit improved macroscopic properties such as enhanced ductility or superplasticity. Also, in order to obtain the optimum properties, it is important to achieve microstructural and chemical homogeneity with minimal defects in a nearly fully dense ceramic. This is facilitated by starting with fine-particle-size powders that have low impurity content.

* Dept. of Chemical Engineering, Clarkson University, Potsdam, New York

Obtaining the ultrafine powders that are needed for exploratory research as well as manufacture has proven to be a problem. A variety of techniques are currently used to produce commercial silicon nitride powders[1]. These include direct nitridation of silicon, carbothermic reduction of silica and gas-phase reaction of $SiCl_4$ and NH_3. Several other gas-phase processes have been reported including the thermal pyrolysis of silane and ammonia[2] and laser pyrolysis of gaseous reactants[3]. Each of these processes has limitations in the morphology, size distribution, and chemical purity of the product.

In 1988, Buss and Ho patented a process[4] for synthesizing ultrafine particles of silicon nitride and other materials in a radio frequency (rf) plasma. The method involves flowing gaseous precursors at low pressure through a glow discharge. Electron-molecule collisions in the plasma result in fragmentation of the starting gases into reactive free radicals which undergo complex gas-phase chemistry leading to particle nucleation. Particles leaving the plasma are collected by filtering the gases pumped from the reactor. The technique is capable of generating gram quantities of silicon nitride powder in a few hours of operation in a laboratory reactor. Properties of the powder were well characterized by a variety of techniques[5].

During the past decade, particle formation and transport in plasmas has become an area of intense interest and activity[6]. It has developed that these particles, occurring in the plasmas used to manufacture microelectronic devices, can result in serious loss of wafer yield. Stimulated by this economic urgency, many laboratories worldwide have begun investigating the mechanisms governing particle nucleation, growth, trapping and agglomeration.

One particularly important achievement was reported by Boufendi and coworkers[7] in France in 1992. They studied formation of silicon particles in a silane/argon plasma by pulsing the plasma on for a short time and collecting the particles for electron microscopy. Remarkably, they found a linear rate of particle growth to the 40 nm size with a very narrow size dispersion. They postulated an initial stage of the plasma in which nucleation occurs, producing a high density of 5 nm size

particles followed by a no-nucleation stage in which these smaller particulates associated into the observed clusters.

We report here experiments aimed at applying this pulsed plasma approach to the synthesis of nano-size silicon nitride powders. Part of the work entails reproducing experiments of the French group with silane/argon to confirm the technique. Some striking differences in particle growth rates and size dispersion are reported. Applying the pulsed plasma technique to the silicon nitride system, we have demonstrated control of average particle size but with persistent size dispersion and agglomeration.

EXPERIMENTAL

A diagram of the apparatus is shown in Fig. 1. The plasma

Figure 1

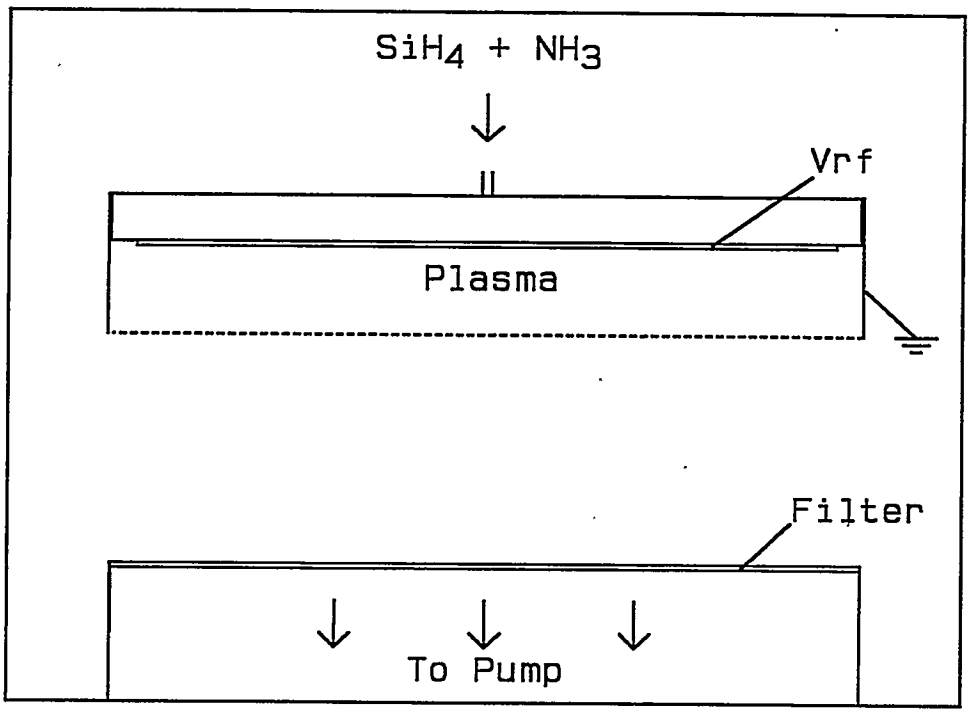

Fig. 1. Diagram of pulsed rf plasma apparatus.

electrode assembly consists of a 15 cm diameter powered electrode, perforated with holes to allow gas flow in a showerhead configuration. The plasma region is enclosed by a grounded aluminum sheet with a grounded high transmission screen across the bottom. The pumping port is located 4 cm beneath the electrode assembly, and is fitted with a single sheet of Whatman #1 filter paper. In order to study the size and morphology of the particles generated, transmission electron microscopy (TEM) was employed *ex situ*. To obtain samples, a TEM sample grid was placed beneath the plasma assembly on the filter paper.

A 10 mWatt helium-neon laser passed through the region beneath the plasma (or through holes in the electrode assembly wall). Laser light scattering from particles was observed by eye as a qualitative characterization of the process.

In a typical experiment, gas flow was first established (eg. 2 sccm SiH_4, 12 sccm NH_3, at 200 mTorr pressure); then the plasma was pulsed with a square wave on/off cycle for 100 periods. The TEM grid was then removed and analyzed. In order to obtain large quantities of powder for bulk analysis, the plasma was pulsed for several hours and the filter with accumulated powder was removed.

RESULTS AND DISCUSSION

Silicon

In a study aimed at duplicating the experimental conditions of Boufendi et al, we investigated the formation of silicon particles in a silane/argon plasma. We find that the growth kinetics differ very markedly from those of the French group. In Fig. 2 is shown the measured size distribution for silicon particles as a function of plasma-on time with the upper and lower solid line giving one standard deviation. Shown for comparison are dashed lines depicting the distribution obtained under apparently similar conditions by Boufendi et al. We observe an initial rapid growth in particle diameter which, for longer plasma on-periods, decreases to a slow growth rate. In addition,

the size dispersion is very large, in fact, with all sizes from zero to approximately twice the average diameter represented. We are unable at this time to resolve the discrepancy between our particle growth

Figure 2

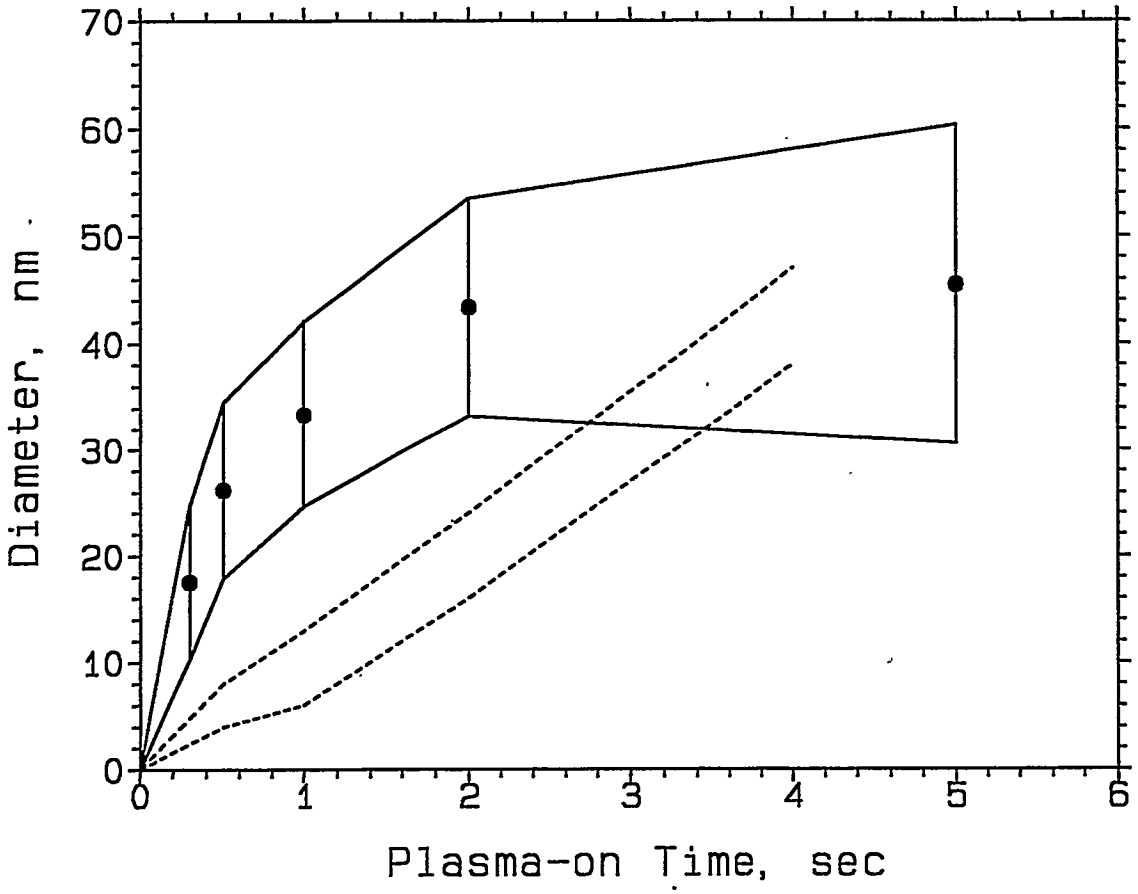

Fig. 2. Silicon particle size distributions obtained from a pulsed silane/argon plasma. Dashed lines show the data of Ref. 7.

dynamics and those of Boufendi et al. Great effort was expended to match conditions of geometry, linear flow velocities, pressure and power. Plasmas are, however, notoriously difficult to reproduce quantitatively in different laboratories. We are not actually able to confirm, at this time, that the plasma density, spatial uniformity, or temperature truly coincide with those of Boufendi et al.

Silicon Nitride

Pulsed rf plasmas of silane/ammonia gas mixtures successfully generated nano-size particles. The chemistry of the particles appears consistent with our earlier observations using a continuous rf plasma[5]. Fourier transform infrared spectra (FTIR) show strong SiH (2100 cm^{-1}) and NH absorptions (3400 cm^{-1}), confirming that the powder has a high hydrogen content. The powders formed in a pulsed plasma have a color associated with a stoichiometric ratio of Si/N, but elemental analysis has not yet been performed. Fig 3. is a TEM picture of silicon nitride particles formed with 100 cycles of a 0.25 sec-on discharge. The average particle size determined from analysis of many TEM photos is

Figure 3

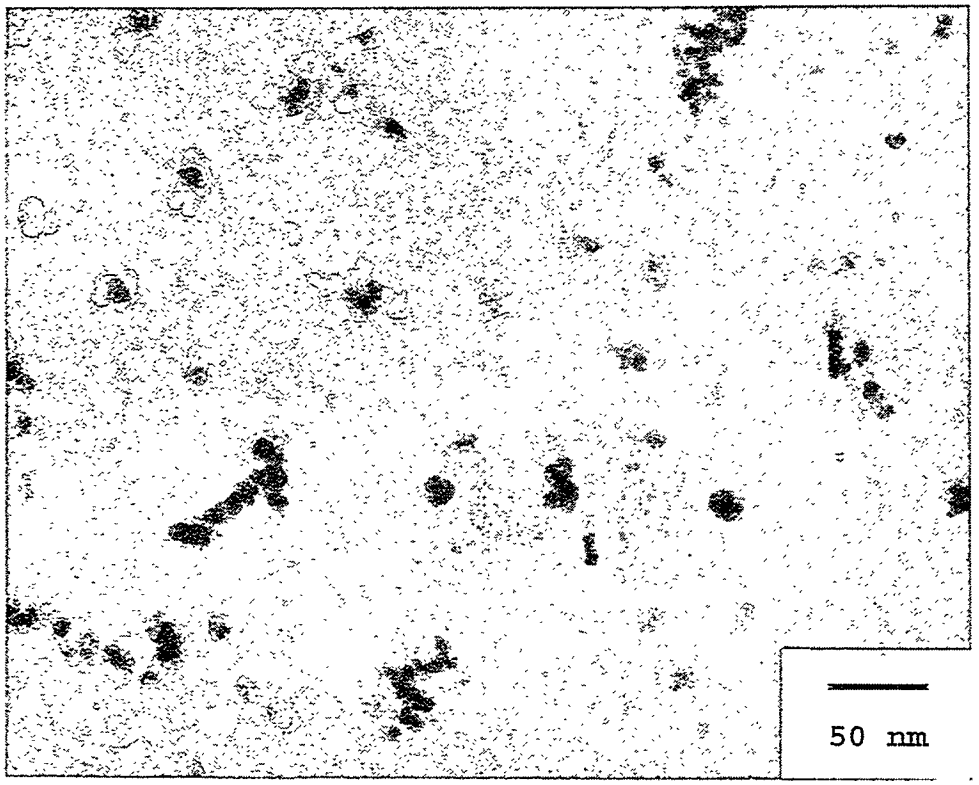

Fig. 3. TEM of particles synthesized in a SiH_4/NH_3 plasma pulsed on for 0.25 sec, off for 2.0 sec.

15 nm diameter. It is clear that many particles have agglomerated into clusters or chains and that the size dispersion is large. Similar pictures were analyzed for different plasma on-times and a sample of the results is shown in Fig. 4. The average diameter is shown with a solid dot and is seen to increase fairly linearly in time. A point has been graphed for each measured particle to show the distribution of sizes. Clusters and agglomerates were not included. It is apparent that

Figure 4

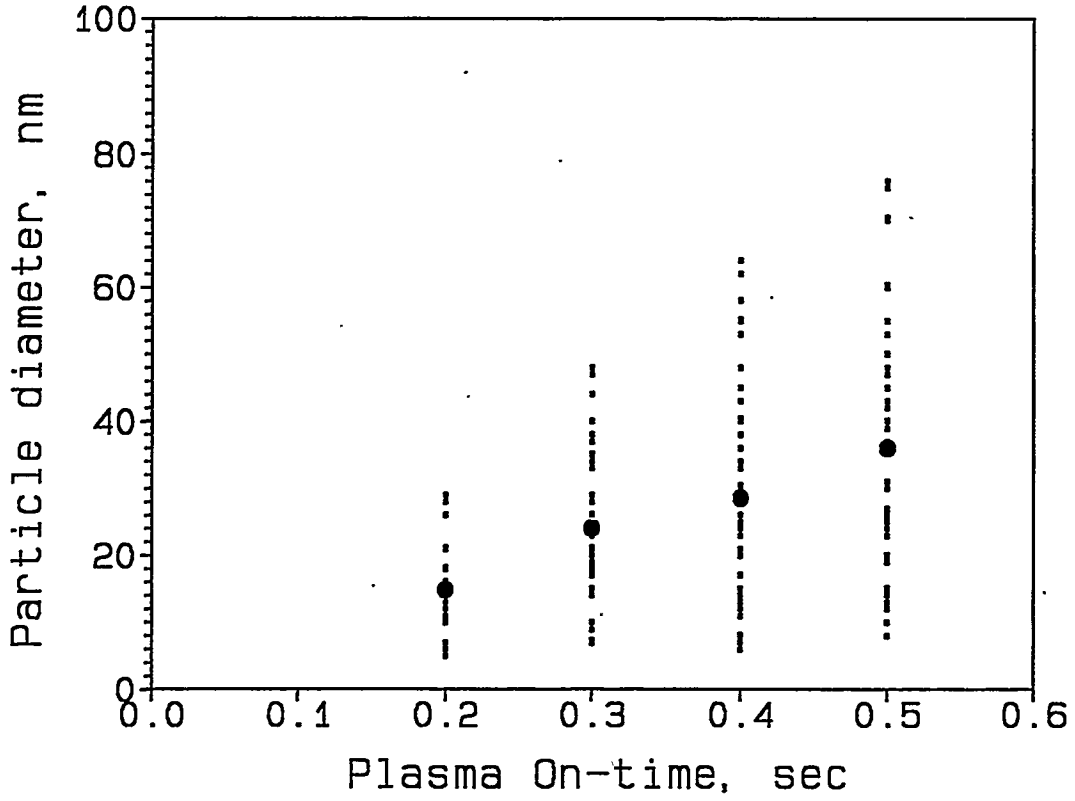

Fig. 4. Particle size distributions from a SiH_4/NH_3 plasma, large dot is the mean diameter.

particle nucleation is an ongoing phenomenon during the plasma-on period. All sizes of particles are approximately equally represented

and the simplest model is that a particle may nucleate at any time and it then grows at a constant rate until the plasma is extinguished.

The observed agglomeration of particles is potentially detrimental to the ultimate goal of producing high density ceramic material. It is generally expected that hard agglomeration into complex shapes will seriously degrade the ability to obtain close packing. It is important to establish the physical mechanisms leading to agglomeration. An isolated body suspended in a plasma acquires a negative potential relative to the plasma because the electron velocity greatly exceeds that of the positive ions. We would expect that the negatively charged particulates should repel each other and remain separated. This would only break down when the particle mass becomes very large. When the plasma is extinguished, though, the particles may be neutralized by the residual ions and could agglomerate through collisions.

Close inspection of the agglomerates seen in TEM photographs reveals that some are very strongly fuzed as if significant material growth has occurred after association of the particles. This would seem to point to a mechanism of agglomeration in the plasma itself at least for some particles. The smooth appearance of the particle surface might suggest melting and neck-formation by mass transport. The temperature of the gas and ions in the plasma is, however, very low, probably less than 50 C. The particle is presumably nucleating and growing by highly exothermic reaction of radicals which might heat the growing particle faster than it can radiate. If the particle were to exceed 1000 C, however, it would desorb the bound hydrogen, in conflict with the post-plasma FTIR results. Thus, particle melting should be discounted.

One additional observation is relevent. When laser light scattering was monitored either in the bulk of the plasma, or beneath the electrode assembly (with and without the lower screen), no particles were observed during the on-cycle. A sudden appearance of light scattering occurred only in the instant after the plasma was extinguished. The individual particles below 100 nm do not scatter enough laser light to be visible by this technique, thus it appears that a burst of agglomeration occurs after the plasma is turned off.

CONCLUSIONS

The pulsed rf plasma technique is capable of generating silicon nitride powder with controlled average size in the 10 nm size regime. Large size dispersion and some degree of agglomeration are always observed. Compaction and sintering studies will be needed to evaluate these particles as precursor candidates for superior silicon nitride ceramics.

ACKNOWLEDGEMENTS

The authors gratefully acknowledge the valuable assistance of Charles Hills for obtaining the TEMs. Also this work was supported by the United States Department of Energy under Contract DE-AC04-94AL85000.

REFERENCES

1. D. L. Segal, Br. Ceram. Trans. J. **85**, 184(1986).

2. S. Prochazka and C. Greskovich, Amer. Ceram. Soc. Bull. **57**, 579(1978).

3. J. S. Haggerty and W. R. Cannon, in *Laser-Induced Chemical Processes*, edited by J. I. Steinfeld (Plenum Press, New York, 1981), p. 165.

4. R. J. Buss and P. Ho, US Patent No. 4,769,064.

5. P. Ho, R. J. Buss, and R. E. Loehman, J. Mater. Res., **4**, 873(1989).

6. see for example, Plasma Sources. Sci. Technol., **3** (1994). Entire volume devoted to the topic.

7. L. Boufendi, A. Plain, J. Ph. Blondeau, A. Bouchoule, C. Laure, and M. Toogood, Appl. Phys. Lett. **60**, 169 (1992).

MECHANICALLY RELIABLE SURFACE OXIDES FOR HIGH-TEMPERATURE CORROSION RESISTANCE*

K. Natesan, B. W. Veal, M. Grimsditch, D. Renusch, and A. P. Paulikas
Argonne National Laboratory
Argonne, IL 60439

ABSTRACT

Corrosion is widely recognized as being of profound technological importance, but an understanding of the underlying phenomena (in order to characteriz material performance) involves factors such as the chemistry and physics of the early stages of oxidation, chemistry and bonding at the substrate/oxide interface, role of segregants on the strength of that bond, transport processes through scale, mechanisms of residual stress generation and relief, and fracture behavior at the oxide/substrate interface. Because of this complexity and the need for a wide range of different techniques, a multilaboratory program has been initiated under the auspices of the DOE Center of Excellence for the Synthesis and Processing of Advanced Materials, with strong interactions and cross-leveraging with DOE Fossil Energy and U.S. industry. The ultimate objective is to systematically generate the knowledge required to establish a scientific basis for designing and synthesizing improved protective oxide scales/coatings (slow-growing, adherent, sound) on high-temperature materials without compromising the requisite properties of the bulk materials. The objectives of program work at Argonne National Laboratory are to (1) correlate actual corrosion performance with stresses, voids, segregants, interface roughness, initial stages of oxidation, and microstructures; (2) study such behavior in growing or as-grown films; and (3) define prescriptive design and synthesis routes to mechanically reliable surface oxides. Several techniques, such as Auger electron spectroscopy, X-ray diffraction, X-ray grazing incidence reflectance, grazing-angle X-ray fluorescence, optical fluorescence, and Raman spectroscopy, are used in the studies. The project has selected Fe-25 wt.% Cr-20 wt.% Ni and Fe-Cr-Al alloys, which are chromia- and alumina-formers respectively, for the studies. This paper will present some of the results on early stages of oxidation and on surface segregation of trace elements.

INTRODUCTION

Protection from corrosion and environmental effects arising from reactions with gases and condensed products is required in order to fully exploit the potential of advanced high-temperature materials designed to improve energy efficiency and minimize deleterious environmental impact. This protection is best afforded by either formation of stable surface oxides that are slow growing, sound, and adherent to the substrate or deposition of coatings that contain or develop oxides with similar characteristics. The benefits of certain alloying additions on the growth and adherence of protective oxide scales on metallic substrates are well known, but there remains the need for a detailed understanding of the mechanisms by which scale properties and coating integrity are improved by compositional, microstructural, and processing modifications.

---

*Work supported by the U.S. Department of Energy, Office of Fossil Energy, Advanced Research and Technology Development Materials Program, Work Breakdown Structure Element ANL–4A and Basic Energy Sciences Materials Program, under Contract W–31–109–Eng–38.

The ultimate objective of this program is to systematically generate a scientific basis for designing and syntheszing of improved protective oxide scales/coatings (slow-growing, adherent, sound) on high-temperature materials without compromising the requisite properties of the bulk materials. Specific objectives are to (1) systematically investigate the relationships among substrate composition and properties and scale/coating adherence, damage tolerance, and micromechanical properties; (2) use such information to predict scale/coating failure; and (3) identify conditions leading to more damage-tolerant coatings and scales that are amenable to legitimate synthesis routes. The initial thrust is on alumina scales and coatings, but chromia-formers are used for comparative analysis. The emphasis is on materials systems with direct relevance to application suggested by the Electric Power Research Institute (EPRI) and DOE's Fossil Energy Program. The objectives of the ANL program are to (1) correlate actual corrosion performance with stresses, voids, segregants, interface roughness, initial stages of oxidation, and microstructures; (2) study such behavior in growing or as-grown films; and (3) define prescriptive design and synthesis routes to mechanically reliable surface oxides. Several techniques, are used in the studies, including Auger electron spectroscopy, X-ray diffraction, X-ray grazing incidence reflectance, grazing-angle X-ray fluorescence, optical fluorescence, and Raman spectroscopy. The project has selected Fe-25 wt.% Cr-20 wt.% Ni and Fe-Cr-Al alloys, which are chromia- and alumina-formers, respectively, for the studies. This paper presents selected results on early stages of oxidation and on surface segregation of trace elements in alumina-forming alloys.

EXPERIMENTAL PROCEDURE

The experimental study has focused on Fe-25 wt.%Cr-20 wt.%Ni and Fe aluminide alloys, both of which are of interest in fossil energy applications. The former is a chromia-former and its composition is the basis for one of the commercial austenitic stainless steels. The latter alloys, which are alumina-formers, are in various stages of development under the sponsorship of DOE Fossil Energy. These alloys can be used as either structural material or as a cladding to protect the structural material against corrosion. Sheets of several Fe_3Al-based alloys were procured from Oak Ridge National Laboratory. Table 1 lists the compositions of the alloys used in the study. Coupon specimens were cut from the sheet material for thermogravimetric experiments and for spectroscopic studies.

Several types of experiments were initiated to examine the oxidation behavior of these alloys, with emphasis on early stages of scaling, microstructural changes in scales, trace-element segregation on the free

Table 1. Nominal chemical composition (wt.%) of alloys used in corrosion tests

Material	Cr	Al	Fe[a]	Other
FA 61	-	15.9	Bal.	-
FA 71	5.5	15.9	Bal.	-
FA 81	2.2	15.9	Bal.	B 0.01
FA 129	5.5	15.9	Bal.	Nb 1.0, C 0.05
FAX	5.5	15.9	Bal.	Nb 1.0, Mo 1.0, Zr 0.15, B 0.04
FAL	5.5	15.9	Bal.	Zr 0.1, B 0.05
FAS	2.2	15.9	Bal.	B 0.05

[a]Bal. = balance.

surface and scale/alloy interface, and scale spallation characteristics. Thermogravimetric experiments were performed at 1000°C with an electrobalance having a sensitivity of 0.1 μg, to establish the effect of alloy composition on long-term oxidation characteristics and scaling kinetics. Specimens were suspended from the balance in a vertical furnace and held for the desired exposure period. Ultrahigh-purity air, further purified by passing over a hot bed of Zr chips, was used in these experiments. Upon completion of the oxidation test, the furnace was opened and the specimen was rapidly cooled in high-purity air. Following thermogravimetric measurement of oxidation, scale surfaces and cross sections of specimens were examined with a scanning electron microscope equipped with an energy-dispersive X-ray (EDX) analyzer.

For the segregation studies, specimens of FA 71 alloy were exposed at 1000°C to high-purity argon for times of 10 min, 1, 5, and 10 h. Subsequently, the specimens were analyzed using Auger electron spectroscopy (AES), along with sputtering, to obtain AES spectra and depth profile analysis for Fe, Cr, Al, O, and S. For Raman and fluorescence spectroscopy studies, specimens of FA 71 and FAL alloys were used to examine the scale composition during scale development and evaluate the effect of exposure temperature on scale adhesion and spallation.

Raman spectroscopy studies were used to identify and monitor the evolution of Fe_2O_3 and Al_2O_3 in scales grown on FA 71 and FAL after sequential treatments in air at temperatures ranging from 300 to 1300°C. These sesquioxides can be readily identified from Raman spectra using the measurements as a "fingerprint" technique. Evidence of additional oxide phases in the scales is present from the spectra, but their identification is not straightforward. Further, some line broadening and spectral line shifts appear (possibly because of strains or impurity effects) but these are not considered in this paper.

The FA 71 and FAL alloys are alumina formers. However, the alumina scales that develop on these alloys after high-temperature oxidation contain a small amount of dissolved Cr. When Cr 3d electrons, from atoms substituting on Al sites, are excited, they de-excite by producing a sharp fluorescence doublet with a wavelength near 7000 Å. (The red gemstone ruby is a Cr-doped alumina; the red coloration comes from the Cr fluorescence.) As alumina scales form on the iron aluminides, the Cr fluorescence doublet becomes very prominent. Depending on scale-growth conditions, the doublet shifts and broadens, apparently as a consequence of varying strains in the alumina scale. The shifts provide a sensitive measure of strain accumulation in the scales and clearly indicate when strain relief occurs.

RESULTS AND DISCUSSION

Figure 1 shows the oxidation data for several of the alumina-forming alloys at 1000°C in air. Oxygen uptake for the alloys is fairly rapid in the initial 10 h, after which the rate of weight change was greatly reduced. Some of the alloys, such as FA 61 and FA 71, exhibited extensive spallation when cooled to room temperature. On the other hand, alloys such as FAL and FA 129 exhibited fairly adherent oxide scales in similar experiments. Figures 2 and 3 show SEM photomicrographs of surfaces of different alloys exposed to air at 1000°C. The ternary alloy FA 71 exhibited severe spallation of the scale, while alloys such as FA 129, FAX, and FAL exhibited adherent alumina scales with several locally spalled regions on the alloy surface. The mode of scale cracking was different in each alloy, indicating that alloy composition

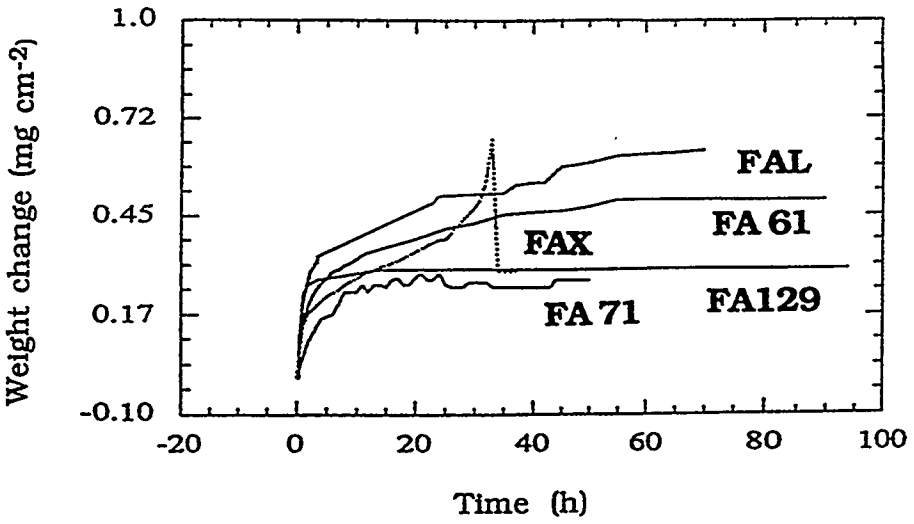

Fig. 1. Weight change data for several Fe aluminide alloys tested in air at 1000°C.

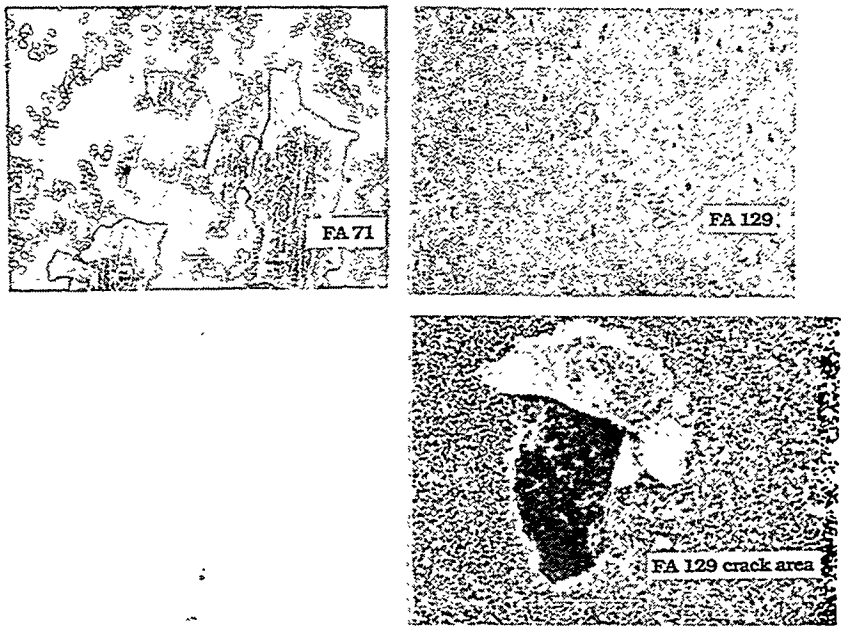

Fig. 2. Scanning electron photomicrographs of surfaces of FA 71 and FA 129 alloys tested in air at 1000°C.

may play a significant role in scale development and subsequent spallation. Figure 4 contains cross-sectional SEM pictures that display the thickness and morphology of scales developed in the alloys after 100 h of exposure at 1000°C.

Figure 5 shows the AES spectra for specimens of FA 71 in the initial condition and after 10 min, 1, 5, and 10 h ofexposure to high-purity argon at 1000°C. The argon contains sufficient oxygen to permit

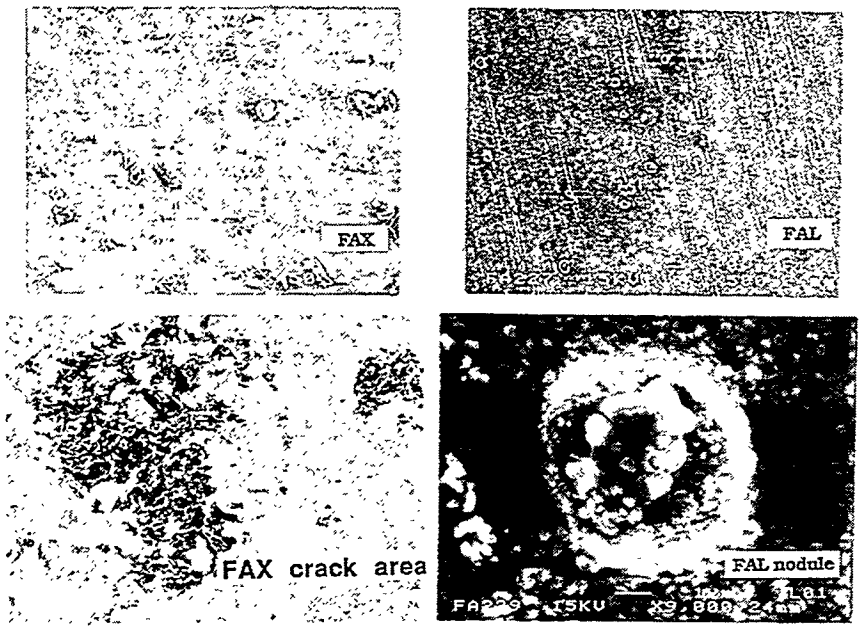

Fig. 3. Scanning electron photomicrographs of surfaces of FAX and FAL alloys tested in air at 1000°C.

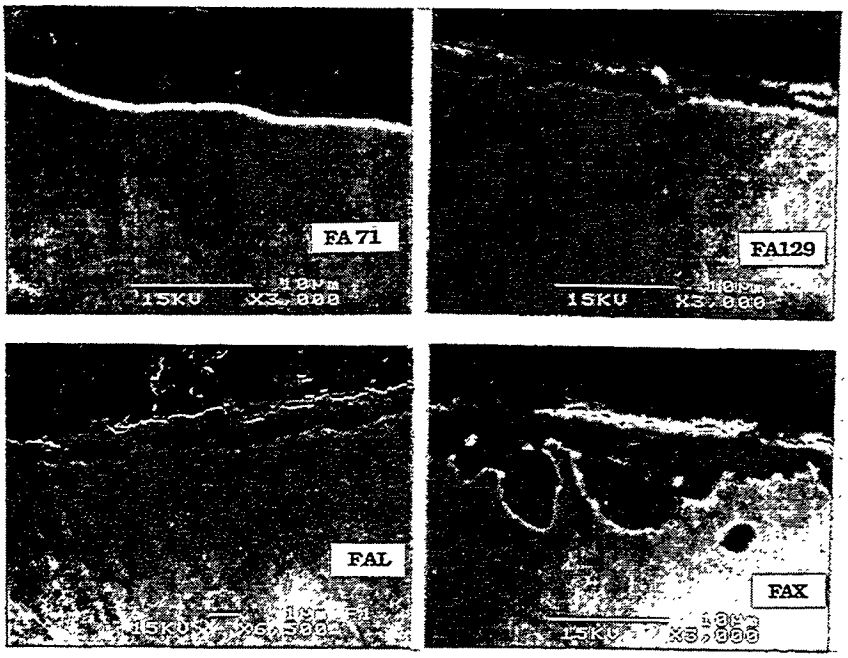

Fig. 4. Scanning electron photomicrographs of cross sections of several Fe aluminide alloys tested in air at 1000°C.

sustained scale growth. It is evident that the surface of the untreated specimen reveals S and that the peak height for S decreases exposure time increased from 0 to 1 h. Although S is absent in the specimen exposed for 5 h, a significant S peak can be observed in the specimen exposed for 10 h. Figure 6 shows the elemental depth profiles obtained by AES analysis for several of the specimens. It is evident that after 10

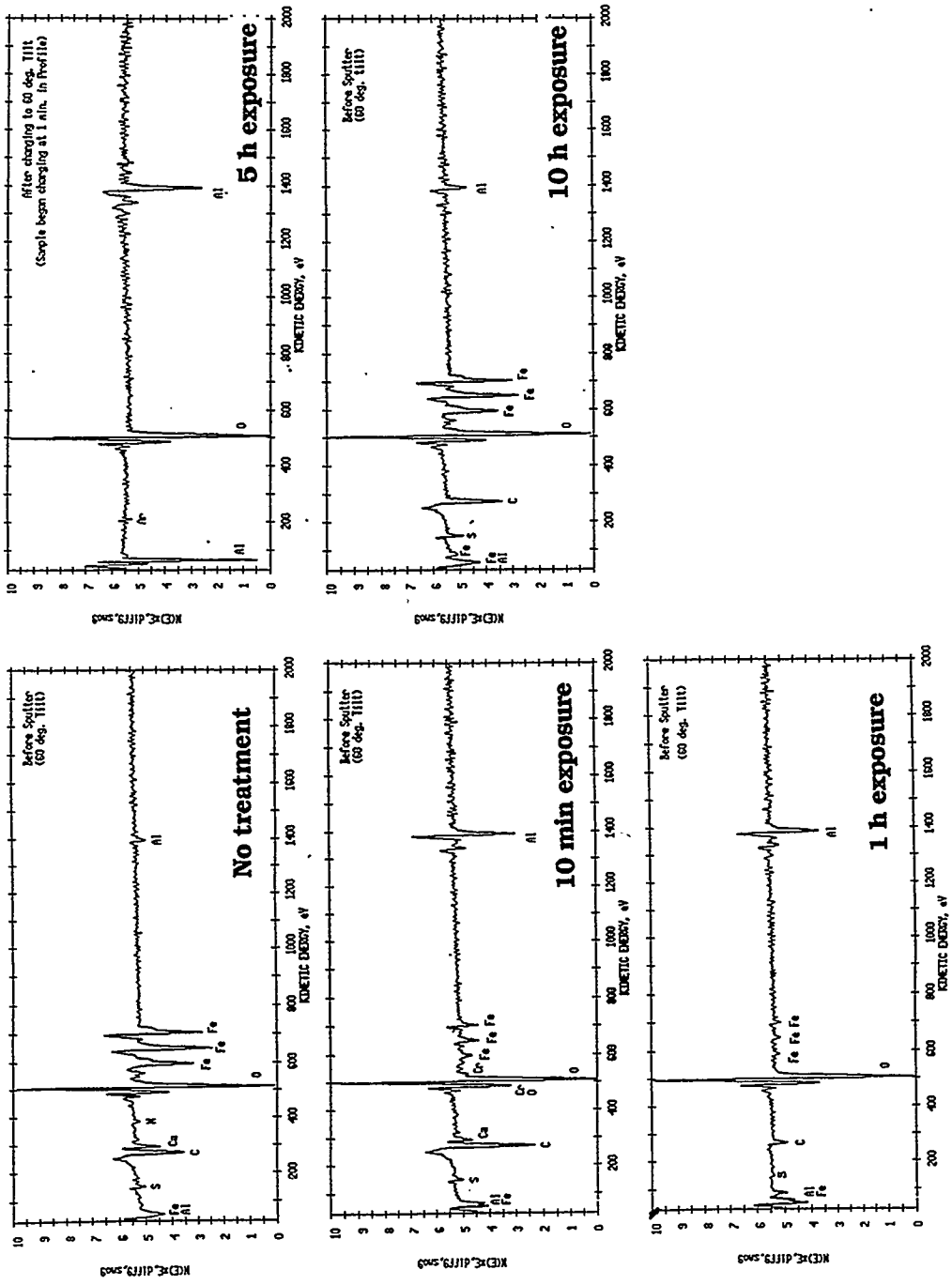

Fig. 5. Auger electron spectroscopy spectra for FA 71 alloy in as-received condition and after exposure in air at 1000°C for several time periods.

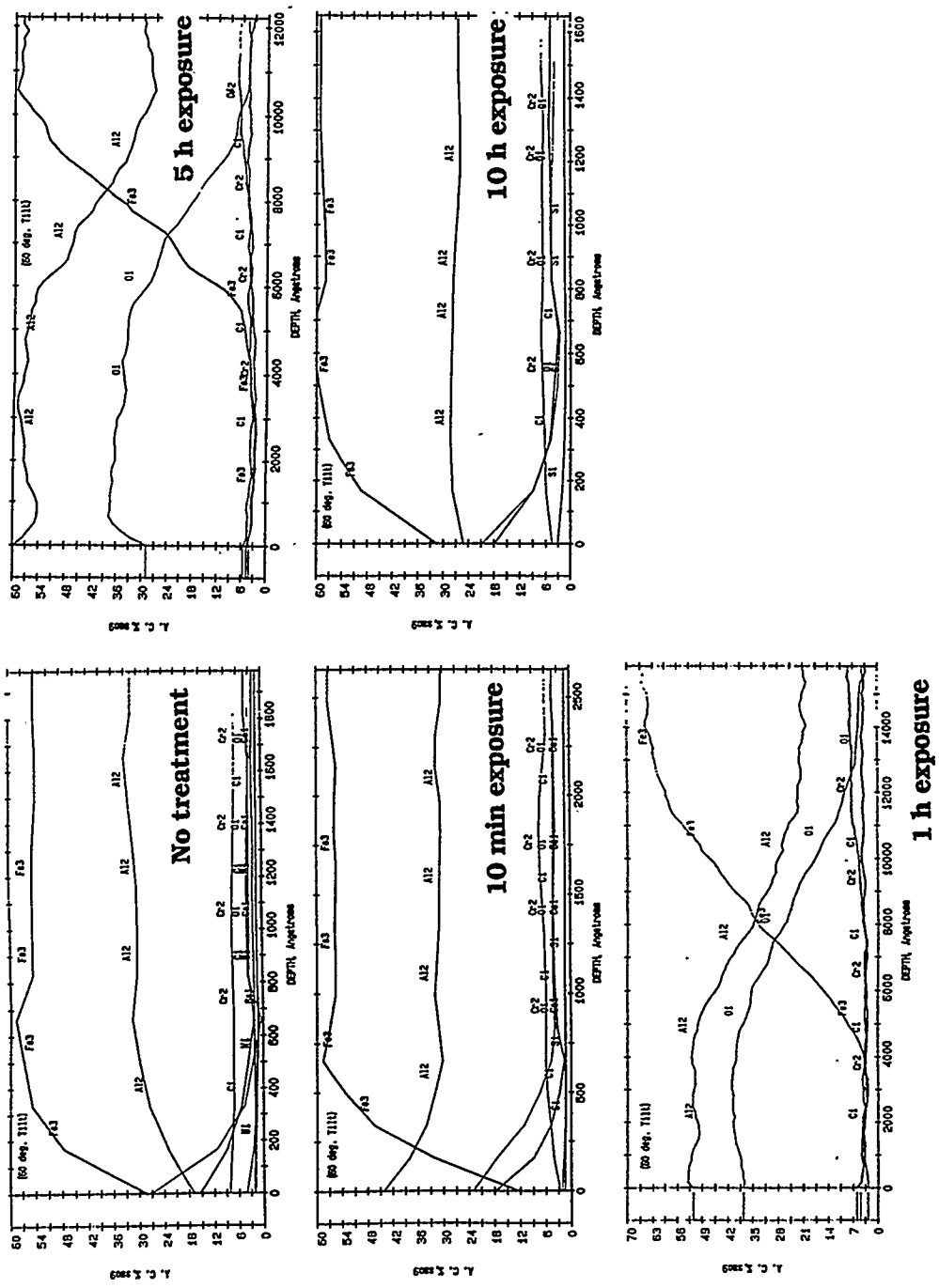

Fig. 6. Auger electron spectroscopy depth profiles for FA 71 alloy in as-received condition and after exposure in air at 1000°C for several time periods.

min of exposure the scale contained significant Fe but that the Al and O concentrations increased to a depth of ≈500 Å. After 1 h of exposure in argon, Fe content in the scale decreased significantly to a depth of ≈4000 Å. Further increase in exposure time to 5 h resulted in almost pure alumina scale of ≈5000 Å thickness. Exposure time of 10 h resulted in destruction of the pure alumina scale, and the elemental depth profiles were similar to those obtained after 10 min exposure of the virgin alloy. These preliminary results indicate that there may be a critical oxide thickness in alumina-forming alloys that can lead to spallation after cycling to room temperature, and that this thickness may be achieved with exposure times of 5-10 h at 1000°C. The observed behavior of scaling and spallation may also be due to segregation of S, initially at the alloy surface, to the scale/alloy interface, which can lead to debonding of the scale.

Figure 7 shows elemental concentrations for Fe, Al, O, and S in the surface of argon-exposed specimens as a function of exposure time. Figures 8 shows the surfaces of FA 71 specimens after 10 min, 1 h, and 5 h of exposure to argon at 1000°C. In 10 min, the alloy shows the grain boundaries of the original material and little or no scaling. In 1 h, the scale is fragmented but analysis showed it to be predominantly alumina. After 5 h of exposure, the oxide exhibited significant texturing, probably dictated by the original polishing lines of the specimen. The scale exhibited a number of transverse cracks (i.e., between the parallel grinding lines) and some spallation. However, the scale composition was predominantly alumina. Figure 9 shows photomicrographs of specimens exposed for (a) 10 h, (b) 10 h followed by polishing and further exposure of 5 h, and (c) 10 h plus polishing and 5 h of exposure repeated twice. It is evident that the scale is very friable and that spallation is expected. This also confirms the

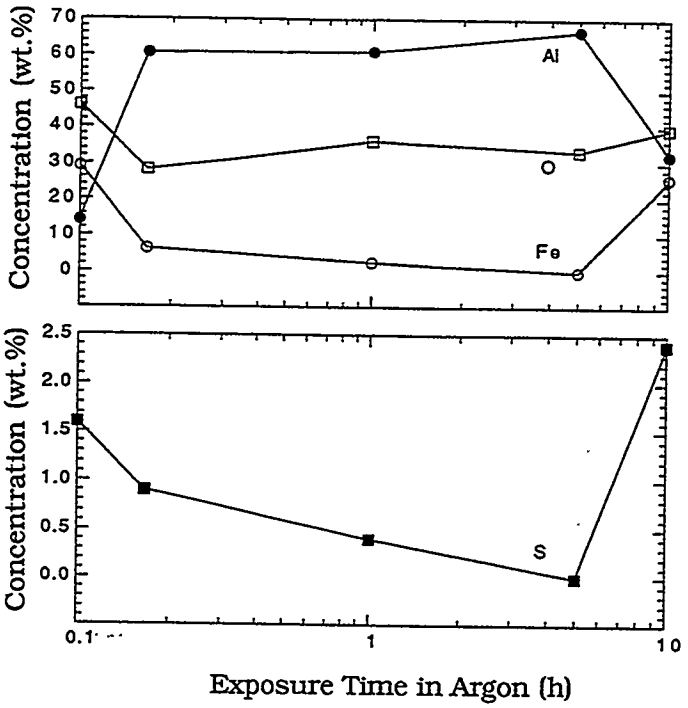

Fig. 7. Variation in concentration of Fe, Al, O, and S on the surfaces of an FA 71 alloy as a function of exposure time in air at 1000°C.

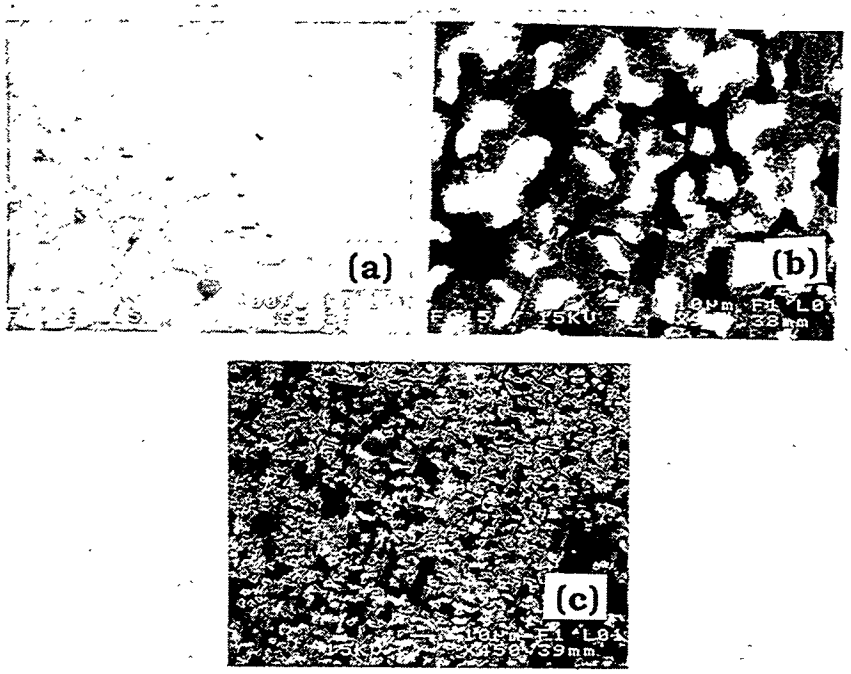

Fig. 8. Scanning electron photomicrographs of surfaces of FA 71 exposed in air at 1000°C for (a) 10 min, (b) 1 h, and (c) 5 h.

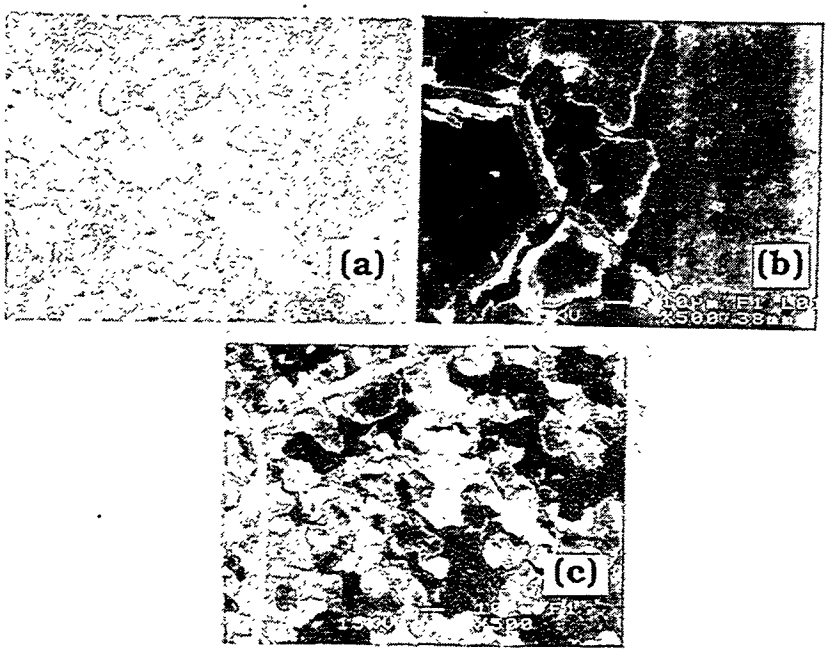

Fig. 9. Scanning electron photomicrographs of surfaces of FA 71 exposed in air at 1000°C for (a) 10 h, (b) 10 h plus polished and re-exposed for 5 h, and (c) 10 h plus re exposure step in b repeated twice.

AES results that scale composition changes from pure alumina to Fe-containing alumina as exposure time increases from 5 to 10 h. Additional experiments are in progress to examine this aspect of scaling and spallation, as well as toevaluate the role of other alloying elements in the scaling/spallation process.

Figure 10 (left panel) shows a series of Raman spectroscopy measurements for the FA 71 alloy. The top spectrum contains data taken at room temperature before oxidation. The spectrum is featureless because the underlying metal provides no Raman sensitivity in this spectral range. Beginning at 300°C, the samples were then oxidized for 1 h, and a Raman spectrum was taken at room temperature. One-hour oxidation treatments, followed by room-temperature measurements, were repeated at 100°C intervals to a final temperature of 1300°C. The data in Fig. 10 indicate that by 500°C, Fe_2O_3 appears prominently in the scale and is replaced by Al_2O_3 at T > 1000°C. Also shown in Fig. 10 (right panel) are room-temperature "ruby line" fluorescence measurements from FA 71 scales after heat treatments of 1 h beginning at 750°C, with sequential oxidation at 50°C intervals. The fluorescence signal first appears at T ≈750°C and grows rapidly in intensity with subsequent oxidation. At temperatures below 950°C, the peak position displays a red shift when samples are oxidized at increasingly elevated temperatures. This shift indicates that an increasing compressive strain is developing in the scale. (We note that the red shift of the ruby doublet is used for measurement and calibration of hydrostatic pressure in diamond-anvil pressure cells.) Strain relief (at room temperature) clearly occurs when reaction temperatures exceed ≈950°C, probably because of crack

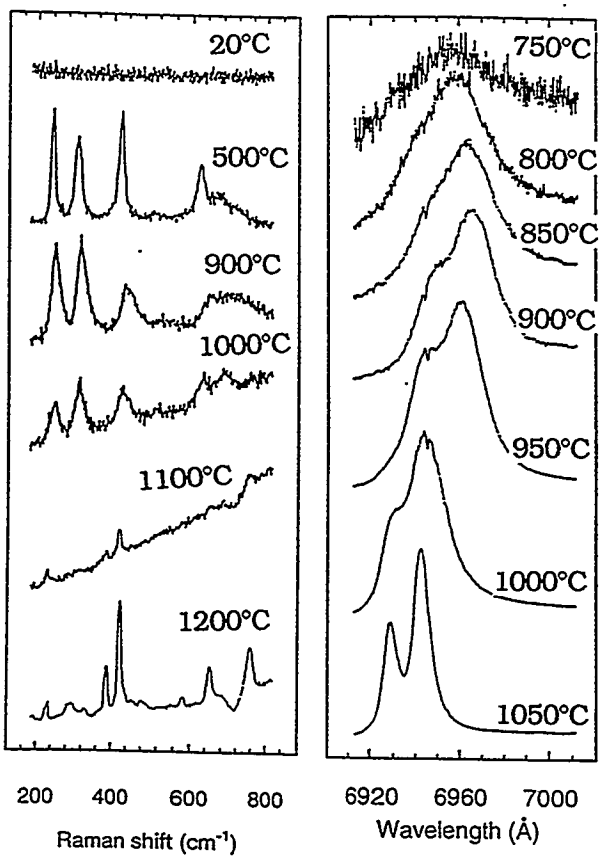

Fig. 10. Raman spectroscopy data obtained for FA 71 alloy after oxidation at several temperatures.

formation in the scales, thus signaling the onset of spallation. The 1050°C spectrum in Fig. 10 is very similar to that of natural unstrained ruby; apparently this spectrum identifies scale delamination.

Figure 11 shows intensity measurements of the Raman signal for Fe_2O_3 and of the ruby fluorescence (data in Fig. 10) plotted vs oxidation temperature. (Raman spectroscopy is not ideal for precise intensity measurements, but dramatic changes occur with oxidation and thus observed trends are clearly meaningful.) The presence of iron oxide in the scale is dominant for temperatures up to ≈750°C. At this temperature, Al_2O_3 first appears and, for subsequent treatments, dominates the scale. Figure 11 shows scale evolution through a transient region heavily influenced by Fe_2O_3 to the formation of the protective Al_2O_3. Curve (a) in Fig. 11, showing a rapid increase in intensity for T > 1000°C, is based on data from sample FA 71. Curve (b) is from sample FAL, which contains the reactive element Zr that is known to provide increased scale adhesion. The rapid growth of scale (a) relative to scale (b) is probably due to increased spallation failure with rapid oxidation of exposed substrate.

Figure 12 shows measurements of the ruby line peak shift vs. oxidation temperature (data in Fig. 10) for samples FA 71 (open circles) and FAL (solid squares). For temperatures below 900°C, the scales are adherent and the ruby lines show a continuous shift to the red as strain buildup increases. At 950°C, an abrupt blue shift (apparent in both FA 71 and in FAL) was observed. We are exploring the possibility that this effect might be associated with the θ-to-α phase transition that occurs near 950°C. With further oxidation at T > 950°C, the FAL scale can acquire increased strain without catastrophic failure. The solid line in Fig. 12 denotes the maximum red shift and hence maximum strain sustained by the scale. It appears that the maximum sustainable strains occur in FAL at T ≈1050°C. Using published values of spectral shift vs. hydrostatic pressure for ruby, and obtaining strain from bulk modulus data, we estimate that the linear strain in the scales processed at 900°C is about 0.8%.

For FA 71, scale failure is evident after 1 h of oxidation at 1000°C (preceded by oxidation at lower temperatures, as discussed above). An abrupt blue spectral shift occurring at 1000°C indicates catastrophic failure of the FA 71 scale. For oxidation temperatures greater than ≈1000°C, the spectra are comparable to those of conventional ruby, suggesting that the scale has completely debonded. At T > 950°C, multiple (shifted) doublets are observed at different points on the oxide scale, indicating varying degrees of scale adhesion. Multiple spectral peaks appearing at T > 950°C are plotted in Fig. 12.

These studies of the Cr fluorescence line in alumina scales provide the first application of Cr fluorescence spectroscopy for determining of strains and strain gradients in thermally grown scales. Further studies are underway to obtain the needed information to quantify both the magnitudes and the gradients of the strains that occur in the oxide scales.

SUMMARY

A multilaboratory program has been initiated by DOE to develop mechanically reliable oxide scales for high temperature corrosion resistance. Work at Argonne National Laboratory has focused on alumina-forming

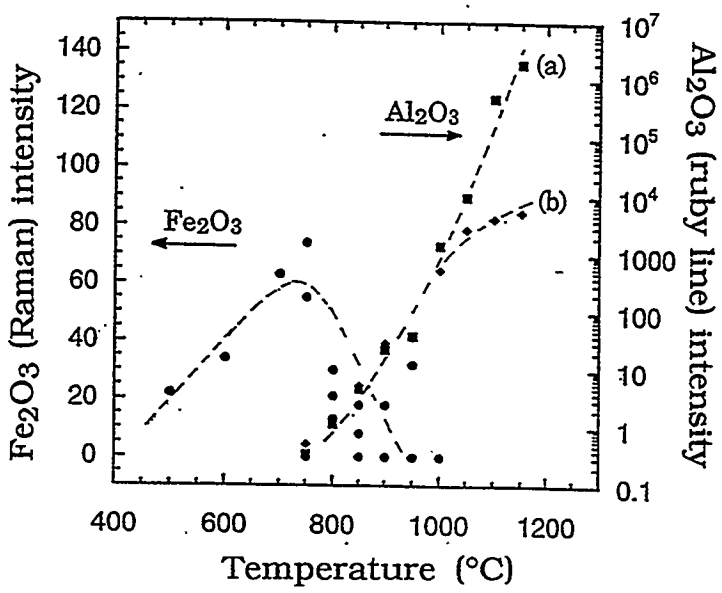

Fig. 11. Raman intensity data for Fe_2O_3 and ruby fluorescence data for FA 71 alloy as a function of oxidation temperature.

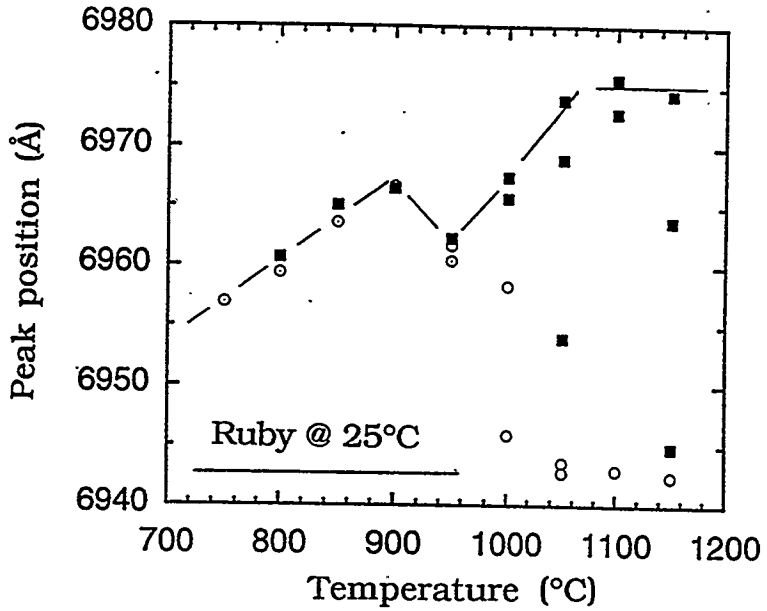

Fig. 12. Data on ruby line peak shift vs. oxidation temperature for FA 71 (open circles) and FAL (solid squares) alloys

alloyswith emphasis on examining the early stages of oxidation of several Fe-Cr-Al alloys and also evaluating the segregation behavior of trace elements in the alloy and their role in the scaling and spallation

processes that occur in oxidation of these alloys. Preliminary results are presented on the segregation data obtained by Auger electron spectroscopy and on scaling/spallation data from Raman spectroscopy.

ACKNOWLEDGMENTS

The authors thank V. Sikka and P. Tortorelli of Oak Ridge National Laboratory for supplying several of the alloys.

PLASMA SYNTHESIS OF ALUMINA FILMS ON METAL & CERAMIC SUBSTRATES

Ian Brown and Zhi Wang

Lawrence Berkeley Laboratory
University of California
Berkeley, CA 94720

ABSTRACT

We are exploring the feasibility of the plasma synthesis of highly-adherent films of alumina and chromia on SiC and FeAl substrates. A magnetically-filtered cathodic arc plasma deposition technique is used in which a high density metal plasma (Al or Cr) is formed and deposited on the substrate in the presence of a low pressure gaseous oxygen background. The substrate is simultaneously repetitively pulse biased, providing a means of controlling the incident ion energy. In the early stages of the process the ion energy is held in the keV range so as to produce atomic mixing at the film-substrate interface (ion stitching), and in the latter stages of deposition the energy is reduced to ~200 eV (IBAD range) to provide a means of controlling the film structure and morphology. Films that are dense and highly adherent can be formed in this way. We have produced near-stoichiometric films of alumina and chromia on small SiC and FeAl substrates and characterized the films in a number of ways, including RBS, X-ray diffraction and adhesion, and we've also done some preliminary temperature cycling experiments. The alumina films are of thickness from 0.2 to 1.5 μ, amorphous prior to heat treatment, and show an α-alumina phase after heat treating at 1000°C for up to 16 hours. The film substrate adhesion is typically greater than ~70 MPa prior to heating, and initial results indicate that the films maintain their adhesion after repetitive cycling in temperature between ambient and 1000°C. Here we describe the plasma processing method and outline the experimental results obtained to-date.

INTRODUCTION

Vacuum arc plasma discharges are intense sources of highly ionized, dense metal plasmas. Plasma generators based on this kind of discharge can be used to deposit thin films of various kinds including metals and alloys, and if the source is operated in a gaseous background then compounds including ceramic oxides can also be formed. We have developed techniques that combine plasma deposition with ion bombardment to create a powerful and adaptable new technology that is environmentally friendly, highly efficient, can be scaled up to large size, and can synthesize films of a range of materials[1-4]. The films can be atomically mixed to the substrate by the ion bombardment phase of the process to produce excellent film/substrate bonding at the atomic level.

A metal plasma of the required species is formed by a vacuum arc plasma gun and directed toward the substrate with a moderate streaming energy, typically of order 100 eV. At the same time, the substrate is

repetitively pulse biased to a moderate negative voltage (typically a few hundred to a few tens of kilovolts), thereby accelerating a fraction of the incident ion flux and energetically bombarding the ions into the substrate and the previously-deposited film. This technique provides a means for precise control of the energy of the depositing plasma ions. We use an early-time high ion energy so as to atomically mix the film into the substrate, and a lower (but optimized) ion energy during the bulk of the film growth so as to add an 'ion assist' to the deposition (similar to an ion beam assisted deposition, or IBAD, process). In this way the film is ion stitched to the substrate and has very strong adhesion, and it is also of high density (void-free), good structure (eg, not columnar), and good morphology (eg, close to atomically smooth).

In the work described here we've used this plasma materials synthesis technique to form films of Al_2O_3 and Cr_2O_3 on SiC and FeAl substrates. The films have been characterized, both before and after 1000°C heat treating, for composition and phase using Rutherford backscattering spectrometry (RBS) and X-ray diffraction analysis, and the film-substrate adhesion has been measured using a Sebastian-type pull tester. In the following we firstly outline the plasma and ion beam processing set-up, the substrate preparation, and the characterization methods used. The experimental results of the program to-date are then presented. Finally, we summarize and comment on the suitability of the method for this field of application.

EXPERIMENTAL PROCEDURE

Plasma Processing

We've made a number of different kinds of vacuum arc plasma guns, from small pulsed versions to a large dc embodiment. The sources can be operated either in a repetitively pulsed mode with pulse duration between 50 μs and 5 ms, or with long pulses (tens or hundreds of milliseconds), or d.c.; arc current is typically in the range 100 - 250 A. The guns are UHV-compatible and the cryogenically-pumped vacuum system base pressure is typically about 1×10^{-6} Torr. For the alumina and chromia films produced in this work, we used a "minigun" (Fig. 1) with arc pulses of 5 ms duration and a repetition rate of about 1 pulse per second. The cathode is a central cylindrical rod of the desired metal plasma species surrounded coaxially by a cylindrical anode. The arc pulses are initiated by a short (~10 μs) high voltage (~10 kV) trigger spark to the cathode. The plasma is created on the cathode surface and leaves the source as a directed plume through the annular anode. It is a fundamental characteristic of this kind of plasma discharge[5,6] that along with the plasma formation, a small fraction of 'macroparticles' is also produced – small particles of metallic cathode debris of dimension in the range 0.1 - 10 μ. If macroparticle filtering is desired, as for the

present purpose, a magnetic duct of suitable size is attached so that the plasma streams directly from the plasma gun into the filter[7]. With optimum magnetic field configuration[8,9] and optimum bias of the filter wall, about 25% of the ions produced in the arc discharge can be transported through the filter. Figure 2 shows plasma flowing through the magnetic filter used in the present work. The overall plasma deposition system thus consists of the repetitively pulsed plasma gun in conjunction with the 90° bent magnetic filter. Plasma exits the filter and deposits onto the appropriately positioned substrate.

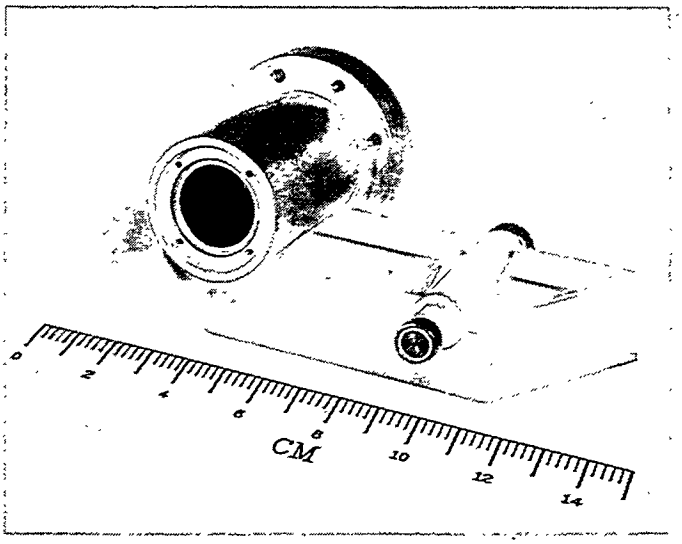

Figure 1. Partially disassembled vacuum arc plasma gun of the kind used here. The cathode assembly is shown removed from the anode.

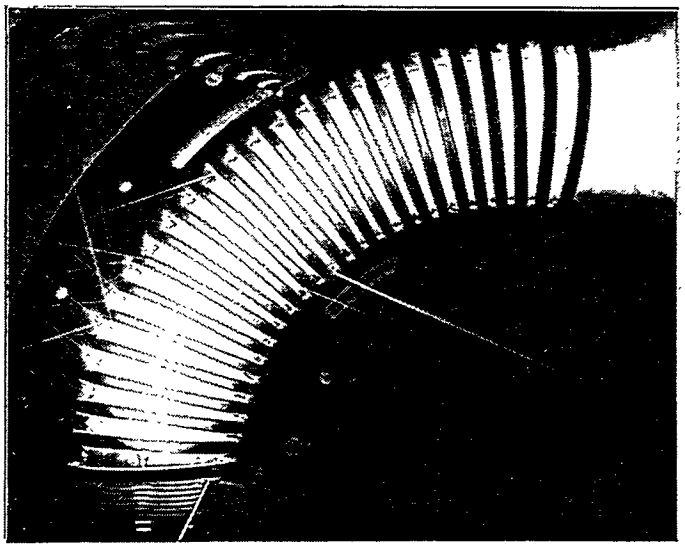

Figure 2. Magnetic filter, showing plasma injected from the gun at the lower left streaming through it and exiting at the upper right.

Films of metallic oxides can be formed simply by carrying out the plasma deposition not in a high vacuum environment, but in a somewhat higher pressure ambient of oxygen gas[10,11]. We have found empirically that a pressure in the range 1 - 100 mTorr is suitable for most metal oxides. Here the oxygen background pressure was 10 to 15 mTorr. The oxygen is both entrained in the plasma stream, ionized, and deposited in the plasma state, as well as reacting at the freshly-deposited metallic surface to form aluminum oxide. The net result is that, for the optimal oxygen pressure, a stoichiometric film of alumina is formed.

Ion energy of the depositing plasma flux is controlled by repetitively pulse biasing the substrate. Typically the pulse duration might be ~10 μs and the duty cycle ~10 - 50%. Pulsing of the bias voltage is necessary (for all but the lowest bias voltages) because a high voltage dc bias would cause an electrical discharge between the substrate and the vessel or the plasma gun; the plasma would be grossly perturbed (because the plasma sheath would expand from the substrate to large distances) and the ions would not be accelerated. The solution is to switch off the bias before such major perturbation can occur (to limit the sheath expansion to modest distances), let the plasma recover, and then repeat the process; ie, to do the biasing in a repetitively pulsed mode. For the early stages of the deposition process the pulse bias is held at a relatively high voltage of 2.2 kV. The mean aluminum ion energy is then 3.75 keV, because the mean ion charge state of the aluminum plasma is 1.7 (ref. 12) and $E_i = QV$. This energy results in implantation into the substrate to a depth of up to ~100 Å and intermixing of the Al film that is deposited during the pulse-off part of the pulse biasing. The aluminum film thus grows on the SiC substrate from a highly mixed interface. When an oxide is to be formed, the oxygen is also intermixed both by direct implantation of ionized oxygen as well as by recoil implantation of oxygen in the surface film. When a film thickness of just a few tens of angstroms has accumulated, the pulse bias voltage is reduced, since intermixing with the substrate is no longer a factor and the higher ion energy would sputter away the already-deposited film. Moreover, it is known from a large body of work on ion assisted deposition that a modest ion energy can be highly advantageous for controlling such characteristics as the density, morphology and structure of the film. For the bulk of the plasma deposition process the pulse amplitude is kept at 200 volts.

Substrate Preparation

The substrates were small coupons of silicon carbide and iron aluminide. The SiC was CVD-produced and was purchased from Morton Advanced Materials; the polished coupons were 0.5" x 0.5" square and 0.1" thick. The FeAl was supplied by ORNL and was in the form of polished 1 cm x 2 cm coupons approx. 1 mm thick.

Characterization

Analysis of film composition was done with Rutherford backscattering spectrometry (RBS) using 1.8 MeV He^+ ions, and X-Ray diffraction analysis was used to determine the crystallographic phase. Film adhesion was measured with a Sebastian-type pull tester using Sebastian studs epoxied to the samples and pulled normal to the substrate by known weights; the epoxy failure limit was typically ~70 MPa, and this thus determined the instrumental limit.

Procedure

Substrate samples were cleaned with alcohol and positioned within the vacuum chamber for the plasma deposition and ion bombardment processing. The oil-free system was cryogenically pumped down to a base pressure of about 1×10^{-6} Torr or better before commencing the plasma process. Oxygen gas was admitted to a pressure of typically 10 to 15 mTorr, and the plasma deposition and ion bombardment processing carried out as described above; the time required for film growth was usually a few tens of minutes. Note that in this plasma processing the energy added to the sample is small and they are not heated significantly. The samples were then removed from the chamber for characterization and testing. Heating was done in air in an oven which could be heated to 1100°C. The samples could be inserted into and removed from the hot oven quickly, and the sample heat-up and cool-down time was thus just a few minutes, determined by the thermal capacity of the small coupons. In the experiments conducted, the samples were maintained at full temperature at times varying between 15 minutes and 16 hours.

EXPERIMENTAL RESULTS

A number of different samples were prepared and studied, of both alumina and chromia and on both silicon carbide and iron aluminide. Several different thicknesses of films were formed, between about 0.2 μ and 1.5 μ. Issues that we considered important to address were:

- Stoichiometry of the plasma deposited film, both pre- and post-heat treatment;
- Crystallographic phase of the film produced, pre- and post-heat treatment;
- Adhesion of the film to the substrate, pre- and post-heat treatment;
- Adhesion of the film to the substrate following thermal cycling of the sample through a number of repeated high temperature excursions.

Stoichiometry

RBS analysis showed that the as-prepared samples were usually slightly oxygen-rich, with composition such as for example $Al_2O_{3.3}$ for an oxygen pressure of 12 mTorr. When the oxygen pressure was too high, for example 26 mTorr as in our early work, the films were significantly oxygen rich, with an Al_2O_5 composition. The post-heating films were, not surprisingly, of good Al_2O_3 stoichiometry.

Crystallography

The as-deposited alumina was typically amorphous with a small amount of κ-Al_2O_3, but for optimized plasma and ion beam processing conditions and oxygen gas pressure, we could form material containing largely α- and κ-Al_2O_3 (Fig. 3). The post-heating films were always largely α-Al_2O_3 (Fig. 4).

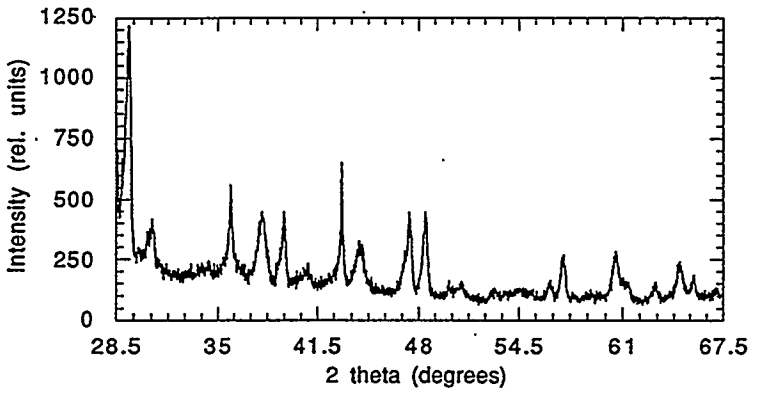

Figure 3. X-ray diffraction spectrum for an alumina film, as-deposited (pre-heating) at optimal conditions, indicating mostly α- and κ-Al_2O_3 phases. Film thickness 0.5 μ; on FeAl.

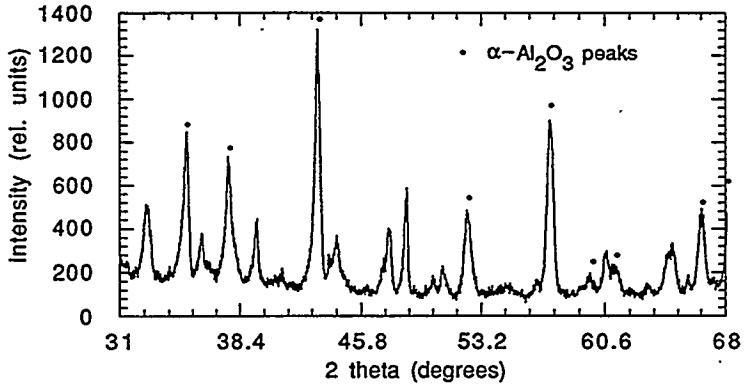

Figure 4. X-ray diffraction spectrum for an alumina film, after heating at 1000°C for 16 hours, indicating mostly α-Al_2O_3 phase. Film thickness 0.5 μ; on FeAl.

Adhesion

The film-substrate adhesion was always good for the as-prepared, pre-heat-treatment films – an adhesion strength as measured with our home-made Sebastian-type pull tester of $\gtrsim 70$ MPa, the instrumental limit of measurement – this for both alumina and chromia films on both FeAl and SiC. Post-heat-treatment, the adhesion strength of the optimally-prepared films is also good for films of thickness $\lesssim 0.5$ μ, but we've had mixed results to-date with films of thickness $\gtrsim 1$ μ. We refer here to heating to 1000°C for a period of either 15 minutes or 16 hours (we've done both), for a single heat cycling.

Adhesion after Repeated Thermal Cycling

We have at the present time data for one set of experimental conditions only. These data are for an alumina film of thickness about 0.25 μ formed on a SiC substrate. The sample was thermally cycled from room temperature to 1000°C though four cycles of 15 minutes duration each; heating and cooling time of the sample was one or two minutes only. The film-substrate adhesion both before and after temperature cycling was excellent, at the instrumental limit of the pull-tester.

CONCLUSION

Films of alumina (and also chromia) have been plasma synthesized on FeAl and SiC substrates. The process is straightforward and produces a mostly α-Al_2O_3 phase. The plasma deposition process is accompanied by a controlled and time-varied ion bombardment such that the film is atomically mixed to the substrate and consequently of high adhesion, and the ion-assist process during the bulk of the film growth helps to form good morphology. For optimally prepared films the film-substrate adhesion is $\gtrsim 70$ MPa, and at least for quarter-micron alumina films on SiC the film retains its integrity and full adhesion strength through a 4-cycle thermal cycling between ambient and 1000°C.

We have reported here on the status at the time of writing of our program to explore the feasibility of the plasma synthesis of alumina and chromia films on silicon carbide and iron aluminide substrates. Clearly there's much work that remains to be done. We can conclude, however, that the plasma and ion beam techniques described here provide a tool that could be valuable for the formation of highly adherent and thermally tolerant ceramic films.

ACKNOWLEDGEMENTS

We are indebted to Peggy Hou, Simone Anders, André Anders and Kin-Man Yu for help in various parts of the work, and to Bob MaGill and Mike Dickinson for support of the experimental equipment. This work was supported by the U.S. Department of Energy, Office of Advanced Research, Fossil Energy, under Contract Number DE-AC03-76SF00098.

REFERENCES

1. I.G. Brown, A. Anders, S. Anders, M.R. Dickinson, I.C. Ivanov, M.A. MacGill, X. Yao and K.M. Yu, Nucl. Instrum. Meth. Phys. Res. B80/81, 1281 (1993).
2. Ian Brown, in *Plasma Synthesis and Processing of Materials*, edited by K. Upadhya (pub. TMS, Warrendale, PA, 1993).
3. A. Anders, S. Anders, I.G. Brown and I.C. Ivanov, Mat. Res. Soc. Symp. Proc. 316, 833 (1994).
4. A. Anders, S. Anders, I.G. Brown, M.R. Dickinson and R.A. MacGill, J. Vac. Sci. Tech. B12, 815 (1994).
5. See, for instance,*Vacuum Arcs - Theory and Application*, edited by J.M. Lafferty, (Wiley, N.Y., 1980).
6. See, for instance,*Vacuum Arc Science and Technology*, edited by R.L. Boxman, P. Martin and D. Sanders, (Noyes, N.Y., 1995).
7. S. Anders, A. Anders and I.G. Brown, J. Appl. Phys. 74, 4239 (1993).
8. A. Anders, S. Anders and I.G. Brown, Plasma Sources Sci. Technol. 4, 1 (1995).
9. S. Anders, A. Anders and I.G.Brown, J. Appl. Phys. 75, 4895 (1994).
10. R.A. MacGill, S. Anders, A. Anders, R.A. Castro, M.R. Dickinson, K.M. Yu and I.G. Brown, "Cathodic Arc Deposition of Copper Oxide Thin Films", submitted to Surface and Coatings Technol.
11. S. Anders, A. Anders, M. Rubin, Z. Wang, S. Raoux, F. Kong and I.G. Brown, "Formation of Metal Oxides by Cathodic Arc Deposition", paper presented at the Int. Conf. on Metallurgical Coatings and Thin Films, San Diego, CA, Apr 24-28, 1995.
12. I.G. Brown, Rev. Sci. Instrum. 10, 3061 (1994).

MECHANICALLY RELIABLE SCALES AND COATINGS

P. F. Tortorelli and K. B. Alexander

Oak Ridge National Laboratory
Oak Ridge, Tennessee 37831-6156

ABSTRACT

As the first stage in examining the mechanical reliability of protective surface oxides, the behavior of alumina scales formed on iron-aluminum alloys during high-temperature cyclic oxidation was characterized in terms of damage and spallation tendencies. Scales were thermally grown on specimens of three iron-aluminum compositions using a series of exposures to air at 1000°C. Gravimetric data and microscopy revealed substantially better integrity and adhesion of the scales grown on an alloy containing zirconium. The use of polished (rather than just ground) specimens resulted in scales that were more suitable for subsequent characterization of mechanical reliability.

INTRODUCTION

In many high-temperature fossil energy systems, corrosion and deleterious environmental effects arising from reactions with reactive gases and condensible products often compromise materials performance and, as a consequence, degrade operating efficiencies. Protection of materials from such reactions is best afforded by the formation of stable surface oxides (either as deposited coatings or thermally grown scales) that are slowly reacting, continuous, dense, and adherent to the substrate. However, the ability of normally brittle ceramic films and coatings to provide such protection has long been problematical, particularly for applications involving numerous or severe high-temperature thermal cycles or very aggressive (for example, sulfidizing) environments. A satisfactory understanding of how scale and coating integrity and adherence are improved by compositional, microstructural, and processing modifications is lacking. Therefore, to address this issue, the present work is intended to define the relationships between substrate characteristics (composition, microstructure, and mechanical behavior) and the structure and protective properties of deposited oxide coatings and/or thermally grown scales. Such information is crucial to the optimization of the chemical, interfacial, and mechanical properties of the protective oxides on high-temperature materials through control of processing and composition and directly supports the development of corrosion-resistant, high-temperature materials for improved energy and environmental control systems.

The work described in this paper is being conducted at Oak Ridge National Laboratory (ORNL) in collaboration with work sponsored by the Department of Energy's Office of Fossil Energy at Argonne National Laboratory (ANL)[1] and Lawrence Berkeley Laboratory (LBL)[2] and in concert with directly related activities that are part of the Office of Basic Energy Sciences' Center of Excellence for the Synthesis and Processing of Advanced Materials. These cooperative efforts allow the integration of several advanced and, in some cases, unique characterization, modeling, and coating/deposition techniques so as to systematically investigate the relationships among corrosion performance, bulk composition, and surface oxide chemistry, structure, adherence, and elastic and plastic properties. However, in order to effectively pursue these types of study, it is necessary to first determine the effects of alloy composition, microstructure, surface condition, etc. on high-temperature oxidation behavior and associated scale integrity and spallation tendencies for a particular system. This paper presents initial results in this regard with respect to alumina scales on iron-aluminum alloys using thermal cycling under oxidizing conditions to gauge scale integrity in terms of gravimetric data and microstructural characterization. A similar characterization effort will then be conducted for as-deposited alumina on similar substrates.[2]

This work will ultimately include several model material systems, which are defined as ones that develop, upon oxidation, slowly growing, chemically stable surface oxides that offer the potential for protection of the metal from rapid reaction at high temperatures and show a substantial sensitivity to small additions of certain alloying elements. Alumina on iron-aluminum alloys appeared to satisfy these criteria[3] and this system was chosen as the initial one for study.

EXPERIMENTAL PROCEDURES

Three iron aluminides were studied. Their compositions and common designations are listed in Table 1. Ingots of these alloys were prepared by arc melting and casting. These were then rolled to a final thickness of between 0.8 and 1.3 mm. Rectangular specimens (typically 12 x 10 mm) were prepared from these sheets. The surface finish was either as-ground (600 grit, SiC paper) or polished (0.3 or 1 μm, alumina paste).

Gravimetric measurements under thermal cycling conditions were used to establish overall corrosion behavior at 1000°C. These cyclic oxidation experiments were conducted in static air by exposing coupons in individual pre-annealed alumina crucibles to a series of (typically) 24-h exposures. At the end of each exposure period, the crucibles were taken

Table 1. Compositions of iron-aluminum alloys used in this study.

Alloy Designation	Concentration[a] (at. %)				
	Al	Cr	Zr	Nb	Other
FA186	28	5			
FA129	28	5	-	0.5	0.2 C
FAL	28	5	0.1	-	0.05 B

[a] Balance is Fe.

from the furnace hot zone into the ambient atmosphere in about 2 min. Both the weight of the specimen, W_S, and that of any spalled scale, W_O (as collected in the crucible holding the coupon), were measured prior to the start of each experiment and after every thermal cycle. In this way, the total reacted mass due to oxidation, W_t, where

$$W_t = \Delta W_S + \Delta W_O, \quad (1)$$

could be measured as a function of oxidation time. Several of the oxidized coupons were examined by scanning electron microscopy (SEM). Two plan-view scale specimens for transmission electron microscopy were prepared from cyclically oxidized FAL and FA129.

RESULTS

Cyclic oxidation results for duplicate FAL specimens with 600 grit surface finishes are shown in Fig. 1. Both ΔW_S and ΔW_O (filled and open symbols, respectively) are plotted versus time; each data point represents one thermal cycle. Note that the weight of spalled material was usually small. In contrast, significant amounts of spalled material were measured for cyclically oxidized FA129 (Fig. 2) and FA186 (Fig. 3). For both of these alloys, ΔW_O was consistently greater than ΔW_S. Comparing Figs. 2 and 3 with Fig. 1, and referring to eq. 1, the total reacted mass due to oxidation (W_t) is therefore significantly greater for FA129 and FA186, as shown in Fig. 4.

Distinct differences in the surface appearance of the respective oxidized iron-aluminide alloys were observed. Visual examination revealed a uniformly dark gray product on the FAL and a lighter, powdery scale on the FA129 and (based on substantially fewer observations) FA186. As typified by the representative SEM micrographs in Fig. 5, the oxidized ground FA129 surfaces exhibited areas of bare metal from where the oxide product had completely spalled and fragmented, loosely-adherent pieces of scale. In contrast, the

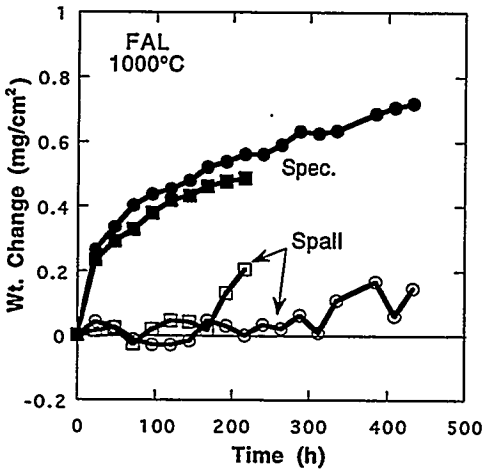

Fig. 1. Weight change versus time for FAL specimens cyclically oxidized in air at 1000°C. Each point represents one thermal cycle. Closed and open symbols represent weight changes of the specimen and spalled material, respectively. The specimens had a 600 grit surface finish.

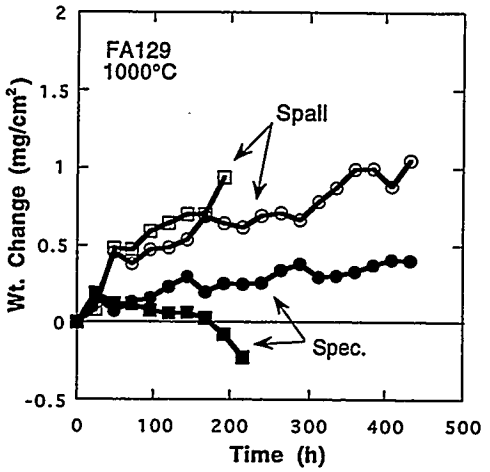

Fig. 2. Weight change versus time for FA129 specimens cyclically oxidized in air at 1000°C. Each point represents one thermal cycle. Closed and open symbols represent weight changes of the specimen and spalled material, respectively. The specimens had a 600 grit surface finish.

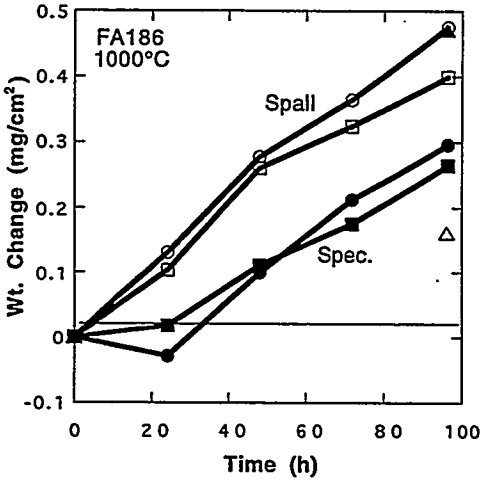

Fig. 3. Weight change versus time for FA186 specimens cyclically oxidized in air at 1000°C. Each point represents one thermal cycle. The triangles are for a specimen that was exposed for one 96-h cycle. Closed and open symbols represent weights of the specimen and amount of spalled material, respectively. The specimens had a 1 μm surface finish. The specimens represented by the circles and triangles were in the as-rolled condition prior to exposure. The squares indicated an annealed condition.

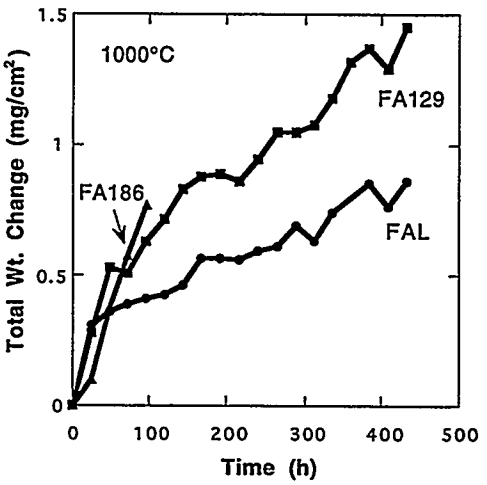

Fig. 4. Total weight change (weight of specimen plus that of spalled material) versus time for FAL, FA129, and FA186 specimens cyclically oxidized in air at 1000°C. Each point represents one thermal cycle.

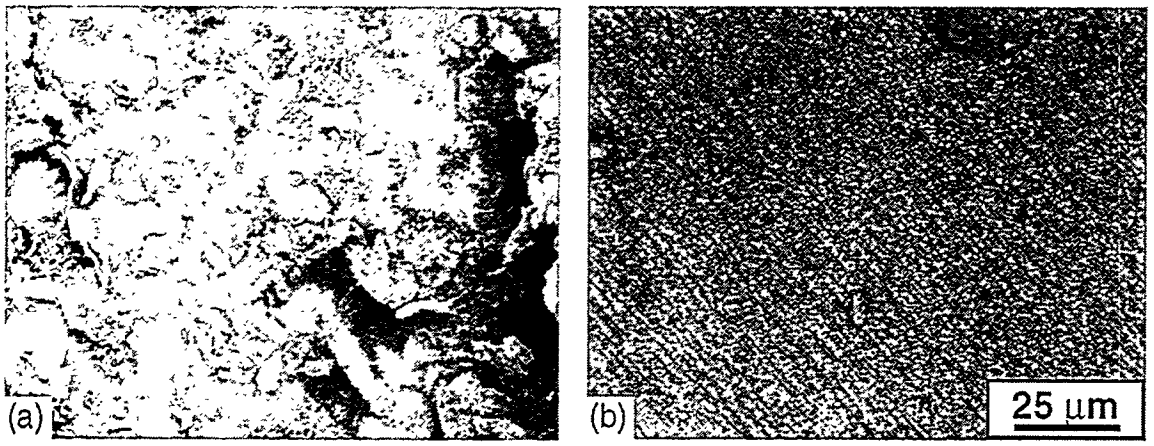

Fig. 5. SEM micrographs of ground (600 grit) iron-aluminum alloys that were oxidized for 48 h (2 24-h cycles) in air at 1000°C. (a) FA129 (b) FAL.

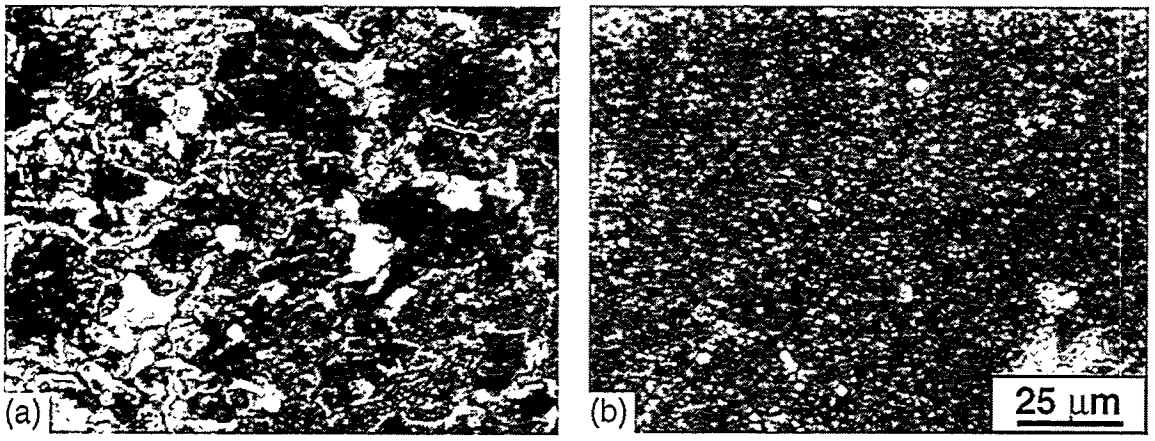

Fig. 6. SEM micrographs of polished (0.3µm) iron-aluminum alloys that were oxidized for 48 h (2 24-h cycles) in air at 1000°C. (a) FA129 (b) FAL.

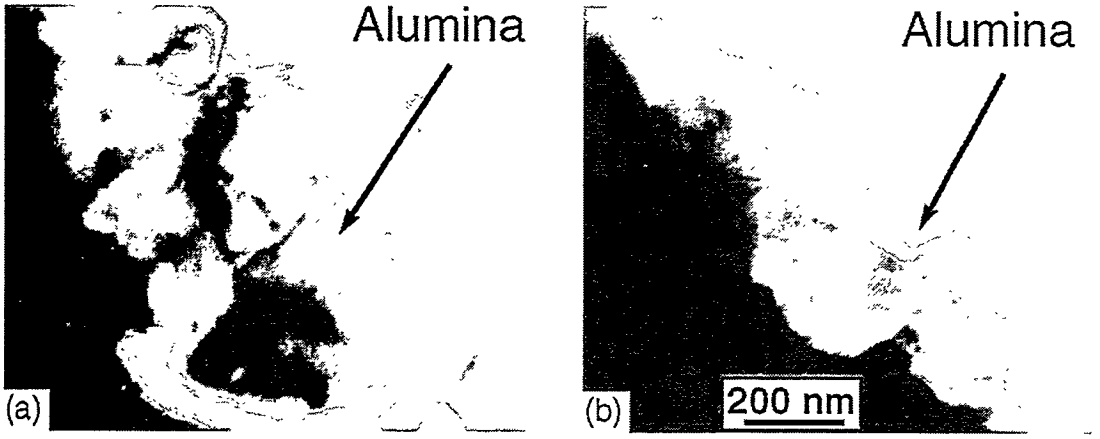

Fig. 7. TEM micrographs of iron-aluminum alloys that were oxidized for 48 h (2 24-h cycles) in air at 1000°C. (a) FA129 (b) FAL.

surface oxides grown on ground FAL were nodular and adherent. In this case, oxide appeared to nucleate along grinding marks - see Fig. 5b. These macro- and microscopic differences were observed regardless of exposure time. The surfaces resulting from cyclic oxidation exposures with specimens that first were polished to a finish of either 0.3 or 1.0 μm showed scale characteristics somewhat different from those observed for the ground specimens. As shown in Fig. 6, there was some, albeit small, areas of adherent scale on FA129, and a finer, less nodular, adherent surface oxide on FAL. Transmission electron microscopy of plan-view scales formed on FAL and FA129 showed very fine-grained oxides (approximately 200 nm) in both cases (Fig. 7).

Weight change measurements for polished specimens of FAL are compared to those for ground surfaces in Fig. 8. The ground specimens had slightly higher specimen weight gains, but all the mass changes shown in Fig. 8 are relatively small. With either type of surface finish, the weights of spalled material were substantially less than the respective changes in specimen weight. For FA129, the ΔW_o of a polished specimen was less than those of the ground ones (Fig. 9), which is consistent with the microscopy results described above. Polished specimens of FA186 were exposed in as-rolled and annealed (1000°C, 1 h) conditions. As shown in Fig. 3 (circles and triangles - as-rolled, squares - annealed), the differences in the gravimetric data due to starting microstructural condition was negligible.

Figure 8 also shows that the gravimetric data for FAL is cycle independent. Two FAL specimens with a 1 μm surface finish that were exposed for 96 h had identical weight changes despite the fact that one had four thermal cycles (square with cross symbols) and the other just one (filled square). In contrast, as shown in Fig. 3, the weight change data for FA186 did depend on the number of cycles - a specimen that was exposed for 96 h prior to cooling to room temperature (triangles) showed substantially different ΔW_s and ΔW_o than those measured for specimens of this alloy that underwent four 24-h thermal cycles from 1000°C (circles and squares).

DISCUSSION

Referring to eq. 1, the principal difference between FAL and the other two iron aluminides was in the weight of spalled scale, ΔW_o. Alloys FA129 and FA186 showed substantial scale spallation during cooling from the oxidation temperature at the end of most exposure periods. On the other hand, W_o for FAL was usually negligible (Fig. 1). These results, which were replicated for several specimens of each composition, are consistent with

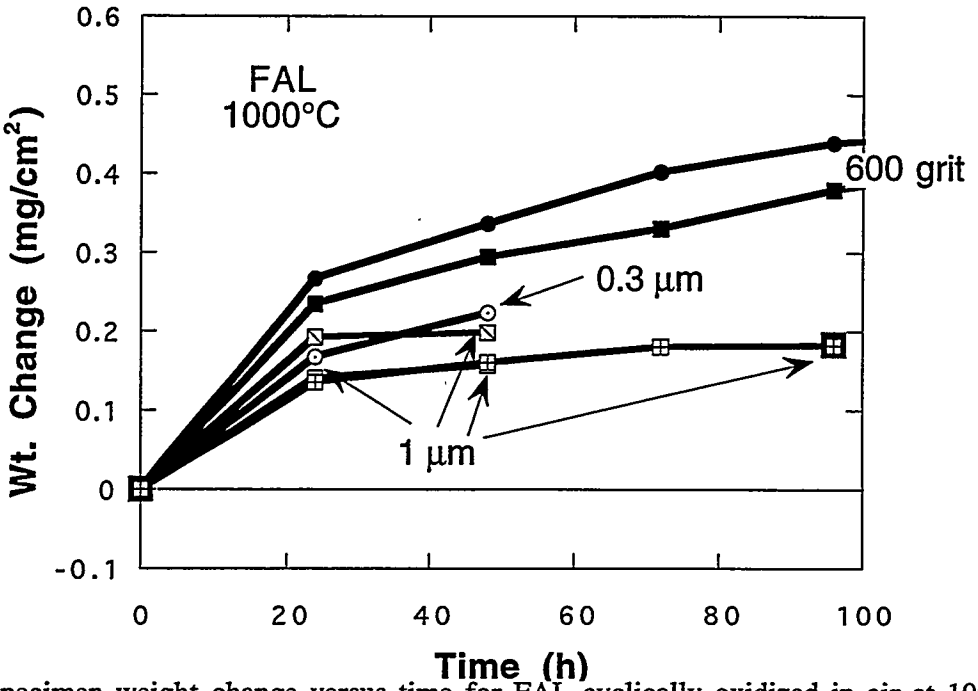

Fig. 8. Specimen weight change versus time for FAL cyclically oxidized in air at 1000°C. Each point represents one thermal cycle. The specimens had either ground (600 grit) or polished (0.3 or 1 µm) starting surfaces as indicated.

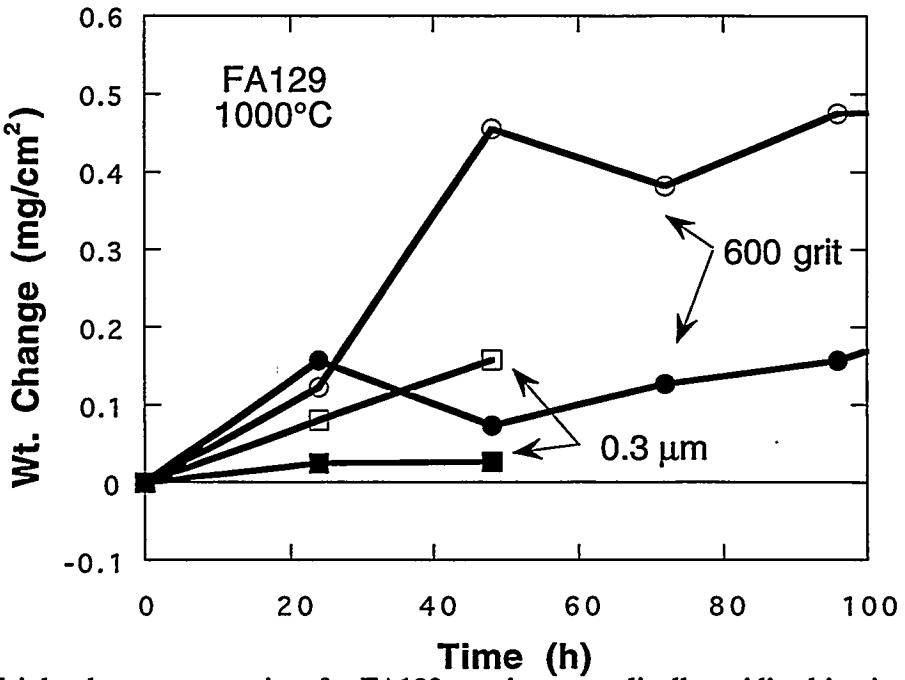

Fig. 9. Weight change versus time for FA129 specimens cyclically oxidized in air at 1000°C. Each point represents one thermal cycle. The specimens had either ground (600 grit) or polished (0.3) starting surfaces as indicated. Closed and open symbols represent weight changes of the specimen and spalled material, respectively.

earlier, preliminary studies showing that zirconium had a beneficial effect on the adherence of scales grown on Fe_3Al alloys at both higher (1300°C)[4] and lower (900°C)[5] temperatures. Zirconium is known to also have a positive effect on scale adherence in other alumina-forming alloys systems (see, for example, ref. 6), but the mechanism by which it provides a beneficial influence in iron aluminides has not been demonstrated. There is some electron microscopy evidence that zirconium ions accumulate in the alumina scale,[7] but these observations do not definitively prove any one particular model for the effect of this element on scale adherence. As the initial transmission electron microscopy revealed that the surface oxides on both FAL and FA129 were fairly fine grained (Fig. 7), the effect of zirconium does not appear to be due to a major modification of the bulk scale microstructure. However, this result is preliminary; the influence of zirconium on scale and interface characteristics will be investigated in more detail using microscopy and other analytical techniques available at ORNL, ANL and LBL.

For spallation-resistant alloys, there should be little influence of cycle frequency on weight-change measurements unless substantial scale cracking occurs. Therefore, the finding that the measured weight changes of FAL undergoing cyclic oxidation at 1000°C are not frequency dependent (Fig. 8) is consistent with the lack of any observations of spallation or visible scale cracking. On the other hand, because of the spallation susceptibilities of FA129 and FA186, the gravimetric results for these alloys do show a dependence on the number of thermal cycles for a given oxidation period (see, for example, Fig. 3). Most of the scale damage is due to thermal cycling; in Fig. 3, W_o is about the same regardless of whether the first cycle was after 24 or 96 h of exposure.

As mentioned above, the present work represents the initial stage in defining the fundamental correlations among properties, structure, and mechanical reliability of the surface oxides as they relate to corrosion performance. This first step includes determination of the effects of starting alloy microstructure, composition, and surface finish on high-temperature cyclic oxidation behavior and associated scale integrity and spallation susceptibility. The results of this work are being used to prepare suitable thermally grown oxides on iron-aluminum alloys for examination by a variety of characterization techniques, including analytical electron microscopy, SEM observation of cracking behavior using a bending stage, and nanoindentation (to determine elastic and plastic properties as well as fracture toughness). In this regard, the oxidation results described above have important implications for the use of these alloys as model materials for such a comprehensive study of the microstructure and properties of alumina scales. The use of polished (rather than just

ground) surfaces on the specimens of FAL results in a more uniform scale upon oxidation such that these characterization techniques can be facilitated. Furthermore, whereas the scales formed on FA129 with a 600 grit surface finish (Fig. 5a) were wholly unsuitable for such analyses, there appears to be some possibility in obtaining information from the pieces of sound, adherent oxide remaining on polished surfaces of this alloy (see, for example, Fig. 7a). This could be a key part of subsequent study as it may be just as crucial to obtain information from spallation-prone scales (in this case, those formed on FA129 and FA186) as it is for adherent surface oxides (such as those grown on FAL). As such, these results may well prove to be an important step in specifying the microstructural, chemical, and mechanical differences of scales exhibiting different degrees of adherence to their alloy substrates.

The present findings on scale damage resulting from cyclic oxidation represent the traditional way of assessing corrosion performance and the mechanical reliability of scales. Because of this, they provide the means of linking oxidation performance of this system with the results forthcoming from use of the characterization techniques listed above. In addition, this study of alumina scales grown on iron-aluminum alloys will form the basis for comparison with results form similar work with as-deposited alumina on the same substrates.

SUMMARY AND CONCLUSIONS

As a part of the initial effort in defining the fundamental relationships among properties, structure, and mechanical behavior of surface oxides that provide corrosion protection at high temperatures, the integrity of alumina scales formed on iron-aluminum alloys during cyclic oxidation was characterized by gravimetric measurements and microscopy. Specimens with ground or polished surface finishes were prepared from three iron-aluminum compositions. Scales were thermally grown using a series of (typically) 24 h exposures to air at 1000°C. Gravimetric data and scanning electron microscopy revealed little scale damage and substantially better adhesion of the alumina grown on the alloy containing zirconium. Thermal cycling caused extensive disruption and spallation of the scales formed on the other two alloys. Transmission electron microscopy showed that scales grown on spallation-resistant and spallation-susceptible iron-aluminum alloys were both fine-grained. Use of polished (rather than just ground) specimens resulted in scales that were more amenable to characterization.

ACKNOWLEDGMENTS

The authors thank M. Howell for experimental support and J. R. DiStefano, B. A. Pint, and I. G. Wright for their thoughtful reviews of the manuscript. This research was sponsored by the Fossil Energy Advanced Research and Technology Development (AR&TD) Materials Program and the Division of Materials Science, U S. Department of Energy, under contract DE-AC05-84OR21400 with Martin Marietta Energy Systems, Inc.

REFERENCES

1. K. Natesan, "Mechanically Reliable Coatings and Scales for High-Temperature Corrosion Resistance," these proceedings.

2. I. W. Brown, "Plasma Synthesis of Alumina Films on Metal and Ceramic Substrates," these proceedings.

3. P. F. Tortorelli and J. H. DeVan, pp. 257-70 in Processing, Properties, and Applications of Iron Aluminides, J. H. Schneibel and M. A. Crimp (eds.), The Minerals, Metals, and Materials Society, Warrendale, PA, 1994.

4. J. H. DeVan, P. F. Tortorelli, and M. J. Bennett, pp. 309-20 in *Proc. Eighth Annual Conf. Fossil Energy Materials*, N. C. Cole and R. R. Judkins (comp.), CONF-9405143, U. S. Department of Energy, August 1994.

5. J. H. DeVan, P. F. Tortorelli, and U. K. Abdali, "Environmental Effects on Iron Aluminides," pp. 216-226 in *Proc. Sixth Annual Conf. Fossil Energy Materials*, N. C. Cole and R. R. Judkins (comp.), U. S. Department of Energy, July 1992.

6. J. Doychak, pp. 977-1016 in Intermetallic Compounds: Vol. 1, Principles, J. H. Westbrook and R. L. Fleischer (eds.), John Wiley & Sons, New York, 1994.

7. J. A. Horton, Oak Ridge National Laboratory, unpublished results.

WELDING AND MECHANICAL PROPERTIES OF CAST FAPY (Fe-16 at. % Al-BASED) ALLOY SLABS

V. K. Sikka, G. M. Goodwin, D. J. Alexander, and C. R. Howell

INTRODUCTION

The low-aluminum-content iron-aluminum program deals with the development of a Fe-Al alloy with aluminum content such as a produce the minimum environmental effect at room temperature. The FAPY is an Fe-16 at. % Al-based alloy developed at the Oak Ridge National Laboratory as the highest aluminum-containing alloy with essentially no environmental effect.[1] The chemical composition for FAPY in weight percent is: aluminum = 8.46, chromium = 5.50, zirconium = 0.20, carbon = 0.03, molybdenum = 2.00, yttrium = 0.10, and iron = 83.71. The cast ingots of the alloy can be hot worked by extrusion, forging, and rolling processes. The hot-worked cast structure can be cold worked with intermediate anneals at 800°C. Typical room-temperature ductility of the fine-grained wrought structure is 20 to 25% for this alloy. In contrast to the wrought structure, the cast ductility at room temperature is approximately 1% with a transition temperature of approximately 100 to 150°C, above which ductility values exceed 20%. The alloy has been melted and processed into bar, sheet, and foil. The alloy has also been cast into slabs, step-blocks of varying thicknessess, and shapes.

The purpose of this section is to describe the welding response of cast slabs of three different thicknesses of FAPY alloy. Tensile, creep, and Charpy-impact data of the welded plates are also presented.

Discussion of Current Activities

Casting

For the welding studies, the FAPY alloy was used in the as-cast condition, prepared by vacuum-induction melting, and cast in graphite molds measuring 100 by 150 mm (4 by 6 in.) in length and having thicknesses of 12, 25, and 51 mm (0.5, 1, and 2 in.). All three plates had good as-cast surfaces. The welding studies were conducted on the plates in the as-cast condition.

Weld Production

Weld joints were prepared by sawing as shown in Fig. 1. The included angle of 60° in the double-vee groove geometry was used for all three slab thicknesses and is typical of industrial practice for plate welding.

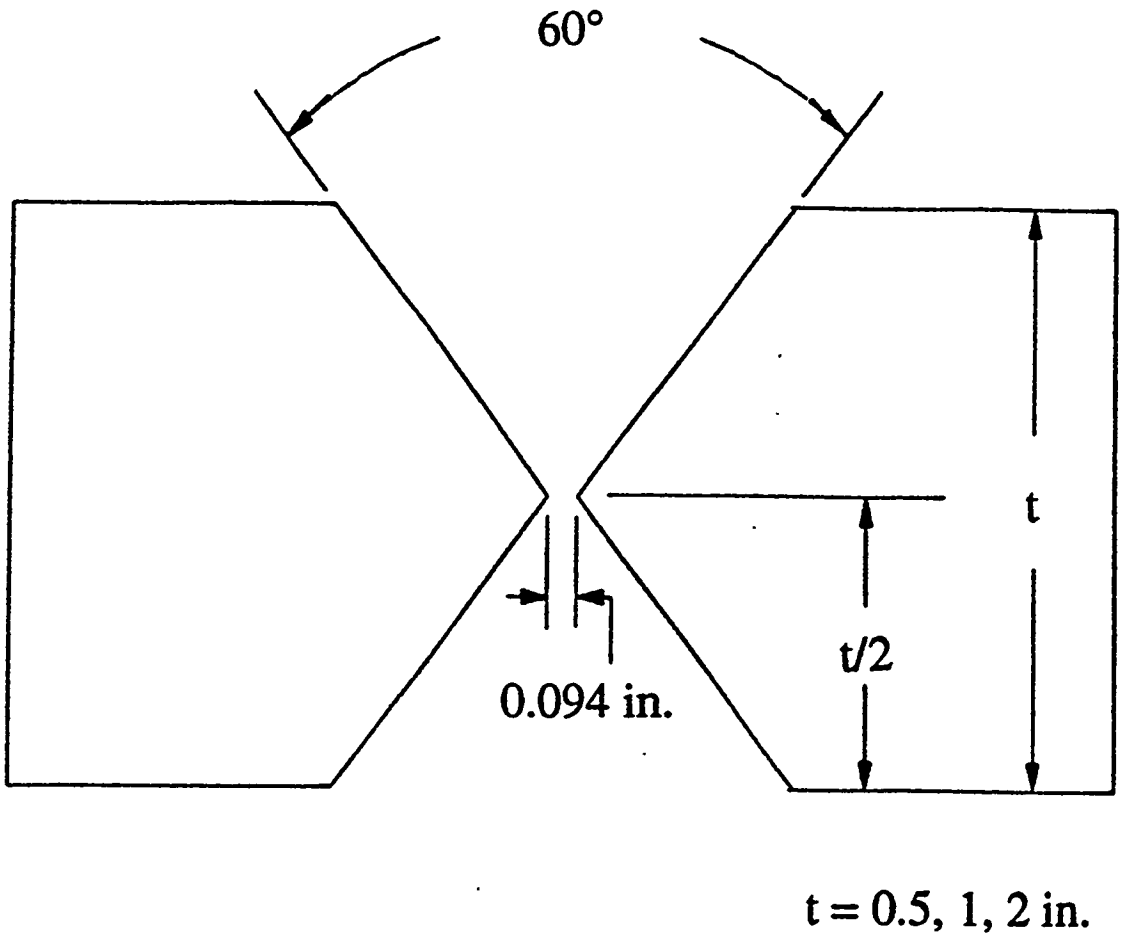

Fig. 1. Joint geometty for FAPY cast slab welds.

Weld wire of 3.2 mm (0.125 in.) diam with a matching composition of FAPY alloy was used for all weldments using the manual gas tungsten arc (GTA) process. The joint surfaces and filler wire were cleaned by wire brushing and solvent degreasing with acetone. A summary of the welding parameters is shown in Table 1.

Preheat, when used, was accomplished with an oxyacetylene torch. Interpass temperature was maintained at 350°C minimum. Postweld heat treatment (PWHT), when used, was done immediately following welding in an air furnace followed by free cooling in still air.

Table 1. Welding parameters for cast FAPY alloy slabs

Process:	Manual gas tungsten arc
Joint geometry:	Double-vee groove, 60° included angle
Base metal:	Cast slabs [100 ¥ 150 ¥ 12, 15, and 51 mm (4 × 6 × 0.5, 1, and 2 in.) thicknesses]
Filler metal:	3.2-mm (0.125 in.) -diam rod, matching composition
Weld current:	100 to 175 A direct current electrode negative
Weld voltage:	10 to 12 V
Torch gas:	Argon, 15 cfh (7.1 L/min)
Backing gas:	Argon, 15 cfh (7.1 L/min)
Approximate number of passes (alternating sides):	12-mm (0.5-in.) slab: 6 25-mm (1-in.) slab: 25 51-mm (2-in.) slab: 65

Completed weldments were examined for possible defects using liquid-dye penetrant. A summary of the inspection results is shown in Table 2. End sections were removed from each weldment for optical metallography.

Table 2. Inspection results of cast FAPY alloy slab welds

Temperature, °C		Slab thickness, mm (in.)		
Preheat	Postheat	12 (0.5)	25 (1)	51 (2)
350	750	No cracks	No cracks	No cracks
200	750	--	--	No cracks
20	20	No cracks	Cracks	--

Mechanical Properties

The welded slabs were cut up for mechanical property determinations. The 12-mm (0.5-in.) -thick plates were used for Charpy-impact testing. The 25- and 51-mm (1- and 2-in.) -thick plates were used for tensile and creep properties. The specimen cut-up diagrams for the Charpy, tensile, and creep specimens are shown in Fig. 2.

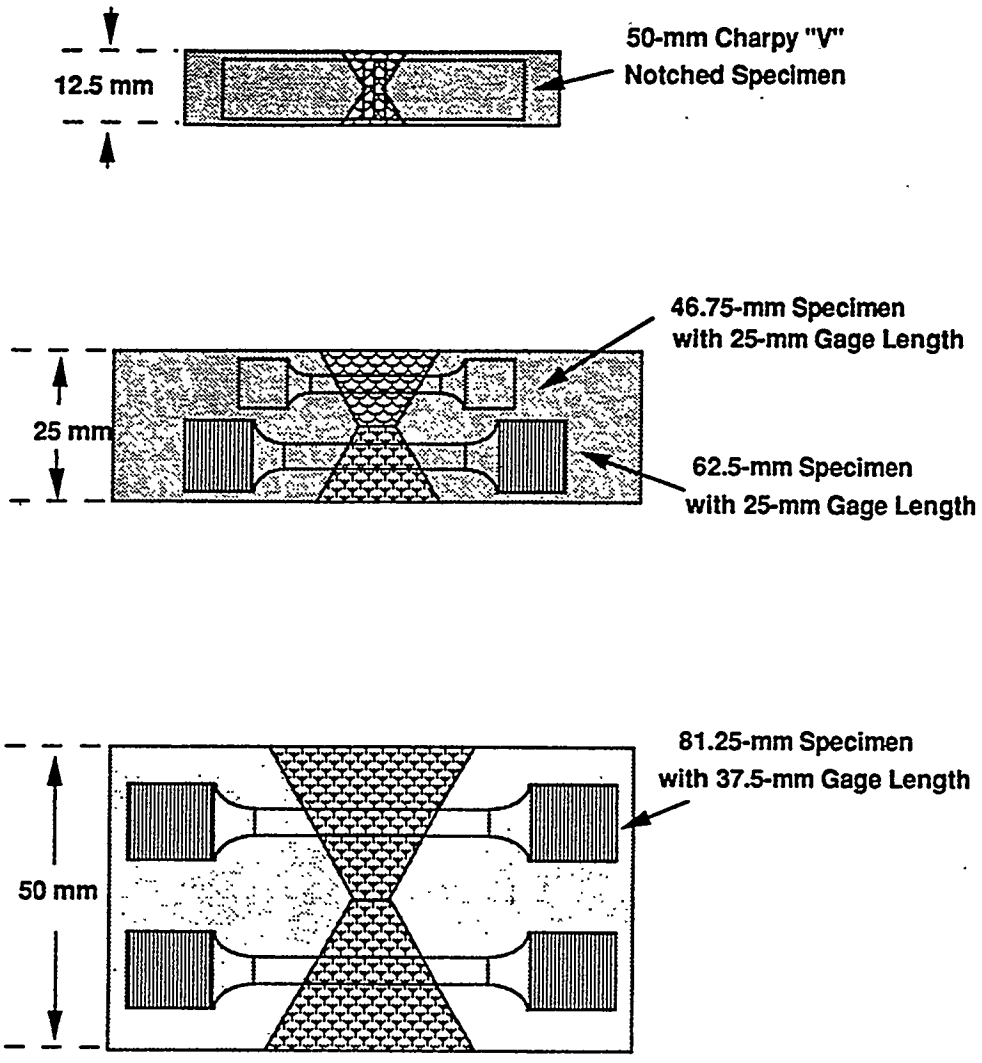

Fig. 2. Schematic showing the location and size of mechanical property specimens machined from welded slabs of FAPY alloy.

Tensile Properties

The tensile data from room temperature to 800°C for the 25- and 51-mm (1- and 2-in.) -thick welded plates are summarized in Table 3. The strength and ductility data of the weldments are plotted and compared with the base-metal data of the cast slabs in Figs. 3 through 6. The following observations are possible from these figures:

1. The 0.2% yield strength of the weldment specimens is essentially the same as the base-metal values for the entire temperature range. This is true for specimens taken from both the 25- and 51-mm (1- and 2-in.) -thick welded plates.

Table 3. Tensile properties of weldment specimens machined from the cast-welded 25- and 51-mm (1- and 2-in.) -thick slabs of FAPY alloy

Specimen No.	Test temperature (°C)	Heat-treatment temperature (°C)		Yield strength (MPa)	Tensile strength (MPa)	Total elongation (%)	Reduction of area (%)
		Preheat	Postheat[a]				
1L[b]	23	350	750	70.91	70.91	1.79	0.08
2L[b]	100	350	750	60.31	79.81	22.88	32.53
3L[b]	200	350	750	47.91	75.07	24.32	44.38
4L[b]	400	350	750	41.19	76.78	25.58	42.89
5L[b]	600	350	750	39.26	39.50	46.16	74.71
6L[b]	800	350	750	11.82	12.22	78.24	83.80
11L[c]	23	200	750	65.39	65.39	0.91	0.00
12L[c]	50	200	750	64.43	65.14	1.62	0.40
13L[c]	100	200	750	57.09	73.77	9.20	9.28
14L[c]	200	200	750	45.36	71.94	20.46	50.37
15L[c]	400	200	750	37.04	73.36	26.35	41.20
16L[c]	600	200	750	37.81	38.93	43.74	72.05
17L[c]	800	200	750	--	11.53	64.13	80.37

[a]Time at temperature: 1 h.
[b]Specimen gauge length: 25 mm (1 in.); strain rate: 3.3×10^{-3}/s.
[c]Specimen gauge length: 51 mm (2 in.); strain rate: 2.2×10^{-3}/s.

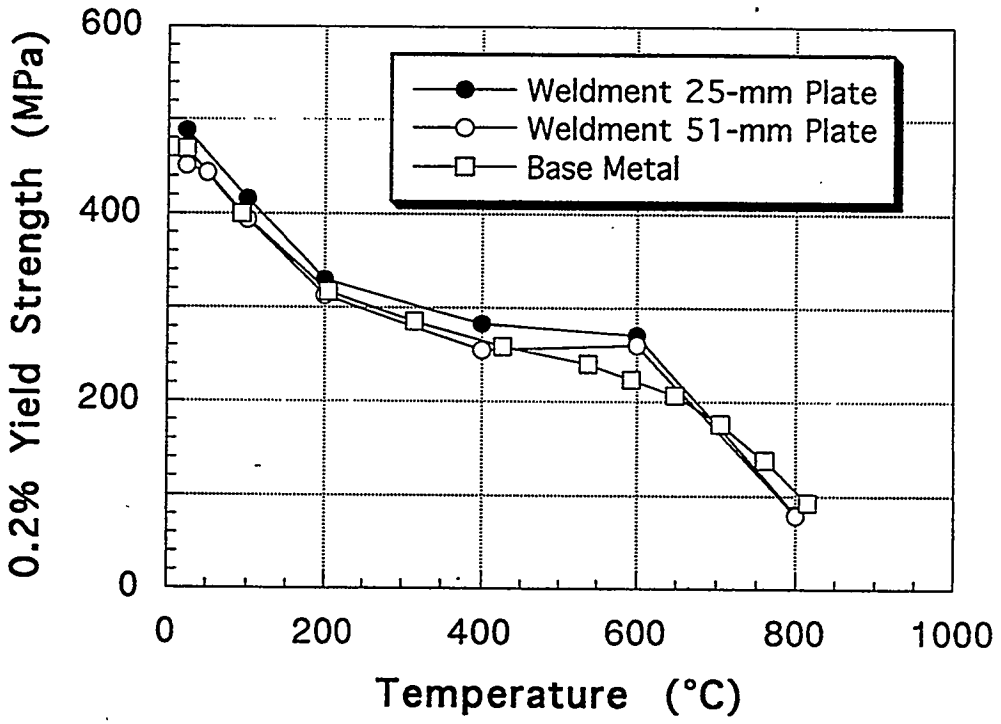

Fig. 3. Comparison of 0.2% yield strength of weldment specimens with base metal of FAPY alloy. The base-metal data are from a previous study on cast slab.

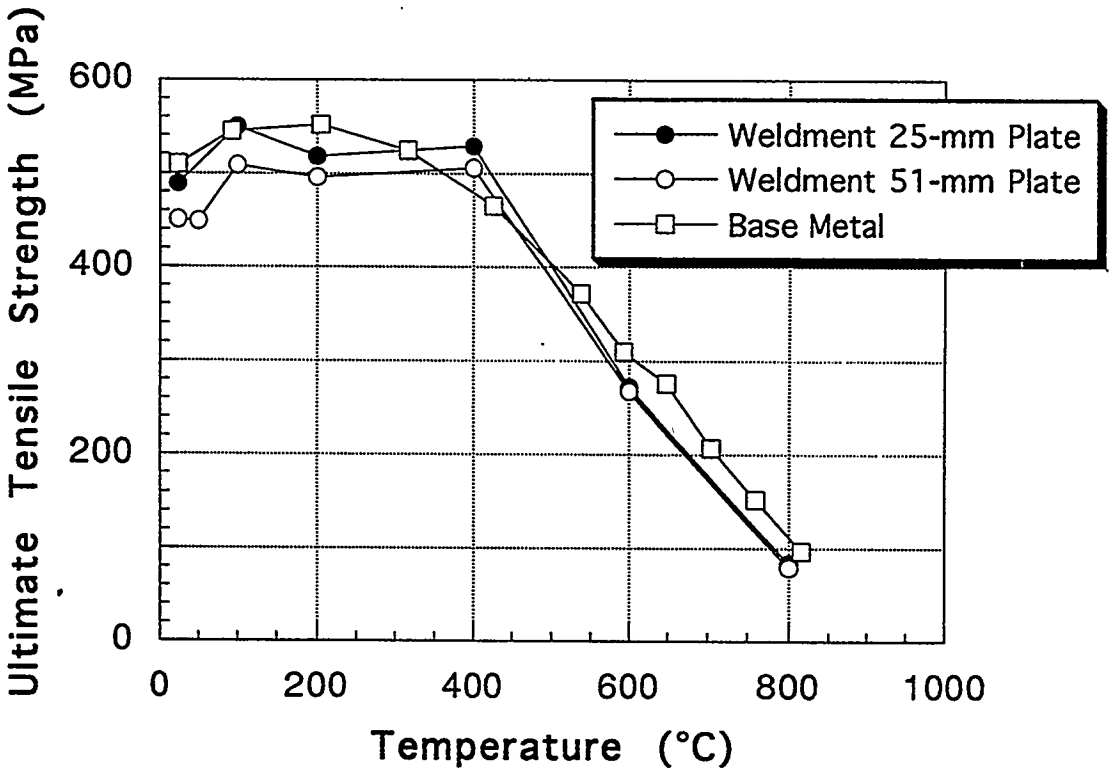

Fig. 4. Comparison of ultimate tensile strength of weldment specimens with base metal of FAPY alloy. The base-metal data are from a previous study on cast slab.

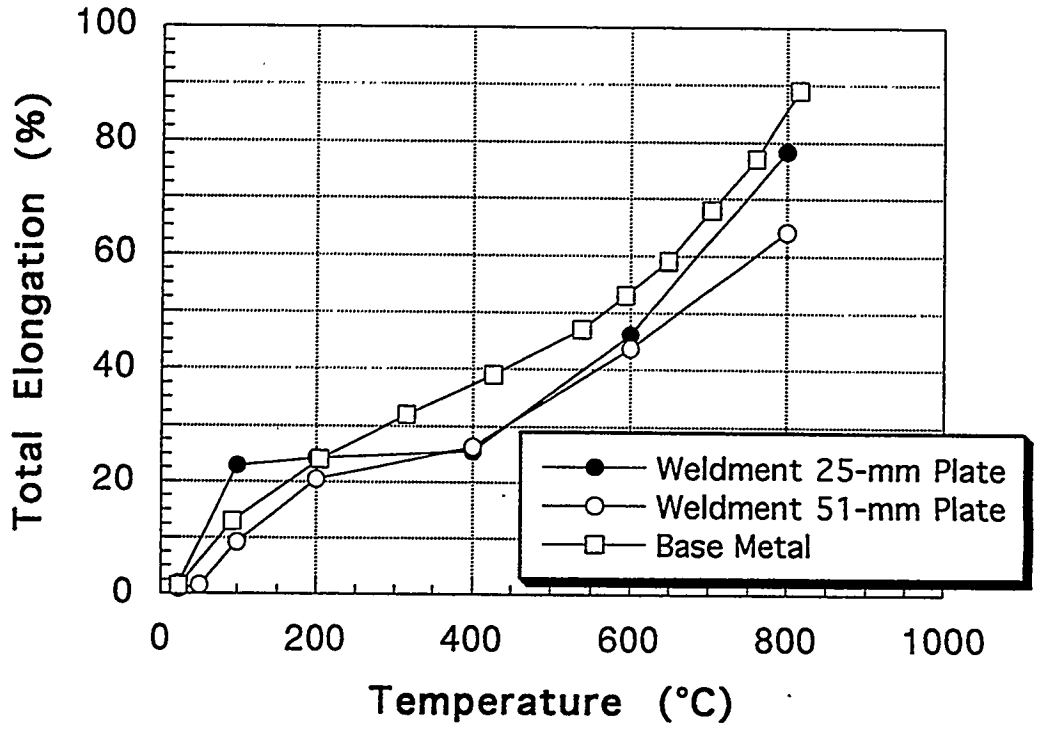

Fig. 5. Comparison of total elongation of weldment specimens with base metal of FAPY alloy. The base-metal data are from a previous study on cast slab.

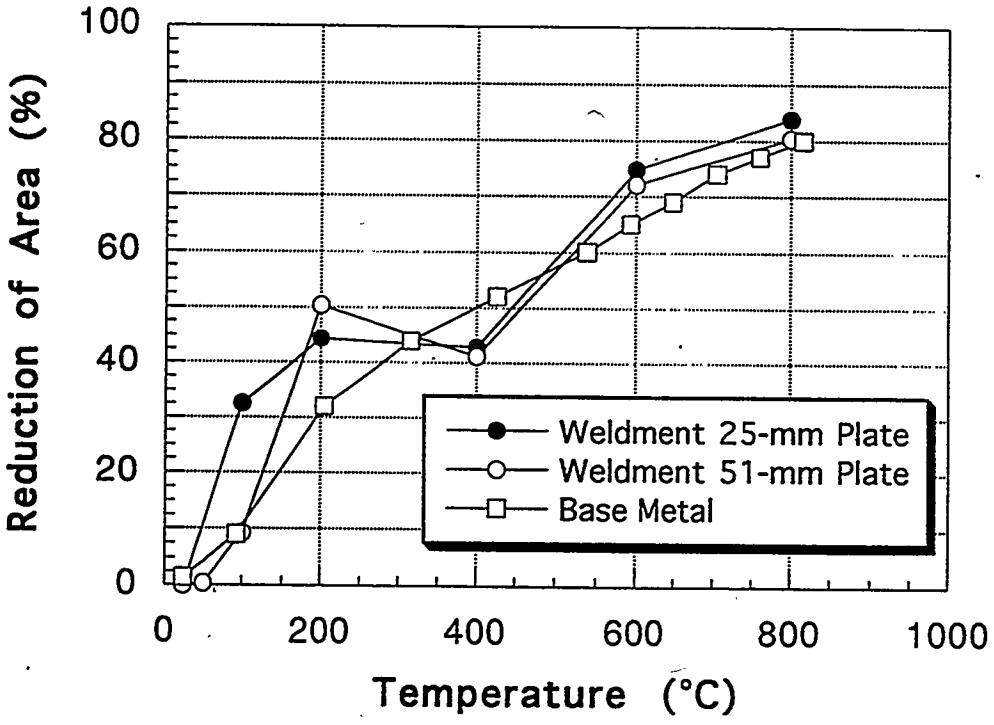

Fig. 6. Comparison of reduction of area of weldment specimens with base metal of FAPY alloy. The base-metal data are from a previous study on cast slab.

2. The ultimate tensile strength of the weldment specimens from the 51-mm (2-in.) -thick plate showed lower values than the base metal in the test-temperature range up to 200°C. This is the same temperature region where ductility of both base metal and weldments is low (see Figs. 5 and 6). The observed results in Fig. 4 imply that the weldment specimens from the 51-mm (2-in.) -thick plates are slightly more brittle in this temperature range than base metal or 25-mm (1-in.) -thick plate.
3. The general trend of total elongation and reduction of area of weldments is the same as that for the base metal (see Figs. 5 and 6).

Creep Properties

The creep data on three weldment specimens machined from 25-mm (1-in.) -thick welded plate are summarized in Table 4. The creep-rupture data on the weldment specimens are compared with the previously developed data on as-cast and wrought base-metal specimens in Fig. 7 which shows that although limited in number, the short-term data on weldment specimens match the data on base-metal, as-cast, and wrought specimens. It should be recognized that long-term data are required to further confirm these observations.

Table 4. Creep properties of weldment specimens*a* machined from the cast-welded 25-mm (1-in.) -thick slab of FAPY alloy

Test No.	Specimen No.	Test temperature (°C)	Stress (MPa)	Time to rupture (h)	Rupture elongation (%)	Reduction of area (%)	Creep rate (%/h)
28312	7L	550	207	2.2	19.20	64.94	--
28321	8L	600	138	2.8	30.38	67.08	--
28314	9L	650	69	13.6	55.96	75.89	--
28313	10L	700	21.69	1389.3	48.90	85.90	--

[a]Weldment prepared with a preheat of 350°C and a postweld heat treatment at 750°C for 1 h.

Charpy-Impact Tests

Full-size Charpy-impact specimens were machined from two welded plates of 12 mm (0.5 in.) thickness. One of the plates contained a weld in the as-welded condition, and the other one was given a PWHT at 750°C for 1 h. The schematic in Fig. 2 shows the cut-up schedule for the Charpy specimens. The crack growth was parallel to the welding direction (T-L orientation). The specimens were tested on a 325-J capacity impact tester, and the data are summarized in

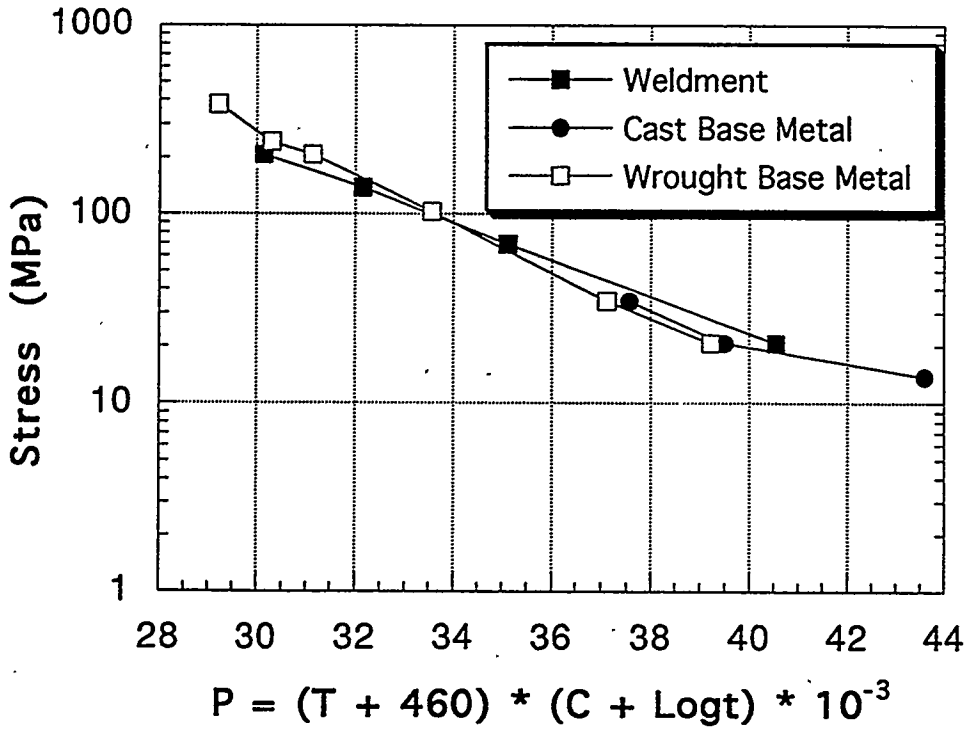

Fig. 7. Comparison of creep rupture properties of weldment specimens with the as-cast and wrought base-metal specimens.

Table 5. The data, plotted in Fig. 8, were fitted with a hyperbolic tangent function. The lower-shelf energy was fixed at 2 J and the upper-shelf energy was fixed at the value of the test at 400°C for each set of specimens (122 J for the as-welded specimens, 144 J for the postweld heat-treated specimens).

The results show that the PWHT does improve the toughness of the material. The ductile-to-brittle transition temperature, defined at an energy level midway between the upper- and lower-shelf energy levels, decreases from 245°C for the as-welded material to 200°C for the material that was given the postweld heat treatment, a 45°C improvement. The transition temperature is still quite high however. The upper-shelf energy also improves with heat treatment, increasing from 122 to 144 J. The specimens tested at 400°C showed completely ductile fracture, and they provide a good estimate of the upper-shelf energy, although only one specimen was tested for each material at high enough temperatures to give fully ductile fracture.

Table 5. Charpy-impact energy data on weldment specimens from 12-mm (0.5-in.) -thick plate of FAPY alloy

Test temperature (°C)	Charpy-impact energy			
	As welded		Postweld heat treated[a]	
	J	ft/lb	J	ft/lb
25	2	1.5	2.6	1.9
100	5.4	4.0	5.3	3.9
150	9.5	7.0	9.2	6.8
175	--	--	20.3	15.0
200	20.3	15.0	72.5	53.5
250	71.2	52.5	--	--
300	100.3	74.0	126.1	93.0
400	122.0	90.0	143.7	106.0

[a]Postweld heat treatment at 750°C for 1 h.

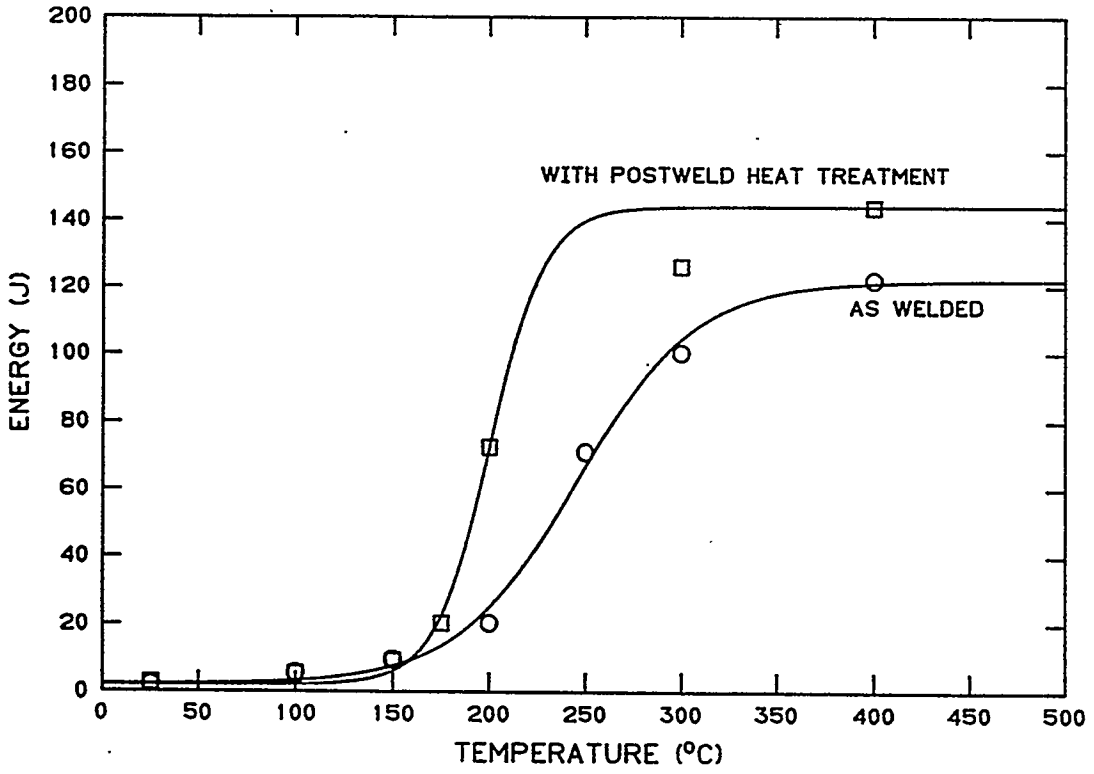

Fig. 8. Plot of Charpy-impact energy of weldment specimens from 12-mm- (0.5-in.-) thick cast plate of FAPY alloy. Postweld heat treatment was carried out at 750°C for 1 h.

The Charpy-impact energy data for the weldment specimens are compared with that of the wrought base-metal data in Fig. 9. This figure shows that the transition temperature is approximately 50° higher for the weldment specimens, and the upper-shelf energy is lower by approximately 100 J. The most likely cause for the higher transition temperature for the weldment specimens is their much coarser grain size as opposed to the wrought material.

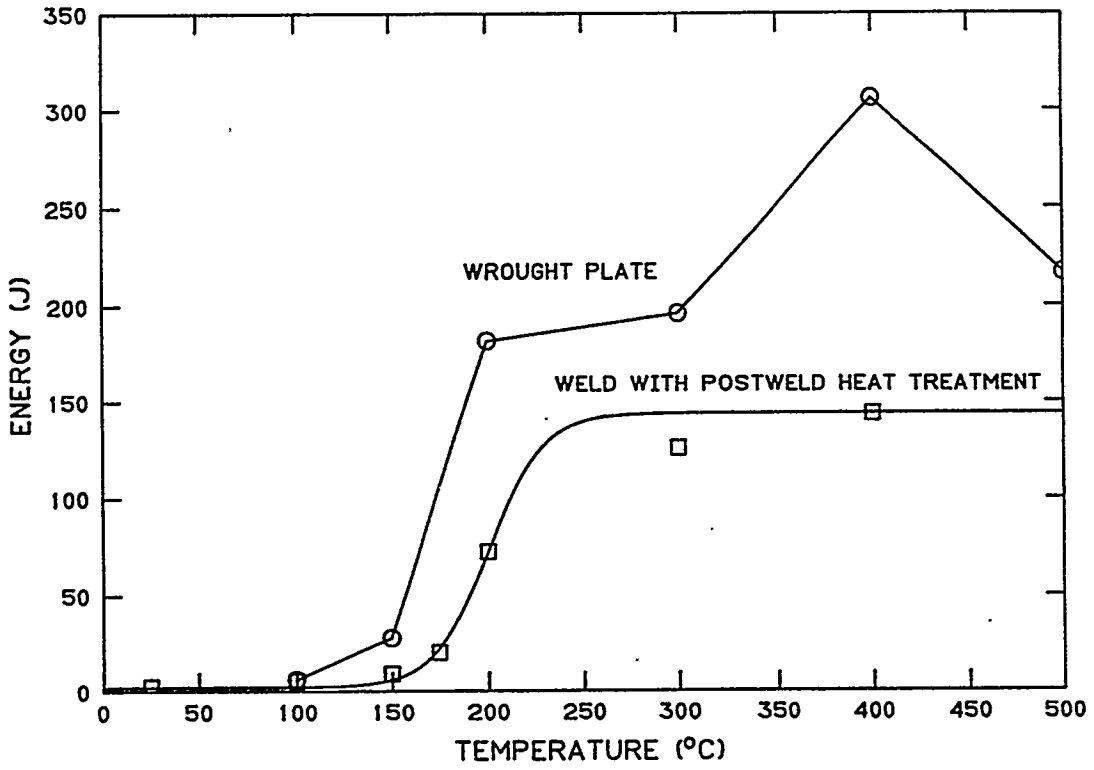

Fig. 9. Comparison of Charpy-impact energy data of weldment specimens with that of base-metal specimens in the wrought condition.

Microstructure and Hardness Data

In addition to the macroetched cross sections, photomicrographs of various regions of the weldment were also taken. The general observations from the weldment photomicrographs are: (1) the weld metal showed a coarse-grained structure similar to the cast base metal, and (2) the region identified as HAZ had an epitaxial grain growth of the base-metal grains into the weld metal.

The microhardness data of the base-metal, HAZ, and weld-metal regions show that they are essentially the same for plates of a given thickness (see Table 6). However, there is approximately a 10- to 20-dph point increase in hardness of thicker plates as opposed to a 12-mm (0.5-in.) -thick plate.

Table 6. Microhardness of base, weld, and heat-affected zone of welds in 12-, 25-, and 51-mm (0.5-, 1-, and 2-in.) -thick welded plates in the as-cast condition

Plate thickness (mm)	Microhardness (dph)			
	Base metal	Weld metal	Heat-affected zone	Base metal and heat-affected zone in unusual area
12	223 ± 4	227 ± 5	223 ± 7	--
25	238 ± 4	237 ± 6	243 ± 3	246 ± 6
51	233 ± 10	252 ± 7	238 ± 4	240 ± 11

DISCUSSION

The vacuum-induction-melted and as-cast plates of 12, 25, and 51 mm (0.5, 1, 2 in.) thicknesses were successfully welded using the GTA process. All of the welds used a filler wire of base-metal composition. The 12-mm (0.5-in.) -thick plate could be welded without a preheat. However, 25 mm (1 in.) and thicker sections required a preheat to make crack-free welds. The preheat temperature for the FAPY alloy can be as low as 200°C, which is no different than that required for most of the ferritic steels. In addition to preheat, a PWHT of 750°C is highly desirable for lowering the transition temperature and increasing the upper-shelf energy during Charpy-impact testing.

The microstructure of the starting plates was coarse due to being in the as-cast condition. For the thinner plate of 12 mm (0.5 in.) thickness, the grain structure was primarily columnar. However, for the plates of 25 and 51 mm (1 and 2 in.) thicknesses, some equiaxed structure was also present in addition to the columnar structure. The weld region also showed a coarse-grained microstructure similar to the cast structure of the base metal. Indications of epitaxial growth of base-metal grains into the weld region were observed. No distinct transition in microstructure was observed from the base- to the weld-metal regions. This observation was confirmed by noting essentially the same microhardness values for base-metal, HAZ, and the weld-metal region. The uniformity in microstructure and microhardness was also confirmed by the failure of

the tensile specimens in the middle of the gage section, which normally happens for a material of uniform properties.

The similarity in microstructure and microhardness of the base and weld metals yielded tensile properties of the weldment specimens to match the base-metal properties. A similar match was also observed for the creep-rupture properties. It is important to note that although the properties of the weldment specimens matched the base-metal properties in the as-cast condition, the ductility values for FAPY alloy are too low at temperatures ≤ 100°C.

An unusual event of cracking was observed in this weldment section of the 51-mm- (2-in.-) thick plate during the etching process to reveal its macrostructure. The acid-etching process is known to produce hydrogen, and it is this hydrogen that is believed to have caused the cracking. This cracking was observed only in the 51-mm (2-in.) -thick plate and not in the plates of 12 and 25 mm (0.5 and 1 in.) thicknesses. Since the hydrogen-related cracking typically requires the combination of stress and the presence of hydrogen, it is believed that a PWHT of 750°C was not adequate to relieve the welding stresses for the 51-mm (2-in.) -thick plate. However, the same PWHT must have been adequate for the thinner sections, which had lower welding stresses to start with because of their thinner sections. Thus, it is believed that a higher PWHT temperature than 750°C may be required for section sizes of ≥ 51 mm (2 in.). Additional work is required to establish the PWHT requirements as a function of section thickness for the FAPY alloy.

SUMMARY AND CONCLUSIONS

The as-cast plates of 12, 25, and 51 mm (0.5, 1, and 2 in.) thicknesses of FAPY alloy were welded using the GTA process and a 3-mm (0.125-in.) -diam filler wire of matching composition. Welds were made without any preheat and with preheats of 200 and 300°C. The crack-free welds could be prepared in 12-mm (0.5-in.) -thick plates. However, the thicker plates required a preheat for crack-free welds, and a temperature of 200°C was acceptable up to plate thickness of 51 mm (2 in.). The preheat temperature for thicker sections may be higher and needs to be determined. The PWHT at 750°C for 1 h was found to lower the transition temperature and increase the upper-shelf energy during Charpy-impact testing of the 12-mm- (0.5-in.-) thick welded plate. Thus, all the other weldment properties were determined in the postweld heat-treated condition. Tensile and creep properties of the weldment specimens matched the properties of the base metal. These results were explained on the basis that the microstructure and microhardness of the weld region were similar to the base metal.

Major conclusions from this study include:

1. The cast plates of the FAPY alloy can be welded by a commonly used GTA process. A filler wire of composition matching the base metal is acceptable. No preheat is required for plates of 12 mm (0.5 in.) thickness. Plates of ≥ 25 mm (1 in.) thickness require a preheat of at least 200°C. A PWHT at 750°C for 1 h is desirable to improve the Charpy-impact properties and to reduce the suceptibility of the weld to hydrogen-related cracking. A PWHT temperature of higher than 750°C is probably required to eliminate the hydrogen-related cracking in the 51-mm- (2-in.-) thick welds. However, a correlation of PWHT as a function of section thickness needs to be developed.
2. Tensile and creep properties of the weldment specimens matched that of the base metal. These results are explained on the basis that the microhardness and microstructure of the welds are very similar to the base metal.

FUTURE WORK

Additional work is required on welding of thicker sections of the FAPY alloy:

1. Prepare welds in a section thickness greater than 51 mm (2 in.), and determine the PWHT temperatures to eliminate hydrogen-related cracking. Macroetching solution can be used to determine the presence of hydrogen-related cracking.
2. Determine the effect of PWHT temperature on Charpy-impact properties. Use these data to select the optimum temperature for the best combination of transition temperature and upper-shelf energy.
3. Determine additional weldment creep tests to obtain data for rupture times exceeding 1000 h.

REFERENCES

1. S. Vyas, S. Viswanathan, and V. K. Sikka, "Effect of Aluminum Content on Environmental Embrittlement in Binary Iron-Aluminum Alloys," *Scr. Metall. Mater.* **27**, 185-190 (1992).

THE INFLUENCE OF PROCESSING ON MICROSTRUCTURE AND PROPERTIES OF IRON ALUMINIDES

R. N. Wright and J. K. Wright

Idaho National Engineering Laboratory
Lockheed Idaho Technologies Company
Idaho Falls, ID 83415-2218

ABSTRACT

An Fe-28%Al alloy containing 5% Cr has been synthesized by reaction of elemental powders, followed by consolidation using hot isostatic pressing or hot extrusion. The resulting materials are fully dense, homogeneous, and have a grain size of less than 5μm. Processing strongly influences the propensity toward secondary recrystallization. While HIPped material is extremely resistant to grain growth, under some circumstances hot extruded material undergoes secondary recrystallization, resulting in grain sizes as large as 25 millimeters. Elevated temperature tensile properties and strain rate sensitivities are reported for fine and very coarse grained materials. Grain boundary sliding is not a significant deformation mode for any of the materials. The properties are compared to those of Fe_3Al processed from conventional hot extruded prealloyed powder. It has been found that the reaction synthesized materials generally have superior elevated temperature tensile strength.

INTRODUCTION

Recent work indicates the problem of limited ductility exhibited by Fe_3Al may be overcome by small additions (2-5 wt%) of chromium (1). Tensile elongations for Fe_3Al + 5% Cr are found to approach 20% with little sacrifice in resistance to oxidation and sulfidation (2). Unfortunately, the yield strength of Fe_3Al rapidly decreases above 500°C, thereby reducing the suitability of this material for high temperature applications (2). Nickel-based materials, suffering from a similar decrease in high temperature strength, are strengthened through the incorporation of oxide particles (oxide-dispersion-strengthened or ODS alloys). The oxide particles impede dislocation motion and prevent grain boundary sliding, thus increasing the high temperature strength and creep resistance of these alloys (3). Since the oxide dispersion affects the mechanisms of deformation, a similar improvement in high temperature strength is expected by incorporating an oxide dispersion into Fe_3Al.

This work reports the high temperature mechanical properties of fully dense Fe_3Al, produced by reaction synthesis from elemental powders followed by hot extrusion, and examines the influence of a dispersion of oxide particles on the observed increase in high temperature strength. In this work, the surface oxide coating the elemental powders prior to reaction synthesis provides the desired dispersion of oxide particles in the processed material. The results are compared to Fe_3Al lacking a dispersion of oxide

particles, processed by hot extrusion of pre-alloyed powders. High temperature characterization of the various materials includes grain growth studies, as well as the determination of their high temperature mechanical properties.

EXPERIMENTAL PROCEDURE

Reaction synthesized material was made using carbonyl iron (8 μm diameter), helium gas atomized aluminum (10 μm diameter) and chromium (1-5 μm diameter) powders, mixed in the proper portions to yield Fe-28%Al-5%Cr. Reaction between the elemental powders occurred during a 2 hour thermal treatment at 1100°C in flowing argon. After canning in mild steel, full density rod was produced by hot extrusion (9:1 reduction in area) at extrusion temperatures of 900°C and 1100°C. Fully dense material was also fabricated by hot isostatic pressing a pre-reacted compact at 207 MPa and 1100°C for 2 hours. Consolidated material lacking an oxide dispersion was produced via extrusion of pre-alloyed powder of composition Fe_3Al + 5%Cr made by gas atomization. Extrusion of this material was carried out at 1000°C with a 9:1 reduction in area.

Grain growth experiments were performed during one hour heat treatments in flowing argon at various temperatures. The mean grain size was determined by the linear intercept method on photomicrographs taken of polished and etched samples. Mechanical properties were evaluated during elevated temperature tensile tests. Round cross section tensile bars, machined by centerless grinding from a portion of each of the materials, were tested in tension at various temperatures in laboratory air. In addition, strain rate jump tests were performed on some tensile specimens to measure the strain rate sensitivity at temperatures of 500, 800, and 900°C. Strain rates for these tests ranged from approximately 10^{-4} to $4x10^{-2}$ s^{-1} and each jump approximately doubled the nominal strain rate.

RESULTS AND DISCUSSION

Figure 1 shows an example of the distribution of particles in the HIPped material, obtained using transmission electron microscopy (TEM). The strain imparted to a preform during HIPping is relatively homogeneous, leaving the distribution of inclusions relatively unchanged from the configuration produced by reaction synthesis. The inclusions appear to originate at the surfaces of individual powder particles and are expected to be largely aluminum-rich oxides, which has been confirmed in a previous study (4). The iron oxide on the elemental iron particles is reduced to iron by the aluminum during the reaction (5); the oxygen available from this reduction reacts to form Al_2O_3.

Extrusion causes extensive deformation to the preform, forming the stringers of particles seen in Figure 2a. Electron diffraction from larger particles indicates their crystal structure to be α-alumina. Qualitative energy dispersive spectroscopy (EDS) reveals the particles are also aluminum-rich, supporting the identification of the particles as α-Al_2O_3. However, it should be noted that EDS and Auger spectroscopy also show the particles to contain small amounts of chromium and possibly iron. Heat treatment of the extruded material at 1300°C for one hour leads to significant coarsening of the oxide particles. Small particles, like those seen in Figure 2a, show considerable growth, as seen in Figure 2b.

Fig. 1. TEM micrograph of HIPped material showing distribution of dispersoid.

The dependence of grain size, measured normal to the extrusion direction, on annealing temperature is shown in Figure 3. The grain size remains relatively constant for one hour anneals below 800°C, regardless of extrusion temperature. Between 800°C and 900°C, the material extruded at 1100°C undergoes extensive grain growth; while the material extruded at 900°C shows a dramatic increase in grain size after annealing above 1100°C. Grain growth parallel to the extrusion direction shows trends similar to those shown in Figure 3, however, the grain sizes in that direction are much larger. It can be seen from Figure 4, an optical micrograph of material extruded at 900°C and heat treated at 1300°, that the grains extend through the entire 25 mm long sample, therefore, an accurate measure of the grain size has not been determined. The material extruded at 1100°C exhibits a maximum grain size in the extrusion direction of approximately 800 μm.

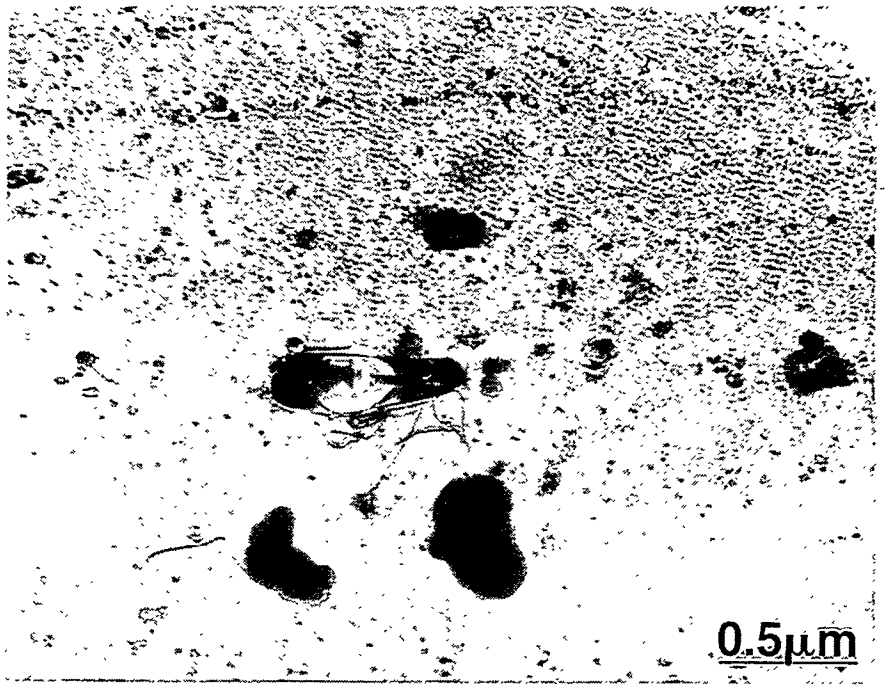

(a)

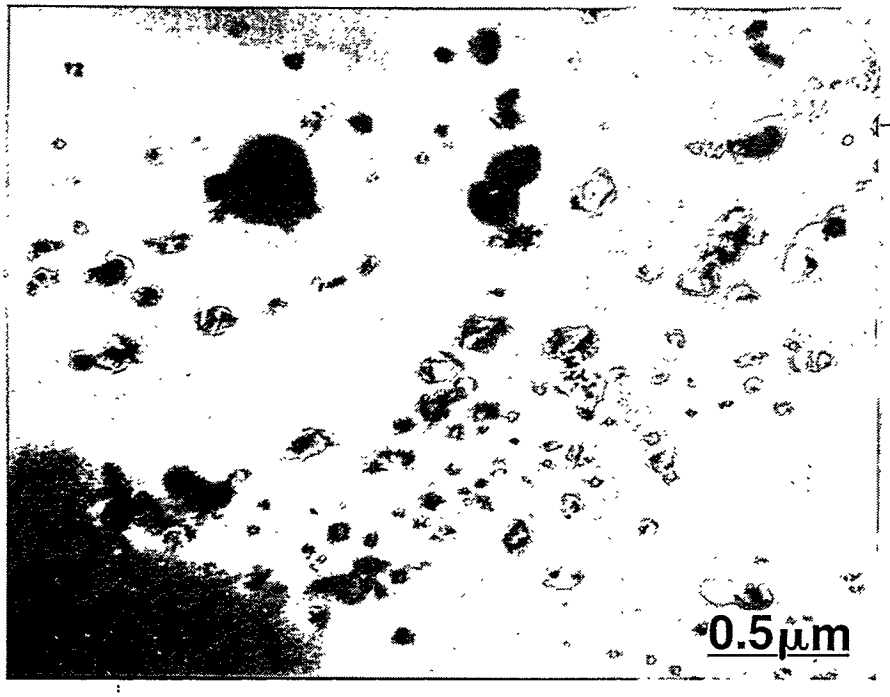

(b)

Fig. 2. TEM micrographs showing (a) stringers of oxide particles in extruded material after 1 hour at 1000°C and (b) increase in particle size after a 1 hour at 1300°C.

The observed grain growth at high temperatures is secondary recrystallization since primary recrystallization is already complete following the one hour anneal at 700°C for either extrusion temperature. A TEM micrograph showing recrystallization after annealing at 700°C is shown in Figure 5. Furthermore, the grain size at higher annealing temperatures remains virtually unchanged after the initial rapid grain growth, behavior characteristic of material having undergone secondary recrystallization (6). The extruded pre-alloyed powder material retains a stable grain size of approximately 50 μm for the annealing temperatures used in this study. Thus, secondary recrystallization appears to be absent in the pre-alloyed material, as well as the HIPped reaction synthesized material where only minor grain growth observed at the annealing temperatures studied.

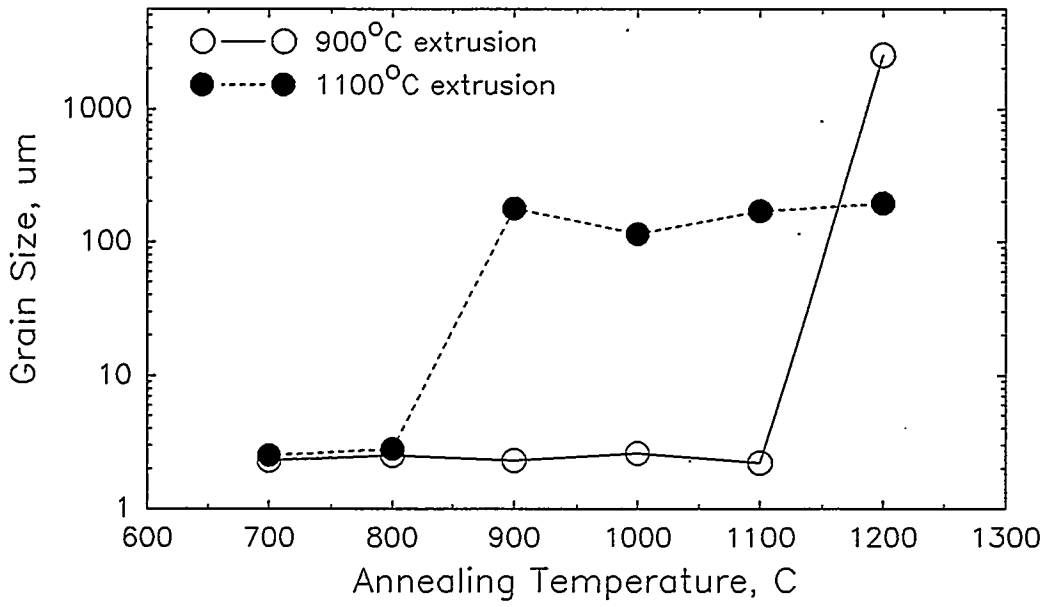

Fig. 3. Effects of annealing on grain size normal to the extrusion direction.

The annealing behavior of the materials in the current study is similar to that of oxide dispersion strengthened nickel (6). Ni-based materials experience severe grain growth at high temperature as a few grains with high mobility boundaries break away from pinning particles and grow rapidly, driven by the reduction in total grain boundary area. The final grain size after secondary recrystallization is determined by the density of nuclei with high boundary mobility (6). Therefore, the exact nature of the annealing response in the Ni-based materials is a function of the processing history, volume fraction of dispersoid and annealing schedule, and is consistent with the behavior of the material used in this study (6).

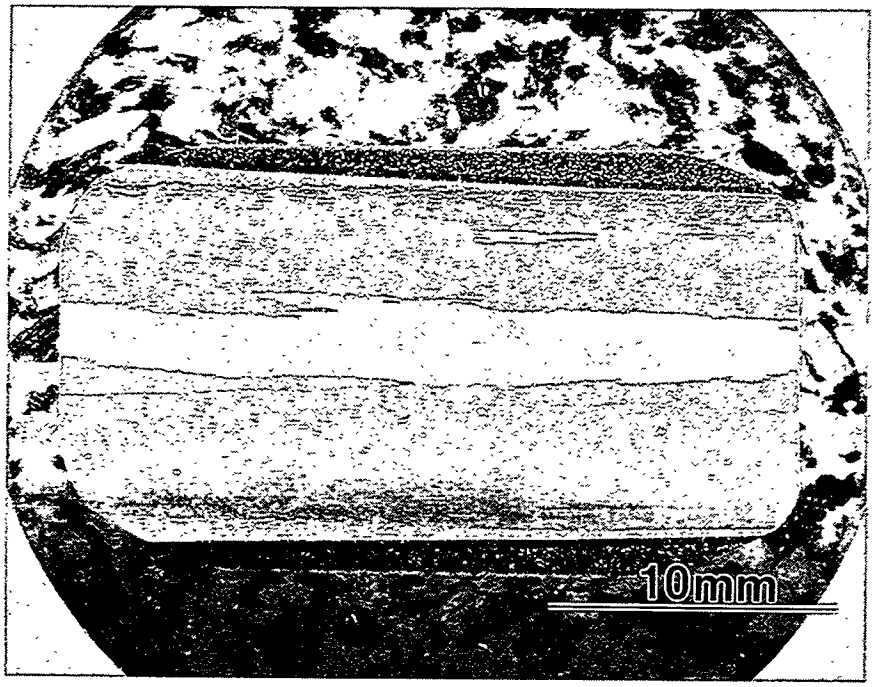

Fig. 4. Optical micrograph of material extruded at 900°C and annealed at 1300°C.

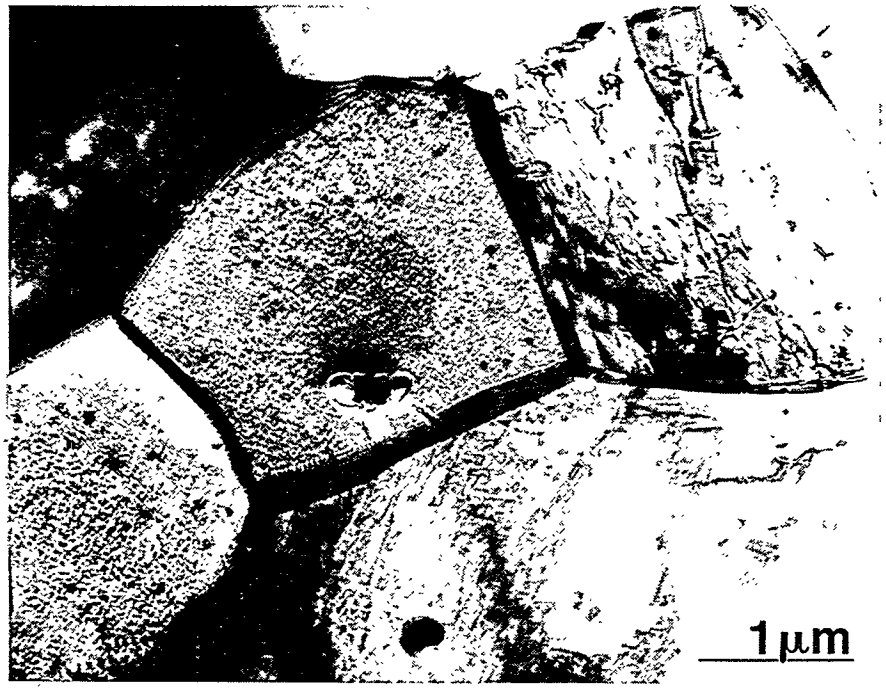

Fig. 5. TEM micrograph of extruded material after annealing 1-hr at 700°C.

Detailed determination of the mechanisms responsible for the unusual grain growth of extruded reaction synthesized material remains under investigation. An analysis by Hillert (7) suggests three conditions are necessary for secondary recrystallization to be observed:

1. Second phase particles prevent normal grain growth.
2. The average grain size cannot exceed a critical value which is determined by dispersoid size and volume fraction.
3. At least one grain much larger than the average grain size must be present.

It has been shown previously that the reaction synthesized material has a critical grain size of about 7 μm (4). Since all of the reaction synthesized materials have approximately the same grain size after primary recrystallization, and all of the grain sizes are below the critical value, it appears differences observed in the tendency to undergo secondary recrystallization are a result of differences in grain shape, texture, and/or the distribution of dispersoid.

Evaluation of the mechanical properties of the reaction synthesized material reveals the oxide dispersion significantly influences the high temperature behavior of chromium-modified Fe_3Al. Figure 6a shows the yield strength of the fine grained ODS alloy to be nearly doubled over that of the pre-alloyed P/M material. The effect appears most dramatic at room temperature; however, the increment of strengthening has been retained at 800°C where the ODS material is still twice as strong despite severely diminished strength for both materials. The 2.7 μm grained material is strongest at all test temperatures while retaining room temperature ductility of approximately 2%; however the yield strengths of the 113 and 1000 μm grained materials do not vary significantly from one another.

The component of strengthening resulting from grain size effects can be seen more clearly from Figure 6b. The grain size and yield strength of HIPped and extruded reaction synthesized material have been plotted along with those from Ceracon consolidated material tested in a previous study (2), and suggests standard Hall-Petch behavior of:

$$\sigma = \sigma_o + kd^{-\frac{1}{2}}$$

where σ_o = 473 MPa and k = 925 MPa $\mu m^{1/2}$. A particle strengthening component of 240 MPa is indicated by the data point (filled) for pre-alloyed material, which should fall on the line of Figure 4b if all strengthening was the result of grain refinement.

In contrast to the yield strength, the strain-rate sensitivity measured at 900°C is not significantly affected by grain size (Figure 7). In addition, the strain rate sensitivity values observed are less than about 0.2 which is relatively low; typically values above 0.5 are characteristic of superplastic materials.

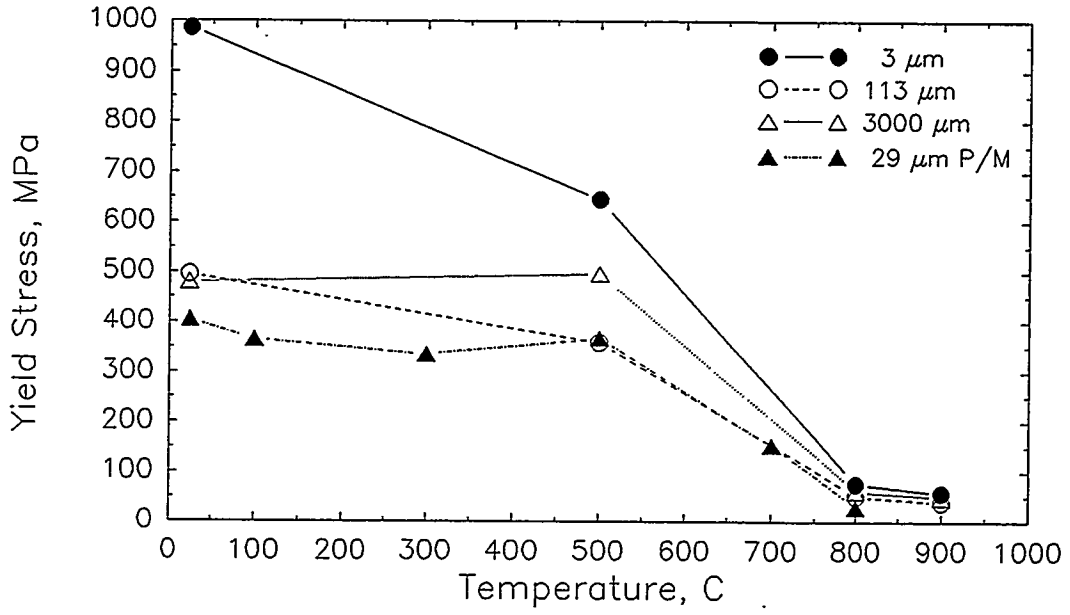

(a)

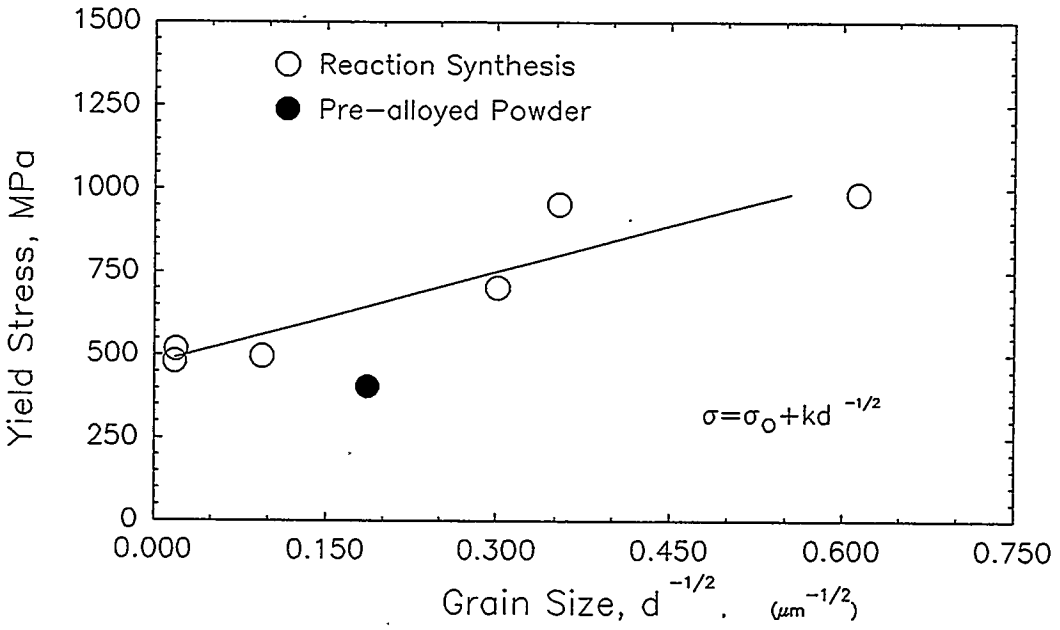

(b)

Fig. 6. Effects of temperature (a) and grain size (b) on yield stress of reaction synthesized Fe_3Al + 5%Cr.

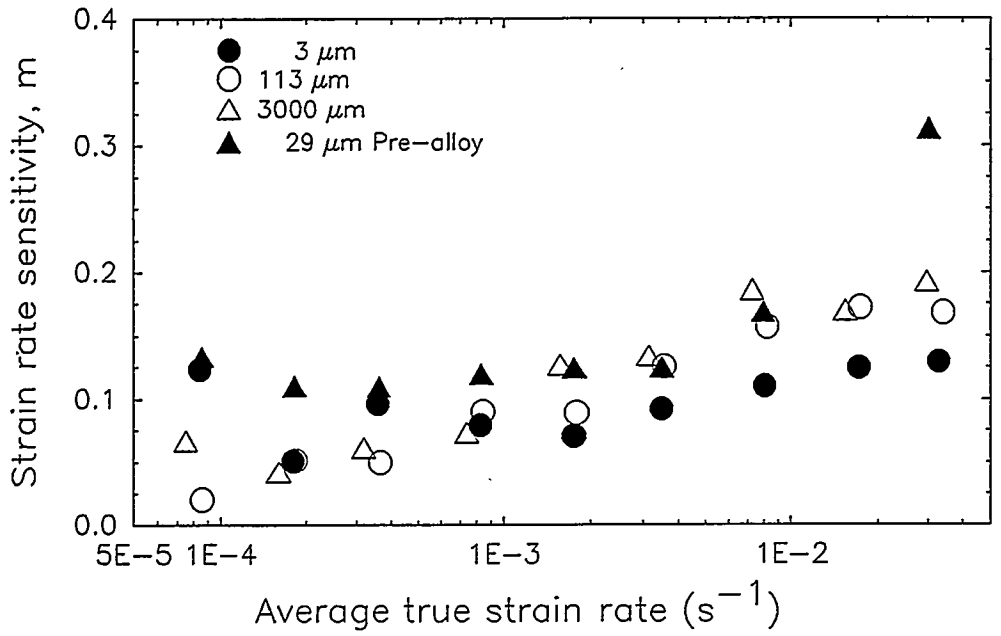

Fig. 7. Effect of grain size on strain rate sensitivity.

The low *m* values measured for this fine grained reaction synthesized material indicate that it is not superplastic even though superplasticity is frequently found in systems with small, stable equiaxed grains. Furthermore, *m* values which do not exhibit a dependence on grain size, as shown in Figure 7, suggest deformation does not occur by grain boundary sliding. A possible explanation for this behavior is that a fraction of the oxide particles reside in the grain boundary, preventing significant grain boundary sliding. These findings are in contrast to reports of superplasticity in a two phase Fe_3Al - Fe_2Nb reaction synthesized material (8) and in Ni_3Al (9).

Generally, large grains are desirable for good creep strength; in these materials, the absence of a grain boundary sliding mechanism holds the promise of reasonable creep properties despite the fine grain size. The total oxygen contents for the extruded and HIPped reaction synthesized materials are all very similar. The HIPped material is known to contain about 0.8 vol% dispersoid and it is expected that the extruded material has a similar oxide content. This value is about a factor of 3 less than commercial ODS alloys. Additional studies are planned to increase the oxide content of the reaction synthesized material, and to evaluate the tensile and creep properties of material with a higher volume fraction of particulate.

CONCLUSIONS

Fine grained Fe_3Al containing an oxide dispersion has been formed using reaction synthesis followed by consolidation by HIPping or extrusion. Materials consolidated by either method are fully dense and have grain sizes below 5 μm. The HIPped material exhibits very little grain growth at 1300°C, while material extruded at 900°C undergoes secondary recrystallization above 1100°C, resulting in a final grain size of greater than 25 millimeters.

The fine grain size after primary recrystallization results in significantly increased yield strength compared to conventional powder metallurgy material of the same composition. In addition to Hall-Petch strengthening, the oxide particles contribute approximately 200 MPa of strengthening at room temperature. Strain rate sensitivity tests indicate that grain boundary sliding is not a significant deformation mechanism up to temperatures of 900°C, even for the fine grained material.

ACKNOWLEDGEMENTS

The authors gratefully acknowledge the assistance of G. L. Fletcher and M. D. Harper in conducting experiments, and L. R. Harper in preparing the manuscript.

REFERENCES

1. C.G. Mckamey, J.H. DeVan, P.F. Tortorelli, and V.K. Sikka, J. Mater. Res., 6, 1779 (1991).
2. C.R. Clark, R.N. Wright, J.K. Wright, and B.H. Rabin, Scripta Met., accepted for publication.
3. R.L. Cairns, L.R. Curwick, and J.S. Benjamin, Metall. Trans., 6A, 179 (1975).
4. B.H. Rabin, J.K. Wright, R.N. Wright, and C.H. Sellers, J. Mater. Res., 9, 1384 (1984).
5. B.H. Rabin and R.N. Wright, Metall. Trans., 22A, 277 (1991).
6. J.J. Petrovic and L.J. Ebert, Metall Trans., 3, 1131 (1972).
7. M. Hillert, Acta Met., 12, 227 (1965).
8. S. Ranganath, A. Dutta, and J. Subrahmanyam, Scripta Met., 25, 1593 (1991).
9. R.N. Wright and J.R. Knibloe, Acta Metall., 38, 1993 (1990).

WELD OVERLAY CLADDING WITH IRON ALUMINIDES

G.M. Goodwin

Oak Ridge National Laboratory
P.O. Box 2008
Oak Ridge, TN 37831-6095

ABSTRACT

The hot and cold cracking tendencies of some early iron aluminide alloy compositions have limited their use in applications where good weldability is required. Using hot crack testing techniques invented at ORNL, and experimental determinations of preheat and postweld heat treatment needed to avoid cold cracking, we have developed iron aluminide filler metal compositions which can be successfully used to weld overlay clad various substrate materials, including 9Cr-1Mo steel, 2-1/4Cr-1Mo steel, and 300-series austenitic stainless steels. Dilution must be carefully controlled to avoid crack-sensitive deposit compositions. The technique used to produce the current filler metal compositions is aspiration-casting, i.e. drawing the liquid from the melt into glass rods. Future development efforts will involve fabrication of composite wires of similar compositions to permit mechanized gas tungsten arc (GTA) and/or gas metal arc (GMA) welding.

INTRODUCTION

We have made significant progress toward development of filler metals for weld overlay cladding using the GTA press on a number of substrate materials including austenitic stainless steel, 2-1/4 Cr-1 Mo steel, and 9 Cr-1 Mo steel. Aspiration casting is the primary technique being used for producing wire, with a smaller effort devoted to development of a shielded metal arc electrode formulation.

Development of Aspiration-Cast Filler Metal

Eleven compositional iterations of cast wire, produced both in-house and through a commercial supplier (Haynes International, Kokomo, IN) have led to optimized compositions which provide crack-free deposits on all three substrate materials. These developmental compositions are summarized in Table 1. A graphic illustration of the influence of aluminum level on cracking is shown in Figure 1. The two deposits on the left of the figure contain greater than 30 atomic % aluminum, and show severe hydrogen cracking, even though preheat of 350°C and postweld heat treatment of 750°C were employed. The two deposits on the right-hand side of the figure, welded under the same conditions, show no evidence of cracking. They contain 20 atomic % aluminum or less. It has been determined that approximately 20 atomic % aluminum or greater is required for optimum corrosion resistance, so in essence, the development effort has involved establishing the compositional window, as illustrated in Figure 2, within which good corrosion resistance and weldability coexist. The final heat of wire, denoted Haynes IV, is in the middle of this window, and represents the optimum composition for overlay cladding with these alloys using the manual GTA welding process. A typical single layer overlay clad (on type 304 stainless steel) is shown in Figure 3. Note that although crack-free deposits can readily produce with several of these filler metal compositions, preheat and postweld heat treatment must still be employed, typically 350°C and 750°C respectively, and dilution must be carefully controlled. Hydrogen cracking is still a problem with these materials.

Development of Shielded Metal-Arc (SMA) Electrodes

Through a cooperative research and development agreement (CRADA) with Devasco International, Houston, TX, we are attempting to extend the technology developed with aspiration-cast wire to the production of shielded metal arc (SMA) electrodes. This effort is considered to be very difficult and high-risk due to the aggressive nature of the fluxing agents which must be used in an electrode coating with the high aluminum contents

Table 1. Composition and Cracking Resistance of Developmental Iron Aluminide Filler Metals

	Nominal Wire Composition, Weight %			
Wire	Al	Cr	Other	Results
Haynes I	30	5	Nb, Ti, C, Mo, Zr, B	No Cracks
Haynes II	30	-	Nb, C, Zr, B	Unusable
ORNL I-01	30	-	Ti, Zr, B	Cracks
ORNL I-02	30	7	Ti, Zr, B	Cracks
ORNL I-03	30	-	C, Mo, Zr, B	Cracks
ORNL II-01	30	5	Nb, Ti, C, Mo, Zr, B	Cracks
ORNL II-02	25	5	Nb, Ti, C, Mo, Zr, B	Cracks
ORNL II-03	20	5	Nb, Ti, C, Mo, Zr, B	No Cracks
Haynes III-01	30	7	Nb, Ti, C, Mo, Zr, B	No Cracks
Haynes III-02	30	-	Mo, Zr, B	No Cracks
Haynes IV	25	7	C, Mo, Zr, B	No Cracks

YP19676

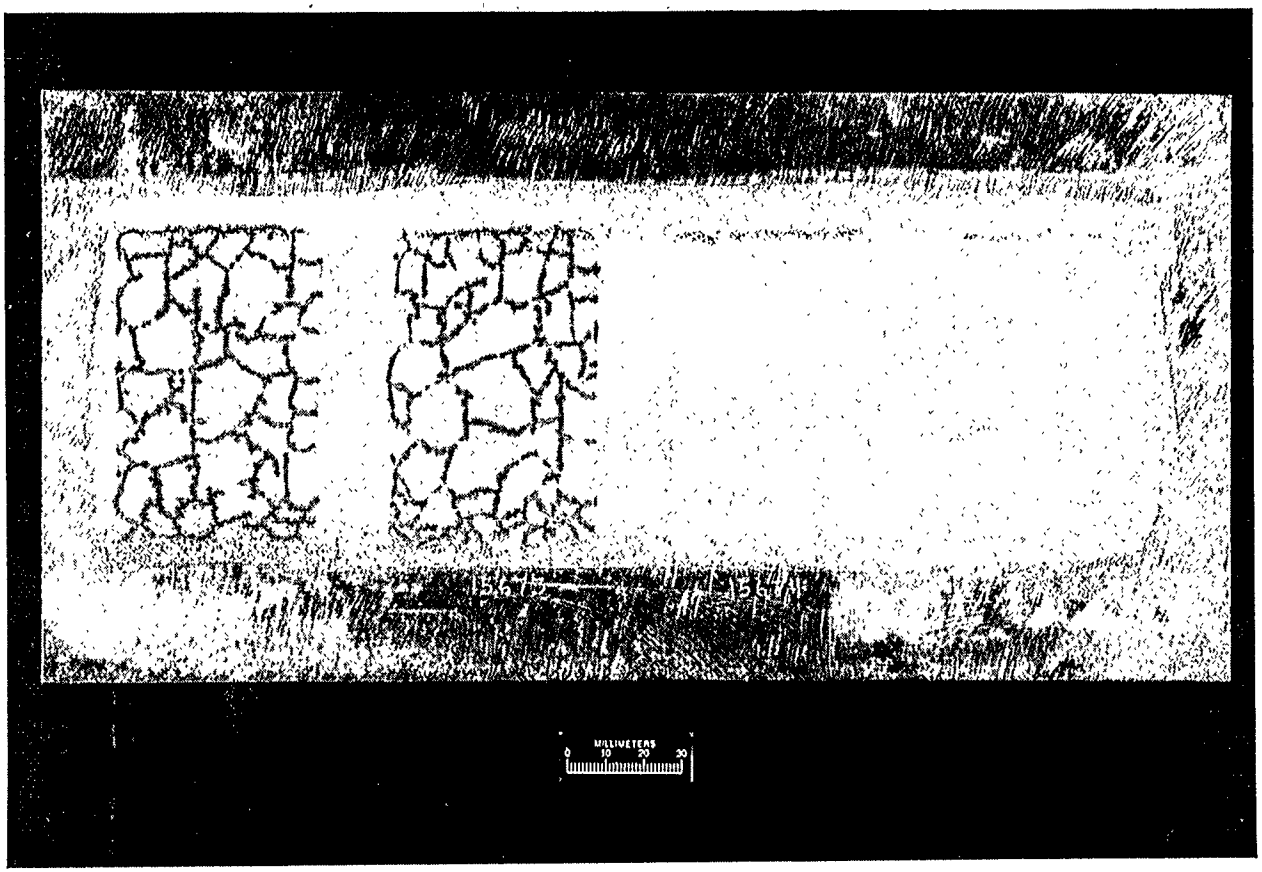

ORNL II-01	ORNL II-02	ORNL II-03	ORNL-385
35.8 a/o Al	31 a/o Al	20.2 a/o Al	8.5 a/o Al

Fig. 1. Iron aluminide weld deposits on 9 Cr-1 Mo plate.

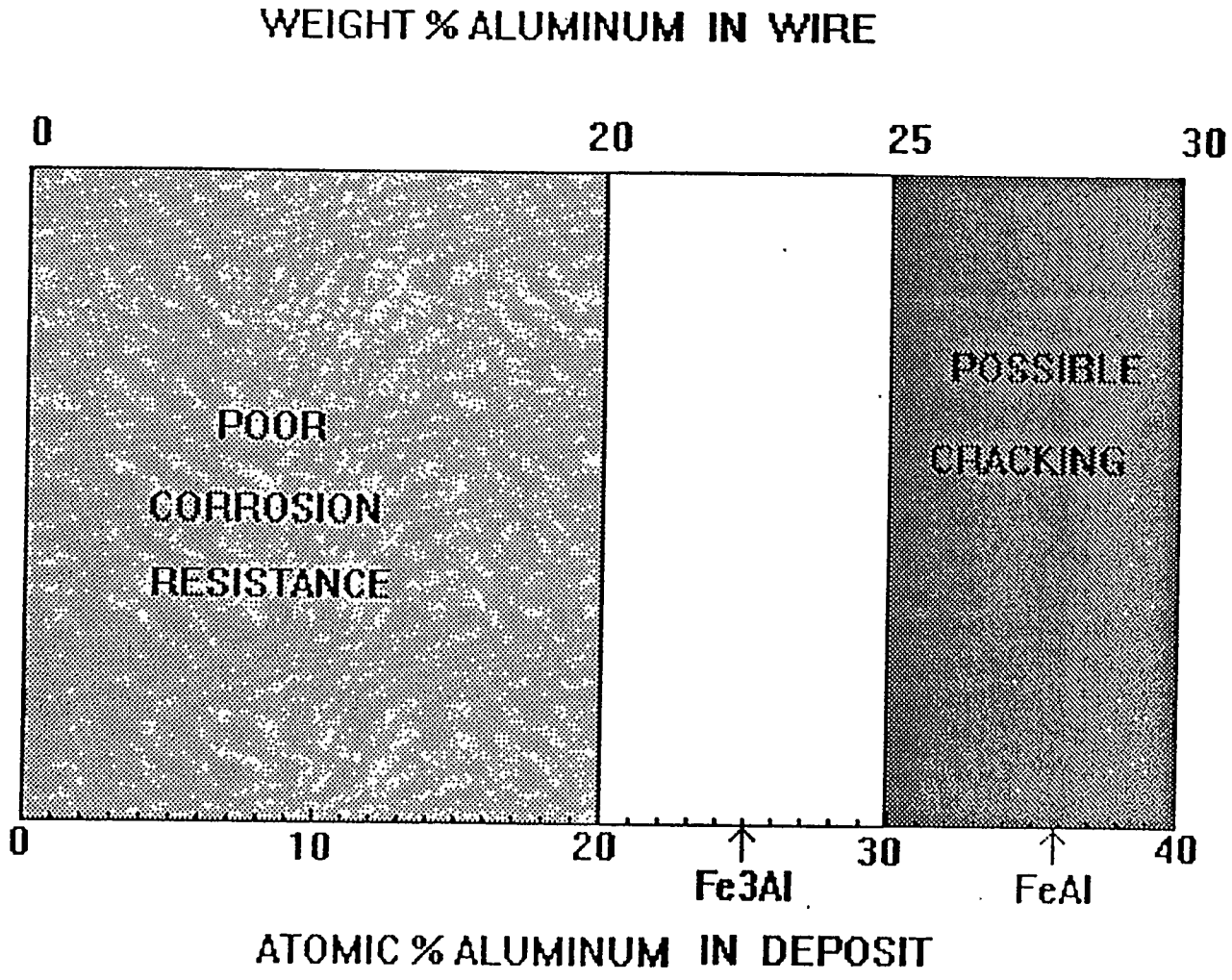

Fig. 2. Compositional window within which good corrosion resistance and weldability coexist.

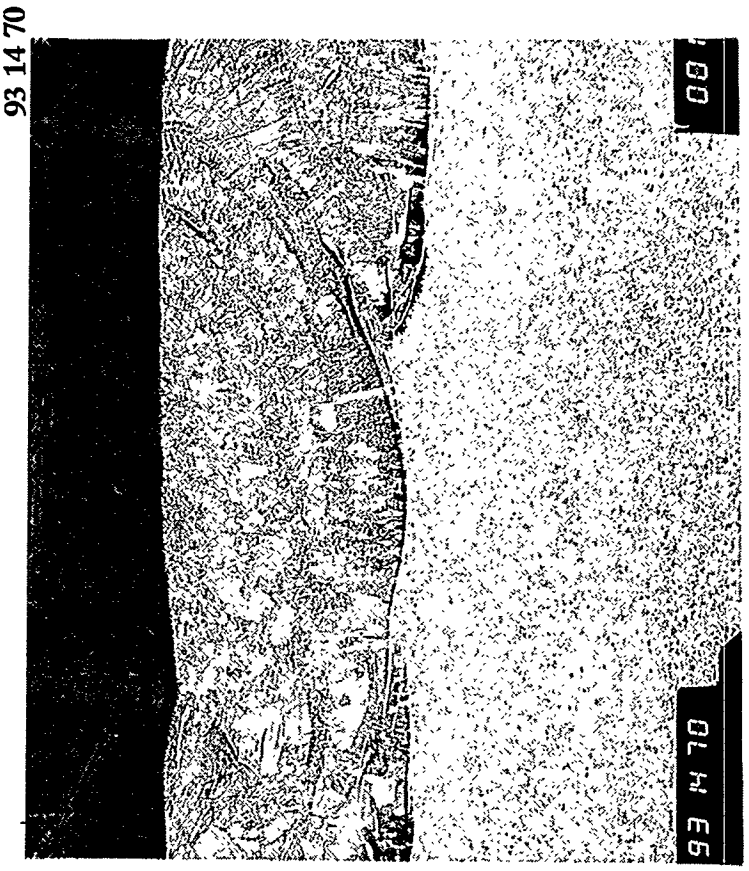

Fig. 3. Typical single layer GTA weld overlay (on type 304 stainless steel). 13x magnification. Deposit is approx. 3 mm thick.

involved here. Several coating formulations have been developed which provide adequate usability, but aluminum recovery in the deposit has been low. This task is continuing.

Development of Powder-Cored Filler Wire

Broader application of these alloys could be achieved, and economics significantly enhanced, by the development of a powder-cored wire formulation. The availability of this wire in coil form would permit careful control of dilution using the mechanized gas tungsten arc (GTA) and gas metal arc (GMA) welding processes, and would ultimately be much cheaper to produce and apply. Toward this end an order has been placed with Stoody Company, Bowling Green, KY, to produce 1/16-in. diam. wire yielding a deposit composition of approximately 15 weight % Al, 7 weight % Cr, 0.1 weight % C, 0.2 weight % Zr, 0.25 weight % Mo, balance Fe. This deposit composition is based on a single layer weld overlay on 2-1/4 Cr-1 Mo steel.

Conclusions

- Significant progress has been made toward development of aspiration-cast filler metal for GTA weld overlay deposits.
- A composition window of aluminum content has been established within which good corrosion resistance and weldability coexist; however,
- Hydrogen cracking is still a problem with these materials.
- Filler metals are being developed for alternate welding processes (mechanized GTA, GMA, SMA) to achieve broader application of the alloys.

HIGH-TEMPERATURE CORROSION BEHAVIOR OF IRON-ALUMINIDE ALLOYS AND COATINGS

P. F. Tortorelli, J. H. DeVan, B. A. Pint, and I. G. Wright

Oak Ridge National Laboratory
Oak Ridge, Tennessee, U. S. A.

and

S. R. J. Saunders

National Physical Laboratory
Teddington, Middlesex, United Kingdom

ABSTRACT

An Fe - 28 at.% Al - 2% Cr alloy doped with Y_2O_3 showed improved scale adhesion relative to a dispersion-free form of the same composition. However, doping with CeO_2 or La_2O_3 was detrimental to oxidation behavior. A study of weld-overlay iron-aluminide coatings showed that, those with sufficiently high aluminum concentrations had sulfidation resistance in H_2S-H_2-H_2O-Ar at 800°C equivalent to the most resistant bulk iron aluminides. These corrosion-resistant coatings have the potential to be effective barriers in high-temperature sulfidizing environments provided the appropriate combinations of filler metal, process parameters, and substrate are used to produce adequate aluminum concentrations and minimal chromium contents. Exposures in an oxidizing/sulfidizing environment containing varying amounts of HCl at 450 and 550°C showed that Fe_3Al alloys had good corrosion resistance.

INTRODUCTION

The iron-aluminum system has been studied by alloy developers for over sixty years.[1] A primary reason is the potential of iron aluminides for excellent high-temperature corrosion resistance in a number of environments. Alumina surface layers will form on iron aluminides even in environments with extremely low oxygen partial pressures.[2] This ability to form Al_2O_3 across a wide range of oxygen activities allows iron aluminides to be corrosion resistant not only in air or oxygen, but also to a variety of mixed gases and salts.[3] Therefore, determining the corrosion behavior of Fe_3Al alloys in aggressive environments at elevated temperatures forms an important part of the development of these aluminides. This paper reports recent results on the high-temperature corrosion behavior of iron aluminides relevant to three areas of alloy and process development for fossil-energy applications: oxidation of selected oxide-dispersion-strengthened (ODS) Fe_3Al alloys, sulfidation of iron-aluminide weld overlays, and corrosion of several iron-aluminum alloys in a simulated coal gasification environment in which the chlorine level was varied.

OXIDATION OF ODS Fe_3Al ALLOYS

As described elsewhere,[4] ODS Fe_3Al alloys are currently being developed to increase the operating temperature regime of these uniquely sulfidation-resistant materials. Determining the effects of a dispersion of oxides on the high-temperature oxidation resistance of Fe_3Al is a key part of this effort. Use of a reactive element (RE) oxide may further improve the adhesion of alumina scales on iron aluminides, as has been shown for the FeCrAl, NiCrAl, and NiAl systems (see, for example, refs. 5-7). The initial results on the effects of Y_2O_3, CeO_2, and La_2O_3 on high-temperature cyclic oxidation of Fe-28% Al-2% Cr (FAS) are summarized here. More details of the work with the Y_2O_3 and CeO_2-doped FAS can be found in ref. 8.

Powders of gas-atomized FAS and submicron oxides (Y_2O_3, CeO_2, or La_2O_3) were mechanically blended in a flowing Ar atmosphere using a high-speed attritor and stainless steel balls. (Unless otherwise noted, all concentrations are in at.%). The blended powder was canned, degassed, and extruded at 1100°C. For comparison, a FAS powder extrusion without an oxide addition, ingot-processed Fe-28% Al-5% Cr-0.1% Zr (FAL), and a commercial ZrO_2-dispersed (0.06% Zr) Fe-20% Cr-10% Al alloy (Kanthal alloy APM) were also tested. Coupons (about 15 mm diam x 1 mm thick) were polished with 0.3 μm alumina prior to oxidation. Cyclic oxidation experiments were conducted at 1200°C in air and in dry, flowing O_2. Admittedly, the exposure temperature of 1200°C is significantly higher than most potential applications for iron aluminides, but it is a convenient way to assess the potential lifetime of these materials based on aluminum consumption. A similar approach was previously used to predict oxidative lifetimes for ingot-processed iron aluminides and for comparison with FeCrAl alloys.[9] In short-term cyclic testing (2 h cycles), specimens were hung in a furnace in flowing O_2 and weight changes were measured continuously using a microbalance to check for any indication of isothermal spallation. (However, spallation was only observed upon cooling.) In long-term testing (100 h cycles), specimens were placed in a static air furnace inside individual alumina crucibles so that any spalled oxide was collected and weighed. In both types of tests, the specimen weight changes were measured before and after oxidation. After oxidation, specimens were examined using scanning electron microscopy (SEM) with energy dispersive x-ray (EDX) analysis.

Specimen weight change data for the various alloys exposed to 2 h cycles are shown in Fig. 1. A fine powdery alumina scale formed on the undoped FAS alloy and led to large weight losses after just a few cycles. In contrast, rapid weight gains were observed for the CeO_2- and La_2O_3-dispersed alloy specimens. The CeO_2-dispersed alloy exposure was

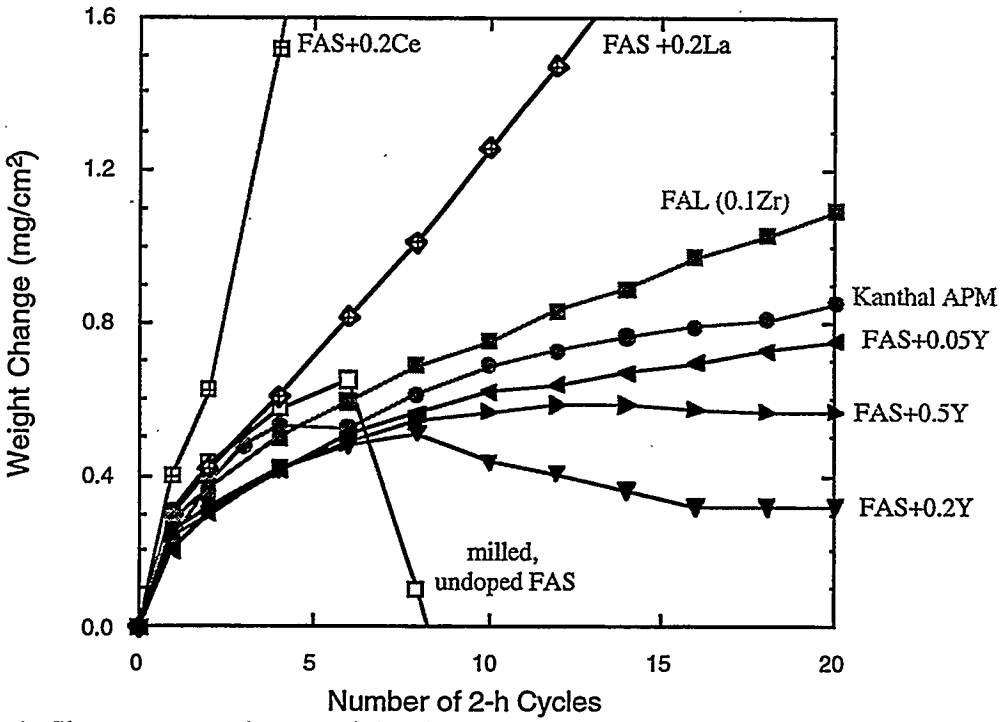

Fig. 1. Short-term specimen weight changes upon cyclic oxidation at 1200°C in O_2 for iron aluminides with various oxide dispersions.

stopped after 14 cycles when breakaway oxidation (formation of FeO_x) began at one edge. The detrimental effects of CeO_2 and La_2O_3 are comparable to that of La_2O_3 in β-NiAl.[7] In all these cases, the additions resulted in accelerated oxidation relative to the undoped alloy. Whether this effect is primarily in the oxide or in the alloy is unclear and is under investigation.

All cyclically exposed alloys had some scale loss except for the ZrO_2-dispersed FeCrAl and the FAS with 0.05% of Y cations. Of the Y_2O_3-dispersed FAS alloys, the 0.2% Y addition had the largest amount of scale spallation (about 40% of area), in agreement with the weight change measurements shown in Fig. 1. In general, spallation to bare metal was observed and voids at the metal-oxide interface were apparent. However, compared to the undoped alloy, all of the Y_2O_3 additions to FAS reduced the amount of scale spallation. Also, Y doping produced a flatter, less convoluted scale than that observed on the undoped FAS, as does Zr in the ingot-processed FAL.

The longer-term cyclic oxidation results are shown in Fig. 2. In contrast to the data in Fig. 1, the specimens were exposed for 100 h each time and the reported results represent total mass change (specimen plus any spalled oxide). In this way, the measurements are proportional to the amount of metal consumed by oxidation. Comparing these total weight

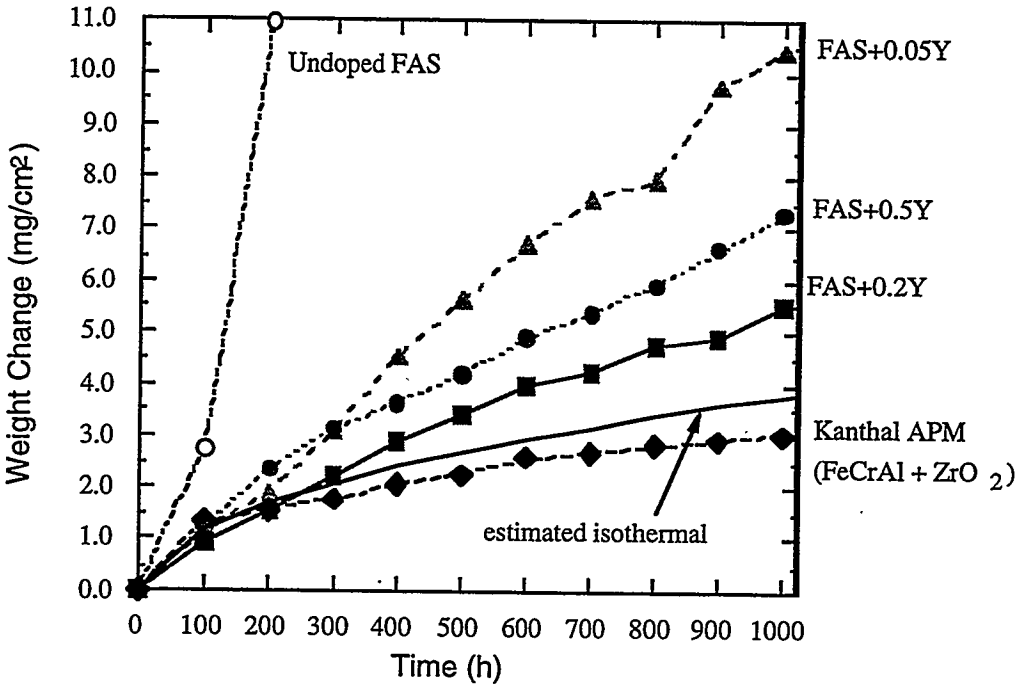

Fig. 2. Total weight gain (including spalled scale) for 100-h cycles at 1200°C in air.

gains, the alloy with the smallest Y_2O_3 addition (0.05% Y) performed worst and that with the 0.2% Y had the best behavior, which is the opposite result of the short-term oxidation results (Fig. 1). Nevertheless, Y_2O_3 additions still improved oxidation resistance relative to the undoped FAS alloy, which went into breakaway oxidation after three cycles. The ability to increase the effectiveness of yttria, and possibly other oxides, in increasing the oxidation resistance of iron aluminides by improving dispersion uniformity and controlling microstructure is currently under study.

The rate at which aluminum in the alloy is consumed is a critical factor in predicting time to breakaway oxidation (as defined above) and the higher Al content of iron aluminides relative to FeCrAl alloys could result in longer oxidative lifetimes. However, scale spallation was more severe for the Y_2O_3-doped FAS alloys than for the ZrO_2-dispersed FeCrAl and, based on the total weight gains (Fig. 2), the aluminum consumption rate was 2 to 4 times higher for the former materials. In previous work on ODS FeCrAl and β-NiAl alloys,[10] Y and Zr dopants were found to have identical beneficial effects on the oxidation behavior. Thus, it appears that the difference in oxidation behavior between the ODS FeCrAl and Fe_3Al alloys cannot be explained by the difference in their dopant oxides. Furthermore, the Zr-containing FAL suffered greater cyclic weight gains and scale spallation than the Zr-doped FeCrAl alloy (Fig. 1). A similar result was also observed for 1300°C oxidative lifetime testing:[9] despite the

lower Al content of a RE-doped FeCrAl alloy, its time to breakaway oxidation was comparable to that for ingot-processed FAL containing 0.1% Zr, thereby indicating a higher Al consumption rate for the FAL alloy.

OXIDATION-SULFIDATION OF IRON-ALUMINIDE WELD OVERLAYS AT 800°C

The oxidation and sulfidation resistance of iron aluminides containing greater than 18 - 25 at.% Al is maintained at temperatures (for example, 800°C) well above those at which these alloys have adequate mechanical strength. Because of this, and possible cost considerations, it is anticipated that appropriate compositions of iron aluminides may find application as coatings or claddings on more conventional higher-strength materials which are less corrosion-resistant at high temperatures. Initial work in this regard focused on examining the sulfidation resistance of iron-aluminide coatings deposited by a weld-overlay technique.

Weld-overlay deposits of Fe-Al alloys were produced on 25 mm-thick 2.25 Cr - 1 Mo (wt%) steel and 50 mm-thick type 304 stainless steel substrates using techniques and filler materials described elsewhere.[11,12] Rectangular pieces, approximately 18 x 12 mm, were cut from the weld overlay specimens. Coupons for the corrosion experiments were then prepared by grinding away the substrate material so that they consisted of only weld metal (approximately 1 - 2 mm thick). Corrosion behavior was characterized by use of a continuous-recording microbalance to measure the weight of these specimens during exposure at 800°C to a flowing (~2 cm^3/s) mixed gas consisting of 5.4% H_2S - 79.4% H_2 - 1.6% H_2O - 13.6% Ar (by volume). The oxygen partial pressure, as determined by a solid-state oxygen cell, was 10^{-22} atm, and the sulfur pressure was calculated to be 10^{-6} atm. This type of experiment has been used to characterize the sulfidation resistance of many iron aluminides and several other alloys.[3,13,14] Due to mixing during welding, the composition of a particular weld overlay depends not only on the elements present in the filler metal but also on the alloy used as the substrate.[11,12] Therefore, it was important to determine the actual concentrations of the appropriate elements in the deposited layers and these are shown in Table 1.

The weight change results for the six overlay coatings exposed to H_2S - H_2 - H_2O - Ar at 800°C are shown in Fig. 3. The curves clearly fell into groups of either low (C1, C2, C3) or high (O1, O2, O3) weight gains. Figure 4 presents a more detailed view of the thermogravimetric data for the coupons in the low weight-gain group and, for the sake of comparison, includes two curves for specimens of wrought FAS. This composition has been shown to be among the most corrosion-resistant Fe_3Al alloys in this gas mixture.[14]

Table 1. Weld Deposit Compositions

Specimen	Substrate	Concentration (at.%)[a]							
		Al	Cr	Nb	Ti	Ni	Mo	Zr	C
C1	Cr-Mo	35.4	2.5	0.2	0.4	-	0.6	0.2	1.0
C2	Cr-Mo	36.7	4.7	0.2	0.4	-	0.6	0.2	1.0
C3	Cr-Mo	35.5	0.7	-	-	-	0.7	0.1	1.0
O1	304	11.1	6.7	<0.01	<0.01	6.6	0.2	0.03	0.5
O2	304	23.1	6.3	0.1	0.1	6.3	0.2	0.1	0.5
O3	Cr-Mo	21.7	2.1	0.1	-	-	0.7	0.1	-

[a] Determined by spark source mass spectrometry. Balance is Fe.

Differences in corrosion behavior between the C and O groups of specimens were also reflected in the respective corrosion product morphologies.[15] The higher-aluminum specimens exhibited thin, fairly uniform scales with just a small amount of powdery, spalled scale. In contrast, significant scale loss (upon cooling and handling), were observed for the three coatings with lower aluminum concentrations. Specimens O1 and O2 had relatively thick, black corrosion products which consisted of dense mattes of aluminum and iron sulfides, as determined by EDX analyses in a SEM. Specimen O3 exhibited a smaller population of the same type of sulfides.

Based on findings from previous iron-aluminide studies,[3,14] the corrosion data shown in Figs. 3 and 4 are consistent with the deposit compositions recorded in Table 1. The coatings exhibiting relatively high weight gains and corrosion rates (O1, O2, O3) have relatively low aluminum and high chromium concentrations. In the case of O1, the aluminum content is very much lower than what has been found to be needed for the best sulfidation resistance,[16] while O2 and O3 exceed this critical concentration somewhat. As expected, O1 showed the greatest sulfidation susceptibility of the group O specimens due to its low aluminum concentration. The somewhat worse behavior of O2 vis-à-vis O3 is probably due to the higher chromium and nickel concentrations of the former. Chromium levels similar to that in O2 exacerbate the sulfidation reaction for Fe_3Al alloys.[14] While the three weld clads with the lower aluminum concentrations exhibited substantial mass gains, their relative corrosion resistance was still somewhat better than that of Fe-Cr-Ni alloys.[13,14]

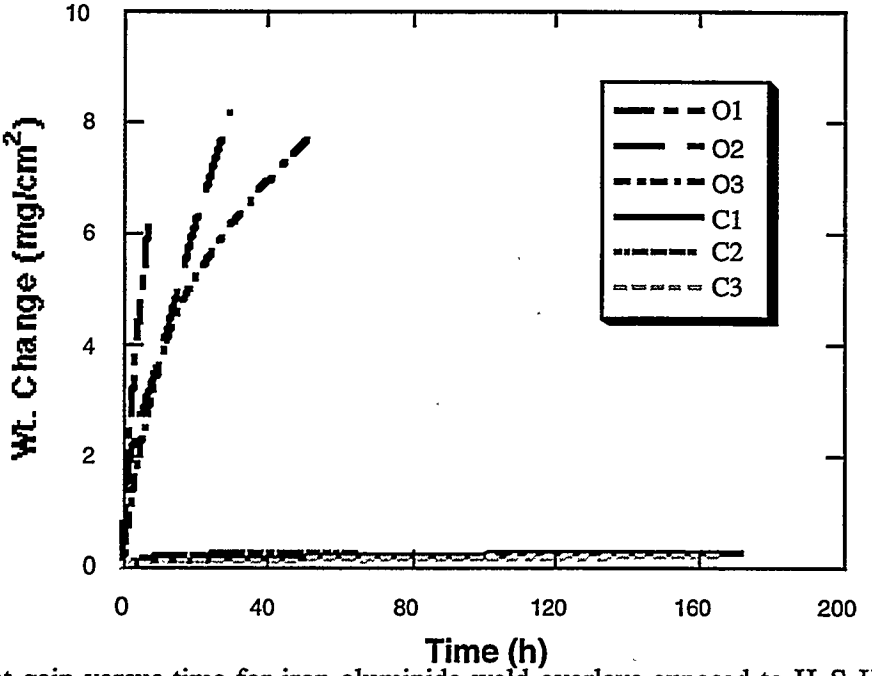

Fig 3. Weight gain versus time for iron-aluminide weld overlays exposed to H_2S-H_2-H_2O at 800°C. Overlay compositions are shown in Table 1.

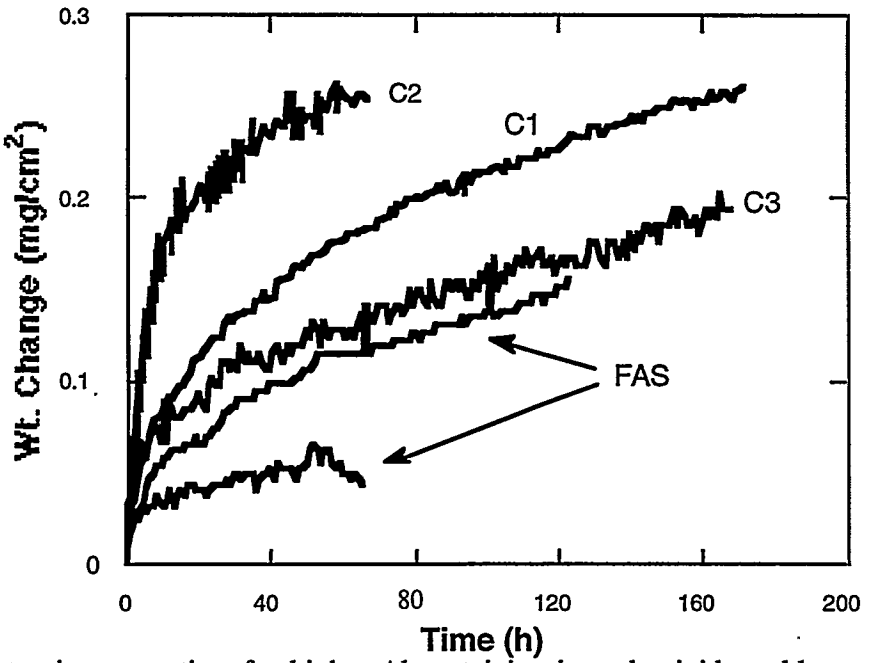

Fig. 4. Weight gain versus time for higher-Al-containing iron-aluminide weld overlays and alloy FAS exposed to H_2S-H_2-H_2O at 800°C. Overlay compositions are shown in Table 1.

The specimens denoted C1, C2, and C3 all have aluminum concentrations well in excess of the critical amount needed for excellent sulfidation resistance in the subject mixed gas.[16] Their oxidation/sulfidation behavior therefore resembles that of the most resistant iron aluminides.[14] The deleterious effect of Cr is normally not observed at the higher aluminum levels in the group C specimens[3,14] and little, if any, detrimental influence of the higher chromium concentration of C2 was detected (Fig. 4). Compared with the results shown in Fig. 3, the weight gains and rates in Fig. 4 are low; differences among the curves are not statistically significant.

The present results show that iron-aluminide weld overlays have the potential to be effective corrosion-resistant coatings in high-temperature sulfidizing environments provided the appropriate combinations of filler metal, process parameters, and substrate are used to produce adequate aluminum concentrations and minimal chromium contents. In the present study, the spread in aluminum concentration between the group O and C specimens is too large to precisely define the clad composition necessary to achieve low corrosion rates. The higher aluminum concentrations of the group C specimens would provide a margin of safety with respect to sulfidation resistance, particularly in view of enrichment of the weld overlay in substrate elements (for example, chromium and nickel) that are deleterious to sulfidation resistance. Furthermore, excess aluminum would delay any onset of breakaway oxidation caused by aluminum depletion.[9] However, weld deposits containing high aluminum concentrations are much more sensitive to hydrogen-induced cracking when exposed to moist air, even after stress relief. In this regard, it must be noted that, as only the coatings themselves were tested in the corrosive environment, the present study was focused on the thermodynamic stability and reaction kinetics of the weld deposits and did not examine the effects of extended defects. The actual protectiveness of a particular layer will also depend on the ability of these layers to provide a physical barrier that doesn't delaminate or allow corrosion of the substrate by ingress of reactive species via cracks or other defects. These aspects will be investigated through exposure of clad substrates to the particular corrosive environment.

EFFECT OF CHLORINE ON THE OXIDATION-SULFIDATION OF IRON ALUMINIDES AT 450 AND 550°C

In some fossil energy applications, iron aluminides will have to show corrosion resistance to product gases that contain small concentrations of HCl in an oxidizing-sulfidizing atmosphere of relatively high p_{S_2} and low p_{O_2}. Because of this, the effect of HCl on the corrosion of FAS, FA129 (Fe-28% Al-5% Cr-0.5% Nb- 0.2% C), and FAP (Fe-16% Al-

5% Cr-1.1% Mo - 0.1% Zr - 0.1% C) in a simulated coal gasification environment has been studied in collaboration with the National Physical Laboratory (NPL) in the United Kingdom. The sulfur and oxygen fugacities of the gas were, respectively, 5×10^{-8} and 1×10^{-26} at 450°C and 2×10^{-6} and 2×10^{-22} at 550°C. Two levels of HCl additions, 1000 and 3283 ppm, were examined. General details of the experiments and initial results (for 1000 ppm HCl) have been described previously.[9] A FeCrAlY alloy was included in the exposures for comparison.

Gravimetric results for exposures in the mixed gas with 3283 ppm of HCl are shown in Fig. 5. As with the results for mixed gas with 1000 ppm HCl,[9] weight changes of FAP were substantially higher than those of the other three alloys and, at 550°C, FAS and FA129 performed somewhat better than the FeCrAlY. Differences in corrosion susceptibility are also shown in Fig. 6, which contains representative cross sections of exposed aluminides. Thin, presumably alumina, scales formed on FAS and FA129 (Fig. 6a and b) and provided adequate protection. Penetration along a few grain boundaries was noted. Such attack has not been noticed for sulfidation of iron aluminides at higher temperatures in the absence of HCl, but the present observations of such were limited to a small fraction of the exposed surface area. In contrast, FAP (Fig. 6c) exhibited significantly thicker scales that included sulfides. The reaction product on the FeCrAlY was thinner than that on FAP, but thicker than those found on FAS and FA129, which is consistent with the gravimetric data for the 550°C exposures in the environments with HCl at concentrations of 1000 ppm (ref. 9) and 3283 ppm (Fig. 5).

In studies conducted in a similar type of mixed-gas at 800°C, but without HCl additions, both higher chromium levels ($\geq$ 2%) and lower aluminum concentrations ($<$ ~18%) contributed to reduced resistance to corrosion.[3,14,16] In the case of the present exposures, a concentration of 5% Cr in Fe_3Al (FA129), which reduces sulfidation resistance at higher temperatures, did not have a significant effect at 450 and 550°C in the presence of HCl. Additionally, the substantial chromium concentration (~20%) of the FeCrAlY, which has a dramatic deleterious effect in the aforementioned high-temperature sulfidizing environment,[3,14,16] appears to have only a minor influence in the mixed gas + HCl; the corrosion susceptibility of this alloy was similar to that of FAS and FA129 at 450°C and only moderately worse at 550°C. On the other hand, the lower aluminum concentration of FAP (16%) appears to have been a major factor in its relatively poor performance under these conditions, as well as at higher temperatures.[3,16]

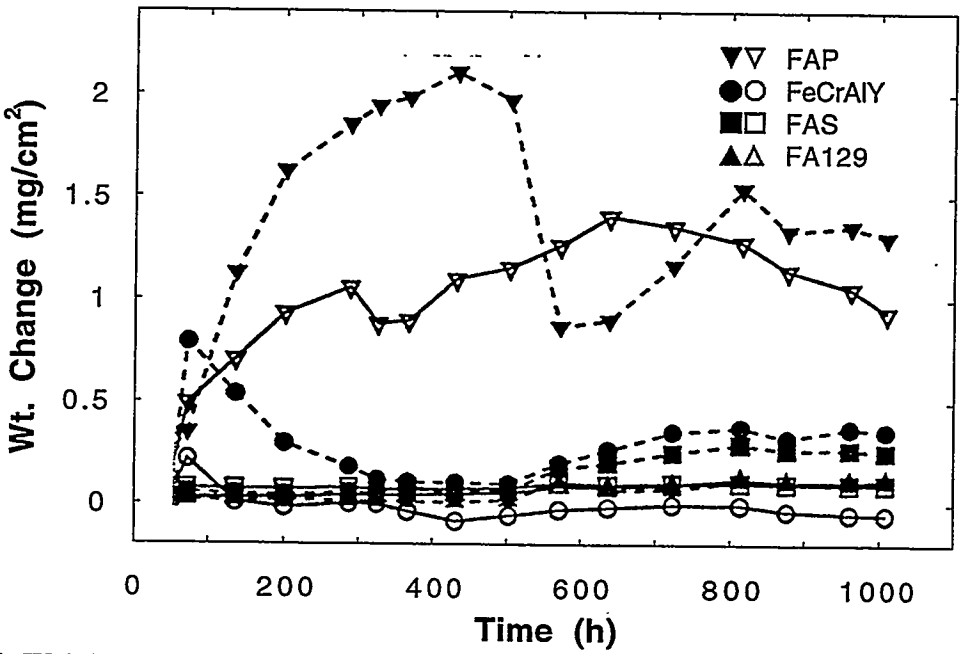

Fig. 5. Weight changes vs. time for exposures in a simulated coal-gasification environment containing 3283 ppm HCl at 550°C.

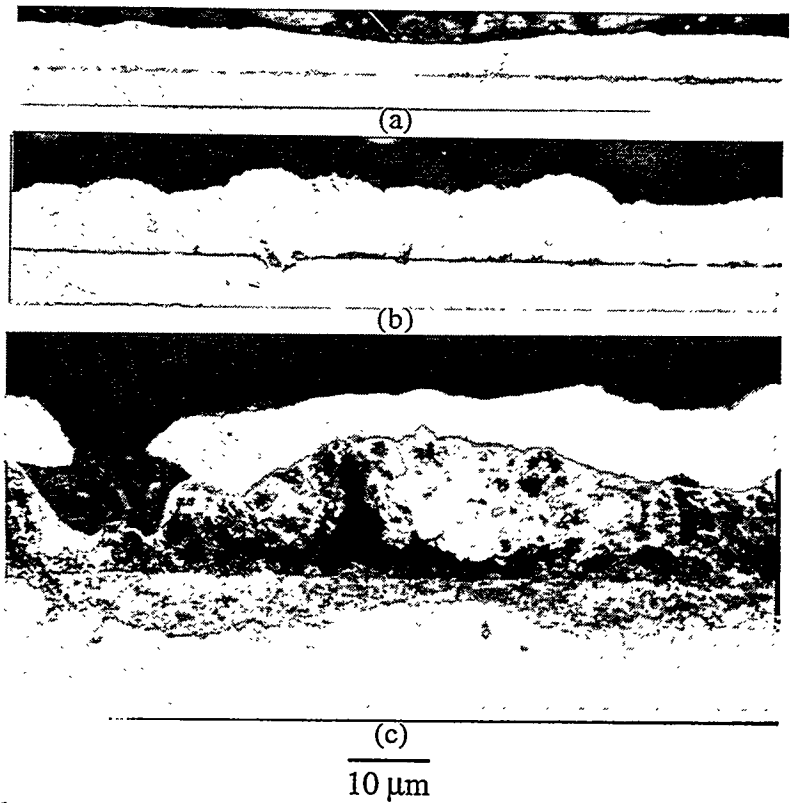

Fig. 6 Polished cross sections of iron aluminides exposed in a simulated coal-gasification environment containing 3283 ppm HCl at 550°C for 1007 h. The specimens were coated with copper prior to sectioning (visible as bright topcoat). (a) FAS (b) FA129 (c) FAP

SUMMARY AND CONCLUSIONS

Oxide-dispersed Fe - 28% Al - 2% Cr alloys doped with Y_2O_3, CeO_2, and La_2O_3 were prepared and cyclically oxidized at 1200°C. Yttria improved scale adhesion relative to the undoped alloy, but was not as effective as zirconia in an FeCrAl alloy. Both CeO_2 and La_2O_3 were detrimental to oxidation behavior.

Specimens of weld-overlay iron-aluminide coatings were exposed to H_2S-H_2-H_2O-Ar at 800°C. The investigation focused only on the weld overlay material and, as such, involved the characterization of the thermodynamic and kinetic stabilities of these coatings rather than their ability to physically separate the corrosive species from susceptible substrate material. Under conditions that produced coatings with sufficiently high aluminum concentrations, corrosion resistance equivalent to the best bulk iron aluminides was found.

Three iron aluminides and a standard FeCrAlY alloy were exposed at 450 and 550°C in an oxidizing/sulfidizing environment containing varying amounts of HCl at the National Physical Laboratory in the United Kingdom. Two 28% Al - 5% Cr alloys, FA129 and FAL, were more resistant than FeCrAlY at 550°C and Fe - 16% Al - 5% Cr (FAP) at both temperatures. For FA129 and FAL, there was little evidence to suggest any accelerating effect of HCl up to a concentration of about 3300 ppm.

ACKNOWLEDGMENTS

The authors thank M. Howell for experimental support and J. R. DiStefano, G. M. Goodwin, and C. G. McKamey for their reviews of the manuscript. This research was sponsored by the Fossil Energy Advanced Research and Technology Development (AR&TD) Materials Program, U S. Department of Energy, under contract DE-AC05-84OR21400 with Martin Marietta Energy Systems, Inc. B. A. Pint is supported by the U S. Department of Energy Distinguished Postdoctoral Research Program administered by the Oak Ridge Institute for Science and Education.

REFERENCES

1. C. G. McKamey, J. H. DeVan, P. F. Tortorelli, and V. K. Sikka, J. Mater. Res. **6**, 1779 (1991).
2. P. Tomaszewicz and G. R. Wallwork, Rev. High Temp. Materials **4**, 75 (1978) 75-105.
3. P. F. Tortorelli and J. H. DeVan, pp. 257-70 in Processing, Properties, and Applications of Iron Aluminides, J. H. Schneibel and M. A. Crimp (eds.), The Minerals, Metals, and Materials Society, Warrendale, PA, 1994.
4. I. G. Wright, C. G. McKamey, and B. A. Pint, "ODS Iron Aluminides," these proceedings.
5. W. J. Quadakkers, K. Schmidt, H. Grubmeier, and E. Wallura, Mater. High. Temperature **10**, 23 (1992).

6. H. T. Michels, Metall. Trans. A **9A**, 873 (1978)

7. B. A. Pint and L. W. Hobbs, pp. 987-92 in High-Temperature Ordered Intermetallic Alloys VI, J. A. Horton, I. Baker, S. Hanada, R. D. Noebe, and D. S. Schwartz (eds.), The Materials Research Society, Pittsburgh, PA, 1995.

8. B. A. Pint, K. B. Alexander, and P. F. Tortorelli, "The Effect of Various Oxide Dispersions on the Oxidation Resistance of Fe_3Al," pp. 1315-20 in High-Temperature Ordered Intermetallic Alloys VI, J. A. Horton, I. Baker, S. Hanada, R. D. Noebe, and D. S. Schwartz (eds.), The Materials Research Society, Pittsburgh, PA, 1995.

9. J. H. DeVan, P. F. Tortorelli, and M. J. Bennett, pp. 309-20 in *Proc. Eighth Annual Conf. Fossil Energy Materials*, N. C. Cole and R. R. Judkins (comp.), CONF-9405143, U. S. Department of Energy, August 1994.

10. B. A. Pint, Oxid. Met. **44**, (1995) in press.

11. G. M. Goodwin, P. J. Masiasz, C. G. McKamey, J. H. DeVan, and V. K. Sikka, pp. 205-10 in *Proc. Eighth Annual Conf. Fossil Energy Materials*, N. C. Cole and R. R. Judkins (comp.), U. S. Department of Energy, 1994.

12. G. M. Goodwin, "Weld Overlay Cladding With Iron Aluminides," these proceedings

13. J. H. DeVan, H. S. Hsu, and M. Howell, Oak Ridge National Laboratory report, ORNL/TM-11176, May 1989.

14. J. H. DeVan, pp. 107-115 in Oxidation of High-Temperature Intermetallics, T. Grobstein and J. Doychak (eds.), The Minerals, Metals, and Materials Society, 1989.

15. P. F. Tortorelli, J. H. DeVan, G. M. Goodwin, and M. Howell, accepted for publication in High-Temperature Coatings I, N. B. Dahotre, J. Hampikian, and J. J. Stiglich (eds.), The Minerals, Metals, and Materials Society, Warrendale, PA, 1994.

16. J. H. DeVan and P. F. Tortorelli, Corros. Sci. **35**, 1065 (1993).

EFFECT OF SURFACE CONDITION ON THE AQUEOUS CORROSION BEHAVIOR OF IRON ALUMINIDES

R. A. Buchanan and R. L. Perrin

Department of Materials Science and Engineering
University of Tennessee
Knoxville, TN 37996-2200

ABSTRACT

The effects of retained high-temperature surface oxides, produced during thermomechanical processing and/or heat treatment, on the aqueous-corrosion characteristics of Fe-Al-based alloys were evaluated by electrochemical methods. Cyclic anodic polarization evaluations were conducted at room temperature in a mild acid-chloride solution (pH = 4, 200 ppm Cl^-) on the Fe_3Al-based iron aluminides, FA-84 (Fe-28Al-2Cr-0.05B, at. %), FA-129 (Fe-28Al-5Cr-0.5Nb-0.2C, at. %), and FAL-Mo (Fe-28Al-5Cr-1Mo-0.04B-0.08Zr, at. %), on the FeAl-based iron aluminide, FA-385 (Fe-35.65Al-0.20Mo-0.05Zr-0.11C, at. %), and on the disordered low-aluminum Fe-Al alloy, FAPY (Fe-16.1Al-5.4Cr-1.1Mo-0.1C, at. %). The surface conditions evaluated were: as-received (i.e., with the retained high-temperature oxides), mechanically cleaned (ground through 600-grit SiC paper), and chemically cleaned (10% HNO_3, 2% HF, at 43 °C). The principal electrochemical parameter of interest was the critical pitting potential, with lower values indicating less resistance to chloride-induced localized corrosion. For all materials evaluated, the critical pitting potential was found to be significantly lower in the as-received condition than in the mechanically-cleaned and chemically-cleaned conditions. Mechanisms responsible for the detrimental high-temperature-oxide effect are under study.

INTRODUCTION

The overall objective of this project is to study the effects of retained high-temperature surface oxides, produced during thermomechanical processing and/or heat treatment, on the aqueous-corrosion and environmental-embrittlement characteristics of several Fe_3Al-based iron aluminides, an FeAl-based iron aluminide, and a low-aluminum Fe-Al alloy. Previous aqueous-corrosion studies of these materials by the present authors and colleagues have examined specimens only with cleaned surfaces (i.e., mechanically ground or polished surfaces).[1-4] The high-temperature surface oxides of the present study are not likely to have the same chemistry nor the same morphology (e.g., thermal cracking) as the passive films formed naturally on a clean surface in an aqueous environment. It was hypothesized that the presence of the high-temperature oxide could decrease the resistance to localized corrosion, which, in turn, could increase the probability of hydrogen production during aqueous corrosion processes, leading to

enhanced environmental embrittlement. To address these issues, the project involves cyclic-anodic-polarization testing to evaluate aqueous-corrosion behavior and U-bend stress-corrosion-cracking testing to evaluate environmental-embrittlement behavior.

To date, most of the anodic polarization testing has been completed, utilizing a mild acid-chloride electrolyte at room temperature. These results are herein reported. Upon completion of this phase of the research, the focus will shift to evaluations of the high-temperature-oxide effects on stress-corrosion cracking properties.

In the mild acid-chloride solution, which was designed to simulate aggressive atmospheric-corrosion, the alloys of this study are susceptible, in varying degrees, to pitting corrosion. An excellent method for evaluating the relative pitting-corrosion susceptibility involves producing and analyzing cyclic anodic polarization curves. A schematic illustration of such a curve is shown in Figure 1, where certain electrochemical parameters are identified. To produce the curve, the corrosion sample first is allowed to stabilize in the electrolyte such that a steady-state, open-circuit, corrosion potential, E_{corr}, is established. Next, with a potentiostatic circuit, the potential of the sample, E, is forced in the positive direction at a given rate while the current density, i, is continuously measured. After the potential has moved away from E_{corr} by a relatively small amount ($\approx$ 50 mV), the current density is directly proportional to the corrosion rate. The potential scan is continued in the positive direction until a predetermined reversing current density, i_r, is reached. At this point, the potential scan direction is reversed, moving in the negative direction, and continued until a very low current density is achieved. In Figure 1, the nearly vertical region in the up-scan portion of the curve, characterized by an average passive current density, i_p, is reflective of passivation, where the material has developed a thin protective oxide/hydroxide passive film, and, therefore, corrodes at a very low rate over a range of potentials. At the critical pitting potential, E_{pit}, pitting corrosion initiates, with a sharp increase in current density. The pitting corrosion accelerates to i_r, and continues during the down-scan portion of the curve until the protection (or repassivation) potential, E_p, is reached (which corresponds to the cross-over point for the up-scan and down-scan curves). With reference to Figure 1, two of the parameters often used to characterize relative resistance to pitting corrosion are: (1) the magnitude of E_{pit}, with higher values corresponding to greater pitting resistance, and (2) the difference between E_{pit} and E_{corr}, i.e., (E_{pit} - E_{corr}), with higher values corresponding to greater pitting resistance.

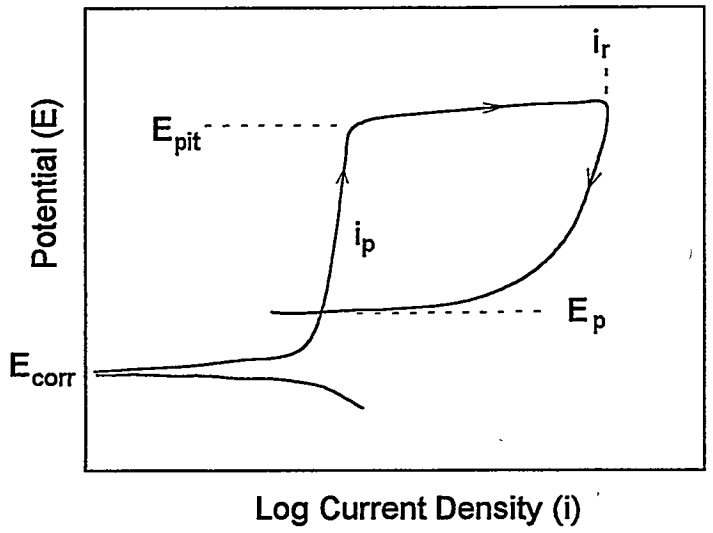

Fig. 1. Schematic illustration of cyclic anodic polarization behavior.

EXPERIMENTAL PROCEDURES

Cyclic anodic polarization tests were conducted at room temperature in a mild acid-chloride solution (pH = 4, 200 ppm Cl^-) on the following materials: the Fe_3Al-based iron aluminides, FA-84 (Fe-28Al-2Cr-0.05B, at. %), FA-129 (Fe-28Al-5Cr-0.5Nb-0.2C, at. %), and FAL-Mo (Fe-28Al-5Cr-1Mo-0.04B-0.08Zr, at. %), a disordered low-aluminum Fe-Al alloy, FAPY (Fe-16.1Al-5.4Cr-1.1Mo-0.1C, at. %), and an FeAl-based iron aluminide, FA-385 (Fe-35.65Al-0.20Mo-0.05Zr-0.11C, at. %). The FA-84, FA-129, FAL-Mo, and FAPY materials, in as-processed sheet form, were kindly supplied by Dr. Vinod Sikka of the Oak Ridge National Laboratory (ORNL); the FA-385 material, in rod form with a cladding, was kindly supplied by Dr. Philip Maziasz of ORNL.

For the FA-84, FA-129, FAL-Mo, and FAPY materials, the surface conditions evaluated were as follows: (1) as-processed (i.e., with the retained high-temperature oxides characteristic of the prior thermomechanical processing methods), (2) mechanically cleaned (ground through 600-grit SiC paper to remove all high-temperature oxides), and (3) chemically cleaned (immersed in a 10% HNO_3, 2% HF solution, at 43 °C, until all high-temperature oxides were removed (approximately 30 minutes), then immersed in 10% HNO_3 at 43 °C for one hour as a passivation treatment). Because of the form of the as-received FA-385 material (rods with protective claddings), it did not

have the high-temperature oxides. To create the high-temperature-oxide surface condition, the FA-385 samples were annealed in air at 750 °C for one hour, then air cooled. This condition will be referred to as the "heat treated" condition, not as the as-processed condition. The mechanically-cleaned and chemically-cleaned conditions were accomplished in the same manner as described for the other materials.

Cyclic anodic polarization tests were performed with a standard polarization cell and an EG&G Model 273 potentiostat. Each sample was mounted in epoxy, attached and electrically connected to a sample holder, and placed in a polarization cell containing the mild acid-chloride electrolyte. Stabilization was allowed to occur for at least one hour, after which E_{corr} was measured. The cyclic polarization curve was then generated at a scan rate of 600 mV/h. The reversing current density was 1000 $\mu A/cm^2$.

RESULTS AND DISCUSSION

The cyclic anodic polarization behaviors of FA-84 (28Al-2Cr) in the as-processed and mechanically-cleaned surface conditions are shown in Figure 2. The as-processed condition, relative to the mechanically-cleaned condition, produced a slightly lower pitting potential (E_{pit}), a lower average passive current density (i_p), and a much higher corrosion potential (E_{corr}). The lower E_{pit} value and the lower (E_{pit} - E_{corr}) value for the as-processed (high-temperature oxide) surface condition both indicated reduced resistance to pitting corrosion.

As seen in Figure 3 for the FA-129 (28Al-5Cr) alloy, the as-processed surface condition performed poorly with respect to both the mechanically-cleaned and chemically-cleaned surface conditions. The as-processed surface condition showed almost no tendency for passivation. For the as-processed surface, the pitting potential was significantly lower, and the corrosion potential higher, than for the other two conditions which involved removal of the high-temperature oxide. Again, the lower E_{pit} value and the lower (E_{pit} - E_{corr}) value for the as-processed surface condition both indicated reduced resistance to pitting corrosion.

As seen in Figure 4 for the FAL-Mo (28Al-5Cr-1Mo) alloy, the pitting potential, E_{pit}, for the as-processed surface condition was significantly lower than E_{pit} values for the mechanically-cleaned and chemically-cleaned surfaces. Also, the range of the passive current density, i_p, was rather small for the as-processed surface condition. It also is noted that the high-temperature oxide on the as-processed surface did not produce a stable i_p, i.e., current-density fluctuations

were obvious. The mechanically and chemically cleaned conditions each had certain advantages. The mechanically-cleaned surface had a slightly higher E_{pit} and a lower E_{corr}. However, the chemically cleaned surface had a significantly lower i_p. The lower i_p suggested that there was either a thickening of the passive film or possibly a Cr enrichment of the passive film caused by the chemical cleaning process.

The cyclic anodic polarization behaviors of the disordered alloy, FAPY (16Al-5Cr-1Mo), in the as-processed and mechanically-cleaned surface conditions are shown in Figure 5. Once again, the as-processed surface performed poorly in comparison to the mechanically-cleaned surface. The as-processed surface condition produced a much lower E_{pit}, with little indication of a passive current density, i_p, and a much higher E_{corr} value.

As seen in Figure 6 for the FeAl-based iron aluminide, FA-385 (36Al-0.2Mo), the heat-treated high-temperature-oxide surface condition produced a much lower E_{pit}, a much lower i_p, and a higher E_{corr} value than the mechanically-cleaned surface condition. The lower E_{pit} value and the lower (E_{pit} - E_{corr}) value for the high-temperature-oxide surface condition both indicated reduced resistance to pitting corrosion.

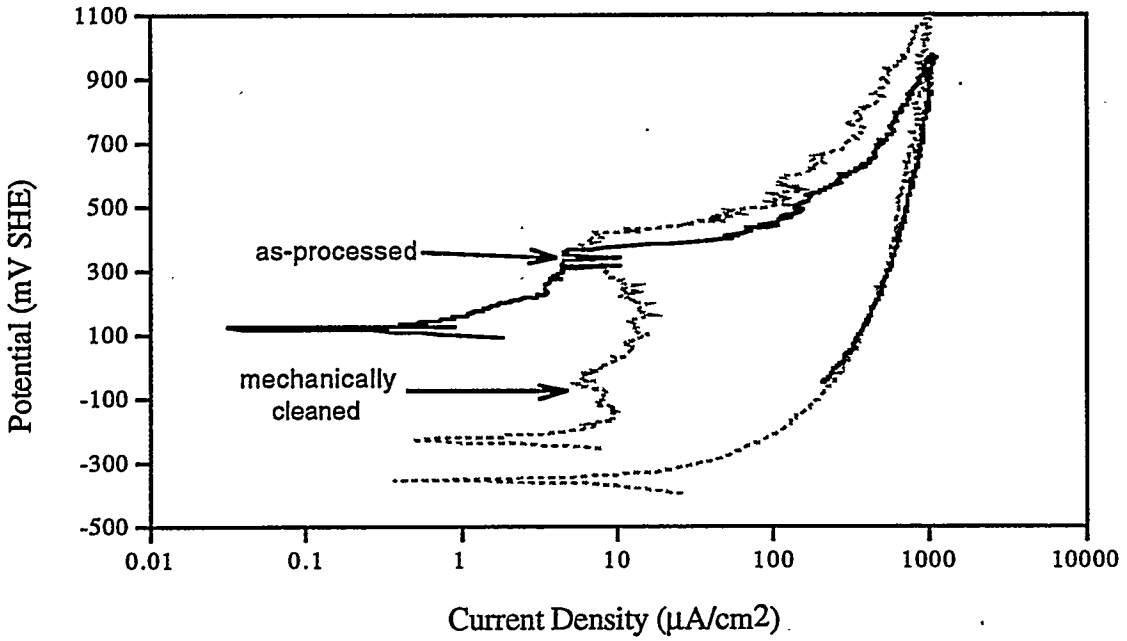

Fig. 2. Cyclic anodic polarization behaviors of FA-84 with as-processed and mechanically-cleaned surfaces.

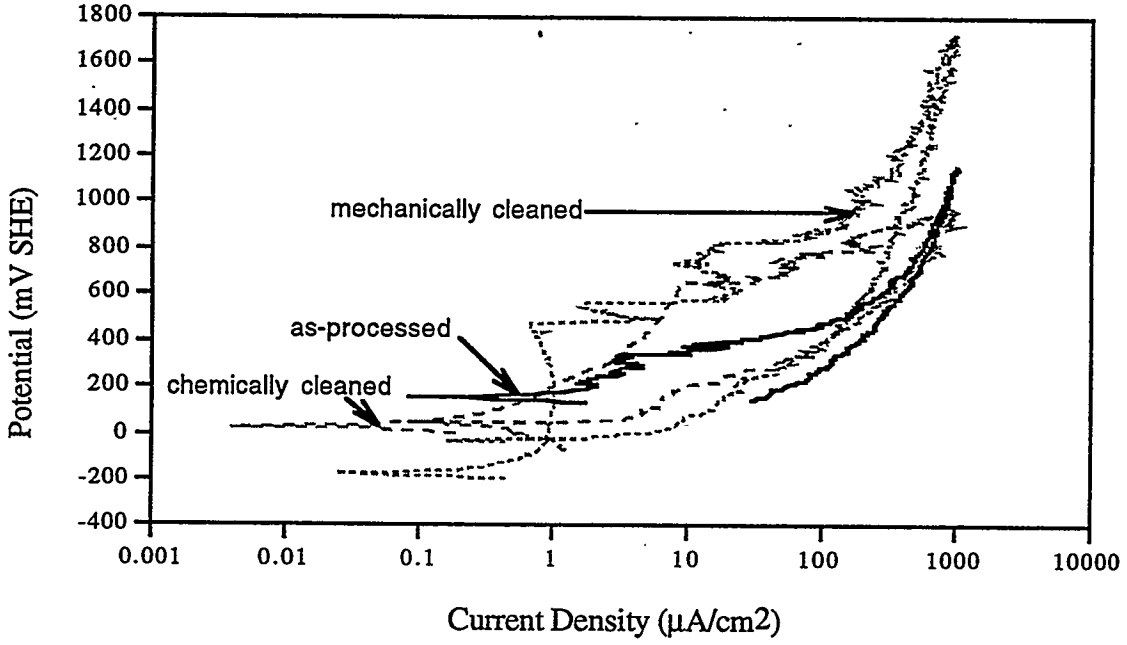

Fig 3. Cyclic anodic polarization behaviors of FA-129 with as-processed, mechanically-cleaned, and chemically-cleaned surfaces.

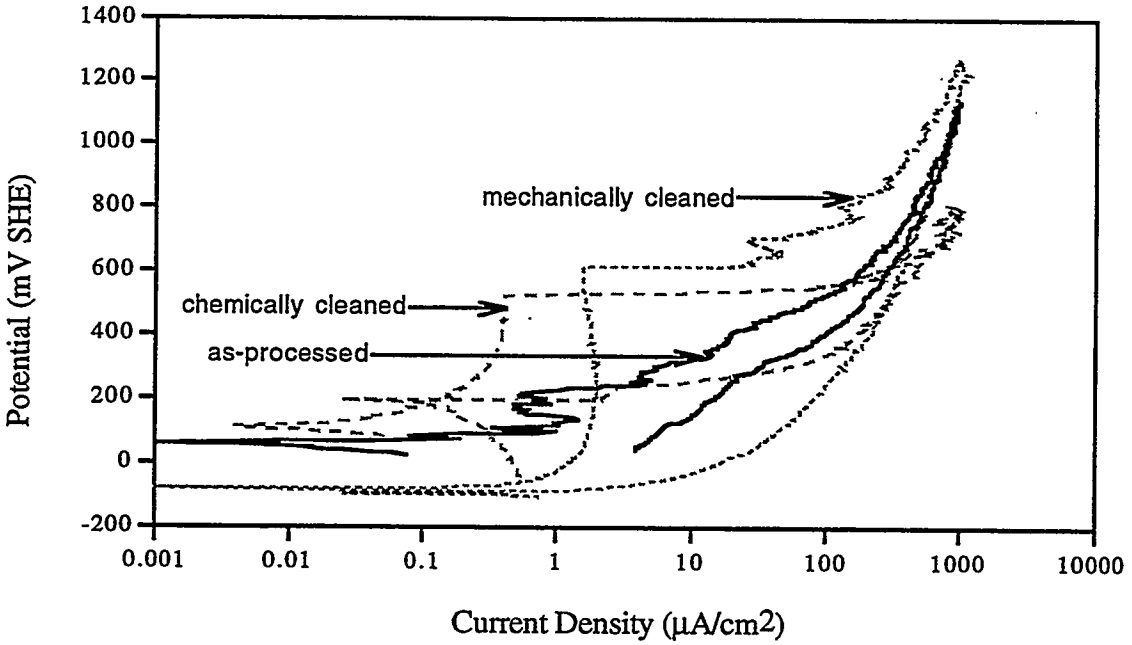

Fig 4. Cyclic anodic polarization behaviors of FAL-Mo with as-processed, mechanically-cleaned, and chemically-cleaned surfaces.

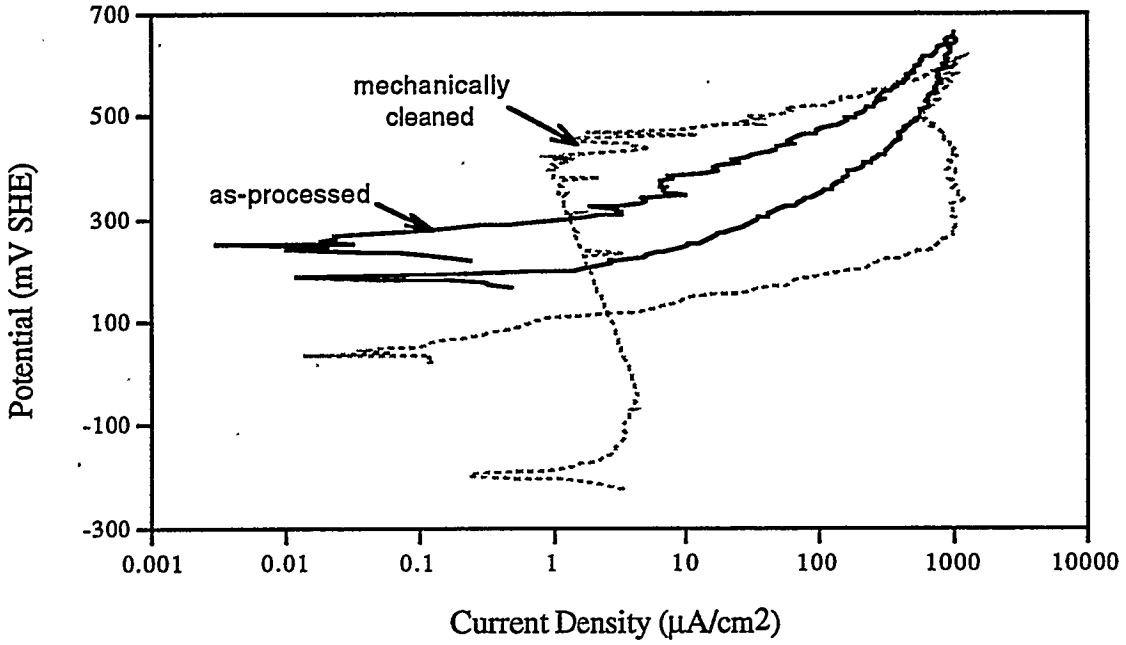

Fig 5. Cyclic anodic polarization behaviors of FAPY with as-processed and mechanically-cleaned surfaces.

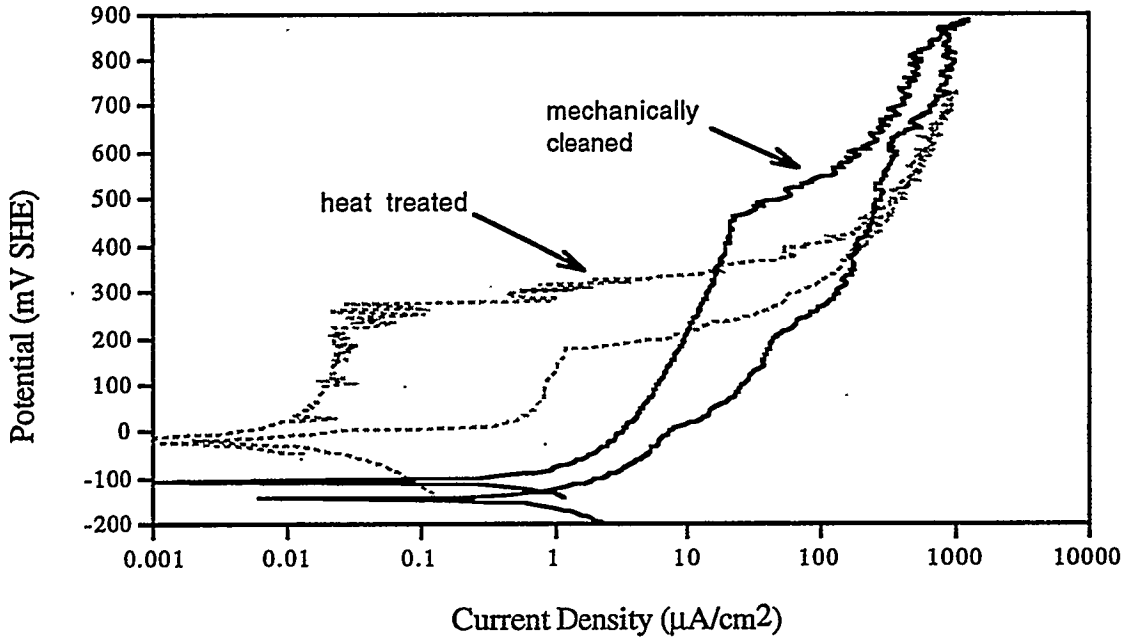

Fig 6. Cyclic anodic polarization behaviors of FA-385 with heat-treated and mechanically-cleaned surfaces.

To provide comparisons of selected results for all materials and surface conditions evaluated, bar graphs of critical pitting potentials, E_{pit}, and the difference between critical pitting and corrosion potentials, (E_{pit} - E_{corr}), are shown in Figures 7 and 8, respectively. It is apparent for all materials that both E_{pit} and (E_{pit} - E_{corr}) were significantly lower for the high-temperature-oxide surfaces, indicating significantly reduced resistance to localized corrosion for these surfaces.

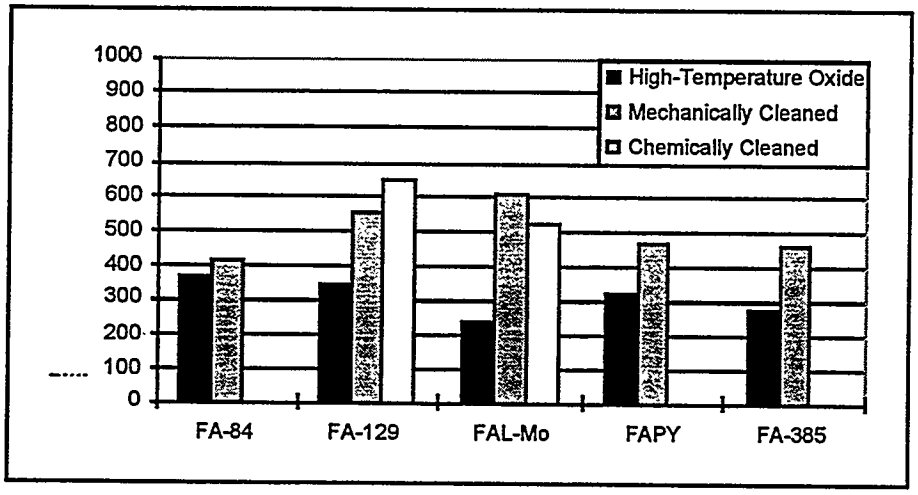

Fig. 7. Critical pitting potential versus material and surface condition.

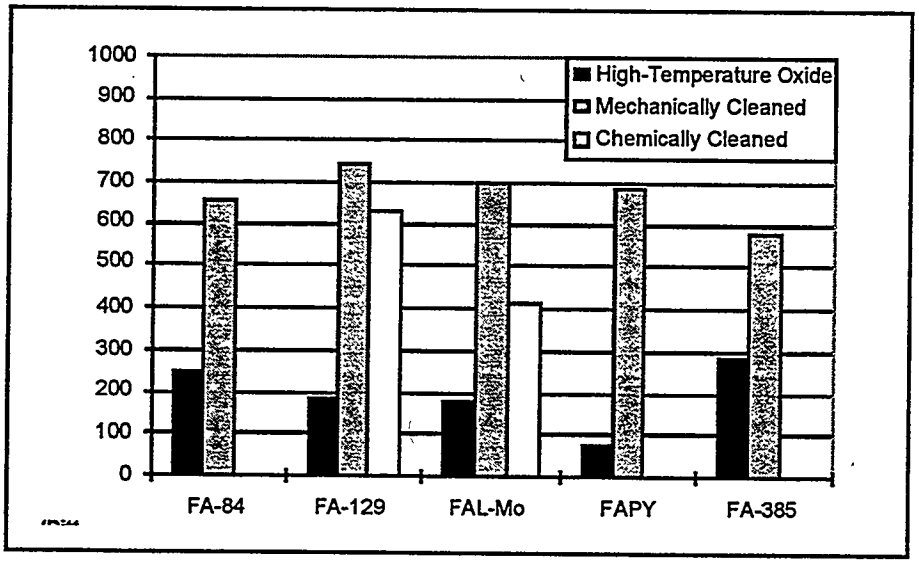

Fig. 8. Difference between pitting and corrosion potentials versus material and surface condition.

Another observation that did not manifest itself directly in the polarization behavior was the appearance of the surfaces of the samples after chemical cleaning. The high-temperature-oxide surfaces of FA-84 and FA-129 were cleaned rather easily in the 10% HNO_3, 2% HF solution but also could be cleaned in a solution containing only 10% HNO_3. However, the oxide surfaces of FAL-Mo and FAPY were slow to clean in the 10% HNO_3, 2% HF solution, and could not be cleaned at all in the 10% HNO_3 solution. Furthermore, after chemical cleaning, the FA-129 and FA-84 samples had shiny smooth surfaces, whereas the FAL-Mo and FAPY samples had shiny rough surfaces. For the FAL-Mo and FAPY samples, the attack of the 10% HNO_3, 2% HF solution was more prominent in areas of exposed base material, i.e., cut faces or where the oxide had flaked off. The difficulties experienced in removal of the high-temperature oxides apparently can be attributed to the presence of Mo in the FAL-Mo and FAPY alloys, which is also partly responsible for the greater aqueous-corrosion resistance exhibited by these alloys.

CONCLUSIONS

Electrochemical aqueous-corrosion studies showed that retained high-temperature surface oxides on iron aluminides (FA-84, FA-129, FAL-Mo, and FA-385) and a related alloy (FAPY), produced during thermomechanical and/or heat treatment processing, caused major reductions in corrosion resistance in an electrolyte designed to simulate aggressive atmospheric corrosion. Removal of the oxides by mechanical grinding, or, more practically, by chemical cleaning restored the corrosion resistance. A standard picking solution employed for stainless steels, nitric plus hydrofluoric acid, worked well for the iron aluminides not containing Mo (FA-84 and FA-129), producing a clean, smooth surface. However, for the Mo-containing materials (FAL-Mo and FAPY), although this solution was effective in removing the oxide, it produced an unacceptably rough surface. Improved chemical cleaning procedures are currently being investigated.

REFERENCES

1. R. A. Buchanan and J. G. Kim, "Fe_3Al-Type Iron Aluminides: Aqueous Corrosion Properties in a Range of Electrolytes and Slow-Strain-Rate Ductilites During Aqueous Corrosion," Final Report, U. S. Dept. of Energy, Fossil Energy AR & TD Materials Program, ORNL/Sub/88-07685CT92/02, National Technical Information Service, Springfield, VA, August, 1992.

2. J. G. Kim and R. A. Buchanan, "Aqueous Corrosion Properties and Slow-Strain-Rate Ductilities of Fe_3Al-Based and Lean-Aluminum Iron Aluminides," Final Report, U. S. Dept.

of Energy, Fossil Energy AR & TD Materials Program, ORNL/Sub/88-07685CT92/03, National Technical Information Service, Springfield, VA, August, 1993.

3. J. G. Kim and R. A. Buchanan, "Pitting and Crevice Corrosion of Iron Aluminides in a Mild Acid-Chloride Solution," Corrosion, Vol. 50, No. 9, pp. 658-668, Sept., 1994.

4. J. G. Kim and R. A. Buchanan, "Localized Corrosion and Stress Corrosion Cracking Characteristics of a Low-Aluminum-Content Iron Aluminum Alloy," Final Report, U. S. Dept. of Energy, Fossil Energy AR & TD Materials Program, ORNL/Sub/88-07685CT92/04, National Technical Information Service, Springfield, VA, October, 1994.

Pack Cementation Cr-Al Coating of Steels and Ge-Doped Silicide Coating of Cr-Nb Alloy

Y. R. He, M. H. Zheng and R. A. Rapp

Department of Materials Science and Engineering
The Ohio State University
2041 College Road
Columbus, OH 43210-1179

ABSTRACT

Carbon steels or low-alloy steels used in utility boilers, heat exchangers, petrochemical plants and coal gasification systems are subjected to high temperature corrosion attack such as oxidation, sulfidation and hot corrosion. The pack cementation coating process has proven to be an economical and effective method to enhance the corrosion resistance by modifying the surface composition of steels. With the aid of a computer program, STEPSOL, pack cementation conditions to produce a ferrite Cr-Al diffusion coating on carbon-containing steels by using elemental Cr and Al powders have been calculated and experimentally verified. The cyclic oxidation kinetics for the Cr-Al coated steels are presented.

Chromium silicide can maintain high oxidation resistance up to 1100°C by forming a SiO_2 protective scale. Previous studies at Ohio State University have shown that the cyclic oxidation resistance of $MoSi_2$ and $TiSi_2$ can be further improved by Ge addition introduced during coating growth. The halide-activated pack cementation process was modified to produce a Ge-doped silicide diffusion coating in a single processing step for the ORNL-developed Cr-Nb advanced intermetallic alloy. The oxidation behavior of the silicide-coated Cr-Nb alloy was excellent: weight gain of about 1mg/cm^2 upon oxidation at 1100°C in air for 100 hours.

INTRODUCTION

For economic reasons, carbon steels or low alloy steels are still the principal materials used in utility boilers, heat exchangers, petrochemical plants and coal gasification systems. The corrosion of these materials by oxidation, sulfidation or hot corrosion at elevated temperatures is a major problem encountered in these systems. One of the approaches to improve the corrosion resistance of steels is to modify the surface composition. Extensive studies have shown that ternary iron-base alloys containing 15-25 wt.% Cr, 4-6 wt.% Al exhibits excellent oxidation resistance at high temperatures due to the synergistic interaction of the two oxidation-resistant elements[1-4]. When exposed to an oxidizing environment at high temperature, a continuous adherent Cr_2O_3 scale is initially formed on the surface of the alloys. The rapid oxidation of Fe and the internal oxidation of Al are prevented by the formation of this scale. The Al atoms diffuse eventually to the Cr_2O_3/alloy interface and form a slowly growing, more stable, Al_2O_3 scale. Therefore, a

surface composition of Fe - (15-25)wt.% Cr - (4-6)wt.% Al (Kanthal- like composition) is desirable to enhance the corrosion resistance of low-alloy steels.

Pack cementation has the advantages of low cost, good adhesion and wide versatility, as compared with other surface modification methods, such as metalliding, hot dipping, ion implantation, laser surface alloying[5]. There has been considerable work to develop a chromized-aluminized coating on steels by pack cementation[6-11]. Kanthal-like surface compositions have been achieved on low-carbon steels by using Cr-Al masteralloys. To reduce the material cost and optimize the pack cementation process, the current research is intended to develop a Kanthal-like Cr-Al coating on carbon-containing steels by using Cr and Al elemental powders in a pack cementation process.

Cr-silicide can maintain reasonable oxidation resistance up to 1100°C[12]. Another goal for this work was to develop a Ge-doped silicide coating on Cr-Nb alloys developed by Oak Ridge National Laboratory (ORNL). The purpose of the Ge addition is to improve the protective SiO_2 film that forms on the silicide coating during high-temperature oxidation. Previous studies by Mueller, et al. show that Ge-doped $(Mo,W)Si_2$ improves the isothermal and cyclic oxidation resistance by increasing the thermal expansion coefficient of the vitreous silica film, and prevents pesting by decreasing the viscosity of the protective film[13, 14]. Cockeram and Rapp have also successfully developed a Ge-doped Ti-silicide diffusion coating on commercially pure Ti, Ti-22Al-27Nb and Ti-20Al-22Nb alloys in a single coating process[15].

PACK CEMENTATION

Halide-activated pack cementation is a high temperature in-situ chemical vapor deposition process. A pack consists of four components: substrate(s) to be coated, metal(s) or masteralloy(s) containing the element(s) to be deposited, halide activator salt(s), and an inert filler. The activator salt reacts with the masteralloy(s) and generates volatile metal halides. Driven by the chemical potential gradients for the elemental components between the pack and the substrate, these halide vapors diffuse through the porous filler material to the substrate surface, where the deposition of the element(s) occurs by one or more reactions[16].

Codeposition of two or more elements in a single processing step by the pack cementation method requires comparable partial pressures of the halide vapors containing these elements. If the partial pressure of one element dominates, the deposition of the other elements will be suppressed.

EXPERIMENTAL PROCEDURES

Nominally pure elemental powders of Al (99.9%, K-109, Transmet Corp.), Cr (99.22%, 100-325 mesh, Shieldalloy Metallurgical Corp.), Si (99%, -325 mesh, Alfa), Ge (99.999%, Eagle Picher Industries) were used. The halide salt activators were NH_4Cl (99.8%, J. T. Baker Inc.), $MgCl_2$, NaF (99.7%, J. T. Baker Chem. Co.). Alumina (98%, 60-325 mesh, Fisher Sci.) was used as an inert filler. The alumina crucible containing the pack was sealed with an alumina lid using high-temperature Ceramabond. The sealed crucible was then cured in an electric oven (90°C) for more than 2 hours, then positioned in the uniform heating zone of a horizontal resistance-heated tube furnace. Prepurified Ar gas flowed through the furnace tube to protect the pack from oxidation. A K-type thermocouple was used to measure the temperature. After holding at the desired temperature for a given time, the crucible was allowed to furnace cool. The coupon retrieved from the pack was cleaned in an ultrasonic cleaner.

A Nikon EPIPHOT-TME optical microscope was used for metallographic examination. X-ray analysis was carried out on a SCINTAG diffractometer. A Phillips XL-30 scanning electron microscope (SEM) with an Energy Dispersive X-ray Spectrometer (EDS) was utilized to analyze the cross-sections of the samples.

RESULTS AND DISCUSSION

Cr-Al Coating on T11 Alloy

A pack containing 18 Cr - 2 Al -2 $MgCl_2$ - 1 NH_4Cl - 77 Al_2O_3 (wt.%) was used to codeposit Cr and Al on T11 steel. The pack cementation cycle consisted of heating to 950°C, holding for 4 hours, then raising the temperature to 1150°C and holding for 3 hours before furnace cooling to room temperature.

Figure 1 shows the cross-section of a T11 steel Cr-Al coated at 950°C for 4 hours. A ferrite coating layer was formed; $Cr_{23}C_6$ was not detected by X-ray diffraction analysis. At this low temperature (950°C), the ferrite-stabilizing Al was transported to the surface, such that the carbon in the steel was again rejected into the austenite core, before the $CrCl_2$ vapor reached a sufficient vapor pressure to form $Cr_{23}C_6$. Once the ferrite case has been initiated, the inward rejection of carbon in front of the growing ferrite permits the addition of Cr to the ferrite layer without carbide formation. Figure 2 (a) displays the cross-section of Cr-Al coated T11 after the complete processing cycle. Pearlite formed beneath the ferrite coating layer due to the rejection of C from the ferrite layer to the austenite core at the processing temperature. The composition profile of Fig. 2 (a) is shown in Fig. 2 (b). Obviously, this composition range is not that desired, and future

experimentation will seek to achieve the Fe-20Cr-5Al composition. The avoidance of Cr carbide formation at the external surface confirmed the applicability of the sequential deposition mode[11], as illustrated in Fig. 3.

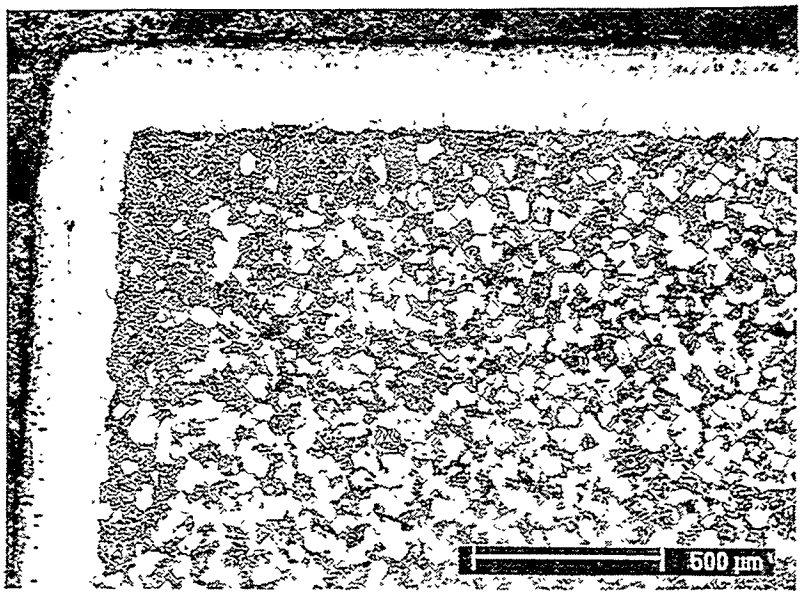

Fig. 1 Cross-section of T11 steel Cr-Al coated at 950°C for 4 hours

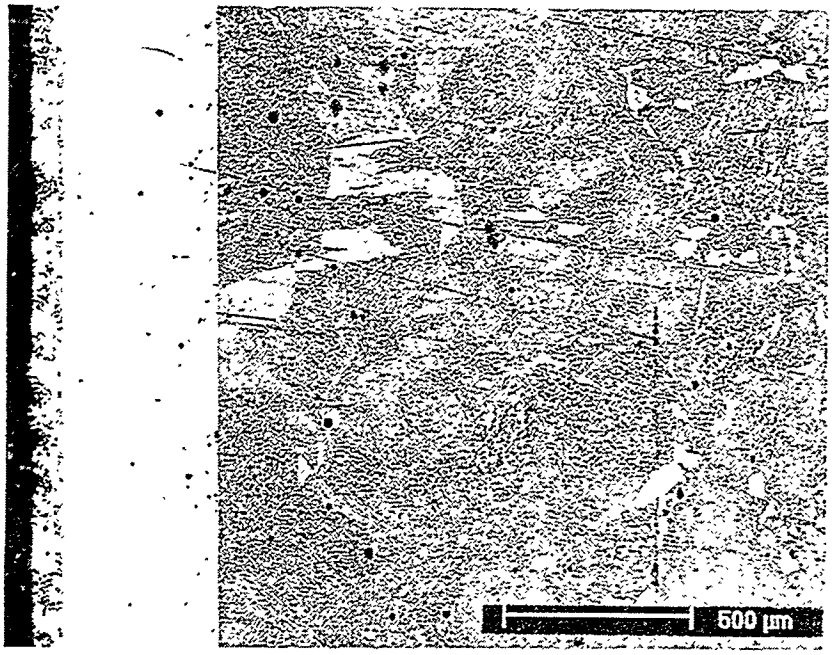

Fig. 2 (a) Cross-section of T11 steel Cr-Al coated at 950°C for 4 hour followed by another 3 hour holding at 1150°C

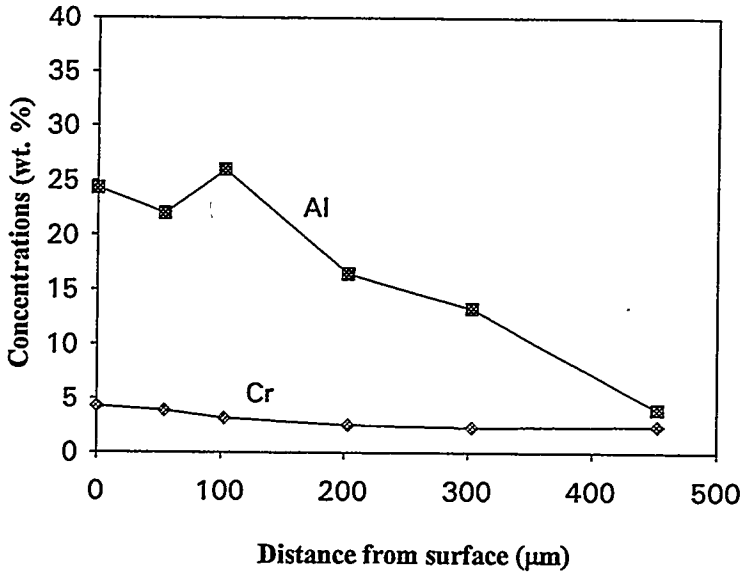

Fig. 2 (b) Composition profile of Cr-Al coated T11steel

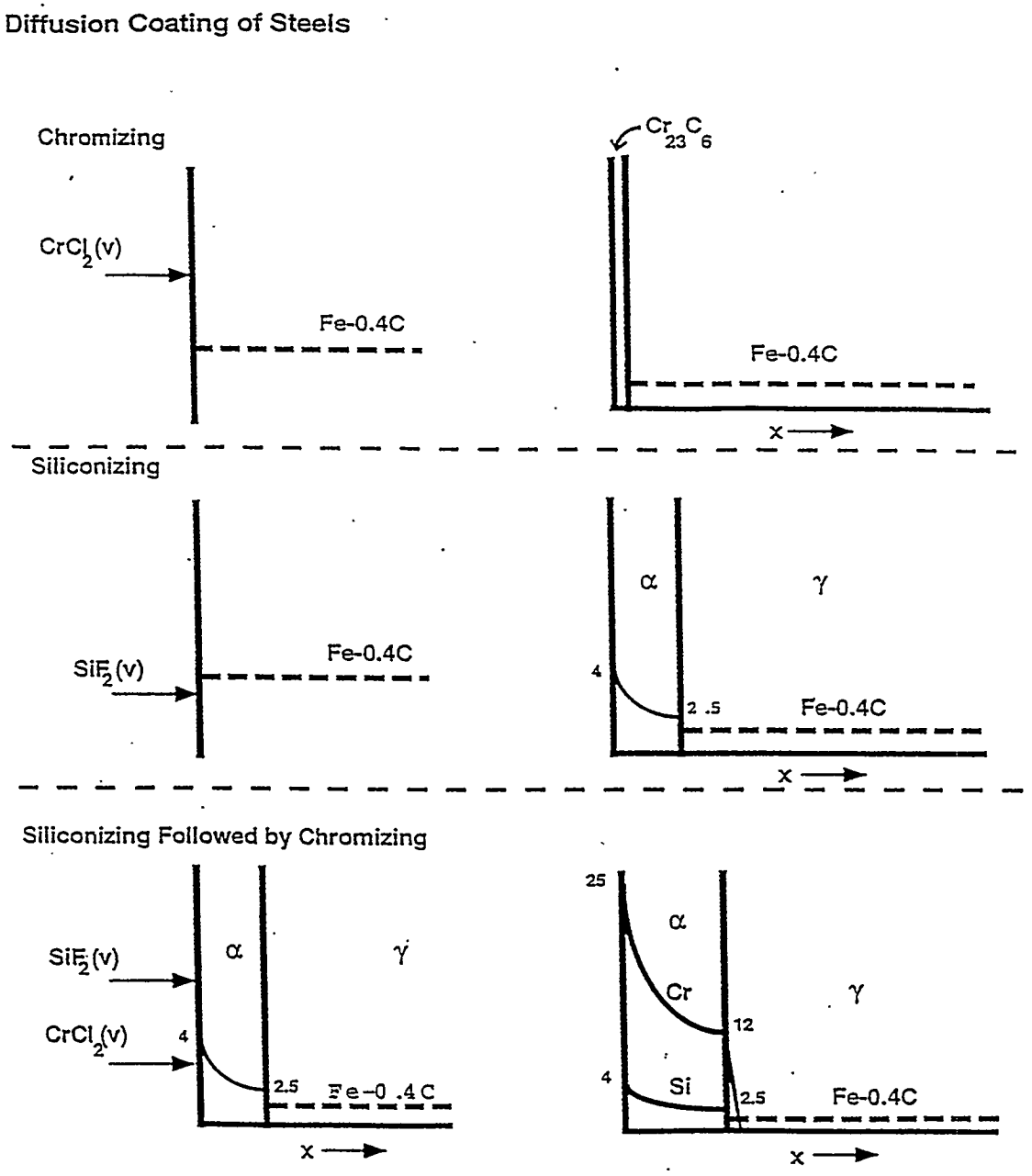

Fig. 3 Processing scheme illustrating mode for codeposition of Cr-Si or Cr-Al to form a ferrite case without a blocking Cr-carbide

Ge-Doped Silicide Coating on Cr-Nb Alloys

With the aid of a computer program, STEPSOL, the equilibrium vapor pressures in a NaF activated pack containing pure Si and pure Ge at 1000°C and 1 atm. total pressure were calculated and are listed in Table 1. Unit activity was used for Si and Ge in the calculation. During pack cementation, Si-Ge alloy is expected to form in the pack from the initial mixture of the pure elemental powders by melting of Ge (melting point 937°C). Therefore, the activities of both Si and Ge in the pack would be less than unity.

Table 1. The STEPSOL computed equilibrium vapor pressure in a NaF-activated pack containing pure Si -pure Ge and Al_2O_3 filler at 1000°C and 1 atm. total pressure

Species	Pressure (atm.)	Species	Pressure (atm.)
Ar	9.94×10^{-1}	GeF_2	1.86×10^{-6}
Na	3.95×10^{-3}	GeF	2.30×10^{-8}
SiF_4	9.17×10^{-4}	Ge	7.15×10^{-9}
NaF	3.66×10^{-4}	SiF	4.8×10^{-10}
SiF_3	7.98×10^{-5}	Si	1.69×10^{-11}
Na_2F_2	3.92×10^{-5}	GeF_3	2.76×10^{-18}
SiF_2	6.32×10^{-6}	GeF_4	8.77×10^{-21}

Four Cr-silicide compounds, Cr_3Si, Cr_5Si_3, CrSi and $CrSi_2$, exist in the Cr-Si system. Due to the lack of standard X-ray diffraction patterns for Cr_5Si_3 and CrSi, EDS data were used to identify the existing phases after pack cementation.

Figures 4 (a) and 4 (b) show the surface morphology and the cross-section of a CN-87 alloy coated at 1000°C for 12 hours in a pack containing 16Si-8Ge (wt.%), respectively. X-ray diffraction analysis on the coupon surface revealed the existence of Cr_3Si and $Cr(Si,Al)_2$. EDS data showed that the externally deposited phase in Fig. 4 (a) was composed of 57.0F, 34.9 Na and 8.1Al (at.%). Previous work found that a Na-Al-oxide byproduct layer formed on the surface of $MoSi_2$ coating resulted from the use of a NaF activator[17]. This Na-rich byproduct passivated the $MoSi_2$ coating by forming a faster growing Na-silicate scale and suppressing accelerated oxidation and pesting of $MoSi_2$ during low-temperature oxidation. Three phases were identified in the back-scattered electron (BSE) image in Fig. 4 (c), a high magnification image of the coating in Fig. 4 (b). EDS analysis shows that the gray phase is composed of 33.9Cr, 14.9Fe, 48.6Si plus 1.0Ge, suggesting the existence of (Cr,Fe)(Si,Ge); the bright phase has the composition 25.9Cr, 20.1 Nb, 5.9Mo, 5.7 Fe, 41.6Si with 0.86Ge; the dark phase consisted of 28.2Cr, 4.8Fe, 62.0Si plus 0.5 Ge, probably in a form of $(Cr,Fe)(Si,Ge)_2$.

A cross-section of CN-87 alloy coated in a pack containing 16Ge-8Si (wt.%) is displayed in Fig. 5. X-ray diffraction analysis detected the existence of Cr_3Si phase in the coating. The coating can be subdivided into three layers. The two phases in the outermost layer in Fig. 5 (b) are a dark phase containing 29.7Cr, 26.9Fe, 42.3Si plus 0.5Ge, and a heterogeneous gray phase containing 34.8Cr, 7.8Fe, 9.8Nb, 3.5Mo, 43.1Si with 0.9Ge. The second layer was mainly composed of a gray phase decorated with some bright and dark phases. EDS analysis indicated the highest Ge content in the gray phase with a composition of 45.6Cr, 12.6Fe, 33.7Si and 1.8Ge. The third layer was very irregular and composed of a dark phase (50.6Cr, 15.7Fe, 2.4Mo, 30.8 Si and 0.1 Ge) and partially transformed Cr_2Nb particles.

Figures 6 (a) and (b) present the surface and cross-section of the CN-87 alloy coated in a pack containing 20Ge-4Si (wt.%), respectively. The $Cr_3NbSi_{2.66}$ phase was identified using X-ray diffraction. The formation of nodules with 10.4Na, 18.8Al, 14.2Si, 48.4O and 8.1F on the surface of the coupon indicated again the existence of a liquid phase during pack cementation. EDS analysis suggested the formation of (Cr,Fe)(Si,Ge) in the outermost layer with the composition of 25.6Cr, 25.1Fe, 47.7Si plus 1.6Ge. The heterogeneous phase in the second layer was composed of 38.7Cr, 9.9Fe, 5.3Nb, 3.3Mo, 40.2Si and 2.7Ge. The major phase in the third layer adjacent to the substrate had the composition of 52.4Cr, 8.2Fe, 37.3Si plus 0.5Ge, which might indicate the presence of $(Cr,Fe)_5Si_3$.

The addition of Ge to Cr-silicide showed some effect on the coating morphology, and increasing the ratio of Ge to Si in the pack suppressed the formation of $CrSi_2$ on the CN-87 alloy, perhaps due to the decrease in Si-fluoride vapor pressures with decreasing ratio of Si to Ge. Higher levels of Ge tended to increase the Ge content in the coating and retard coating growth. Also, the Ge concentration is higher in the inner layer for each coating. A similar effect was also observed in the development of the $(Mo,W)(Si,Ge)_2$ coating[13] and the Ge-doped Ti-silicide coating[17].

Figure 7 shows the surface morphology of a CN-80 alloy coated in a NaF activated pack containing 16Si-8Ge. X-ray diffraction analysis detected the formation of $CrSi_2$. Oxidation tests were conducted at 950°C and 1100°C by P. Tortorelli at ORNL. As shown in Fig. 8, the Ge-doped Cr-disilicide coating prevented the CN-80 alloy from suffering significant oxidation at high temperatures. The weight gain was about $1mg/cm^2$ upon oxidation at 1100°C in air for 100 hours.

CONCLUSIONS

Codeposition of Cr and Al in a pack cementation can be achieved using pure elemental powders, but the ideal surface composition has not been achieved. Cr-carbide formation has been prevented by first diffusing ferrite-stabilizing Al into the substrate at lower temperature.

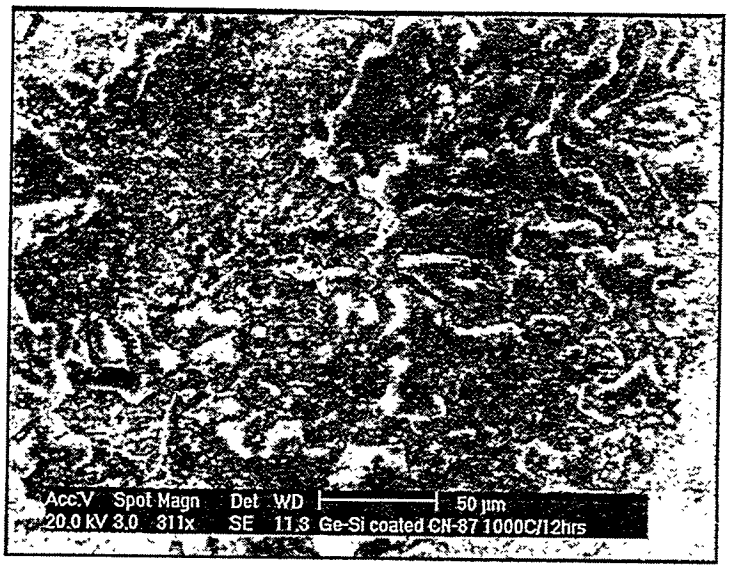

Fig. 4 (a) Surface morphology of CN-87 alloy coated at 1000°C for 12 hours in a NaF activated pack containing 16Si-8Ge.

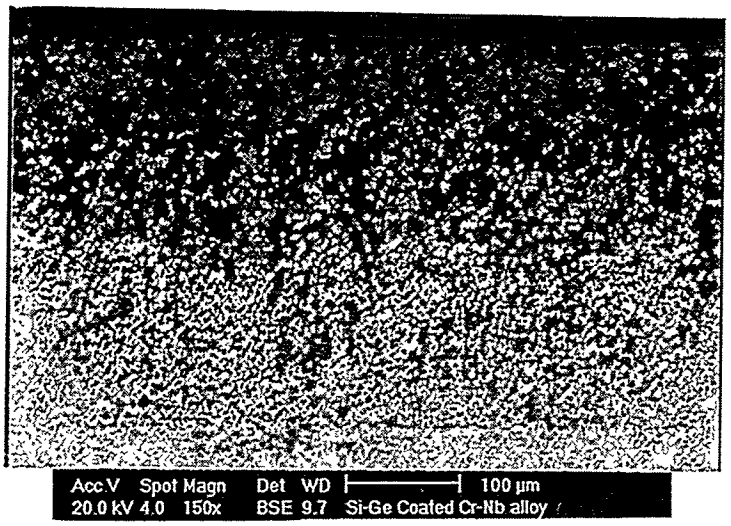

Fig. 4 (b) Cross-section of CN-87 alloy coated at 1000°C for 12 hours in a NaF activated pack containing 16Si-8Ge.

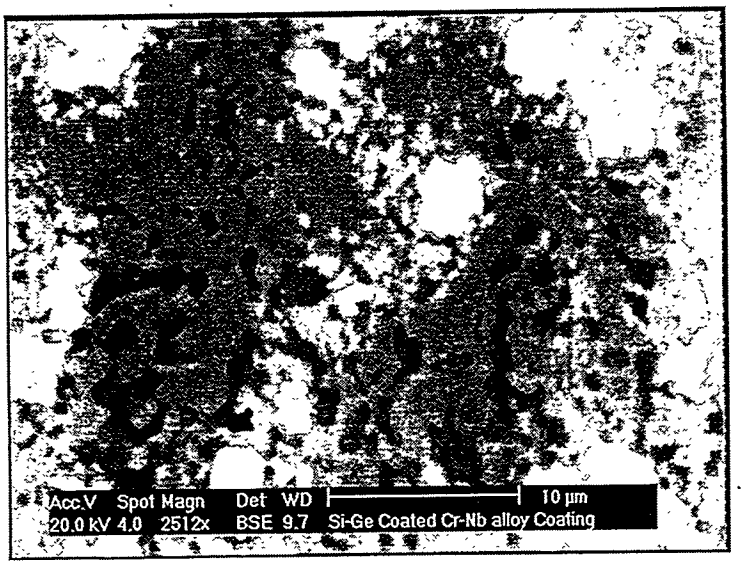

Fig. 4 (c) A high magnification image of the cross-section of Fig. 4 (b).

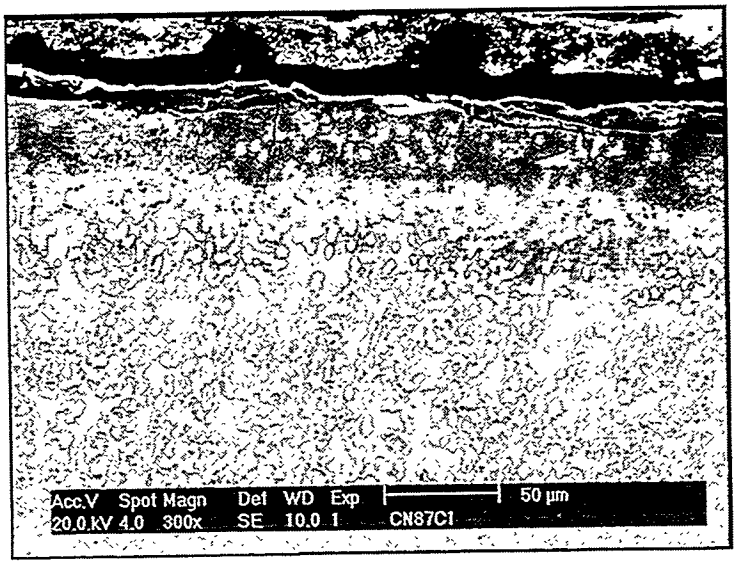

Fig.5 (a) Cross-section of CN-87 alloy coated at 1000°C for 12 hours in a NaF-activated pack containing 8Si-16Ge.

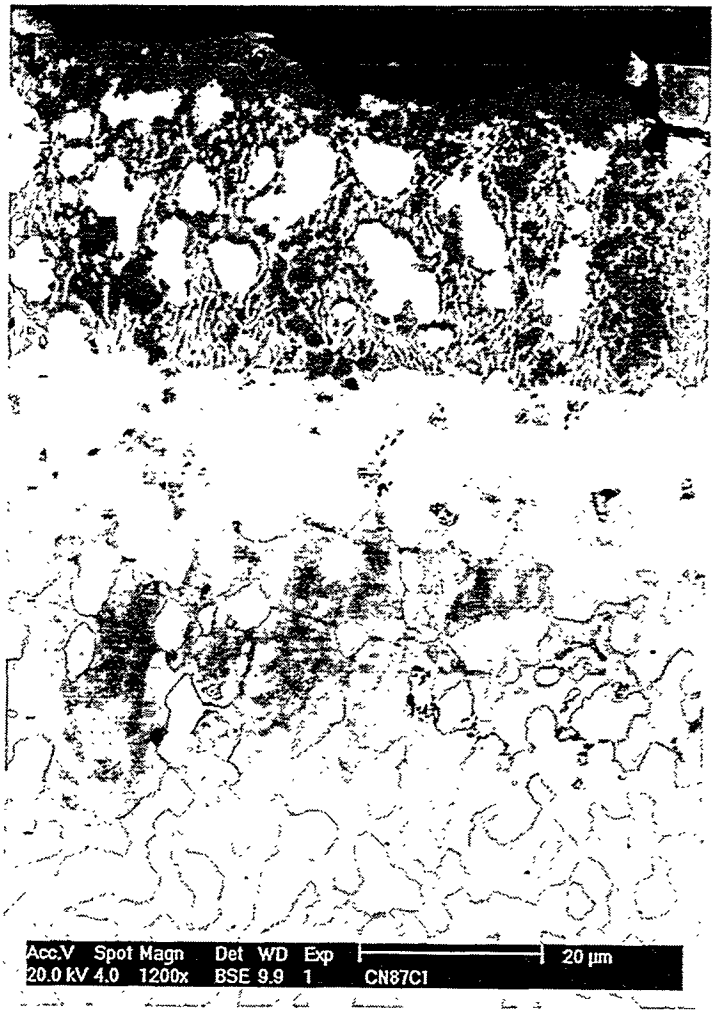

Fig. 5 (b) A high magnification image of Fig. 5 (a)

Ge-doped Cr-silicide diffusion coating was able to be developed on Cr-Nb alloys in a single pack cementation process. The morpology and composition of the coating depended not only on the composition of the pack, but also on the composition of the substrate alloy. Oxidation in air shows that the Ge-doped Cr-silicide coating prevented the Cr-Nb alloy from suffering significant oxidation.

REFERENCES

1. F. H. Stott, G. C. Wood and M. G. Hobby, "A Comparison of the Oxidation Behavior of Fe-Cr-Al, Ni-Cr-Al, and Co-Cr-Al Alloys", Oxid. Met., 3 (2), p. 103, 1971.

2. J. K. Tien and F. S. Pettit, "Mechanism of Oxide Adherence on Fe-25Cr-4Al (Y or Sc) Alloys", Met. Trans., 3 (6), p. 1587, 1972.

3. F. A. Golightly, F. H. Scott and G. C. Wood, "The Influence of Yttrium Addition on Oxide-scale Adhesion to an Iron-Chromium-Aluminum Alloy", Oxid. Met., 10 (3), p. 163, 1976.

4. V. K. Tolpygo and H. J. Grabke, "Microstructural Characterization and Adherence of α-Al_2O_3 Oxide Scales on Fe-Cr-Al and Fe-Cr-Al-Y Alloys", Oxid. Met., 41 (516), p. 343, 1994.

5. P. G. Cappelli, " Coating Processes", High Temperature Alloys for Gas Turbines, D. Coutsouradis, P. Felix, H. Fischmeister, L. Habraken, Y. Lindblom and M. O. Speidel (Eds), Applied Science Publishers, London, p. 177, 1978.

6. D. M. Miller, S. C. Kung, S. D. Scarberry and R. A. Rapp, "Simultaneous Chromizing-Aluminizing Coating of Austenitic Stainless Steels", Oxid. Met., 29, p. 239, 1988.

7. P. A. Choquet, E. R. Naylor and R. A. Rapp, "Simultaneous Chromizing and Aluminizing of Iron-base Alloys", Materials Science and Engineering, A 121, p. 413, 1989.

8. S. C. Kung and R. A. Rapp, "Analyses of the Gaseous Species in Halide-Activated Cementation Coating Packs", Oxid. Met., 32, p. 89, 1989.

9. R. Bianco, M. A. Harper and R. A. Rapp, "Codepositing Elements by Halide-Activated Pack Cementation", JOM, Nov., p. 68, 1991.

10. F. D. Geib and R. A. Rapp, "Simultaneous Chromizing-Aluminizing Coating of Low-Alloy Steels by a Halide-Activated, Pack-Cementation Process", Oxid. Met., p. 213, 1993.

11. N. He, G. Wang and R. A. Rapp, "The Common Component Effect in Multiphase, Multicomponent Equilibria ", High Temperature Science, submitted for publication, 1994.

12. G. H. Meier, "Fundamentals of the Oxidation of High-Temperature Intermetallics", Oxidation of High-Temperature Intermetallics, T. Grobstein and J. Doychak (Eds), TMS Publishers, Pennsylvania., p. 1, 1988.

13. A. Mueller, G. Wang and R. A. Rapp, "Deposition and Cyclic Oxidation Behavior of a Protective (Mo, W)$(Si,Ge)_2$ Coating on Nb-Base Alloys", J. Electrochem. Soc., 139(5), p. 1266, 1992.

14. A. Mueller, G. Wang and R. A. Rapp, "Oxidation Behavior of tungsten and Germanium--Alloyed Molybdenum Disilicide Coatings", Materials Science and Engineering, A155, p. 199, 1992.

15. B. V. Cockeram and R. A. Rapp, "Development and Growth of Boron-Modified and Germanium-Doped Titanium-Silicide Diffusion Coatings by the Halide-Activated Pack Cementation Method", Oxid. Met., submitted for publication, 1995

16. L. L. Seigle, "Thermodynamics and Kinetics of Pack Cementation Processes", Surface Engineering, R. Kossowsky and S. C. Singhal (Eds), Martinus Nijhoff Publishers, Boston, p. 345, 1984.

17. B. V. Cockeram, G. Wang and R. A. Rapp, "Preventing the Accelerated Low-Temperature Oxidation of $MoSi_2$ (Pesting) by the Application of Superficial Alkali Salt Layers", Oxid. Met., accepted for publication, 1995

MICROSTRUCTURE CHARACTERIZATION AND WELDABILITY EVALUATION OF THE WELD HEAT AFFECTED ZONE (HAZ) IN 310HCbN TUBING

C.D. Lundin and C.Y.P. Qiao

Materials Joining Research
Materials Science and Engineering
The University of Tennessee, Knoxville

ABSTRACT

Metallographic evaluation on the Gleeble simulated HAZ samples of 310HCbN tubing material was performed in order to reveal potential degradation in mechanical properties and corrosion resistance. The carbide evolutionary process in the HAZ samples was studied. It is indicated that 310HCbN material showed a weld HAZ sensitization tendency that is associated with the formation of $Cr_{23}C_6$.

INTRODUCTION

310HCbN tubing has been accepted for boiler applications under Code Case 2115. It has been employed by utilities in the United States for replacement of conventional stainless steels. Excellent high temperature mechanical properties, such as creep and high temperature tensile strength, have been reported [1]. However, need for the detailed information on aged base metal and weld HAZ microstructures and their relationship to material properties is apparent. In addition, weldability and welded fabrication associated property variations should be studied for optimum use of the material.

Weldability and microstructural evaluations of 310HCbN were conducted at Oak Ridge National Laboratory and the University of Tennessee [2-4]. The weldability assessment was conducted using the Varestraint hot cracking test and a newly developed tubing weld cracking (TWC) test. It is concluded that 310HCbN possesses an excellent hot cracking resistance. In addition, the TWC test is proven to be a viable tubing material weld hot cracking evaluation method.

The weld HAZ microstructural evaluation was conducted using Gleeble simulated HAZ samples and electric resistance spot welded samples. The metallographic evaluation was performed using OLM, SEM and STEM. The microstructural changes and secondary phase evolution processes as a function of the weld HAZ peak temperature were investigated. The

results from this study were used to explain the HAZ hot cracking mechanism as well as the weld HAZ stress corrosion cracking sensitivity (ASTM 262 Practice A).

EXPERIMENTAL PROCEDURES

The material used in this study is a commercial heat of 310HCbN tubing. The composition of the 310HCbN heat is presented in Table 1. The 310HCbN tubing was in the annealed condition.

Table 1. Composition of the 310HCbN tubing.

C	Mn	P	S	Si	Ni	Cr	Mo	V	Nb
0.061	1.19	0.010	<0.001	0.36	19.92	24.06	0.07	0.04	0.45
Ti	Co	Cu	Al	B	W	Fe	N	O	Ta
<0.01	0.27	0.09	0.023	0.002	<0.01	53.3	0.26	0.005	<0.01

* The chemical composition was analyzed at ABB Combustion Engineering.

The microstructural evaluation was carried out on the base metal and Gleeble simulated HAZ samples. For the Gleeble simulated HAZ samples, seven different peak temperatures (900°C, 1000°C, 1100°C, 1200°C, 1250°C, 1300°C and 1320°C) were selected. Optical light, scanning electron and transmission electron microscopy was employed for the metallographic examinations. The ASTM 262 Practice A was conducted on the Gleeble simulated HAZ samples. Limited precipitate particle characterization was performed using EDS and x-ray diffraction techniques.

RESULTS AND DISCUSSIONS

The previous investigations [3] at the University of Tennessee revealed that 310HCbN tubing possesses an excellent weld hot cracking resistance (using both Varestraint and TWC tests). Thus, the emphasis in this tubing evaluation of 310HCbN was concentrated on the HAZ microstructural evolution and aging. One of the major microstructural concerns is the carbide evolution behavior and its relationship to the mechanical properties and metallurgical and corrosion behavior.

Optical Microstructural Evaluation

Figure 1 shows the optical microstructural morphology of base metal and the simulated HAZ samples (etched with aqua regia). Clearly, the carbides and nitrides are uniformly distributed

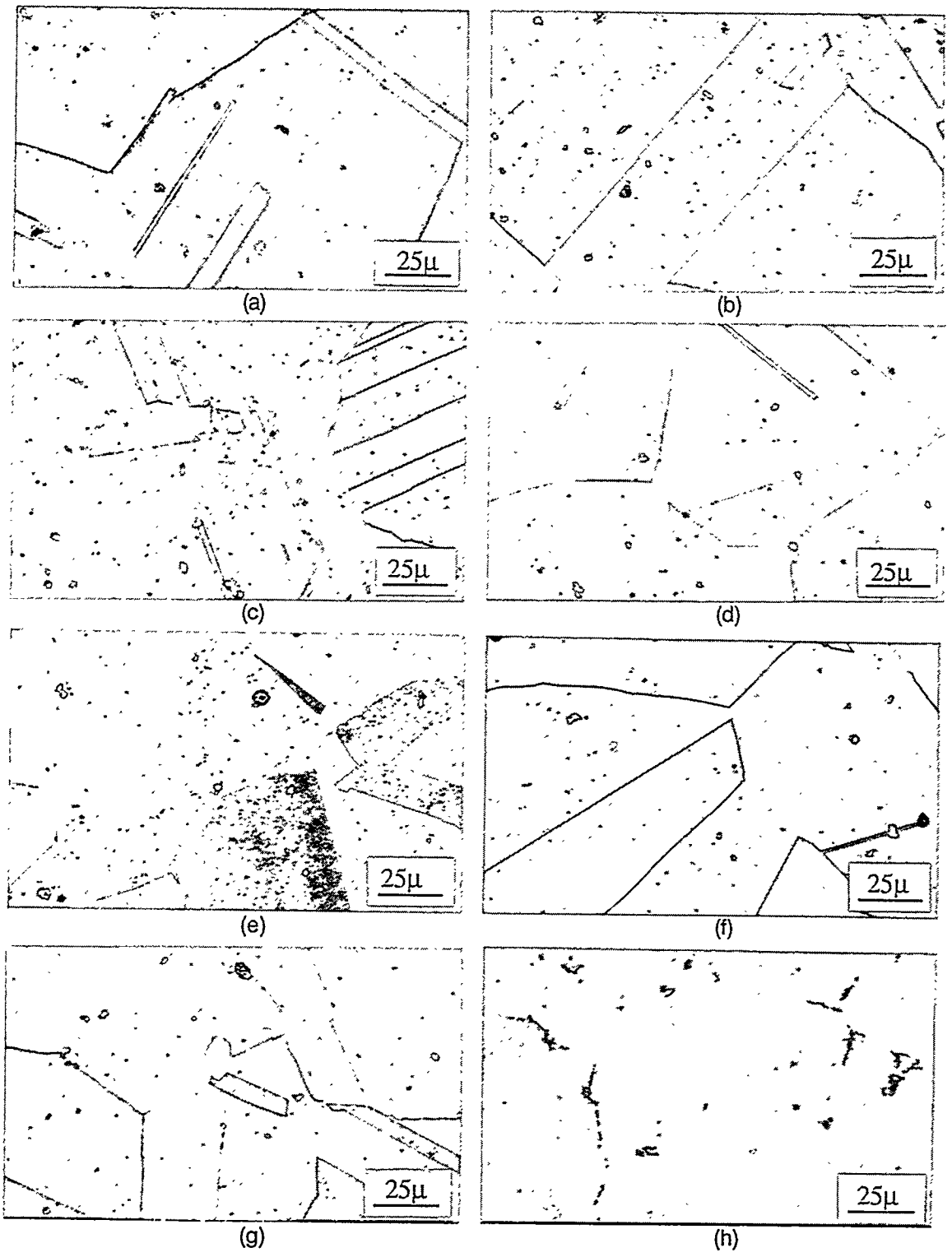

Figure 1. Optical microstructural morphology of base metal and the simulated HAZ samples. (a) Base Metal, (b) HAZ (PT: 900°C), (c) HAZ (PT: 1000°C), (d) HAZ (PT: 1100°C), (e) HAZ (PT: 1200°C), (f) HAZ (PT: 1250°C), (g) HAZ (PT: 1300°C), and (h) HAZ (1320°C).

in the base material matrix in the annealed condition. In the samples with the simulated peak temperatures of 900°C and 1000°C, a greater amount of precipitate was observed compared to the base metal, especially for the small size particles. The precipitate is slightly reduced in the sample with a simulated peak temperature of 1100°C compared to base metal. This may reflect the initiation of precipitate dissolution for certain precipitate particles (e.g. $M_{23}C_6$). In addition, fine precipitates were observed and it is believed that MC type carbides start to form under this HAZ thermal expose. When the simulated peak temperature is in excess of to 1200°C, the fine precipitates increase and it is expected that the newly formed precipitates are dominantly NbC and/or NbN carbides. A similar microstructural morphology was found in sample with the simulated peak temperatures of 1250°C and 1300°C. Additionally, evidence of a reaction between carbides and matrix was observable although it appears that the reaction is in the initial stages. In the simulated HAZ sample with a peak temperature of 1320°C (ZDT), significant evidence of a liquation reaction is apparent. It is noticed that the liquated areas are distributed both intergranularly and intragranularly.

HAZ Sensitization Evaluation

Figure 2 presents the microstructural morphologies of the Gleeble simulated HAZ samples after electrolytic etching with oxalic solution (ASTM A262 Practice A). It is evident that the base metal is not sensitized. It is also shows that the precipitates are uniformly distributed in the base material. In the simulated HAZ samples with the peak temperatures of 900°C and 1000°C, a ditched type grain boundary morphology is present with grains completely surrounded. This is an indication of sensitization. This temperature range (900°C-1000°C) reflects the lower boundary of the HAZ. Therefore, intergranular type localized corrosion may take place in the as welded HAZ if aqueous conditions prevail. The cause of the sensitization is the formation of $Cr_{23}C_6$ type carbides along the grain boundaries and a Cr depleted zone adjacent to the grain boundaries.

It should be noticed that for the HAZ sample with the peak temperature of 1100°C, the grain boundaries were not ditched. Further, the amount of precipitates shown in the sample with the peak temperature 1100°C is significantly reduced compared to that in the simulated HAZ with peak temperatures of 900°C and 1000°C. This observation indicates that dissolution of $Cr_{23}C_6$ occurred for the 1100°C thermal history. Evidence of grain boundary ditching begins to be seen in the sample with a peak temperature of 1200°C and more evidence of grain boundaries is found in the sample with a peak temperature of 1250°C. However, this is step structure in the simulated

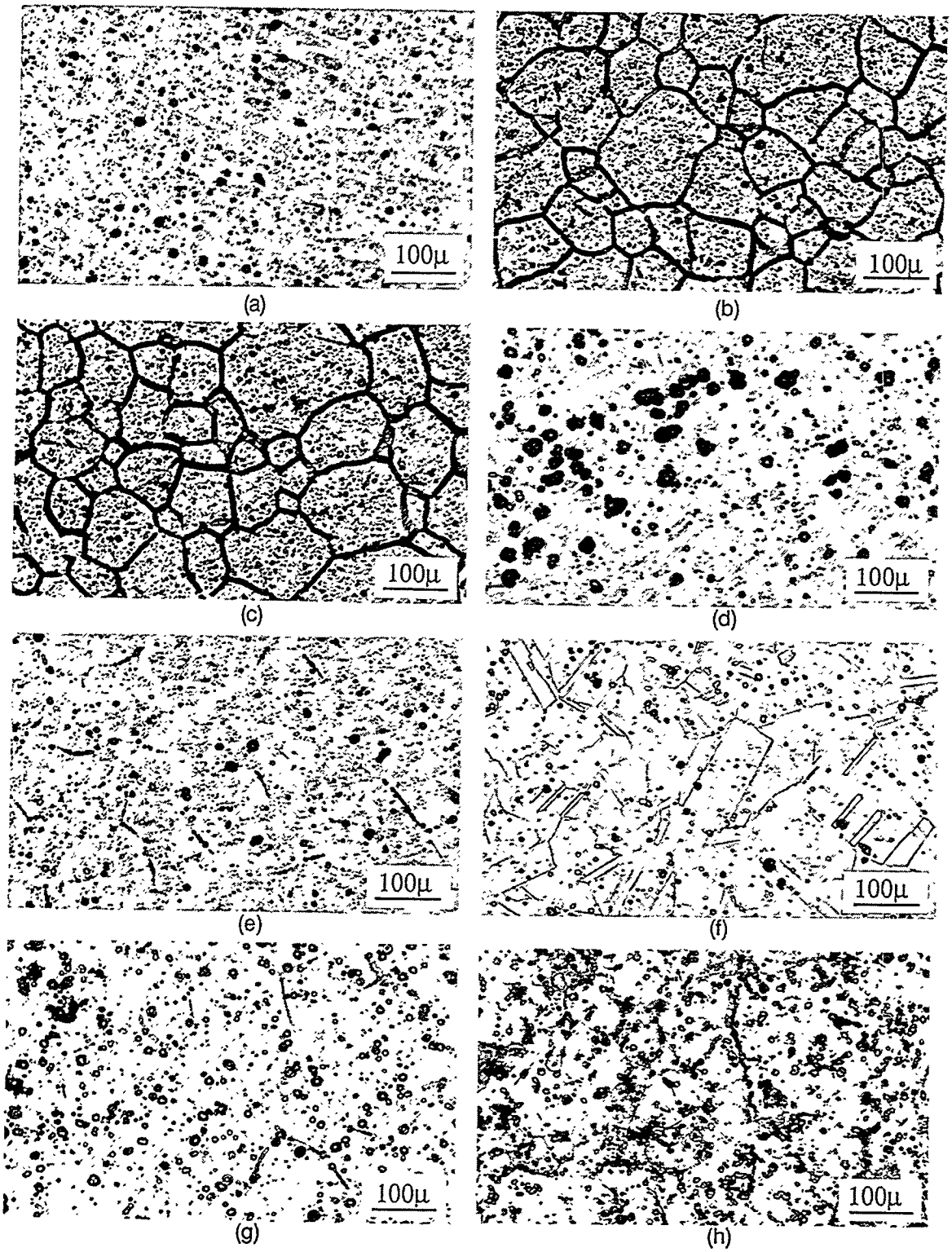

Figure 2. Microstructures in the base metal and the simulated HAZs after A262 Practice A test. (a) Base Metal, (b) HAZ (PT: 900°C), (c) HAZ (PT: 1000°C), (d) HAZ (PT: 1100°C), (e) HAZ (PT: 1200°C), (f) HAZ (PT: 1250°C), (g) HAZ (PT: 1300°C), and (h) HAZ (1320°C).

HAZ sample with a peak temperature of 1250°C. A dual structure is evident in the simulated HAZ sample with a peak temperature of 1300°C and this becomes aggravated when the peak temperature is increased to 1320°C (ZDT). The explanation of the higher temperature range sensitization is due to the dissolution of MC and/or MN type precipitates and followed by relatively fast cooling. In this case, reformation of MC and/or MN type precipitates upon cooling is limited and during cooling in the lower temperature portion of welding thermal cycle, $Cr_{23}C_6$ is formed. This discussion indicates that "knife line" type attack may occur in the weld HAZ of as-welded 310HCbN.

TEM Microstructural Evaluation

In order to confirm the above observations and postulation, carbides and/or nitrides particles were extracted from the base material and EDS checked. Figure 3 shows the SEM morphology of particles extracted from the 310HCbN base material. The dominant particles are within the size range of 1μ to 10μ. The EDS examination results revealed that most of the particles are Nb rich carbides or nitrides. A small amount of Ti and Cr may be contained in the NbC and NbN. A typical EDS spectrum for particle "a" in Figure 3 is exhibited in Figure 4.

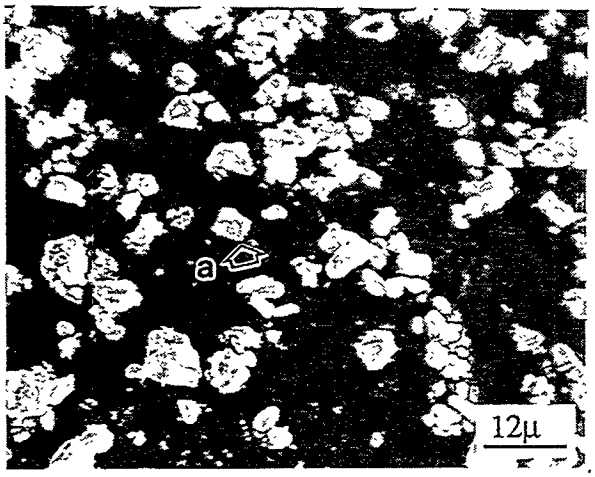

Figure 3. SEM morphologies of carbides extracted from base metal.

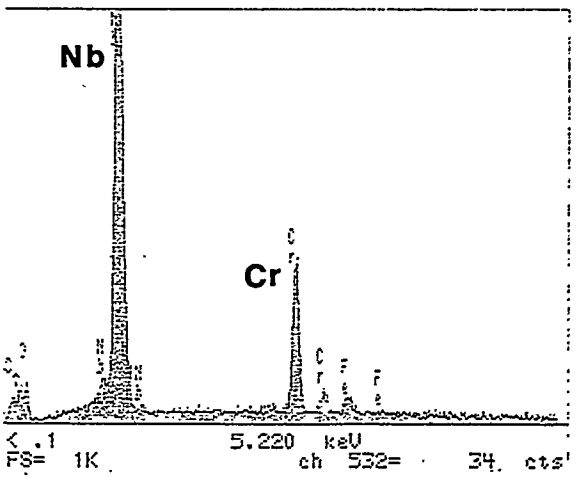

Figure 4. EDS spectrum for particle "a" in Figure 3.

Figure 5 shows the typical TEM microstructural morphologies of the base metal in which intragranular carbides are predominantly present. The dislocation density in the matrix of base material is low.

Typical TEM microstructural morphologies in the simulated HAZ samples with the peak temperatures of 900°C and 1000°C are presented in Figures 6 and 7, respectively. Evidence of an increased amount of precipitates and the appearance of intergranular precipitates are clearly indicated. The increase in carbides is due to the formation of $Cr_{23}C_6$ (preferentially along the grain boundaries). A typical EDS spectrum for these carbides is exhibited in Figure 8.

Typical TEM microstructural morphology of the simulated HAZ samples with a peak temperature of 1100°C is shown in Figure 9. Amount of precipitates (both intergranular and intragranular) in this sample is apparently reduced. Fine particles that are rich in Cr and Nb were present. A typical EDS spectrum of these particles is exhibited in Figure 10.

When the peak temperature increases to 1200°C, Nb rich type carbides become predominant and the size of Nb rich carbides increased compared to those observed in Figure 9 (1100°C) (see Figure 11). Figure 12 shows a typical TEM microstructural morphology in a sample with a peak temperature of 1250°C. More fine, rectangular, bar shaped carbides were formed at this temperature. A typical TEM microstructural morphology of the simulated HAZ sample with a peak temperature of 1300°C is shown in Figure 13. Clearly, the intergranular precipitates are dominant. A typical EDS spectrum of the particles in Figure 12 is shown in Figure 14. It is noticed that Nb content in carbides is increased in the simulated HAZ sample with a peak temperature of 1300°C compared to that in the simulated HAZ sample with a peak temperature of 1100°C. A typical TEM microstructural morphology of the simulated HAZ sample with a peak temperature of 1320°C is shown in Figure 15. The quantity of precipitate is further increased in this sample both intergranularly and intragranularly compared to that in the simulated HAZ sample with a peak temperature of 1300°C.

The HAZ hardness as a function of HAZ peak temperature in 310HCbN material is presented in Figure 16. In general, the variation of hardness in the HAZ is relatively small. Compared to base metal (190 HV), the entire HAZ region showed a lower hardness. As indicated in Figure 16, the maximum hardness was reached with a peak temperature of 1100°C, in which the fine Nb rich particles started to form according to the above metallographic evaluation results. It should be noted that hardness in weld HAZ is not only affected by the precipitate distribution but also associated by grain size, thus, the combined information should be considered in order to interpret the HAZ hardness behavior. Nevertheless, the microhardness measurements agree with the metallographic examination results.

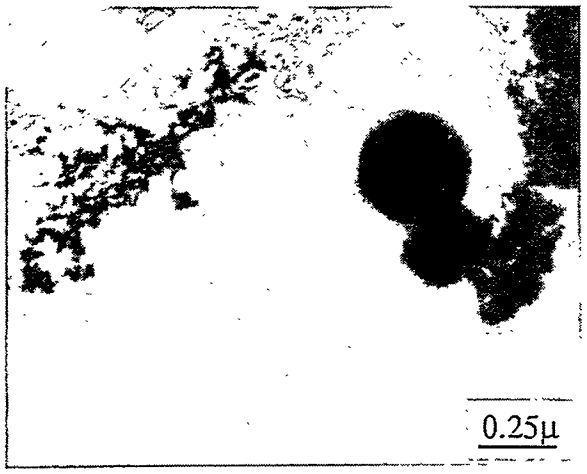

Figure 5. TEM microstructure of base metal.

Figure 6. TEM microstructure in the simulated HAZ with a peak temperature of 900°C.

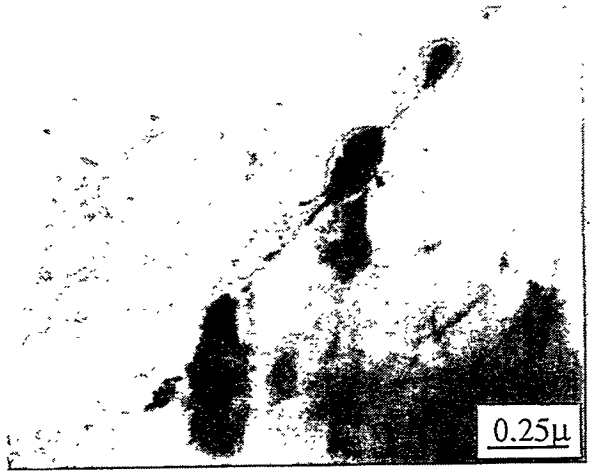

Figure 7. TEM microstructure in the simulated HAZ with a peak temperature of 1000°C.

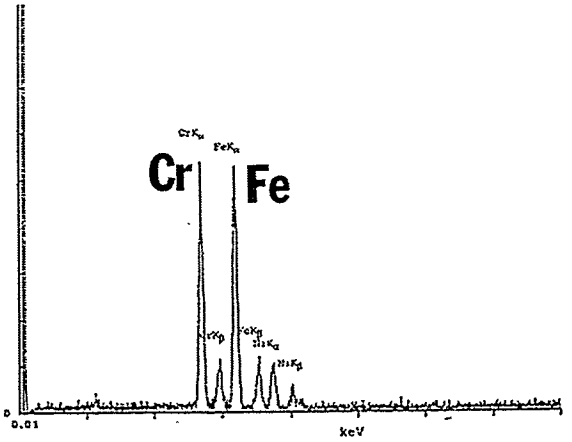

Figure 8. Typical EDS spectrum for the carbides in Figures 6 and 7.

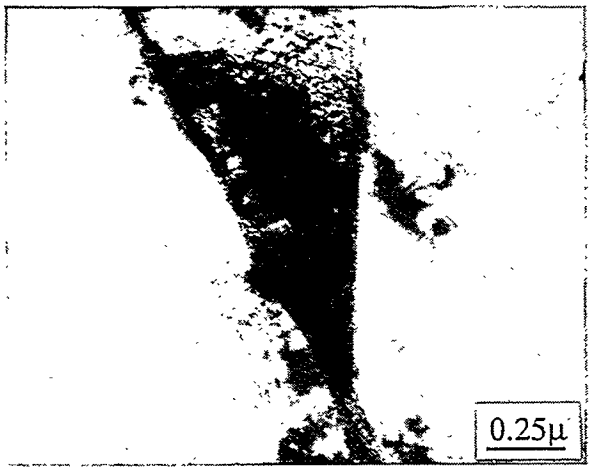

Figure 9. TEM microstructure in the simulated HAZ with a peak temperature of 1100°C.

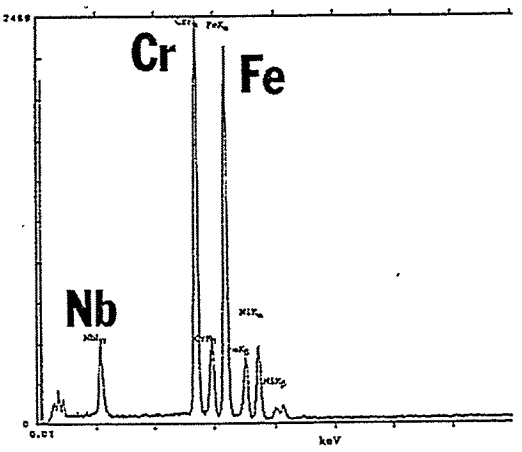

Figure 10. Typical EDS spectrum of the particles in Figure 9.

Figure 11. TEM microstructure in the simulated HAZ with a peak temperature of 1200°C.

Figure 12. TEM microstructure in the simulated HAZ with a peak temperature of 1250°C.

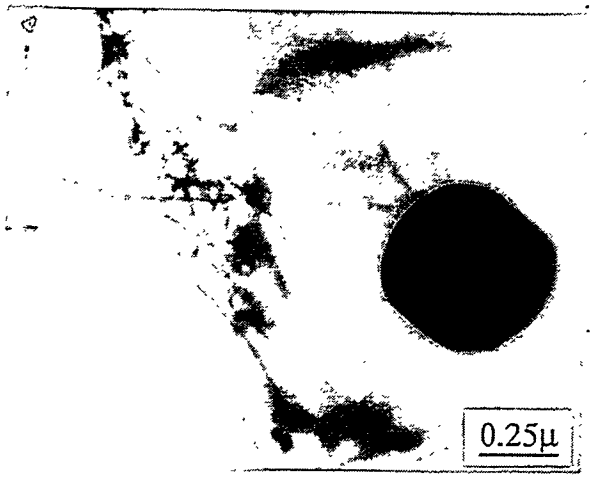

Figure 13. TEM microstructure in the simulated HAZ with a peak temperature of 1300°C.

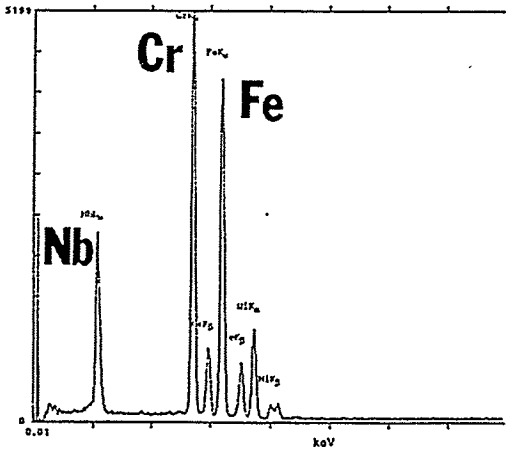

Figure 14. Typical EDS spectrum of the particles in Figure 13.

Figure 15. TEM microstructure in the simulated HAZ with a peak temperature of 1320°C.

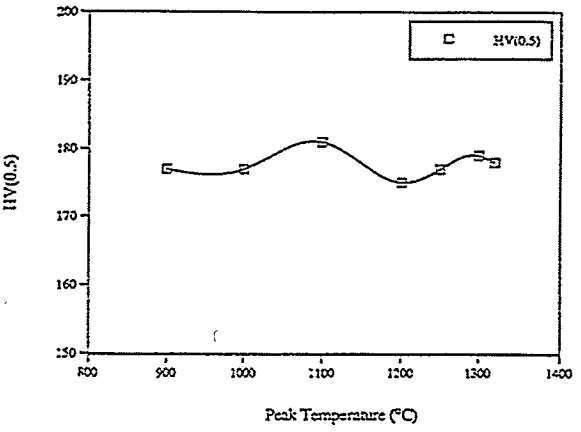

Figure 16. HAZ microhardness in the simulated HAZs.

SUMMARY

1. Metallographic examination indicated that carbide evaluation in the weld HAZ is the major factor causing the mechanical property and corrosion resistance changes in 310HCbN material.
2. A sensitized HAZ microstructure was found in the simulated HAZ samples of 310HCbN with peak temperatures of 900°C and 1000°C. The formation of $M_{23}C_6$ type carbides along the grain boundaries is directly responsible for this sensitization.
3. A dual type structure was observed in the simulated HAZ sample with peak temperature of 1320°C in A262 Practice A. This may imply that a "knife line" attack tendency may be present for 310HCbN.
4. This investigation also showed that carbides (both Nb rich MC type or Cr rich $M_{23}C_6$) evolution processes can occur in the weld HAZ of 310HCbN. The formation of MC type precipitates in the weld HAZ may enhance the reheat cracking tendency because fine MC type carbides preferentially form intragranularly at the dislocation and/or stack faulting sites.

ACKNOWLEDGMENTS

This study was financially supported by the U.S. Department of Energy, through Fossil Energy Materials Program operated at Oak Ridge National Laboratory. Advice from program/technical managers of ORNL, N.C. Cole, R.R. Judkins, R.W. Swindeman, and P.T, Carlson during the study is greatly appreciated.

REFERENCES

1. Sumitomo Metal Industries, Ltd Report, "Characteristics of a New Steel Tube (HR3C) with High Elevated Temperature Strength and High Corrosion Resistance for Boiler," December 1987.

2. R.W. Swindeman, Private Conversation, March 1995.

3. C.D. Lundin and C.Y.P. Qiao, "Investigation on the Weldability of High Temperature Alloy Tubing Materials," pp. 365-375, Proceedings of the Eighth Annual Conference on Fossil Energy Materials," CONF-9405143, ORNL/FMP-94-1, 1994.

4. C.D. Lundin and C.Y.P. Qiao, "Preliminary Metallographic Examination of Service Exposed SA 213 (Grade HR3C) Hot Reheat Tubing at TVA Gallatin Unit 2," Technical Report, The University of Tennessee, March 1995.

THE EFFECTS OF MICROSTRUCTURAL CONTROL ON THE MECHANICAL BEHAVIOR OF Cr_2Nb-BASED ALLOYS

J.A. Cook[1], P.K. Liaw[1], and C.T. Liu[2]

1. Department of Materials Science and Engineering
434 Dougherty Eng. Bldg.
University of Tennessee
Knoxville, TN 37996-2200

2. Oak Ridge National Laboratory
Metals and Ceramics Division
P.O. Box 2008
Oak Ridge, TN 37831-6115

ABSTRACT

Microstructural evaluations and mechanical testing of Laves-phase alloys based on Cr_2Nb were examined in order to optimize microstructural and mechanical properties by thermomechanical treatment at temperatures up to 1600°C. At ambient temperatures, single-phase Cr_2Nb alloys are very hard and brittle due to the complicated crystal structure (C-15). The following results were revealed through examination of the Cr-Cr_2Nb two-phase region: (a) with increasing amounts of the soft chromium-rich phase, the compression strength and hardness decrease; (b) the annealing treatments studied thus far provided the best break-up of the coarse/brittle Laves-containing eutectic phase in the 94 at.% Cr - 6 at.% Nb (CN-7) alloy; (c) two different anneals, 1 hour at 1600°C + 4 hours at 1200°C and 4 hours at 1550°C + 2 days at 1200°C, lead to a substantial improvement in the room temperature strength and compressive ductility over previous annealing treatments. Hot Isostatic Pressing has led to only a marginal reduction in casting defects and refinement of the eutectic structure. A combination of hot forging and annealing has been initially promising in refining the brittle eutectic structure.

INTRODUCTION

The necessity for very high-temperature applications of structural materials with the desired properties of low density, good mechanical properties and environmental resistance has directed research efforts beyond titanium, nickel, and iron aluminides. Chromides, such as Cr_2Nb-based alloys, are a strong candidate for use at very high temperatures. However, after a careful review of the literature, little work appears to have been conducted in developing a good understanding of the effect of microstructural control on the mechanical behavior of Cr_2Nb-based alloys.

Development of this alloy is being carried out for use as critical hot components, such as in advanced fossil energy conversion systems. Cr_2Nb has a C15 (Laves phase) structure which is a relatively complicated crystal structure when compared with the more widely studied B2, $L1_2$, and $D0_{19}$ structures [1]. The crystal structure is so complex that dislocation motion is difficult at ambient temperatures. With regard to the Von Mises criteria, Cr_2Nb does not have a sufficient number of independent slip systems for uniform, extensive plastic deformation [2]. Since it has been shown [2] that the single-phase Cr_2Nb Laves alloys are extremely brittle at ambient temperatures, work has been concentrated on the Cr-Cr_2Nb two-phase compositions. The introduction of a soft Cr-rich phase has been shown [2] to have promising effects on improving the mechanical properties of Cr_2Nb intermetallics.

The objective of this research is to improve the ambient-temperature strength and ductility of a two-phase Cr-Cr_2Nb Laves phase alloy via thermomechanical treatments as well as the study of the effect of microstructural control on the mechanical behavior of this material. In addition, secondary processing techniques, such as hot forging and Hot Isostatic Pressing (HIPping), will be used to suppress casting defects and further refine the brittle eutectic structure. Theoretical modeling will be developed to relate microstructural features with the mechanical properties. Moreover, the results of this research can provide invaluable information for the development and selection of reliable intermetallics for high-temperature structural applications.

EXPERIMENTAL PROCEDURE

The materials which have been studied in this research are four compositions of the Cr-Cr_2Nb two-phase intermetallic system. The four alloy compositions are reported in Table 1. As shown in Table 1, the CN-45 composition contains 17 at.% Nb. It was once believed that the eutectic composition of this two-phase alloy was that of the CN-4 alloy (12 at.% Nb). However, work by Takeyama and Liu [2] has since shown that the eutectic composition is more like that of the CN-45 composition (17 at.% Nb). The recent work done by Thoma and Perepesko [3] has indicated that the actual eutectic composition is closer to 18.5 at.% Nb, which is the composition of the CN-84 alloy investigated in this study.

Chromium-niobium alloys weighing 350 g were prepared by arc melting and drop casting into pre-heated copper molds. High-purity niobium and chromium metal chips were used as charge materials in order to reduce the interstitial impurity (i.e. oxygen), and the alloys were melted in a high-vacuum (10^{-5} Pa) furnace. The preheating of the copper mold to 100°C before drop casting was done in order to control alloy solidification and reduce thermal shock and microporosity formation during drop casting [4,5].

Table 1. Alloy Compositions for the Cr_2Nb-based Alloys

Alloy	Atomic percent	Weight percent
CN-7	Cr-94% Nb- 6%	Cr-89.76% Nb-10.24%
CN-4	Cr-88% Nb-12%	Cr-80.41% Nb -19.59%
CN-45	Cr -83% Nb-17%	Cr-73.21% Nb-26.79%
CN-84	Cr -81.5% Nb-18.5%	Cr-71.14% Nb-28.86%

Table 1 lists the composition (at.%) of CN (Cr-Nb) alloys investigated in this work. The alloys used in this study have nominal compositions of chromium with a variation of 6 to 18.5 at.% Nb. The alloys were placed in a covered alumina crucible and annealed under vacuum at 1600°C for 1 hour (h) + 4 h at 1200°C.

Optical micrographs for CN-7 and CN-4 at this annealing treatment are shown in Figs. 2 and 3, respectively. An additional annealing treatment of 2 days (d) at 1580°C + 2 d at 1200°C was performed on two (CN-4 and CN-7) of the four alloy compositions listed in Table 1 and shown by the optical micrographs in Figs. 4 and 5. Other annealing treatments which have been performed [6] include 1 h at 1400°C, 1 h at 1500°C, 1h at 1550°C, 4 h at 1550°C + 2 d at 1200°C, 1h at 1580°C, and 2 d at 1580°C. The effects of annealing on the microstructures and mechanical properties of these alloys were emphasized in this investigation. Microstructures of these alloys were examined by optical microscopy. The metallographic specimens were polished through 1 μm using conventional techniques. Samples were then etched in a solution of 15 gm KOH, 15 gm $K_3Fe(CN)_6$, and 90 ml H_2O for approximately 5 seconds.

Microhardness readings were taken for each specimen using a LECO M-400 Hardness Tester using an indenter load of 1 kg. An average of three to five readings taken randomly across the sample gives the reported hardness values. Compression specimens having a diameter of 6 mm and a length of 9 mm were cut by electro-discharged machining (EDM) from the annealed ingots. The specimens were tested under compression on an Instron testing machine at room temperature and 1000°C at a nominal strain rate of 3.3×10^{-3} s^{-1}. The elevated-temperature tests were carried out in vacuum (less than 7×10^{-4} Pa).

Coarsening studies were performed on the CN-4 and CN-7 compositions at 1200°C for the following times: 3h, 6h, 1d, 3d, 7d, 14d, and 30d. The microstructures were then examined in the scanning electron microscope in order to evaluate the volume fraction of precipitates within the Cr-rich phase. Image analysis techniques will be used to determine the average particle size and

distribution due to different annealing times. Hot Isostatic Pressing (HIPping) to suppress and/or remove casting defects was carried out by Dr. Sarit Bhaduri of the Department of Mines, University of Idaho. HIPping was performed at 1610°C at a pressure of roughly 193 MPa. Hot forging was performed at 1200°C in vacuum to roughly 20% deformation at a strain rate of 3×10^{-4} s^{-1}.

RESULTS AND DISCUSSION

Microstructure and Phase Composition

The CN alloys contain two phases, the Cr_2Nb intermetallic phase and the chromium-rich solid solution which can contain as much as 5 at.% Nb at the eutectic temperature of 1620°C. Recent work by Liu et.al., [5] however, has revealed that the eutectic temperature may actually be closer to 1670°C, which agrees well with the results reported by Thoma and Perepesko [3].

The compositions of the phases in the alloys CN-7, CN-4, and CN-45 were determined by electron microprobe analyses for an average of three points in each respective phase, as reported in Table 2. From the phase diagram in Fig. 1, we see that the intermetallic phase in the eutectic structure has an average composition of 70 at.% Cr - 30 at.% Nb, which, according to the results in Table 2, reveals that the phase identified by microprobe analyses in the eutectic structure is in fact the Cr_2Nb Laves-type intermetallic phase. Figure 2 shows the optical micrograph of CN-7 annealed for 1 h at 1600°C + 4 h at 1200°C. In this alloy, the Cr-rich patches cover most areas, and a small amount of the Laves-containing eutectic phase can be seen along the Cr-rich boundaries. At lower annealing temperatures, such as 1100°C-1300°C, which have been studied [2,4,5], this brittle eutectic phase exists as an interconnected skeleton along the Cr-rich regions as seen in Fig. 6, but in the case of the microstructure seen in Fig. 2, the anneal has broken up the eutectic phase that was once interconnected along the Cr-rich regions. The 88 at.% Cr - 12 at.% Nb (CN-4) alloy is shown in Fig. 3 with the same annealing history as CN-7 in Fig. 2. As seen in Figure 3, the lighter patches in the CN-4 composition are the chromium-rich phase which is surrounded by the Laves-containing brittle eutectic phase. Some very fine dark spots can be seen within the Cr-rich patches in both Figures 2 and 3, and these are the Cr_2Nb precipitates that precipitate out of the supersaturated Cr-rich matrix upon annealing. In each of these alloy compositions, the Cr-rich phase is the matrix, thus indicating from the phase diagram that these are hypoeutectic compositions.

It has been shown [4] that the precipitation of the Cr_2Nb Laves-phase particles from the Cr-rich phase is sluggish. These precipitates are extremely fine, with a size of less than 1 μm for an alloy annealed for 3 d at 1100°C [2,4]. Annealing at temperatures of 1500°C to 1600°C did

Table 2. Electron Microprobe Analysis of the Cr_2Nb Alloys

Alloy	Anneal Condition	Cr_2Nb phase in Eutectic structure (at.%)	Cr-rich phase (at.%)
CN-7	1h/1600°C + 4h/1200°C	Cr = 68.8 % Nb = 31.2 %	Cr = 96.2 % Nb = 3.8 %
CN-4	1h/1600°C + 4h/1200°C	Cr = 69.3 % Nb = 30.7 %	Cr = 96.6 % Nb = 3.4 %
CN-45	1h/1600°C + 4h/1200°C	Cr = 68.6 % Nb = 31.4 %	Cr = 97.2 % Nb = 2.8 %

* analysis of the Cr-rich phase also includes the fine Cr_2Nb precipitates

not reveal the fine Cr_2Nb particles within the Cr-rich phase. These precipitates were partially dissolved due to an increase in the solubility of Nb in Cr at these temperatures and the remainder of the particles migrated to the Laves-containing eutectic phase, thereby coarsening it. Thus, we see that there are two competing mechanisms occurring during the annealing treatment; (1) break-up of the eutectic phase and (2) coarsening of the Laves-containing eutectic phase due to Cr_2Nb particles migrating from the Cr-rich phase at high temperatures. Upon furnace cooling from 1580°C and/or 1600°C, very fine particles once again precipitate out in the Cr-rich phase. Additional annealing at 1200°C causes a coarsening of these fine particles. This result can especially be seen in the micrographs shown in Figs. 4 and 5 for CN-7 and CN-4 annealed 2 d at 1580°C + 2 d at 1200°C.

Hardness

Microhardness results are presented in Table 3 for the CN-7, CN-4, and CN-45 alloys under different annealing conditions. The effects of annealing temperature on hardness are shown in Fig. 7 for the CN-4 alloy. No microcracking was observed at the tips of the microhardness indents as was previously reported for alloys in the as-cast condition [2]. The hardness decreases with decreasing niobium concentration and increasing amount of the soft Cr-rich phase. Previous work by Liu [7] has indicated that the hardness tends to decrease as the coarsening of the fine Cr_2Nb particles within the Cr-rich phase occurs for temperatures ranging from 950°C to 1200°C, as shown in Fig. 7. In the present investigation, it was found that annealing at high temperatures near the eutectic temperature (1550°C to 1600°C) leads to an increase in hardness, as reported in Table 3.

Table 3. Microhardness Values (DPH) for the Cr_2Nb-based Alloys

Annealing Treatment	CN-4	CN-7	CN-45
6 h/1200°C	476	373	
24h/1200°C	453	339	
3d/1200°C	454	327	
7d/1200°C	423	324	
14d/1200°C	416	319	
30d/1200°C	405	308	
1h/1400°C	465	367	616
1h/1500°C	494	393	618
1h/1550°C	502	424	618
1h/1580°C	513	406	613
2d/1580°C	508	445	–
2d/1580°C + 2d/1200°C	418	341	–
1h/1600°C + 4h/1200°C	479	429	–

* all anneals shown are performed on as-cast material, unless otherwise noted

Annealing at these high temperatures has the following effects: (a) dissolution of the fine Cr_2Nb precipitates in the Cr-rich phase due to an increase in the solubility limit of Nb in Cr; (b) coarsening of the Laves-containing eutectic phase due to migration of the Cr_2Nb particles from the Cr-rich phase, (c) break-up of the eutectic phase, and; (d) re-precipitation of extremely fine Cr_2Nb particles in the Cr-rich phase upon cooling from the high-temperature anneals. It is this fine re-precipitation that is believed to lead to the increase in hardness. Upon additional annealing of the sample at 1200°C after annealing for 1 h at 1600°C or 2 d at 1580°C, we see that the hardness once again decreases due to the coarsening of the Cr_2Nb precipitates within the Cr-rich region as discussed in the work by Liu [7] and seen by the results presented in Table 3 and Fig. 7. In addition, we see that the hardness also decreases when the material is annealed for prolonged periods at a fixed temperature, such as the drop in hardness values from the coarsening studies reported in Table 3 for the CN-4 and CN-7 compositions that were annealed at 1200°C over a period ranging from 6 hours to 30 days. Once again, this drop in hardness is attributed to the particle coarsening behavior of the Cr_2Nb precipitates within the Cr-rich regions. These coarsening studies at 1200°C were done in order to further understand the precipitation and growth kinetics of the Cr_2Nb particles in the supersaturated Cr-rich regions.

Compression Testing

The 0.2 % yield strength and compressive ductility of 94 at.% Cr-6 at.% Nb (CN-7) and 88 at.% Cr-12 at.% Nb (CN-4) alloys at room temperature are reported in Table 4. At room temperature, the yield strengths of CN-7 and CN-4 are higher than 700 and 900 MPa, respectively, for an annealing condition of 3 d at 1100°C. A substantial improvement in room-temperature yield strength and compressive ductility was seen for the CN-7 and CN-4 alloys annealed for 1 h at 1600°C + 4 h at 1200°C. The CN-45 alloy tested for this annealed condition showed reasonable ductility with very high strength at room temperature, as reported in Table 4. Some improvement in strength, together with a significant increase in room temperature compressive ductility was seen for the alloys annealed for 4 h at 1550°C + 2 d at 1200°C. The improvement in ductility in all cases can be attributed to the break-up of the coarse/brittle eutectic structure due to these high temperature anneals (1 h at 1600°C and 4 h at 1550°C).

Table 4. Compressive Properties of CN Alloys Tested at Room Temperature in Air

Alloy No.	Heat Treatment	Composition (at.%)	Strength, MPa (ksi)		Ductility (%)
			Yield	Ultimate	
CN-7	3d/1100°C	94 Cr-6 Nb	702(102)	1261(183)	9.5
CN-7	1h/1600°C +4h/1200°C	94 Cr-6 Nb	1029(149)	1733(251)	20.7
CN-7	4h/1550°C +2d/1200°C	94 Cr-6 Nb	668(97)	1477(215)	23
CN-4	3d/1100°C	88 Cr-12 Nb	960(139)	1760(255)	5.4
CN-4	1h/1600°C +4h/1200°C	88 Cr-12 Nb	1327(192)	1546(224)	8.8
CN-4	4h/1550°C +2d/1200°C	88 Cr-12 Nb	1247(181)	1345(195)	10.1
CN-4	HIP @ 1610°C +3d/1200°C	88 Cr-12 Nb	1077(157)	1562(227)	10
CN-45	1h/1600°C +4h/1200°C	83 Cr-17 Nb	1763(256)	1824(265)	12.2
CN-45	4h/1550°C +2d/1200°C	83 Cr-17 Nb	1698(246)	1840(267)	8.9

Hot Isostatic Pressing (HIPping) at 1610°C + annealing 3 d at 1200°C of the CN-4 composition showed only a marginal break-up of the brittle eutectic phase and negligible improvement in room temperature strength and compressive ductility over other anneals that have been performed as reported in Table 4.

As shown in Table 5, samples annealed for 1 h at 1600°C + 4 h at 1200°C showed some improvement in strength at 1000°C over similar tests performed on samples annealed for 3 d at 1100°C. However, there was little change in compressive ductility from the previous tests performed for samples annealed 3 d at 1100°C. As the test temperature increased, the strength decreased and the ductility increased for all tests. The CN-45 alloy showed very limited ductility when compared with the CN-4 and CN-7 results at 1000°C. For the CN-4 alloy annealed 1 h at 1600°C + 4 h at 1200°C, the yield strength at 1000°C is approximately 780 MPa, which is substantially stronger than conventional nickel-base superalloys; for example, the yield strength of IN713C at 1000°C is about 300 MPa [8]. At 1000°C, both CN-7 and CN-4 can be deformed with compressive ductilities larger than roughly 20 %. These results reveal that the two-phase intermetallic alloys based on Cr_2Nb have high strength with decent ductility at all test temperatures. In addition, we can see that the break-up of the Laves-containing eutectic phase via annealing at higher temperatures (1550° to 1600°C) results in a considerable increase in strength and compressive ductility at room temperature and a slight increase in strength with good ductility at 1000°C in vacuum.

FUTURE WORK

Despite the improvements seen as a result of annealing at temperatures above 1580°C, there is the disadvantage of Cr vaporization from the surface of the material and in extreme cases, partial melting of the material, thus providing less usable material for testing as one must remove and/or avoid these areas when machining specimens for mechanical testing. In an attempt to alleviate this problem, a combination of hot forging and annealing at lower temperatures (1500°C and below) has shown to be promising in effectively refining the brittle eutectic structure. Continued work will be undertaken to further explore this method of microstructural refinement and ductility enhancement. It is hoped that a theoretical model, such as finite-element modeling of compression tests, can be developed which will correlate the effects of changes in the microstructure via thermomechanical treatment with the mechanical behavior of these two-phase alloys based on Cr_2Nb. These studies will lead to a mechanistic understanding of the effects of microstructural control via thermomechanical treatment on the fracture behavior of these alloys. Other image analysis techniques will be used to determine average particle size and distribution due to different annealing times studied in the coarsening experiments. It is hoped that these

studies will help to shed some light on the precipitation kinetics of the Cr_2Nb phase within these alloys. In addition, tensile tests will be performed on the alloys at different temperatures and anneal conditions in order to study the effect of microstructural refinement of the brittle eutectic structure on the strength and ductility of the material in tension.

Table 5. Compressive Properties of CN Alloys Tested at 1000°C in Vacuum

Alloy No.	Heat Treatment	Composition (at.%)	Strength, MPa (ksi)		Ductility (%)
			Yield	Ultimate	
CN-7	3d/1100°C	94 Cr-6 Nb	436(63)	738(107)	32.7
CN-7	1h/1600°C +4h/1200°C	94 Cr-6 Nb	580(84)	1069(155)	27.9
CN-7	4h/1550°C +2d/1200°C	94 Cr-6 Nb	405(59)	790(115)	31.4
CN-4	3d/1100°C	88 Cr-12 Nb	685(99)	856(124)	22.8
CN-4	1h/1600°C +4h/1200°C	88 Cr-12 Nb	778(113)	1079(157)	19.8
CN-4	4h/1550°C +2d/1200°C	88 Cr-12 Nb	711(103)	845(123)	17.1
CN-4	HIP @ 1610°C +3d/1200°C	88 Cr-12 Nb	658(96)	711(112)	16.6
CN-45	1h/1600°C +4h/1200°C	83 Cr-17 Nb	994(144)	1076(156)	8.1
CN-45	4h/1550°C +2d/1200°C	83 Cr-17 Nb	1698(246)	1840(267)	10.3

ACKNOWLEDGMENTS

The authors wish to give thanks to Nancy Cole and Rod Judkins of the Oak Ridge National Laboratory for financial support of this program. Thanks are due to C.A. Carmichael, D.H. Pierce, J. Wright, T. Henson, and M. Williams for their technical assistance. This work is sponsored by the Fossil Energy AR & TD Materials Program, U.S. Department of Energy, under subcontract 11X-SP173V to the University of Tennessee with Martin Marietta Energy Systems, Inc.

REFERENCES

1. T. Takasugi, S. Hanada, and K. Miyamoto, *J. Mater. Res.*, vol. 8, no. 12, (Dec. 1993), pp. 3069-3077.

2. M. Takeyama and C.T. Liu, *Materials Science and Engineering*, A132, (1991), pp. 61-66.

3. D.J. Thoma and J.H. Perepesko, *Materials Science and Engineering*, vol. A156, (1992), pp. 97-108.

4. C.T. Liu, J.A. Horton and C.A. Carmichael, pp. 297-307 in *Proc. 7th Annual Conf. on Fossil Energy Materials*, ORNL/FMP-93/1, Oak Ridge National Laboratory, July 1993.

5. C.T. Liu, J.A. Horton and C.A. Carmichael, pp. 377-390 in *Proc. 8th Annual Conf. on Fossil Energy Materials*, ORNL/FMP-94/1, Oak Ridge National Laboratory, August 1994.

6. J.A. Cook, P.K. Liaw and C.T. Liu, pp. 401-412 in *Proc. 8th Annual Conf. on Fossil Energy Materials*, ORNL/FMP-94/1, Oak Ridge National Laboratory, August 1994.

7. J.A. Cook, P.K. Liaw, and C.T. Liu, Fracture Behavior of Cr_2Nb-based Intermetallics, in *Fatigue and Fracture of Ordered Intermetallic Materials II*, TMS (the Minerals, Metals and Materials Society) Proceedings of the 1994 Materials Week in Rosemont, Ill (in press).

8. C.T. Liu, pp. 375-383 in *Proc. 6th Annual Conf. on Fossil Energy Materials*, ORNL/FMP-92/1, Oak Ridge National Laboratory, July 1992.

9. *Engineering Properties of Alloy 713C*, International Nickel, New York, 1968.

10. H.J. Goldschmidt and J.A. Brand, *J. Less-Common Met.*, 3 (1961) p. 44.

11. T.B. Massalski, J.L. Murray, L.H. Bennett and H. Baker (eds.) *Binary Alloy Phase Diagram*, American Society for Metals, Metals Park, OH, 1986.

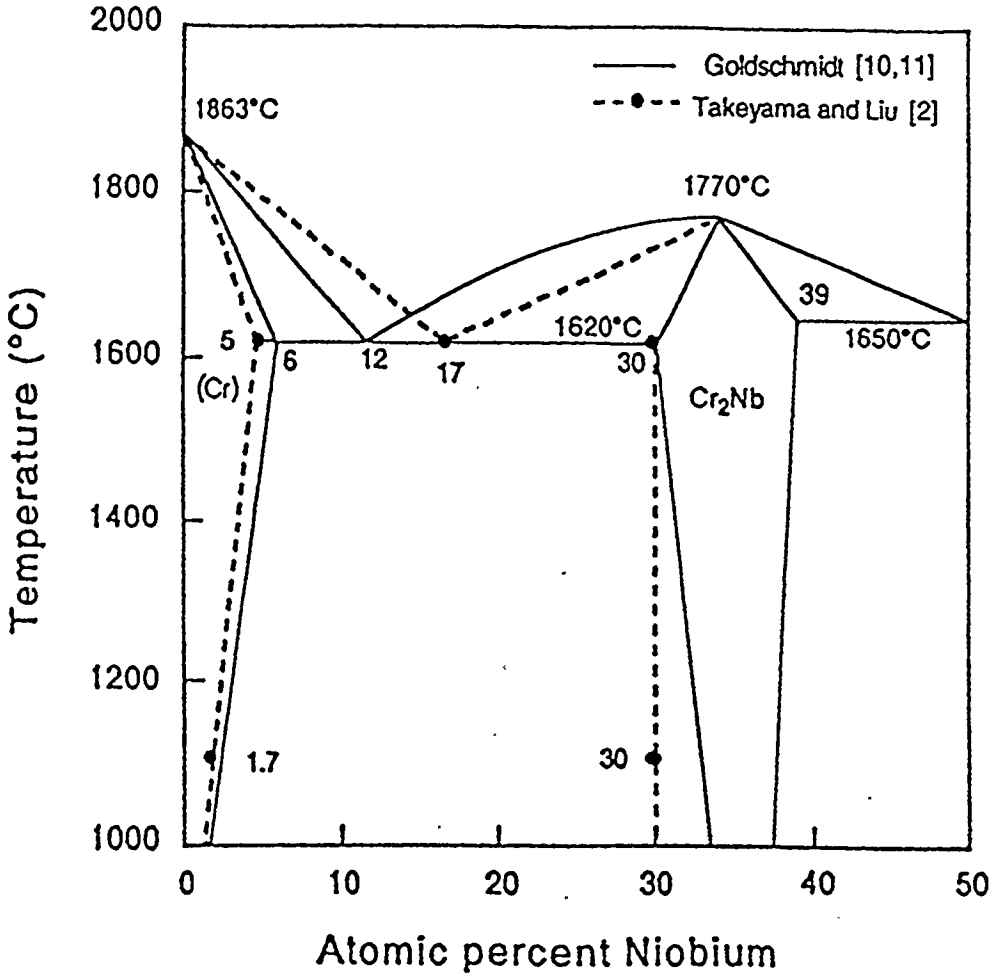

Figure 1. The Chromium-Niobium Binary Phase Diagram.

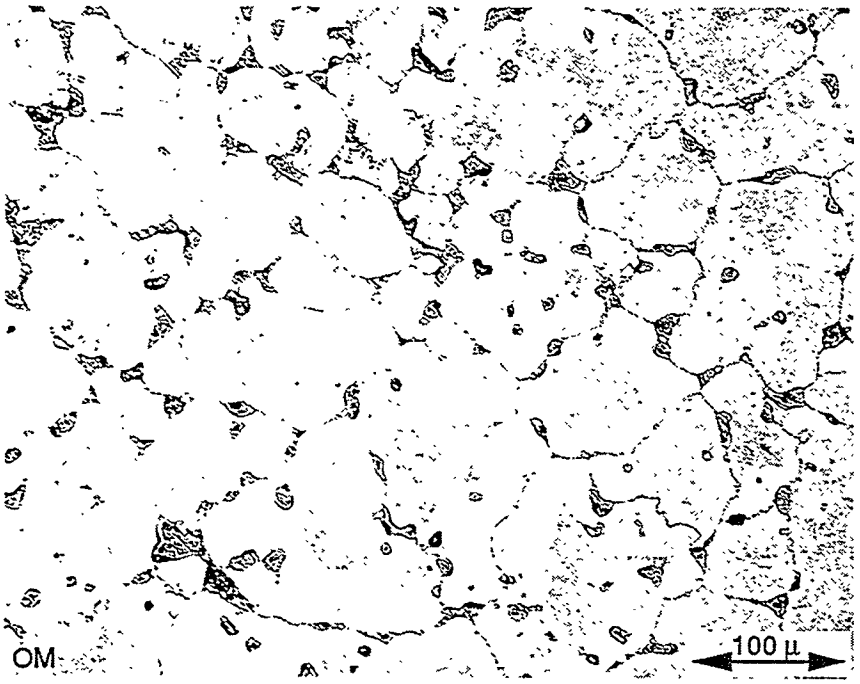

Figure 2. Sample CN-7 (94 at.% Cr-6 at.% Nb) annealed 1 hour at 1600°C plus 4 hours at 1200°C in vacuum. Cr-rich regions (light) surrounded by Laves-containing eutectic phase (dark).

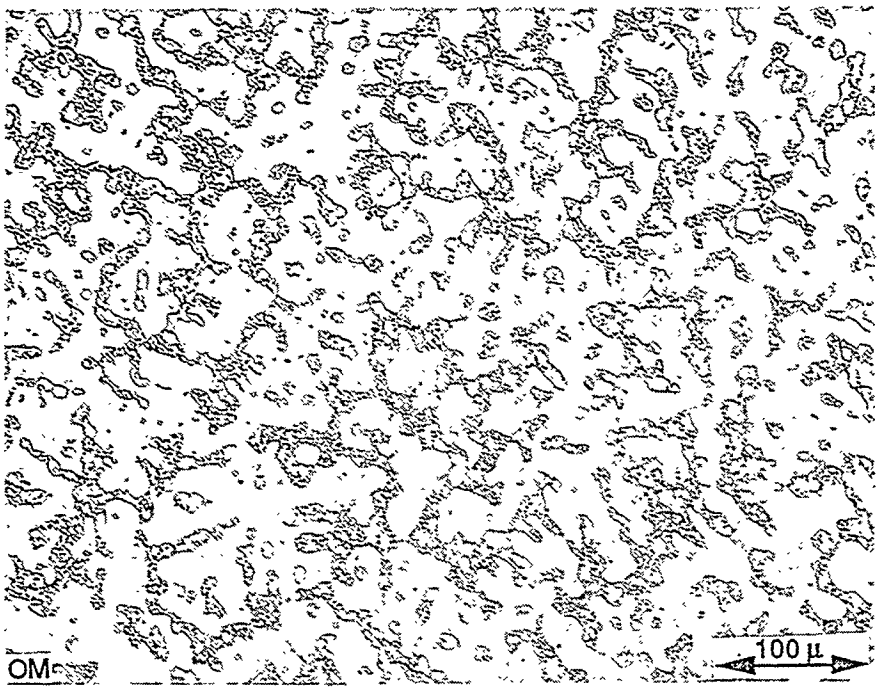

Figure 3. Sample CN-4 (88 at.% Cr-12 at.% Nb) annealed for 1 hour at 1600°C plus 4 hours at 1200°C in vacuum. Cr-rich regions (light) surrounded by Laves-containing eutectic phase (dark).

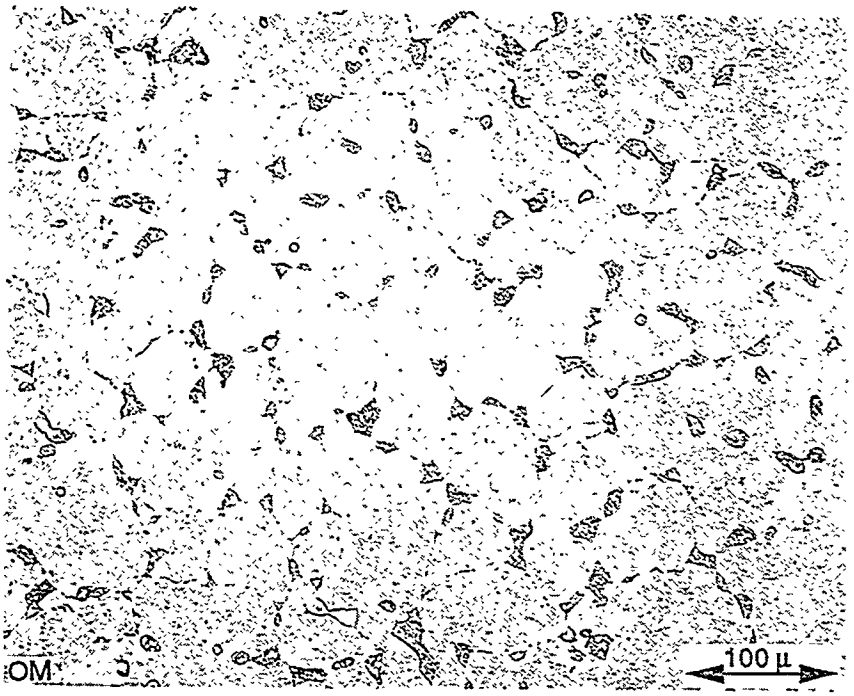

Figure 4. CN-7 - annealed for 2 days at 1580°C plus 2 days at 1200°C in vacuum.

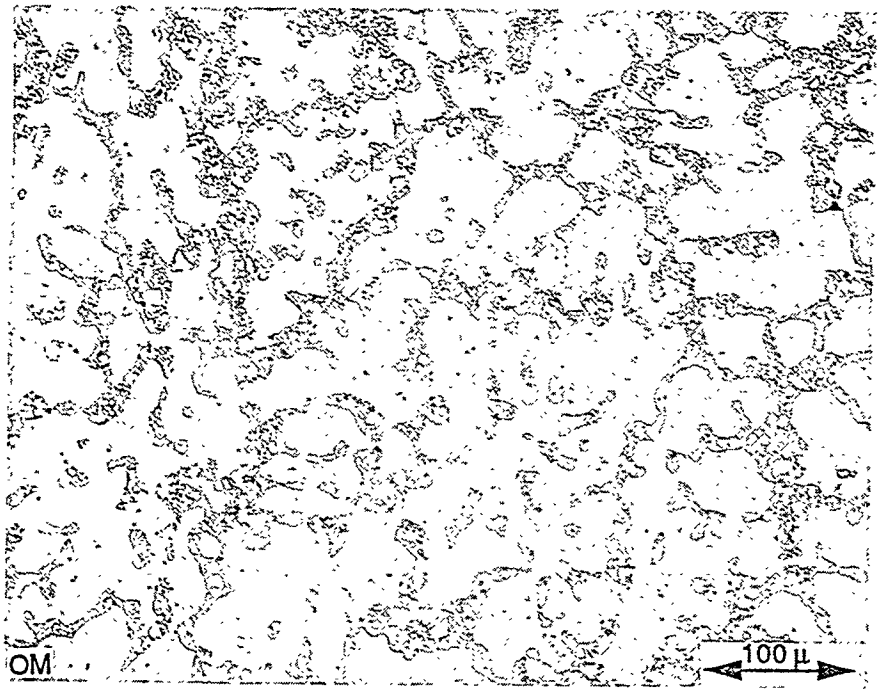

Figure 5. CN-4 - annealed for 2 days at 1580°C plus 2 days at 1200°C in vacuum.

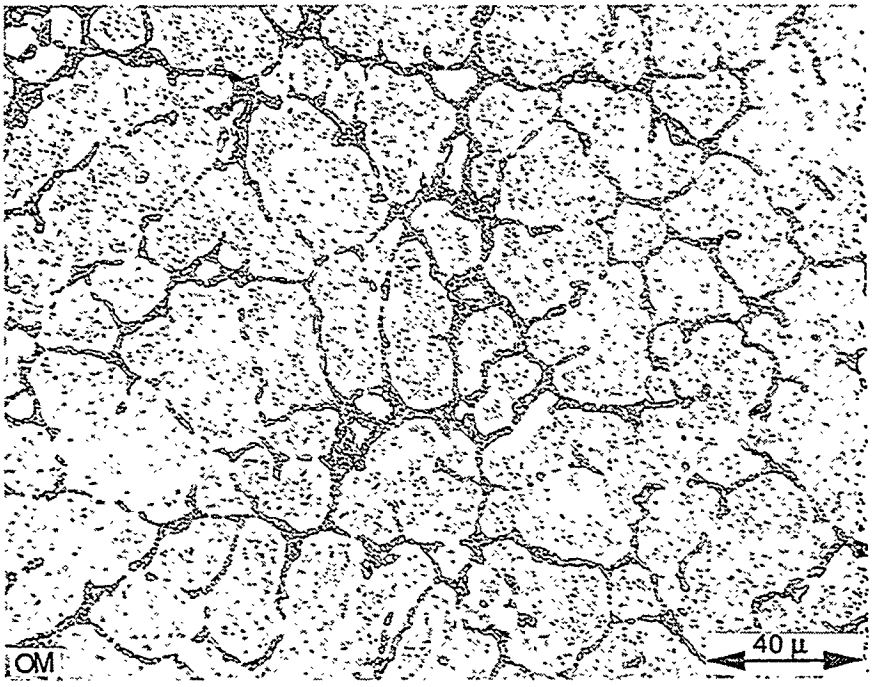

Figure 6. Sample CN-7 (94 at.% Cr-6 at.% Nb) annealed 1 day at 1300°C in vacuum. Cr-rich regions (light) surrounded by Laves-containing eutectic phase (dark).

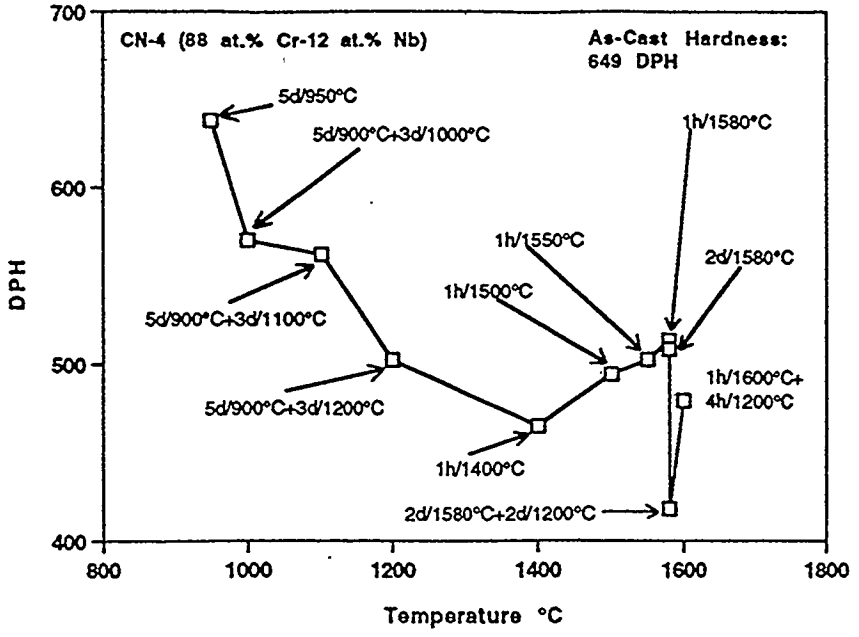

Figure 7. Hardness profile for CN-4 for a variety of annealing treatments illustrating how precipitate coarsening at lower annealing temperatures (950-1200°C) can reduce the hardness of the material.

SESSION III - WORKSHOP ON MATERIALS CHALLENGES IN ADVANCED FOSSIL FUELED POWER SYSTEMS

SUMMARY

WORKSHOP ON NEW MATERIALS DEVELOPMENT AND APPLICATIONS

A *Workshop on Materials Challenges in Advanced Fossil Fueled Power Systems* was held as part of the Ninth Annual Conference on Fossil Energy Materials. The workshop opened with a plenary session that included several brief overviews from a panel of sponsors, system designers, manufacturers, producers, and users who presented different perspectives on issues for their particular systems. Systems discussed included integrated gasification combined cycle (IGCC), pressurized fluidized bed combustion (PFBC), hot gas filters, and indirectly fired combined cycles. A question and answer session followed the presentations.

Workshop panelists and the primary emphasis areas of their presentations were:

Dan Seery	Senior Program Manager; United Technologies Research Center; East Hartford, Connecticut	Combustion 2000, HIPPS system design
Gerry Bruck	Program Manager, Advanced Fossil Energy Systems; Westinghouse Electric Corporation; Pittsburgh, Pennsylvania	Materials selections for advanced coal-fueled power systems
Larry Ruth	Division Director/DOE Pittsburgh Energy Technology Center; Pittsburgh, Pennsylvania	Combustion 2000, HIPPS, and LEBS
Ted McMahon	Project Manager/Coal Gasification and Hot-Gas Cleanup Division; DOE Morgantown Energy Technology Center; Morgantown, West Virginia	Hot-gas cleanup materials
John Mundy	DOE-Basic Energy Sciences; Division of Materials Sciences, Washington, DC	BES Materials R&D and its relationship to Fossil Energy
Tom Gibbons	Director, Materials and Water Chemistry, Power Plant Laboratories; ABB Combustion Engineering; Windsor, Connecticut	Materials selections for pulverized coal power plants
Juhani Isaksson	Ahlstrom Pyropower; Karhula, Finland and San Diego, California	Circulating pressurized fluidized bed combustion systems and hot-gas filtration
Nguyen Minh	Space Systems Engineering, Aerospace Systems and Equipment; AlliedSignal Inc.; Torrance, California	HIPPS design and ceramic heat exchangers
Mo Bary	Program Manager, Black & Veatch, Overland Park, Kansas	Warren Station EFCC Repowering Project

Following the plenary session, four separate working group sessions were conducted. The working groups addressed issues related to:

Session A - Hot Gas Filters
Session B - Metallic Heat Exchangers
Session C - Ceramic Heat Exchangers
Session D - Metallic Components

The conference and workshop are part of the overall AR&TD Materials Program strategic planning. This workshop provided the opportunity to have major materials issues discussed from a systems point of view by the expert panelists followed by detailed discussions in the working groups on how best to address these issues in the context of the AR&TD Materials Program. Results of the workshop will be incorporated into program planning activities.

SESSION IV - NEW ALLOYS AND FUNCTIONAL MATERIALS

ODS IRON ALUMINIDES

I. G. Wright, C. G. McKamey, and B. A. Pint

Oak Ridge National Laboratory
P. O. Box 2008
Oak Ridge, TN37831-6156

ABSTRACT

Since oxide dispersion-strengthened (ODS) FeCrAl-based alloys have sufficient creep strength and good oxidation resistance at the very high temperatures of interest for the primary heat exchanger in advanced, closed-cycle gas turbine systems, they constitute viable alternative candidates to ceramics. A major life-limiting factor of these alloys is the ability to continue to form a protective scale of aluminum oxide, a factor proportional to the total amount of aluminum contained in the alloy. Fe_3Al has oxidation resistance comparable to that of the FeCrAl-based alloys, and significantly superior sulfidation resistance. Also, because of its larger reservoir of aluminum, Fe_3Al would be expected to exhibit longer lifetimes at the temperatures of interest. Since the strengthening effects of ODS processing are expected to confer similar high-temperature creep properties to those found for the FeCrAl-based alloys, ODS-Fe_3Al is considered to have excellent potential for the very high-temperature heat exchanger application. The program effort on ODS Fe_3Al includes examination of the properties of available ODS-FeCrAl alloys; development of mechanical alloying parameters for ODS-Fe_3Al; determination of the effects of a dispersion of reactive element oxides on the high-temperature oxidation behavior of Fe_3Al; and evaluation of methods for joining them.

INTRODUCTION

There has been a recent increase of interest in advanced cycles that involve indirectly-fired gas turbines, in which coal- or gas-fired high-temperature heat exchangers are used to heat a working fluid in a closed system[1]. In a program conducted as part of the European COST-501 Concerted Action Project (Round 2, Work Package 4), available alloys based on FeCrAl-Y_2O_3 (listed in Table 1) were evaluated for use in the main heat exchanger in a similar closed-cycle gas turbine application[2,3,4,5,6,7,8,9,10,11,12]. One of the currently available ODS FeCrAl alloys was found to meet the strength requirements for this application, in which the working fluid at 0.9 MPa (131 psi) flowing at 5,889 kg/hr (12,955 lb/hr) was to be heated from 800 to 1100°C (1472 to 2012°F) over a tube length of 4 m (13 ft).

FeCrAl-based alloys have long been regarded as having excellent resistance to high-temperature oxidation, with reactive metal or reactive metal oxide additions playing some beneficial role[13,14,15]. However, much of the information on oxidation behavior was generated from relatively short-term exposures. In the very high-temperature heat exchanger application, an area of unexpected

but major concern with these alloys is their ability to maintain a protective oxide scale for the extended times necessary for commercial application. After extended exposure times, these alloys

Table 1. Nominal Compositions of Available Ferritic ODS Alloys (weight percent)

Alloy	Fe	Cr	Al	Mo	Ti	Y_2O_3
MA 956	Bal	20.0	4.5	—	0.5	0.5
PM 2000	Bal	20.0	5.5	—	0.5	0.5
ODM 751	Bal	16.5	4.5	1.5	0.6	0.5
ODM 331	Bal	13.0	3.0	1.5	0.6	0.5

suffer increasing loss of scale through spallation, as indicated by the trend to weight losses as shown in Fig. 1. The oxidation life of these alloys is determined by their ability to form or reform a protective alumina scale, and can be related to the time for the aluminum content of the alloy to be depleted to some minimum level; this, in turn, is a function of the total aluminum content of the alloy. This dependence on total available aluminum content is illustrated by results[8] from the COST-501 project as summarized in Fig. 2, which relates the effective life of the alloy tube (represented as 'time to breakaway') to its wall thickness.

The major factors that result in depletion of the reservoir of aluminum in the alloy are the inherent growth rate of the oxide, a process that consumes aluminum, and the tendency for the scale to spall, which also results in a net loss of aluminum from the alloy together with a (temporary) increase in oxide growth rate in the area affected by spallation. When the alloy aluminum reservoir falls below the minimum level at which an alumina layer can be reformed, less-protective oxides of the other alloy

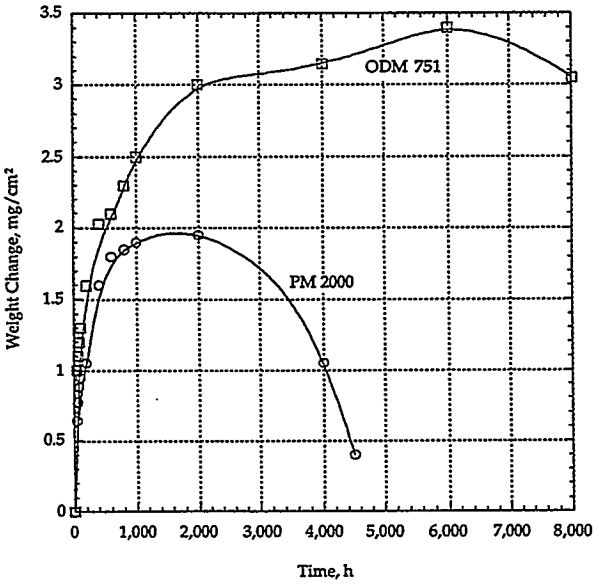

Figure 1. Oxidation kinetics for ODS-FeCrAl-Y_2O_3 alloys in air at 1200°C cycled to room temperature every 48 hr (after ref. 8).

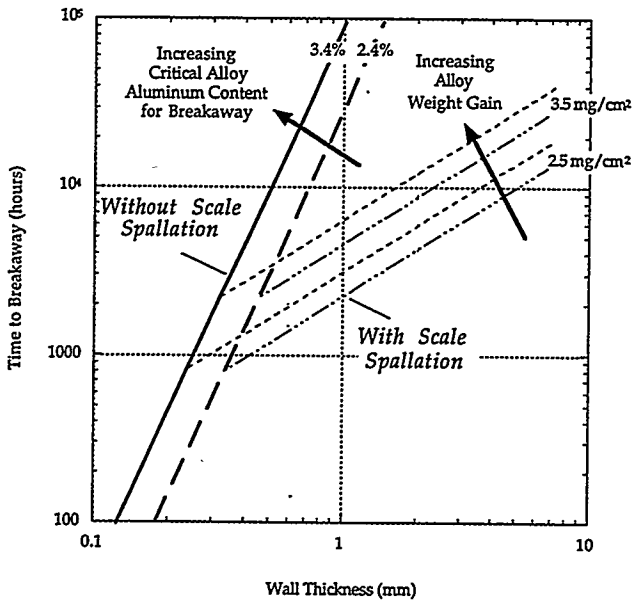

Figure 2. Effects of alloy oxidation rate, oxide spallation, and tube wall thickness on lifetime (time to onset of breakaway oxidation) of ODS-FeCrAl alloys (after ref. 8).

constituents will form in areas where the initial scale spalls, and the rate of oxidation may rapidly increase as the alloy undergoes breakaway oxidation. A further complication is that, according to results from the COST-501 project, differences among alloys that are insignificant for oxidation growth rate and tendency to spall can dramatically affect the time to breakaway. Hence, similar components manufactured from alloys of nominally similar compositions may fail at quite different times.

Iron-aluminum alloys have the obvious potential to provide longer service lives because of their inherently larger aluminum reservoirs (15.8 vs 3 to 5.5 wt.% Al), provided that their oxidation and mechanical properties are similar to the FeCrAl-based alloys. Iron-aluminum alloys have been regarded for many years as having excellent resistance to high-temperature oxidation[16,17,18,19], and this has been confirmed by the recent work at ORNL on Fe_3Al alloys[20]. However, until this recent work , the development of usable ferritic alloys was restricted by their poor mechanical properties, especially the lack of ambient-temperature ductility which impaired fabricability. The lack of strength at temperatures above about 600°C is still a problem for the conventionally-cast alloys. The potential for increasing the creep rupture strength of iron aluminides by ODS processing was demonstrated in the 1960's[21]: the incorporation of 12 volume percent of approximately 1 μm Al_2O_3 to Fe-40 at. percent Al improved the high-temperature (732°C) creep strength by a factor of 4, compared to the dispersion-free, cast alloy.

Overall, there appears to be a niche application for an ODS version of Fe_3Al in components such as heat exchanger tubes that must operate at very high temperatures and for which the obvious competition is from ceramic materials. The work in this program is aimed at evaluating this potential.

PRELIMINARY EXAMINATION OF AVAILABLE FERRITIC ODS ALLOYS

A sample of an ODS FeCrAl alloy in the form of a round bar approximately 13 mm (0.5 in.) diameter was obtained from Dour Metal for characterization. Chemical analysis of the alloy showed that it was probably Dour Metal alloy ODM 331, rather than ODM 751 (see Table 1). The grain size of the as-received alloy was determined by metallographic techniques to be approximately 2 μm , as shown in Fig. 3. Round specimens with a gage diameter of approximately 3 mm (0.12 in.) and a gage length of 12.7 mm (0.50 in.) were machined from the as-received bar, and subjected to creep-rupture testing in air. The first creep test at 1000°C (1832°F) and 55 MPa (8 ksi) failed in only a few minutes, before sufficient data could be recorded. A subsequent test at 816°C (1500°F) with a stress of 34.5 MPa (5 ksi) produced the data plotted in Fig. 4; the rupture-life was less than 5 hours, with a final elongation of 119.3 percent, and the minimum creep rate (MCR) was approximately 7.75%/h. This unexpectedly-low creep-rupture resistance was attributed to the small grain size of the as-received material.

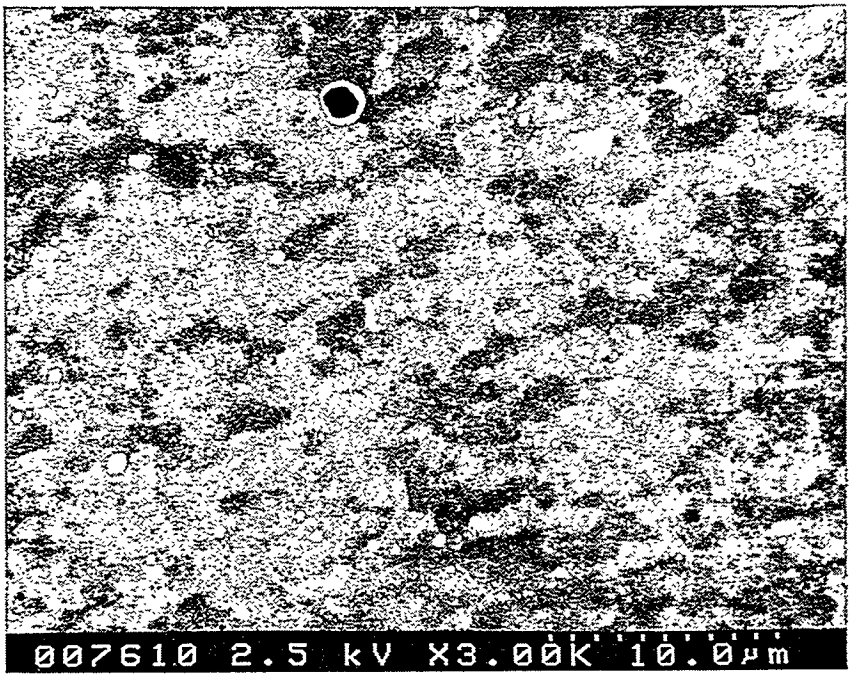

Figure 3. Secondary scanning electron image of a transverse cross section of ODM-331 showing the small grain size and the presence of cavities and oxide particles.

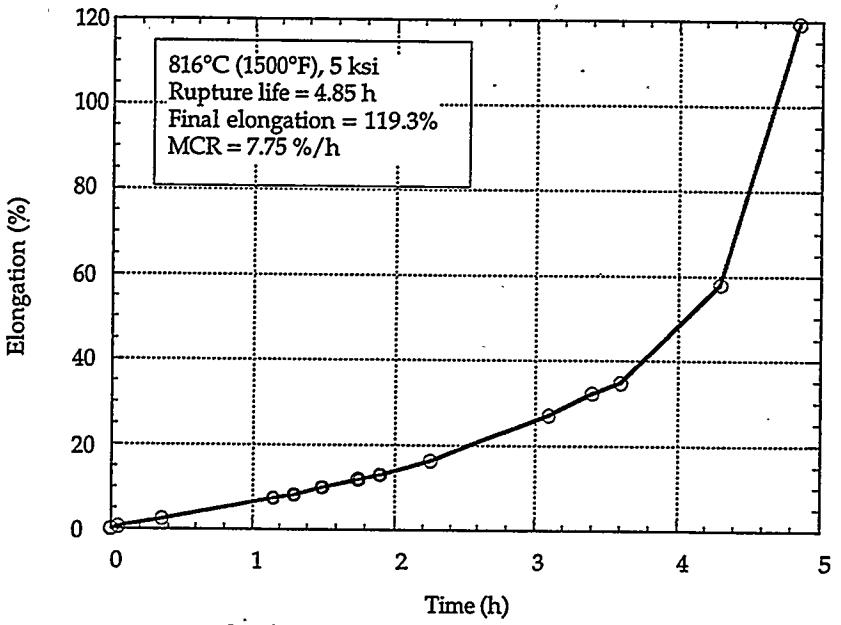

Figure 4. Creep-rupture curve for ODM-331 in the as-received and machined condition, tested at 816°C at a stress of 34.5 MPa (5 ksi).

In an attempt to produce larger, elongated grains to increase the creep strength, a heat treatment of 25 hours at 1350°C (2462°F) in vacuum was performed on a small sample of the alloy. However, no etchant could be found that would satisfactorily reveal the grain structure resulting from the heat treatment. A drawback of this heat treatment was obvious evaporation of chromium from the outer surface of the specimen, and an observed increase in the size of some of the oxide particles in the matrix. In the absence of a means of measuring the alloy grain size, further testing of this alloy was postponed.

A second series of tests was conducted on a sample of an ODS Fe_3Al-based alloy produced at ORNL (designated FAS-3Y). The nominal composition of this alloy was Fe-28Al-2Cr-0.05B (at.%), to which 0.2 cation% Y_2O_3 was added by mechanical alloying (see following section). Tensile specimens with gage dimensions of 12.7 x 0.75 x 3.2 mm (0.50 x 0.030 x 0.126 in.) were punched from the as-rolled sheet and heat treated for 8 h at 1275°C (2327°F) in argon to produce the large-grained banded grain structure shown in Fig. 5. The results of tensile tests conducted in air at room temperature, 800, and 1000°C (1472 and 1832°F) using a strain rate of 3.3×10^{-3} s^{-1} are shown in Table 2. Typical data for monolithic FAS, two other monolithic ORNL-developed iron aluminide alloys, and the Dour Metal alloy ODM-331, are included for comparison. At room temperature, the FAS-3Y alloy had a similar tensile strength but a lower ductility compared to the FA-180 alloy, as

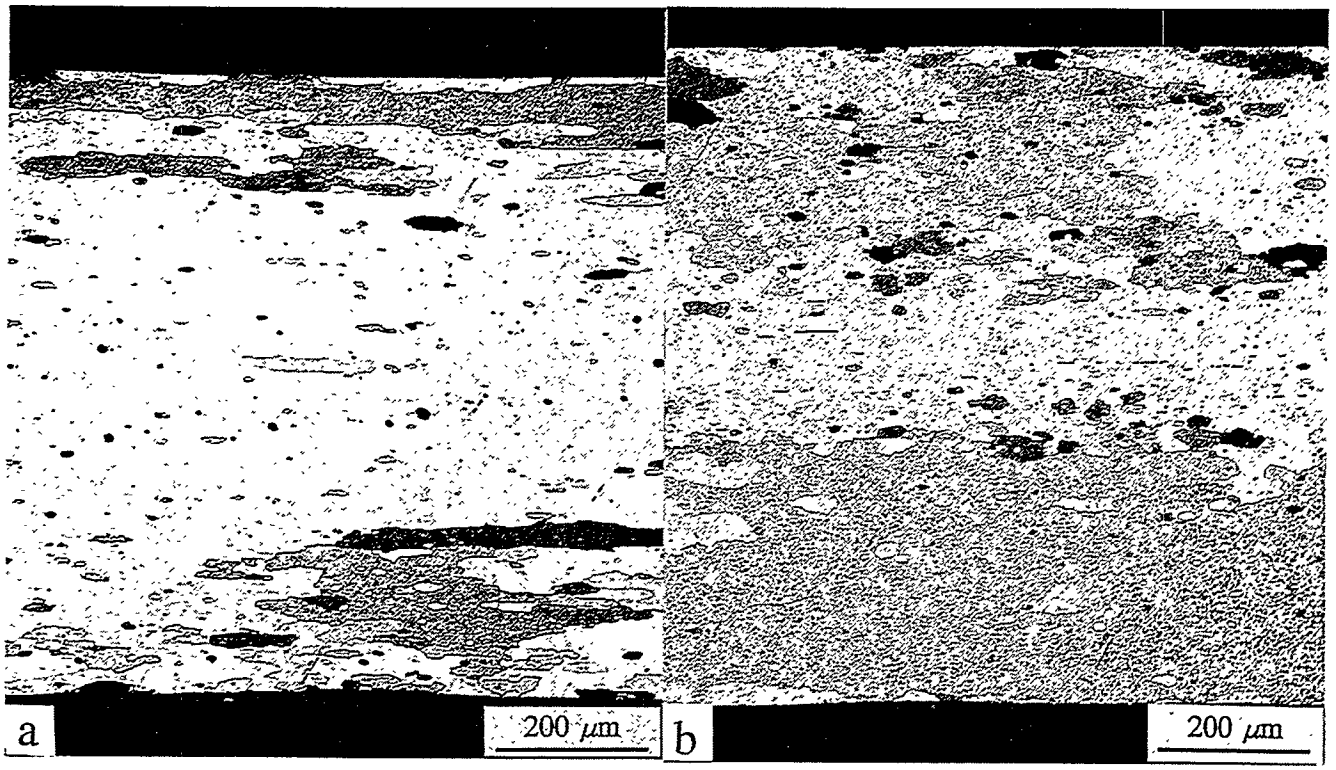

Figure 5. Optical micrographs of FAS-3Y after a heat treatment of 8 h at 1275°C in air; shown is the through-thickness direction (a) parallel to and (b) perpendicular to the rolling direction.

Table 2. Comparison of Tensile Properties of Alloy FAS-3Y With Other Iron-Based Alloys

Property	FAS-3Y	FAS	FA-129	FA-180	ODM-331
20°C					
YS (MPa)	643	394	380	620	
UTS (MPa)	959	679	900	900	
Elongation (%)	2	9	15	8	
800°C					
YS (MPa)	110			140	
UTS (MPa)	120			148	
Elongation (%)	36			79	
900°C					
YS (MPa)					160
UTS (MPa)					170
Elongation (%)					10
1000°C					
YS (MPa)	43			27	
UTS (MPa)	49			27	
Elongation (%)	12			137	

FA-129 = Fe-28Al-5Cr-0.5Nb-0.2C (at.%)
FA-180 = Fe-28Al-5Cr-0.5Nb-0.8Mo-0.025Zr-0.05C-0.005B (at.%)

expected for an oxide-dispersion-strengthened alloy. The FAS-3Y specimen failed in a ductile-dimple manner, with particles at the base of the dimples. Since tensile properties are usually better in iron aluminides with finer-grained microstructures, it is anticipated that the strength of this alloy will improve with heat treatment at a lower temperature.

A creep-rupture test of this alloy was initiated at 800°C (1472°F) with an initial stress of 34.5 MPa (5 ksi). At this stress, the minimum creep rate appeared to be almost zero. After approximately 240 hours, the stress was increased to 48.3 MPa (7 ksi) and the test was allowed to proceed to rupture. As shown in Fig. 6, rupture occurred suddenly after 383.45 hours, at a specimen elongation of about 3 percent. Another test at 1000°C (1832°F) started at 13.8 MPa (2 ksi). Since there was no discernible creep after 240 hours, the stress was increased to 20.7 MPa (3 ksi), and then to 27.6 MPa (4 ksi) before failure occurred after 477 hours, with a final elongation of 6.9 percent. Further creep tests on FAS-3Y will be initiated following the fabrication of a new sample of FAS-3Y material and the development of thermomechanical processing to produce the desired large, elongated grain structure.

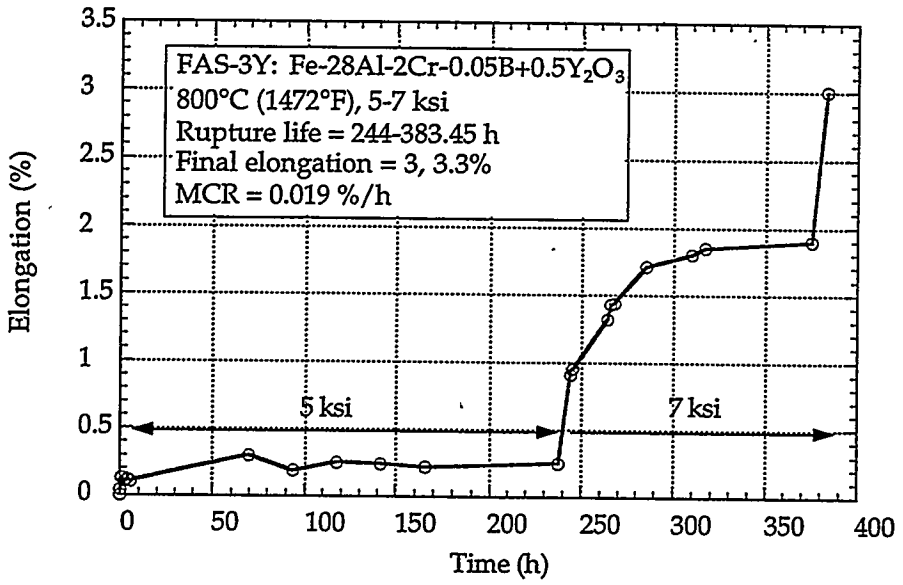

Figure 6. Creep-rupture curve of FAS-3Y heat treated 8 h at 1275°C and tested at 800°C.

The limited creep-rupture data generated so far on the FAS-3Y material suggests a lower creep resistance than the ODM alloys produced by Dour Metal. However, with the limited number of samples available, the best fabrication and heat treating conditions to produce the desired

microstructure for maximum strength have not been determined. Plans have been made to obtain a larger sample of this alloy from a commercial vendor.

DEVELOPMENT OF MECHANICAL ALLOYING PARAMETERS FOR ODS Fe_3Al

Initial investigation of mechanical alloying parameters used a Svegvari Type 01STD attritor mill (purchased from Union Process Inc., Akron, Ohio), which has a capacity of 0.75 litres (0.26 ft^3). This mill was top-loaded (and unloaded) and was fitted with a water-cooled lid and paddle bearing. A typical charge consisted of 150 g (0.33 lb) of powder, and 1500 g (3.3 lb) of stainless steel balls (powder:ball ratio of 1:10). Prealloyed Fe_3Al (FAS) powder was used, together with reactive metal oxide powder which was obtained with an average particle size of less than 1μm. The FAS powder was obtained from Ametek, and consisted of spherical particles having a particle size range of 150 μm to 45 μm, (mesh size -100/+325). In use, the loaded and assembled mill was purged with argon for 5 min. prior to the start of milling; a continuous flow of argon was maintained during milling. At the end of a run, the lid was removed and the cooled powder exposed to the ambient laboratory air. The effect of increasing milling time was evaluated through examination of the powder size and shape by scanning electron microscopy; the extent of mechanical alloying was assessed by light microscopy of metallographically-prepared samples of the powder. The mechanical alloying process incorporates the oxide dispersoid into the alloy structure by a repetitive process of welding and smearing of the alloy powder particles onto the mill walls and the balls, followed by detachment of fragments of the powder. A layered structure is developed which contains entrapped particles of the dispersoid; with time, the layers become sufficiently fine that the alloy powder particles attain a homogeneous composition, with a uniform distribution of the dispersoid particles. Figure 7 shows the change in powder particle size as a function of milling time. The most obvious initial effect of milling is flattening of the original spherical particles into discs, which assume irregular shapes with increased milling time. Further milling results in the transformation from flattened plates to agglomerates of much smaller particles. Once the powder structure observed after 50 hours of milling is attained, further milling produces little alteration in alloy structure or actual particle size.

The milling parameters chosen for the processing of powder intended for subsequent consolidation and preparation of test specimens were 500 rpm for 48 hours. A larger Svegvari attritor mill, Type 01HD with a capacity of 1.4 litres (0.49 ft^3), was used to prepare these materials. The milling conditions were the same as those used in the smaller mill. The amount of powder per batch was increased to 300g (0.66 lb) and the larger mill is capable of running 24 hours per day.

A search was made for facilities capable of producing larger batches of mechanically-alloyed powder, of the order of several kilograms to commercial alloy-production sizes. The following possible sources were identified: INCO, Dour Metal of Belgium; PM Hochtemperatur-Metall of Germany; AEA Technology of Risley, U. K.; and CRM of Italy. INCO (Huntington, West Virginia) uses ball milling to produce Ni-based ODS-alloys only and has no current capability that could address the needs of the iron aluminide program; there was also concern about contamination of any mill that was used. INCO International (Hereford, U.K.) produces only Fe-based ODS alloys, but it also has no available mill capacity. Dour Metal has produced tubes of ODS-FeCrAl-Y_2O_3 using in-house

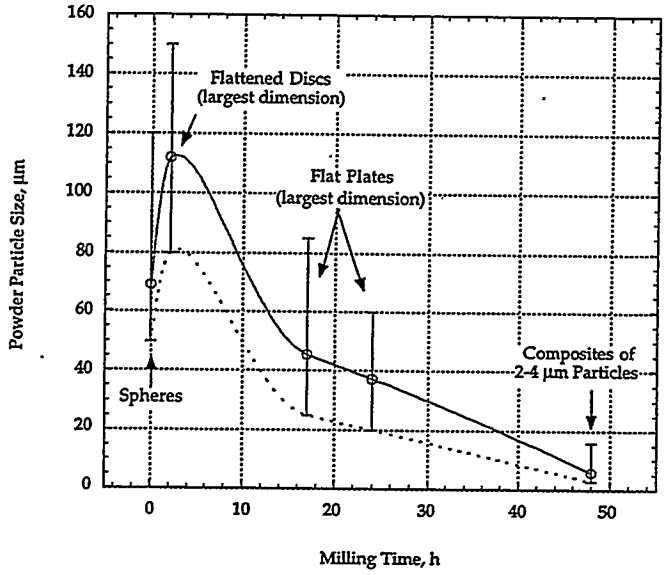

Figure 7. Plot of the average particle size of FAS-3Y alloy powder as a function of milling time.

processing that starts with ball milling. They also have made an ODS version of Fe-40 at.% Al using alumina as the dispersoid. PM Hochtemperatur-Metall uses ball milling to produce ODS-FeCrAl-Y_2O_3 on a commercial basis, but has not made tubing. AEA, Risley, U.K. has a small-capacity centrifugal mill of new design; this equipment has the potential for better processing control than conventional attritor or ball milling, but is as yet not available in a commercial size. CRM has a small-capacity ball mill, and has been involved with ODS-Fe-40Al. Arrangements currently are being made to work with both Dour Metal and PM Hochtemperatur-Metall to produce several 20 kg (44 lb) batches of ODS-Fe_3Al powder from prealloyed FAS powder made by Ametek corp. The mechanically-alloyed powder will be used by ORNL to optimize the thermomechanical processing required to produce the required grain size and structure and to measure the properties relevant to the envisioned application.

EFFECTS OF A DISPERSION OF OXIDES ON THE HIGH-TEMPERATURE OXIDATION BEHAVIOR OF Fe_3Al

Mechanically-alloyed powders of Fe_3Al containing additions of the following reactive element oxides: Y_2O_3 (0.05, 0.1, 0.2, 0.3, 0.5 cation %), ZrO_2 (0.2 cat.%), La_2O_3 (0.05, 0.2 cat.%), Al_2O_3 (0.2 cat.%), CeO_2 (0.2 cat.%), Nd_2O_3 (0.2 cat. %), and Yb_2O_3 (0.2 cat. %) were made at ORNL using nitrogen-atomized prealloyed FAS powder in the Svegvari 01HD mill. These powders were canned in mild steel, and extruded at 1050°C (1922°F) with a reduction ratio of 12:1 to produce rods approximately 25 mm (1.0 in.) in diameter. After decanning, disc-shaped specimens were cut from these rods and subjected to oxidation testing with no further heat treatment, that is, with a relatively small alloy grain size. The specimen surfaces were polished with 0.3 μm (12 x 10^{-6} in.) alumina and washed before exposure. The details of the test procedures and some of the cyclic oxidation results are presented elsewhere [22]. Figures 8 and 9 summarize the kinetics of isothermal oxidation in air, and cyclic oxidation in oxygen, respectively, both at 1200°C (2192°F), for the FAS alloy with and without a dispersion of Y_2O_3. Ignoring the initial rapid

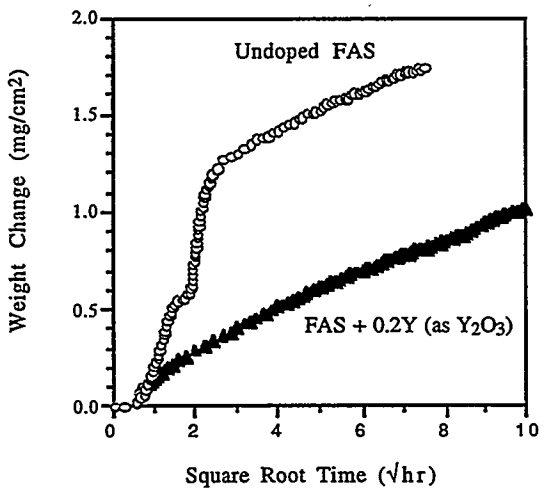

Figure 8. Comparison of the isothermal oxidation kinetics of conventionally-produced and and ODS-FAS (FAS-3Y); 1200°C in oxygen.

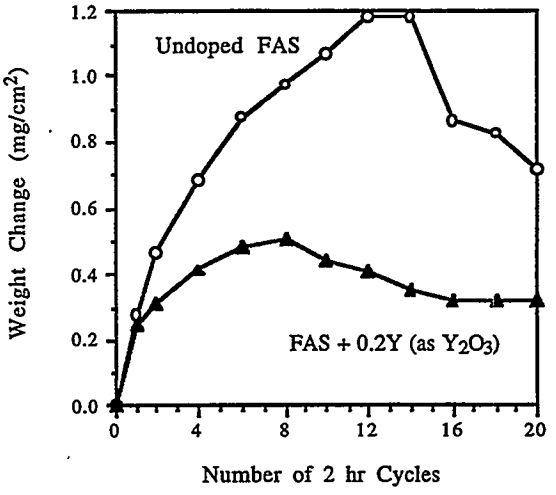

Figure 9. Comparison of the cyclic oxidation kinetics of conventionally-produced ODS-versions of Alloy FAS (FAS-3Y); 1200°C in air.

oxidation of the undoped alloy during the first 4 hours of isothermal exposure, the oxidation rates of the two alloys at longer times appear quite similar; both alloys exhibited oxidation rates that are slightly slower than parabolic, suggesting that the oxide scales become more protective with time. In the cyclic oxidation test, the weight gain of the ODS alloy was very similar to that in the isothermal test up to approximately 16 hours (and obviously slower than that of the undoped alloy), after which it

apparently suffered some degree of scale spallation. The reason for the increased weight gain of the undoped alloy in this test was because it suffered from scale spallation at the end of each cycle. The areas over which spallation occurred were extremely small and, since the spalled scale did not fully detach, a net increase in weight was measured up to the 14th cycle, or 28 hours, after which actual scale loss apparently occurred.

Figures 10 and 11 compare the isothermal and cyclic oxidation behavior of the FAS-3Y alloy with a commercially-available ODS-FeCrAl-Y_2O_3 alloy, MA956 (see Table 1) at 1200°C (2192°F) in air, and in oxygen, respectively. The kinetics of isothermal oxidation to 100 hours appear essentially

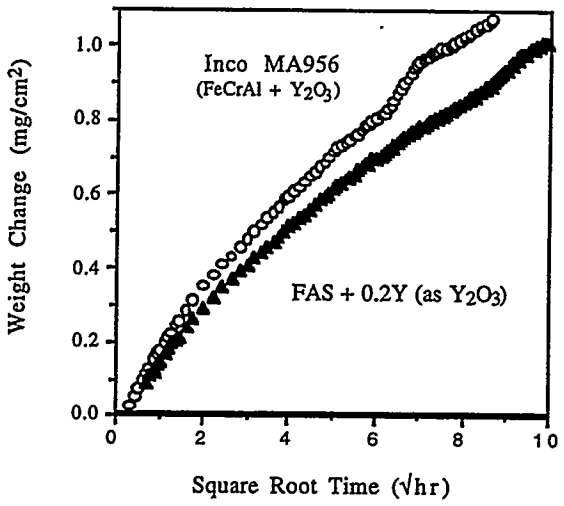

Figure 10. Comparison of the isothermal oxidation kinetics of ODS-FAS (FAS-3Y) with a commercial ODS-FeCrAl-Y_2O_3; 1200°C in air.

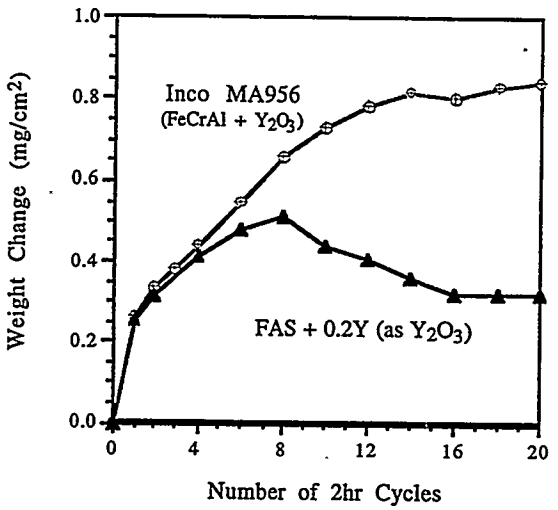

Figure 11. Comparison of cyclic oxidation kinetics of ODS-FAS (FAS-3Y) with a commercial ODS-FeCrAl-Y_2O_3; 1200°C in oxygen.

the same, as might be expected for alloys that are intended to form a protective alumina scale. Under isothermal conditions, the rate of consumption of aluminum to form the protective scale would be very similar for the two alloys. In the cyclic oxidation test, the weight gain of the MA956 after 40 hours was almost the same as that measured in the isothermal test, indicating no scale spallation. As noted above, the weight gains measured for the FAS-3Y indicated some scale spallation. This is a surprising result, since a dispersion of a reactive element oxide with the appropriate particle size and distribution generally has been found to improve the overall scale adherence on alumina-forming alloys. Such spallation would obviously increase the rate of depletion of the aluminum reservoir of the FAS-3Y alloy. Although this reservoir is much larger than that in alloy MA956, the rate of spallation must be minimized to maintain the potential service lifetime advantage of FAS-3Y[22].

There are several possible reasons for the difference in scale spallation behavior between the two alloy types, ranging from inhomogeneity in FAS-3Y to a fundamental difference in the functioning of the reactive element effect in Fe_3Al compared to FeCrAl-Y_2O_3. The possibility that there are inherent differences in scale spallation behavior between FeCrAl-based and iron aluminide-based alloys[20] and the effects of different types and levels of reactive element oxides on the oxidation behavior of Fe_3Al are the subject of ongoing research.

SUMMARY AND CONCLUSIONS

Heat exchangers for cycles which require a working fluid to be heated to temperatures of 1100-1200°C (2012-2192°F) provide a potential application in which the exceptional high-temperature oxidation and sulfidation resistance of iron aluminides can be exploited. The alternative materials choices for such an application are ODS-FeCrAl-based alloys and ceramics. An ODS-version of Fe_3Al has the obvious advantage over ceramics that it has metallic characteristics, and is expected to exhibit a significantly longer service life than ODS-FeCrAl alloys. Creep tests with a non-optimized ODS-Fe_3Al indicated significantly improved strength compared to non-ODS iron aluminides, but lower creep resistance compared to a commercial ODS-FeCrAl alloy. The isothermal oxidation rate of the ODS-Fe_3Al was essentially the same as that of a commercial ODS-FeCrAl alloy at 1200°C (2192°F), but there was evidence of inferior resistance to cyclic oxidation. The main issues to be resolved are the ability of optimized ODS processing of Fe_3Al to achieve an equivalent improvement in high-temperature creep strength to that found with ODS-FeCrAl alloys and a method for improving the resistance to scale spallation of Fe_3Al.

ACKNOWLEDGMENTS

The authors thank colleagues at ORNL: V. K. Sikka, K. S. Blakely, J. L. Wright, M. Howell, J. R. DiSteffano, and P. F. Tortorelli for their contributions and invaluable discussions. This research was sponsored by the Fossil Energy Advanced Research and Technology Development (AR&TD) Materials Program, U. S. Department of Energy, under contract DE-AC05-84OR21400 with Martin Marietta Energy Systems, Inc. B. A. Pint is supported by the U. S. Department of Energy's Distinguished Postdoctoral Research Program administered by the Oak Ridge Institute for Science and Education.

REFERENCES

1. F. Starr, A. R. White, and B. Kazimierzak, pp. 1393-1412 in *Materials for Advanced Power Engineering*, Proc. 5th COST 501 Conf., Liege, Belgium, D. Coutsouradis, et al., eds., Kluwer Academic Pub., Dordrecht (1994).
2. D. Sporer, and O. Lange, ibid, pp. 1469-1488.
3. J. Beckers-Lecomte, D. Coutsouradis, and B. Kazimierzak, ibid, pp. 1489-1498.

4. H. Cama, and T. A. Hughes, ibid, pp. 1497-1506.
5. D. M. Jaeger, and A. R. Jones, ibid, pp. 1507-1514.
6. D. M. Jaeger, and A. R. Jones, ibid, pp. 1515-1522.
7. B. Dubiel, W, Osuch, M. Wrobel, A. Czyrska-Filemonowicz, and P. J. Ennis, ibid, pp. 1523-1532.
8. W. J. Quadakkers, K. Bongartz, F. Stubbier, and H. Schuster, ibid, pp. 1533-1542.
9. J. P. Banks, D. D. Gohil, H. E. Evans, D. J. Hall, and S. R. J. Saunders, ibid, pp. 1543-1552.
10. J. Bennett, R. Perkins, J. B. Price, and F. Starr, pp. 1553-1562.
11. G. P. De Gaudenzi, F. Umberti, F. Bregani, and G. P. Toledo, ibid, pp. 1563-1572.
12. R. C. Hurst, M. Rees, and J. D. Parker, ibid, pp. 1573-1582.
13. W. Hessenbruch, *Metals and Alloys for Use at High Temperatures, Part 1, Non-Scaling Alloys*, J. Springer, Berlin (1940).
14. I. I. Kornilov, Profigrafkniga, Moscow (1945), cited by Setterlund and Prescott, 1961.
15. C. S. Wukusic, *The Physical Metallurgy and Oxidation Behavior of Fe-Cr-Al-Y Alloys*, Report No. GEMP-414 by General Electric Nuclear Energy Div. on USAEC Contract No. AT (40-1)-2847 (1966).
16. C. Sykes and J. W. Bampfylde, JISI, 130 (II), 389 (1934).
17. R. B. Setterlund and G. R. Prescott, Corrosion 17, 277t-282t (1961).
18. J. F. Nachman and W. J. Buehler, *The Fabrication and Properties of 16-ALFENOL (Fe_3Al)—A Non-Strategic Aluminum-Iron Alloy*, U. S. Naval Ordnance Lab. Report No. 2819, (April, 1953).
19. J. F. Nachman and W. J. Buehler, *Thermenol (Fe_3Al-3Mo), A Non-Strategic Aluminum-Base Alloy for High-Temperature Service*, U. S. Naval Ordnance Lab. Report No. 3700, (June 1954).
20. See, for example, J. H. DeVan, P. F. Tortorelli, and M. J. Bennett, pp. 309-320 in *Eighth Annual Conf. on Fossil Energy Materials*, N. C. Cole and R. R. Judkins (comp.), CONF-9405143, U. S. Department of Energy, August 1994.
21. A. U. Seybolt, Trans. ASM, 59, 861-875 (1966).
22. P. F. Tortorelli, J. H. DeVan, B. A. Pint, and I. G. Wright, paper presented at the *Ninth Annual Conference on Fossil Materials*, Oak Ridge, TN, May 1995.

EFFECTS OF COMPOSITION AND HEAT TREATMENT AT 1150°C ON CREEP-RUPTURE PROPERTIES OF Fe_3Al-BASED ALLOYS

C. G. McKamey, P. J. Maziasz, and Y. Marrero-Santos

Metals and Ceramics Division
Oak Ridge National Laboratory
Oak Ridge, TN 37831-6115

ABSTRACT

The effects of composition and heat treatment at 1150°C on the creep-rupture properties of Fe_3Al-based alloys were studied. Tests of alloy FA-180 (Fe-28Al-5Cr-0.5Nb-0.8Mo-0.025Zr-0.05C-0.005B, at.%) with this heat treatment were performed in air using various test temperatures and stresses in order to obtain creep activation energies and constants. An activation energy for creep of approximately 150 kcal/mole was determined, a value which is approximately twice that obtained earlier for the binary alloy heat treated at 750°C. Tests were also conducted on alloys containing various combinations of Cr, Mo, Nb, Zr, C, and B in order to better understand the effect of composition on the improved creep resistance with heat treating at 1150°C. The results suggest an interaction of Mo with Zr and Nb to produce increased creep life.

INTRODUCTION

Past studies have shown that binary Fe_3Al possesses low creep-rupture strength compared to many other alloys, with creep-rupture lives of less than 5 h being reported for tests conducted at 593°C and 207 MPa (ref. 1). The combination of poor creep resistance and low room-temperature tensile ductility due to a susceptibility to environmentally-induced dynamic hydrogen embrittlement[2,3] has limited use of these alloys for structural applications, despite their excellent corrosion properties.[4] Improvements in room temperature tensile ductility have been realized mainly through alloying effects, changes in thermomechanical processing to control microstructure, and by control of the specimen's surface condition.[3,5] Ductilities of 10-20% and tensile yield strengths as high as 500 MPa have been reported.[6,7] In terms of creep-rupture strength, small additions of Mo, Nb, and Zr have produced significant improvements, but at the expense of weldability and room-temperature tensile ductility.[1,8-11] Recently an alloy containing these additions, designated FA-180, was shown to exhibit a

creep-rupture life of over 2000 h at 593°C and 207 MPa after a heat treatment of 1 h at 1150°C.[12,13] The increased strength was attributed to the dissolution of coarse particles and reprecipitation of finer Nb-, Mo-, and Zr-based precipitates which strengthened grain boundaries and pinned dislocations.[12-15] This study presents the results of creep-rupture tests at various test temperatures and stresses and discusses the results as part of our effort to understand the strengthening mechanisms involved with heat treatment at 1150°C. Creep-rupture tests of several different compositions of Fe_3Al-based alloys were also conducted in order to better understand the composition dependence of the 1150°C heat treatment.

EXPERIMENTAL PROCEDURES

Alloys used in this study were prepared by arc-melting and drop-casting into a chilled copper mold. Fabrication to 0.8-mm-thick sheet was accomplished by hot-rolling, beginning at 1000°C and finishing at 600-650°C. After a stress relief anneal of 1 h at 700°C, flat tensile specimens (0.8 x 3.18 x 12.7 mm) were mechanically punched from the rolled sheet. Before testing, the specimens were further annealed in air for 1 h at 1150°C and air cooled. Creep-rupture tests were performed in air at temperatures between 500 and 775°C and at stresses of 69-434 MPa (10-63 ksi). Minimum creep rates (MCR) were measured as the slope of the linear portion of the test curve. The data were plotted to a power-law equation in order to obtain creep exponents and activation energies. Optical metallography and scanning electron microscopy (SEM) were used to study the microstructures and fracture modes.

RESULTS AND DISCUSSION

Effect of Heat Treatment at 1150°C on Creep of Alloy FA-180

Tables I and II list the results of creep-rupture tests conducted as a function of test temperature and stress, respectively. The results of tests at temperatures between 593 and 700°C showed that, under a stress of 207 MPa, this alloy had good creep resistance to a temperature of 650°C, but the creep-rupture life decreased dramatically at 675°C. Other data in Tables I and II indicate that with a lower applied stress this alloy could be used at temperatures higher than 650°C. For example, using a stress of 69 MPa, a creep-rupture life of over 500 h was attained at 675°C and almost 200 h at 700°C (Table I). All of the fractured specimens showed a ductile failure mode in which creep voids were observed to have coalesced at grain boundaries and triple points.

Table I. Creep-rupture test results for tests conducted at constant stress

Test #	Stress (MPa)	Tempera-ture (°C)	Rupture Life (h)	Elongation (%)	MCR[a] (%/h)
404/405	207	700	0.6	26.2	13.6
407/431		675	0.8	27.0	20.8
410		650	1059.0	11.0	0.002
411		593	1959.2	9.7	0.003
418/420	69	775	5.1	72.6	4.0
417/419		750	12.5	72.2	1.6
421/422		725	54.5	52.2	0.4
415/416		700	192.1	60.4	0.03
412		675	591.0	45.0	0.002

[a]MCR = minimum creep rate measured in the linear portion of the creep curve.

Table II. Creep-rupture test results for tests conducted at constant temperature

Test #	Temperature (°C)	Stress (MPa)	Rupture Life (h)	Elongation (%)	MCR[a] (%/h)
407/431	675	207	0.8	27.0	20.8
425/430		172	14.2	27.0	1.4
408/413/414		138	52.2	29.0	0.1
427		103	252.4	24.8	0.01
412		69	591.0	45.0	0.002
484	500	434	8.4	29.6	2.0
483		414	14.8	30.8	1.9
429		379	28.2		0.2
476		365			0.2
426		345	54.0	25.1	0.3
484		328			0.02
428		310	27.9		0.05

[a]MCR = minimum creep rate measured in the linear portion of the creep curve.

If one assumes that the mechanisms of dislocation creep in intermetallic alloys do not differ from those in conventional alloys,[16-19] then the creep data can be fitted to a power-law creep equation of the form

$$\dot{\varepsilon} = A\sigma^{n}(e^{-Q/RT}) ,$$

where $\dot{\varepsilon}$ is the minimum creep rate (MCR) , A is a constant, σ is the test stress, n is the creep exponent, Q is the activation energy for creep, T is the temperature in Kelvin (K) and R is

the universal gas constant with a value of 1.987 cal/mol/°C. By rearranging this equation and inserting the data for constant stress or constant temperature tests, the activation energy for creep (Q) and the creep exponent (n) were obtained (see Figs. 1 and 2). The average activation energy was determined to be approximately 150 kcal/mole which indicates a much stronger temperature dependence of the creep rate for this alloy compared to binary Fe-28Al or the ternary alloys containing additions of only Mo or Nb/Zr (~80 kcal/mol).[1,20] The binary alloy has been shown to have very poor creep resistance under the test conditions used in the current study[1] and a heat treatment at 1150°C produced absolutely no improvement,[21] as was expected for a binary alloy with no precipitate formers. A creep exponent of 7-12 was determined from constant-temperature tests at 500 and 675°C, numbers which suggest that

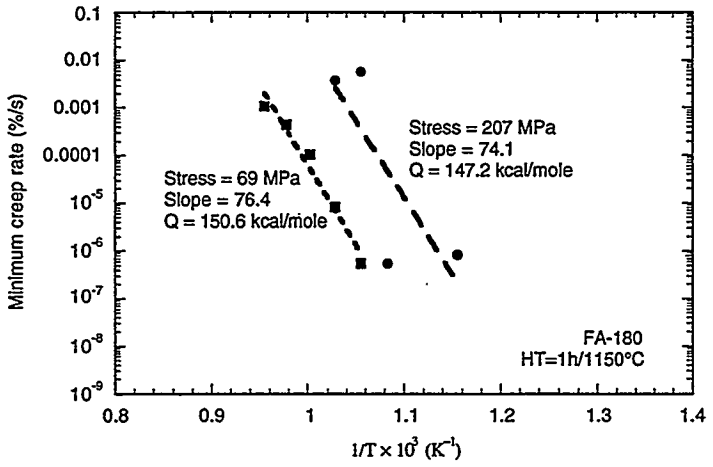

Fig. 1. Minimum creep rate versus temperature for FA-180. The slope represents the activation energy for creep.

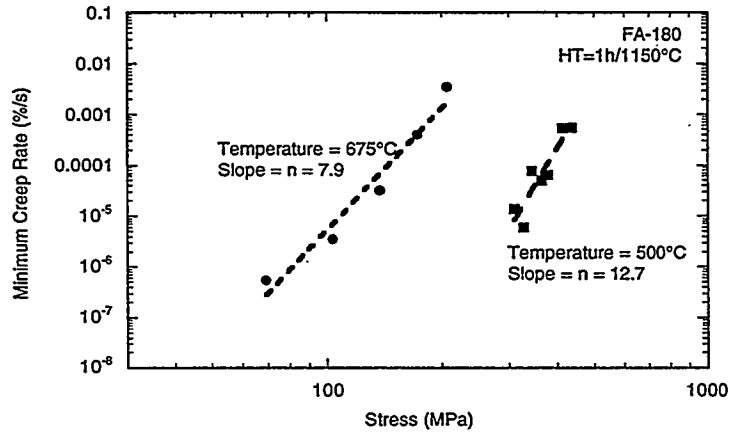

Fig. 2. Minimum creep rate versus stress for FA-180. The slope equals the creep exponent n.

the increased creep strength with the 1150°C heat treatment probably involves particle strengthening.[16-18] This was substantiated by the analytical electron microscopy (AEM) results reported earlier.[12,13] In this study, no dependence of the creep exponent on the test stress, as was reported earlier for binary and ternary alloys,[1] was observed.

Creep-Rupture of Various Fe_3Al Compositions Heat Treated at 1150°C

In order to gain an understanding of the relationship between composition and the improvement in creep-rupture life with a 1-h heat treatment at 1150°C, several alloys containing various amounts and combinations of Cr, Nb, Mo, Zr, B, and C were included in this study. Some of those compositions and the results of creep tests conducted at 593°C with a stress of 207 MPa are listed in Table III. The general conclusion from these results is that, while the addition of Nb, Zr, or Mo, alone or in combination with Cr, B, or C, do not provide significant strengthening, the proper combination of Nb, Zr, and Mo does result in creep-rupture lives of over 2000 h. Figures 3 and 4 show that the best creep properties were attained in alloys containing at least 0.5 at. % Nb and 0.8 at.% Mo, with a small amount of zirconium. The particular level of zirconium needed is difficult to ascertain from these results, but appears to be low (on the order of 0.1 at.% or less). Other studies have shown that approximately 0.1% Zr will be required to promote scale adhesion for protection against corrosion in harsh environments.[4] But the more zirconium added, the more embrittle will be the alloy.[14] Therefore, the level of zirconium will have to be carefully controlled. Indications are that the zirconium interacts with molybdenum to produce its contribution to the strengthening. These results support previous analytical electron microscopy results which indicated that Zr, Mo, and Nb-based precipitates, formed during cooling from 1150°C, are the strengthening agents in these alloys.[12,13,21] These are also the same additives which were shown to produce some improvement in creep life after a heat treatment at 750°C.[9,14]

The results shown in Table III for alloys FA-92, FA-88, FA-128, and FA-129 indicate that the presence of large amounts of carbon should be avoided if creep resistance is important for the intended application. The effect of boron on creep strength is less obvious, but suggestions are that large amounts of boron (on the order of 0.2 at.%; see results for FA-122 versus FA-126 in Table III) can result in reduced creep life. The amount of reduction may actually depend on which other elements are present.

CONCLUSIONS

In an earlier study, the creep-rupture strength of Fe_3Al-based alloy FA-180 (Fe-28Al-5Cr-0.5Nb-0.8Mo-0.025Zr-0.05C-0.005B, at.%) was shown to be improved significantly by heat treating for 1 h at 1150°C. This strengthening was attributed to the formation of fine

Table III. Creep-rupture test results versus composition after heat treatment for 1 h at 1150°C (all tests were conducted at 593°C and 207 MPa)

Alloy	Composition (at.%)	Life (h)	Elongation (%)	MCR (%/h)
FA-61C	Fe-28Al	0.2	6	45
FA-124	-5Cr-.05B	3	24	4.2
FA-128B	-5Cr-.5Nb-.05B	35	47	0.6
FA-129	-5Cr-.5Nb-.2C	8	45	1.2
FA-122B	-5Cr-.1Zr-.05B	149	17	0.0045
FA-126	-5Cr-.1Zr-.2B	4	54	5.8
FA-62B	-2Mo	91	19	0.1
FA-73	-2Mo-.05B	19	25	0.5
FA-74	-2Mo-.1B	24	16	0.4
FA-75	-2Mo-.2B	77	26	0.1
FA-114	-2Mo-.05Zr-.05B	2541	9.5	0.0005
FA-92	-2Mo-.1Zr-.2B	1022	25	0.0015
FA-88	-2Mo-.1Zr-.2C	194	52	0.05
FA-166	-5Cr-1Mo-.5Nb-.02Zr	696	12	0.002
FA-130	-5Cr-.5Mo-.5Nb-.1Zr-.05B	2203	16	0.0009
FA-133L	-5Cr-.5Mo-.5Nb-.1Zr-.2B	1534	28	0.002
FA-169	-5Cr-.25Mo-.5Nb-.025Zr-.05C	34	49	0.6
FA-174	-5Cr-.4Mo-.2Nb-.025Zr-.05C	8	28	1.8
FA-175	-5Cr-.4Mo-.025Zr-.05C	15	27	1.3
FA-178	-5Cr-.4Mo-.025Zr-.05C-.005B	17	34	0.9
FA-176	-5Cr-.4Mo-.025Zr-.5Nb-.05C-.005B	56	26	0.1
FA-170	-5Cr-.4Mo-.025Zr-.5Nb-.05C	51	41	0.5
FA-177	-5Cr-.4Mo-.025Zr-.2Nb-.05C-.005B	21	41	1.0
FA-179	-5Cr-.6Mo-.025Zr-.5Nb-.05C-.005B	48	31	0.3
FA-180	-5Cr-.8Mo-.025Zr-.5Nb-.05C-.005B	1924	11	0.0006
FA-183	-5Cr-.8Mo-.025Zr-.3Nb-.05C-.005B	2	22	5.9
FA-184	-5Cr-.8Mo-.025Zr-.1Nb-.05C-.005B	24	30	0.7

matrix and grain boundary precipitates. In this study, the activation energy for creep in alloy FA-180 was determined to be approximately 150 kcal/mole which is twice that determined earlier for binary Fe_3Al. Creep exponents of 7-12 were determined, consistent with a precipitation-strengthening mechanism.

Creep-rupture tests of many alloys containing different compositions of Mo, Zr, Nb, Cr, B, and C support the earlier results of analytical electron microscopy that indicated that the strengthening in these alloys is produced by the presence of fine Zr(Nb,Mo)-based precipitates. The role of boron is still unclear, but the presence of carbon in amounts of 0.1 at.% or more was found to decrease creep strength significantly.

ACKNOWLEDGEMENTS

This research was sponsored by the U.S. Department of Energy, Office of Fossil Energy, Advanced Research and Technology Development Materials Program and by the

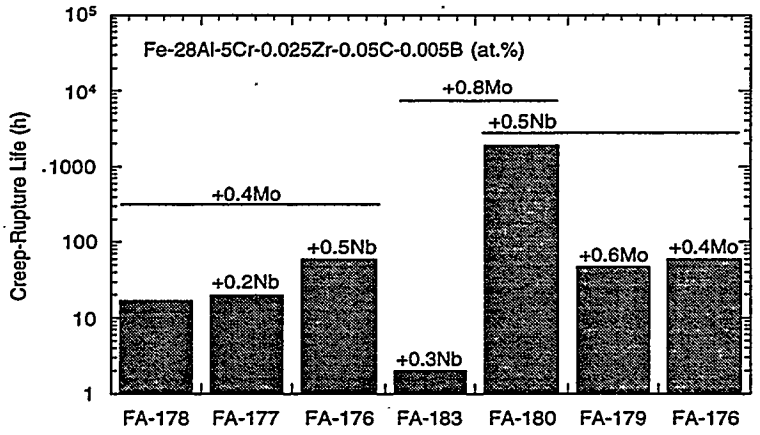

Fig. 3. Effect of addition of niobium and molybenum on creep-rupture life of a Fe_3Al-based alloy tested at 593°C and 207 MPa.

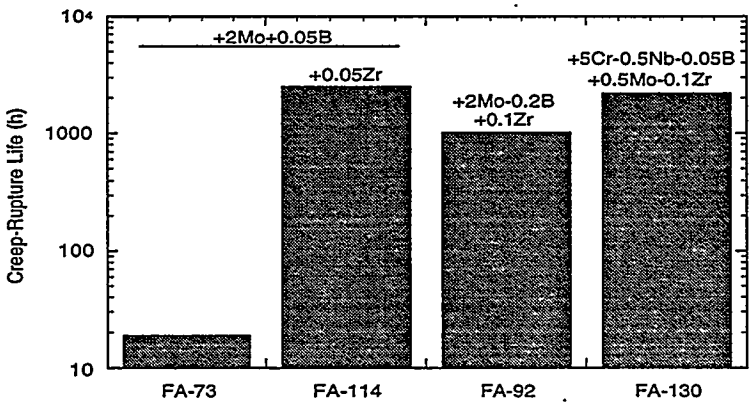

Fig. 4. Effect of addition of zirconium on creep-rupture life of molybdenum-containing Fe_3Al alloys tested at 593°C and 207 MPa.

Assistant Secretary for Energy Efficiency and Renewable Energy, Office for Industrial Technologies, Advanced Industrial Materials Program, under contract DE-AC05-84OR21400 with Martin Marietta Energy Systems, Inc., and by the American Chemical Society's Project SEED (Summer Educational Experience for the Disadvantaged) program at the Oak Ridge National Laboratory managed by the Martin Marietta Energy Systems, Inc.

REFERENCES

1. C. G. McKamey, P. J. Maziasz, and J. W. Jones, J. Mater. Res. 7(8), 2089 (1992).
2. C. T. Liu, C. G. McKamey, and E. H. Lee, Scripta Metall. Mater. 24(2), 385 (1990).
3. C. T. Liu and C. G. McKamey, in High Temperature Aluminides and Intermetallics, edited by S. H. Whang, C. T. Liu, D. P. Pope, and J. 0. Stiegler, The Metallurgical Society, Warrendale, PA: 1990, pp. 133-151.
4. P. F. Tortorelli and J. H. DeVan, in Processing, Properties, and Applications of Iron Aluminides, edited by J. H. Schneibel and M. A. Crimp, TMS, Warrendale, PA, 1994, pp. 257-70.
5. C. G. McKamey and C. T. Liu, in Proceedings of ADVMAT/91, First International Symposium on Environmental Effects on Advanced Materials, edited by R. D. Kane, NACE, Houston, TX, 1992, paper no. 17-1.
6. V. K. Sikka, SAMPE Quart. **22**(4), 2 (1991).
7. V. K. Sikka, S. Viswanathan, and C. G. McKamey, Structural Intermetallics, edited by R. Darolia, J. J. Lewandowski, C. T. Liu, P. L. Martin, D. B. Miracle, and M. V. Nathal, The Metallurgical Society, Warrendale, PA, 1993, pp. 483-91.
8. C. G. McKamey, J. H. DeVan, P. F. Tortorelli, and V. K. Sikka, J. Mater. Res. **6**(8), 1779 (1991).
9. P. J. Maziasz and C. G. McKamey, Mater. Sci. & Eng., **A152**, 322 (1992).
10. D. M. Dimiduk, et al., Acta Metall. **36**, 2947 (1988).
11. D. G. Morris, M. Nazmy, and C. Noseda, Scripta Metall. Mater. **31**, 173 (1994).
12. C. G. McKamey and P. J. Maziasz, in Processing, Properties, and Applications of Iron Aluminides, edited by J. H. Schneibel and M. A. Crimp, TMS, Warrendale, PA, 1994, pp. 147-58.
13. C. G. McKamey and P. J. Maziasz, Proceedings of Eighth Annual Conference on Fossil Energy Materials, ORNL/FMP-94/1, Oak Ridge National Laboratory, Oak Ridge, TN, August 1994, pp. 169-83.
14. C. G. McKamey, P. J. Maziasz, G. M. Goodwin, and T. Zacharia, Mater. Sci. & Eng. **A174**, 59 (1994).
15. C. G. McKamey, Y. Marrero-Santos, and P. J. Maziasz, in High Temperature Ordered Intermetallic Alloys VI, edited by J. A. Horton, I. Baker, S. Hanada, R. D. Noebe, and D. S. Schwartz, Mater. Res. Soc. Symp. Proc. **364**, Pittsburgh, PA, 1995, pp. 249-54.
16. F. Garofalo, Fundamentals of Creep and Creep-Rupture in Metals, The Macmillan Co., New York, 1965.
17. O. D. Sherby and P. M. Burke, Prog. Mater. Sci. **13**, 325 (1967).
18. N. S. Stoloff and R. G. Davies, Prog. Mater. Sci. **13**, 1 (1966).
19. I. Jung, M. Rudy, and G. Sauthoff, in High Temperature Ordered Intermetallic Alloys II, edited by N. S. Stoloff, C. C. Koch, C. T. Liu, and O. Izumi, Mater. Res. Soc. Symp. Proc. **81**, Pittsburgh, PA, 1987, pp. 263-274.
20. A. Lawley, J. A. Coll, and R. W. Cahn, TMS AIME **218**, 166 (1960).
21. C. G. McKamey, unpublished results, 1994.

ENVIRONMENTAL EMBRITTLEMENT OF IRON ALUMINIDES UNDER CYCLIC LOADING CONDITIONS

A. Castagna, D. A. Alven and N. S. Stoloff

Rensselaer Polytechnic Institute
Troy, NY 12180-3590

ABSTRACT

The tensile and fatigue crack growth behavior in air in hydrogen and in oxygen of an Fe-Al-Cr-Zr alloy is described. The results are compared to data for FA-129. A detailed analysis of frequency effects on fatigue crack growth rates of FA-129, tested in the B2 condition, shows that dislocation transport of hydrogen from the surface is the rate limiting step in fatigue crack growth.

INTRODUCTION

Iron aluminides are currently being studied for use in applications where low cost, relatively low weight, moderate strength at temperatures up to 500°C, and excellent corrosion resistance are desired. Binary iron aluminides do not possess high ductility at room temperature in air; however, iron aluminides have demonstrated ductility of 12%-16% when tested in vacuum or gaseous oxygen environments.[1-4] This indicates that Fe_3Al is an inherently ductile material and an environmental interaction causes the low ductility in air.

The purpose of this research was to examine the effects of environment on the mechanical properties of two Fe_3Al base intermetallics. In particular, fatigue crack growth resistance and tensile behavior were examined in various environments, and the resulting data used to gain insight into the role of hydrogen in embrittlement of the iron-aluminum alloys.

EXPERIMENTAL PROCEDURE

Alloy Composition and Heat Treatment

Two alloys were examined in this study, an Fe-28%Al alloy designated FA-129, and an Fe-Al-Cr-Zr-C alloy, see Table 1. The alloys can exist in the B2 or DO_3 ordered state, depending on the temperature from which each is quenched. Both alloys were fabricated at the Oak Ridge National Laboratory (ORNL) by vacuum induction melting, extrusion to a 2.54 cm thickness, and either hot or warm rolling to the final thickness of near 5mm.

The annealing parameters for both alloys consisted of a 700°C anneal for 1 hour with a mineral oil quench, which was then repeated. This resulted in a partially ordered B2 type superlattice.

Tensile tests on Fa-129 have previously been described (3,4). The strain rate for tensile tests on Fe-Al-Cr-Zr reported here was 3×10^{-4} s^{-1}. All specimens were cyclindrical; some were notched (1.0mm deep, 0.689mm radius). The stress concentration factor was 3.9. Tests were conducted in air, 1 atm O_2 and 1 atm H_2 gas.

TABLE 1

Compositions of Iron Aluminides

	a%						
	Fe	Al	Cr	Mo	Nb	Zr	C
FA-129	66.2	28.1	5.0	--	0.5	--	0.2
Fe-Al-Cr-Zr-C	bal	28	5.0	--	--	0.5	0.05

Compact tension specimens were used in all fatigue tests and were cut such that the crack propagation direction would be perpendicular to the rolling direction. The Zr-containing alloy was 34.9mm x 33.5mm x 4.3mm thick, while FA-129 specimens were 25mm x 24mm x 5.1mm thick. Crack length was monitored via the d.c. potential drop method. Calibration curves were created relating crack length to potential drop by optically measuring the crack length with a calibrated traveling microscope. Tests were conducted in the three environments used for tensile experiments. The R-ratio was 0.5 and the frequency was 20Hz unless otherwise noted.

EXPERIMENTAL RESULTS

Tensile Experiments

Tensile stress strain curves for the Fe-Al-Cr-Zr alloy are shown in Fig. 1 and data from these tests are summarized in Table 2. Note that elongations and % reduction in area are similar in air and in oxygen, but are much reduced in 1 atom H_2 gas. Notch sensitivity ratios of 0.74 were noted in both air and oxygen, but could not be measured in H_2 gas.

Fatigue Crack Growth Experiments

Fatigue crack growth behavior of the Fe-Al-Cr-Zr alloy is summarized in Fig. 2 and Table 3. Note that oxygen again provides the lowest crack growth rates. However, in all environments, the slope m in the Paris crack growth equation:

$$\left(\frac{da}{dN}\right)=C\Delta K^m \qquad \text{Eq. (1)}$$

is much lower than for FA-129, and thresholds are higher.(3,4) A comparison of the behavior of Fa-129, and the disordered alloy FAP-Y Fe-Al-Zr-C is shown in Fig. 3.

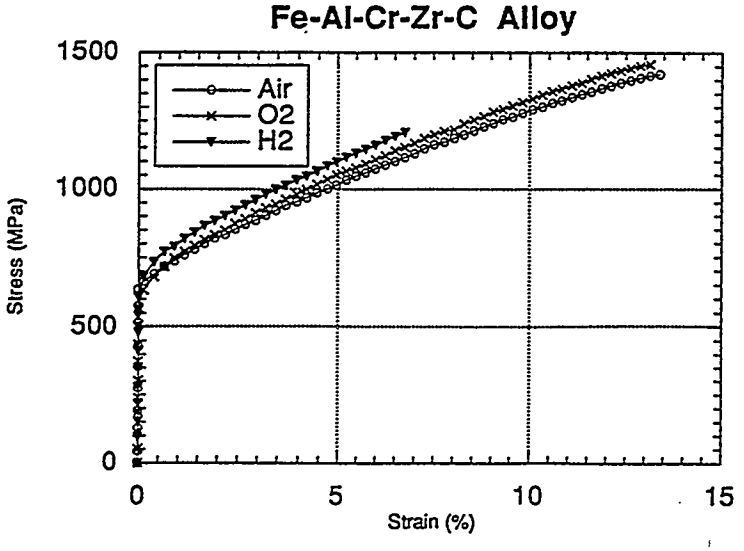

Fig. 1 Stress Strain Curves for Fe-Al-Cr-Zr, 25°C.

TABLE 2

Summary of Tensile Data for Fe-Al-Cr-Zr-C

	Ductility	RA	YS	UTS	UTS w/notch	NSR
	%	%	MPa	MPa	MPa	
Air	13.8	11.6	686	1460	1076	0.74
H_2	6.1	6.3	678	1197	-	-
O_2*	13.1	13.0	682	1456	1081	0.74

*Average of two tests

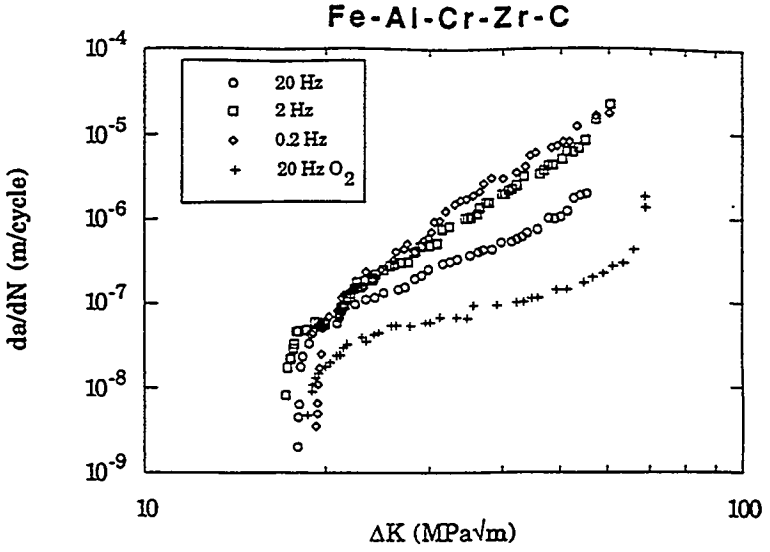

Fig.2 Effects of Environment on Fatigue Crack Growth Behavior of Fe-Al-Cr-Zr

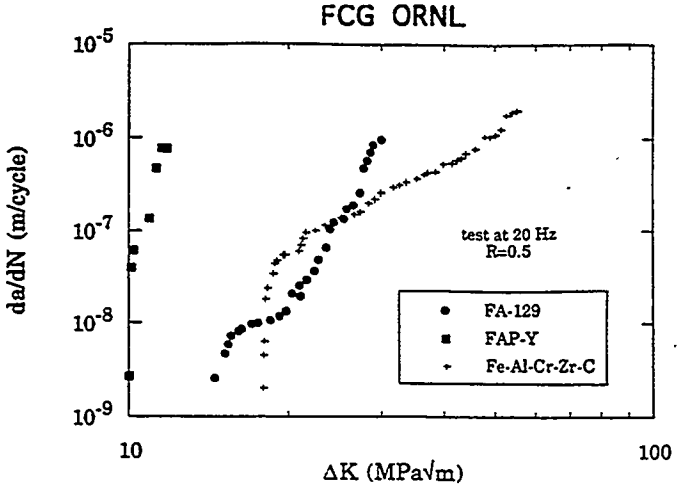

Fig. 3 Crack Growth Rates of Three Fe-Al Alloys

TABLE 3

Results of Fe-Al-Cr-Zr-C Crack Growth Experiments

Test	m	ΔK_{th} (MPa$\sqrt{m}$)	ΔK_c(MPa$\sqrt{m}$)
20 Hz in Air	3.0	18.0	55.0
2 Hz in Air	4.4	17.0	60.3
0.2 Hz in Air	5.6	19.2	64.3
20 Hz in O_2	2.5	18.6	68.7

Effect of Frequency on Fatigue Crack Growth of Fa-129

The da/dN vs. ΔK curves for B2 ordered FA-129 fatigued at frequencies of 20Hz, 2Hz, 0.2Hz, and 0.08Hz in air at 25°C are shown in Fig. 4. Also shown are data for the test at 20Hz in oxygen, which is considered to be inert. The effect of frequency on the FCG resistance was not examined in the oxygen environment. However, little or no effect is expected as oxygen has been shown to yield at least as high ductilities as a high-vacuum environment. As seen in Fig. 4, lower frequencies enhance crack growth rates at higher stress intensities. Frequency has a pronounced influence on the measured critical stress intensity. The highest K_C, 60MPa$\sqrt{m}$, is seen at the highest frequency of 20Hz. K_C steadily drops as frequency is decreased, to K_C = 50.4 MPa$\sqrt{m}$ at a frequency of 0.08Hz.

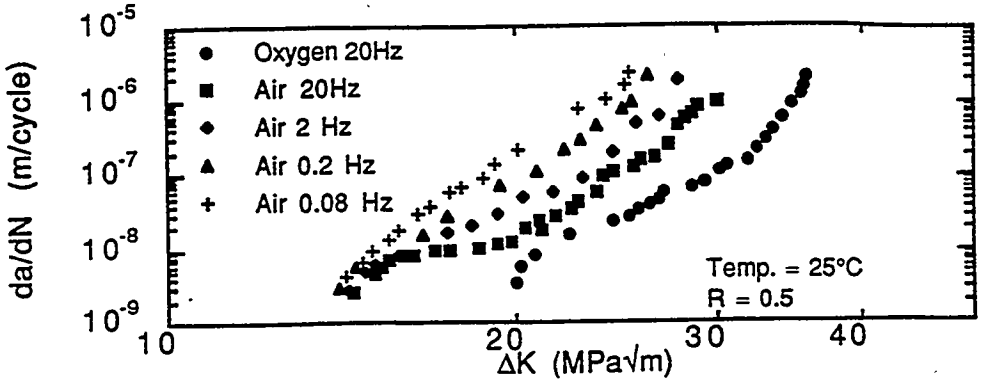

Fig. 4 Effect of Frequency on B2 Ordered FA-129 Fatigued in Air

Frequency has almost no effect on threshold stress intensity. In all tests in air ΔK_{TH} was measured between 14 and 14.5 MPa$\sqrt{m}$. The curves appear to diverge when the stress intensity range reaches about 15 MPa$\sqrt{m}$ and the growth rate reaches 5 x 10^{-9}-1 x 10^{-8} m/cycle.

Fractography

The fracture surface of B2 ordered FA-129 fatigued in hydrogen gas shows mostly cleavage facets, together with some fatigue striations.

Decreasing the test frequency of B2 ordered FA-129 tested in air made cleavage faceting more pronounced and introduced a small amount of intergranular fracture. The fracture surface at 2.0Hz showed mostly a transgranular tearing fracture mode, similar to that seen in air at 20Hz. At 0.2Hz, the fracture surface showed cleavage facets with well defined river patterns, as well as some intergranular facets. At 0.08Hz, the fracture surface displayed an even greater degree of transgranular cleavage faceting, and occasional intergranular facets.

DISCUSSION

Tensile and Fatigue Behavior of Fe-Al-Cr-Zr

The Fe-Al-Cr-Zr alloy behaves similarly to FAP-Y in that ductility is the same in air and oxygen, but is reduced in hydrogen gas(3,7). These results suggest that the small amount of Zr in this alloy inhibits moisture-induced embrittlement. In fatigue, however, oxygen clearly provides superior crack growth resistance.

Another characteristic of the Fe-Al-Cr-Zr alloy is the observation of higher threshold and critical values of stress intensity than in FA-129. This factor, combined with the low Paris exponent, shows that the crack growth resistance of the Zr-containing alloy is very high.

Frequency Dependence of Crack Growth in FA-129

The frequency effect on crack growth rate for B2 ordered FA-129 (see Fig. 4) has been analyzed following a model of McEvily and Wei (5). The crack growth rate can be expressed as a superposition of mechanical fatigue, $(da/dN)_r$, and a corrosion-fatigue interaction term $(da/dN)_{cf}$, as shown in Eq. 2.

$$\left(\frac{da}{dN}\right)=\left(\frac{da}{dN}\right)_r+\left(\frac{da}{dN}\right)_{cf} \qquad \text{Eq. (2)}$$

If the corrosion-fatigue crack growth rate $(da/dN)_{cf}$ truly reflects a synergistic combination of applied stress intensity and exposure to an embrittling environment, then this term should incorporate both a stress intensity term and some measure of the exposure to hydrogen. In the case of bulk-transport limited embrittlement the environmental term may involve the penetration depth of hydrogen ahead of the crack tip, r. Corrosion fatigue exhibiting this dependence may then be expressed by Eq. 3.

$$\left(\frac{da}{dN}\right)_{cf}=A\Delta K^m r^n \qquad \text{Eq. (3)}$$

Dislocation-assisted transport has been observed in a number of materials and is responsible for penetration of hydrogen much further than would be expected from bulk diffusion (6-9). A hydrogen atmosphere develops about a dislocation generated near the crack tip and as the dislocation travels away from the tip, it drags the hydrogen with it. The penetration distance of hydrogen ahead of the crack tip is equal to the dislocation velocity times the time available per cycle, or V/2f. One model, proposed by Tien and Richards(6), predicts the maximum possible dislocation velocity that can be achieved before the hydrogen atmosphere is stripped from the dislocation. This velocity can be used to determine the maximum penetration distance that can be accounted for by dislocation assisted transport. Tien and Richards expressed the maximum penetration, r_{max}, as

$$r_{max}=V_{max}t=\frac{D}{kT}\frac{E}{30b}\frac{1}{2f} \qquad \text{Eq. (4)}$$

where E is the binding energy of hydrogen to the dislocation and is approximately 0.3eV (10), k is the Boltzmann constant, t is time, and b is the Burgers vector (3Å for B2 ordered FA-129). The maximum penetration depth due to dislocation transport calculated from Eq. 4 for B2 ordered Fa-129 is tabulated in Table 4 for frequencies from 20 to 0.08 Hz. The

values of r_{max} in Table 4 are several orders of magnitude larger than calculated penetration depths due to bulk diffusion, and range from 129Å to 3μm.

Eq. 3 can be rearranged to yield the following:

$$Log\left(\frac{da}{dN}\right)_{cf} = Log(A) + m\ Log(\Delta K) + n\ Log(r) \qquad \text{Eq. (5)}$$

If Eq. 3 is an accurate representation of $(da/dN)_{cf}$, then a plot of Eq. 5 at a constant ΔK should yield a straight line with the intercept given by Log(A)+m Log(ΔK) and a slope of n. These plots for ΔK=21, 23, 25, and 27 MPa$\sqrt{m}$ are shown in Fig. 5. The correlation is excellent, and from a least squares curve fit the exponent n of Eq. 5 is found to be 0.52.

TABLE 4

Penetration Depth of Hydrogen Due to Dislocation Transport in B2 Ordered FA-129 at Room Temperature

Frequency (Hz)	20	2	0.2	0.08
r_{max}(m)	1.29×10^{-8}	1.29×10^{-7}	1.29×10^{-6}	3.24×10^{-6}

In order to find the values of A and m, Eq. 5 is rearranged into the following form:

$$Log\left[\frac{\left(\frac{da}{dN}\right)_{cf}}{r_{max}^{0.52}}\right] = Log(A) + m\ Log(\Delta K) \quad (6) \qquad \text{Eq. (6)}$$

Eq. 6 is plotted for all values of ΔK and frequencies in Fig. 6. The validity of Eq. 6 is clear as the $(da/dN)_{cf}$ vs. ΔK curves at various frequencies can be collapsed onto a single frequency-modified curve. A least-squares fit of the data in Fig. 6 shows that A=3.78×10^{-18} and m=10.31.

The excellent correlation of the fatigue data to Eqs. 3, 5 and 6 indicates that in B2 ordered FA-129 fatigued at room temperature, hydrogen

moves into the lattice ahead of the crack tip by a dislocation-assisted transport mechanism.

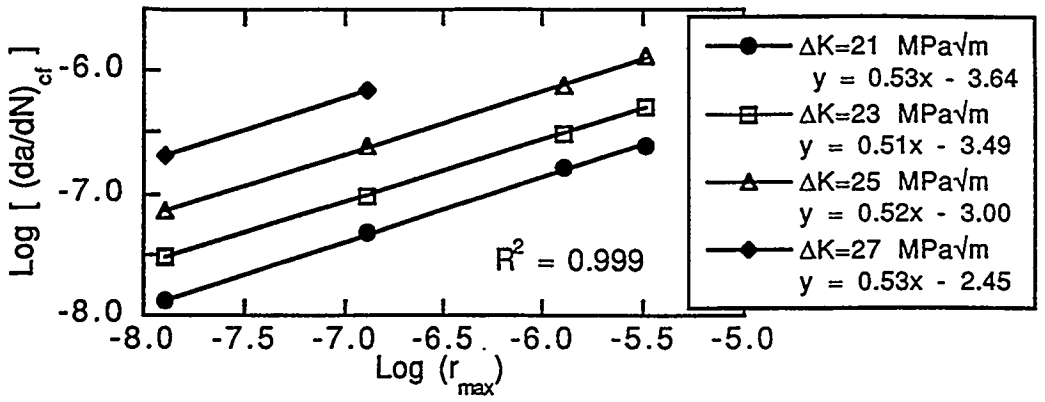

Fig. 5 Log-Log Plot of $(da/dN)_{cf}$ vs. Hydrogen Penetration Depth Due to Dislocation Transport in B2 Ordered Fa-129 Fatigued in Air at 25°C.

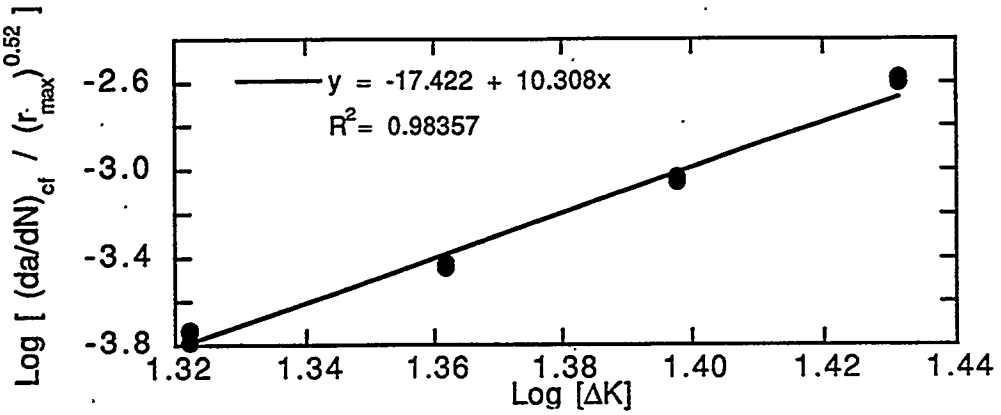

Fig. 6 Plot of Ratio of $(da/dN)_{cf}$ to Hydrogen Penetration Depth Due to Dislocation Transport vs. Applied Stress Intensity in B2 Ordered FA-129 Fatigued in Air at 25°C.

The physical meaning of the exponent n in Eq. 3 must be related to the quantity of hydrogen that dislocations carry into the plastic zone. For example, it is likely that the exponent n will scale with the quantity of hydrogen each dislocation is capable of dragging with it, or the density of dislocations capable of dragging hydrogen atoms, or both. It is, therefore, significant that the exponent n was found to be a constant with respect to frequency. Even though the degree of embrittlement increased dramatically with frequency, the exponent n was unchanged, signifying that embrittlement does little to change the mobility, ease of dislocation

generation, or hydrogen carrying capability of dislocations. Therefore, hydrogen enhanced plasticity or inhibited dislocation motion in the presence of hydrogen can be ruled out in B2 ordered FA-129.

CONCLUSIONS

The Zr-containing Fe_3Al alloy shows better resistance to fatigue crack growth than does FA-129. The crack growth rate of B2 ordered FA-129 can be expressed as a superposition of purely mechanical fatigue and a corrosion-fatigue interaction term (5). There is a significant rate effect in the corrosion-fatigue contribution to crack growth of iron-aluminides. Dislocation-assisted diffusion is responsible for transport of hydrogen atoms into the bulk of the material for B2 ordered FA-129, and this process is the rate limiting step in hydrogen embrittlement during crack growth.

ACKNOWLEDGEMENTS

The authors are grateful to the DOE Fossil Energy Program for providing financial support under Martin Marietta Energy Systems Subcontract Number 19X-SF521C. The authors also are grateful for helpful discussions with Dr. V. K. Sikka of ORNL and to Dr. Sikka for providing test alloys.

REFERENCES

1. C.T. Liu, H.E. Lee and C.G. McKamey, Scripta Met. 23, 1989, p. 875.

2. C. G. McKamey, J. H. DeVan, P. F. Tortorelli and V. K. Sikka, J. Mat. Res. 6, 1991, p. 1779.

3. A. Castagna, Ph.D. Thesis, Rensselaer Polytechnic Inst., 1994.

4. A. Castagna and N. S. Stoloff, Mater. and Design 14, 1993, p. 73.

5. A. J. McEvily and R. P. Wei, in Corrosion-Fatigue: Chemistry, Mechanics and Microstructure, O. F. Devereux, A. J. McEvily, R. W. Staehle, Eds., (NACE, Houston, 1972), NACE-2, p. 381.

6. J. K. Tien and R. J. Richards, Scripta Metall. 9, 1975, p. 1097.

7. A. Castagna and N. S. Stoloff, Mat. Sci. & Eng. A192/193, 1995 p. 399.

THE EFFECT OF GRAIN REFINEMENT ON THE ROOM-TEMPERATURE DUCTILITY OF AS-CAST Fe_3Al-BASED ALLOYS

S. Viswanathan, V. K. Andleigh, and C. G. McKamey

Oak Ridge National Laboratory
P.O. Box 2008
Oak Ridge, TN 37831-6083

ABSTRACT

Fe_3Al-based alloys exhibit poor room-temperature ductility in the as-cast condition. In this study, the effect of grain refinement of the as-cast alloy on room-temperature ductility was investigated. Small melts of Fe-28 at. % Al-5 at. % Cr were inoculated with various alloying additions and cast into a 50- × 30- × 30-mm graphite mold. The resulting ingots were examined metallographically for evidence of grain refinement, and three-point bend tests were conducted on samples to assess the effect on room-temperature ductility. Ductility was assumed to correlate with the strain corresponding to the maximum stress obtained in the bend test. The results showed that titanium was extremely effective in grain refinement, although it severely embrittled the alloy in contents exceeding 1%. Boron additions strengthened the alloy significantly, while carbon additions reduced both the strength and ductility. The best ductility was found in an alloy containing titanium, boron, and carbon. In order to verify the results of the grain refinement study, vacuum-induction melts of selected compositions were prepared and cast into a larger 25- × 150- × 100-mm graphite mold. Tensile specimens were machined from the ingots, and specimens were tested at room temperature. The results of the tensile tests agreed with the results of the grain refinement study; in addition, the addition of molybdenum was found to significantly increase room-temperature tensile ductility over that of the base alloy.

INTRODUCTION

The primary reason for the poor room-temperature ductility of Fe_3Al-based alloys is generally accepted to be environmental embrittlement due to hydrogen produced by the reaction of aluminum with water vapor present in the test atmosphere.[1] In the as-cast condition, another possible reason for the low room-temperature ductility is the large grain size (0.5 to 3 mm) of the cast material.[2] While recent studies on iron aluminides in the wrought condition have led to higher room-temperature ductility and increased high-temperature strength,[1] limited studies have been conducted on iron aluminides in the as-cast condition. The purpose of this study was to induce grain refinement of the as-cast alloy through alloying additions to the melt and study the effect on room-temperature ductility as measured by the strain corresponding to the maximum stress obtained in a three-point bend

test. A base charge of Fe-28% Al-5% Cr alloy was used; as in previous studies, this ternary alloy exhibited the highest tensile ductility of several alloys tested.[2]

DISCUSSION OF CURRENT ACTIVITIES

Grain Refinement Study

As part of a study on wrought alloys, a large number of cast alloy samples with a variety of alloying additions had been produced in the form of 450-g chill-cast ingots.[3] Samples were obtained close to the hot-top sections of these ingots; were polished and then swab-etched using a solution of 25 mL acetic acid, 15 mL nitric acid, 15 mL hydrochloric acid, and 5 mL water; and finally, were examined under an optical microscope. In this preliminary screening, only samples containing titanium and boron showed evidence of grain refinement; samples containing other additions (including Ce, Hf, Mg, Mn, Mo, Nb, Si, V, Y, and Zr) did not show any evidence of grain refinement. Consequently, the effects of titanium and boron were examined in detail in this study.

For the grain refinement study, approximately 10 kg of a base charge material of Fe-28% Al-5% Cr alloy was prepared by melting elemental materials in air in an induction furnace under an argon blanket, and cast into a graphite mold to produce rods of approximately 35 mm diam and 200 mm length. The rods were ground to 28 mm diam and cut to provide cylinders consisting of approximately 300 g of base charge material. These cylinders were subsequently melted in an induction furnace specially constructed for this study, alloyed with a variety of inoculants designed to promote grain refinement, and cast into a preheated graphite mold to produce 30- × 50- × 30-mm ingots. Table 1 indicates nominal compositions for the heats in the grain refinement study. A mold preheat temperature of 400°C was used throughout the study. Although the pouring temperature of the metal was not measured, it is estimated that it was in the range of 1500 to 1600°C since the liquidus temperature of Fe_3Al-based alloys is approximately 1470°C. Also, although an argon blanket was used during melting, an oxide layer formed on the melt surface, and a preheated graphite rod was quickly inserted into the melt prior to pouring to break up the surface oxide layer and allow a smooth pour. Figure 1 illustrates the graphite mold used in the study.

Table 1. Nominal compositions of cast ingots in grain refinement study

Heat No.	Composition (at. %)					
	Fe	Al	Cr	Ti	C	B
GR-07	Balance	28.0	5.0			
GR-09	Balance	28.0	5.0	1.0	0.1	
GR-10	Balance	28.0	5.0	1.0	0.1	0.12
GR-11	Balance	28.0	5.0	2.0		
GR-12	Balance	28.0	5.0	1.0	0.1	0.52
GR-19	Balance	28.0	5.0	1.5		
GR-20	Balance	28.0	5.0			0.12
GR-21	Balance	28.0	5.0			0.52
GR-26	Balance	28.0	5.0			
GR-27	Balance	28.0	5.0	1.0	0.1	0.02
GR-28	Balance	28.0	5.0			0.02
GR-30	Balance	28.0	5.0		0.1	
GR-34	Balance	28.0	5.0	1.0		0.02
GR-36	Balance	28.0	5.0	1.5		0.02

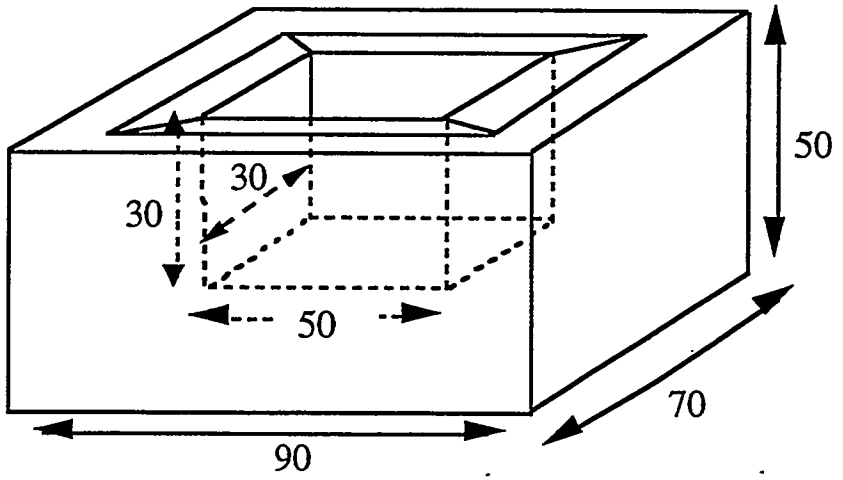

Fig. 1. Graphite mold used in grain refinement study (dimensions in mm).

Ingots were sectioned to obtain metallography and bend test specimens. Metallography specimens were polished, swab-etched, and examined under an optical microscope; ingot compositions were subsequently checked by energy dispersive spectroscopy (EDS). In cases where there was evidence of grain refinement, vertical sections were macroetched to reveal ingot macrostructure. Two bars of 4- × 4-mm cross section and 40 mm length were electrodischarge machined from locations toward the bottom of the ingot. After machining, bar edges were ground lightly on 600-grit silicon carbide paper, and the bars were electropolished in a solution of 7 parts methanol and 1 part sulfuric acid at 7.5 V for about 100 s. Two bend test specimens of 20 mm length were typically obtained from each bar. Specimens were ultrasonically cleaned for 3 min and washed in acetone before testing. A gage length of 10 mm was used in the three-point bend test configuration. The stress and strain were calculated from the equations:

$$\sigma = 3PL/2wt^2 \tag{1}$$

and

$$\varepsilon = 6ty/L^2 \ , \tag{2}$$

where σ = stress, ε = strain, P = load, y = displacement, L = gage length, w = specimen width, and t = specimen thickness.

Results of Grain Refinement Study

Figure 2 illustrates the results of the grain refinement study. As shown in Fig. 2(*a*), the base charge material produced an ingot consisting entirely of columnar grains. The addition of 1% Ti, 0.1% C, and 0.12% B produced some grain refinement in the center of the ingot, although a columnar zone is seen along the edge of the ingot [see Fig. 2(*b*)]. The addition of 0.52% B provided a marginal increase in grain refinement in the center of the ingot [see Fig. 2(*c*)], while the addition of 2% Ti provided extensive grain refinement over the entire ingot [see Fig. 2(*d*)]. Additions of titanium at levels less than 1% did not produce grain refinement, and additions of other alloying elements at levels up to 2% also did not have an effect. It must be noted that because of the high-thermal gradients expected in the solidifying metal due to the use of a small graphite mold, preferentially giving rise to columnar grains, this test provides a very severe test of grain refinement efficacy.

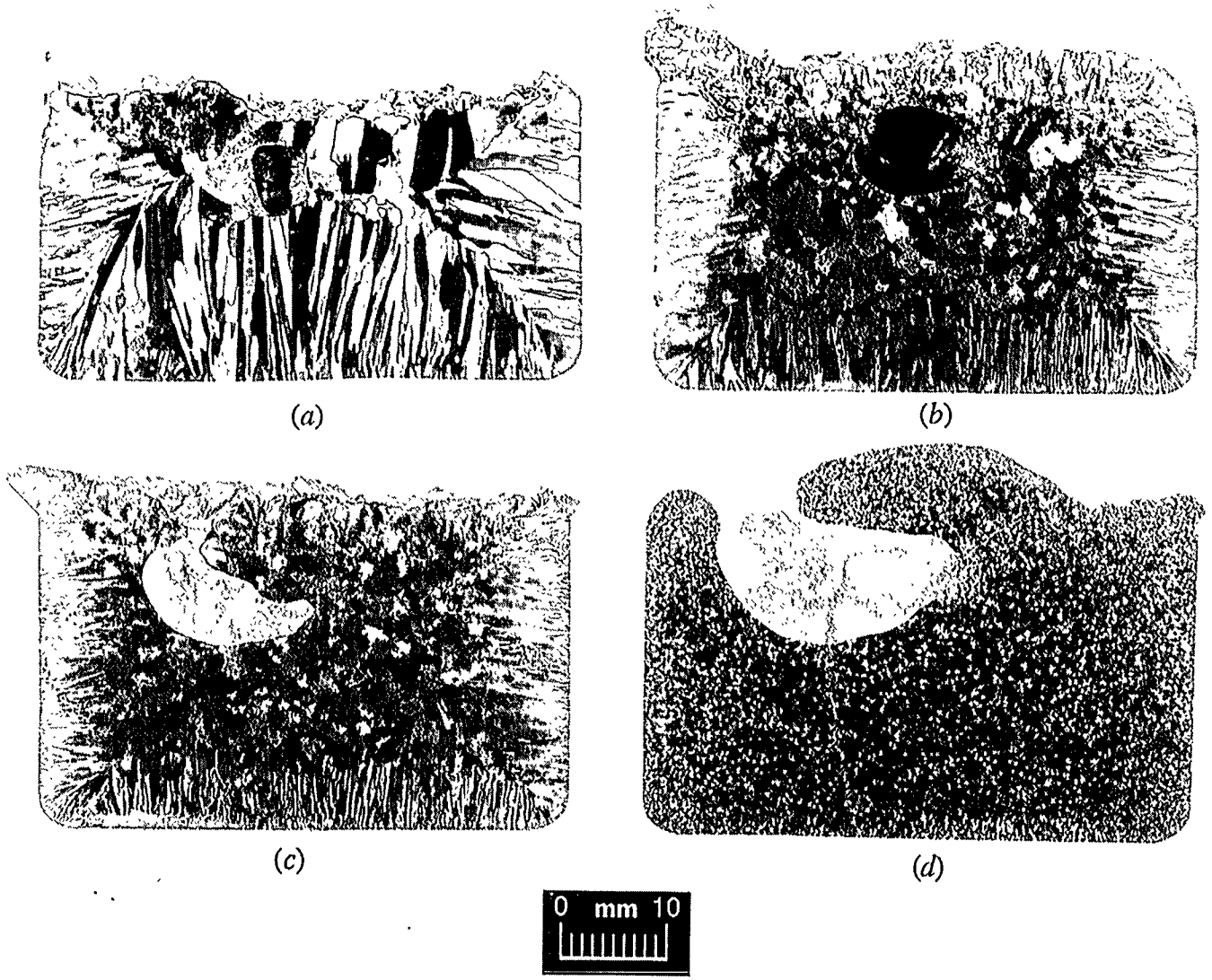

Fig. 2. Photographs of macroetched sections of ingots from grain refinement study: (*a*) base charge, (*b*) 1% Ti-0.12% B-0.1% C, (*c*) 1% Ti-0.51% B-0.1% C, and (*d*) 2% Ti.

Figure 3 shows the results of the three-point bend tests. Figure 3(*a*) shows the maximum stress values obtained, and Fig. 3(*b*) shows the strains corresponding to the maximum stress. For each case, the values obtained may be compared to that obtained for the base charge of Fe-28% Al-5% Cr alloy. The trends obtained for maximum stress and strain are similar and indicate that the addition of titanium or carbon alone serves to embrittle the material, lowering both the stress and strain values obtained. The addition of both titanium and carbon produced the lowest values of stress and strain at failure. The addition of boron improved both the maximum stress and the strain obtained, although ductility was somewhat affected as boron was increased. The effect of boron on the strength of the alloy may also be the reason that boron decreases the weldability of iron-aluminide alloys. Interestingly, the effects of boron and carbon seemed to offset each other with respect to the maximum stress obtained; carbon-containing alloys seemed to require more boron to produce the same strength levels as alloys containing no carbon. Boron also had a strong effect on the maximum strain obtained, inasmuch as the presence of any boron in the alloy provided moderate ductility at least equal to the base charge material, even in the presence of carbon. The maximum ductility was obtained in an alloy containing 1% Ti, 0.1% C, and 0.52% B, although this value was almost identical to that obtained for the alloy containing 0.02% boron alone.

The results of the study clearly establish the grain refinement propensity of titanium and the effect of boron on ductility, although titanium also serves to embrittle the material. In general, the addition of alloying elements other than boron invariably served to decrease both the maximum stress and the maximum strain obtained, indicating that for as-cast Fe_3Al-based alloys, the addition of alloying elements designed to serve as inoculants is likely to have a negative effect on ductility, even when grain refinement is obtained.

Scale-up Study

In order to verify the results of the grain refinement study, a vacuum-induction melt of the 1% Ti, 0.1% C, and 0.52% B alloy that exhibited the maximum ductility in the grain refinement study was prepared and cast into a 25- × 150- × 100-mm graphite mold. Tensile specimens were machined from the ingot, and specimens were tested at room temperature. The results were compared with that for the base ternary alloy obtained previously.[2] In addition, the effect of molybdenum additions to the base ternary alloy was also investigated. Table 2 indicates nominal compositions for the heats in the scale-up study. Figure 4 illustrates the graphite mold used in the scale-up study.

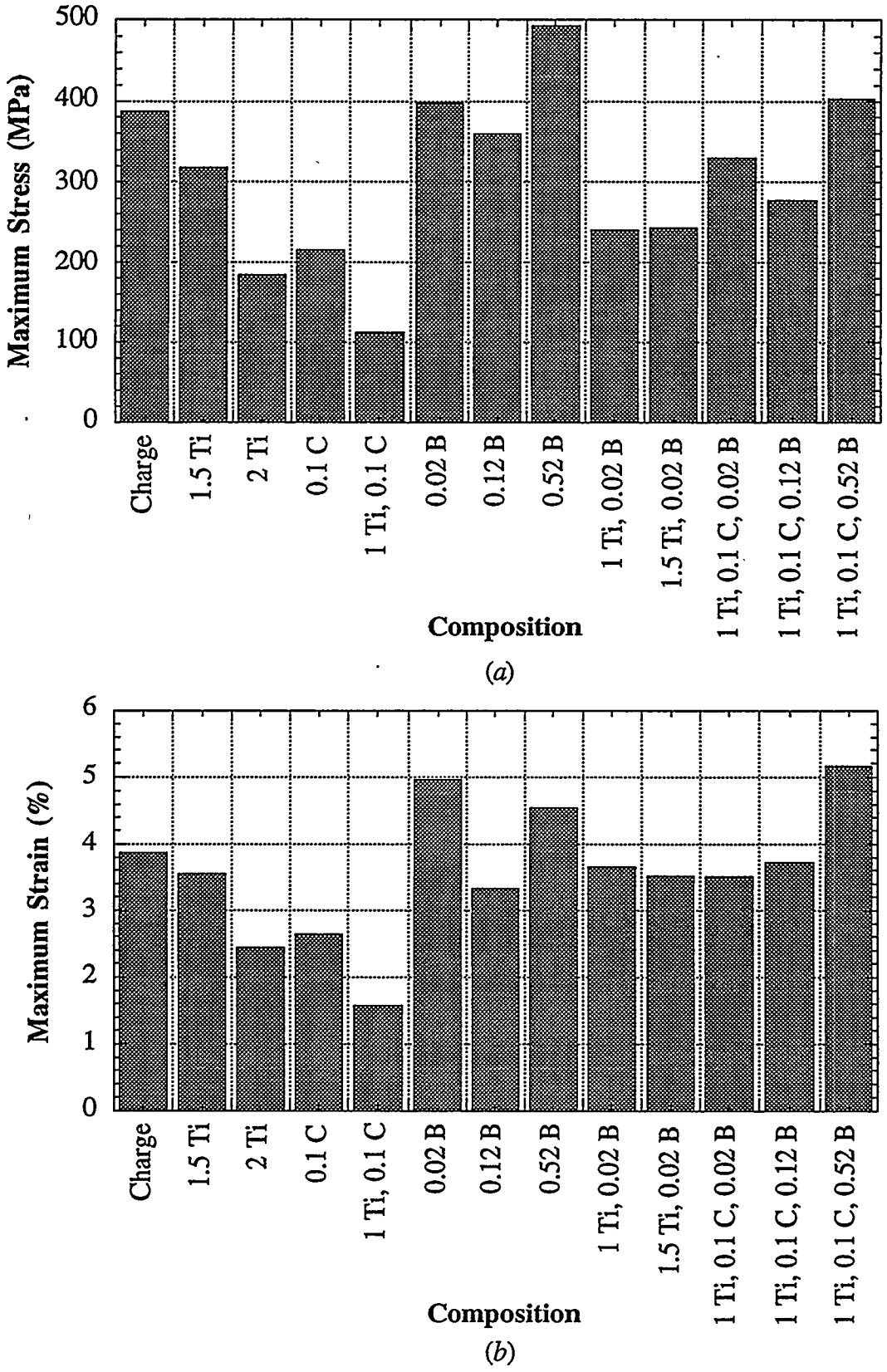

Fig. 3. Results of three-point bend tests: (*a*) maximum stress and (*b*) maximum strain.

Table 2. Nominal compositions of cast ingots in scale-up study

Heat No.	Composition (at. %)						
	Fe	Al	Cr	Mo	Ti	C	B
16097	Balance	28.0	5.0		1.0	0.1	0.52
15897	Balance	28.0	5.0	0.02			
16094	Balance	28.0	5.0	0.05			
16095	Balance	28.0	5.0	0.1			
16096	Balance	28.0	5.0	0.25			

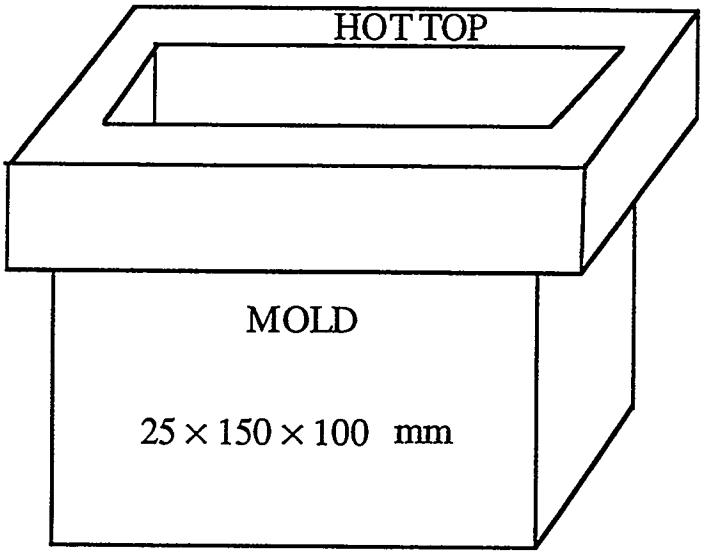

Fig. 4. Graphite mold used in scale-up study (dimensions in mm).

Figure 5 shows the results of room-temperature tensile tests for specimens in the scale-up study. Figure 5(*a*) indicates the effects of alloying on the yield and tensile strength, while Fig. 5(*b*) shows the effect on tensile elongation. Alloying had almost no effect on the yield strength, while tensile strength increased from 250 to 300 MPa. It is likely that yield strength is dominated by the large grain size of the as-cast material and, consequently, is not greatly affected by alloying. The 1%Ti, 0.1% C, and 0.52% B alloy that exhibited the maximum ductility in the grain refinement study did not exhibit increased ductility in the scale-up study. However, equally significant, there was no drop in ductility as might have been expected due to the addition of titanium and carbon. Interestingly, the

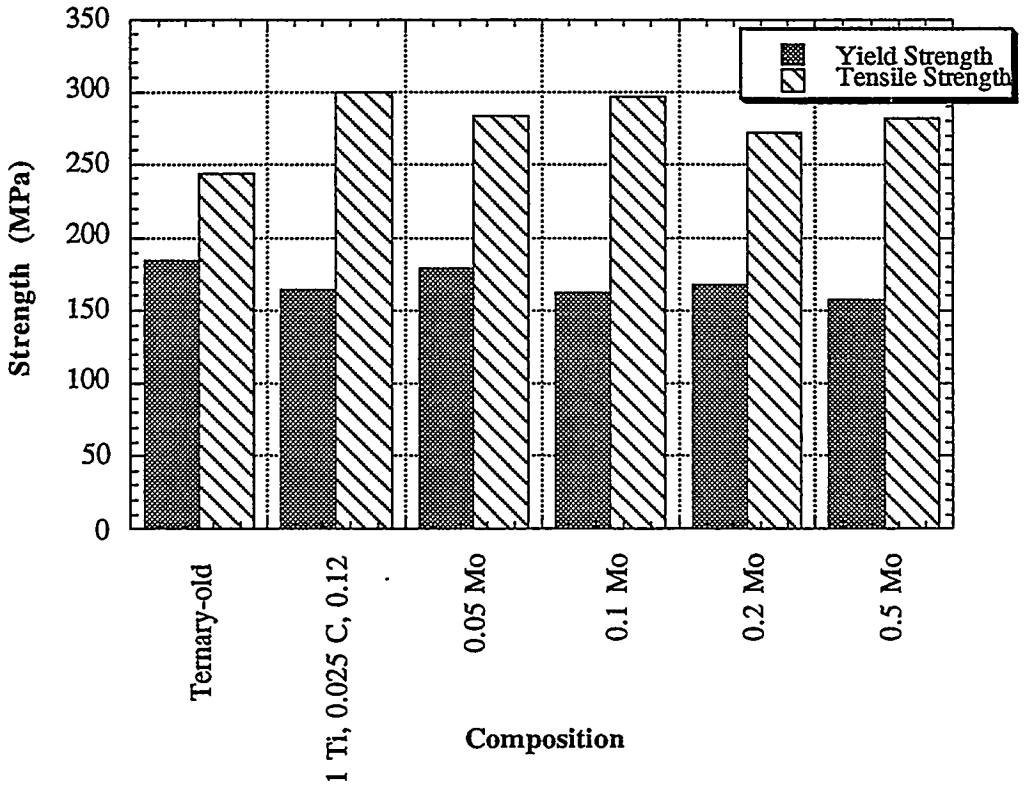

(*a*)

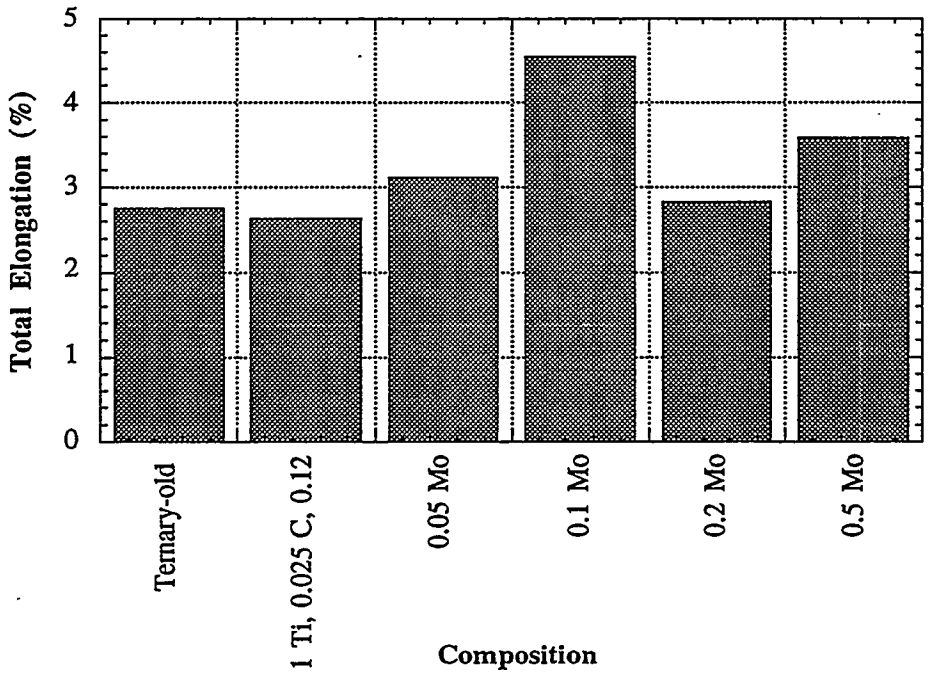

(*b*)

Fig. 5. Results of tensile tests for scale-up study: (*a*) yield strength and ultimate tensile strength and (*b*) total elongation.

addition of molybdenum produced a significant increase in room-temperature ductility over the base alloy, at a level of 0.1%. Additions less than or greater than 0.1% did not seem to change the ductility significantly, although marginal increases may be noted at the 0.05 and 0.5% levels. The reason for the increase in room-temperature ductility on the addition of molybdenum is under investigation, although there is some indication that the molybdenum may serve to tie up the carbon and prevent it from segregating to the grain boundaries, where it can cause embrittlement. The 4.5% tensile elongation obtained at a level of 0.1% molybdenum is the highest recorded in any as-cast Fe_3Al-based alloy cast in the same size and type of ingot mold as that used in this study.

ACKNOWLEDGMENTS

The authors wish to thank J. D. Vought for melting and casting the base charge material; B. G. Whitson and K. M. Byrd for the construction of the melting apparatus; G. W. Garner, E. C. Hatfield, and C. R. Howell for their assistance with the grain refinement experiments; the staff of the Metallography Department for their assistance; C. A. Carmichael for help with bend tests; B. G. Gieseke and G. M. Goodwin for reviewing the paper; K. Spence for editing; H. S. Payne and the Science and Engineering Research Semester (SERS) Program, U.S. Department of Energy, for supporting one of the authors (V. K. Andleigh) from September to December 1993; and M. L. Atchley for final preparation of the manuscript.

Research for this work was sponsored by the U.S. Department of Energy, Office of Fossil Energy, Advanced Research and Technology Development Materials Program, [DOE/FE AA 15 10 10 0, Work Breakdown Structure Element ORNL-2(H)] under contract DE-AC05-84OR21400 with Lockheed Martin Eenrgy Systems.

REFERENCES

1. C. T. Liu, in *High Temperature Ordered Intermetallics V*, eds., I. Baker, J. D. Whittenberger, R. Darolia, and M. H. Yoo (Mater. Res. Soc. Symp. Proc. 288, Pittsburgh, PA, 1993) p. 3.

2. S. Viswanathan, C. G. McKamey, P. J. Maziasz, and V. K. Sikka, in *Processing, Properties, and Applications of Iron Aluminides*, eds. J. H. Schneibel and M. A. Crimp (The Minerals, Metals, and Materials Society, Warrendale, PA, 1994) pp. 159-169.

3. C. G. McKamey, C. T. Liu, S. A. David, J. A. Horton, D. H. Pierce, and J. J. Campbell, *Development of Iron Aluminides for Coal Conversion Systems*, ORNL/TM-10793, Martin Marietta Energy Systems, Inc., Oak Ridge Natl. Lab., 1988.

WELDABILITY OF POLYCRYSTALLINE ALUMINIDES

A. A. Fasching*, G. R. Edwards*, R. P. Burt*, and S. A. David#

Center for Welding and Joining Research
Department of Metallurgical and Materials Engineering
Colorado School of Mines
Golden, CO 80401

#Metals and Ceramic Division
Oak Ridge National Laboratory
Materials Joining Group
Oak Ridge, TN 37831

ABSTRACT

Slow strain rate tensile tests were conducted in varying water vapor atmospheres on weldments refined by magnetic arc oscillation with average fusion zone grain sizes ranging between 115 and 530μm. Fracture strength and percent strain to fracture were measured for each fusion zone microstructure. The fracture strength data followed Hall-Petch behavior, and water vapor significantly reduced fracture strength. The finer grain size fusion zones were found to be less susceptible to hydrogen cracking and more tolerant of high hydrogen concentrations than coarse fusion zone grain structures. Microstructural refinement via arc oscillation was also found to be suitable only for well-controlled fabrication environments.

INTRODUCTION

Iron aluminide alloy FA-129 is susceptible to cold cracking during gas-tungsten arc (GTA) welding and previous work has shown that iron aluminides are susceptible to environmental embrittlement when tensile tested in the presence of water vapor[1,2]. To further investigate hydrogen cold cracking in iron aluminides and, specifically, to study the effect of fusion zone grain size on cracking susceptibility, welds were produced using magnetic arc oscillation to refine the fusion zone grain structures. Weldments with average fusion zone grain sizes ranging between 115 and 530μm were slow strain rate tensile tested in varying water vapor atmospheres. The results of the investigation are presented within this paper.

EXPERIMENTAL PROCEDURE

An experiment was developed to test the resilience of the refined fusion zone microstructures to hydrogen embrittlement in water vapor atmospheres. Alloy FA-129 samples were welded in pure

argon, then slow strain rate tensile tested in argon containing varying concentrations of water vapor. The tests were strain controlled at a rate of 2.78×10^{-6}/s. Four different weldments were produced using different welding and oscillation parameters, shown in Table 1. The different heat inputs and oscillation parameters produced four unique microstructures for evaluation. The microstructure of the welds differed significantly from that of the base material; consequently, all of the applied strain concentrated within the fusion and heat affected zones, and fracture occurred within the same region.

Table 1 Welding Parameters Used to Produce Fusion Zones of Differing Grain Sizes

Microstructure Type	Current (amps)	Arc Gap (inches)	Heat Input (J/mm)	Oscillation Frequency (Hz)	Oscillation Amplitude Setting	Oscillation Orientation Relative to Welding Direction
A	38	0.060	80.9	--	--	--
B	31	0.060	73.3	--	--	--
C	31	0.060	73.3	10.0	250 (0.8mm)	90 degrees
D	31	0.060	73.3	10.0	250 (0.8mm)	45 degrees

Alloy FA-129 samples were tensile tested in a plexiglas environmental chamber designed specifically for the MTS system. The moisture probe was located directly between the grips in the back of the chamber. For all tests, the chamber was purged with Grade 5 argon until the moisture reading was less than 200 ppm. Argon was continually passed through the system during testing and a measurement was recorded both before and after testing. For tests conducted in moisture, the chamber was purged and then water was bubbled through distilled water using an ultra-slow flow rate meter. Once again the atmosphere was allowed to equilibrate prior to testing.

RESULTS

The unoscillated microstructures produced are shown in Figures 1a and 1b, and the transversely oscillated fusion zone microstructures are shown in Figures 1c and 1d. The welds of the unoscillated Microstructure A, shown in Figure 1a, consisted of large columnar grains. The second unoscillated microstructure (Microstructure B), shown in Figure 1b, also exhibited a columnar grain

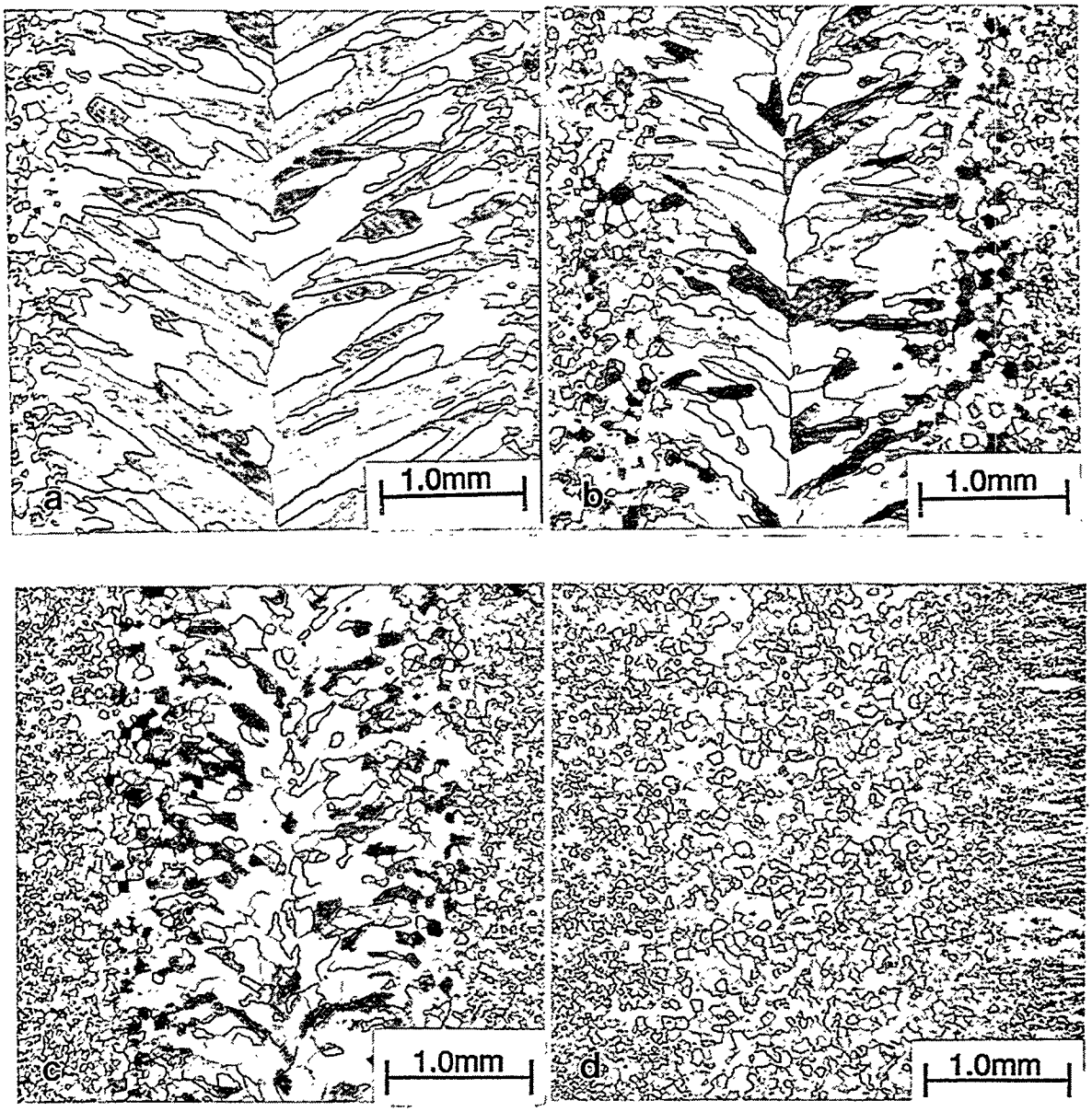

Fig. 1. Microstructures used for weldments used in slow strain rate testing. a) Microstructure A (H.I.=81 J/mm), b) Microstructure B (H.I.=73 J/mm), c) Microstructure C (90° at Freq.=10 Hz, Amp.=0.8mm), and d) Microstructure D (45° at Freq.=10 Hz, Amp.=0.8mm).

structure and a well defined centerline. In this lower heat input weld, however, the grains were not as large as grains in the higher heat input weld. The transversely oscillated fusion zone (Microstructure C), Figure 1c, looked similar to the unoscillated fusion zone (Microstructure B) in Figure 1d; however, in this microstructure there was no clear centerline. The grains in this microstructure were still elongated. Finally, the fusion zone created by oscillating the arc at 45 degrees to the welding direction (Microstructure D) resulted in a nearly equiaxed, fine-grained fusion zone (Figure 1d). Also, no clear centerline or fusion line was apparent in this weldment.

Fusion zone grain size measurements were made using a Leco image analyzer system. The results of the grain size measurements are shown in Table 2. The average grain size and aspect ratio of each microstructure are reported as well. As shown in Figure 1, the weld with the highest heat input contained the largest grains and the largest aspect ratio (Figure 1a). Oscillating the arc at a 45-degree angle to the welding direction produced the smallest grains with the smallest aspect ratio (Figure 1d).

Table 2 Grain Dimensions of FA-129 Fusion Zones

Microstructure	average length (l), μm	average width (w), μm	average thickness (t), μm	average grain size, μm	aspect ratio (l/w)
A	1,250	168	176	530	7.4
B	637	141	109	300	4.5
C	300	123	94	172	2.4
D	139	107	100	115	1.3

Slow strain rate tensile test were conducted on welds of all four microstructures in both pure argon and argon containing four water vapor levels. Load at fracture and strain at fracture were recorded for each sample. Welds of Microstructure C broke at the fusion line. The fracture surfaces were either transgranular cleavage or a mixed mode of intergranular and transgranular cleavage.

Fracture strength versus moisture content was plotted for welds representing each fusion zone grain size, as shown in Figure 2. A linear regression was performed on the data for each grain size. The correlation coefficient (R) is shown and describes the accuracy of the fit. (An R value equal to one designates a perfect fit.) The slope of the line for the coarsest (530 μm) fusion zone is slightly steeper than that for the most refined (115 μm) fusion zone. The data for the two intermediate grain sizes plot nearly on top of one another. Percent strain at fracture versus the moisture content in the

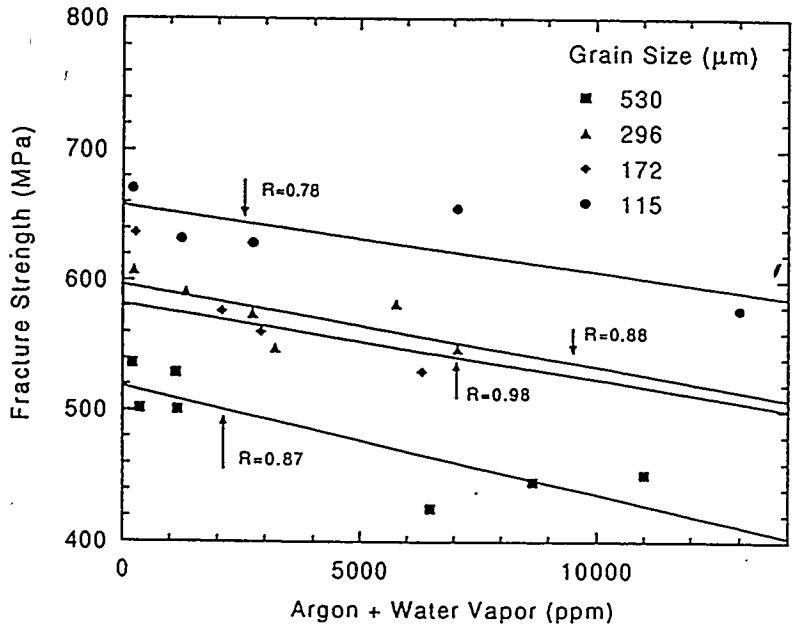

Fig. 2. Fracture strength versus water vapor content in the atmosphere showing the effect of fusion zone grain size on the mechanical properties of the weldment.

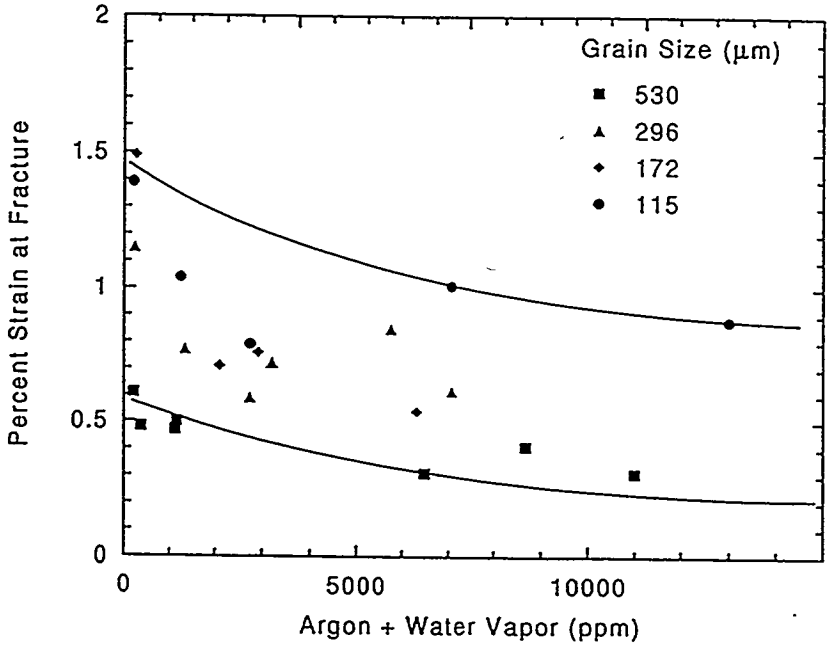

Fig. 3. Percent elongation at fracture for weldments of different fusion zone grain size tested in atmospheres of varying levels of water vapor.

atmosphere was also plotted for each of the fusion zone grain sizes as shown in Figure 3. These data, while not as well defined as the fracture strength data, exhibited the same basic trends. The most refined fusion zone (115 μm) exhibited the highest percent elongation at fracture and the coarsest fusion zone (530 μm) showed the least elongation at fracture.

Figure 4 is a Hall-Petch style plot where each range of the water vapor levels tested is shown. Since testing occurred over a range of water vapor concentrations, points were read from the linear regression fits of the data in Figure 3 at the specific levels plotted. Again a linear regression was conducted on each of these data and the slope of each line was determined. Again the correlation coefficient (R) is shown for each line. The slopes of the lines in Figure 4 correspond to the k_F value in the Hall-Petch equation. The k_F value was plotted as a function of water vapor concentration, as indicated in Figure 5. The data fit a square root function showing $k_F = 70 + 0.25M^{1/2}$ (MPa $mm^{1/2}$), where M is the water vapor concentration in parts per million. The σ_o term is also a function of water vapor, where $\sigma_o = 472 - 1.5M^{1/2}$ (MPa). The plot of σ_o versus water vapor concentration is also shown in Figure 5.

DISCUSSION

Iron aluminides are embrittled when tested in water vapor atmospheres at strain rates slower than 10^{-3} /s (ref.3). A slow strain rate test (10^{-8}/s) was developed to evaluate the hydrogen embrittlement of alloy FA-129 weldments. The slowest reasonable strain rate was selected to maximize the time for hydrogen to diffuse. Slow strain rate tensile testing revealed that welds containing fine-grained fusion zones resisted hydrogen embrittlement in the presence of water vapor significantly better than welds of coarse-grained fusion zones. Microstructure D, the smallest and most equiaxed fusion zone, exhibited the highest fracture strength and the most ductility at fracture. The trends were very clear for the fracture strength data, and a first order polynomial equation was fit to these data. The values of the correlation coefficient (R) for each fusion zone grain structure are shown in Figure 2. These values ranged from 0.7 to 0.99. Variations in moisture level over the duration of the test and normal experimental error can account for some of the scatter seen in the fracture data. However, the linear regression fits accurately describe the trend of these data.

Using points from the linear fits in Figure 2, the fracture strength was plotted as a function of the inverse square root of fusion zone grain size, as shown in Figure 4, for four water vapor levels. Again, a first order polynomial equation was fit to the data for each water vapor concentration, and the correlation coefficient (R) is shown. The data for the coarsest fusion zone, Microstructure A, fall below the linear regression line. Microstructure A had a very large aspect ratio and an obvious

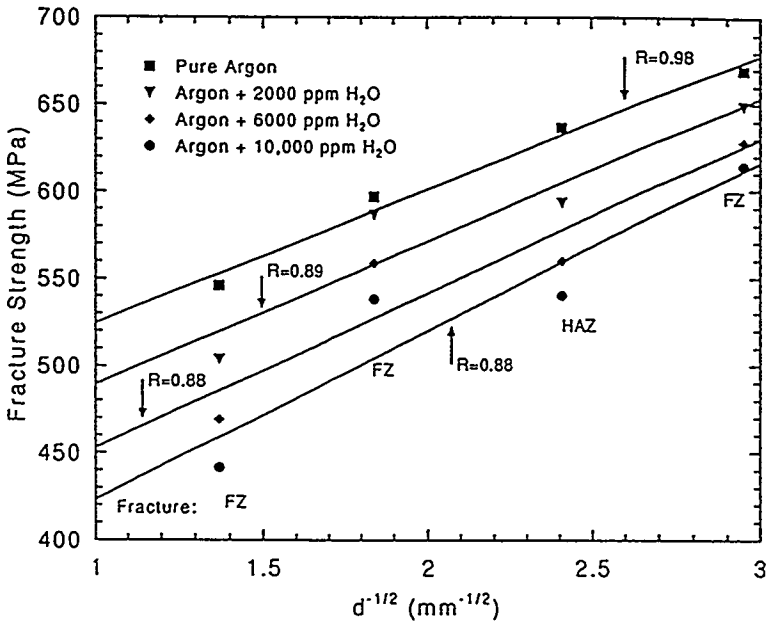

Fig. 4. Hall-Petch plot for iron aluminide alloy FA-129 weldments tested in varying water vapor atmospheres.

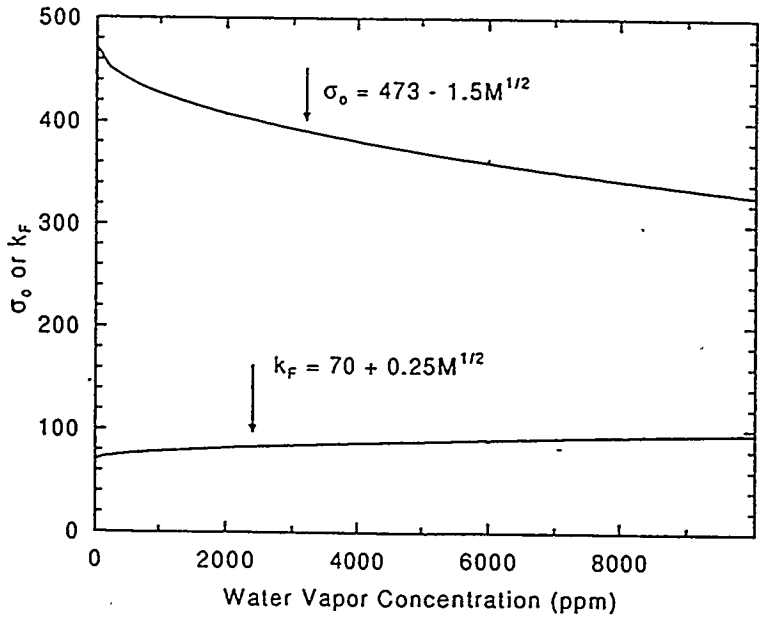

Fig. 5. k_F and σ_o as a function of water vapor concentration for aluminide alloy FA-129 weldments.

centerline. The effect of the directional grains and the centerline was lessened by averaging of the grain size in three directions. Hence, the linear regression predicts a higher fracture strength for Microstructure A (530 μm) than was measured, as shown on Figure 4. The data points of Microstructure C (172 μm) also fall below the linear regression line. In this case, failure occurred in the heat affected zone causing the measured fracture strength to be less than that of the actual weldment.

The slopes of these lines, shown in Figure 4, slightly increased as water vapor concentration increased, indicating that k_F is a function of water vapor concentration. The slope varied from 77 in pure argon to 97 MPa $mm^{1/2}$ in argon containing 10,000 ppm water vapor. This change in slope is small and the experimental scatter of the data could account for the difference.

The y-intercept decreased significantly as water vapor concentration increased, indicating that σ_o, the flow stress, was a strong function of water vapor concentration. The flow stress ranged from 448 MPa in pure argon to 327 MPa in argon containing 10,000 ppm water vapor; thus, a 30 percent decrease in flow stress occurred over the range of water vapor concentrations tested. Figure 5 shows that σ_o was a much stronger function of water vapor concentration than k_F.

These results and other results beyond the scope of this paper show that arc oscillation requires tight control of the welding process[4]. Optimal refinement parameters are sensitive to welding water vapor concentration, material composition, and heat input[4]. Magnetic arc oscillation was shown to be an effective method for refining fusion zone grain structures in iron aluminide alloy FA-129; however, it was found to be best suited for well-controlled fabrication environments. Other techniques such as inoculation should be investigated to refine the fusion zone grain structures in field situations where precise parameter control is not available.

CONCLUSIONS

1. Arc oscillation was shown to be an effective method for refining fusion zone microstructures in iron aluminide alloy FA-129 by changing the thermal gradients in the weld pool and affecting the competitive growth process.
2. Slow strain rate tensile tests showed fine-grained iron aluminide fusion zones to be less susceptible to hydrogen cracking and more tolerant of high hydrogen concentrations than coarse fusion zone grain structures. The fracture strength data was found to obey the Hall-Petch relationship.
3. Microstructural refinement by arc oscillation is suitable for well-controlled fabrication environments. Optimal refinement parameters were sensitive to numerous processing variables including welding water vapor concentration, material composition, and heat input.

4. Fusion zone inoculation or another method of fusion zone grain refinement should be considered to refine weldments produced in field fabrication situations.

CURRENT AND FUTURE WORK

Work now centers on using weld pool inoculation to refine the fusion zone. The study will follow the same format as the arc oscillation study. The method will first be tested and optimized by welding in a pure argon environment. Slow strain rate tensile tests will then be performed in atmospheres of varying water concentrations on welds refined in pure argon to determine the effect of grain size on hydrogen embrittlement. Finally, successful refinement of the fusion zone by inoculation while welding in environments of varying water vapor concentration will be attempted.

Powdered titanium and niobium carbide have been selected as the inoculants for the study (based on compatible physical properties and availability). The inoculant is added to the weld by machining a groove in the base plate, which is then filled with the powder and covered with an iron aluminide protective cap. The GTA welds are made using the same experimental equipment used in previous work.

Preliminary welds made by inoculating the fusion zone have shown significant fusion zone refinement. Figure 6 shows the fusion zone microstructure of an FA-129 iron aluminide weld inoculated with titanium powder (99.5%, -325 mesh). The heat input was 142 J/mm and the average grain size was 65μm. It has not yet been determined if the titanium reacted with the base plate or environment; however, particles were visible in the weldment microstructure and account for approximately 2.5 volume percent of the fusion zone (Figure 7). Further analysis will be done to identify these particles as well as to characterize the reproducibility and cracking susceptibility of weldments prepared by this method.

REFERENCES

1. C.T. Liu, C.G. McKamey, and E.H. Lee, Scripta Metall., 24 (1990) p. 385-390.

2. S.A. David, T.Zacharia, and R.W. Reed, Proceedings of the Fourth Annual Conference on Fossil Fuel Materials, ORNL/FMP-90/1 (U.S. Dept. of Energy, Oak Ridge, TN, August 1990), p. 207.

3. N.S. Stoloff, D.J. Duquette, "Moisture and Hydrogen-Induced Embrittlement of Iron Aluminides", Journal of Metals, December 1993.

4. A.A. Fasching "Grain Refinement and Hydrogen Embrittlement in Iron Aluminide Alloy FA-129 Weldments", Thesis #4686, Colorado School of Mines, Golden, CO, May 1995.

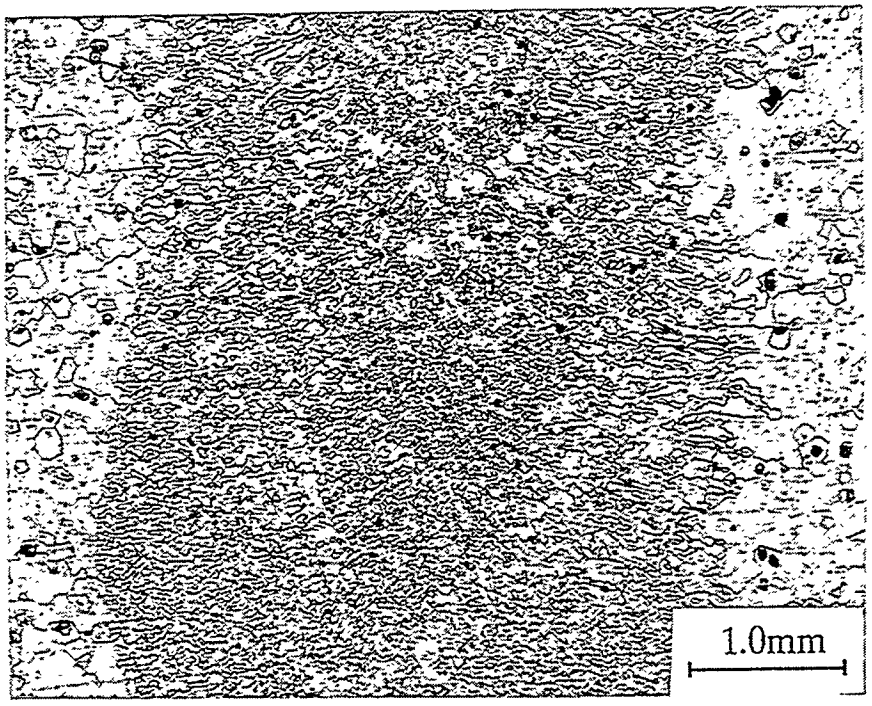

Fig. 6. Refined microstructure of titanium-inoculated FA-129 iron aluminide weld.

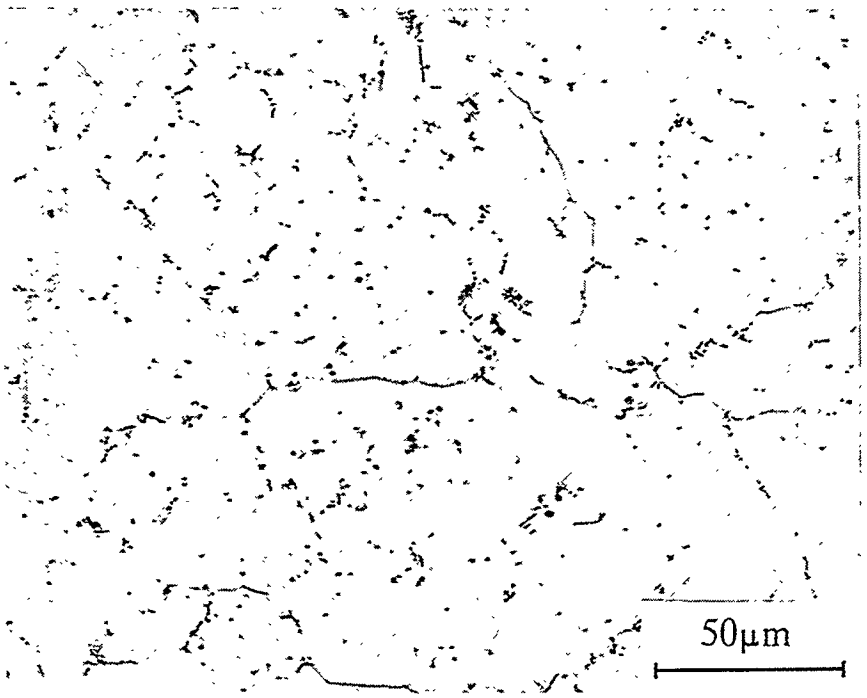

Fig. 7. Unidentified particles in titanium-inoculated FA-129 iron aluminide fusion zone.

ELECTRO-SPARK DEPOSITED COATINGS FOR PROTECTION OF MATERIALS

R.N. Johnson

Battelle Pacific Northwest Laboratory
P.O. Box 999, K3-59
Richland, WA 99352

ABSTRACT

Electro-Spark Deposition (ESD) is a micro-welding process that uses short duration, high-current electrical pulses to deposit or alloy a consumable electrode material onto a metallic substrate. The coating is fused (metallurgically bonded) to the substrate with such a low total heat input that the bulk substrate material remains at or near ambient temperature. Rapid solidification of the deposit typically results in an extremely fine-grained deposit that may be amorphous for some materials. Nearly any electrically conductive metal, alloy or cermet can be applied to metallic substrates.

The ESD process allows multi-layer coatings to be built-up using different materials to create graded structures or surface compositions that would be difficult to achieve by other means. A series of iron-aluminide coatings based on Fe_3Al and FeAl in combination with refractory metal diffusion-barrier coatings and supplementary additions of other elements are in corrosion testing at ANL. The most recent FeAl coatings are showing a factor of three better corrosion performance than the best previous coatings.

Technology transfer activities are a significant portion of the ESD program effort. Notable successes now include the start-up of a new business to commercialize the ESD technology, major new applications in gas turbine engines and steam turbine blade coatings, and in military, medical, metal-working, and recreational equipment applications.

INTRODUCTION

The objective of this program is to develop advanced materials coatings capable of operating in fossil energy environments beyond current materials limits, and to provide improvements in materials performance, durability and cost effectiveness for both new and existing power systems. Ultimately, new materials performance limits can enable new systems concepts.

A corollary objective is to further advance the Electro-Spark Deposition (ESD) technology and equipment, and to develop broad commercial applications through technology transfer activities.

Just as high-performance jet engines would not be possible today without protective coatings, so also does the next generation of high efficiency energy systems depend on protective coatings to survive the necessarily higher temperatures and more corrosive environments. The ESD coating process has been identified as one of the principal enabling technologies for such future systems. One of the reasons for this is that the exceptional structure produced in these metallurgically-bonded

coatings makes them virtually immune to damage or spalling under severe service conditions and temperatures that destroy most other coatings. Additional attractions are that the process is portable (allowing coatings or surface treatments to be performed in the field), environmentally benign (creates no noxious wastes, fumes, or effluents), and highly cost-effective.

The Fossil Energy program currently funds the only research being conducted in the U.S. on this unique process. This program not only develops advanced coatings for fossil energy applications, but also contributes to improvements in understanding the basic phenomena occurring in the complex process parameters and surface effects and their relation to the quality, reproducibility, and rate of coating. The advances so far achieved are resulting in increased capabilities, reduced costs, and wider technology transfer opportunities.

BACKGROUND

Electro-spark deposition is a pulsed-arc micro-welding process that uses short-duration, high current electrical pulses to weld a consumable electrode material to a metallic substrate. The short duration of the electrical pulse allows an extremely rapid solidification of the deposited material and results in an extremely fine-grained, homogenous coating that may be amorphous for some materials. The microstructures produced by ESD can provide exceptional corrosion-resistance and wear-resistance for many materials.

The ESD process is one of the few methods available by which a fused, metallurgically-bonded coating can be applied with such a low total heat input that the bulk substrate material remains at or near ambient temperatures. This eliminates thermal distortions or changes in metallurgical structure of the substrate. Since the coating is metallurgically bonded, it is inherently more resistant to damage and spalling than the mechanically-bonded coatings produced by most other low-heat-input processes such as detonation gun, plasma spray, electro-chemical plating, etc. Nearly any electrically-conductive metal, alloy or cermet can be applied by ESD to metallic substrates.

Further background information on the ESD process is provided in References 1 and 2.

DISCUSSION OF PRIOR ACTIVITIES

Data collected so far indicate that ESD coatings tend to show lower corrosion rates in most environments than the same material would in either bulk form or as a coating applied by other processes. For example, ESD-applied coatings of chromium carbide-15% nickel exhibit significantly

lower corrosion rates in aqueous and liquid metal environments than similar detonation-gun applied coatings.[3] The superior performance of the former is attributed to the extremely fine-grained, nearly amorphous structure inherent to the ESD coatings compared to the larger-grained, more heterogeneous detonation-gun coatings.

In tests at Argonne National Laboratory (ANL), this same ESD coating (chromium carbide-15% nickel) showed four times better sulfidation resistance than Type 310 stainless steel at 875°C.[4] Normally, this composition would not be expected to perform that well because of the strong susceptibility of a nickel matrix to sulfidation attack. Again, the fine grain structure is believed to be a major factor in the corrosion resistance. This observation is in agreement with other Fossil Energy Materials Program work that indicates one mechanism of improving lifetimes of protective oxide films and scales is to maintain as fine a grain structure as possible.[5] Further improvement in corrosion resistance of the chromium carbide coating was achieved by alloying aluminum into the surface by further ESD treatment.

One of the most significant advances in ESD coatings for use in sulfidation environments has been the successful development of Fe_3Al as a coating material. Oak Ridge National Laboratory (ORNL) has demonstrated the exceptional corrosion properties of Fe_3Al in bulk form, but alloying the Fe_3Al to achieve acceptable mechanical properties while maintaining optimum corrosion performance appears to be a challenge. As one alternative approach, ORNL supplied electrode materials to us for use in ESD coating development. (Using Fe_3Al as a coating material allows the selection of the substrates material for optimum mechanical properties and economy while retaining the corrosion resistance offered by the coating.) The coating results to date have been outstanding. The ESD parameters have been developed to the point that consistent, defect free coating over 100 μm thick can be applied relatively rapidly with good transfer efficiency. The Fe_3Al appears to produce some of the best and most economical coatings of all the materials evaluated for ESD application.

Further coating development is proving that the corrosion performance of the Fe_3Al coating can be significantly enhanced by the use of multi-layer ESD coating techniques. Sulfidation corrosion tests at ANL [6,7], for example, showed the beneficial effects of applying a Nb-1Zr diffusion barrier coating. The corrosion rate of an ESD coating of Fe_3Al was reduced by a factor of 2 in tests at 500°C when an intermediate ESD coating of Nb-1Zr was first applied to the steel, when compared to the same Fe_3Al coating applied directly to the steel.

Analyses of the Fe_3Al coatings with and without the Nb-1Zr diffusion barrier coating led to the conclusion that one of the principal reasons for the improved corrosion performance of the Fe_3Al coating over the Nb-1Zr layer was the higher aluminum content of the coating surface.[8] Scanning

Electron Microprobe (SEM) analyses showed that the intermediate diffusion barrier reduced the dilution of substrate elements into the coating weld zone and resulted in about 50% more aluminum in the surface of the coating (15% vs 9.5%).

After attempting unsuccessfully to alloy aluminum into the Fe_3Al surface by ESD treatments without generating surface cracks,[9] we obtained rods of FeAl from ORNL. This material proved to be nearly ideal for further increasing the aluminum content of the ESD coatings.

DISCUSSION OF CURRENT ACTIVITIES

Improved Iron Aluminide Coatings

We have now produced FeAl coatings as thick as 100 μm deposited on Type 316 stainless steel and on Alloy 800 with none of the cracking defects that were observed when aluminum electrodes were used.

Seven groups of test specimens incorporating FeAl in the coating were prepared for corrosion testing at ANL. Most are still in test, but results to date show that the already-attractive corrosion performance of the best previous Fe_3Al coatings is improved by about a factor of 3 when FeAl is applied directly to the Type 316 stainless steel substrates. Figure 1 shows comparison of the Fe_3Al , FeAl, and bare 316 SS weight changes in coal gasification atmospheres at 650°C.[2,10]

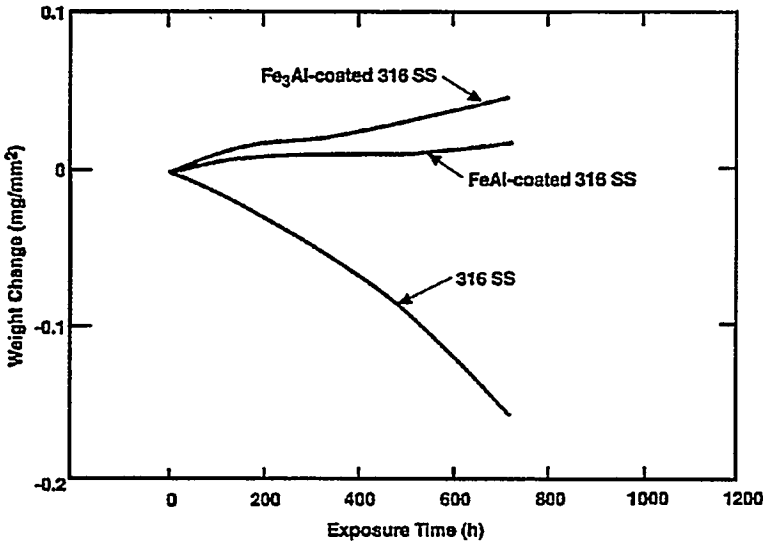

Figure 1.Corrosion of ESD Coatings in coal gasification atmospheres at 650°C.[2,10]

The remaining ESD coating candidates still in test at ANL consist of various combinations of Fe_3Al , FeAl, Nb, and Mo, applied to Type 316 stainless steel substrates. The Nb and Mo represent refractory metal diffusion barriers applied between the stainless steel substrate and the iron aluminde coating to inhibit the diffusion of nickel to the surface and the diffusion of sulfur or oxygen to the substrate, both of which are mechanisms of corrosion failure. The application of the diffusion barrier also reduces the weld dilution effects during the coating process and results in the surface composition of the coating more nearly approaching the composition of the electrodes used.

Test specimens of the advanced coatings were delivered to Argonne National Laboratory for corrosion testing in fossil energy environments. The success of using FeAl as a coating material now opens the potential for further improving the performance of Fe_3Al alloys. The Fe_3Al alloys so far can provide better mechanical properties in structural applications than FeAl, while an FeAl coating could improve the corrosion performance in applications where the higher aluminum content is desirable. It is possible such treatments could also improve the resistance of Fe_3Al to hydrogen embrittlement (described by McKamey and Liu[11]). Plate or sheet substrates of Fe_3Al have been requested from ORNL for further exploration of these potential improvements.

Technology Transfer Activities

A major manufacturer of heavy equipment (rail cars, ships, etc.) performed field evaluations of ESD hardsurfaced weld-wire feed-rollers, and reported a minimum of 5X increase in service life. Use of ESD is now saving over $100,000 per year for this application alone. Other applications are now being evaluated.

Consultations and test specimens of Electro-Spark Deposited (ESD) coatings were provided to Westinghouse Steam Turbine Division in Orlando, FL. Corrosion tests to date in wet steam containing NaCL and NaOH on coated U-bend specimens show that our recommended ESD coatings of Hastelloy C-22™ provides outstanding prevention of chloride and caustic stress corrosion cracking. The next phase of longer term (1 yr) materials tests are in progress to qualify the ESD coatings for large steam turbine applications. No other coating process has been found that is capable of economically providing the required surface treatment to some of the difficult geometries involved.

A presentation was given to Air Force Air Logistics Center personnel at Randolf AFB on the potential uses of Electro-Spark Deposited coatings to replace chromium plating as a hard surfacing on aircraft components. The Air Force is phasing out chromium plating in many applications and is searching for more environmentally benign coating technologies. Until now, the best candidate replacements have been various forms of thermal spray coatings, but these are proving to be

inadequate in several applications, due to delamination failures. (ESD coatings in similar conditions are virtually immune to such failures.) Further discussions with the Air Force are in progress.

Visits and consultations on the Electro-Spark Deposition process were provided to a major manufacturer of gas turbine engines. The manufacturer is now successfully using the ESD process for several applications, including modification of aluminide diffusion coatings, recovery of out-of-tolerance parts, and hard surfacing of critical turbine blade wear locations. This the second, but largest, successful application of the ESD technology in the gas turbine field so far.

A new commercial application for Electro-Spark Deposited coatings is resulting from consultation and work provided to a small Seattle-based fabricator as part of our technology transfer activities. ESD coatings of titanium carbide provided a required increase in gripping force in special collets where all other coatings and materials failed. There now appears to be a significant market for these and similar collets.

Other technology transfer activities included:

- Consultations were provided to a diffusion coating manufacturer on possible uses of ESD-applied FeAL to protect welds on previously aluminized components. (Follow-on tests are in progress.)
- Control rod drive rollers were coated for tests at Bettis Atomic Power Laboratory.

REFERENCES

1. R. N. Johnson, "Principles and Applications of Electro-Spark Deposition," Surface Modification Technologies, T.S. Sudarshan and D.G. Bhat, eds., The Metallurgical Society, January 1988, pp. 189-213.

2. R. N. Johnson, "Electro-Spark Deposited Coatings for High Temperature Wear and Corrosion Applications." presented at Symposium on High Temperature Coatings I (HTC-I '94), TMS, Rosemount, IL, October 1994 (to be published in the Proceedings).

3. R. N. Johnson, "Coatings for Fast Breeder Reactors," in Metallurgical Coatings, Elsevier Sequoia, S.A. , New York, 1984, pp. 31-47.

4. K. Natesan and R. N. Johnson, "Corrosion Resistance of Chromium Carbide Coatings in Oxygen-Sulfur Environments," Surface and Coatings Technology, Vol. 33, 1987, pp. 341-351.

5. I. G. Wright and J. A. Colwell, "A Review of the Effects of Micro-Alloying Constituents on the Formation and Breakdown of Protective Oxide Scales on High Temperature Alloys at Temperatures Below 700°C," ORNL/Sub/86-57444/01, September 1989.

6. K. Natesan and R. N. Johnson, "Development of Coatings with Improved Corrosion Resistance in Sulfur-Containing Environments," presented at the International Conference on

Metallurgical Coatings, San Diego, April 1990, published in Surface and Coatings Technology, Vol. 3/44, 1990, pp. 821-835.

7. R. N. Johnson, "Electro-Spark Deposited Coatings for Protection of Materials in Sulfidizing Environments," Proceedings of the Fourth Annual Conference on Fossil Energy Materials, ORNL/FMP-90/1, August 1990, pp. 321-329.

8. R. N. Johnson, "Electro-Spark Deposited Coatings for Protection of Materials in Sulfidizing Atmospheres," Proceedings of the Fifth Annual Conference on Fossil Energy Materials, ORNL/FMP-91/1, September 1991, pp. 281-288.

9. R. N. Johnson, "Electro-Spark Deposited Coatings for Fossil Energy Environments," in Proceedings of the Seventh Annual Conference on Fossil Energy Materials, ORNL/FMP-93/1, July 1993, pp. 289-295.

10. K. Natesan and W. D. Cho, "High Temperature Corrosion of Iron Aluminides," in Proceedings of the Eighth Annual Conference on Fossil Energy Materials, ORNL/FMP-94/1, May 1994.

11. C. G. McKamey and C. T. Liu, "Environmental Embrittlement of Iron Aluminides in Moisture-Containing Atmospheres," in Proceedings of the Environmental Effects on Advanced Materials, NACE Conference, June 1991.

Cr_2Nb-BASED ALLOY DEVELOPMENT

C. T. Liu, P. F. Tortorelli, J. A. Horton, D. S. Easton, J. H. Schneibel,
L. Heatherly, C. A. Carmichael, M. Howell, and J. L. Wright

Oak Ridge National Laboratory
Oak Ridge, Tennessee 37831

ABSTRACT

Two-phase Cr-Cr_2Nb alloys (designated as CN alloys) were prepared by arc melting, followed by directional solidification, HIPping, or hot extrusion at 1450 to 1500°C. The microstructure of CN alloys containing 6 to 12 at.% Nb depended strongly on alloying additions, heat treatment, and material processing. Tensile properties were sensitive to defects. Hot extrusion at 1480°C was most effective in reducing as-cast defects and refining the cast Cr-Cr_2Nb eutectic structure and thus improving ductility. Beneficial alloying elements that modified the eutectic microstructure, improved oxidation resistance, or increased high-temperature strength were identified. One particular composition had a room-temperature fracture strength of 548 MPa and an ultimate tensile strength of 388 MPa, and 23% elongation at 1200°C. Another CN alloy showed a fracture toughness of 7.6 MPa$\sqrt{m}$ at room temperature and 24.4 MPa$\sqrt{m}$ at 1000°C. Silicide coatings applied by a pack cementation process substantially improved the oxidation resistance of the Cr-Cr_2Nb alloys at 950 and 1100°C.

INTRODUCTION

The objective of this task is to develop a new generation of structural materials based on intermetallic alloys for use as critical hot components in advanced fossil energy conversion systems. The intermetallic phase, Cr_2Nb, with a complex cubic structure (C-15)[1,2] has been selected for this development because of its high melting point (1770°C),[2-4] relatively low material density (7.7 g/cm^2),[5] excellent high-temperature strength (at 1000 to 1250°C),[6,7] and potential resistance to oxidation and corrosion.[3,8,9] This intermetallic phase, like many other Laves phases, has a wide range of compositional homogeneity[2,4] suggesting the possibility of improving its mechanical and metallurgical properties by alloying additions.

The major engineering concern with Cr_2Nb and other A_2B Laves phases is their poor fracture toughness and fracture resistance at ambient temperatures.[3,6,7,10] The single-phase Cr_2Nb is very hard (~800 DPH) and brittle at room temperature.[11] Because of this brittleness, the development effort has concentrated on two-phase structures containing the hard intermetallic phase Cr_2Nb and the softer Cr-rich solid solution phase. Previous studies indicate that the two-phase CN alloys exhibited significant plastic deformation prior to fracture under compressive tests at room temperature.[6,7,11] The alloys showed excellent compressive strength at room and elevated temperatures, with the yield strength much

superior to nickel-base superalloys and Ni_3Al alloys at and above 1000°C. The CN alloys, however, showed poor fracture strength in tension at ambient temperatures.

Potential applications of Cr-Cr_2Nb alloys include hot components (for example, air heat exchangers and turbine blades) in advanced energy conversion systems and heat engines, wear-resistant parts in coal handling systems (e.g., nozzles), drill bits for oil/gas wells, and valve guides in diesel engines. Current studies are focused on enhancement of fracture resistance in tension at ambient temperatures and oxidation resistance above 1000°C. This report summarizes recent progress on controlling microstructure and improving the mechanical and metallurgical properties and the high-temperature corrosion behavior of Cr-Cr_2Nb alloys through alloying additions, material processing, and heat treatment.

ALLOY PREPARATION AND PROCESSING

Cr(Nb)-Cr_2Nb alloys weighing 400 g were prepared by arc melting and drop casting in a copper mold (2.5 cm diam x 7.6 cm long) preheated at 100 to 300°C. High-purity niobium and chromium metal chips were used as charge materials. The alloy ingots generally contain certain defects, including oxide inclusions and as-cast porosity ranging in size from a few to several hundred microns. The alloys also exhibit a coarse eutectic structure including interconnected Cr_2Nb plates, which adversely affect their mechanical (tensile) properties.

In order to minimize the casting defects and to refine the cast eutectic structure, selected alloy ingots were clad inside molybdenum billets and hot extruded at 1450 to 1500°C at an extrusion ratio of 4 to 1. Some alloys were successfully hot extruded into 1.3 cm bar stock, and others were cracked into pieces. The tendency for cracking was not simply correlated with alloy composition. It appeared that the cracking may be related to casting defects.

Preparation of CN alloys using elemental powders has just been initiated. In this case, the powders were mixed completely to give the correct alloy compositions and then placed inside molybdenum cans. The filled cans were then degassed in a vacuum chamber and sealed by electron-beam welding. They were hot extruded at 1480°C to produce CN alloys. Initial results indicate the as-extruded bars contained many foreign particles which were identified as aluminum and niobium oxides by energy dispersive x-ray spectroscopy (EDS). The amount of the oxide phase depended on the way the powders were prepared prior to insertion into the molybdenum cans. Significant recent progress was made in decreasing the amount of the oxide phases by reducing interstitial contamination during the powder processing.

MICROSTRUCTURAL ANALYSIS

Alloying additions, heat treatment, and material processing all strongly affect the microstructure of Cr(Nb)-Cr_2Nb alloys. Figure 1 compares the as-cast microstructure of two alloys, CN-96 and -97 containing 12% Nb and other alloying additions. (All compositions are at.% unless otherwise noted.) The compositional difference of the two alloys is that CN-97 had 0.1 wt% of a minor alloying addition (designated as X5). As shown in Fig. 1, the base alloy CN-96 exhibits a typical lamellar-type eutectic structure (Fig. 1a) while the doped alloy CN-97 shows blocky particles in the eutectic structure. In these photos, the Cr-rich phase appears as light gray while the Cr_2Nb is darker. The primary Cr-rich patches precipitated out fine Cr_2Nb particles after annealing at 1200 to 1300°C (as shown in Fig. 2 for CN-103).

Hot extrusion at 1450 to 1500°C was apparently effective in breaking the interconnected Cr_2Nb phase in the eutectic structure. This is shown in Fig. 3 for CN-90 containing 6% Nb and other alloying additions. The coarse Cr_2Nb plates that formed around primary Cr-rich patches (Fig. 3a) were broken into blocky particles (Fig. 3b) after hot extrusion at 1480°C.

The alloys CN-80, -85, and -87 were examined by transmission electron microscopy (TEM). All the alloys were hot extruded at 1480°C and annealed for 3 d at 1200°C. Alloy disks were prepared by ion milling at 6 kV and were examined in a Philips CM30 at 300 kV. Figure 4 is a TEM micrograph showing Cr_2Nb particles observed in CN-85 which was annealed for 3 d at 1200°C. The blocky particles contain numerous microtwins. This may be due to the C14 → C15 transformation. The study of the crystal structure of these particles

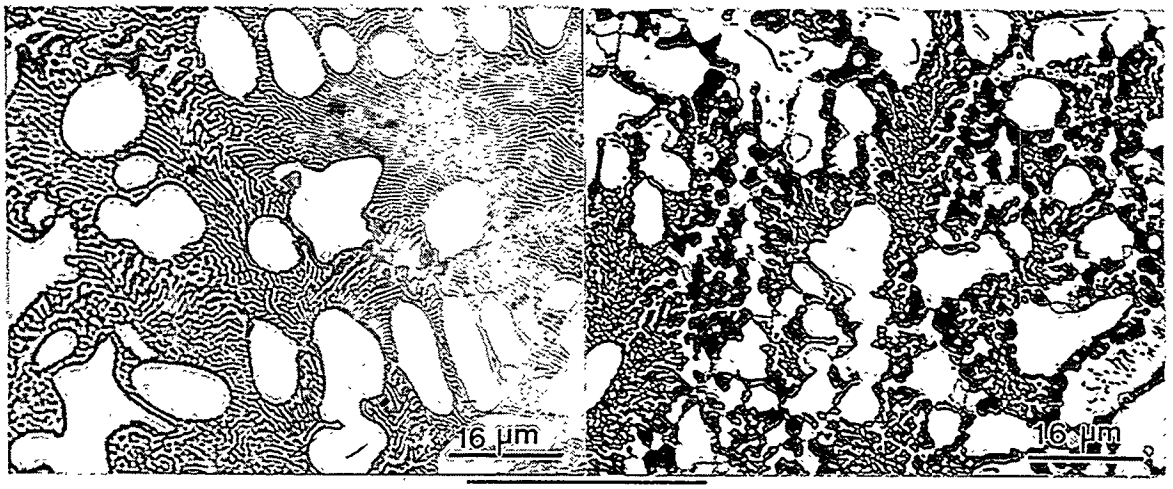

Fig. 1. Optical micrograph of as-cast (a) CN-96 and (b) CN-97 containing 12 at.% Nb and other alloying additions. The difference in composition is that CN-97 has 0.1 wt% X5.

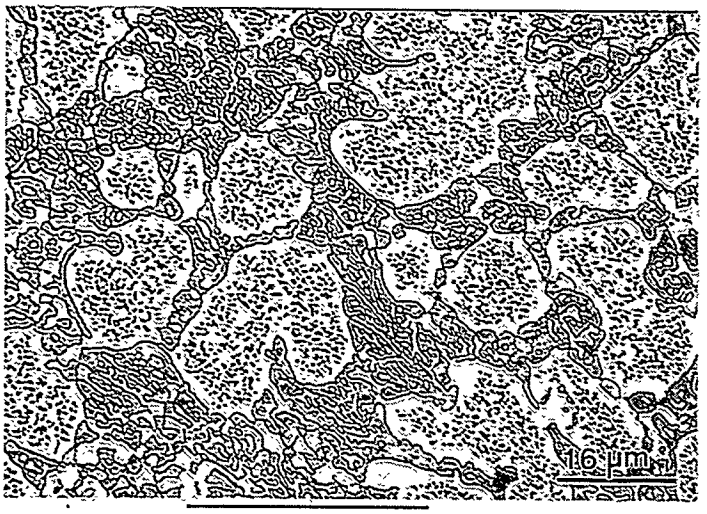

Fig. 2. Optical micrograph of CN-103 containing 10 at.% Nb and 0.1 wt% X5. The alloy was annealed for 1 d at 1300°C and 2 d at 1200°C.

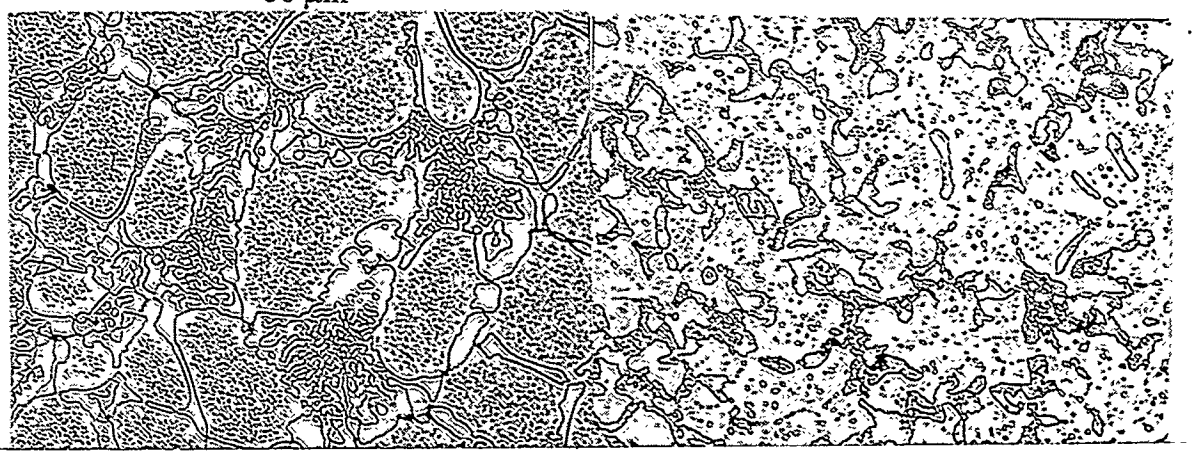

in CN-80, -85, and -87 dissolves a small amount (≤1%) of niobium. The Cr_2Nb-type phase, on the other hand, contains more than 27% Nb, and the exact amount of niobium in this phase depends on the partitioning of alloying additions in the CN alloys. The element X1 partitions more or less equally in the Cr_2Nb and the Cr-rich phases in CN-80 and -85, and preferentially in the Cr_2Nb phase in CN-87 (containing 20% X4). A careful examination of the Cr_2Nb compositions suggest X1 essentially occupies the chromium subsites. The element X2 in CN-85 and -87 partitions strongly in the Cr_2Nb-type phase, as shown in Table 1. The element X4 was distributed roughly equal in the two phases in CN-87. The partitioning behavior of these alloying elements could not be rationalized by considering both reactivity and atomic size of the alloying elements.

TENSILE PROPERTIES

Button-type tensile specimens with gage dimensions 0.31 cm diam x 0.95 cm long were machined by electro-discharge machining, followed by grinding. The tensile specimens

MICROSTRUCTURAL ANALYSIS

Alloying additions, heat treatment, and material processing all strongly affect the microstructure of Cr(Nb)-Cr_2Nb alloys. Figure 1 compares the as-cast microstructure of two alloys, CN-96 and -97 containing 12% Nb and other alloying additions. (All compositions are at.% unless otherwise noted.) The compositional difference of the two alloys is that CN-97 had 0.1 wt% of a minor alloying addition (designated as X5). As shown in Fig. 1, the base alloy CN-96 exhibits a typical lamellar-type eutectic structure (Fig. 1a) while the doped alloy CN-97 shows blocky particles in the eutectic structure. In these photos, the Cr-rich phase appears as light gray while the Cr_2Nb is darker. The primary Cr-rich patches precipitated out fine Cr_2Nb particles after annealing at 1200 to 1300°C (as shown in Fig. 2 for CN-103).

Hot extrusion at 1450 to 1500°C was apparently effective in breaking the interconnected Cr_2Nb phase in the eutectic structure. This is shown in Fig. 3 for CN-90 containing 6% Nb and other alloying additions. The coarse Cr_2Nb plates that formed around primary Cr-rich patches (Fig. 3a) were broken into blocky particles (Fig. 3b) after hot extrusion at 1480°C.

The alloys CN-80, -85, and -87 were examined by transmission electron microscopy (TEM). All the alloys were hot extruded at 1480°C and annealed for 3 d at 1200°C. Alloy disks were prepared by ion milling at 6 kV and were examined in a Philips CM30 at 300 kV. Figure 4 is a TEM micrograph showing Cr_2Nb particles observed in CN-85 which was annealed for 3 d at 1200°C. The blocky particles contain numerous microtwins. This may be due to the C14 → C15 transformation. The study of the crystal structure of these particles

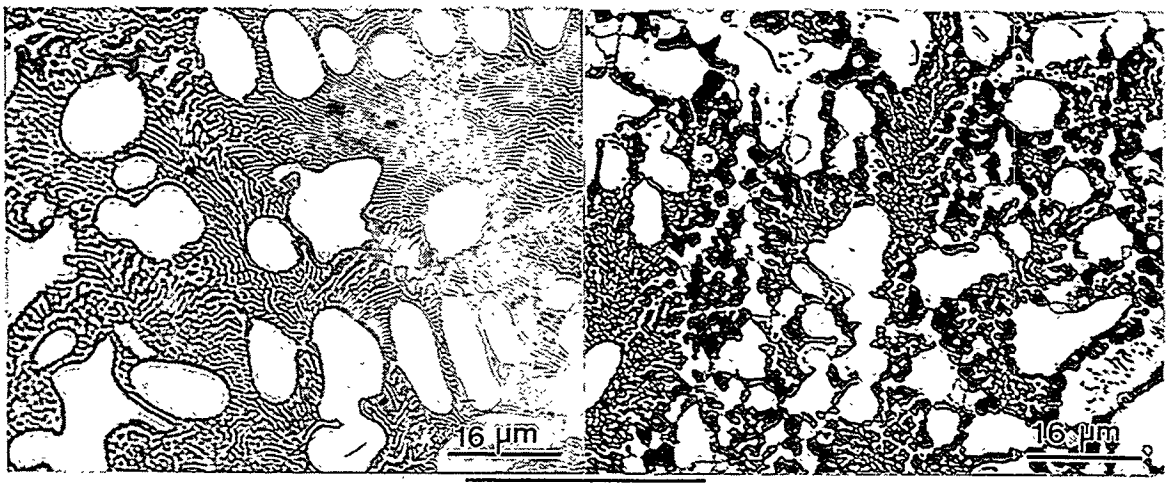

Fig. 1. Optical micrograph of as-cast (a) CN-96 and (b) CN-97 containing 12 at.% Nb and other alloying additions. The difference in composition is that CN-97 has 0.1 wt% X5.

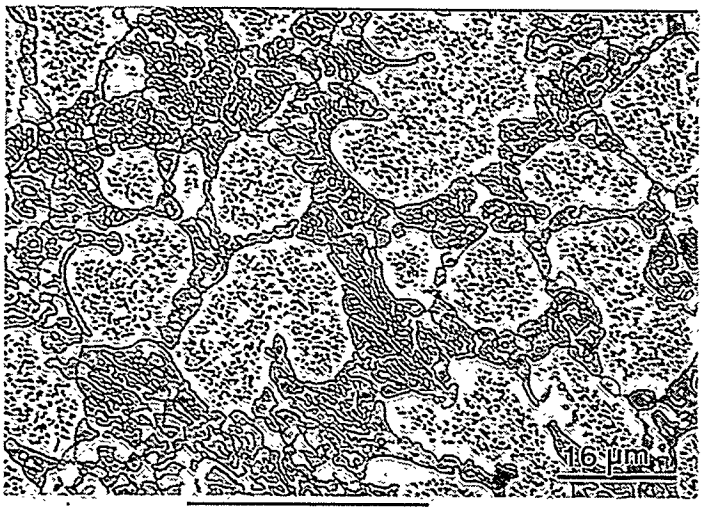

Fig. 2. Optical micrograph of CN-103 containing 10 at.% Nb and 0.1 wt% X5. The alloy was annealed for 1 d at 1300°C and 2 d at 1200°C.

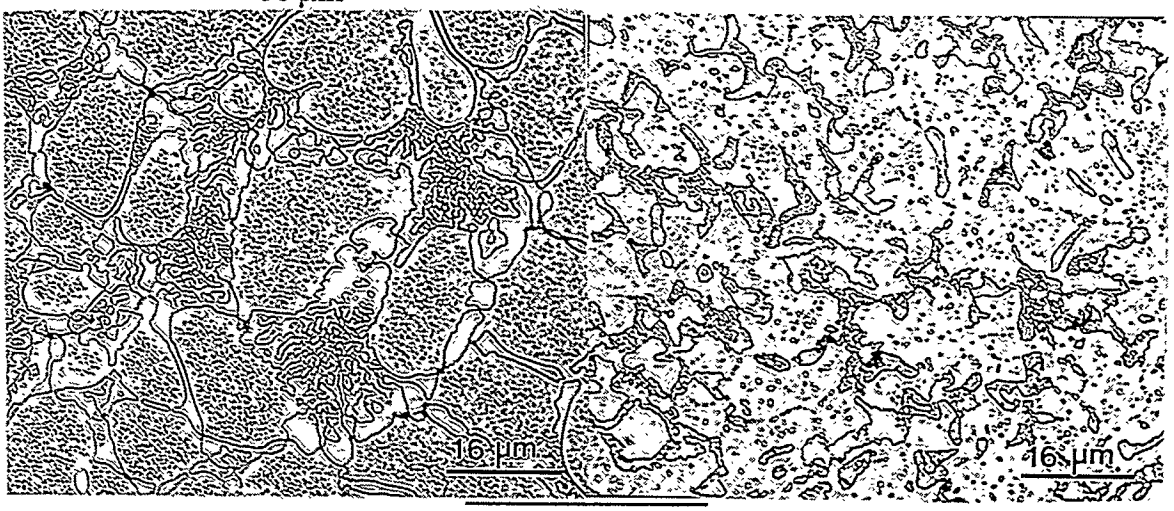

(a) (b)

Fig. 3. Comparison of optical micrograph of CN-90 in (a) as-cast plus 1 d at 1200°C anneal and (b) hot extrusion at 1480°C plus 1 d at 1200°C anneal.

is in progress. Dislocations and dislocation networks are generally observed in the Cr-rich phase, but they are very seldom observed in Cr_2Nb particles.

An EDAX 9100 spectrometer was used to perform EDS in conjunction with the TEM studies. The EDS analyses were made on precipitates that intersected the ion milling perforations, thereby minimizing the contributions from surrounding matrix material. The results were averaged and are shown in Table 1. Here X1, X2, X3, and X4 represent the beneficial elements added to the Cr-Nb alloys. X1 was added for refining the coarse eutectic structure, X2 was for improving oxidation resistance, X3 for enhancing the high-temperature strength, and X4 for ease of fabrication. The Cr-rich solid solution (that is, the matrix phase)

Fig. 4. TEM micrograph of CN-85 (Cr-Nb-1.5Al-5X1-4X2) hot extruded at 1480°C.

Table 1. Partitioning of Alloying Additions in CN Alloys* as Determined by EDS/TEM

Alloy (at. %)	Cr_2Nb Phase (at. %)	Cr-rich Matrix (at. %)
CN-80: Cr-12Nb-1.5Al-6X1	Nb = 33 Cr = 59 X1 = 6 Al = 2	Nb = 1 Cr = 90 X1 = 8 Al = 1
CN-85: Cr-6Nb-1.5Al-5X1-4X2	Nb = 32 Cr = 51 X1 = 7 X2 = 10 Al = 0	Nb = 1 Cr = 90 X1 = 6 X2 = 1.5 Al = 1.5
CN-87: Cr-8Nb-1.5Al-5X1-4X2-20X4	Nb = 27 Cr = 27 X1 = 10 X2 = 10 X4 = 24 Al = 2	Nb = 0.4 Cr = 73.5 X1 = 4.8 X2 = 2.3 X4 = 16.5 Al = 2.5

*The alloys were fabricated by hot extrusion at 1480°C and annealed for 1 to 3 d at 1200°C.

in CN-80, -85, and -87 dissolves a small amount (≤1%) of niobium. The Cr_2Nb-type phase, on the other hand, contains more than 27% Nb, and the exact amount of niobium in this phase depends on the partitioning of alloying additions in the CN alloys. The element X1 partitions more or less equally in the Cr_2Nb and the Cr-rich phases in CN-80 and -85, and preferentially in the Cr_2Nb phase in CN-87 (containing 20% X4). A careful examination of the Cr_2Nb compositions suggest X1 essentially occupies the chromium subsites. The element X2 in CN-85 and -87 partitions strongly in the Cr_2Nb-type phase, as shown in Table 1. The element X4 was distributed roughly equal in the two phases in CN-87. The partitioning behavior of these alloying elements could not be rationalized by considering both reactivity and atomic size of the alloying elements.

TENSILE PROPERTIES

Button-type tensile specimens with gage dimensions 0.31 cm diam x 0.95 cm long were machined by electro-discharge machining, followed by grinding. The tensile specimens were polished by "0"-grade Emery paper and tested in an Instron testing machine at room temperature in air and at 1200°C in vacuum at a crosshead speed of 0.25 cm/min. Since the tensile properties are sensitive to defects in the alloys, the CN alloys at room temperature were tested using different fabrication conditions to show the defect effect. Table 2 summarizes the tensile results for CN alloys in as-cast, directionally solidified, hot-isostatically pressed (HIPped), and hot extruded conditions. Note that all the specimens were annealed 1 to 3 d at 1200°C prior to tensile testing.

The alloy Cr-5.6Nb-1.5Al-6X1 prepared by arc melting showed a fracture strength at room temperature of 143 MPa. The fracture strength increased to 294 MPa when the alloy was prepared by directional solidification via levitation-zone remelting at the University of Tennessee. The strength further increased to 399 MPa when the arc-cast material was HIPped at 1480°C at 413 MPa (60 ksi). HIPping was used to reduce cast defects in the CN alloys. The best fracture strength at room temperature was obtained for a specimen produced by hot extrusion at 1480°C, which supposedly further reduced cast defects and refined the cast microstructure in CN alloys. A fracture strength as high as 548 MPa was obtained for hot-extruded Cr-12Nb-1.5Al-6X1 (CN-80).

At 1200°C, the CN alloys exhibited significant plastic deformation in tension, with 23% elongation for CN-80, which also had excellent strength at this temperature (see Table 2). For comparison, the strength of Ni-base superalloys, the state-of-the-art high-temperature materials, drops to almost nil at 1200°C. The strength appeared to increase with the niobium

Table 2. Effect of Processing and Alloy Composition on Tensile Properties of CN Alloys

Alloy Composition	Processing*	Fracture Strength (MPa)	Yield Strength (MPa)	Elongation (%)
	Room Temperature			
Cr-5.6Nb-1.5Al-6X1	AM	143		
Cr-5.6Nb-1.5Al-6X1	DS	294		
Cr-5.6Nb-1.5Al-6X1	HIP	399		
Cr-6.0Nb-1.5Al-5X1-4X2 (CN-90)	HE	435		
Cr-12Nb-1.5Al-6X1 (CN-80)	HE	548		
	1200°C			
Cr-6.0Nb-1.5Al-5X1-4X2-2X3 (CN-90)	HE	384	302	13.4
Cr-10Nb-1.5Al-5X1-4X2 (CN-89)	HE	269	238	1.6
Cr-12Nb-1.5Al-6X1 (CN-80)	HE	388	290	23.0

*AM = arc melt; DS = directional solidification; HIP = hot isostatic pressing; HE = hot extrusion at 1480°C.

concentration (or the amount of the Cr_2Nb phase). The data suggest that alloying with 2% X3 significantly increases the strength of CN alloys at 1200°C.

The fracture mode of CN-80 was examined by scanning electron microscopy (SEM). The alloy showed a mixture of both brittle cleavage fracture and intergranular fracture at room temperature. On the other hand, it exhibited a ductile fracture with a dimple appearance at 1200°C. It is known that Cr-based alloys can be embrittled by as little as 100 ppm (or less) of nitrogen or oxygen.[12,13] In order to detect segregation of these interstitial elements in CN-alloys, CN-80 was fractured in an ultra-high vacuum and analyzed by Auger electron spectroscopy (AES). Limited analyses gave no indication of nitrogen or oxygen segregated to grain-boundary facets or cleavage planes in this alloy.

FRACTURE TOUGHNESS

The fracture toughness of CN-87 (Cr-8Nb-1.5Al-5X1-4X2-20X4) hot extruded at 1480°C was determined by three-point bend testing of Chevron-notched specimens. The alloy exhibited a fracture toughness of 7.6 MPa$\sqrt{m}$ at room temperature. The toughness increased substantially with temperature, to 18.3 and 24.4 MPa$\sqrt{m}$ at 800 and 1000°C, respectively. The alloy was so ductile at 1200°C that it could not be fractured by bend testing. The fracture toughness of CN-87 at room temperature is comparable to that of a Cr_2Hf/Cr alloy reported recently by Kumar and Miracle.[12] Figure 5 shows the crack growth modes in CN-87 at room temperature and 800°C. The alloy exhibited a mixed fracture mode at room temperature (Fig. 5a) and a more ductile fracture with Cr-rich patches necking down to a chisel point at 800°C (Fig. 5b).

Fig. 5. SEM fractographs of CN-87 hot extruded at 1480°C and fractured by bend testing at (a) room temperature and (b) 800°C.

HIGH-TEMPERATURE OXIDATION BEHAVIOR

It has been previously demonstrated[9] that the presence of significant concentrations of element X1 substantially increased the isothermal oxidation rates and spallation susceptibilities of Cr-Cr_2Nb alloys, while the addition of X2 completely offset these deleterious effects. The presence of this latter element resulted in the best overall oxidation behavior of all Cr-Cr_2Nb compositions.[9] The effects of X2 were manifested as relatively low weight gains, substantially reduced scale cracking and spallation, and elimination of the

dependence of oxidation behavior on niobium content (that is, on the relative amounts of the Cr-rich and eutectic phases). Its beneficial influence was attributed to improvement in the oxidation resistance of the Cr-rich regions (despite its partitioning to the Cr_2Nb phase),[9] which otherwise showed preferential susceptibility to degradation upon exposure to high-temperature air.[8,14] Recent work has shown that the positive effect of X2 on oxidation resistance is maintained under the more severe oxidation conditions associated with thermal cycling. This is shown by the cyclic oxidation results in Fig. 6: the alloy containing X2 (CN-87, see Table 1) showed relatively low weight gains and significantly improved spallation resistance (as characterized by the weight of spalled material) when compared to a Cr-Cr_2Nb composition containing X1 (CN-80).

Element X2 continued to impart a beneficial effect on the rate of isothermal weight gain and spallation resistance up to 1100°C, as shown by comparison of the curves for uncoated CN-80 and -87 in Fig. 7a and b, respectively. However, the oxidation rate at this temperature was still relatively high (as it is for all chromia-formers). Therefore, it was deemed necessary to examine the possibility of using coatings to reduce the oxidization at higher temperatures. To this end, some preliminary experiments were conducted by depositing a germania-doped silicide coating on CN-80 and CN-87 by pack cementation at The Ohio State University.[15] The details of the coating process for these alloys are described elsewhere.[16] In isothermal microbalance exposures in dry air, specimens coated in this manner exhibited very low weight gains at 950 and 1100°C (Fig. 7). The oxidation rate was essentially controlled by the

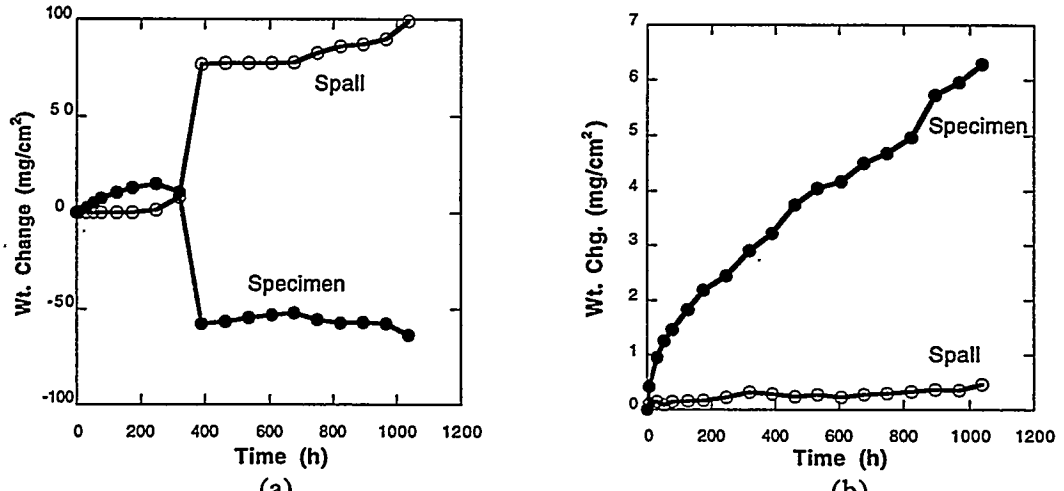

Fig. 6. Weight change versus time for specimens cyclically oxidized in air at 950°C. Each point represents one thermal cycle. Closed and open symbols represent weight changes of the specimen and spalled material, respectively. (a) CN-80 (b) CN-87

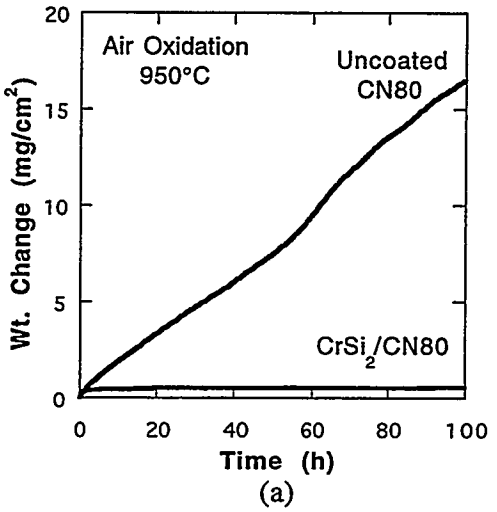

(a)

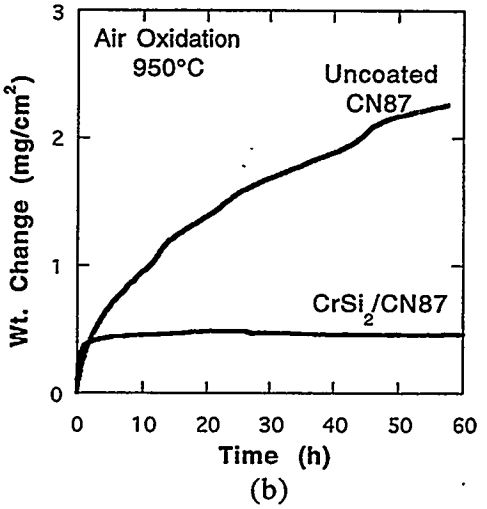

(b)

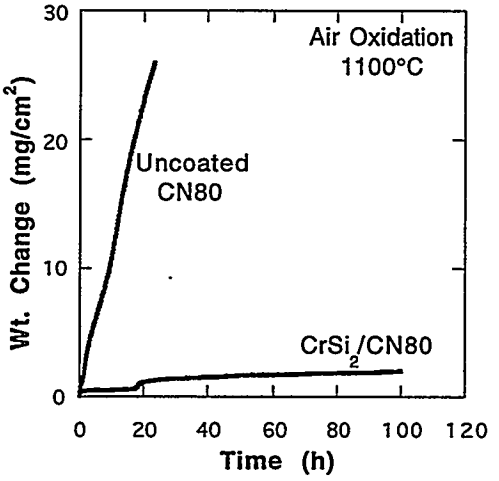

(c)

Fig. 7. Weight change versus time for coated and uncoated Cr-Cr_2Nb alloys isothermally exposed to dry, flowing air at elevated temperatures. The silicide coating was applied by a pack cementation process. (a) CN-80, 950°C. (b) CN-87, 950°C. (c) CN-80, 1100°C.

coatings as there was little difference between the 950°C gravimetric results for coated CN-80 and CN-87 (compare Fig 7a with 7b) despite the significant differences in their oxidation rates when uncoated.

While these initial results with coated Cr-Cr_2Nb are quite encouraging, particularly as the coatings have not yet been optimized for these substrates,[16] the influence of thermal stresses produced during cyclic oxidation on the integrity and adherence of these surface layers, and of the oxide scales that formed on them, must be assessed in some detail. In one microbalance experiment, the exposure was twice interrupted by cooling to room temperature with subsequent reheating to the oxidation temperature. The results, shown in Fig. 8, indicated an abrupt weight gain (probably due to cracking of the scale on the coating) after a thermal cycle, but a rapid healing of any cracks such that the same low oxidation rate was quickly reestablished. While final conclusions regarding the utility of this approach for

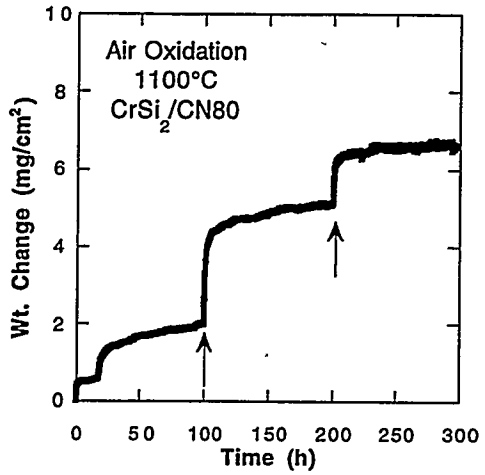

Fig. 8. Weight change versus time for silicide coated CN-80 isothermally oxidized in air at 1100°C. Arrows indicated times at which specimen was cooled to room temperature and then reheated to the exposure temperature.

corrosion protection of these alloys await more rigorous cyclic oxidation testing and coating optimization, the present results indicate that such surface treatments offer excellent promise as effective routes to oxidation resistance for temperatures (such as 1100°C) where the superior strength of Cr-Cr_2Nb alloys can be exploited.

SUMMARY AND CONCLUSIONS

Two-phase Cr-Cr_2Nb alloys (designated as CN alloys) were prepared by arc melting, followed by directional solidification, HIPping, or hot extrusion at 1450 to 1500°C. The secondary processing was used to reduce cast defect structures in CN alloys.

The microstructure of CN alloys containing 6 to 12% Nb depended strongly on alloying addition, heat treatment, and material processing. Hot extrusion at 1480°C was most effective in reducing as-cast defects and refining the cast Cr-Cr_2Nb eutectic structure.

Several beneficial alloying elements have been identified. Element X1 refined the coarse eutectic structure but reduced oxidation resistance. X2 substantially improved both isothermal and cyclic oxidation resistance. X3 strengthened CN alloys at high temperatures. X5 is used to control the morphology of the eutectic structure.

Tensile properties were sensitive to defects in CN alloys. The best results were obtained from hot-extruded CN-80 (Cr-12Nb-1.5Al-6X1) which showed a fracture strength of 548 MPa at room temperature, and an ultimate tensile strength of 388 MPa, with an elongation of 23%, at 1200°C.

The alloy CN-87 fabricated by hot extrusion at 1480°C showed a fracture toughness of 7.6 MPa$\sqrt{m}$ at room temperature. The toughness increased substantially with temperature and reached 24.4 MPa$\sqrt{m}$ at 1000°C.

A silicide coating applied by a pack cementation process substantially improved the oxidation resistance of the Cr-Cr_2Nb alloys at 950 and 1100°C. Such surface layers offer the potential to afford corrosion resistance to these alloys at temperatures (such as 1100°C) at which thermally grown oxides on CN compositions are not protective and, thus, may allow the superior strength of Cr-Cr_2Nb alloys to be exploited.

ACKNOWLEDGMENTS

The authors thank C. G. McKamey and S. J. Pawel for their reviews of the manuscript. This research was sponsored by the Fossil Energy Advanced Research and Technology Development (AR&TD) Materials Program, U. S. Department of Energy, under contract DE-AC05-84OR21400 with Martin Marietta Energy Systems, Inc.

REFERENCES

1. F. Laves, p. 124 in Theory of Alloy Phases, American Society for Metals, Metals Park, OH, 1956, .

2. D. J. Thoma and J. H. Perepezko, Mat. Sci. and Eng. **A156**, 97-108 (1992).

3. H. J. Goldschmidt and J. A. Brand, J. Less-Common Met. **3**, 44 (1961).

4. T. B. Massalski, J. L. Murray, L. H. Bennett, and H. Baker (eds.), Binary Alloy Phase Diagram, American Society for Metals, Metals Park, OH, 1986.

5. A. I. Taub and R. L. Fleischer, Science **243**, 616 (1989).

6. C. T. Liu, pp. 375-383 in *Proc. 6th Annual Conf. Fossil Energy Materials*, N. C. Cole and R. R. Judkins (comp.), U. S. Department of Energy, July 1992.

7. C. T. Liu, J. A. Horton, and C. A. Carmichael, pp. 297-307, in *Proc. 7th Annual Conf. on Fossil Energy Materials*, N. C. Cole and R. R. Judkins (comp.), U. S. Department of Energy, July 1993.

8. P. F. Tortorelli, L. J. Carsen, and J. H. DeVan, pp. 309-318 in *Proc. 7th Annual Conf. on Fossil Energy Materials*, N. C. Cole and R. R. Judkins (comp.), U. S. Department of Energy, July 1993.

9. P. F. Tortorelli and J. H. DeVan, pp. 391-400 in *Proc. 8th Annual Conf. on Fossil Energy Materials*, N. C. Cole and R. R. Judkins (comp.), U. S. Department of Energy, August 1994.

10. C. T. Liu, J. A. Horton, and C. A. Carmichael, pp. 377-390 in *Proc. 8th Annual Conf. on Fossil Energy Materials*, N. C. Cole and R. R. Judkins (comp.), U. S. Department of Energy, August 1994..

11. M. Takeyama and C. T. Liu, Mat. Sci. and Eng. **A132**, 61 (1991).

12. K. S. Kumar and D. B. Miracle, Intermetallics **2**, 257-274 (1994).

13. H. L. Wain, F. Henderson, S.T.M. Jonstone, J. Inst. Met. **83**, 1954-55 (1993).

14. P. F. Tortorelli and J. H. DeVan, "The Nature of Scales Grown on Binary Cr-Nb Alloys," pp. 229-236 in *Proc. Symp. on Oxide Films on Metals and Alloys*, B. R. MacDougall, R. S. Alwitt, and T. A. Ramanarayanan (eds.), Proceedings Vol. 92-22, The Electrochemical Society, 1992.

15. M. A. Harper and R. A. Rapp, pp. 379-86 in Heat Resistant Materials, K. Natesan and D. J. Tillack, (eds.), ASM International, Materials Park, OH, 1991.

16. Y-R. He and R. A. Rapp, "Pack Cementation Cr-Al Coating of Steels and Ge-Doped Silicide Coating of Cr-Nb Alloy," these proceedings.

INVESTIGATION OF AUSTENITIC ALLOYS FOR ADVANCED HEAT RECOVERY AND HOT GAS CLEANUP SYSTEMS

R. W. Swindeman and W. Ren

Oak Ridge National Laboratory
P. O. Box 2008
Oak Ridge, TN 37831-6155

ABSTRACT

Alloys for design and construction of structural components needed to contain process streams and provide internal structures in advanced heat recovery and hot gas cleanup systems were examined. Emphasis was placed on high-strength, corrosion-resistant alloys for service at temperatures above 1000°F (540°C). Data were collected that related to fabrication, joining, corrosion protection, and failure criteria. Alloys systems include modified type 310 and 20Cr-25Ni-Nb steels and sulfidation-resistance alloys HR120 and HR160. Types of testing include creep, stress-rupture, creep crack growth, fatigue, and post-exposure short-time tensile. Because of the interest in relatively inexpensive alloys for high temperature service, a modified type 310 stainless steel was developed with a target strength of twice that for standard type 310 stainless steel.*

INTRODUCTION

The objective of the research on austenitic alloys is to provide databases and design criteria that will assist contractors in selecting optimum alloys for construction of components needed to contain process streams in advanced heat recovery and hot gas cleanup systems. Typical components include: steam line piping and superheater tubing for low emission boilers (600 to 700°C), heat exchanger tubing for topping cycle systems (650 to 800°C), foil materials for recuperators on advanced turbine systems (700 to 750°C), heat exchanger tubing for pulsed combustors (650 to 950°C), and tubesheets, plenums, and liners for hot gas cleanup systems (850 to 1000°C). The near term objective is to gather data that will permit the consideration of a modified

* Research sponsored by the U.S. Department of Energy, Office of Fossil Energy, Advanced Research and Technology Development Materials Program {DOE/FE AA 15 10 10 0, Work Breakdown Structure element ORNL-2(B)] under contract DE-AC05-84OR21400 with Martin Marietta Energy Systems, Inc.

310 stainless steel and a modified 20Cr-25Ni-Nb stainless steel for applications to 925° C in oxidizing environments or to 870° C slightly sulfidizing environments. Planned future work includes the collection of data that will permit the consideration of aluminide clad stainless steels for applications to 1000° C in sulfidizing environments.

BACKGROUND

In the United States, new power generation needs are being met by the use of co-generation and the installation of medium-size gas turbines. Research in the fossil power industry is largely focused on condition assessment and the repair of aging components. Research related to inspection, damage assessment, and repair is actively supported by fossil power and petrochemical industries. In both industries, replacement of components with "new² and "advanced² materials is sometimes required, and research on the performance of the advanced materials for such components is in progress. Development of advanced materials for the fossil power industry is largely performed in Japan under sponsorship of the Electric Power Research Institute (1). Alloys such as tungsten-vanadium-modified 2 1/4 Cr, 9Cr, and 12Cr steels have reached ASME Code status. These steels are candidates for the construction of piping, headers, and tubing in the low emission boiler (LEB) project (2). More research is needed before the complex metallurgical constitution of these alloys is fully understood. Austenitic stainless steels for service to higher temperatures in the fossil power industry include niobium-modified 310 stainless steel (3) and titanium-zirconium-modified 20Cr-25Ni-Nb stainless steel (4). Both of these alloys are intended for superheater tubing, and service temperatures are limited to approximately 730° C. Both steels are candidates for heat exchanger tubing in the LEB and the advanced topping cycle. For higher temperature service in the petrochemical industry, a commercial modified alloy 800 has been developed (5), and, for sulfidation resistance, a commercial cobalt-bearing alloy has been produced (6). Both alloys are "new² and much has to be learned about their high temperature performance. Three commercial stainless steels that have been used in the construction of components in advanced fossil energy systems include type 310S stainless steel, a silicon-aluminum modified steel, and a rare earth modified steel. Compositions are listed in Table 1. A careful review of the performance and costs of the materials indicated that there was a need for an additional material. A modified 310 stainless steel having strength equivalent to alloy 800H would have applications above 800° C (7).

Table 1. Typical Compositions of High Temperature Austenitic Alloys (wt%)

ELEMENT	310HCbN	NF-709	HR-120	HR-160	RA85H	253MA
Fe	Balance	Balance	36	4	Balance	Balance
Ni	20	25	37	Balance	14.5	11
Cr	25	20	25	28	18.5	21
Co				30		
C	0.05	0.07	0.05	0.05	0.2	0.08
Si	0.5	0.5	0.6	2.8	3.5	1.7
Mn	1.6	1	0.7	0.5	0.8	0.6
Nb	0.4	0.25	0.7			
Mo		1.5				
N	0.25	0.18	0.2			0.17
Al			0.1		1.0	
Ti		0.06	0.1			
B		0.004	0.004			
Rare earth						0.04

Notes: NF-709 is a trademark of Nippon Steel Corporation, HR-160 and HR-120 are registered trademarks of Haynes Alloys, International, RA85H is a registered trademark of Rolled Alloys, Inc., and 253MA is a registered trademark of AVESTA AB.

EXPERIMENTAL WORK ON MODIFIED 310 STAINLESS STEEL

Commercial alloys were obtained from alloy suppliers, and small heats of experimental alloys were purchased from various sources. Products were fabricated into convenient forms (plates and sheets) for weldability studies, mechanical testing, and corrosion testing. Short-time tensile and stress-rupture testing was used to establish optimum solution treating conditions, and longer creep and stress-rupture testing was performed in the temperature range of interest for the alloys.

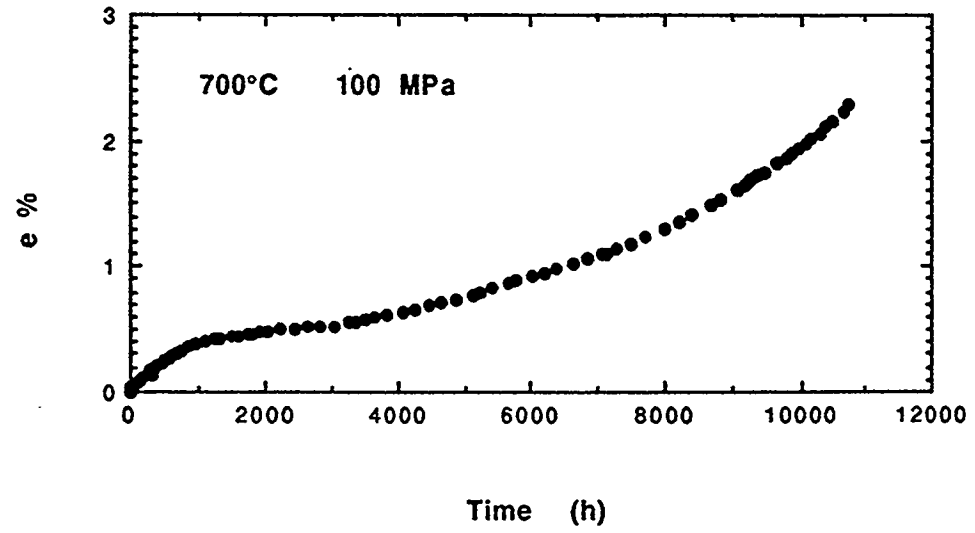

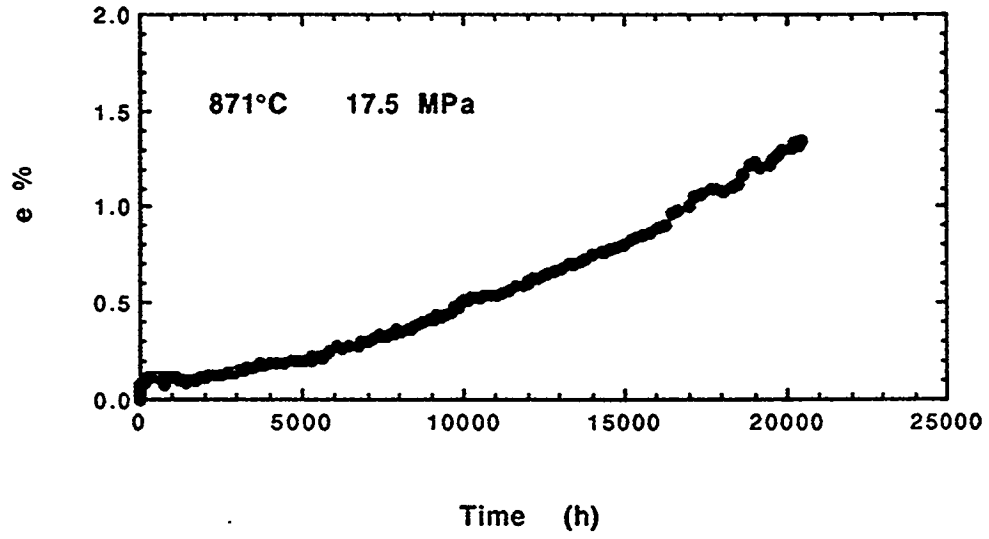

Fig. 1. The 310TaN stainless steel exhibits very little primary creep at all temperatures.

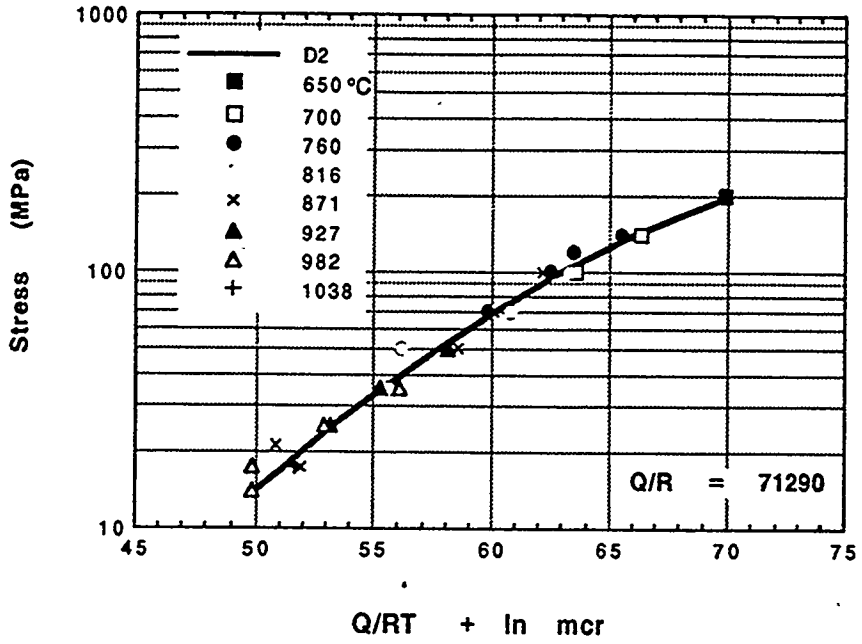

Fig. 2. Parametric analysis of MCR data produced an activation energy near 144 Kcal and a stress exponent near 5.

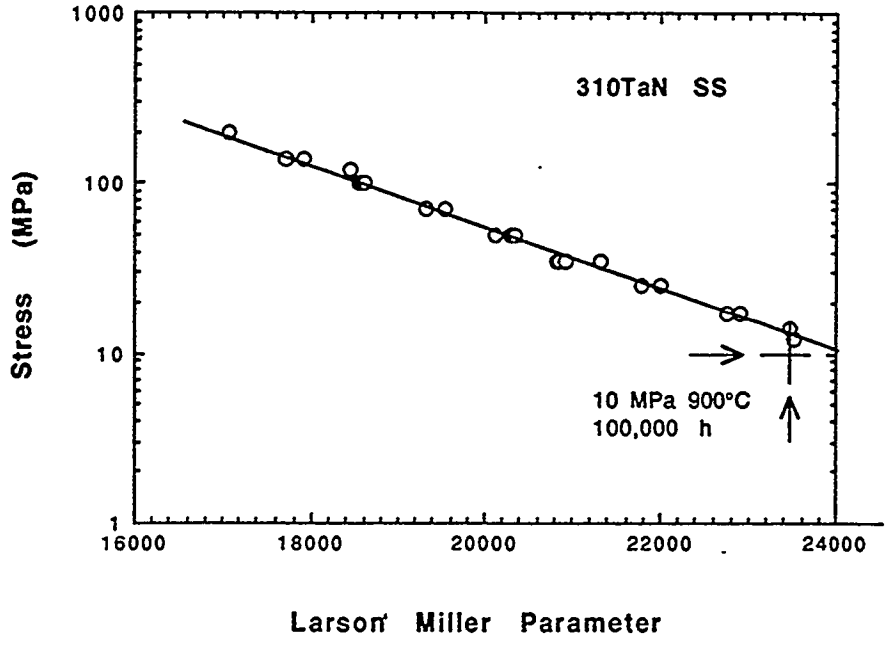

Fig. 3. Parametric analysis of rupture data to 10,000 h suggests that the target strength can be achieved.

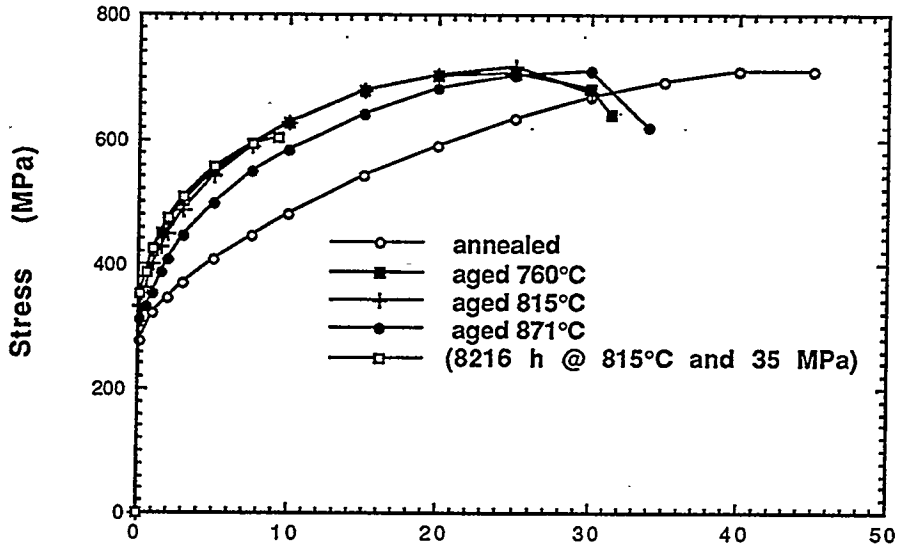

Fig. 4. Aging for 1000 hours produces a reduction of ductility in 310TaN stainless steel.

For modified 310 stainless steel it was found that an anneal at 1200° C produced the best creep-rupture strength for temperatures above 800° C. Creep curves to time beyond 10,000 hours indicated relatively stable behavior, as shown the creep curves plotted in Fig. 1. The minimum creep rates determined from tests in the temperature range of 650 to 1038° C were correlated on the basis of a constant activation energy near 144 kcal/mole. The trend is shown in Fig. 2. Larson-miller parametric analysis of the stress-rupture data for the modified 310 stainless steel indicated that a single parametric constant near 15 correlated rupture data over a broad range of temperatures and times, as shown in Fig. 3. Analysis further indicated that the target strength of 10 MPa for 100,000 h at 900° C could be achieved. Tensile and bend tests were performed on aged specimens. Room temperature tensile stress versus strain curves for aged specimens were compared to unaged material in Fig. 4. It was observed that 1000 h of aging reduced the ductility of modified 310 stainless steel by 30 per cent.

DESIGN CRITERIA FOR VERY HIGH TEMPERATURES

Components in several advanced fossil energy systems are expected to experience very high temperatures, and the potential for creep damage, fatigue, thermal-fatigue, and creep-fatigue crack growth are significant. Issues that are of concern include the proper selection of design margins on life. To some extent, design engineers rely on construction codes such as those developed by the

American Petroleum Institute or the American Society of Mechanical Engineers. However, several of the candidate materials for components are not code-approved materials, and, even for the code-approved materials, data for design at very high temperatures are often lacking. For these reasons, exploratory research on creep, creep-fatigue, fatigue, and crack growth of several candidate alloys has been in progress (8,9).

Early work involved studies of alloy 333 and 556, which were candidates for used in pressurized fluidized bed (PFBC) hot gas cleanup systems. More recently alloy 160 has been investigated. Techniques for creep- and fatigue-crack growth measurements were developed for temperatures to 950°C, and experiments were performed on alloy 160. Tensile and creep tests were included on base metal and weld metal.

PUBLICATIONS

1. M. Ohgami, et al., "Mechanical Properties of 9Cr-0.5Mo-1.8W Steel Tubes Exposed in a Fossil Power Plant, paper presented at the International Symposium on Improved Technology for Fossil Power Plants-New & Retrofit Applications, March 1-3, 1993, Washington, D.C.

2. D. Sopocy, et al., "Using the State of the Art Power Plant SOAPP Workstation for Planning and Conceptual Design, paper presented at the International Symposium on Improved Technology for Fossil Power Plants-New & Retrofit Applications, March 1-3, 1993, Washington, D.C.

3. K. Yoshikawa, et al., Development of New Boiler Tubes with High Elevated Temperature Strength and Corrosion Resistance,² paper 5-167, First International Conference on Improved Coal Fired Power Plants, EPRI publication CS-5581-SR, Electric Power Research Institute, Palo Alto, California, 1988.

4. T. Takahashi, el al., Development of a High Strength 25Ni-20Cr Steel for Tubes in Ultra Supercritical Power Boilers,² paper 41-1 in Second International Conference on Improved Coal Fired Power Plants, EPRI publication GS-6422, Electric Power Research Institute, Palo Alto, California, 1989.

5. S. C. Ernst and G. Y. Lai, "A New High Strength Fe-Ni-Cr-Nb-N Alloy for Elevated Temperature Applications,² pp. 115-121 in Heat Resistant Materials, ASM International, Materials Park, Ohio, 1991.

6. C. M. Anthony, S. K. Srivastava, and G. Y. Lai, pp. 667-73 in Heat Resistant Materials, ASM International, Materials Park, Ohio, 1991.

7. R. W. Swindeman, The Potential of Modified Type 310 Stainless Steel for Advanced Fossil Energy Applications, ORNL-TM-12057, Oak Ridge National Laboratory, Oak Ridge, TN March, 1992 .

8. R. W. Swindeman and D. L. Marriott, "Criteria for Design with Structural Materials in Combined-Cycle Applications above 815°C,² J. Engineering for Gas Turbines and Power, **116**, 352-59 April, 1994 .

9. W. Ren, et al., Creep and Creep Crack Propagation Behavior of Haynes HR160 Superalloy, Final Report for SURA/ORAU/ORNL 1994 Summer Cooperative Program, October , 1994.

FIRESIDE CORROSION TESTING OF CANDIDATE SUPERHEATER TUBE ALLOYS, COATINGS, AND CLADDINGS - PHASE II

J. L. Blough
M. T. Krawchuk
S. F. Van Weele

Foster Wheeler Development Corporation
12 Peach Tree Hill Road
Livingston, NJ 07039

ABSTRACT

A number of developmental and commercial tubing alloys and claddings have previously been exposed in Phase I to laboratory fireside corrosion testing simulating a superheater or reheater in a coal-fired boiler. This program is exposing samples of TP 347, RA-85H, HR-3C, 253MA, Fe_3Al + 5Cr, 310 modified, NF-709, 690 clad, and 671 clad, which showed good corrosion resistance from Phase I, to the actual operating conditions of a 250-MW, coal-fired boiler. The samples were installed on air-cooled, retractable corrosion probes, installed in the reheater cavity, and are being controlled to the operating metal temperatures of an existing and advanced-cycle coal-fired boiler. The exposure will continue for 4000, 12,000, and 16,000 hours of operation. After the three exposure times, the samples will be metallurgically examined to determine the wastage rates and mode of attack.

The probes were commissioned November 16, 1994. The temperatures are being recorded every 15 minutes, and the weighted average temperature calculated for each sample. Each of the alloys is being exposed to a temperature in each of two temperature bands—1150 to 1260°F and 1260 to 1325°F. After 2000 hours of exposure, one of the corrosion probes was cleaned and the wall thicknesses were ultrasonically measured. The alloy performance from the field probes will be discussed.

INTRODUCTION

High-temperature fireside metal wastage in conventional coal-fired steam generators can be caused by gas-phase oxidation or liquid-phase coal-ash corrosion. Gas-phase oxidation is usually not a problem if tube and support materials are selected for their oxidation resistance at operating temperatures and for spalling, flaking, or other reactions to their environment. Coal-ash corrosion, on the other hand, usually results in accelerated attack and rapid metal wastage—even of stainless steels. The cause of this type of corrosion is generally accepted as the presence of liquid sulfates on the surface of the metal beneath an overlying ash deposit[1-4].

While substantial progress has been achieved through laboratory testing, actual utility service exposures are evidently necessary to verify any conclusions drawn from laboratory testing. A number

of important environmental parameters cannot be fully simulated in the laboratory[5]:

- The actual composition of the deposits formed on the tubes is more complex than the composition of the simulated ash.
- The SO_3, formed by heterogeneous reaction on cooled surfaces, is variable.
- Very large temperature gradients occur within the ash deposits.
- The ash and fuel gas move past tubes at high velocity; the rate varies with design.
- The composition of the corrosive deposits changes with time.
- Metal and flue gas temperatures fluctuate.
- Fly-ash erosion removes the protective oxides, exposing a clean surface to fresh ash.

Foster Wheeler Development Corporation (FWDC) has performed a number of literature reviews and recent updates discussing the variables affecting the corrosion mechanism[6-8]. Additionally, Foster Wheeler is conducting two sizable research projects—one a laboratory and in situ field testing at three utilities of commercially available alloys[5,9-14] and this program (ORNL-FW2), combining laboratory and field testing to more completely cover the controlling variables for a longer duration[10].

PHASE I RESULTS

In Phase I of this ORNL program, "Fireside Corrosion Testing of Candidate Superheater Tube Alloys, Coatings, and Claddings," 20 commercial and developmental alloys were evaluated[10]. The coupons of the metals were exposed to synthetic coal ash and synthetic flue gases at 650 and 700°C (1202 and 1292°F) for up to 800 hours.

Chromium content was found to be the largest factor in determining the resistance of an alloy to liquid coal-ash corrosion. For stainless steels and nickel alloys, additions of chromium up to 25 percent provide increased resistance to coal-ash attack; however, above the 25-percent chromium level, there appears to be minimal benefit from more chromium, possibly because of the higher nickel content of those alloys. Silicon and aluminum were also beneficial, but to a lesser extent. The iron aluminide intermetallics also show a chromium dependence. Aluminides containing 5-percent chromium performed markedly better overall than those containing 2-percent chromium. The more resistant alloys show lower corrosion rates at longer exposure times, indicating the formation of a passive layer; the less-resistant alloys exhibit increasing corrosion rates at longer exposures. Lower-chromium alloys generally suffered greater wastage rates at the higher testing temperature [700°C (1292°F)], while higher-chromium alloys suffered the same amount of wastage at 650 (1202) as at 700°C (1292°F).

Both the alkali content in the ash and SO_2 concentration in the flue gas affect the corrosivity of the alkali-iron trisulfates in the ash layer. An increase in either resulted in a more corrosive environment and higher wastage rates.

PHASE II CORROSION PROBE TESTING

In this project, the field tests will comprise corrosion probe testing, coal characterization, and deposit analysis. The coals and their deposits, which are formed on the tube surfaces, will be analyzed to provide fuel characterization, a deposit analysis data bank, and possibly a corrosivity index for predicting corrosivity under various combustion conditions. The equipment and the procedures for this phase have been previously used and perfected at three different utilities for over 3 years of in situ testing at each station.

The utility for test exposures should be burning an aggressive fuel to adequately evaluate the candidate alloys. The coal being burned at Tennessee Valley Authority's (TVA's) Gallatin Station had been previously analyzed, and numerous corrosion indices predicted high corrosivity in addition to the fact that installed T22 and Type 304SS tubing experienced about 7 years of life in the superheaters and reheaters of Units 1 and 2.

Selection of Materials for Corrosion Probes

FWDC laboratory-tested 20 different materials[10]. Because this quantity was impractical from both an economic and a probe-length standpoint, fewer (the nine listed in Table 1) had to be selected for the field tests. These materials provide a range of compositions and cost for both the commercially available and developmental alloys and claddings.

Field Corrosion Probe Design

The corrosion probes were designed to provide realistic exposures of metal samples to both actual boiler environments and also at the higher anticipated metal temperatures of an advanced plant. The parameters are independence from the main boiler, removal without a boiler outage, and a fail-safe design, one that removes the probe from the boiler if there are any malfunctions. With these features, years of testing will not be compromised with a sudden system overheating.

The probes will be exposed for 4000, 12,000, and 16,000 hours. This will be accomplished by utilizing two probe test locations. At one test location, the probe will be exposed for 16,000 hours. At

Table 1. Chemical Composition of Candidate Alloys (%)

Alloy	Cr	Ni	Others
Type 347	17-19	9-13	(Nb + Ta) = 10 × C (min.)
85 H	18	15	Al = 1, Si = 3.9
NF 709	20	25	Mo = 1.5, Mn = 1.0, Si = 0.6
690 Clad	30	58	
671 Clad	48	52	
Fe_3Al + 5% Cr	5	---	Al = 17
HR-3C	25	20	Nb = 0.4
253 MA	21	11	Si = 1.7
Modified 310	25	20	Modified

the other test location, the probe will be removed after 4000 hours and a new probe inserted for the remaining 12,000 hours.

Each probe is a 2.56-m (8.4-ft)-long, 60.20-mm (2.37-in.)-OD tube that extends into the furnace for approximately 2.3 m (7.6 ft). Ring samples [38.1 mm (1.5 in.) wide] of the candidate alloys listed in Table 1 were installed at the end of the probe farthest from the furnace wall. The probe is cooled by air that flows in the annular region between the probe tube ID and the tapered inner tube OD. The tapered inner tube was designed to obtain two bands of temperature on the outer surface of the samples. The alloy samples were duplicated in such a manner as to expose each alloy to a temperature in each of the temperature bands [621 to 677°C (1150 to 1250°F) and 677 to 727°C (1250 to 1340°F)].

Each probe has a retraction mechanism, and three K-type thermocouples in duplicate to monitor the mean tube wall at the beginning and end of each test section group. A 19.95-mm (3/4-in.) O.D. thermowell with sheathed thermocouple was mounted between the corrosion probes to measure flue gas temperature. Each probe has its own cooling-air control valve.

The control system monitors the selected control thermocouple and modulates the airflow to maintain an average surface metal temperature for each temperature band. The probes retract automatically if failure of the cooling-air supply system or any other malfunction (instrument signal, power failure, or computer failure) causes the probe temperature to exceed the set limit of 746°C (1375°F) for 2 minutes. FWDC personnel access the field computer automatically for probe status and temperature data each morning at 6 a.m. or manually through its modem.

The locations in this plant (shown in Figure 1) were chosen because of cavity access and because they best represent the locations for the reheater or superheater outlet on the "Advanced Cycle" unit.

The ideal coal-ash corrosion probe exposure is if only one coal is being burned at the plant. This practice is not common at many utilities; in fact, many are buying coal on the spot market. Gallatin burns a number of eastern high-sulfur coals, mainly Island Creek, Warrior, Dotiri, and Pattiki, which are known to be corrosive and prone to alkali-iron-trisulfate formation. The Borio Index for these coals typically range from 2.0 to 4.1, and the chloride level is 450 to 3000 ppm.

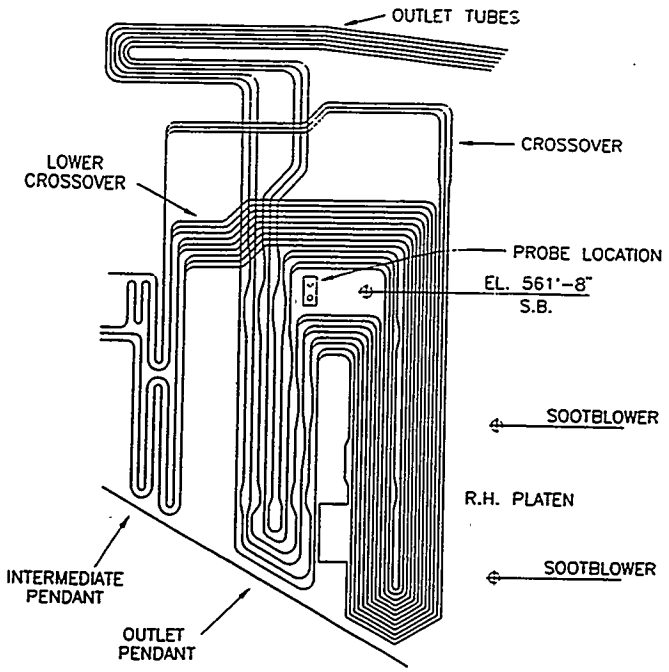

Fig. 1. Side elevation of reheater at TVA Gallatin Unit 2

Post-Exposure Analysis

Quarterly Examinations

During the quarterly inspections, FWDC personnel at the site will manually retract the probes, selectively remove deposits, and make ultrasonic wall thickness measurements on the "A" samples of the probe set.* The "B" probe will be left untouched at this time. The quarterly inspections will

*To aid in describing the operations, "A" (inspected quarterly) and "B" (untouched) have been assigned to the two probes in a set. The operations will be performed on the "A" or "B" probes in each 4000-, 12,000-, and 16,000-hour-exposure set.

provide preliminary nondestructive corrosion data before the three destructive examinations. With these data, corrosion can be tracked, and a total loss of data can be avoided if there is a catastrophic failure. The automatic retraction feature, if cooling air is lost and test specimen temperatures become excessive, minimizes the possibility of such a catastrophic failure.

The laboratory analysis of the removed deposits at FWDC will characterize the composition and determine whether alkali sulfates are present and aid in interpreting the effect of fuel changes on coal-ash corrosion.

Destructive Testing

At 4000, 12,000, and 16,000 hours, probes (A-1," "A-2," and "B" respectively) will be removed and sent to FWDC for metallurgical evaluation, which includes:

- Visual examination and selective photographic documentation
- Selective removal of deposits
- Disassembly of probes
- Cutting of two transverse sections through the center of the ring sample
- Light grit blasting and NaOH cleaning of one transverse ring section of each sample
- Visual examination of the cleaned samples
- Wall thickness measurements at 45-deg points or maximum loss areas on the leading 180-deg side of cleaned transverse ring from each alloy
- Mounting of the uncleaned ring samples to analyze the scale/deposit
- Microscopic measurement of the penetration and calculation of total metal loss
- Selective SEM/EDX examination to analyze corrosion mechanism.

Exposure Results to Date

The 4000- and 16,000-hour corrosion probes continued to be exposed in the reheater cavity of the TVA Gallatin Station Unit 2. The temperature plots for March are shown in Figure 2. The upper curve is the flue gas temperature [average 807°C (1484°F)] measured by a separate thermowall. The lower two bands are the mean wall thermocouples at the beginning and end of each test section in the two probes. The nine alloys listed in Table 1 are contained in each test section. The weighted average temperature is calculated for each test section in each of the two probes and is shown in Table 2.

On March 8, 1995, the probes were pulled for maintenance and ultrasonic inspection of the 4000-hour probe. On each ring the measurements were taken at two cleaned locations of approximately 10:00 and 2:00 with the oncoming flue gas at 12:00. Thickness losses were calculated, and the range of wall loss is given in Table 3. These thickness losses were obtained from an ultrasonic

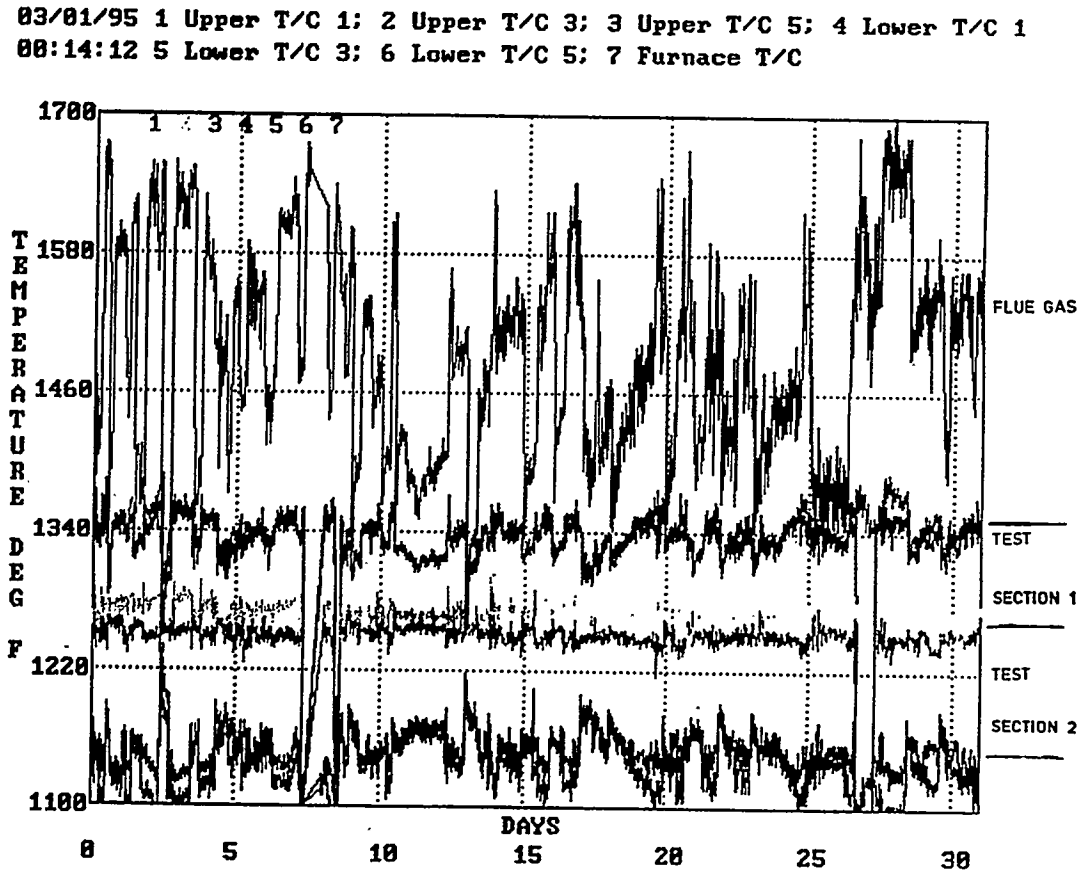

Fig. 2. Temperature profile, March 1995.

Table 2. Average Exposure Temperature

Test Section	4000-Hour Probe [°C (°F)]	16,000-Hour Probe [°C (°F)]
1	726-683 (1339-1261)	723-678 (1334-1252)
2	683-618 (1261-1144)	678-619 (1252-1147)

reading and, therefore, should be taken as only relative values. They do not include any internal penetration measurements and are not as accurate as micrometer and microscopic examination. Figure 3 shows the two probes in the retracted position. The nearby soot blower can be seen to the right of the corrosion probes. The 4000-hour probe was carefully cleaned (as shown in Figure 4) with a wire wheel and/or sanding disk to remove the deposit and scale without removing any metal.

The thickness losses for each alloy are generally higher, as would be expected, in the hotter Section 1 samples vs. the Section 2 sample. There are some exceptions, but these results are only interim ultrasonic measurements.

Table 3. Ultrasonic Measurement Results (mils)

Material	Test Section 1 Thickness Loss	Test Section 2 Thickness Loss
800HT	1-4	
800HT	0-6	0-3
85H	0-4	0-2
347	0-2	0-6
NF709	0	0-5
253MA	4-5	2-6
671	6-14	8-9
690	0	0-5
Fe_3Al	0	0
310	0-2	0-4
800HT	0-5	0
800HT		0

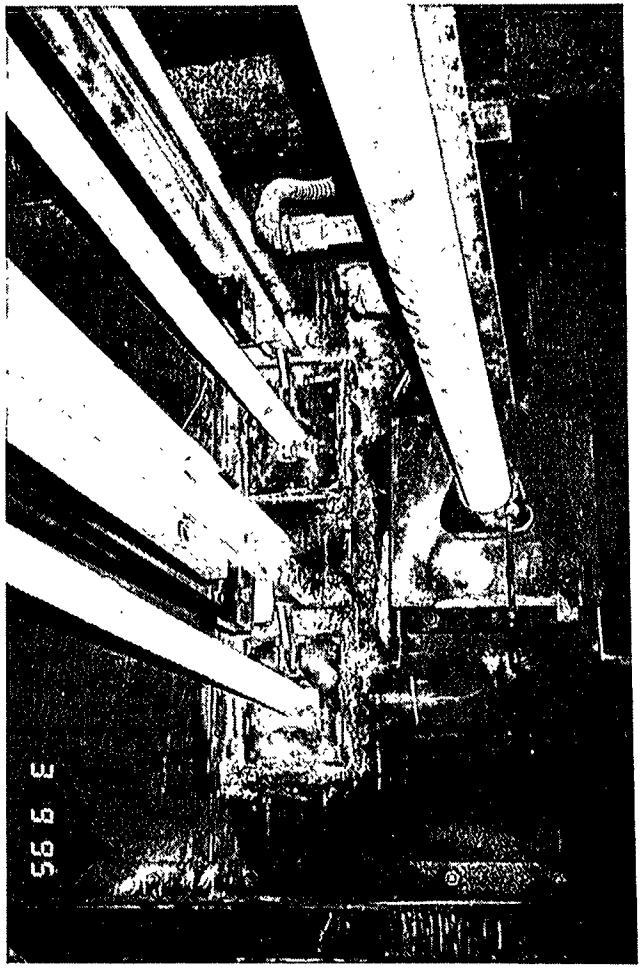

Fig. 3. Corrosion probe in retracted position.

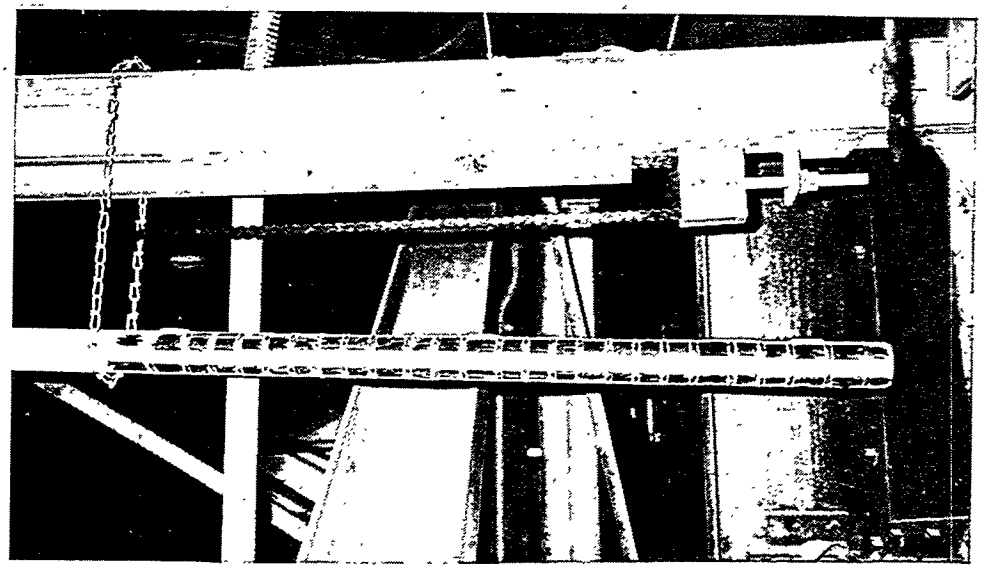

Fig. 4. Cleaned 4000-hour probe.

There was quite a variation in the thickness readings and, therefore, no elemental dependency could be determined. The stability of the readings on the 671 sample was a problem, but there was a consistently higher loss than would have been expected from the previous lab data.

Again, these ultrasonic readings every 2000 hours are a check on the status of the alloys and determine relative losses, not absolute measurements which can only be done when microscopic examination for penetration is performed.

CONCLUSIONS

The air-cooled retractable corrosion probes are working successfully and are providing exposure of each of the nine alloys to two different temperatures. The ultrasonic readings indicate that the exposure at the TVA Gallatin Unit 2 is aggressive.

Future metallographic and corrosion deposit analyses will verify the wastage rates and corrosive attack mechanisms (i.e., coal ash, erosion-assisted oxidation, etc.).

REFERENCES

1. W. Nelson and C. Cain, Jr., "Corrosion of Superheaters and Reheaters of Pulverized-Coal-Fired Boilers," *Transactions of the ASME, Journal of Engineering for Power,* July 1960, pp. 194-204.

2. W. T. Reid, "Formation of Alkali Iron Trisulphates and Other Compounds Causing Corrosion in Boilers and Gas Turbines," Project Review July 1, 1966-June 30, 1968, prepared by Battelle Memorial Institute, Columbus, OH, June 1968.

3. W. T. Reid, *External Corrosion and Deposits: Boilers and Gas Turbines,* American Elsevier Publishing Company, New York, 1974.

4. G. J. Hills, "Corrosion of Metals by Molten Salts," *Proceedings of the Marchwood Conference: Mechanism of Corrosion by Fuel Impurities,* Johnson and Littler, eds., Butterworths, London, 1963.

5. J. L. Blough, G. J. Stanko, M. Krawchuk, W. Wolowodiuk, and W. Bakker, "In Situ Coal Ash Corrosion Testing for 2 Years at Three Utilities," International EPRI Conference on Improved Technology for Fossil Power Plants New and Retrofit Applications, Washington, DC, March 1-3, 1993.

6. I. M. Rehn, "Fireside Corrosion of Superheater and Reheater Tubes," Palo Alto, CA: Electric Power Research Institute, 1980. CS-1653.

7. I. M. Rehn, "Fireside Corrosion of Superheater Alloys for Advanced Cycle Steam Plants," Palo Alto, CA: Electric Power Research Institute, 1987. EPRI 5195.

8. S. Van Weele and J. L. Blough, "Literature Search Update—Fireside Corrosion Testing of Candidate Superheater Tube Alloys, Coatings, and Claddings," Livingston, NJ: Foster Wheeler Development Corporation, September 1990. FWC/FWDC/TR-90-11.

9. W. Wolowodiuk, S. Kihara, and K. Nakagawa, "Laboratory Coal Ash Corrosion Tests," Palo Alto, CA: Electric Power Research Institute, July 1989. GS-6449.

10. S. Van Weele and J. L. Blough, "Fireside Corrosion Testing of Candidate Superheater, Tube Alloys, Coatings, and Claddings," Livingston, NJ: Foster Wheeler Development Corporation, August 1991. ORNL/SUB/89-SA187/02.

11. S. Kihara, K. Nakagawa, A. Ohtomo, H. Aoki, and S. Ando, "Simulating Test Results for Fireside Corrosion of Superheater & Reheater Tubes Operating at Advanced Steam Conditions in Coal-Fired Boilers, *High Temperature Corrosion in Energy Systems,* TMS/AIME, M. F. Rothman, ed., 1984, pp. 361-376.

12. W. Wolowodiuk, et al., "Coal-Ash Corrosion Investigations," *Proceedings of the First International Conference on Improved Coal-Fired Power Plants.* Palo Alto, CA: Electric Power Research Institute, November 1986.

13. J. L. Blough, M. T. Krawchuk, G. J. Stanko, and W. Wolowodiuk, "Superheater Corrosion Field Test Results," Palo Alto, CA: Electric Power Research Institute, November 1993. TR-103438.

14. J. L. Blough and W. T. Bakker, "Measurement of Superheater Corrosion Caused by Molten Alkali Sulfates," First International Conference on Heat-Resistant Materials, to be presented at the ASM International, Lake Geneva, WI, September 22-26, 1991.

15. T. Hammond, W. Wolowodiuk, J. L. Blough, J. Brooks, "Replacement of Reheater at TVA's Gallatin Station Unit 2," presented at the Third International Conference on Improved Coal-Fired Power Plants (ICPP), San Francisco, April 1991.

16. R. W. Borio and R. P. Hensel, "Coal-Ash Composition as Related to High-Temperature Fireside Corrosion and Sulfur-Oxides Emission Control," *Transactions of the ASME, Journal of Engineering for Power,* Vol. 94, 1972, pp. 142-148.

A NOVEL CARBON FIBER BASED POROUS CARBON MONOLITH

T. D. Burchell, J. W. Klett, and C. E. Weaver

Oak Ridge National Laboratory
P.O. Box 2008
Oak Ridge, Tennessee 37831-6088

ABSTRACT

A novel porous carbon material based on carbon fibers has been developed. The material, when activated, develops a significant micro- or mesopore volume dependent upon the carbon fiber type utilized (isotropic pitch or polyacrylonitrile). The materials will find applications in the field of fluid separations or aa a catalyst support. Here, the manufacture and characterization of our porous carbon monoliths are described.

INTRODUCTION

A novel adsorbent carbon composite material has been developed[1,2] comprising carbon fibers and a binder. The material, called carbon fiber composite molecular sieve (CFCMS), was developed through a joint research program between Oak Ridge National Laboratory (ORNL) and the University of Kentucky, Center for Applied Energy Research (UKCAER).

The materials are manufactured from milled carbon fibers and powdered phenolic resin, which are slurried in water and vacuum molded. The molding process allows the manufacture of slabs, tubes or more complex geometries with contoured surfaces. The "green" (as molded) artifact is heated at 130°C to cure the phenolic resin and then carbonized at 650°C. The resultant monoliths have bulk densities in the range 0.2 - 0.4 g/cm^3 and crush strength of 1 - 2 MPa. Two carbon fiber types have been utilized in our work to date. First, petroleum-pitch derived isotropic carbon fibers have been fabricated into monoliths and activated in steam or CO_2 at 850°C. The material develops significant microporosity, with mean pore sizes in the range 0.5 - 1.0 nm, and micropore volumes in the range 0.2 - 0.5 cm^3/g. Second, monoliths have been manufactured from polyacrylonitrile (PAN) derived carbon fibers. These materials develop significant mesoporosity in the size range 2-50 nm and mesopore volumes typically exceeding 0.5 cm^3/g, making them potential catalyst support materials. In both cases the composites are strong and porous, allowing fluids to easily flow through the material.

The isotropic pitch derived carbon fiber porous carbon monolith, when activated, provides a high micropore surface area (> 1900 m^2/g) capable of rapid adsorption and desorption. The activated fiber micropore distribution is very narrow, with mean micropore sizes < 1 nm, allowing molecular sieving on the basis of molecular size and shape. A potentially large application for our carbon-fiber based porous monoliths is gas separation using the Pressure Swing Adsorption (PSA) process.

Separation by adsorption is based on the selective accumulation of one or more components of a gas mixture on the surface of a microporous solid. When a gaseous mixture is exposed to an absorbent for sufficient time, an equilibrium is established between the adsorbed phase and the gas phase. The gas phase becomes richer in the less selectively adsorbed component. The attractive forces responsible for adsorption

are of the Van der Waals type. Desorption can be achieved either by increasing the temperature of the system or by reducing the adsorbate pressure. The desorption step also regenerates the adsorbent surface for reuse during the subsequent adsorption step. Thus, the adsorptive separation process consists of a cyclic sequence of adsorption and desorption steps. When desorption is achieved by decreasing the pressure, the process is called pressure swing adsorption. One of the components of a gas mixture is selectively adsorbed at higher partial pressure and desorbed subsequently by lowering the partial pressure. The change in partial pressure of the component gas can be caused either by decreasing the total pressure, changing the composition of the gaseous mixture, or by a combination of both.

Here we report the synthesis and characterization of CFCMS material, particularly with respect to micropore and mesopore structure. Moreover, the results of CO_2 uptake studies on microporous monoliths are reported.

EXPERIMENTAL

Nitrogen adsorption isotherms were measured at 77 K using our Autosorb-1 instrument. Micropore size analysis used a variety of methods, including the Brunauer, Emmett and Teller[3] (BET) method for surface area and the Dubinin-Redushkevich (DR) method for micropore volume and micropore size. Additional micropore size estimates were obtained using the Horvath-Kawazoe (HK) and Dubinin-Astakhov (DA) methods. Mesopore (2-50 nm) and macropore (>50 nm) size, area, and volume data were obtained using a Micromeritics Autopore II mercury intrusion apparatus. Intrusion measurements were performed over the pressure range vacuum (~10μm Hg) to 90,000 psia. Equilibration times of 10 and 60 seconds were used for the low and high pressure measurements, respectively. CFCMS materials were subjected to microstructural examination using an ISI SS40 scanning electron microscope (SEM). CO_2 uptake was measured using a Mettler thermal microbalance. Specimens were thoroughly outgassed by heating them to 300°C under vacuum on the microbalance. The specimens were then cooled under vacuum to room temperature and the balance back-filled with CO_2. The weight loss and gain was measured when the specimen temperature was swung from 30 to 110°C and back to 30°C.

RESULTS AND DISCUSSION

CFCMS Synthesis

The CFCMS material was fabricated at ORNL using a process initially developed by the DOE for the production of thermal insulators for NASA space missions[4]. Carbon fibers derived from either isotropic petroleum pitch, or PAN, were mixed in a water slurry with powdered phenolic resin. The slurry was transferred to a molding tank and the water drawn through a porous mold under vacuum. The resulting green artifact was dried, cured in air at 60°C, and stripped from the mold. The composite was cured at ~150°C in air prior to carbonization at 650°C under an inert gas. The CFCMS synthesis route is illustrated in Fig. 1. A schematic diagram of the molding arrangement is shown in Fig. 2. The fabrication process allows the manufacture of slab or tubular forms. Moreover, we believe that it will be possible to mold contoured plates, and tubes, to near net shape via this synthesis route. Once carbonized, CFCMS is readily machined to more complex geometries. Typical carbonized bulk densities of our CFCMS materials are 0.3-0.4 g/cm^3.

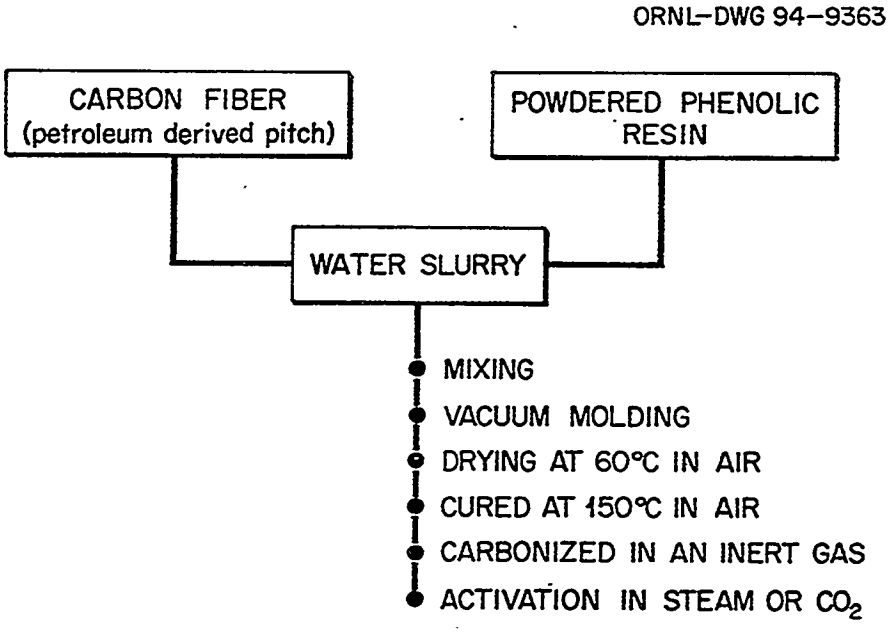

Fig. 1. CFCMS synthesis route.

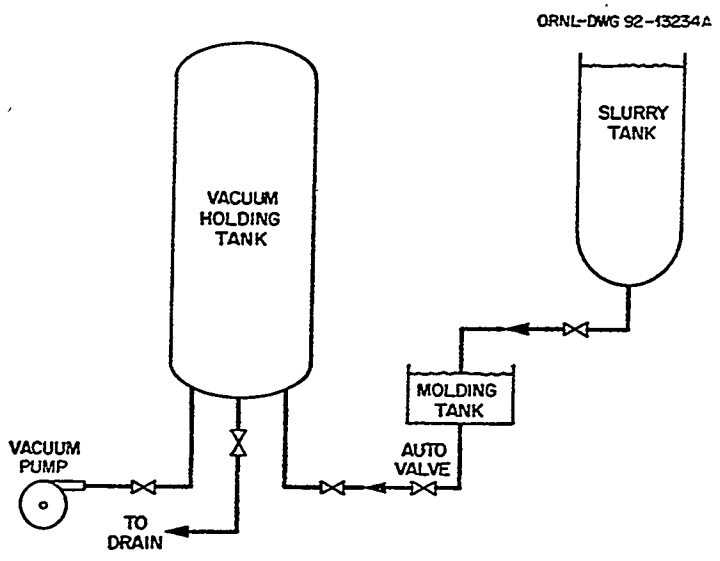

Fig. 2. Schematic illustration of the CFCMS molding apparatus.

Characterization

Microporous Carbon Fiber Monoliths

Figure 3 (×200 magnification) shows the structure of our CFCMS material manufactured from isotropic pitch derived carbon fibers. The chopped fibers are bonded at their contact points. The carbon fibers are

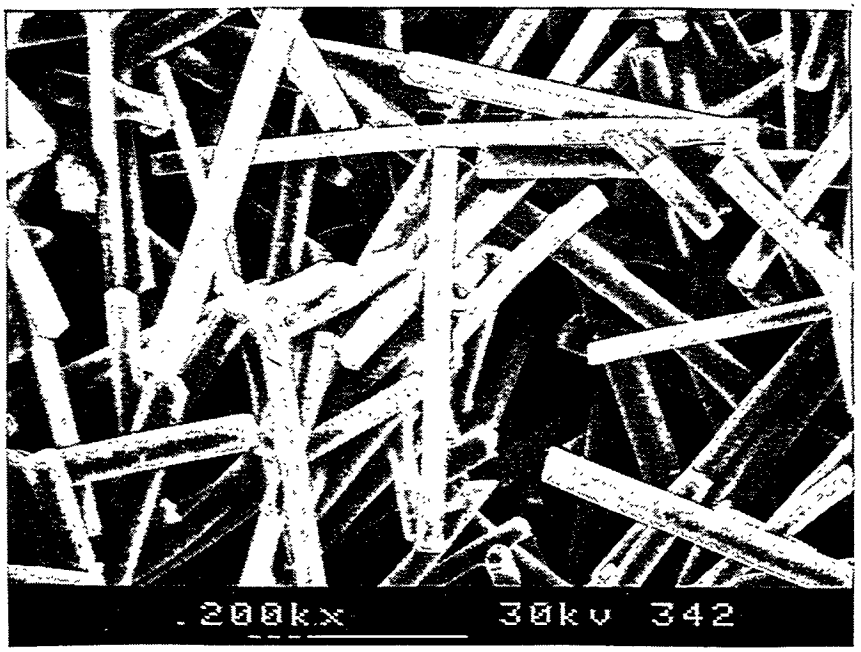

Fig. 3. SEM micrograph of carbon fiber composite molecular sieve (magnification x 200).

approximately 10-20 μm diameter, whereas the macro-voids between the fibers are typically >30 μm in size. The resultant open structure allows free flow of fluids through the material and ready access to the carbon fiber surface. Previously, we reported the carbon fiber length distribution[1]. The distribution mode is ~400 μm and the fiber lengths are widely distributed and range from 100 to 1000 μm. Mercury porosimetry data for the CFCMS material in the unactivated condition are shown in Fig. 4, and indicate the macropore size range to be approximately 10-100 μm. The macropores are the voids between the fibers, and mercury porosimetry data for macropore sizes are in agreement with visual observations made from SEM images (Fig. 3).

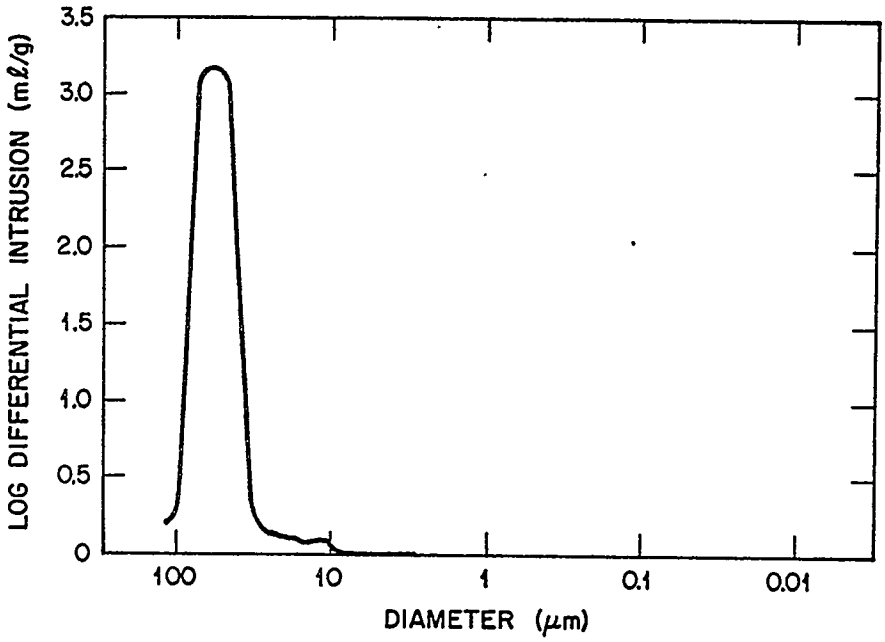

Fig. 4. CFCMS macropore size distribution for a pitch derived carbon fiber monolith obtained from mercury intrusion data.

A series of CFCMS materials were prepared at ORNL and activated at UKCAER. Details of the activation conditions are given in Table 1 along with the results of our analysis of the microporosity.

Table 1. Activation conditions and micropore characterization data.

Spec. Ident.	Activation Conditions				Micropore Analysis Data				
	Temp (°C)	Time (mins)	Agent	Burn -off (%)	BET Area (m^2/g)	Micropore Width (nm)			DR Pore Vol (cm^3/g)
						HK	DA	DR	
160	800	30	H_2O	7	394	0.48	1.3	0.58	0.20
161A	950	10	CO_2	6	292	0.48	1.8	1.21	0.13
161B	950	10	CO_2	6	281	0.47	1.9	1.34	0.10
166	800	180	H_2O	17	762	0.48	1.48	0.75	0.39
167	800	360	H_2O	28	891	0.49	1.5	0.76	0.49
170	950	180	CO_2	32	1132 1038	0.47	1.6	0.78 0.76	0.48
46	850	90	H_2O	28	1461	0.62	1.3	0.67	0.73

The BET surface areas reported in Table 1 ranged from 281 to 1461 m^2/g, and the mean micropore size (DR method) varied from 0.58-1.34 nm. Moreover, the micropore volumes (DR method) varied from 0.1 - 0.73 cm^3/g. The large surface area, combined with a large volume of micropores, suggests these materials might have a strong affinity for the adsorption of light gases. Therefore, CO_2 adsorption studies were performed, and our data are reported in Table 2.

Table 2. CO_2 uptake data and micropore data

Spec. Ident.	CO_2 Uptake data				Micropore Analysis Data				
	Sample Mass (mg)	Wt% CO_2 Uptake	Vol CO_2 Ads. (cm^3)	Spec. CO_2 Ads. Capacity (cm^3/g)	BET Surf. Area (m^2/g)	Micropore Width (nm)			DR Pore Vol (cm^3/g)
						HK	DA	DR	
160	89.50	7.8	3.95	44	394	0.48	1.3	0.58	0.20
161	72.45	6.9	2.53	35	292	0.48	1.8	1.21	0.13
166	89.95	8.9	4.05	45	762	0.48	1.5	0.75	0.39
167	92.27	8.7	4.04	44	891	0.49	1.5	0.76	0.49
170	74.89	10.3	3.9	52	1132	0.47	1.6	0.76	0.48
46	73.88	8.5	3.2	43	1461	0.62	1.3	0.67	0.73
Coconut shell carbon	90.22	8.3	3.8	42	168	0.5	1.6	-	-

Large CO_2 uptakes were measured for the CFCMS samples. As a comparison a commercial coconut shell carbon was evaluated, and was shown to have adsorbed ~20% less CO_2 than our best CFCMS. Moreover, the adsorption process was significantly slower in the case of the coconut shell carbon, where resorption of the CO_2 on cooling from the temperature swing took >2 hours compared with <1 hour for the CFCMS materials. The superior adsorption kinetics of the CFCMS are ascribed to the small diameter of the carbon fibers (10-20 μm) compared to the ~2-3 mm of the coconut shell carbon. The diffusion path for the CO_2 to an adsorption site is, therefore, substantially shorter in the case of the CFCMS. The CO_2 adsorption capacity of CFCMS is clearly related to the BET surface area and micropore volume, as shown in Figs. 5 and 6, respectively. The weight percent of CO_2 adsorbed increases with increasing pore volume and BET surface area, apparently reaching peak adsorption capacity at micropore volumes of ~0.5 cm^3/g and BET surface areas of ~1000 m^2/g (e.g., sample 170). Figure 7 shows CO_2 uptake plotted as a function of micropore size (DR method). The optimum pore size appears to be ~0.8 nm. Significantly, samples 161 and 160 showed the lowest CO_2 uptakes (6.9 and 7.8% respectively), yet they possessed the largest and smallest mean micropore sizes (1.21 and 0.58 nm) respectively, suggesting a strong sensitivity of CO_2 uptake to the micropore size.

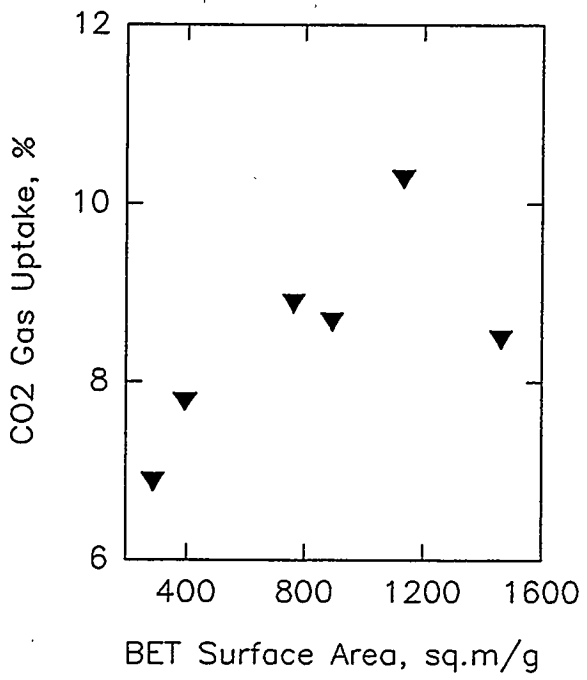

Fig. 5. The relationship between CO_2 uptake and BET surface area for CFCMS.

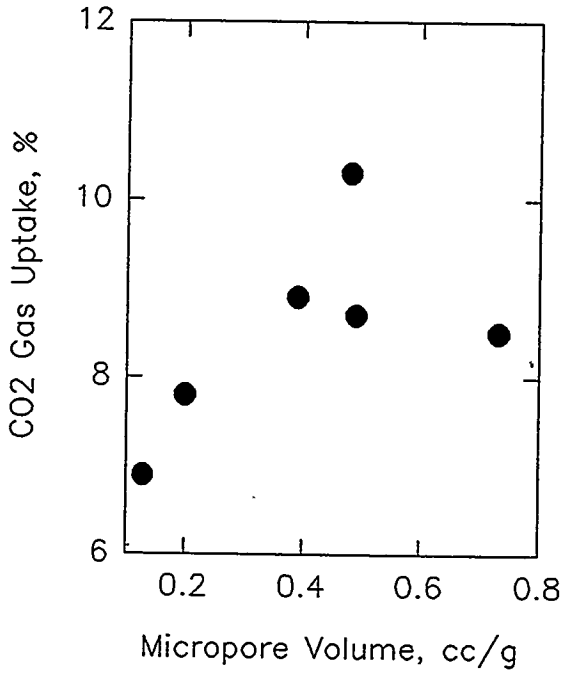

Fig. 6. The relationship between CO_2 uptake and micropore volume for CFCMS.

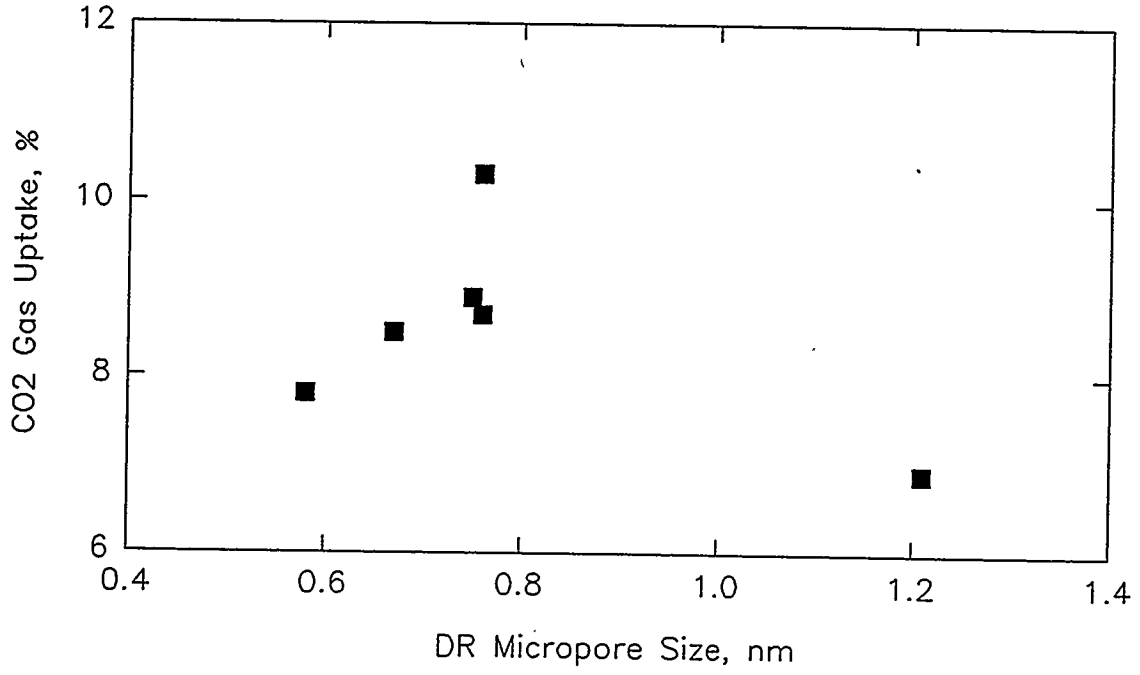

Fig. 7. The relationship between CO_2 uptake and mean micropore size for CFCMS.

Mesoporous Carbon Fiber Monoliths

A series of carbon fiber monoliths[5] were prepared from PAN derived carbon fibers and activated to burn-offs (% weight loss on activation) up to ~22%. Subsequent characterization using mercury porosimetry revealed the material to be highly mesoporous. Figure 8 shows the cumulative mesopore surface area as a function of pore diameter. The surface area is clearly associated with pores of size <50nm, i.e., the mesopores. The carbonized monoliths exhibited surface areas >500 m^2/g and mesopore volumes >1 cm^3/g. In contrast, the as-received PAN fibers exhibited a mesopore volume of only 0.28 cm^3/g. Evidently, the carbonization process radically affects the PAN fiber pore structure, possibly by opening the surface pores sufficiently to make the internal pores accessible. Access to the fiber's internal pore structure could occur when reactive species such as O_2, CO_2, H_2O and CO (which were adsorbed during monolith manufacture) are subsequently desorbed during carbonization and gasify the carbon.

The effect of steam activation on the mesopore volume is shown in Fig. 9. The mesopore volume was found to rapidly decrease with increasing burn-off, from >1 cm^3/g at zero burn-off to <0.4 cm^3/g at ~10% burn-off. Similarly, the mesopore surface area was found to decrease with increasing burn-off, falling from

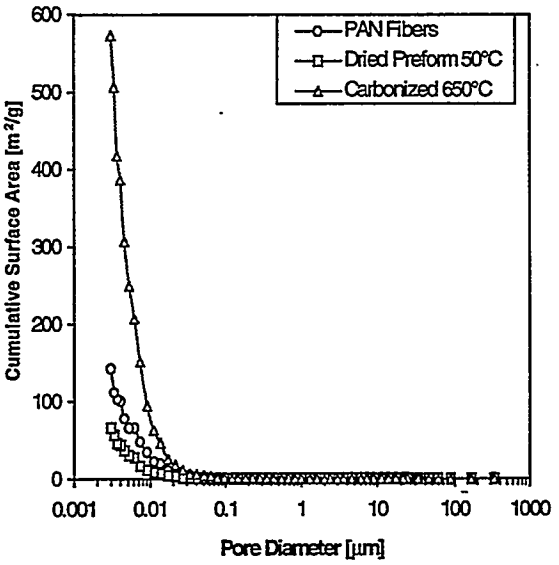

Fig. 8. Mesopore surface area as a function of pore diameter obtained from mercury intrusion data for our PAN derived carbon fiber porous carbon monoliths.

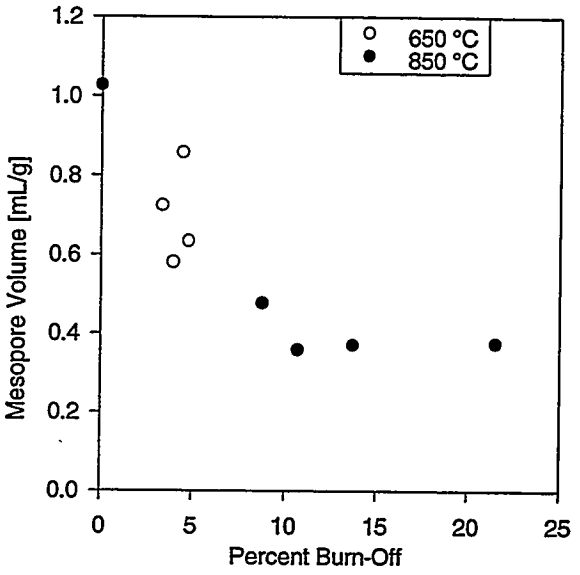

Fig. 9. Mesopore volume as a function of burn-off for our PAN derived carbon fiber porous monoliths.

>500 m^2/g at zero burn-off to <200 m^2/g at ~10% burn-off (Fig. 10). The mean mesopore diameter is shown as a function of burn-off in Fig. 11. In the carbonized condition, the carbon fiber monoliths exhibited a mean mesopore width of ~7.2 nm. Activation caused the mean mesopore size to increase, reaching ~8.7 nm at the peak burn-off considered here.

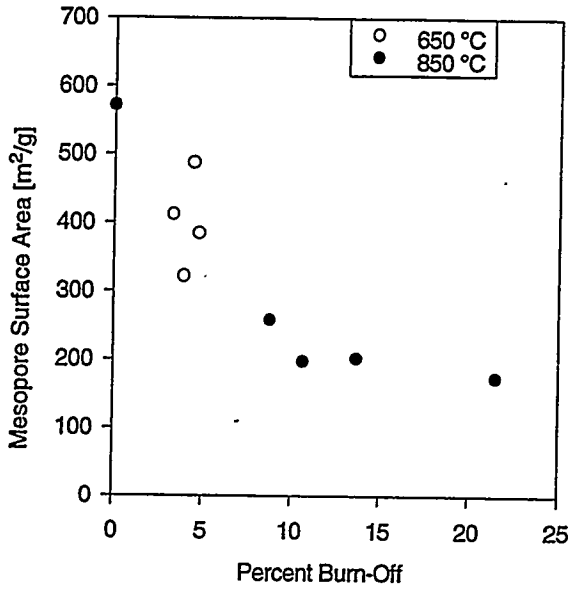

Fig. 10. Mesopore surface area as a function of burn-off for our PAN fiber derived porous carbon monoliths.

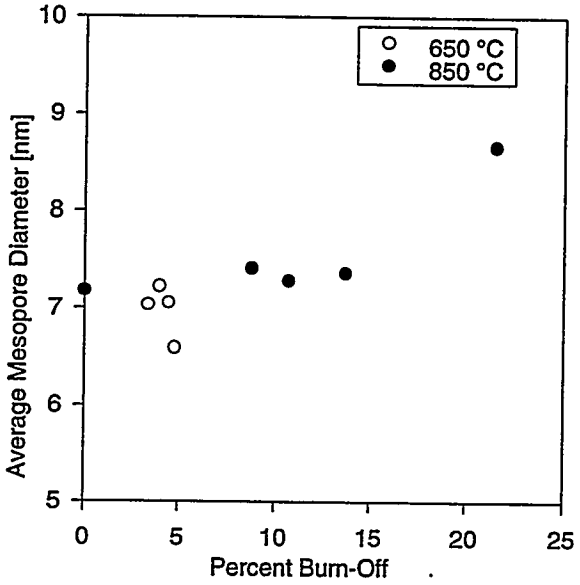

Fig. 11. Mean mesopore diameter as a function of burn-off for our PAN fiber derived porous carbon monoliths.

The large volume of mesopores observed in the PAN derived fiber monoliths is attributed to the fibril structure of PAN carbon fibers[6]. Typically[7], the crystallite size in a PAN fiber is ~1.6 nm. Moreover, there is extensive folding of the fibril nature of these crystallites, creating extensive pore networks in the mesopore size range, as confirmed by the data in Fig. 8. The modest increase of mesopore size with increasing burn-off (Fig. 11) suggests that the steam activation process affected very little change to the internal pore structure of the fiber. However, steam activation substantially reduced both the specific mesopore volume and associated specific mesopore surface area (Figs. 9 and 10). Moreover, SEM examination showed that the carbon fiber diameter reduced substantially during activation, indicating the fibers are consumed radially by a process of gasification of their external surface. The observed variations of pore size, pore volume, and surface area with burn-off could be readily explained if activation of the PAN carbon fibers occurred via a constant penetration depth, moving-front reaction. In such a process the pore structure would first be developed by gasification of the pore walls, increasing the pore size and volume. With further burn-off, the fiber itself is consumed, thus destroying the pore structure. As the reaction front moves from the periphery of the fiber toward its core, reducing the fiber diameter, the total volume of pores being created or developed is reduced. The high mesopore volume in the carbonized monolith suggests that, in this instance, activation is not required. Significant reductions in process time, and a beneficial cost saving, may thus be realized.

CONCLUSIONS

A novel porous monolithic carbon fiber composite material, known as CFCMS, has been developed and shows considerable potential for use in PSA gas separation systems. The material can be fabricated in large sizes yet retains the advantageous gas adsorption and separation properties of its precursor isotropic pitch derived carbon fibers. The CFCMS material structure contains large voids (>30 μm) between the 10-20 μm diameter fibers which allows for free flow of fluids through the material. A series of microporous CFCMS materials have been prepared and characterized. Their CO_2 adsorption characteristics were examined and

determined to be superior to a commercially available activated carbon. The CO_2 adsorption capacity of CFCMS materials is related to both the BET surface area and the micropore volume, and appears to be particularly sensitive to the mean micropore size.

Mesoporous CFCMS materials were prepared from PAN derived carbon fibers. The materials exhibited mesopore volumes in excess of 1 cm^3/g and, therefore, are candidates for catalyst support applications. Steam activation of the monoliths increased the mean mesopore size only modestly, but reduced the mesopore volume and mesopore surface area significantly. The largest mesopore volumes were associated with the samples that had not been activated, but rather had only been carbonized. An activation and pore structure development mechanism was postulated to explain the pore characterization data obtained from mercury intrusion analysis.

ACKNOWLEDGEMENTS

Research sponsored by the U.S. Department of Energy, Office of Fossil Energy, Advanced Research and Technology Development Materials Program [DOE/FE AA 15 10 10 0, Work Breakdown Structure Element ORNL-1(E)] under contract DE-AC05-84OR21400 with Martin Marietta Energy Systems, Inc.

REFERENCES

1. T. D. Burchell, "Carbon Fiber Composite Molecular Sieves," in *Proc. Eighth Annual Fossil Energy Materials Conference*, Oak Ridge, Tennessee, May 10-12, 1994. CONF-9405143, ORNL/FMP-94/1, pp. 63-70, Pub. Oak Ridge National Lab., Aug. 1994.

2. Frank Derbyshire, "Activation and Micropore Structure Determination of Carbon Fiber Composite Molecular Sieves," in *Proc. Eighth Annual Fossil Energy Materials Conference*, Oak Ridge, Tennessee, May 10-12, 1994. CONF-9405143, ORNL/FMP-94/1, pp. 137-143, Pub. Oak Ridge National Lab., Aug. 1994.

3. S. Brunauer, P. H. Emmett, and E. Teller, *J. Am. Chem. Soc.,* Vol 60, p. 309 (1938).

4. George C. Wei and JM Robbins, "Carbon-Bonded Carbon Fiber Insulation for Radioisotope Space Power Systems," *Ceramic Bulletin*, Vol. 64, No. 5, p. 691 (1985).

5. J. W. Klett and T. D. Burchell, "Carbon Fiber Carbon Composites for Catalyst Supports," *Proc. 22nd Conf. on Carbon, San Diego, California, July 1995*, Pub. American Carbon Society.

6. R. J. Diefendorf and E. W. Tokarsky, *Polymer Eng. Sci.*, Vol. 15, P. 150 (1975).

7. J. P. Donnet and R. C. Bansal, *Carbon Fibers*, Pub. Marcel Dekker, Inc., New York (1990).

CARBON-FIBER COMPOSITE MOLECULAR SIEVES FOR GAS SEPARATION

M. Jagtoyen, F. Derbyshire, G. Kimber, Y. Q. Fei

University of Kentucky Center for Applied Energy Research,
3572 Iron Works Pike, Lexington KY 40511-8433, USA

ABSTRACT

The progress of research in the development of novel, rigid, monolithic adsorbent carbon fiber composites is described. Carbon fiber composites are produced at ORNL and activated at the CAER using steam or CO_2 under different conditions, with the aims of producing a uniform degree of activation through the material, and of closely controlling pore structure and adsorptive properties. The principal focus of the work to date has been to produce materials with narrow porosity for use in gas separations.

Carbon fiber composites are prepared at ORNL, usually in plate or tubular form, by vacuum molding from water slurries containing phenolic resin and chopped isotropic petroleum pitch fibers. The composites are activated at the CAER in steam or CO_2, using samples of dimensions up to 1.5 x 4 x 12 cm that are cut from the original larger plates. One of the objectives is to produce uniformly activated composites, which is especially critical when attempting to active large monoliths. It has been found that there are appreciable variations in the density and permeability of the as-formed composites that must relate to the forming technique. These variations are expected to exert some influence on the rate and extent of reaction and surface area development. In attempting to uniformly activate the composites, two reactor configurations have been investigated. In the more successful arrangement, steam is introduced at several points along the length of the composite. A reduction in steam partial pressure from 95 vol% to 44 vol% significantly improved the uniformity of surface area distribution. Activation with CO_2 was still better, which is attributed to the much slower reaction rate than with steam.

Measurements of composite dimensions have shown that there is an overall shrinkage during activation. A direct correlation is found between dimensional shrinkage and burnoff, and is similar for CO_2 and steam activation. The causes of the shrinkage are not yet clear. At levels of burnoff above about 40%, the extent of contraction is sufficient to produce stresses that result in fracture.

Activated composites have been evaluated for the separation of CH_4-CO_2 mixtures, and an apparatus has been constructed specifically for this purpose. Samples activated to low burnoff (5-7% wt loss) with low surface areas (from 300-500m^2/g) give much better separation of CO_2 and CH_4 than samples produced at higher burnoff, and there appears to be no benefit in producing composites at burnoffs higher than 10%. The greater separation efficiency obtained at low burn-off means that the most effective CFCMS can be produced at relatively low cost. Continuing work will attempt to define the parameters that influence this gas separation, and whether these are applicable to other gas mixtures.

INTRODUCTION

This project involves collaborative research between the ORNL and the CAER, for the development of novel, rigid, monolithic adsorbent carbon fiber composites that can be produced in single pieces to a given size and shape. The concept has resulted in the filing of a patent application that is held jointly between researchers at these two organizations. Because of their potential molecular sieve properties, the composites have been termed carbon fiber composite molecular sieves, or CFCMS. The carbon fiber composites are produced at the ORNL and activated at the CAER using steam or CO_2 under different conditions, with the aims of producing a uniform degree of activation, and of closely controlling pore structure and adsorptive properties. The principal aims of the work to date have been to produce uniformly activated samples with narrow porosity for use in gas separations, although numerous other areas of application are envisaged.

The project originated in research conducted at the ORNL in the 1980s[1]. A carbon fiber composite material was developed as a low-density, mechanically strong thermal insulator for a radioisotopic heat source on spacecraft for the Galileo and Ulysses Missions. The material was prepared by vacuum molding from water slurries containing chopped carbonized rayon fibers (~ 6.5 μm diameter x ~ 0.15 mm) and a particulate phenolic resin. The slurry was vacuum molded into tubular or plate configuration, followed by drying, curing, and carbonization to 1600°C.

The basis for the present project was to use the above technique to produce high surface area carbon fiber composites through the activation of similar composites, in which porosity is developed in the carbon fibers to produce high surface areas for adsorption. One of the principal changes, compared to the original work, is to utilize lower cost carbon fibers that are produced form isotropic pitches (other types of fiber will also be included in the studies). In recent years, a great interest has developed in the activated forms of such isotropic carbon fibers, where high surface areas can be produced by partial gasification in steam or other oxidizing gas[2,3]. Moreover, while porosity can be generated in most types of carbon fiber, low-modulus fibers produced from isotropic pitch are particularly suited for activation due to their unique structure in which the random packing of small crystallites allows the development of an extensive pore structure. It was also assumed that the ease and kinetics of activation should be much more favorable than with high performance fibers which, in addition to possessing different structure, have been subjected to elevated temperatures. Early results confirmed this supposition, in that it was found that isotropic fibers that had been heat treated to 1600°C were much more difficult to activate than fibers that had been heat treated to 1100°C.

The interest in activated carbon fibers as adsorbents is that they have novel properties that make them more attractive than conventional forms of activated carbons (powder or granular) for certain applications[3]. Among their possible uses, activated carbon fibers are of interest for: the adsorption and recovery of organic vapors; environmental protection; the removal of SO_x and NO_x from flue gas; the improvement of air quality; and water treatment[3-8]. Difficulties in handling and utilizing activated fibers can be surmounted by their incorporation into composites, such as woven and non-woven fabrics, felt, and paper. Hence, the interest in producing rigid adsorbent composites.

This paper provides an account of studies of composite activation, the measurement of physical properties (dimensional changes during activation, gas permeability), and the results of preliminary experiments to evaluate the effectiveness of CFCMS for the separation of gas mixtures.

DISCUSSION OF CURRENT ACTIVITIES

Experimental

Composite Preparation

Carbon fiber composites are prepared at ORNL by vacuum molding from water slurries containing phenolic resin and chopped isotropic petroleum pitch fibers, (P-200, ~ 17.5 μm diameter, average length 380μm, supplied by courtesy of Ashland Carbon Fibers Division, Ashland Inc.). The slurry is vacuum molded into tubular, plate or rod configuration, followed by drying, curing, and carbonization to about 650°C. The carbon fiber composites are supplied to the CAER usually in the form of plates (28 x 12 x 1.5 cm).

Activation

The composites are activated in steam or CO_2, using smaller samples (dimensions 1.5 x 4 x 12 cm) that are cut from the original plates. Activation is conducted in a Lindberg tube furnace at temperatures between 800 and 950°C, for reaction times from 0.5-4 hours. Surface areas and pore size distributions are

determined for samples taken from selected areas of the activates, using a 10 port automated surface area analyzer, OMNISORB 610. The high efficiency of this instrument allows the measurement of surface area and the characterization of pore sizes down to 4 A, using nitrogen at 77K and CO_2 at 298K as adsorbents.

Results and Discussion

Activated carbon fibers produced from isotropic petroleum pitch have been reported to develop high surface areas (in some cases up to 2000 $m^2 g^{-1}$), with almost all of the pore volume present in micropores (< 2nm diameter pores)[3]. These properties are retained by the composites, as illustrated in Table 1, where the nitrogen BET surface area is shown as a function of burn-off in steam (percent weight loss during activation). It can be seen that high surface areas can be attained at moderate burn-off.

The pore size distribution is narrow, although it broadens with increasing activation: the average pore width increases from 0.58 to 0.83 nm as the burn-off with steam increases from 16 to 31%. The sample at 16% burn-off has the narrowest pore size distribution with almost all pores less than 6 nm in diameter, while the more activated samples have significant proportions of pores from 6-8 nm in diameter. Depending on the application, a compromise may be required between pore size distribution and total surface area. Samples activated in CO_2 show the same trend in surface area development as the steam activated samples. At comparable levels of burnoff the BET surface area is 566 m^2g^{-1} for steam and 527 m^2g^{-1} for CO_2 while the pore widths are similar, 0.58 nm vs 0.62nm, Table 1.

Table 1: Surface area and average pore size for CFCMS at different levels of burnoff in steam and CO_2

Burnoff	BET(m^2g^{-1})	Average pore size(nm)
Steam (concentration: 97 vol %)		
16	566	0.58
20	936	0.75
31	1240	0.83
CO_2 (concentration: 100 vol %)		
13	512	0.60
18	527	0.62
36	800	0.76

Uniformity of Composites and Activated Composites

One of the main concerns in this work is to be able to uniformly activate the composites: this consideration will become especially critical when attempting to activate large monoliths, where diffusion of activating gas to the center of the artifacts could present a limiting factor. Consequently, a great deal of effort has been taken to ensure uniform activation. Since the start of the project, the activation procedure has been progressively modified in order to establish furnace conditions that will help to realize this objective. One factor that cannot be controlled through the activation however, is the uniformity of the composite blocks as they are received from ORNL. Before discussing further the activation process, the uniformity of the as-received composites will be addressed.

Uniformity of as-received composites. A sample of composite, 28 x 12 x 1.5 cm, supplied by ORNL (UK-10-2) was examined for consistency of density, thickness and permeability by removing 18 nominally 1" cores and measuring them individually.

The results showed that density was the least variable parameter. Even so, the variation was 0.347 to 0.382 g/cc. The thickness of the block was extremely variable with a range of 13.4 to 17.8 mm. The thicker areas did not seem to be directly linked to the higher density areas. Similarly, no correlation was obvious between density and permeability (for measurement details see later section). Thus, there is far from equal resistance to flow over the whole plate area, which could obviously affect the distribution of the activating gas, and the removal of the products of the gasification reactions. These variations in the physical parameters must result from the forming technique and are expected to exert some influence on the rate and extent of activation reaction and surface area development.

Uniformity of Activation. The principal parameters that can be varied in the activation process are, the reactor design and configuration, the partial pressure of the activating gas, total flow rate, temperature and reaction time.

Two different reactor arrangements have been investigated. In the first configuration, steam was introduced at several points along the length of the composite. In the second, the steam was introduced at one end only and passed downstream over the composite. The uniformity of activation was tested by measuring BET surface areas on sub-samples taken from different positions in the composite (dimensions 1.5 x 4 x 12 cm). The first reactor was found to give a much smaller spread of results, with standard deviations in BET surface area of 2-12% as opposed to 18-50% for the other reactor.

Another factor that will influence uniformity of the composites is the partial pressure of the activating gas. In initial experiments, essentially pure steam (95 vol%) was used as the activating agent. Water at a flow rate of 60cc/hr was mixed with nitrogen at 80cc/min. These conditions resulted in non-uniform surface area development throughout the sample (deviation around 10-30%), which was attributed to the high concentration of steam. When the steam concentration was reduced to 61vol % and 44 vol%, the uniformity improved significantly. The standard deviation in surface area along the 12cm length of sample came down to 7 and 2% respectively. In future studies a concentration of 44 vol% H_2O in N_2 or less will be used to achieve uniform activation.

Activation with CO_2 is found to give more uniform surface area development than steam, with only a 8% variation in BET surface area. CO_2 activation gives a slightly different pore size distribution than steam activation[9]. There is a significantly slower reaction rate than with steam, since the larger dimension of the CO_2 molecule results in a slower diffusion into the porous system and is more restricted in its access to the micropores. The CO_2 activation runs were therefore carried out at higher temperatures (850-950°C), for 1-3 hours, and at a rate of 2l/min.

Dimensional Changes

There is an overall shrinkage of the composites during activation. The changes have been measured in all three directions of the composite. A direct correlation is found between dimensional shrinkage and burnoff, and is similar for CO_2 and steam activation.

It has been reported that carbon shrinkage can be caused by direct reaction between O_2 and C, as carbon is directly removed from exterior surfaces. At temperatures above 800°C, oxygen is known to react more than 100 times faster with carbon than steam and CO_2, which leads to a diffusion-controlled reaction involving a shrinking core type of mechanism, and there is minimal contribution to porosity development. In the present studies, there should only be low concentrations of oxygen present, and the causes of the shrinkage are not clear. External burn-off in the activant gas could make some contribution, but this is expected to be small. Another factor might be degradation of the binder. In any event, at high levels of burnoff, above about 40%, the extent of contraction produces stresses in the composites that result in fracture in a plane parallel to the plane of deposition when the composite was first formed by filtration.

Permeability and Adsorptive Properties

The permeability of the composites and activates has been measured by a simple apparatus where the sample under test is sealed in a plastic funnel using foam rubber. Air is passed through the sample at a rate of 15-60 l/min, and the differential pressure over the sample is measured using a water manometer. For a composite of thickness 13mm, an air flow of 15 l/min through a disc of diameter 25 mm (i.e. 30 m^3/min per m^2) generates a pressure differential less than 0.5 psi. This permeability is comparable to that of an equivalent bed depth of 2 mm sized granules, and much higher than for a similar bed of 14 micron sized powder. The high permeability is due to the very open structure of the composites.

The rate of gas adsorption on CFCMS has been compared with that on other carbons by thermogravimetric analysis using NO as the test adsorbate. The rate of adsorption on activated carbon fiber composites is found to be much higher than on a granular commercial coconutshell derived carbon, Figure 1, due to the essential absence of diffusion limitations in the carbon fiber composite. Only when the granular carbon is reduced to a comparable particle size (average diam 14 microns vs 12-15 microns fiber diameter) do the rates begin to correspond. The high adsorption rate is another benefit of the open architecture of the composite since the fibers within are almost as accessible as free fibers. The materials will therefore have high potential for processes requiring rapid adsorption and desorption rates, e.g. gas separation, solvent recovery etc.

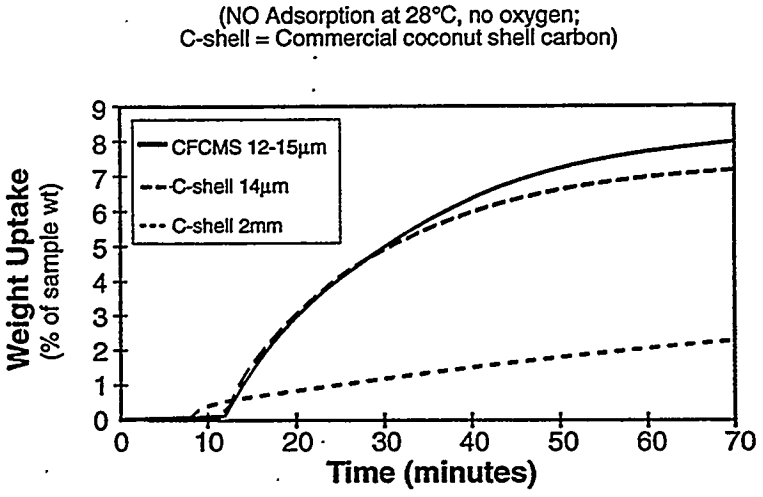

Figure 1: Adsorption rates of CFCMS compared with a commecial granular activated carbon at two particle sizes, granulars at 2mm and finely ground to 14µm.

Gas Separation

The unique properties of the activated composites - narrow, unimodal pore structure, high surface area, rapid rates of adsorption and desorption, the ability to form specific shapes of high permeability and strength - suggest that, among other applications, they may be suitable for molecular separation on the basis of size and shape. The system CH_4 - CO_2 was selected as the model mixture, following studies of the adsorption of these gases by TGA which showed that the carbons have high capacity for adsorbing CO_2 (up to 10 wt%) while much less methane is adsorbed, Figure 2.

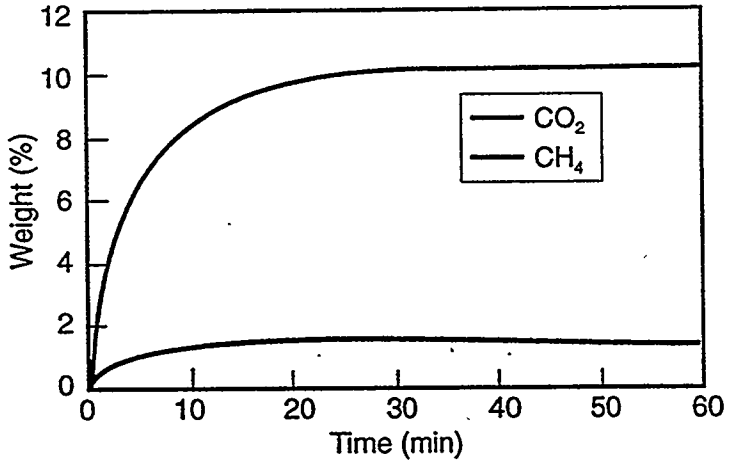

Figure 2: Adsorption of CH_4 and CO_2 on CFCMS using TGA (STP).

An apparatus was then constructed to examine the effectiveness of CFCMS for gas separation, Figure 3. Samples have been tested using a mixture of 75% CH_4 and 25% CO_2. The composition and flow rate of the emergent gases are detected as a function of time using a mass spectrometer and a mass flow meter. The sample is sealed in place using a rubber seal. Helium is first purged through the system and when the gas analysis indicates that virtually pure helium is emerging at the outlet, the valve is switched and the 75%CH_4/ 25% CO_2 mixture is introduced at a fixed controlled flow rate (usually 50 ml/min). The outlet flow rate and composition is then monitored and recorded for 10 minutes. Initially, for an activated sample there is a period of time when the outlet flow is very low, as most of the CH_4 and CO_2 flowing into the sample is adsorbed. Then, relatively pure methane begins to be detected. After about 10 minutes, the outlet gas composition has returned to that of the original mixture 75% CH_4, 25% CO_2. The volumes of gas produced per gram of composite with 95%, 90% and 85% CH_4 concentration are then calculated.

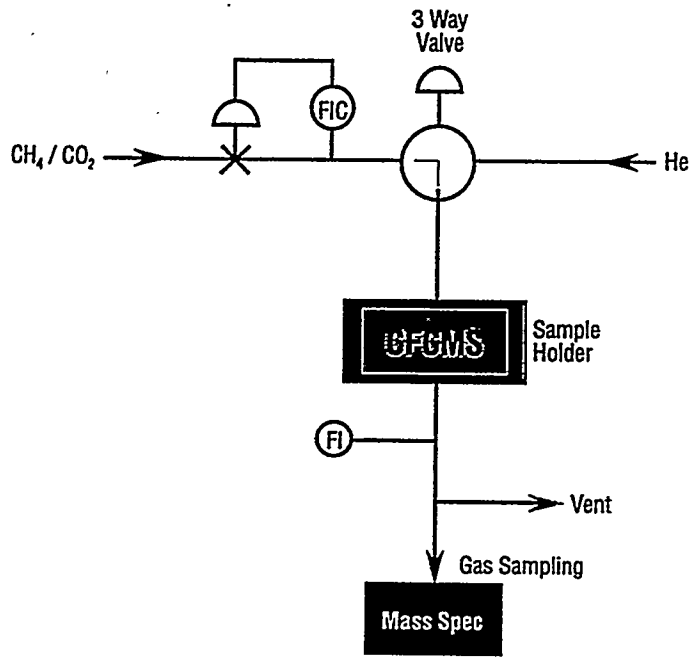

Figure 3: Schematic Arrangement of Apparatus for testing Gas Separation.

Results of the gas separation experiments are shown in Table 2. Samples activated to low burnoff (5-7% wt loss) and low surface areas (from 300-500m^2/g) show excellent separation of CO_2 and CH_4, compared to samples produced at higher burnoff (10-30% wt. loss, surface area 500-1000m^2/g). The volumes of effluent gas produced at 95 and 90% methane concentration are shown in Table 2 as a function of burn-off. The most effective carbons are produced at low burn-off, and there appears to be no benefit in producing composites at burnoffs higher than 10%. The same trend is reflected in the relationship between micropore volume and efficiency for separation, Table 2, from which it appears that the ideal micropore volume should be less 0.15 cc/g. These results are rather unexpected. The greater separation efficiency obtained at low burn-off means that the most effective CFCMS can be produced at relatively low cost. However, there remain the questions of defining the parameters that influence this gas separation, and whether these are applicable to other gas mixtures.

The influence of average pore diameter on the separation process and production of high purity methane is shown in Figure 4. From these data, the optimum pore diameter is seen to be in the range 0.7 - 1.0 nm. However, other parameters such as surface chemistry cannot be neglected. Future work will be directed to further elucidating the CFCMS parameters that are most important to the separation process.

Table 2: Volume of CH_4 produced at 95-85% concentration from a mixture of 75%CH_4/25%CO_2

Sample	Cumul. vol of CH_4 out(cc)		Bum -off	Activation			BET s.area	pore volume	pore diameter
	95%	90%	(wt %)	agent	temp (°C)	time (hr)	(m^2/g)	(cc/g)	(A)
SA124	-	47	24	CO_2	900	3	632	0.2	5.8
SA139	33	69	8	H_2O	850	1/4	444	0.26	12.0
SA 132	35	67	8	CO_2	850	2	424	0.19	7.6
SA 135	39	78	12	CO_2	850	4	548	0.23	5.9
SA 136	44	80	7	CO_2	1000	1/60	291	0.11	11.0
SA 137	53	87	7	CO_2	950	1/6	397	0.13	8.8

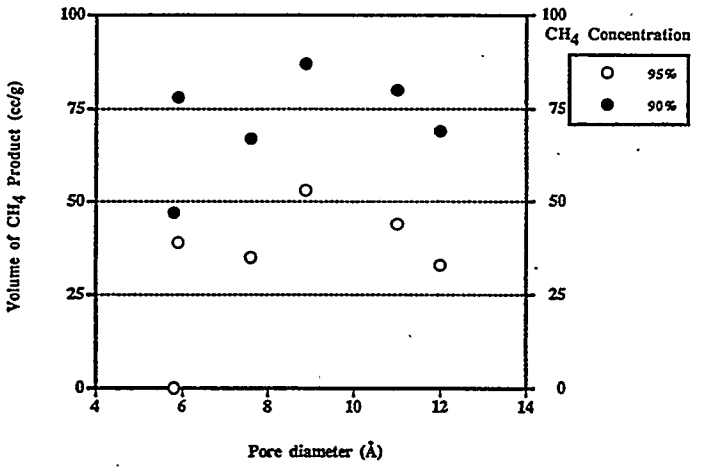

Figure 4: Relationship of average pore diameter to volume of effluent gas produced with high CH_4 purity.

REFERENCES

1. G. C. Wei, and J. M. Robbins, Ceramic Bull. , 64(5), p. 691, 1985.
2. M. W. Thwaites, M. L. Stewart, B. E. McNeese, and M. Sumner, Fuel Proc. Tech., 34, 137, 1993.
3. M. Suzuki, Proc. Biennial Carbon Conference, Buffalo, 1993.
4. I. Mochida, Y-N. Sun, H. Fijitsu, S. Kisamori, and S. Kawano, Nippon Kagaku Kaishi, (J. Chemical Society of Japan), 6, 885-890, 1991.
5. I. Mochida, T. Hirayama, S. Kisamori, S. Kawano, and H. Fijitsu, Langmuir, 8 (9), 2290, 1992.
6. K. L. Foster, R. G. Fuerman, J. Economy, S. M. Larson, and M. J.Rood, Chem. Mater., 4, 1068-1073, 1992.
7. J. Economy, K. Foster, A. Andreopoulos, and H. Jung, Chemtech, 597-603, October 1992.
8. M. Suzuki, Water Science technology, 23, p. 1649, 1991.
9. T. Wigmans, Carbon Vol. 27. No. 1. pp. 13-22, 1989.

STABILITY OF SOLID OXIDE FUEL CELL MATERIALS

T.R. Armstrong, L.R. Pederson, J.W. Stevenson, and P.E. Raney

Materials Sciences Department
Pacific Northwest Laboratory[1]
P.O. Box 999
Richland, WA 99352

ABSTRACT

The phase stability and sintering behavior of materials used in SOFCs has been evaluated. The sintering behavior of Ca and Sr doped lanthanum manganite (the preferred SOFC cathode material) is highly dependent on the relative proportion of A and B site cations in the material. Ca and Sr doped lanthanum chromite (the preferred interconnect material) have been shown to rapidly expand in reducing atmospheres at temperatures as low as 700°C. This expansion is due to the reduction of Cr^{4+} to Cr^{3+} in reducing environments.

INTRODUCTION

Doped lanthanum chromite and lanthanum manganite have been extensively studied over the past two decades for use in high-temperature solid oxide fuel cells (SOFC). Lanthanum chromite for use as an interconnect and lanthanum manganite as the SOFC cathode. The requirements on materials used in SOFCs is severe. The chosen interconnect material must be stable in both oxidizing and reducing atmospheres, have a high electronic conductivity, high thermal conductivity, a thermal expansion match to yttria stabilized zirconia, and be chemically compatible with the other fuel cell materials. The material chosen for the cathode must be stable in air at 1000°C and have high electronic conductivity. The thermal expansion must be compatible with the yttria-stabilized zirconia (YSZ) electrolyte, and chemical interaction with the electrolyte and interconnect materials must be minimal. Also, the cathode material must maintain a porous microstructure during operation to allow adequate diffusion of gaseous oxygen through the cathode to the cathode/electrolyte interface

[1]Operated for the U.S. Department of Energy by Battelle Memorial Institute under contract DE-AC06-76RLO 1830

Reproducible fabrication of SOFCs requires a thorough knowledge of the sintering behavior of the chosen cathode and interconnect material. Important factors affecting densification include temperature, type and amount of dopant, and cationic stoichiometry (i.e., relative proportion of A and B site cations). Additionally, these materials must be stable over a wide range of temperatures and oxygen partial pressures. The objective of this work is two-fold: 1) to evaluate the sintering behavior of doped lanthanum manganite with and without the addition of sintering aides and 2) to evaluate the phase stability of lanthanum chromite over a range of oxygen partial pressures and temperatures.

SINTERING OF LANTHANUM MANGANITE

Doped $LaMnO_3$ has a perovskite-type structure. The sintering behavior of these manganites is highly dependent on the ratio of A-site cations (La, Sr, Ca) to B-site cations (Mn) in the material. LSM-16, LSM-24, and LCM-20 were prepared with A/B cation ratios of 0.91, 0.95, 0.98, 1.00, 1.02, and 1.05. LSM-10 with A/B = 0.98 was also prepared. Since A and B sites are present in a 1:1 ratio, and all ions present in the structure occupy regular lattice sites[1], those ratios would correspond to $(La_{1-y}M_y)_{0.91}MnO_3$, $(La_{1-y}M_y)_{0.95}MnO_3$, $(La_{1-y}M_y)_{0.98}MnO_3$, $(La_{1-y}M_y)MnO_3$, $(La_{1-y}M_y)Mn_{0.98}O_3$, and $(La_{1-y}M_y)Mn_{0.95}O_3$ (M = Ca or Sr), respectively, assuming single phase materials. While compositions near the stoichiometric point (A/B = 1) were single phase perovskites, other compositions contained small amounts of additional phases, as discussed below. Although manganites can also exhibit oxygen nonstoichiometry, that nonstoichiometry in highly doped manganites tends to be relatively small[2]. For convenience, therefore, an oxygen stoichiometry of 3 (rather than $3 \pm \delta$) is used in this article.

Sintered (1350°C for 1 hour) densities for LSM-16, LSM-24 and LCM-20 (calcined at 650°C for 0.5 hour) are shown as a function of A/B cation ratio in Figure 1. The green densities were essentially independent of A/B cation ratio, whereas the sintered densities were highly dependent on the A/B ratio, with A-cation deficient compositions (A/B ratio < 1) exhibiting substantially higher densities than the stoichiometric and B-cation deficient manganites. This pronounced effect of A/B cation ratio on densification behavior was also observed in measurements of the linear shrinkage of green compacts as a function of temperature. For example, sintering shrinkage plots for LSM-24 are shown in Figure 2.

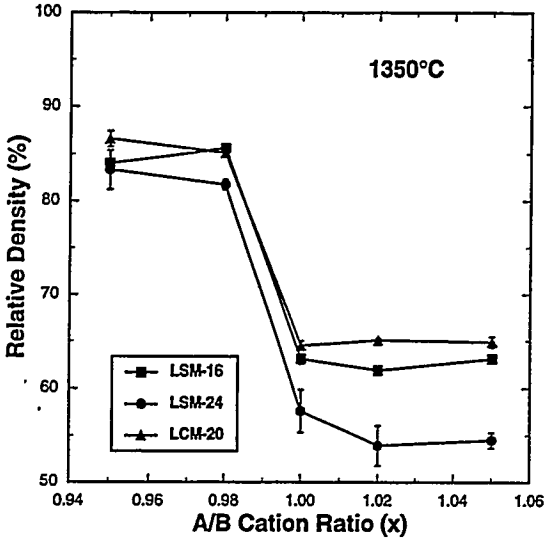

Figure 1. Relative densities of lanthanum manganites as a function of A/B ratio. Specimens sintered in air at 1350°C for 1 hour.

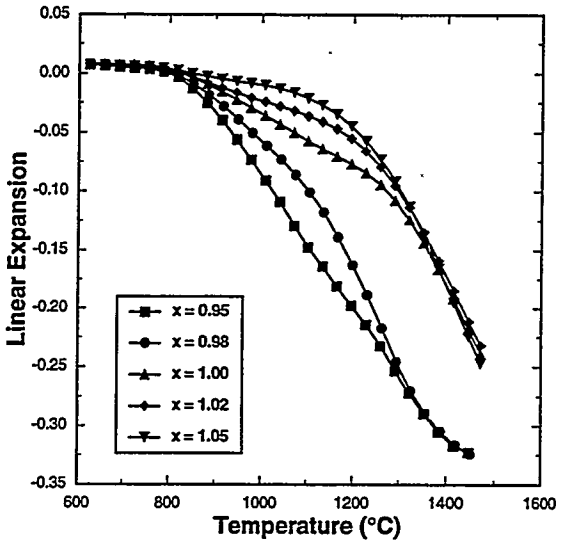

Figure 2. Sintering shrinkage plots for LSM-24 with varying A/B ratio. Specimens heated at 2°C/min in air.

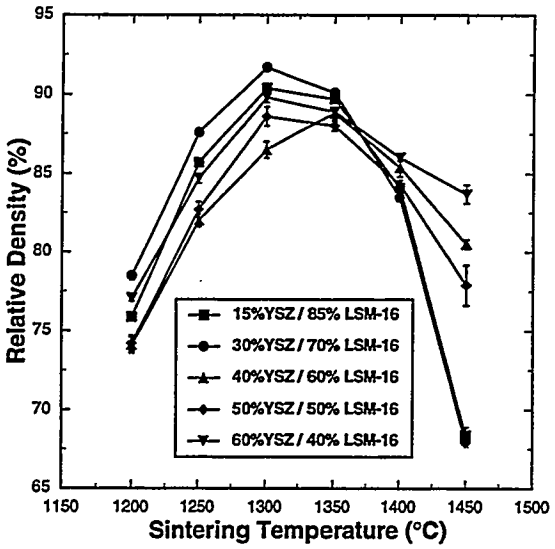

Figure 3. Relative densities of LSM-16/ YSZ mixtures sintered in air at the indicated temperatures.

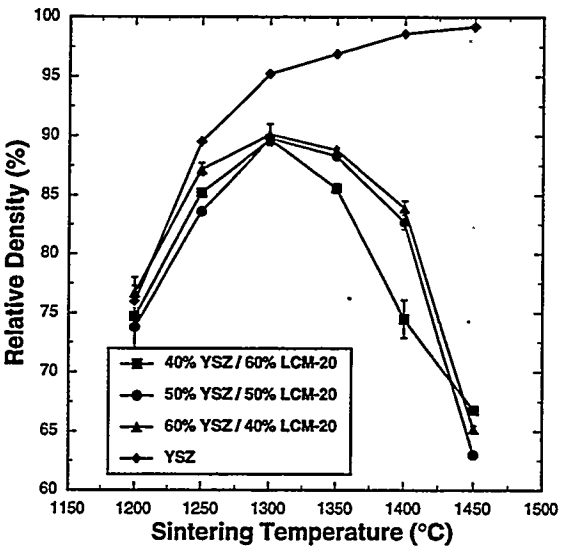

Figure 4. Relative densities of LCM-20/ YSZ mixtures sintered in air at the indicated temperatures.

These plots show an enhancement of shrinkage for the A cation deficient manganites. The shape of these shrinkage plots is consistent with a solid state sintering mechanism, with no signs of sudden shrinkage events (nearly vertical regions in the plot) resulting from liquid phase formation.

The higher densities obtained in the A-site cation deficient manganites suggests that the diffusion of A-site cations is the limiting factor in mass transport during densification[3]. Preparation of manganites with A/B < 1.00 should result in an excess concentration of A-site vacancies within the structure. When additional A-site vacancies are present in the structure, A-site cation diffusion occurs more readily, allowing for higher sintered densities. This agrees with conclusions drawn by van Roosmalen et al.[4] for undoped lanthanum manganite. Since sintered density was not significantly affected by B-site cation deficiency, the diffusion of B-site cations does not appear to be a limiting factor during sintering.

Sintered densities of mixtures of YSZ/LSM-16 and YSZ/LCM-20 are shown in Figures 3 and 4, respectively. Sintered densities for YSZ alone (also shown in Figure 4) increased uniformly with increasing sintering temperature. For the manganite/YSZ mixtures, however, densities increased with increasing temperature until reaching a maximum around 1300°C. At higher temperatures, the densities tended to decrease substantially with increasing temperature. High porosity is essential for the SOFC cathode. It is clear from Figures 3 and 4 that the degree of porosity of the sintered mixtures can be varied over a wide range by changing the sintering temperature. In practice, the introduction of pore formers, such as organic materials which can be removed at low temperatures, may be a preferable means of obtaining the desired level (and morphology) of porosity.

One of the potential advantages of the addition of YSZ to lanthanum manganite is an improved thermal expansion match between the cathode and the YSZ. The average TECs (between 25 and 1000°C) of LSM-16 (10.0×10^{-6} K^{-1}) and LCM-20 (10.5×10^{-6} K^{-1}) were close to that of YSZ (10.2×10^{-6} K^{-1}). The average TEC for LSM-24 was considerably higher (11.2×10^{-6} K^{-1}). These observed values for Sr-doped lanthanum manganite are similar to those reported by Aizawa et al.[5] and somewhat lower than values reported by Srilomsak et al.[6]. For LCM-20, the deviation from YSZ could be eliminated by adding 15% or 50% YSZ. For LSM-16, the addition of 50% YSZ also resulted in a

close match to YSZ. However, a 15% addition of YSZ to LSM-16 did not improve the match to YSZ but instead resulted in an increased thermal expansion (11.1×10^{-6} K^{-1}).

Some SOFC designs require co-sintering of the cathode and YSZ. Successful co-sintering requires a close match in the sintering behavior of both materials. Plots of sintering shrinkage (with and without YSZ additions) as a function of temperature are shown for LSM-16 and LCM-20 in Figures 5 and 6, respectively. The mismatch between the shrinkages of YSZ and the manganites without YSZ additions is apparent. In the case of LSM-16, the addition of 15 vol.% YSZ improved the match to YSZ significantly, except at high temperature (above 1400°C) where there was evidence of swelling of the specimen. Increasing the addition to 50 vol.% had little further effect on the shrinkage behavior. For LCM-20, the match was improved slightly by the YSZ additions. At high temperatures, substantial swelling was observed in the YSZ/LCM specimens; swelling also occurred to a lesser degree in the YSM/LSM specimens. This swelling may occur as a result of oxygen evolution from the perovskite lattice at elevated temperatures. If the specimen has sintered sufficiently to close off the internal pores from the surface, oxygen leaving the lattice will be trapped within the bulk of the specimen and may cause bloating. This mechanism may explain the low densities observed for the YSZ/manganite mixtures sintered at high temperatures (Figures 3 and 4).

The sintering behavior of doped lanthanum manganite and yttrium manganite was determined to be highly sensitive to changes in the A/B cation ratio. Manganites synthesized with a deficiency of A-site cations exhibited enhanced densification behavior relative to B-site cation deficient manganites. Maximum sintered densities of mixtures of lanthanum manganite and YSZ were obtained by sintering at 1300°C. Higher sintering temperatures resulted in lower densities. The addition of YSZ to the manganites resulted in reduced electrical conductivity but allowed for tailoring of the thermal expansion and sintering shrinkage. Small quantities of $La_2Zr_2O_7$ were formed during sintering of mixtures of YSZ and slightly A cation deficient manganites (i.e., A/B = 0.98). The formation of $La_2Zr_2O_7$ during sintering was suppressed in mixtures of YSZ and Mn-enriched manganites (A/B = 0.91). Thus, judicious selection of the A/B cation ratio and amount of YSZ addition may result in SOFC cathodes with adequate electrical conductivity, thermal expansion and sintering shrinkage matched to the YSZ electrolyte, and minimal deleterious interaction with the YSZ.

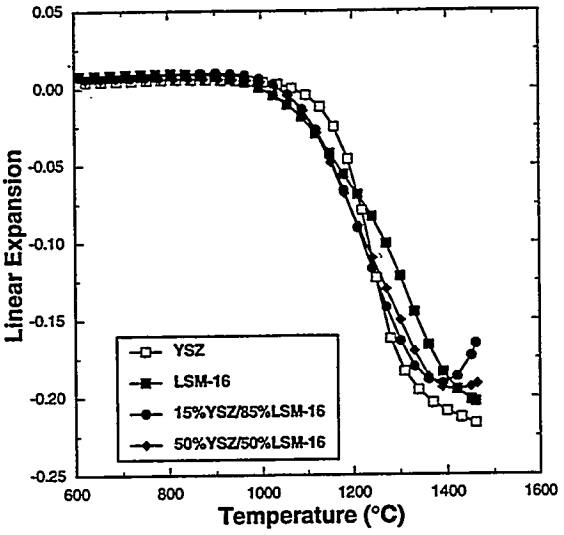

Figure 5. Sintering shrinkage plots for LSM-16/YSZ mixtures. Specimens heated at 2°C/min in air.

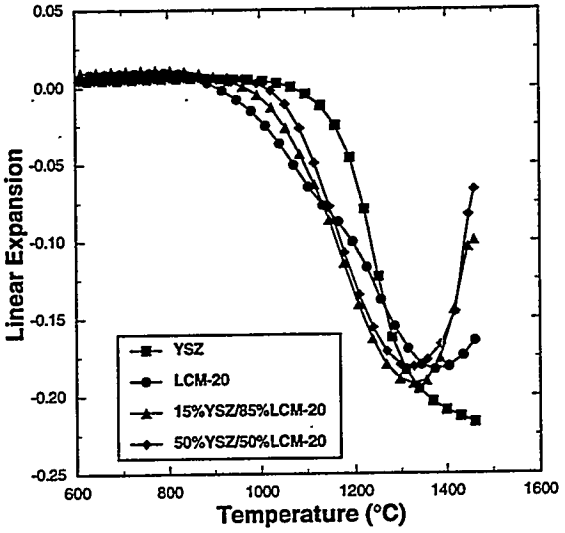

Figure 6. Sintering shrinkage plots for LCM-20/YSZ mixtures. Specimens heated at 2°C/min in air.

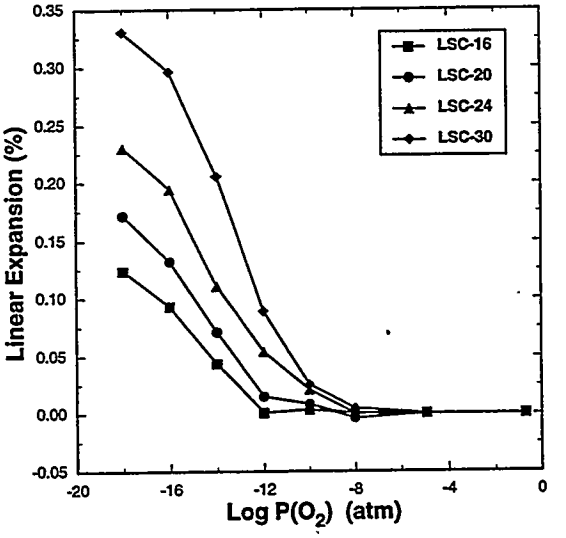

Figure 7. Linear Expansion of $La_{1-x}Sr_xCrO_3$ as a Function of Oxygen Partial Pressure at 1000°C.

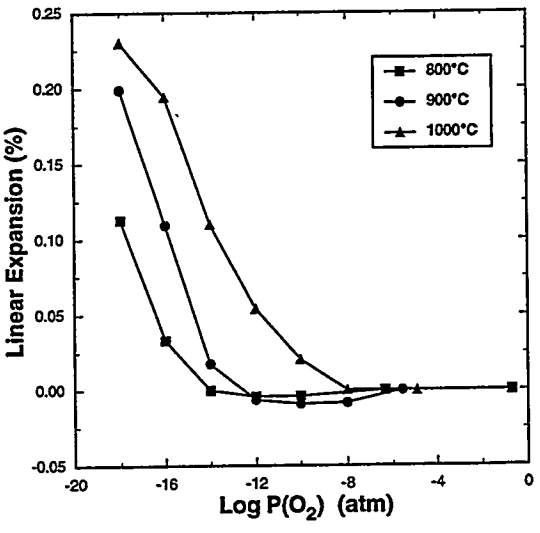

Figure 8. Linear Expansion of LSC-24 as a Function of Temperature and Oxygen Partial Pressure.

close match to YSZ. However, a 15% addition of YSZ to LSM-16 did not improve the match to YSZ but instead resulted in an increased thermal expansion (11.1×10^{-6} K^{-1}).

Some SOFC designs require co-sintering of the cathode and YSZ. Successful co-sintering requires a close match in the sintering behavior of both materials. Plots of sintering shrinkage (with and without YSZ additions) as a function of temperature are shown for LSM-16 and LCM-20 in Figures 5 and 6, respectively. The mismatch between the shrinkages of YSZ and the manganites without YSZ additions is apparent. In the case of LSM-16, the addition of 15 vol.% YSZ improved the match to YSZ significantly, except at high temperature (above 1400°C) where there was evidence of swelling of the specimen. Increasing the addition to 50 vol.% had little further effect on the shrinkage behavior. For LCM-20, the match was improved slightly by the YSZ additions. At high temperatures, substantial swelling was observed in the YSZ/LCM specimens; swelling also occurred to a lesser degree in the YSM/LSM specimens. This swelling may occur as a result of oxygen evolution from the perovskite lattice at elevated temperatures. If the specimen has sintered sufficiently to close off the internal pores from the surface, oxygen leaving the lattice will be trapped within the bulk of the specimen and may cause bloating. This mechanism may explain the low densities observed for the YSZ/manganite mixtures sintered at high temperatures (Figures 3 and 4).

The sintering behavior of doped lanthanum manganite and yttrium manganite was determined to be highly sensitive to changes in the A/B cation ratio. Manganites synthesized with a deficiency of A-site cations exhibited enhanced densification behavior relative to B-site cation deficient manganites. Maximum sintered densities of mixtures of lanthanum manganite and YSZ were obtained by sintering at 1300°C. Higher sintering temperatures resulted in lower densities. The addition of YSZ to the manganites resulted in reduced electrical conductivity but allowed for tailoring of the thermal expansion and sintering shrinkage. Small quantities of $La_2Zr_2O_7$ were formed during sintering of mixtures of YSZ and slightly A cation deficient manganites (i.e., A/B = 0.98). The formation of $La_2Zr_2O_7$ during sintering was suppressed in mixtures of YSZ and Mn-enriched manganites (A/B = 0.91). Thus, judicious selection of the A/B cation ratio and amount of YSZ addition may result in SOFC cathodes with adequate electrical conductivity, thermal expansion and sintering shrinkage matched to the YSZ electrolyte, and minimal deleterious interaction with the YSZ.

STABILITY OF LANTHANUM CHROMITE IN REDUCING ENVIRONMENTS

$(La_{1-x}Sr_x)CrO_3$ and $(La_{1-x}Ca_x)CrO_3$ powders, where x was varied from 0.1 to 0.4, were synthesized using the glycine-nitrate process[7]. All powders synthesized for this study had an A/B cation ratio equal to unity. The powders were precalcined at 650°C for 0.5 hour to decompose any residual organic material and then calcined at 1000°C for 1 hour. The powders were uniaxially pressed into bars at 55 MPa followed by isostatic pressing at 138 MPa for dilatometric studies. Samples were sintered in air at 1500° to 1650°C for 5 hours. Additional samples were prepared with the general formula $La_{0.7}Ca_{0.3}(Cr_{0.9}M_{0.1})O_3$ (where M was Ti, Co, Fe, Ni, Zn, Ga, Al, Mn or Cu) to evaluate the effects of isovalent and aliovalent B-site dopants on the dimensional stability.

The dependence of the physical properties of sintered lanthanum chromites upon ambient oxygen partial pressure and temperature (using electrical conductivity, dilatometry, thermogravimetric analysis, and oxygen permeation measurements) were studied. $La_{1-x}A_xCrO_3$ and $Y_{1-x}Ca_xCrO_3$, where A is Ca or Sr and x was varied from 0.1 to 0.4 were evaluated in this study. The oxygen partial pressure was varied using a CO_2 buffered Ar - 4%H_2 gas system, enabling expansion measurements to be made over a partial pressure range from 10^{-5} to 10^{-18} atmosphere at 800, 900, and 1000°C

Figure 7 is a plot of the isothermal linear expansion of $La_{1-x}Sr_xCrO_3$ where x was varied from 0.15 to 0.5 as a function of the oxygen partial pressure at 1000°C. All samples evaluated showed no effect of reducing environment from ambient pressure to 10^{-8} atmosphere. As the P(O2) was lowered further, the samples steadily expanded. The critical oxygen partial pressure (onset of expansion) was the same for all samples 10^{-10} atm. The data further show that the expansion increases with increasing acceptor dopant concentration. Similar results were observed for the $La_{1-x}Ca_xCrO_3$ and $Y_{1-x}Ca_xCrO_3$ systems, however, the magnitude of the expansion varies slightly.

Figure 8 shows the effect of decreasing $P(O_2)$ on the linear expansion of LSC-24 as a function of temperature. This sample showed no effect of reducing environment from ambient pressure to 10^{-8} atmosphere at 1000°C. As the $P(O_2)$ was lowered further, the sample steadily expanded, reaching a maximum expansion of ≈0.23% at 10^{-18}

atmospheres. Figure 8 also clearly shows that the onset (critical oxygen partial pressure) of expansion moved towards lower oxygen partial pressures with decreasing temperature. Both figures 7 and 8 indicate that the magnitude of expansion decreases with decreasing temperature.

Acceptor doping of lanthanum chromite (substitution of Sr or Ca for La) can be charge compensated either electronically (through the conversion of Cr^{3+} to Cr^{4+}) or ionically (through the creation of oxygen vacancies), as shown by the electroneutrality relation in Equation 1 (Kroger-Vink notation; brackets denote concentration).

$$[Sr'_{La}] = [Cr^{\bullet}_{Cr}] + 2[V^{\bullet\bullet}_{O}] \quad (1)$$

At high oxygen partial pressures, this compensation is electronic, as verified experimentally in a study by Pederson and Dake using XPS[8] in which the Cr^{4+} concentration was found to be equivalent to the A-site acceptor concentration. At low oxygen partial pressures, charge compensation is dominated by the formation of oxygen vacancies, as shown in Equation 2.

$$La^{x}_{1-x}M'_{x}Cr^{x}_{1-x}Cr^{\bullet}_{x}O^{x}_{3} \rightarrow La^{x}_{1-x}M'_{x}Cr^{x}_{1-x+2\delta}Cr^{\bullet}_{x-2\delta}O^{x}_{3-\delta}[V^{\bullet\bullet}_{O}]_{\delta} + \frac{\delta}{2}O_2 \quad (2)$$

TGA analysis on these samples by the authors has verified an appreciable decrease in mass due to oxygen evolution during reduction[9]. The weight loss (vacancy formation) and gain due to oxygen removal and uptake from the lattice correspond well with the observed reversible linear expansion as well as with electrical conductivity measurements carried out by others[10,11]. Based on this information, it would be expected that increasing the acceptor concentration in lanthanum chromites would result in increased expansion upon reduction as the higher initial concentration of Cr^{4+} is reduced to Cr^{3+}, resulting in an increased concentration of oxygen vacancies in the lattice.

The removal of oxygen from the perovskite lattice results in an increase in lattice cell dimensions, and, therefore, an increase in specimen volume as indicated by Srilomsak et al.[12] and Armstrong et al.[9]. The observed expansion may result from the increase in cation size accompanying the reduction of Cr^{4+} to Cr^{3+} and/or an electrostatic repulsive forces

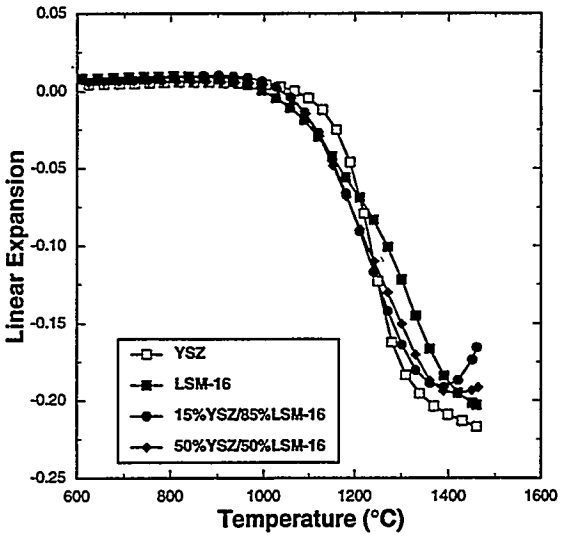

Figure 5. Sintering shrinkage plots for LSM-16/YSZ mixtures. Specimens heated at 2°C/min in air.

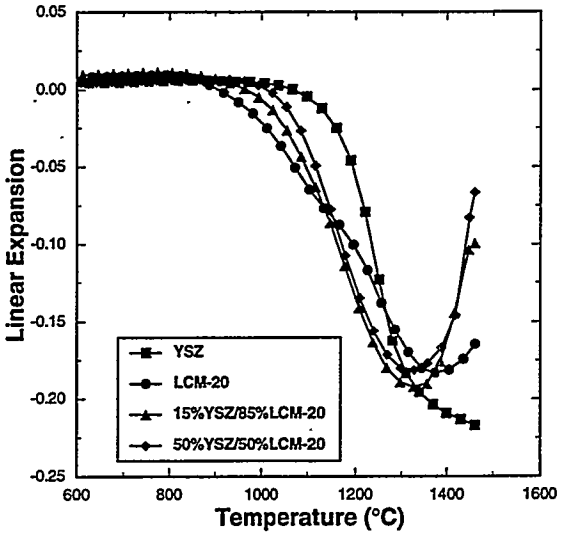

Figure 6. Sintering shrinkage plots for LCM-20/YSZ mixtures. Specimens heated at 2°C/min in air.

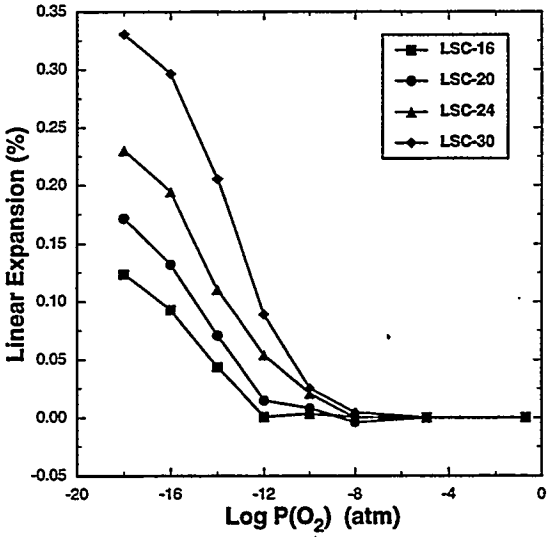

Figure 7. Linear Expansion of $La_{1-x}Sr_xCrO_3$ as a Function of Oxygen Partial Pressure at 1000°C.

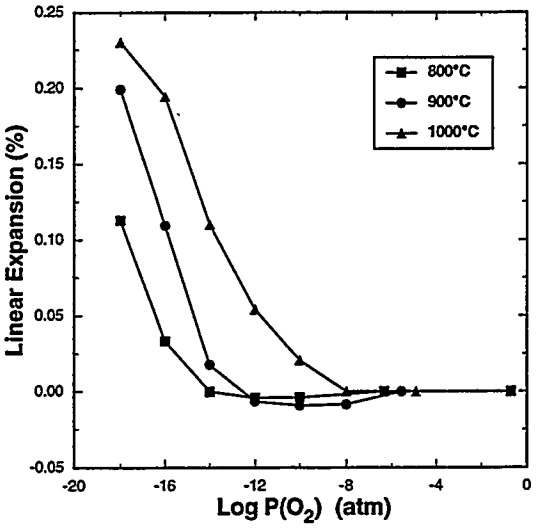

Figure 8. Linear Expansion of LSC-24 as a Function of Temperature and Oxygen Partial Pressure.

between adjacent Cr cations separated by oxygen vacancies.

Figure 9 shows data for linear expansion as a function of dopant content from this study and from Schafer and Schmidberger[13] in 10^{-15} atm $P(O_2)$ at 1000•C. In both studies, it is apparent that the relationship between expansion and dopant content was approximately linear over a wide range of composition. The relationship between sample expansion and dopant concentration (denoted by the slope) is 0.013% expansion/mole % dopant for LSC and 0.015% expansion /mole% dopant for LCC materials. It is clear, however, (from the fact that the linear fits shown in Figure 9 have negative y-intercepts) that this linearity cannot hold for very low dopant levels. The data presented in Figure 9 show very good agreement over the entire composition range for the LSC materials. However, there is a large disparity between the expansion measurements for the two sets of LCC data presented in this figure. The data presented by the authors are similar to that of LSC. The data by Schafer and Schmidberger[13] show a significant deviation. While still linear, their data shows nearly a 1:1 correlation between the expansion and the Ca concentration. The data of Schafer more closely match the expansion data at 10^{-18} atmospheres obtained in the present investigation.

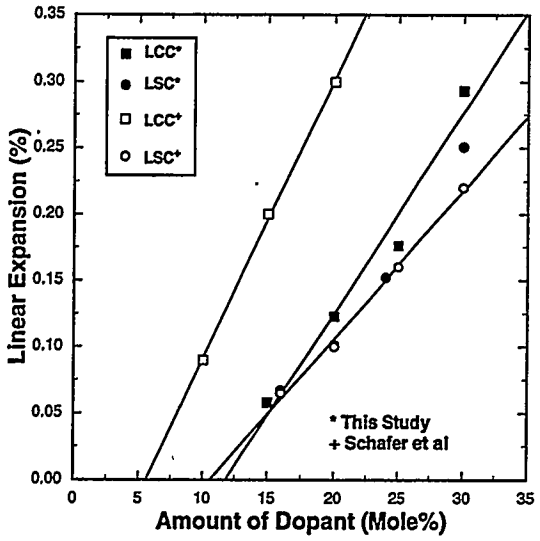

Figure 9. Maximum Linear Expansion at 10-15 atm (1000°C) for LSC and LCC compared to Similar Data From Ref. 13.

REFERENCES

1. B.C. Tofield and W.R. Scott, J. Solid State Chem., **10**, 183 (1974).

2. J.W. Stevenson, M.M. Nasrallah, H.U. Anderson, and D.M. Sparlin, J. Solid State Chem., **102**, 175 (1993).

3. J.W. Stevenson, P.F. Hallman, T.R. Armstrong, and L.A. Chick, Accepted J. Am. Ceram. Soc.**78** [3] 507 (1995)

4. J.A.M. van Roosmalen, E.H.P Cordfunke, and J.P.P. Huijsmans, Solid State Ionics, **66**, 285 (1993).

5. M. Aizawa, H. Nishiyama, A. Ueno, M. Kuroishi, S. Yoshino, K. Eguchi, and H. Arai, Proc. 36th Int. SAMPE Symp., p. 1231 (1991).

6. S. Srilomsak, D.P. Schilling, and H.U. Anderson, in 1st Intl. Symp. on SOFC/1989,
S.C. Singhal, Editor, PV 89-11, p.129, The Electrochemical Society Proceedings Series, Pennington, NJ (1989).

7. L. A. Chick, L. R. Pederson, G. D. Maupin, J. L. Bates, L. E. Thomas, and G. J. Exarhos, Mater. Lett., **10**, 6 (1990).

8. L. R. Pederson and L. S. Dake, in Ceramic Transactions, 5, Advanced Characterization Techniques for Ceramics, ed. by W. S. Young, G. L. McVay and G. E. Pike (1988).

9. T. R. Armstrong, J. W. Stevenson, P. E. Raney, and L. R. Pederson, 1994 Fuel Cell Seminar Abstracts, p. 105, Courtesy Associates (1994).

10. I. Yasuda and T. Hikita, J. Electrochem. Soc., 140, 1689 (1993).

11. H. U. Anderson, J. H. Kuo, and D. M. Sparlin, in Proceedings of the 1st Int. Symposium on Solid Oxide Fuel Cells, ed. S. C. Singhal, Electrochem. Soc., Pennington, NJ, p. 111 (1989).

12. S. Srilomsak, D. P. Schilling and H. U. Anderson, in Proceedings of the 1st Int. Symposium on Solid Oxide Fuel Cells, ed. S. C. Singhal, Electrochem. Soc., Pennington, NJ, p. 129 (1989).

13. W. Schafer and R. Schmidberger, in High Tech Ceramics, Ed. by P. Vincenzini, Elsevier Science Publishers, p. 1737 (1987).

Ceramic Catalyst Materials

A. G. Sault and T. J. Gardner
Fuel Science Department
Sandia National Laboratories
Albuquerque, NM 87185-0710

A. Hanprasopwattanna, J. Reardon, and A. K. Datye
Department of Chemical and Nuclear Engineering
University of New Mexico
Albuquerque, NM 87131

ABSTRACT

Hydrous titanium oxide (HTO) ion-exchange materials show great potential as ceramic catalyst supports due to an inherently high ion-exchange capacity which allows facile loading of catalytically active transition metal ions, and an ability to be cast as thin films on virtually any substrate. The ion-exchange capacity arises from the inclusion of sodium ions within the titania matrix during synthesis. Thin film forms of titania and HTO materials possess several advantages over the bulk oxide forms for catalyst support applications. By coating titania and HTO materials onto inexpensive, high surface area substrates such as silica and alumina, the economics of using these materials is greatly improved, particularly for the HTO materials, which are substantially more expensive in the bulk form than other oxide supports. In addition, the development of thin film forms of these materials allows the catalytic and mechanical properties of the final catalyst formulation to be separately engineered. In order to fully realize the potential of thin film forms of titania and HTO, improved methods for the deposition and characterization of titania and HTO films on high surface area substrates are being developed. By varying deposition procedures, titania film thickness and substrate coverage can be varied from the submonolayer range to multilayer thicknesses on both silica and alumina. HTO films can also be formed, but the quality and reproducibility of these films is not nearly as good as for pure titania films. The films are characterized using a combination of isopropanol dehydration rate measurements, point of zero charge (PZC) measurements, BET surface area, transmission electron microscopy (TEM), and elemental analysis. In order to assess the effects of changes in film morphology on catalytic activity, the films are being loaded with MoO_3 using either incipient wetness impregnation or ion-exchange of heptamolybdate anions followed by calcining. The MoO_3 is then sulfided to form MoS_2, and tested for catalytic activity using pyrene hydrogenation and dibenzothiophene (DBT) desulfurization, model reactions that simulate reactions occurring during coal liquefaction. Comparison with bulk titania and HTO supports, as well as uncoated silica and alumina, demonstrates the superiority of the thin film materials as supports for MoS_2 catalysts. In addition to use as supports for MoS_2 catalysts, the thin film materials are also being investigated as supports for rhodium catalysts for alkane hydrogenolysis, and iron catalysts for selective dehydrogenation. Results of catalytic activity measurements are being correlated with characterization results to determine the influence of changes in film properties on catalyst activity.

INTRODUCTION

The use of thin film materials as catalysts for coal liquefaction and related reactions provides several potentially important advantages over conventional catalyst technology. First, the use of thin films deposited on inexpensive high surface area substrates allows the use of relatively expensive catalytic materials in a cost

effective manner. Many potentially useful catalytic materials are too expensive to be used in a bulk form, but become economical in thin film form due to lower raw materials costs. Second, the ability to tailor the catalytic properties of thin film materials independently of the physical properties of the support increases catalyst design flexibility. Changes can be made in catalytic properties without changing physical factors that affect reactant and product diffusion within catalyst particles. Third, thin film technology allows the use of materials with advantageous catalytic properties that lack the structural strength needed in commercial applications. By coating a structurally weak material onto a much stronger substrate, catalysts can be designed that incorporate previously unusable catalytic functions while maintaining the mechanical strength needed to withstand the physical demands encountered in commercial catalytic reactors. Fourth, the properties of thin film materials may differ in important ways from the corresponding bulk materials. Thus, thin film catalyst materials offer the potential to access new catalytic behaviors unattainable with bulk materials.

Two materials that could benefit from development of thin film forms are titania and hydrous titanium oxide (HTO) ion exchange materials. Titania-supported catalysts often show significantly different catalytic behavior than silica or alumina supported catalysts, but the surface areas of bulk titania materials are generally inferior to those obtainable with silica or alumina. Thus, development of titania thin film technology would allow application of the catalytic properties of titania supports without the disadvantage of low surface area. HTO materials are formed by the reaction of a metal alkoxide (*e.g.*, titanium tetraisopropoxide (TTIP)) with a solution of NaOH in a suitable solvent (*e.g.*, methanol or toluene), followed by hydrolysis with an acetone/water mixture.[1] The resulting amorphous powders have surface areas on the order of 300 m^2/g, and contain up to one sodium ion for every two titanium atoms. These sodium ions can be quantitatively exchanged for metal cations in aqueous solution, providing a simple and effective method for preparing supported metal catalysts. With proper control of ion-exchange conditions, high metal loadings can be achieved with essentially atomic dispersion.[2,3] For certain classes of metals, these high dispersions can be retained even after reduction to the metallic state,[4] resulting in extremely efficient usage of expensive noble metals. Furthermore, experimental sulfided NiMo/HTO catalysts exhibit activities for reactions relevant to coal liquefaction exceeding those of currently available commercial catalysts.[1] In spite of these encouraging results, HTO materials suffer from high manufacturing costs and poor mechanical properties . Thus, HTO materials would also benefit greatly from the further development of thin film forms. Within the context of the DOE Fossil Energy Materials Program, the emphasis of this project is to study sulfided NiMo thin film catalysts for coal liquefaction, but it is important to note that the technology resulting from this project has general applicability for a number of diverse catalytic applications. Thus, in addition to studies of sulfided NiMo catalysts supported on thin titania and HTO films, we are also investigating the use of these materials as supports for metal catalysts for hydrogenolysis (cracking) and oxide catalysts for selective dehydrogenation.

DISCUSSION OF CURRENT ACTIVITIES

In previous work,[5] emphasis was placed on the development of deposition techniques for coating nonporous silica spheres with titania and HTO films. We have now extended these studies to high surface area silica and alumina materials. Substantial effort is also being devoted to loading these films with MoS_2 and testing the resulting materials for hydrodesulfurization (HDS) of DBT. This model reaction is highly relevant to direct coal liquefaction, since heteroatom removal is an important step in the liquefaction process.

Titania Thin Film Characterization

The use of specific rates of isopropanol dehydration to measure titania surface areas on silica has been developed as part of this program. Because titania is several orders of magnitude more active for isopropanol dehydration than silica, the rate of isopropanol dehydration over titania coated silica materials can be used to calculate the titania surface area alone. Calibration of the technique is provided by measurement of the reaction rate on bulk titania materials with known BET surface area. While the basic technique is well established, several outstanding issues with regard to this measurement have been addressed and resolved within the past year. The first issue regards the effects of impurities on the measured rates. It is well known that sodium is a strong poison for dehydration catalysts. Because many high surface area silica materials contain sodium as an impurity, sodium must be removed by acid treatments prior to application of the titania coating and measurement of dehydration rates. Even though silica itself is inactive for dehydration, it is apparent from studies of films prepared on washed (low Na) and unwashed (high Na) silica that sodium can migrate from the silica onto the titania film and thereby poison activity, resulting in artificially low activities and an underestimation of titania surface areas.

A second issue involves the effect of pretreatment on specific dehydration activities of titania coatings. For virtually all films studied, dehydration rates over untreated films correspond to titania surface areas that exceed the BET surface area of the material as a whole. Clearly, specific dehydration rates over the untreated films must be substantially higher than over the bulk titania materials used for calibration. After pretreating the titania films in flowing helium at 500°C, titania surface areas measured by dehydration are always equal to or lower than the total BET surface area. In cases where the two techniques agree, the entire silica surface must be covered by titania. In cases where the titania surface area is less than the total, only partial coverage has been obtained. These pretreatment studies clearly show that the use of bulk titania materials to calibrate specific rates of isopropanol dehydration is valid only for films pretreated at 500°C or higher, and that films treated at lower temperatures have a very different surface structure and specific activity than the bulk materials.

Both sodium content and pretreatment affect the specific activity of HTO materials as well. Acidification of HTO materials to remove sodium is facile compared to removal of sodium from silica, since sodium ions present in HTO are designed to be easily ion-exchangeable. The question of pretreatment and correspondence between the specific activity of bulk standards and thin film materials remains problematic, however. Comparisons among the activities of three bulk HTO samples pretreated at different temperatures demonstrate the difficulties involved. As the pretreatment temperature rises from 300°C to 500°C, the BET surface area drops from 321 m^2/g to 107 m^2/g, and the specific dehydration rate falls from 9.8×10^{-8} moles/m^2/s to 1.6×10^{-6} moles/m^2/s. A change in surface structure must accompany the loss in surface area and result in the observed drop in specific activity. Even after accounting for the effects of pretreatment temperature, the use of bulk HTO standards to calibrate HTO film surface area measurements is currently unsatisfactory. For pretreatment at either 400 or 500°C, HTO film surface areas derived from isopropanol dehydration exceed the total BET surface areas by 50-100%. This result indicates that under the pretreatment conditions attempted to date, the structure of the thin film HTO materials does not correspond to that of the bulk HTO materials. While this result currently precludes the use of isopropanol dehydration for measurement of HTO film surface areas, it does provide an important indication that HTO films may be fundamentally different from the bulk materials. Further work is in progress to resolve this issue.

A final issue with regard to the use of isopropanol dehydration to measure titania surface area arises in the extension of this technique to alumina substrates. While α-Al_2O_3 is inactive for dehydration reactions,[6] and therefore amenable to the isopropanol dehydration method for determining titania film surface area, it is available only with very low surface areas (~10 m^2/g). γ-Al_2O_3 is available with higher surface areas, and is therefore more desirable as a film substrate material, but suffers from the drawback of possessing a high dehydration activity.[6] Consequently, the dehydration reaction cannot differentiate between surface area due to titania and surface area of the γ-Al_2O_3 substrate. For this reason, we investigated a different method for determining film surface area, based on measurement of the point of zero charge (PZC).[7] PZC can be determined either by measuring the mobility of suspended solid particles under the influence of an applied electric field, or by measuring the asymptotic pH obtained in a suspension of the solid as the concentration of solid becomes large. Since different materials have different PZC's, is has been asserted that the PZC of a mixture of solids varies linearly with the fractional surface area of each phase.[7] This method has been tested for physical mixtures of titania and silica and a linear relationship is found (figure 1). Using this relationship as a calibration,

Figure 1: Point of Zero Charge Calibration Curve

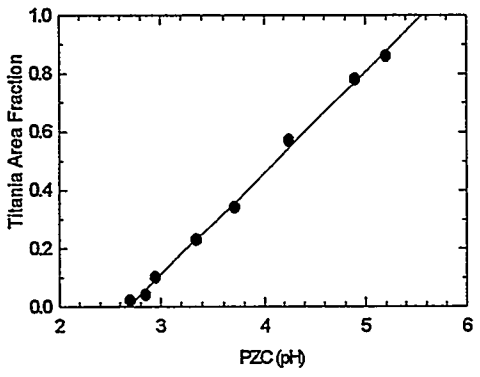

the PZC method was used to measure the titania surface area of titania coated silica materials, and compared to the results of isopropanol dehydration. The comparison gives fair agreement (±20%) between the two techniques, and provides confidence that the PZC method is valid for thin films, as well as physical mixtures of two components.

Titania Thin Film Formation and Characterization on Silica

In the past, much effort was dedicated to the growth of monolayer and multilayer films on nonporous silica spheres. These spheres present several advantages over high surface area silica, including ease of characterization by TEM and an absence of problems related to diffusion limitations during dehydration activity measurements, but suffer from the disadvantage that they have low surface areas (12 m^2/g) and are therefore not practical for industrial application. In the past year we have completed work on titania films on the spheres, and extended this work to high surface area silica gels using the knowledge gained with the spheres to guide our efforts.

Multilayer films of titania on silica spheres have been prepared and total and specific surface areas measured. These films are prepared by careful addition of controlled amounts of water to a solution of titanium *t*-butoxide (TBOT) in ethanol, followed by addition of silica spheres and refluxing of the mixture at the boiling point of ethanol. After refluxing, the spheres are filtered, washed with ethanol, and dried under vacuum. As reported in a previous annual report,[5] the multilayer films are clearly visible as 2-10 nm layers in TEM images, and appear uniform, smooth and dense. In spite of this appearance, isopropanol dehydration and total BET surface area measurements show that the surface area of the films can be up to six times greater than that of the uncoated silica spheres (70 m^2/g *vs.* 12 m^2/g). Furthermore, the multilayer film surface areas decrease with pretreatment temperature, but in the best case, the surface area after pretreatment at 500°C remains four times greater than that of the uncoated spheres. This surface area undoubtedly arises from cracking or porosity in the films, as TEM indicates that surface roughness is insufficient to account for the surface area.

Attempts to coat high surface area silica gels with multilayer titania coatings using the technique developed for silica spheres met with little success. Apparently the sensitivity of TBOT to hydrolysis in the presence of water results in some minor precipitation of titania, which, while insufficient to negatively impact film growth on spheres, blocks pore entrances in high surface area silicas and prevents multilayer formation. In an attempt to avoid this problem, we are investigating the use of water soluble precursors, such as the lactamide complex $[CH_3CH(O)CO_2NH_2]_2Ti(OH)_2$. A silica gel with a surface area of 159 m^2/g was dispersed in an aqueous solution of the lactamide precursor, with urea added to induce precipitation, and the mixture was then refluxed for 20 hours. After filtering, washing with water, drying, and calcining at 550°C for 16 hours, the resulting material contained 39 wt% titania, and possessed a surface area of 350 m^2/g as measured by both

BET and isopropanol dehydration. Thus, the surface area of the material was effectively doubled by the addition of the titania coating, and the entire silica surface was coated. TEM images (figure 2) of this sample show the amorphous silica matrix, as well as the presence of 2-4 nm anatase crystallites dispersed throughout the material. The presence of these crystallites is consistent with the increased surface area.

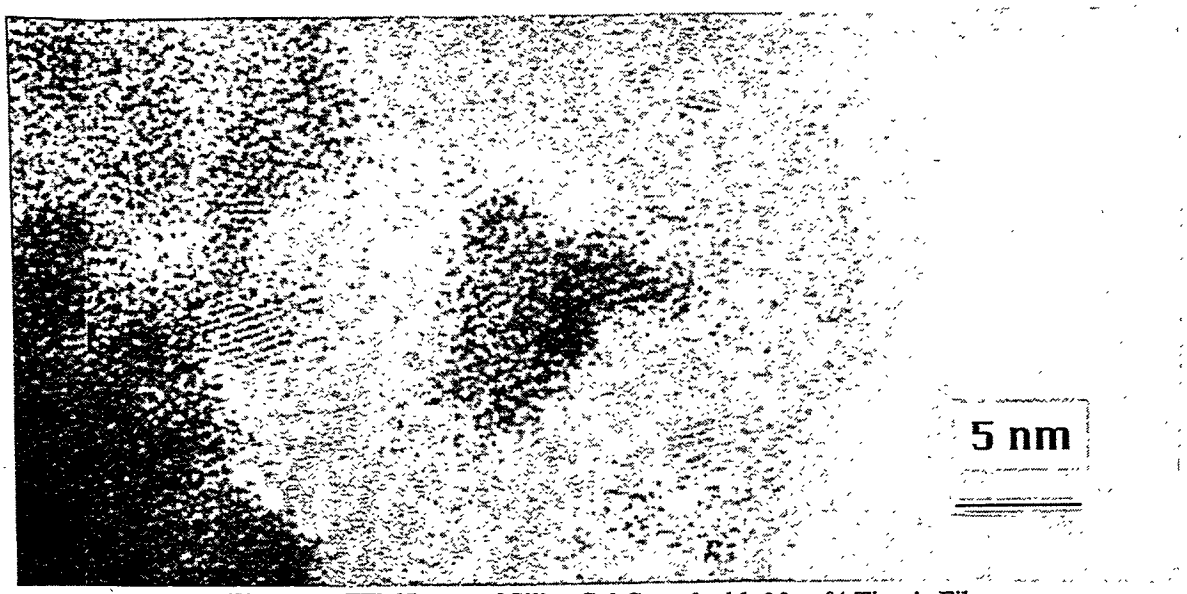

Figure 2: TEM Image of Silica Gel Coated with 39 wt% Titania Film

HTO Thin Film Formation and Characterization on Silica

HTO coatings cannot be formed by the same process used for titania films since the hydrolysis of the titanium precursor is much faster in the presence of NaOH, and refluxing a mixture of the HTO precursor solution with silica spheres results in heterogeneous precipitation of bulk HTO particles and very poor film qualities. The best HTO films are formed by filtering the HTO precursor through the silica spheres, and then washing the spheres with hexane and water to complete the hydrolysis. This procedure results in submonolayer coverages of the HTO film on the silica spheres as measured by isopropanol dehydration, and TEM shows the films to be much rougher than titania films. These submonolayer HTO films are now being used to sort out differences in Rh^{3+} ion-exchange behavior between bulk and thin film HTO materials, and also to investigate how changes in rhodium ion-exchange parameters affect the rhodium loading, distribution, and hydrogenolysis activity. Although not important from the aspect of developing improved coal liquefaction catalysts, experiments with noble metals are important for determining the generic applicability of HTO thin films as catalysts supports.

Like the submonolayer coatings, multilayer coatings of HTO films also require substantially different deposition techniques than multilayer titania coatings. Addition of water to the precursor mixture is not

effective since the accelerated hydrolysis of the HTO precursor relative to TBOT results in precipitation of bulk HTO. Instead, an attempt was made to achieve multilayer HTO coatings by using multiple deposition steps. Accordingly, the procedure outlined above for producing submonolayer coatings was repeated a total of four times, and the resulting materials were dried overnight at 110°C. BET measurements of silica spheres coated in this manner show a substantial increase in total surface area, but until TEM measurements are made, we cannot be sure that this increase is the result of a high surface area coating, rather than the presence of some precipitated bulk HTO material. An HTO coating prepared in this manner on a high surface area silica gel shows no change in BET surface area, indicating that at most a monolayer film was formed. Because of the difficulties described earlier with using the isopropanol dehydration rate to measure HTO surface area, we are currently unable to distinguish between monolayer and submonolayer HTO coatings, but anticipate that analysis of these films by TEM will help to clarify this question.

Titania Thin Film Formation on Alumina

In addition to our work with silica substrates, we have also directed effort toward developing coating techniques for alumina substrates. Monolayer films have been formed on a low surface area α-alumina using methods similar to those developed for silica substrates. The films do not alter the BET surface area of the substrate, and calculations based on bulk titania content indicate that the amount of titania present is adequate to form a complete a monolayer. These films do not alter the appearance of the substrate as viewed by TEM, indicating the absence of any agglomeration or particle formation. PZC and isopropanol dehydration measurements are underway to further characterize the films, and studies on higher surface aluminas are planned for the coming year.

MoS_2 Formation and Hydrodesulfurization Activity on Titania Thin Films

Titania films on both silica and α-alumina substrates have been loaded with molybdenum using incipient wetness techniques, calcined at 500°C, and sulfided at 400°C in a 10% H_2S in hydrogen mixture to produce MoS_2 particles. For comparison, uncoated substrates have also been prepared with similar MoS_2 loadings. TEM analysis has been performed on both the alumina and silica substrates and testing for HDS activity has been performed on the silica substrate materials. TEM of coated (17 wt% TiO_2) and uncoated silica containing ~6 wt% MoS_2 (figure 3) shows important differences between the morphologies of the MoS_2 particles in the two cases. On pure silica multilayered MoS_2 structures are visible, while on the titania coated silica MoS_2 tends to form mostly single layer structures. Furthermore, the MoS_2 particles in the coated sample tend to be associated with the small crystalline titania particles rather than with the silica support.

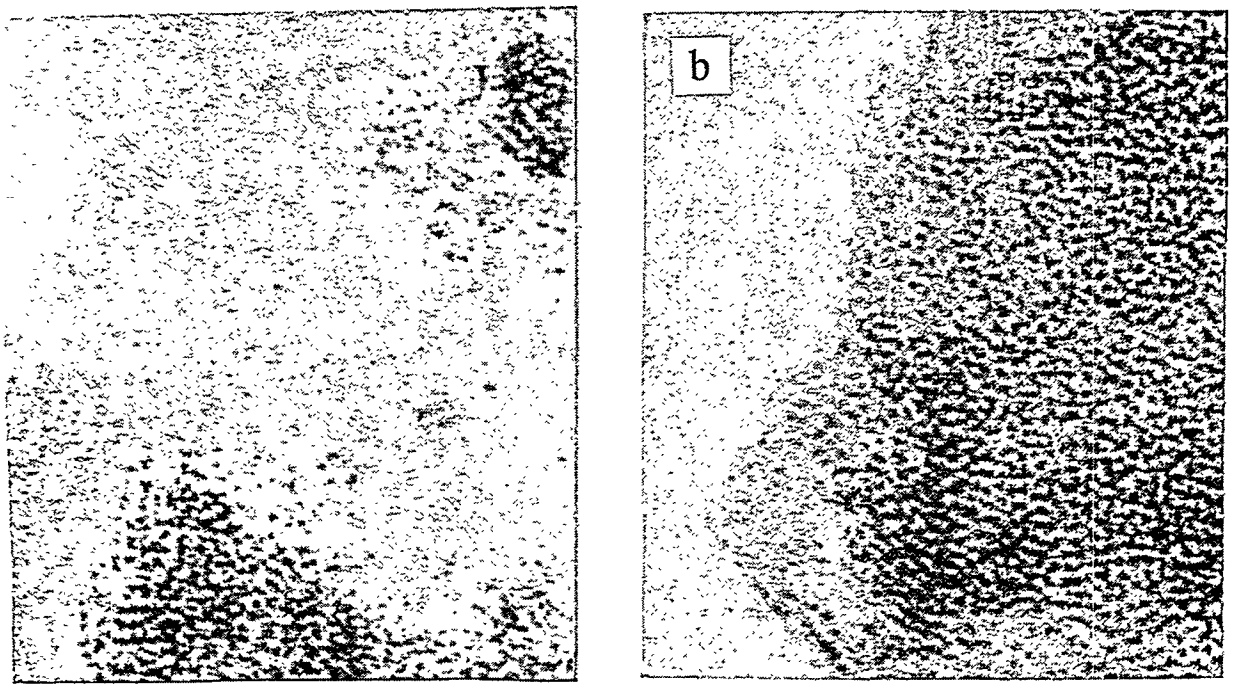

Figure 3: TEM Images of a) 6 wt% MoS_2 on Silica and b) 6 wt% MoS_2 on Titania Coated Silica.

Batch HDS activity measurements on the coated and uncoated silica materials show that the catalytic activity reflects the differences in MoS_2 morphology (Table I). For the same MoS_2 loading, the activity of the titania coated silica is approximately 7 times greater than that of the uncoated silica. Either the single layer

Table I

Batch HDS activity of supported MoS_2 Catalysts

350°C, 1200 psig H_2, 50 mg catalyst, 100 mg DBT in 1000 mg hexadecane (solvent)

Sample	Psuedo-First Order Rate Constant (moles DBT/mole Mo/s)
6 wt% MoS_2/SiO_2	0.87
6 wt% MoS_2/17 wt% TiO_2/SiO_2	6.13
12 wt% MoS_2/17 wt% TiO_2/SiO_2	5.68
18 wt% MoS_2/17 wt% TiO_2/SiO_2	2.39

structures are inherently more active than multilayered structures, or the formation of single layers increases the fraction of molybdenum atoms located on particle edges, which are widely believed to be the active sites in this class of catalysts. Note also that the as the MoS_2 loading increases on the titania coated materials, the

activity per molybdenum atom declines. This decrease is expected since the weight loading at which the amount of MoS_2 exceeds the monolayer capacity of the support is near 10-12 wt%. Above this loading, multilayer structures must necessarily form, and the apparent advantages of single layer particles are lost. At the time of writing, TEM images of the higher weight loading materials were unavailable, but it is anticipated that these images will show an increase in the number of multilayer particles as the loading increases.

Although activity testing for the coated alumina particles is not yet complete, TEM images of these materials provide some information and allow the prediction of catalytic behavior. Upon initial inspection, TEM images of α-alumina loaded with an amount of molybdenum equivalent to a ~1.7 layers of MoS_2 give little evidence for an effect of the titania monolayer (figure 4). Upon closer examination, however, the MoS_2 particles on the uncoated alumina appear to consist of extended single layers of MoS_2 exposing few edge sites. On the alumina coated with a monolayer of titania, the surface appears much rougher than the uncoated alumina, and the MoS_2 particles appear much less continuous, and therefore likely to expose a higher fraction of molybdenum at the active edge sites. For this reason it is anticipated that the titania coated material will show superior activity to the uncoated alumina.

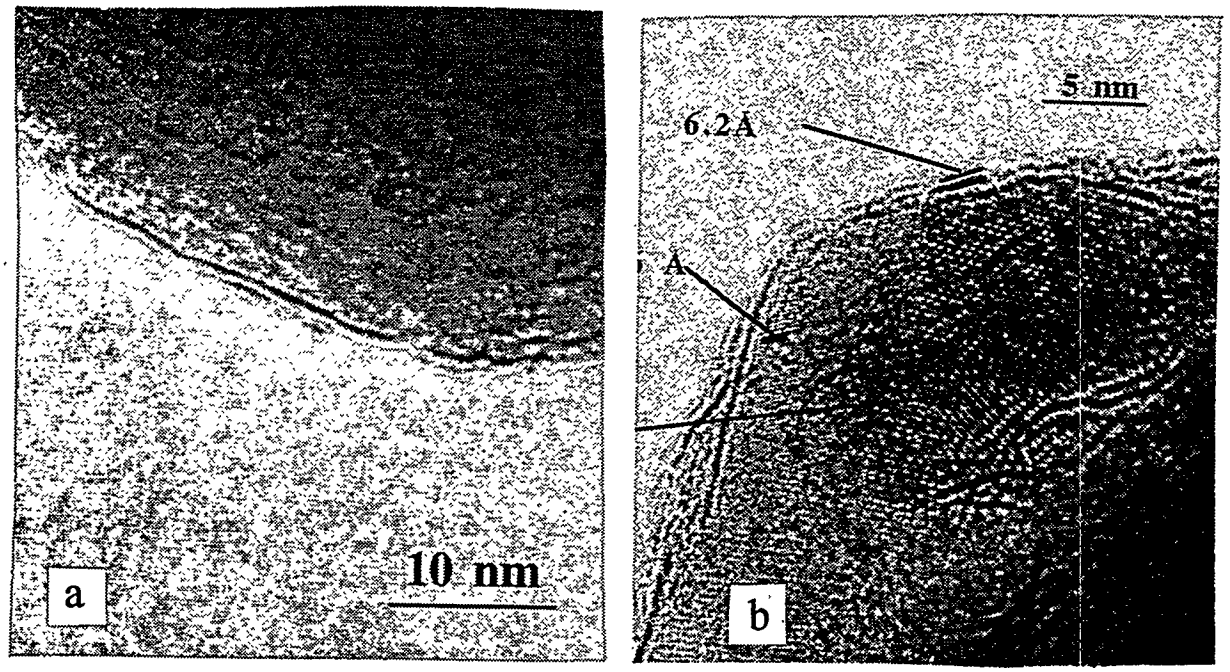

Figure 4 - TEM images of a) MoS_2 on α-Alumina and b) MoS_2 on Titania Coated α-Alumina.

CONCLUSIONS

Substantial progress has been made in the development of thin film deposition techniques for forming titania and HTO films on silica and alumina substrates. On nonporous silica spheres monolayer and multilayer

titania coatings can be formed with surface areas exceeding those of the substrate. On high surface area silica gels, multilayer coatings have also been formed using a water soluble titania precursor. Titania film deposition on alumina substrates is also under investigation, and initial results suggest that techniques developed for silica substrates will be effective with alumina substrates as well. MoS_2 particles have been formed on both coated and uncoated silica and alumina substrates, analyzed by TEM, and tested for HDS catalytic activity. Although testing is still underway, TEM results show clear differences between MoS_2 particles supported on coated and uncoated substrates. These morphological differences are reflected in the catalytic activity of the materials, with the coated materials showing superior activity.

Substantial progress has also been made in the development of thin film deposition techniques for the HTO system. Results to date show that substantial coverages of HTO materials can be achieved on both silica spheres and high surface area silica gels. The ion-exchange and catalytic behavior of these films is under investigation. In addition to their utility as MoS_2 catalyst supports for direct coal liquefaction, these materials also offer significant advantages as supports for a diverse range of catalytic applications, including hydrogenolysis and selective dehydrogenation. In addition to evaluation of HTO thin film materials as supports for coal liquefaction catalysts, we are therefore also exploring the generic applicability of HTO thin film technology by evaluating these materials for both hydrogenolysis and selective dehydrogenation.

REFERENCES

1. (a) R. G. Dosch, H. P. Stephens, F. V. Stohl, B. C. Bunker, and C. H. F. Peden, "Hydrous Metal Oxide-Supported Catalysts: Part I. Preparation and Physical and Chemical Properties," *Sandia Report* (SAND89-2399). (b) R. G. Dosch, H. P. Stephens, and F. V. Stohl, "Hydrous Metal Oxide-Supported Catalysts: Part II. Catalytic Properties and Applications," *Sandia Report* (SAND89-2400). (c) R. G. Dosch and L. I. McLaughlin, "Hydrous Metal Oxide-Supported Catalysts: Part III. Development of NiMoHMO Catalysts," *Sandia Report* (SAND92-0388).

2. S. L. Anderson, A. K. Datye, E. J. Braunschweig, and C. H. F. Peden, *Appl. Catal.*, 82 (1992)185.

3. T. J. Gardner, C. H. F. Peden, and A. K. Datye, *Catal. Lett.*, 15 (1992) 111.

4. A. G. Sault, *J. Catal.*, in press.

5. A. G. Sault, T. J. Gardner, S. Srinivasan, A. Hanprasopwattanna, and A. K. Datye, in Proceedings of the Eighth Annual Conference on Fossil Energy Materials, Department of Energy, Oak Ridge, TN, May, 1994, p.145.

6. C. R. Narayanan, S. Srinivasan, A. K. Datye, R. Gorte, and S. Biaglow, *J. Catal.*, 138 (1992) 659.

7. S. Subramanian, J. S. Noh, and J. A. Schwartz, *J. Catal.*, 114(1988) 433.

APPENDIX A

FINAL PROGRAM
FOR THE NINTH ANNUAL
CONFERENCE ON FOSSIL ENERGY MATERIALS

FINAL PROGRAM
CONFERENCE ON FOSSIL ENERGY MATERIALS
Oak Ridge, Tennessee
May 16-18, 1995

SESSION I - Ceramic Composites

Tuesday, May 16, 1995

7:00 a.m. Registration and Refreshments

8:00 *Welcome and Introductory Remarks,* Program Managers, Department of Energy and Oak Ridge National Laboratory

8:10 *Keynote Address* - Dr. John Longwell, Chairman of the Committee on the Strategic Assessment of the U.S. Department of Energy's Coal Program

9:00 *AR&TD Materials Program Overview* - James P. Carr, DOE/HQ Program Manager

9:30 *Oxidation-Resistant Interfacial Coatings for Continuous Fiber Ceramic Composites,* D. P. Stinton, Oak Ridge National Laboratory

9:55 *Modeling of Fibrous Preforms for CVI Fabrication,* T. L. Starr, Georgia Institute of Technology

10:20 **BREAK**

10:45 *Engineering Scale Development of the Vapor-Liquid-Solid (VLS) Process for the Production of Silicon Carbide Fibrils and Linear Fibril Assemblies,* M. A. Tenhover, The Carborundum Company and F. Ko, APD Inc.

11:10 *Mechanical Properties of Ceramic Composite Tubes,* W. A. Curtin, Virginia Polytechnic Institute and State University

11:35 *Joining of SiC Ceramics and SiC/SiC Composites,* B. H. Rabin, Idaho National Engineering Laboratory

12:00 *Comparison of High Temperature Mechanical Properties of Two Monolithic SiC Ceramics and an Al_2O_3 SiC Composite,* K. Breder, Oak Ridge National Laboratory

12:25 **LUNCH**

1:45 *Factors Effecting the Corrosion Rates of Ceramics in Coal Combustion Systems,* J. P. Hurley, University of North Dakota

2:10 *Corrosion Performance of Materials for Advanced Combustion Systems,* K. Natesan, Argonne National Laboratory

2:35 *Mullite Coatings for Corrosion Protection of Silicon Carbide,* V. Sarin, Boston University

3:00 *Mechanical Behavior of Ceramic Composite Hot-Gas Filters After Exposure to Severe Environments,* D. J. Pysher, 3M Company

3:25 **BREAK**

3:50 *Fracture Behavior of Advanced Ceramic Hot-Gas Filters,* J. P. Singh, Argonne National Laboratory

4:15 *High Temperature Corrosion of Advanced Ceramics Material for Hot-Gas Filters and Heat Exchangers,* R. E. Tressler, Pennsylvania State University

4:40 *Thermal and Structural Analyses of a Filter Vessel Ceramic Tubesheet,* R. H. Mallett, Mallett Technology, Inc.

5:05 *Processing of Nanosize Silicon Nitride and Alumina Powders,* S. G. Malghan, National Institute of Standards and Technology

5:30 **ADJOURN**

FINAL PROGRAM
CONFERENCE ON FOSSIL ENERGY MATERIALS
Oak Ridge, Tennessee
May 16-18, 1995

SESSION II - Ceramics and New Alloys

Tuesday, May 16, 1995
6:30 - 8:30 p.m.

POSTER PRESENTATIONS - BUFFET RECEPTION

Development of Nondestructive Evaluation Methods and Prediction of Effects of Flaws on the Fracture Behavior of Structural Ceramics, W. A. Ellingson and J. P. Singh, Argonne National Laboratory

Fabrication of Fiber-Reinforced Composites by Chemical Vapor Infiltration, D. P. Stinton and W. M. Matlin, Oak Ridge National Laboratory

Transport Properties of Ceramic Composites, T. L. Starr, Georgia Institute of Technology

Development of Materials for Microwave-Heated Diesel Particulate Filter, M. A. Janney, Oak Ridge National Laboratory

High Temperature Inorganic Membranes for Separating Hydrogen, D. E. Fain, Oak Ridge K-25 Site

Mixed Oxygen Ion/Electron-Conducting Ceramics for Oxygen Separation, L. R. Pederson, Pacific Northwest Laboratory

Proton Conducting Cerate Ceramics, L. R. Pederson, Pacific Northwest Laboratory

Synthesis of Silicon Nitride Powders in Pulsed Rf Plasmas, R. J. Buss, Sandia National Laboratories

Mechanically Reliable Surface Oxides for High-Temperature Corrosion Resistance, K. Natesan, Argonne National Laboratory

Plasma Synthesis of Alumina Films on Metal and Ceramic Substrates, I. Brown, Lawrence Berkeley Laboratory

Mechanically Reliable Scales and Coatings, P. F. Tortorelli, Oak Ridge National Laboratory

Welding and Mechanical Properties of Cast FAPY (Fe-16 at. % Al-Based) Alloy Slabs, V. K. Sikka, Oak Ridge National Laboratory

The Influence of Processing on the Microstructure and Properties of Iron Aluminides, R. N. Wright, Idaho National Engineering Laboratory

Weld Overlay Cladding With Iron Aluminides, G. M. Goodwin, Oak Ridge National Laboratory

High-Temperature Corrosion Behavior of Iron-Aluminide Alloys and Coatings, P. F. Tortorelli, Oak Ridge National Laboratory

Effect of Surface Condition on the Aqueous Corrosion Behavior of Iron Aluminides, R. A. Buchanan, University of Tennessee

Pack Cementation Cr-Al Coating of Steels and Ge-Doped Silicide Coating of Cr-Nb Alloy, R. A. Rapp, Ohio State University

Microstructure Characterization and Weldability Evaluation of the Weld Heat Affected Zone (HAZ) in 310HCbN Tubing, C. D. Lundin, University of Tennessee

The Effects of Microstructural Control on the Mechanical Behavior of Cr_2Nb-Based Alloys, P. Liaw, University of Tennessee

SESSION III - WORKSHOP ON MATERIALS CHALLENGES IN ADVANCED FOSSIL FUELED POWER SYSTEMS

Wednesday, May 17, 1995

8:00 - 11:45	**PLENARY SESSION** - Panel Discussion Moderator - Rod Judkins	
	Larry Ruth	Pittsburgh Energy Technology Center; Pittsburgh, Pennsylvania
	Dan Seery	United Technologies Research Center; East Hartford, Connecticut
	Nguyen Minh	AlliedSignal Inc.; Torrance, California
	Tom Gibbons	ABB Combustion Engineering; Windsor, Connecticut
9:45 - 10:00	**BREAK**	
	Ted McMahon	Morgantown Energy Technology Center; Morgantown, West Virginia
	Juhani Isaksson	Ahlstrom Pyropower; Karhula, Finland
	Gerry Bruck	Westinghouse Electric Corporation; Pittsburgh, Pennsylvania
	Mo Bary	Black & Veatch, Overland Park, Kansas
	John Mundy	DOE-Basic Energy Sciences; Washington, DC
11:45 - 1:00	**LUNCH**	
1:00 - 2:30	**SESSION A - HOT GAS FILTERS** Rapporteurs - Dave Stinton and John Hurley	
	SESSION B - METALLIC HEAT EXCHANGERS Rapporteurs - Ian Wright and Ken Natesan	
2:30 - 2:45	**BREAK**	
2:45 - 4:15	**SESSION C - CERAMIC HEAT EXCHANGERS** Rapporteurs - Dave Stinton and Kristin Breder	
	SESSION D - METALLIC COMPONENTS Rapporteurs - Ian Wright and Bob Swindeman	
4:15 - 4:30	**BREAK**	
4:30 - 5:30	**SUMMARY SESSION**	

FINAL PROGRAM
CONFERENCE ON FOSSIL ENERGY MATERIALS
Oak Ridge, Tennessee
May 16-18, 1995

SESSION IV - New Alloys and Functional Materials

Thursday, May 18, 1995

7:30 **Registration Desk Opens**

8:00 Welcome and Introductory Remarks

8:10 *Keynote Address,* Mr. Marvin Singer, DOE/Fossil Energy, Deputy Assistant Secretary for Advanced Research and Special Technologies

8:30 *ODS Iron Aluminides,* I. G. Wright, Oak Ridge National Laboratory

8:55 *Effects of Composition and Heat Treatment at 1150°C on Creep-Rupture Properties of Fe_3Al-Based Alloys,* C. G. McKamey, Oak Ridge National Laboratory

9:20 *Environmental Embrittlement of Iron Aluminides Under Cyclic Loading Conditions,* N. S. Stoloff, Rensselaer Polytechnic Institute

9:45 *The Effect of Alloying and Grain Refinement on the Room-Temperature Ductility of As-Cast Fe_3Al-Based Alloys,* Srinath Viswanathan, Oak Ridge National Laboratory

10:10 **BREAK**

10:30 *Weldability of Polycrystalline Aluminides,* G. R. Edwards, Colorado School of Mines

10:55 *Electro-Spark Deposited Coatings for Protection of Materials,* R. N. Johnson, Pacific Northwest Laboratory

11:20 Overview of BES and FE Joint Project, *Mechanically Reliable Scales and Coatings for High-Temperature Corrosion Resistance,* P. F. Tortorelli, Oak Ridge National Laboratory

11:45 *Cr_2Nb-Based Alloy Development,* C. T. Liu and P. F. Tortorelli, Oak Ridge National Laboratory

12:10 **LUNCH**

1:30 *Investigation of Austenitic Alloys for Advanced Heat Recovery and Hot-Gas Cleanup Systems,* R. W. Swindeman, Oak Ridge National Laboratory

1:55 *Fireside Corrosion Testing of Candidate Superheater Tube Alloys, Coatings, and Claddings - Phase II,* J. L. Blough, Foster Wheeler Development Corporation

2:20 *A Novel Carbon Fiber-Based Porous Carbon Monolith,* T. D. Burchell, Oak Ridge National Laboratory

2:45 *Carbon Fiber Composite Molecular Sieves for Gas Separation,* M. Jagtoyen, University of Kentucky

3:10 **BREAK**

3:30 *Stability of Solid Oxide Fuel Cell Materials,* L. R. Pederson, Pacific Northwest Laboratory

3:55 *Ceramic Catalyst Materials,* A. G. Sault, Sandia National Laboratories

4:20 **ADJOURN**

APPENDIX B

LIST OF ATTENDEES

LIST OF ATTENDEES

Ninth Annual Conference on Fossil Energy Materials
May 16-18, 1995
Oak Ridge, Tennessee

Charles T. Alsup
Morgantown Energy Technology Center
P.O. Box 880
3610 Collins Ferry Road
Morgantown, WV 26505
(304) 285-5432
FAX 304-285-4403

Paul Apen
Los Alamos National Laboratory
MS-D453
Los Alamos, NM 87545
(505) 665-7513
FAX 505-665-2964

Pronob Bardhan
Corning Incorporated
SP-DV-1-9
Corning, NY 14831
(607) 974-3800
FAX 607-974-2171

Mohammad Bary
Black & Veatch
11401 Lamar
Overland Park, KS 66211
(913) 339-7842
FAX 913-339-2934

David Beecy
Department of Energy
Office of Advanced Research
FE-72, B-119
19901 Germantown Road
Germantown, MD 20585
(301) 903-2787
FAX 301-903-8350

T. M. Besmann
Oak Ridge National Laboratory
P.O. Box 2008
MS-6063
Oak Ridge, TN 37831-6063
(615) 574-6852

Nick Biery
University of Tennessee
Department of Materials Science & Engineering
434 Doughtery Engineering Building
Knoxville, TN 37996-2200
(615) 974-6356
FAX 615-974-4115

Neil Birks
Materials Science & Engineering Department
University of Pittsburgh
848 Benedum Hall
Pittsburgh, PA 15261
(412) 624-9743
FAX 412-624-8069

Norm Bornstein
United Technologies Research Center
411 Silver Lane
East Hartford, CT 06108
(203-727-7487
FAX 203-727-7879

Daniel Boss
BIRL
1801 Maple Avenue
Evanston, IL 60201
(708) 491-3373
FAX 708-467-1022

William H. Boss
University of Tennessee Space Institute
UTSI-MS23
Goethert Parkway
Tullahoma, TN 73788
(615) 393-7414
FAX 615-393-7518

Ron Bradley
Oak Ridge National Laboratory
P.O. Box 2008
Oak Ridge, TN 37831-6067
(615) 574-6094
FAX 615-574-6098

Kristin Breder
Oak Ridge National Laboratory
P.O. Box 2008
Oak Ridge, TN 37831-6062
(615) 574-5089

Ian Brown
Lawrence Berkeley Laboratory
University of California
Berkeley, CA 94720
(510) 486-4174
FAX 510-486-4374

Gerald Bruck
Westinghouse Electric Corporation
Science and Technology Center
1310 Beulah Road
Pittsburgh, PA 15235-5098
(412) 256-2102

R. A. Buchanan
The University of Tennessee
Department of Materials Science
and Engineering
434 Dougherty Engineering Building
Knoxville, TN 37996-2200
(615) 974-4858

Tim Burchell
Oak Ridge National Laboratory
P.O. Box 2008
Oak Ridge, TN 37831-6088
(615) 576-8595

Rick Buss
Sandia National Laboratories
Properties of Organic Materials
Dept. 1812
MS-0367
Albuquerque, NM 87185-0367
(505) 844-3504
FAX 505-844-9624

Jason Canon
Oak Ridge National Laboratory
P.O. Box 2008
Oak Ridge, TN 37831-6062
(615) 574-5089

Gary A. Carlson
Sandia National Laboratories
Department 6211
MS-0710
P.O. Box 5800
Albuquerque, NM 87185-0710
(505)-844-8116
FAX 505-845-9500

J. P. Carr
U.S. Department of Energy
Fossil Energy
Office of Advanced Research
FE-72,
19901 Germantown, MD 20874
(301) 903-6519
FAX 301-903-8350

Nancy C. Cole
Oak Ridge National Laboratory
P.O. Box 2008
4500, MS-6153
Oak Ridge, TN 37831-6084
(615) 574-4824
FAX 615-574-5118

Jeff Cook
University of Tennessee
Department of Materials Science
and Engineering
434 Dougherty Engineering Building
Knoxville, TN 37996-2200
(615) 974-5336
FAX 974-4115

Kevin Cooley
Oak Ridge National Laboratory
P.O. Box 2008
Oak Ridge, TN 37831-6063
(615) 574-4559

William Curtin
Virginia Polytechnic Institute & State
University
Department of Engineering Science
and Mechanics
College of Engineering
Blacksburg, VA 24061-0219
(703) 231-5316

Steve Dekanich
Martin Marietta Energy Systems, Inc.
P.O. Box 2003
Oak Ridge, TN 37830-7271
(615) 576-2288

Alan Dragoo
Department of Energy
Office of Basic Energy Sciences
Chief of Metallurgy and Ceramics Branch
ER-131
19901 Germantown Road
Germantown, MD 20874-1290
(301) 903-3428

John DuPont
Lehigh University
Whitaker Lab
5E. Packer Avenue
Bethleham, PA 18015
(610) 758-3942
FAX 610-758-4244

G. R. Edwards
Colorado School of Mines
Center for Welding and Joining Research
Golden, CO 80401
(303) 273-3773
FAX 303-273-3795

William A. Ellingson
Argonne National Laboratory
9700 South Cass Avenue
Argonne, IL 60439
(708) 252-5068
FAX 708-252-4798

Douglas Fain
Oak Ridge K-25 Site
P.O. Box 2003
1004-L, MS 7271
Oak Ridge, TN 37831-7271
(615) 574-9932
FAX 615-576-2930

Albert Z. Fresco
Dupont Lanxide Composites, Inc.
1300 Marrows Road
P.O. Box 6077
Newark, DE 19714-6077
(302) 456-6241

Thomas B. Gibbons
ABB Combustion Engineering
Power Plant Laboratories
1000 Prospect Hill Road
Windsor, CT 06095
(203) 285-3593

G. M. Goodwin
Oak Ridge National Laboratory
P.O. Box 2008
4508, MS-6096
Oak Ridge, TN 37831-6096
(615) 574-4809
FAX 615-574-7721

Robert Hallstrom
Quality Assurance Department
DB Riley, Inc.
5 Neponset Street
Worcester, MA 01606
(508) 854-3927
FAX 508-852-7548

Yirong He
Department of Materials Science & Engineering
The Ohio State University
477 Watts Hall
2041 College Road
Columbus, OH 43210
(614) 292-3373-
FAX 614-292-1537

E. E. Hoffman
U. S. Department of Energy
Oak Ridge Operations
P.O. Box 2008
MS-6269
Oak Ridge, TN 37831
(615) 576-0735

Linda Horton
Oak Ridge National Laboratory
P.O. Box 2008
Oak Ridge, TN 37831-6134
(615) 574-5081

John Hurley
University of North Dakota EERC
P.O. Box 9018 University Station
Grand Forks, ND 58202
(701) 777-5159
FAX 701-777-5181

Juhani Isaksson
A. Ahlstrom Corporation
Ahlstrom Pyropower
Kanslerinkatu 14
Fin 33720
Tampere,
Finland
358-31-316-5076
FAX 358-31-316-5078

Marit Jagtoyen
The University of Kentucky
Center for Applied Energy Research
3572 Iron Works Pike
Lexington, KY 40511-8433
(606) 257-0213

Mark Janney
Oak Ridge National Laboratory
P.O. Box 2008
4508, MS-6087
Oak Ridge, TN 37831-6087
(615) 574-4281

R. N. Johnson
Pacific Northwest Laboratory
P. O. Box 999, K3-59
Battelle Boulevard
Richland, WA 99352
(509) 375-6906
FAX 509-375-3864

Roddie R. Judkins
Oak Ridge National Laboratory
P.O. Box 2008
4508, MS-6084
Oak Ridge, TN 37831-6084
(615) 574-4572
FAX 615-574-5812

Bruce Kang
Mechanical & Aerospace Engineering Department
West Virginia University
P.O. Box 6106
Morgantown, WV 26506
(304) 293-3111
FAX 304-293-6689

James Kelly
Rolled Alloys
125 West Sterns Road
P.O. Box 310
Temperance, MI 48182
(313) 847-0561

Frank Ko
APD Inc.
2500 Pearl Buck Road
Bristol, PA 19007
(215) 785-3230

Libby Kupp
Pennsylvania State University
226 Steidle Building
University Park, PA 16802
(814) 865-3953
FAX 814-865-2917

Peter Liaw
The University of Tennessee
Department of Materials Science & Engineering
434 Doughtery Engineering Building
Knoxville, TN 37996-2200
(615) 974-6356
FAX 615-974-4115

C. T. Liu
Oak Ridge National Laboratory
P.O. Box 2008
Oak Ridge, TN 37831-6156
(615) 574-4459

John P. Longwell
Department of Chemical Engineering
Massachusetts Institute of Technology
Room 66-456
Cambridge, MA 02139
FAX 617-258-5042

Rick Lowden
Oak Ridge National Laboratory
P.O. Box 2008
Oak Ridge, TN 37831-6087
(615) 576-2769

Subhaus G. Malghan
National Institute of Standards and Technology
Materials Building 223/A256
Gaithersburg, MD 20899
(301) 975-6101
FAX 301-990-8729

Robert Mallett
Mallett Technology
100 Park Drive, Suite 204
P.O. Box 14407
Research Triangle Park, NC 27709
(919) 406-1500
FAX 919-549-9679

Mahendra Mathur
U.S. DOE/PETC
P.O. Box 10940
Pittsburgh, PA 15236
(412) 892-4605
FAX 412-892-5104

W. M. Matlin
The University of Tennessee
Department of Materials Science & Engineering
434 Doughtery Engineering Building
Knoxville, TN 37996-2200
(615) 974-6356
FAX 615-974-4115

Phil Maziasz
Oak Ridge National Laboratory
P.O. Box 2008
MS-6115, 4500S
Oak Ridge, TN 37831-6114
(615) 574-5082

Claudette McKamey
Oak Ridge National Laboratory
P.O. Box 2008
MS-6114, 4500S
Oak Ridge, TN 37831-6114
(615) 574-6917

Jerry McLaughlin
Oak Ridge National Laboratory
P.O. Box 2008
Bldg. 4515, MS-6063
Oak Ridge, TN 37831-6063
(615) 574-4559

Theodore J. McMahon
U. S. Department of Energy
Morgantown Energy Technology Center
P.O. Box 880
MS CO4
Morgantown, WV 26505
(304) 285-4865
FAX 304-285-4403

Nguyen Minh
AlliedSignal
2525 W 190th Street
Department 93140, MS T-41
Torrance, CA 90504-6099
(310) 512-3515

John N. Mundy
U. S. Department of Energy
BES
Division of Material Sciences
ER-131, MSG 236
Washington, DC 20585
(301) 903-4271

K. Natesan
Argonne National Laboratory
9700 South Cass Avenue
Argonne, IL 60439
(708) 252-5103
FAX 708-252-3604

Dick Nixdorf
President
Cer-Wat Corporation
1701 Louisville Drive
Suite C
Knoxville, TN 37922
(615) 588-8342
FAX 615-588-3453

L. R. Pederson
Pacific Northwest Laboratory
MS K2/44
P.O. Box 999
Richland, WA 99352
(509) 375-2731
FAX 509-375-2186

Robert Perrin
The University of Tennessee
Department of Materials Science
and Engineering
434 Dougherty Engineering Building
Knoxville, TN 37996-2200
(615) 974-4858

Bruce Pint
Oak Ridge National Laboratory
P.O. Box 2008
Oak Ridge, TN 37831-6156
(615) 576-2897
FAX 615-574-5118

Doug Pysher
3M Company
3M Center
Bldg 201-4N-01
St. Paul, MN 55144-1000
(612) 737-1797
FAX 612-737-4682

C. Y. (Paul) Qiao
The University of Tennessee
Materials Science & Engineering Department
434 Dougherty Engineering Building
Knoxville, TN 37996-2200
(615) 974-5310
FAX 615-974-0880

Barry H. Rabin
Idaho National Engineering Laboratory
P.O. Box 1625
Idaho Falls, ID 83415
(208) 526-0058
FAX 208-526-0690

George Roettger
Oak Ridge K-25 Site
P.O. Box 2003
1004-L, MS-7271
Oak Ridge, TN 37831-7271
(615) 574-7539

Glenn Romanoski
Oak Ridge National Laboratory
P.O. Box 2008
4508, MS- 6088
Oak Ridge, TN 37831-6088
(615) 574-4838
FAX 615- 586-8424

Larry Ruth
Department of Energy
PETC
P.O. Box 10940
Pittsburgh, PA 15236
(412) 892-4461
FAX 412-892-5917

Stephen M. Sabol
Westinghouse Electric Corporation
4400 Alafaya Trail
MC-303
Orlando, FL 32826-2399
(407) 281-5136
FAX 407-281-2334

Sankar Sambasivan
BIRL
1801 Maple Avenue
Evanston, IL 60201
(708) 491-4619
FAX 708-467-1022

Vinod K. Sarin
Boston University
College of Engineering
44 Commington Street
Boston, MA 02215
(617) 353-6451
FAX 617-353-5548

Allen G. Sault
Sandia National Laboratories
Department 6211
P.O. Box 5800
Albuquerque, NM 87185
(505) 844-8723
FAX 505-845-9500

Otto J. Schwarz
Oak Ridge National Laboratory
P.O. Box 2008
Oak Ridge, TN 37831-6087
(615) 576-2769

Rodger Seeley
Babcock & Wilcox International
581 Coronation Blvd.
Cambridge, Ontario
Canada NIR 5V3

Dan Seery
United Technologies Research Center
411 Silver Lane
East Hartford, CT 06108
203) 727-7150
FAX 203-727-2151

Vinod Sikka
Oak Ridge National Laboratory
P.O. Box 2008
4508, MS-6083
Oak Ridge, TN 37831-6083
(615) 574-5112

Marvin I. Singer
U. S. Department of Energy
Fossil Energy
FE 70,
4G-052/FORS
Washington, DC 20585
(202) 586-1577

J. P. Singh
Argonne National Laboratory
Bldg. 212
9700 South Cass Avenue
Argonne, IL 60439
(708) 252-5123
FAX 708-252-3604

Robert G. Smith
3M Company
Bldg. 203-1-01
3M Center
St. Paul, MN 55144-1000
(612) 733-2564
FAX 612-737-5484

Karl Spear
Pennsylvania State University
118 Steidle Bldg
University Park, PA 16802
(814) 863-0990
FAX 814-865-2917

Thomas L. Starr
Georgia Institute of Technology
Materials Science and Engineering
Bunger-Henry Building, Room 276
Atlanta, GA 30332-0245
(404) 853-0579
FAX 404-853-9140

David P. Stinton
Oak Ridge National Laboratory
P.O. Box 2008
4515, MS-6063
Oak Ridge, TN 37831-6063
(615) 574-4556

N. S. Stoloff
Rensselaer Polytechnic Institute
Materials Engineering Department
Troy, NY 12180-3590
(518) 276-6371
FAX 518-276-8554

Robert W. Swindeman
Oak Ridge National Laboratory
P.O. Box 2008
MS-6155, 4500S
Oak Ridge, TN 37831-6155
(615) 574-5108
FAX 615-574-5118

Mike Tenhover
The Carborundum Company
P.O. Box 832
Niagara Falls, NY 14302

Peter F. Tortorelli
Oak Ridge National Laboratory
P.O. Box 2008
Oak Ridge, TN 37831-6156
(615) 574-5119

Mladen Trubelja
Pennsylvania State University
110 Steidle Bldg
University Park, PA 16802
(814) 865-0634
FAX 814-865-2917

Özer Ünal
Ames Laboratory
207 Metals Development
Ames, IA 50011
(515) 294-4892
FAX 515-294-8727

John Vaklyes, Jr.
CeraMem Separations
952 East Fir Street
Palmyra, PA 17078
(717) 838-7911
FAX 717-838-7880

Stuart Van Weele
Foster Wheeler
12 Peach Tree Hill Road
Livingston, NJ 07039
(908) 236-1463
FAX 908-236-1352

Norm Vaughn
Oak Ridge National Laboratory
P.O. Box 2008
Oak Ridge, TN 37831-6087
(615) 576-2769

Srinath Viswanathan
Oak Ridge National Laboratory
P.O. Box 2008
4508, MS-6083
Oak Ridge, TN 37831-6083
(615) 576-9917

Jim Wessel
Dow Corning Corporation
1800 M Street, NW
Washington, DC 20036
(202) 785-0585
FAX 202-785-0421

Jeff Williams
Oak Ridge National Laboratory
P.O. Box 2008
Oak Ridge, TN 37831-6063
(615) 576-2896

Ian Wright
Oak Ridge National Laboratory
4500S, MS-6156
P.O. Box 2008
Oak Ridge, TN 37831-6156
(615) 574-4451
FAX 615-574-5118

Jill K. Wright
Idaho National Engineering Laboratory
P.O. Box 1625
Idaho Falls, ID 83415-2218
(208) 526-9723
FAX 208 526-0690

Richard N. Wright
Idaho National Engineering Laboratory
P.O. Box 1625
Idaho Falls, ID 83415-2218
(208) 526-6127
FAX 208 526-0690

Kim A. Wynns, P.E.
Alon Processing, Inc.
Grantham Street
Tarentum, PA 15084
1-800-367-2556

CONF-9505204
ORNL/FMP-95/1

INTERNAL DISTRIBUTION

1. D. J. Alexander
2. P. Angelini
3. R. L. Beatty
4. T. M. Besmann
5. A. Bleir
6. R. A. Bradley
7. K. Breder
8. T. D. Burchell
9. J. Canon
10. P. T. Carlson
11-14. N. C. Cole
15. K. M. Cooley
16. S. DeKanich
17. J. R. DiStefano
18. D. E. Fain
19. G. M. Goodwin
20. L. L. Horton
21. M. A. Janney
22-24. R. R. Judkins
25. M. A. Karnitz
26. J. R. Keiser
27. W. Y. Lee
28. C. T. Liu
29. R. A. Lowden
30. W. M. Matlin
31. P. J. Maziasz
32. D. J. McGuire
33. C. G. McKamey
34. J. C. McLaughlin
35. K. L. More
36. A. Pasto
37. B. Pint
38. G. E. Roettger
39. G. R. Romanoski
40. A. C. Schaffhauser
41. J. H. Schneibel
42. O. J. Schwarz
43. J. Sheffield
44. V. K. Sikka
45. P. S. Sklad
46. D. P. Stinton
47. R. W. Swindeman
48. T. N. Tiegs
49. N. Vaughn
50. P. F. Tortorelli
51. S. Viswanathan
52. J. Williams
53. D. F. Wilson
54. I. G. Wright
55-56. Central Research Library
57. Document Reference Section
58. ORNL Patent Section
59-60. Laboratory Records Department
61. Metals and Ceramics Records Office
62. LRD-RC

EXTERNAL DISTRIBUTION

63-66. 3M COMPANY, 3M Center, St. Paul, MN 55144
J. H. Eaton (Bldg 203-1-01)
M. L. Leitheiser
D. Pysher
R. G. Smith (Bldg 203-1-01)

67. A. AHLSTROM CORPORATION, Ahlstrom Pyropower, Kanslerinkatu 14, Fin 33720, Tampere, Finland
J. Isaksson

68. ABB Lummus Crest, 15 Broad St., Bloomfield, NJ 07003
M. Greene

69. ABB COMBUSTION ENGINEERING, 911 W. Main St., Chattanooga, TN 37402
D. A. Canonico

70. ABB COMBUSTION ENGINEERING, 1000 Prospect Hill Road, Windsor, CT 06095
T. B. Gibbons

71. ADIABATICS, INC., 3385 Commerce Dr., Columbus, IN 47201
P. Badgley

72. ADVANCED REFRACTORY TECHNOLOGIES, INC., 699 Hertel Avenue, Buffalo, NY 14207
K. A. Blakely

73. AEA INDUSTRIAL TECHNOLOGY, Harwell Laboratory, Materials Development Division, Bldg. 393, Didcot, Oxfordshire, OX110RA ENGLAND
H. Bishop

74. AIR PRODUCTS AND CHEMICALS, INC., 7201 Hamilton Blvd., Allentown, PA 18195-1501
P. Dyer

75. ALBERTA RESEARCH COUNCIL, Oil Sands Research Department, P. O. Box 8330, Postal Station F, Edmonton, Alberta, CANADA T6H5X2
L. G. S. Gray

76. ALLEGHENY LUDLUM STEEL, Technical Center, Alabama and Pacific Avenues, Brackenridge, PA 15014
J. M. Larsen

77. ALLIEDSIGNAL, 2525 W 190th Street, Dept. 93140, Torrance, CA 90504-6099
N Minh (MS T-41)

78. ALLIEDSIGNAL ENGINES, 111 S. 34th Street, Phoenix, AZ 85071-2181
T. Strangman (MS 553-12)

79. ALLISON ENGINE COMPANY, Materials Engineering, P.O. Box 420, Indianapolis, IN 46206-0420
L. E. Groseclose

80-82. ALLISON GAS TURBINE DIVISION, P. O. Box 420, Indianapolis, IN 46206-0420
P. Khandalwal (Speed Code W-5)
R. A. Wenglarz (Speed Code W-16)
J. R. Whetstone

83-84. ALON PROCESSING, INC., Grantham Street, Tarentum, PA 15084
W. P. Heckel, Jr.
K. A. Wynns

85. AMAX R&D CENTER, 5950 McIntyre St., Golden, CO 80403
T. B. Cox

86-87. AMERCOM, Advanced Material Division, Atlantic Research Corporation 8928 Fullbright Avenue, Chatsworth, CA 91311
J. O. Bird
W. E. Bustamante

88. AMOCO CHEMICAL COMPANY, P. O. Box 3011, D-2, Naperville, IL 60566-7011
N. Calamur

89. ANSTO, New Illawarra Rd, Lucas Heights NSW 2234 PMB, 1 Menai NSW 2234, Australia
A.B.L. Croker

90. APD INC., 2500 Pearl Buck Road, Bristol, PA 19007
F. Ko

91. A. P. GREEN REFRACTORIES COMPANY, Green Blvd., Mexico, MO 65265
J. L. Hill

92-94. ARGONNE NATIONAL LABORATORY, 9700 Cass Ave.,
Argonne, IL 60439
W. A. Ellingson
K. Natesan
J. P. Singh

95. ARMY MATERIALS TECHNOLOGY LABORATORY SLCMT-MCC,
Watertown, MA 02172-0001
D. R. Messier

96. AVCO RESEARCH LABORATORY, 2385 Revere Beach Parkway,
Everett, MA 02149
R. J. Pollina

97-98. BABCOCK & WILCOX, Domestic Fossil Operations,
20 South Van Buren Ave., Barberton, OH 44023
M. Gold
D. Wasyluk

99-102. BABCOCK & WILCOX, Lynchburg Research Center, P. O. Box 11165,
Lynchburg, VA 24506
R. Goettler
J. A. Heaney
W. Long
H. H. Moeller

103. BABCOCK & WILCOX INTERNATIONAL, 581 Coronation Blvd.,
Cambridge, Ontario, Canada N1R 5V3
R. Seeley

104. BATTELLE COLUMBUS LABORATORIES, 505 King Ave.,
Columbus, OH 43201
D. Anson

105. BENNETT, Michael J., Three Chimneys, South Moreton Oxon, United Kingdom

106-107. BETHLEHEM STEEL CORPORATION, Homer Research Laboratories,
Bethlehem, PA 18016
B. L. Bramfitt
J. M. Chilton

108-109. BIRL, 1801 Maple Avenue, Evanston, IL 60201
D. Boss
S. Sambasivan

110. BLACK & VEATCH, 11401 Lamar, Overland Park, KS 66211
M. Bary

111. BOSTON UNIVERSITY, 44 Washington Street, Boston, MA 02215
V. K. Sarin

112-115. BRITISH COAL CORPORATION, Coal Technology Development Division, P. O. Box 199, Stoke Orchard, Cheltenham, Glocester, ENGLAND GL52 4ZG
J. Oakey
N. Sims
M. A. Smith
I. Summerfield

116-117. CANADA CENTER FOR MINERAL & ENERGY TECHNOLOGY, 568 Booth St., Ottawa, Ontario Canada K1A OG1
R. W. Revie
M. Sahoo

118. CATERPILLAR INC., Technology Center, P.O. Box 1875, Perioria, IL 61656-1875
D. I. Biehler

119. CERAMEM SEPARATIONS, 952 Eat Fir Street, Palmyra, PA 17078
J. Vaklyes, Jr.

120. CER-WAT CORPORATION, INC., 1701 Louisville Dr., Suite C, Knoxville, TN 37921
D. Nixdorf

121. CHEVRON RESEARCH & TECHNOLOGY COMPANY, 100 Chevron Way, Richmond, CA 94802-0627
D. J. O'Rear

122. CIEMAT, Avda. Complutense, 22, 28040-Madrid (SPAIN)
G. M. Calvo

123. COAL & SYNFUELS TECHNOLOGY, 1401 Wilson Blvd., Suite 900, Arlington, VA 22209
E. Tilley-Hinkle

124. COAL & SYNFUELS TECHNOLOGY, 1616 N. Fort Myer Dr., Suite 1000, Arlington, VA 22209
J. Bourbin

125-126. COAL TECHNOLOGY CORPORATION, 103 Thomas Road, Bristol, VA 24201
R. A. Wolfe
R. E. Wright

127. COLORADO SCHOOL OF MINES, Dept. of Metallurgical Engineering, Golden, CO 80401
G. R. Edwards

128-130. CONSOLIDATION COAL COMPANY, 4000 Brownsville Road, Library, PA 15129
F. P. Burke
S. Harding
D. Nichols

131. CORNING INCORPORATED, SP-DV-1-9, Corning, NY 14831
P. Bardhan

132. CUMMINS ENGINE COMPANY, Box 3005, MC 50183, Columbus, IN 47202-3005
T. M. Yonushonis

133. DB Riley, Inc., 5 Neponset Street, Worcester, MA 01606
R. Hallstrom

134. DEVASCO INTERNATIONAL, INC., 9618 W. Tidwell, Houston, TX 77041
J. L. Scott

135. J. DOWICKI, P.E., 19401 Framingham Dr., Gaithersburg, MD 20879

136. DUPONT LANXIDE COMPOSITES, INC., Pencader Plant, Box 6100, Newark, DE 19714-6100
J. K. Weddell

137-138. DUPONT LANXIDE COMPOSITES, INC., 1300 Marrows Road, P.O. Box 6077, Newark, DE 19714-6077
A. Z. Fresco
D. Landini

139. EC TECHNOLOGIES, INC., 3614 Highpoint Dr., San Antonio, TX 78217
D. J. Kenton

140-142. EG&G IDAHO, INC., Idaho National Engineering Laboratory, P.O. Box 1625, Idaho Falls, ID 83415
B. H. Rabin
R. N. Wright
J. K. Wright

143-147. ELECTRIC POWER RESEARCH INSTITUTE, P.O. Box 10412, 3412 Hillview Avenue, Palo Alto, CA 94303
W. T. Bakker
R. A. Brown
S. Gehl
R. Goldstein
J. Stringer

148. ENERGY AND ENVIRONMENTAL RESEARCH CENTER, Box 8213, University Station, Grand Forks, ND 58202
J. P. Hurley

149. ENERGY AND WATER RESEARCH CENTER, West Virginia University, Morgantown, WV 26505-5054
C. L. Irwin

150. ENVIRONMENTAL PROTECTION AGENCY, Global Warming Control Division (MD-63), Research Triangle Park, NC 27711
K. T. Janes

151. ERC, INC., P. O. Box 417, Tullahoma, TN 37388
Y. C. L. Susan Wu

152-153. EXXON RESEARCH AND ENGINEERING COMPANY, Clinton Township, Route 2 East, Annandale, NJ 08801
M. L. Gorbaty
S. Soled

154. FERRO CORPORATION, Filtros Plant, 603 West Commercial St. E., Rochester, NY 14445
P. S. Way

155. FORSCHUUGS ZENTRUM JÜLICH GmbH, ICT, Postfach 1913, D-5170 Jülich, Germany
H. Barnert-Wiemer

156-157. FOSTER WHEELER DEVELOPMENT CORPORATION, Materials Technology Dept., John Blizard Research Center, 12 Peach Tree Hill Road, Livingston, NJ 07039
J. L. Blough
S. Van Wheele

158. FRAUNHOFER-INSTITUT für WERKSTOFFMECHANIK, Wohlerstrass 11, 79108 Freiburg, West Germany
R. Westerheide

159. GAS RESEARCH INSTITUTE, 8600 West Bryn Mawr Avenue,
Chicago, IL 60631
H. S. Meyer

160. GENERAL APPLIED SCIENCE LABS, 77 Raynor Avenue,
Ronkonkoma, NY 11779
M. Novack

161. GEORGIA INSTITUTE OF TECHNOLOGY, Georgia Tech Research
Institute, 123D Baker Bldg., Atlanta, GA 30332-0245
T. L. Starr

162. GRI, 8600 W. Bryn Mawr, Chicago, IL 60656
D. Scarpiello

163. HAYNES INTERNATIONAL, INC., 1020 W. Park Avenue,
Kokomo, IN 46904
G. Y. Lai

164-165. HOSKINS MANUFACTURING COMPANY, 10776 Hall Rd.,
Hamburg, MI 48139
R. B. Brennan
F. B. Hall

166. ILLINOIS INSTITUTE OF TECHNOLOGY, METM Dept., Perlstein Hall,
IIT, Chicago, IL 60616
J. A. Todd-Copley

167. INCO ALLOYS INTERNATIONAL, INC., P. O. Box 1958,
Huntington, WV 25720
S. Tassen

168. INTECH, INC., 11316 Roven Dr., Potomac, MD 20854-3126
P. Lowe

169-170. IOWA STATE UNIVERSITY, Ames Laboratory, 107 Metals Development,
Ames, IA 50011
D. J. Sordelet
Ozer Unal

171. LIQUID CARBONIC INDUSTRIAS S.A, Avenida Rio Branco, 57-6° Andar,
Centro - 20090-004, Rio De Janeiro, Brazil
M. Saddy

172. JET PROPULSION LABORATORY, 4800 Oak Grove Dr., MS-79-21,
Pasadena, CA 91020
R. L. Chen

173. LANXIDE CORPORATION, 1 Tralee Industrial Park, Newark, DE 19711
E. M. Anderson

174. LAVA CRUCIBLE-REFRACTORIES CO., P.O. Box 278,
Zelienople, PA 16063
T. Mulholland

175-179. LAWRENCE BERKELEY LABORATORY, University of California,
1 Cyclotron Road, Berkeley, CA 94720
I. Brown - MS 53
T. M. Devine
P. Y. Hou - MS 62-203
G. Rosenblatt
S. Visco

180. LAWRENCE LIVERMORE NATIONAL LABORATORY, P.O. Box 808,
Livermore, CA 94551
J. H. Richardson (L-353)

181. LEHIGH UNIVERSITY, Energy Research Center, 5 E Packer Avenue,
Bethlehem, PA 18015
J. N. DuPont

182-184. LOCKHEED MARTIN-KAPL, P.O. Box 1072, MS G2-312,
Schenectady, NY 12301
J. J. Letko (MS D2-121)
G. A. Newsome
J. Woods

185. E. LORIA, 1829 Taper Drive, Pittsburgh, PA 15241

186-189. LOS ALAMOS NATIONAL LABORATORY, P.O. Box 1663,
Los Alamos, NM 87545
P. Apen - MS D453
R. G. Castro - MS G720
J. D. Katz
D. Phillips

190. LURGI LENTJES BABCOCK, Duisburger Strasse 375, D-46041 Oberhausen,
Germany
G. von Wedel

191. MALLETT TECHNOLOGY, 100 Park Drive, Suite 204, P.O. Box 14407,
Research Triangle Park, NC 27709
R. Mallett

192-193. MANUFACTURING SCIENCES CORPORATION, 804 Kerr Hollar Road, Oak Ridge, TN 37830
R. Hayes
T. Muth

194. MASSACHUSETTS INSTITUTE OF TECHNOLOGY, Department of Chemical Engineering, Room 66-456, Cambridge, MA 02139
J. Longwell

195. MER CORPORATION, 7960- S. Kolb Road, Tucson, AZ 85706
L. Leaskey

196-197. MOBIL RESEARCH & DEVELOPMENT CORPORATION, P. O. Box 1026, Princeton, NJ 08540
R. E. Searles
S. T. Viscontini

198-201. NASA LEWIS RESEARCH CENTER, 21000 Brookpark Road, Cleveland, OH 44135
J. P. Gyekenyesi
N. Jacobson - MS 106-1
S. R. Levine
R. Miller - MS 24-1

202-204. NATIONAL INSTITUTE OF STANDARDS AND TECHNOLOGY, Materials Building, Gaithersburg, MD 20899
S. J. Dapkunas
L. K. Ives (Bldg. 220, Rm. A-215)
S. G. Malghan

205. NATURAL GAS AND OIL TECHNOLOGY PARTNERSHIP, 12434 Penthshire, Houston, TX 77024
R. M. Whitsett

206. NEW ENERGY AND INDUSTRIAL TECHNOLOGY DEVELOPMENT ORGANIZATION, 1800 K Street, N.W., Suite 924, Washington, DC 20006
T. Fukumizu

207-209. NEW ENERGY AND INDUSTRIAL TECHNOLOGY DEVELOPMENT ORGANIZATION, Sunshine 60 Bldg., P.O. Box 1151, 1-1 Higashi-Ikebukuro 3-Chome, Toshima-Ku, Tokyo, 170, Japan
S. Hirano
H. Narita
S. Ueda

210-211. NETHERLANDS ENERGY RESEARCH FOUNDATION ECN, P.O. Box 1, 1755 ZG Petten, The Netherlands
P. T. Alderliesten
M. Van de Voorde

212. NORCONTROL, Duran Marquina 20, 15080 La Coruna, Spain
S. Gomez

213. NORTH CAROLINA A&T STATE UNIVERSITY, Department of Mechanical Engineering, Greensboro, NC 27411
J. Sankar

214. OFFICE OF NAVAL RESEARCH, Code 431, 800 N. Quincy St., Arlington, VA 22217
S. G. Fishman

215-216 OHIO STATE UNIVERSITY, Department of Metallurgical Engineering, 116 W. 19th Avenue, Columbus, OH 43210
Y. He
R. A. Rapp

217-219. PACIFIC NORTHWEST LABORATORIES, P.O. Box 999, Richland, WA 99352
J. L. Bates
R. N. Johnson
L. R. Pederson

220. PALL CORPORATION, 5E Packer Avenue, Whitaker Laboratory #5, Bethlehem, PA 18015
Tanweer Haq

221-224. PENNSYLVANIA STATE UNIVERSITY, 101 Steidle Building, University Park, PA 16802
L. Kupp
K. Spear
R. Tressler
M. Trubelja

225. PSI TECHNOLOGY COMPANY, 20 New England Business Center, Andover, MA 01810
L. Bool

226. RENSSELAER POLYTECHNIC INSTITUTE, Materials Engineering Department, Troy, NY 12180-3590
N. S. Stoloff

227. RIBBON TECHNOLOGY CORPORATION, P.O. Box 30758,
Columbus, OH 43230
T. Gaspar

228. RILEY STOKER CORPORATION, 5 Neponset Street, Worcester, MA 01606
D. P. Kalmanovitch

229. RISO NATIONAL LABORATORY, P.O. Box 49, DK-4000, Roskilde,
DENMARK
Aksel Olsen

230. ROLLED ALLOYS, 125 West Sterns Road, Temperance, MI 48182
J. C. Kelly

231. SANDIA NATIONAL LABORATORIES, 7011 East Avenue, P.O. Box 969
Livermore, CA 94551-0969
J. E. Smugeresky (MS-9402)

232-237. SANDIA NATIONAL LABORATORIES, P.O. Box 5800,
Albuquerque, NM 87185
L. L. Baxter
R. Bradshaw
R. Buss
G. Carlson
G. Samara
A. Sault

238-239. SARGENT AND LUNDY, 55 E Monroe Street, Chicago, IL 60603
R. J. Kerhin
D. G. Sloat

240-241. SCIENCE APPLICATIONS INTERNATIONAL CORPORATION,
1710 Goodridge Dr., McLean, VA 22102
J. T. Bartis
J. Ward (MS 2-20-1)

242. SFA PACIFIC, INC., 444 Castro Street, Suite 920, Mountain View, CA 94041
N. Korens

243. SHELL DEVELOPMENT COMPANY, P.O. Box 1380,
Houston, TX 77251-1380
L. W. R. Dicks

244. G. SORELL, 49 Brookside Terrace, N. Caldwell, NJ 07006

245. SOUTHERN RESEARCH INSTITUTE, 2000 Ninth Avenue South,
Birmingham, AL 35202
H. S. Starrett

246. SOUTHWEST RESEARCH INSTITUTE, 6620 Culebra Road,
P.O. Drawer 28510, San Antonio, TX 78284
F. F. Lyle, Jr.

247. SRI INTERNATIONAL, 333 Ravenswood Avenue, Meno Park, CA 04025
Y. D. Blum

248. SRS TECHNOLOGIES, 990 Explorer Blvd., Huntsville, AL 35806
J. H. Laue

249. STANTON ENERGY INDUSTRY CONSULTANTS, INC., RD #1, Liberty Court,
New Stanton, PA 15672-9621
R. J. Steffen

250. STATE ELECTRICITY COMMISSION OF VICTORIA, Herman Research
Laboratory Library, Howard St., Richmond, Victoria, 3121 Australia
H. Hodgskiss

251-252. STRESS ENGINEERING SERVICES, INC., 415 Glensprings Drive, Suite 200,
Cincinnati, OH 45246
C. Haynes
D. Marriott

253. SUNDSTRAND, 4747 Harrison Ave., Rockford, IL 61125
D. Oakey

254. SUPERKINETICS, 2881 Tramway Place, NE,
Albuquerque, NM 87122
J. V. Milewski

255. TECHNIWEAVE, INC., 109 Chestnut Hill Road, Rochester, NH 03868
J. A. LeCoustaouec

256. TECHNOLOGY ASSESSMENT AND TRANSFER, 133 Defense Highway,
Suite 212, Annapolis, MD 21401
J. Hanigofsky

257. TECHNOLOGY MANAGEMENT INC., 9718 Lake Shore Blvd.,
Cleveland, OH 44108
B. P. Lee

258. TELEDYNE ALLVAC, P.O. Box 5030, Monroe, NC 28110
A. L. Coffey

259-260. TENNESSEE VALLEY AUTHORITY, 3N66A Missionary Ridge Place,
Chattanooga, TN 37402-2801
J. B. Brooks
C. M. Huang

261. TEXAS EASTERN TRANSMISSION CORPORATION, P.O. Box 2521, Houston, TX 77252
D. H. France

262. THE AMERICAN CERAMIC SOCIETY, INC., 735 Ceramic Place, Westerville, OH 43081
L. Sheppard

263. THE CARBORUNDUM COMPANY, Technology Division, P. O. Box 832, Niagara Falls, NY 14302
M. Tenhover

264. THE JOHNS HOPKINS UNIVERSITY, Materials Science & Engineering, Maryland Hall, Baltimore, MD 21218
R. E. Green, Jr.

265. THE MATERIALS PROPERTIES COUNCIL, INC., United Engineering Center, 345 E. Forty-Seventh St., New York, NY 10017
M. Prager

266. THE NORTON COMPANY, High Performance Ceramics Division, Goddard Road, Northboro, MA 01532-1545
N. Corbin

267. THE RALPH M. PARSONS COMPANY, 100 West Walnut St., Pasadena, CA 91124
J. B. O'Hara

268. THE TORRINGTON COMPANY, Advanced Technology Center, 59 Field Street, Torrington, CT 06790
W. J. Chmura

269. THIRD MILLENNIUM TECHNOLOGY, INC., 120 Sherlake Drive, P.O. Box 23556, Knoxville, TN 37933-1556
C. F. VanConant

270. TRW, 1455 E. 195th Street, Cleveland, OH 44110
M. Kurup

271-273. UNITED TECHNOLOGIES RESEARCH CENTER, Materials Department, 411 Silver Lane, East Hartford, CT 06108
N. S. Bornstein
J. E. Holowczak
D. Seery

274. UNIVERSITY OF CALGARY, 2500 University Dr. NW, Calgary, Canada
S. X. Mao

275. UNIVERSITY OF CALIFORNIA, Department of Materials Science and Mineral Engineering, University of California, Building 66-Room 247, Berkeley, CA 94720
R. O. Richie

276-277. UNIVERSITY OF KENTUCKY, Center for Applied Energy Research, 3572 Iron Works Pike, Lexington, KY 40511-8433
F. Derbyshire
M. Jagtoyen

278. UNIVERSITY OF NORTH DAKOTA, P.O. Box 9018, University Station, Grand Forks, ND 58202
J. P. Hurley

279. UNIVERSITY OF PITTSBURGH, Materials Science & Engineering Department, 848 Brenedum Hall, Pittsburgh, PA 15261
N. Birks

280. UNIVERSITY OF SOUTH AUSTRALIA, Department of Metallurgy, The Levels SA 5095 Australia
K. N. Strafford

281-286. UNIVERSITY OF TENNESSEE, Department of Materials Science and Engineering, 434 Doughtery Engineering Building, Knoxville, TN 37996
N. Biery
R. A. Buchanan
P. Liaw
C. D. Lundin
R. Perrin
P. Qiao

287-289. UNIVERSITY OF TENNESSEE SPACE INSTITUTE, Tullahoma, TN 37388
W. H. Boss
J. W. Muehlhauser
M. White

290. UNIVERSITY OF WASHINGTON, Department of Materials Science and Engineering, 101 Wilson, FB-10, Seattle, WA 98195
T. G. Stoebe

291. UOP, 50 E. Algonquin Road, Des Plaines, IL 60017-5016
G. J. Antos

292-293. U.S. BUREAU OF MINES, Tuscaloosa Research Center, P. O. Box L, Tuscaloosa, AL 35486
J. C. Debsikdar
J. Kwong

294. U.S. BUREAU OF MINES, P. O. Box 70, Albany, OR 97321
J. Woodyard

295. U.S. DEPARTMENT OF TREASURY, 1500 Pennsylvania Ave., N.W., Rm. 5132, Washington, DC 20220
J. Benton

296. VEBA OEL, P. O. Box 45, 4650 Gelsenkirchen-Buer, Germany
D. Fuhrmann

297-298. VIRGINIA POLYTECHNIC INSTITUTE AND STATE UNIVERSITY, Department of Materials Engineering, Blacksburg, VA 24061
W. Curtin
K. L. Reifsnyder

299. WESSEL, James K.,127 Westview Lane, Oak Ridge, TN 37830

300-301. WEST VIRGINIA UNIVERSITY, Mechanical & Aerospace Engineering Department, P.O. Box 6106, Morgantown, WV 26505
B. Kang
B. Cooper

302. WESTERN RESEARCH INSTITUTE, 365 N. 9th Street, P. O. Box 3395, University Station, Laramie, WY 82071
V. K. Sethi

303. WESTINGHOUSE ELECTRIC CORPORATION, 4400 Alafaya Trial, Orlando, FL 32826-2399
S. M. Sabol - MC 303

304-308. WESTINGHOUSE ELECTRIC CORPORATION, Research and Development Center, 1310 Beulah Road, Pittsburgh, PA 15235-5098
M. A. Alvin
G. Bruck
D. L. Keairns
T. Lippert
S. C. Singhal

309. WORCESTER POLYTECHNIC INSTITUTE, 100 Institute Road, Worcester, MA 01609
E. Ma

310. DOE CHICAGO OPERATIONS OFFICE, 9800 S. Cass Ave., Argonne, IL 60439
J. Jonkouski

311. DOE IDAHO OPERATIONS OFFICE, 765 DOE Place, Idaho Falls, ID 83406
J. B. Malmo

312-326. DOE MORGANTOWN ENERGY TECHNOLOGY CENTER, P.O. Box 880, Morgantown, W VA 26505
C. T. Alsup
R. A. Bajura
R. C. Bedick
D. C. Cicero
F. W. Crouse, Jr.
R. A. Dennis
U. Grimm
J. S. Halow
N. T. Holcombe
W. J. Huber
T. J. McMahon
W. R. Miller
H. M. Ness
J. E. Notestein
C. M. Zeh

327-328. DOE OAK RIDGE OPERATIONS OFFICE, Oak Ridge, P. O. Box 2008, Oak Ridge, TN 37831-6269
Assistant Manager for Energy Research and Development
E. E. Hoffman
M. H. Rawlins

329-330. DOE OFFICE OF BASIC ENERGY SCIENCES, Materials Sciences Division, ER-131, 19901 Germantown Road, Germantown, MD 20874-1290
A. Dragoo
J. N. Mundy

331. DOE OFFICE OF COAL TECHNOLOGY, FE-232 GTN, Washington, DC 20585
M. Perlsweig

332. DOE OFFICE OF ENERGY EFFICIENCY AND RENEWABLE ENERGY, CE-12, Forrestal Building, Washington, DC 20545
J. J. Eberhardt

333-334. DOE OFFICE OF ENERGY RESEARCH, 14 Goshen Court, Gaithersburg, MD 20882-1016
N. F. Barr
F. J. Wobber

335-342. DOE OFFICE OF FOSSIL ENERGY, Washington, DC 20585
W. Fedarko (FE-232)
K. N. Frye (FE-13)
S. C. Jain (FE-231)
C. E. Pax (FE 73)
T. B. Simpson (FE-231)
M. I. Singer (FE-70)
H. E. Thomas (FE-73)
G. F. Wheeler (FE-231)

343. DOE OFFICE OF INDUSTRIAL TECHNOLOGIES, 1000 Independence Avenue S.W., Washington, DC 20585
S. Dillich (EE-20)

344. DOE OFFICE OF NAVAL REACTORS, NE-60, Crystal City Bldg., N.C.-2, Washington, DC 20585
J. Mosquera

345. DOE OFFICE OF PETROLEUM RESERVES, Analysis Division, FE-431, 1000 Independence Ave., Washington, DC 20585
D. de B. Gray

346-358. DOE PITTSBURGH ENERGY TECHNOLOGY CENTER, P. O. Box 10940, Pittsburgh, PA 15236
A. H. Baldwin
J. L. Balzarini
R. A. Carabetta
R. C. Dolence
P. Goldberg
J. D. Hickerson
J. J. Lacey
S. R. Lee
M. E. Mather
G. V. McGurl
J. A. Ruether
L. Ruth
T. M. Torkos

359-360. DOE, OFFICE OF SCIENTIFIC AND TECHNICAL INFORMATION, P.O.Box 62, Oak Ridge, TN 37831

For distribution by microfiche as shown in DOE/OSTI-4500, Distribution Category UC-114 (Coal Based Materials and Components)